



HAL
open science

Interactions between the climate and the carbon cycle at centennial-to-orbital timescales over the past 2 million years

Etienne Legrain

► To cite this version:

Etienne Legrain. Interactions between the climate and the carbon cycle at centennial-to-orbital timescales over the past 2 million years. Earth Sciences. Université Grenoble Alpes [2020-..], 2023. English. NNT: 2023GRALU027. tel-04763849

HAL Id: tel-04763849

<https://theses.hal.science/tel-04763849v1>

Submitted on 3 Nov 2024

HAL is a multi-disciplinary open access archive for the deposit and dissemination of scientific research documents, whether they are published or not. The documents may come from teaching and research institutions in France or abroad, or from public or private research centers.

L'archive ouverte pluridisciplinaire **HAL**, est destinée au dépôt et à la diffusion de documents scientifiques de niveau recherche, publiés ou non, émanant des établissements d'enseignement et de recherche français ou étrangers, des laboratoires publics ou privés.

THÈSE

Pour obtenir le grade de

DOCTEUR DE L'UNIVERSITÉ GRENOBLE ALPES

Présentée par :

Etienne LEGRAIN

École doctorale : STEP - Sciences de la Terre de l'Environnement et des Planètes

Spécialité : Sciences de la Terre et de l'Environnement

Unité de recherche : Institut des Géosciences de l'Environnement

Interactions entre le climat et le cycle du carbone à des échelles de temps centennales à orbitales au cours des 2 derniers millions d'années

Interactions between the climate and the carbon cycle at centennial-to-orbital timescales over the past 2 million years

Direction de thèse :

Frédéric PARRENIN

Directeur de recherche, Université Grenoble Alpes, IGE, CNRS

Directeur de thèse

Emilie Capron

Chargée de recherche, Université Grenoble Alpes, IGE, CNRS

Co-encadrante de thèse

Thèse soutenue publiquement le 17 octobre 2023, devant le jury composé de :

Didier VOISIN

Professeur des universités, Université Grenoble Alpes

Président

Valérie MASSON-DELMOTTE

Directrice de recherche, LSCE, CEA

Rapporteuse

Eric WOLFF

Professeur, University of Cambridge, Royaume-Uni

Rapporteur

Maria Fernanda SÁNCHEZ GOÑI

Professeur, Université PSL, EPHE

Examinatrice

Thomas STOCKER

Professeur, University of Bern, Suisse

Examinateur

Frédéric PARRENIN

Directeur de recherche, Université Grenoble Alpes, IGE, CNRS

Directeur de thèse

Emilie CAPRON

Chargée de recherche, Université Grenoble Alpes, IGE, CNRS

Invitée



Remerciements

Le manuscrit de thèse apparaît comme un acte solitaire qui s'écrit à la 1^{ère} personne du singulier. Rien n'est pourtant aussi faux que de considérer le diplôme de doctorat comme la simple finalisation d'un parcours individuel. De ce fait, cette liste de remerciement est un acte nécessaire mais bien insuffisant pour illustrer ce que je dois aux personnes mentionnées ci-dessous, et toutes celles que j'ai injustement oubliées.

Emilie, je voulais te remercier. Pour beaucoup de choses, à vrai dire, mais si je les cite toutes je pourrais écrire un nouveau chapitre. J'ai eu la chance de bénéficier d'un encadrement exceptionnel, tant sur le plan humain que scientifique. Je n'aurais pu espérer un cadre plus favorable pour réaliser une thèse. Merci de m'avoir fait confiance, dès notre première discussion, plus d'un an avant le début du projet, puis tout au long de cette thèse, en m'apportant en permanence ton soutien, ta confiance, tes réflexions et tes idées. J'espère que l'on pourra continuer à travailler ensemble bien au-delà de la thèse !

Merci Fred d'avoir co-dirigé cette thèse, sans limiter ton encadrement à un rôle lointain mais en partageant tes thématiques de recherche, et en prenant systématiquement le temps de discuter avec moi. L'une de ces discussions a d'ailleurs abouti à l'un des chapitres de cette thèse ! Merci pour ta disponibilité, ta réactivité, et ton intérêt tout au long de ces trois ans. J'espère que l'on pourra continuer à travailler sur les modèles conceptuels dans un futur proche!

I warmly thank Valérie Masson-Delmotte, María Fernanda Sánchez Goñi, Thomas Stocker, Didier Voisin and Eric Wolff for assessing my thesis and coming to Grenoble for the defense. I also warmly thank Amaëlle Landais and Thomas Bauska for being part of my thesis committee.

Greg, je ne compte même plus le nombre de fois où tu m'as apporté ton aide durant cette thèse, que ce soit pour me former à la mesure des gaz, changer des filtres, réparer mes boulettes, serrer des boulons, déplacer des caisses, scier de la glace, emballer de la glace, annoter de la glace, manger des glaces (et des burgers). Tu n'apparais nulle part officiellement dans mon encadrement et pourtant j'ai eu l'impression d'avoir eu trois encadrants pendant cette thèse, tant je n'aurais pas pu faire grand-chose sans toi. Un grand merci.

PH, je voulais te remercier pour le rôle si particulier que tu tiens dans mon parcours de recherche. Merci de m'avoir permis de travailler sur tes thématiques, et d'avoir poursuivi notre collaboration bien au-delà de ce stage initial de 5 mois. Merci de m'avoir offert ce contrat de pré-doc, comme tu aimes à l'appeler, qui m'a permis de continuer mes recherches avec toi en ayant une source de revenus, alors que tu savais pertinemment que, payé ou non, je n'aurais lâché ces lapse rates pour rien au monde !

Un grand merci à toi, Amaëlle, tout d'abord pour ton aide dans le cadre de nos collaborations scientifiques, mais également pour l'aide que tu m'as apportée pour l'obtention de cette thèse. Je ne réalise toujours pas qu'une chercheuse aussi occupée que toi ait pu prendre 1h au téléphone pour essayer de caser un étudiant de M2 que tu ne connaissais même pas. Avec succès, qui plus est !

J'ai également une pensée et un remerciement particulier pour Daniele Pinti, qui est la première personne à m'avoir encadré sur un long stage de recherche, et qui m'a contaminé très rapidement avec son enthousiasme et sa passion pour les eaux gazeuses.

Merci à l'IGE, et notamment aux personnels administratifs et techniques de m'avoir fourni le cadre et le soutien parfait pour réaliser cette thèse ! Merci en particulier à Amélie, qui a supporté avec patience et bienveillance mes erreurs et approximations administratives. Merci également à Romain, pour avoir réparé cette cellule de CO₂ avec autant de rapidité et d'efficacité. Merci enfin à la direction, d'avoir financé notre projet d'échange avec le LSCE.

Merci aux membres de l'équipe ICE³, pour m'avoir intégré dans cette équipe et d'avoir ainsi pu me permettre d'étendre ma culture générale sur les différentes thématiques de recherche, mais aussi sur la vie et le fonctionnement d'un groupe de recherche.

Merci à toutes les personnes hors-IGE avec lesquelles j'ai pu collaborer ces dernières années : merci Laurie, pour ces supers simulations et ces discussions modélisations ; merci Didier pour ton aide dans cette étude de modélisation conceptuelle ; merci Nathaëlle, d'avoir pris le temps de m'expliquer les rouages de l'extraction de sortie de modèles ; merci Natalia, Aline et Nathan, pour ces discussions qui m'ont beaucoup appris sur les carottes marines. Un grand merci à vous, Frédéric, Antoine et Amaëlle, pour avoir mesuré et m'avoir permis d'utiliser ces si précieux enregistrements de $\delta^{15}\text{N}$.

Thank you to our colleagues from the University of Bern for their constructive comments on the CO₂ study and for this pleasant collaboration initiated well before my PhD !

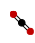
Merci à vous David et Marie, de m'avoir permis de participer à vos passionnantes études : espérons que ce ne soit que le début de la collaboration !

Merci à toi Axel, d'être tombé du ciel par un matin pluvieux en me proposant ton aide pour me dépêtrer d'un problème bien au-delà de mes compétences.

Merci à toi Antoine, d'avoir découpé et mis au froid mes précieux échantillons de thèse avant même que celle-ci ne commence.

Merci à Gilles Delaygue, Jérôme Nomade et Pierre Valla, de m'avoir permis d'effectuer de l'enseignement durant cette thèse, à défaut d'avoir pu récolter des morilles.

Un merci également aux personnes qui ont partagé successivement mon bureau durant ces années : Xavier, Albane et Elsa. Bien que je n'aie pas souvent été assis derrière ce bureau, il était toujours très agréable de pouvoir boire un thé, discuter sur le canapé, et se plaindre de la chaleur ensemble.

 Un merci particulier à Elsa pour cette magnifique idée de puce CO₂, qui représente sans aucun doute ma plus grande fierté vis-à-vis de ce manuscrit.

Merci également à Alexis, pour l'obtention du canapé de thèse, et pour être venu l'user par la suite autour d'une tasse de thé et de discussions de science, de SUVs, et d'avenir.

Cette vie grenobloise a été rendue particulièrement agréable grâce aux copains du labo. Je remercie ici une liste de personnes dans une tentative ratée d'être exhaustif : Aïsa, Alexis, Ari, Audrey, Axel, Claire, Elliot, Guillaume, Lauranne, Luc, Olivier, Pierre, Sara, Sarah... J'ai également eu la chance de connaître beaucoup de personnes du LSCE, devenues très rapidement mes amis, et qui ont permis de rendre le plateau de Saclay moins gris pendant mon séjour là-bas: Antoine, Cécile, Clémence, Marie, Niels, Romilly, Thomas...

Une thèse ne se restreint pas aux portes du labo, mais représente 3 années d'une vie. Merci à mes copains, d'avoir mouliné avec moi lorsque le cerveau, lui, ne voulait plus mouliner.

Merci à mes parents et à mon frère pour avoir toujours montré beaucoup d'intérêt pour mon parcours et ce projet de thèse, et pour m'avoir permis de poursuivre mes études sans jamais avoir besoin de me soucier du reste. Ça a du bon d'être le petit dernier.

Merci enfin à toi, de partager les incertitudes et difficultés associées à ce choix de vie, et de m'avoir apporté quotidiennement l'énergie et le bonheur nécessaires à la réalisation d'une thèse, et bien au-delà.

Abstract

Short- and long-term future climate projections strongly depend on our understanding of the processes related to changes in the carbon cycle and how the latter interacts with climate for the centuries to millennia to come. Past climates offer a diversity of climatic conditions that provide the necessary hindsight to explore these interactions at different time scales. My PhD work combines experimental analyses performed on Antarctic ice together with a surface temperature synthesis and conceptual modelling to investigate the impact of carbon cycle changes on the Earth's climate at centennial-to-orbital timescales. My results provide new insights:

(i) At orbital scale: The causes of the Mid-Pleistocene-Transition (MPT, $\sim 1.2 - 0.6$ Ma), during which the glacial-interglacial periodicity changed from ~ 40 to ~ 100 ka cycles are widely debated. Based on a new conceptual model of global ice volume, I demonstrate that the orbital forcing played a key role in triggering the MPT. In addition, I show that an additional gradual forcing within the Earth's internal system is required to fully simulate the MPT. These results support the hypothesis that a long-term decrease in atmospheric CO_2 concentrations throughout the Pleistocene triggered the MPT.

(ii) At multi-millennial scale: Having a comprehensive picture of the climate during warm periods require combining climate reconstruction from various archives across the globe. Here, I present the first surface temperature data synthesis at global scale across the interglacial Marine Isotope Stage 7 (MIS 7, $\sim 245-190$ ka). My results show that (i) the intensities of the two MIS 7 warm phases are similar in magnitude apart in the southern high latitudes, (ii) the high-latitudes climatic changes are correlated with variations in the atmospheric CO_2 concentrations and (iii) the surface temperature changes are correlated with the obliquity variations during this period, underlying similarities between MIS 7 and pre-MPT interglacials.

(iii) At multi-centennial scale. Glacial-interglacial transitions (also referred to as terminations) are the largest global warming periods of the past 2 Ma. The interactions at play between the carbon cycle and the climate during these intervals remains not well constrained. Based on new and published records of $\delta^{15}\text{N}$ of N_2 and atmospheric CO_2 concentrations measured on the air

trapped in the EPICA Dome C ice core, I evidence a multi-centennial scale lag of the atmospheric CO₂ concentrations decrease over the Antarctic climate cooling at the end of four of the past five terminations. This delay, similar to the one observed during the millennial-scale variability of the last glacial period, suggests that terminations are ultimately ended by millennial-scale events. The analysis of the sequence of events at the end of termination also suggests the enhancement of a mid-to-low latitude carbon sink that may constrain the exact timing of the atmospheric CO₂ decrease.

(iv) At centennial scale. Increases of atmospheric CO₂ concentrations at a rate superior to 1.5 ppm.century⁻¹ have been identified in high-resolution Antarctic ice core records over the past 500 ka. Combining a new atmospheric CO₂ record spanning the 260-190 ka period with published ones, I find that 18 of the 20 identified centennial-scale events occur in an orbital context of high obliquity. New simulations performed with the Earth System Model LOVECLIM support the hypothesis that the occurrence of centennial-scale carbon cycle variations is tight to the obliquity context and also point toward the continental biosphere as the obliquity-dependent source of carbon during these rapid events.

Overall, my results evidence two main characteristics of the Pleistocene climate: (i) the pervasive role of the orbital forcing in the climate-carbon cycle interactions regardless of the timescale considered, and (ii) a close interplay between the processes acting at different timescales on the carbon cycle-climate interactions.

Keywords : Paleoclimate, atmospheric CO₂ concentrations, climate variability, Antarctic ice cores, conceptual modelling, multi-archive surface temperature synthesis

Résumé

Les projections climatiques futures dépendent de notre compréhension des processus liés aux changements dans le cycle du carbone et de la manière dont ce dernier interagira avec le climat pour les siècles et les millénaires à venir. Cette thèse combine des analyses expérimentales réalisées sur de la glace Antarctique avec une synthèse des températures de surface et de la modélisation conceptuelle, permettant ainsi d'étudier l'impact des changements dans le cycle du carbone sur le climat à des échelles temporelles centennales à orbitales. Mes résultats apportent de nouvelles perspectives :

(i) À l'échelle orbitale : Les causes de la Transition du Pléistocène Moyen (MPT, $\sim 1,2 - 0,6$ Ma) font l'objet d'un large débat. Basé sur un nouveau modèle conceptuel du volume global de glace, je démontre que le forçage orbital a joué un rôle clé dans le déclenchement de la MPT, combiné à un changement graduel au sein du système interne terrestre. Ces résultats soutiennent l'hypothèse qu'une diminution sur le long terme des concentrations atmosphériques de CO_2 durant le Pléistocène a déclenché la MPT.

(ii) À l'échelle pluri-millénaire : Obtenir une représentation complète du climat pendant les périodes chaudes nécessite de se baser sur différentes archives sur toute la surface terrestre. Ici, je présente la première synthèse de données de température de surface à l'échelle mondiale pendant le stade marin isotopique 7 (MIS 7, $\sim 245-190$ ka). Mes résultats montrent que (i) les intensités des deux phases chaudes du MIS 7 sont similaires sauf dans les hautes latitudes australes, (ii) les changements climatiques dans les hautes latitudes sont corrélés avec les variations des concentrations atmosphériques de CO_2 et (iii) les variations de température de surface sont corrélées avec les variations de l'obliquité pendant cette période, mettant en évidence des similitudes entre le MIS 7 et les interglaciaires pré-MPT.

(iii) À l'échelle pluri-centennale : Les transitions glaciaire-interglaciaire (terminaisons) sont les périodes de réchauffement global les plus importantes des 2 derniers millions d'années. Les interactions en jeu entre le cycle du carbone et le climat pendant ces intervalles restent mal contraints. Sur la base de nouvelles et anciennes mesures des concentrations de $\delta^{15}\text{N}$ de N_2 et de CO_2 atmosphérique issues de la carotte EPICA Dome C, je mets en évidence un retard à

l'échelle pluri-centennale de la diminution des concentrations de CO₂ atmosphérique par rapport au refroidissement climatique Antarctique à la fin de quatre des cinq dernières terminaisons. Ce décalage, similaire à celui observé pendant la variabilité à l'échelle millénaire de la dernière période glaciaire, suggère que les terminaisons sont achevées par des événements milléniaux. L'analyse de la séquence d'événements à la fin de la terminaison suggère également que le renforcement d'un puits de carbone situés aux basses et moyennes latitudes pourrait avoir déterminé le moment exact de la diminution des concentrations de CO₂.

(iv) À l'échelle centennale : Plusieurs augmentations abruptes des concentrations atmosphériques de CO₂ ont été identifiées par des mesures de l'air inclus dans la glace de l'Antarctique. En combinant un nouvel enregistrement des concentrations de CO₂ atmosphérique sur la période 260-190 ka avec des enregistrements publiés, je constate que 18 des 20 événements centennaux identifiés se produisent dans un contexte d'obliquité élevée. De nouvelles simulations réalisées avec le modèle du système terrestre LOVECLIM confirment cette influence de l'obliquité et pointent vers la biosphère continentale comme source de carbone modulée par l'obliquité lors de ces événements rapides.

Dans l'ensemble, mes résultats soulignent deux caractéristiques du climat du Pléistocène : (i) le rôle prédominant du forçage orbital dans les interactions entre le climat et le cycle du carbone, et (ii) une interaction forte entre les processus agissant à différentes échelles temporelles.

Mots-clés : Paléoclimat, concentrations atmosphériques de CO₂, variabilité climatique, carottes de glace Antarctiques, modélisation conceptuelle, synthèse de températures de surface.

Table of contents

Remerciements.....	3
Abstract.....	6
Résumé.....	8
Table of contents.....	10
Table of abbreviations.....	12
Foreword.....	14
Chapter 1 : Context and objectives of the PhD project.....	18
1.1. Coupling of the Earth's climate and carbon cycle variations	19
1.2. Paleoclimate: beyond the instrumental record.....	28
1.3. Climate and carbon cycle: a long-term perspective.....	34
1.4. Focus on the climate variations of the past 800 ka.....	40
1.5. PhD objectives.....	47
Chapter 2 : Experimental analyses of CO ₂ and CH ₄ concentrations in the EPICA Dome C ice core.....	49
2.1. Greenhouse gas extraction from ice cores: diversity and heterogeneity of methods.....	50
2.2. Measurements of CO ₂ concentrations at IGE.....	53
2.3. Measurements of CH ₄ concentrations at IGE.....	65
2.4. Perspectives	69
Chapter 3 : The role of the carbon cycle in triggering the Mid-Pleistocene Transition.....	72
3.1. Introduction.....	73
3.2. Publication: A gradual change is more likely to have caused the Mid-Pleistocene Transition than an abrupt event.....	75
3.3. Complementary analyses.....	104
3.4. Perspectives.....	115
Chapter 4 : Interactions between the Antarctic climate and the carbon cycle during glacial terminations.....	119
4.1. Introduction	120
4.2. Publication: Evolution of the Antarctic climate-atmospheric CO ₂ phasing over the past five glacial terminations (in prep).....	124
4.3. Perspectives.....	153

Chapter 5 : Spatio-temporal climatic variability at millennial-to-orbital scale during MIS 7...157	
5.1. Introduction.....	158
5.2. Publication: Spatio-temporal pattern of surface temperature changes during Marine Isotopic Stage 7 (in prep).....	161
5.3. Perspectives.....	204
Chapter 6 : Centennial-scale variations in the carbon cycle over the past 500,000 years.....	208
6.1. Introduction	209
6.2. Publication: High obliquity favours centennial-scale variations in the carbon cycle (in revision)	212
6.3. Perspectives.....	257
Chapter 7 : Conclusions and perspectives	261
7.1. Conclusions and perspectives.....	262
7.2. Concluding remarks.....	266
General references.....	269
Appendices.....	288
Résumé en français.....	360

Table of abbreviations

AICC2012 : Antarctic Ice Core Chronology 2012
AICC2023 : Antarctic Ice Core Chronology 2023
AIM : Antarctic isotopic maximum
AMOC : Atlantic Meridional Overturning Circulation
BE-OI : Beyond EPICA- Oldest Ice
CDJ : Carbon Dioxide Jump
CFA : Continuous Flow Analysis
CH₄ : Methane
CO₂ : Carbon dioxide
DO : Dansgaard-Oeschger
EDC : EPICA Dome C
EMIC : Earth system Model of Intermediate Complexity
EPICA: European Project for Ice Coring in Antarctica
FID : Flame Ionization Detector
Ga : Billion years
GC : Gas Chromatograph
GCM : General Circulation Model
GtC : Gigatons of Carbon
HS : Heinrich Stadial
IGE : Institut des Géosciences de l'Environnement
IPCC : Intergovernmental Panel on Climate Change
IPICS : International Partnership on Ice Core Sciences
IRD : Ice Rafted Debris
ka : Thousand years
LSCE : Laboratoire des sciences du climat et de l'environnement
Ma : Million years
MIS : Marine Isotope Stage
MPT : Mid-Pleistocene Transition
PETM : Paleocene–Eocene Thermal Maximum
PMIP : Paleoclimate Modeling Intercomparison Project
T : Termination
TCD : Thermal Conductivity Detector
WAIS : West Antarctic Ice Sheet

Foreword

It is unequivocal that human activities have heated our climate [IPCC report, AR6 WGI]. Anthropogenic activities have released carbon initially stored in the lithospheric realm into the atmosphere. These fossil carbon emissions have induced a major perturbation of the pre-industrial climate. The increase in atmospheric concentrations of carbon dioxide (CO₂) and methane (CH₄) combined with the other human drivers (aerosols, ozone and land-used changes) have caused a total increase of the global surface temperature of 1.14 (0.9 to 1.4) °C in 2013–2022 compared to 1850–1900 [Forster et al., 2023]. The consequences of the current greenhouse gas release in the atmosphere will continue after they have stopped, due to the inertia of both carbon cycle and climate, which retroaction processes at play between these components imply a delayed response to the initial perturbation (e.g. ice sheet melting) [IPCC SPR1.5, 2018]. Future climatic projections beyond the end of the century remain challenging because the observations of the climate-carbon cycle interactions are restricted to the last few decades. These interactions will be a determinant factor for the future evolution of the Earth’s climate at short (end of the century) and long (multi-millennia) terms. A better understanding of these interactions at multiple timescales is thus key to characterize the climate of the future and to help the adaptation of our societies to the ongoing and future climate change.

The speed and amplitude of the anthropogenic carbon emissions and their consequences on Earth’s climate have no equivalent in the past. Nevertheless, variations of the climate and the carbon cycle dynamics are registered in the paleoclimatic archives for millions of years. Especially, the climate of the past 2 million of years (Ma) is punctuated by an alternance of warm (i.e. interglacial) and cold (i.e. glacial) periods. These climates span a large range of temperatures, precipitation patterns and ice volume extension as well as a large diversity in atmospheric CO₂ and CH₄ concentrations. For instance, some of the past warm periods, lasting 5-30 thousand of years (ka), registered polar surface temperature in the range of those expected at the end of the century [Past Interglacial Working Group of PAGES, 2016; Fischer et al., 2018]. In parallel, the transitions from cold to warm periods, known as glacial terminations, are characterized by a 4-7 °C increase in global average temperature and a 60-100 ppm increase in

CO₂ concentrations in about 10 ka [Bereiter et al., 2015; Tierney et al., 2020]. They represent major climatic transitions involving large changes in the carbon cycle dynamics.

Due to its relatively-close proximity with present day, the past 2 Ma offers numerous records retrieved in natural paleoclimate archives. These archives cover a wide range of time intervals and geographical locations at different temporal resolutions. These characteristics allow to investigate the interactions between the carbon cycle and the climate at centennial-to orbital-scale. Hence, characterising and understanding the carbon cycle-climate interactions over the past 2 Ma can provide unique insights to better constrain the future centennial-to-orbital-scale climatic variations in response to the current disruption in the carbon cycle.

My PhD project takes place in this context, relying on the use of several key climatic intervals of the past 2 Ma as natural laboratories to characterise and understand the interactions between the carbon cycle and the climate at multiple timescales. This PhD project was based at IGE where I measured new CO₂ and CH₄ records on the Antarctic EPICA Dome C (EDC) ice core. My project also benefited from data measured by F. Prié, A. Grisart and A. Landais at LSCE, where I also spent three weeks in December 2021.

The following manuscript is organised in seven Chapters. *Chapter 1* introduces existing knowledges necessary to contextualize and understand the purpose of this PhD. *Chapter 2* is a methodological chapter providing an overview of the experimental techniques in place at IGE used to produce new CO₂ and CH₄ highly resolved records measured on the Antarctic EDC ice core. *Chapter 3* focuses on the orbital-scale variations of the climate and the interactions with carbon cycle and orbital forcing during the past 2 Ma through conceptual modelling. It is composed of a published article in *Communications Earth & Environment* [Legrain et al., 2023]. *Chapter 4* investigates the evolution of the phasing between the Antarctic climate and the carbon cycle during the glacial terminations of the past 500 ka using high-resolution records retrieved from the air trapped in ice. This chapter is composed of a manuscript in preparation. *Chapter 5* focuses on the spatio-temporal evolution of the warming during a past warm interglacial period (~245-190 ka) and its link to the carbon cycle and the orbital background conditions using a new surface temperature synthesis. This chapter is composed of a manuscript in preparation. *Chapter 6* investigates the centennial-scale variations in the carbon cycle based on the combination of new and published CO₂ and CH₄ records together with climatic and carbon cycle simulations from an Earth system Model of Intermediary Complexity. This chapter is composed of a manuscript currently in revision for Nature. Lastly, *Chapter 7* concludes this PhD thesis and proposes some future research directions. At the end of the

manuscript are also included *Appendices* that gathered: (i) one co-authored study that presents the new Antarctic Ice Core Chronology 2023 for polar ice cores published in November 2023 in *Climate of the Past* and (ii) three papers related to the research project I carried out during my Master thesis and that I pursued in parallel of my PhD project: two first-authored papers published in April 2022 in *Quaternary Research* and in September 2023 in *Quaternary Science Reviews*, and one co-authored paper published in May 2023 in *Quaternary Science Reviews*.

Chapter 1

Context and objectives of the PhD project

Chapter 1 introduces existing knowledge necessary to contextualize and understand the purpose of my PhD project. First, I provide a brief presentation of the Earth's climate and the carbon cycle. Second, I characterize the main features of the climate of the past 2 Ma. Third, I develop the main objectives of my PhD work.

1.1. Coupling of the Earth's climate and carbon cycle variations

1.1.1 Earth's climate: forcings and realms

The Earth's climate is composed of multiple realms, i.e. atmosphere, biosphere, lithosphere, cryosphere and hydrosphere (Fig. 1.1). It is a complex interactive system since the destabilization of one of its realms has repercussions on the other components. Such destabilization could be induced by forcings external to the climate system:

- (i) The solar incoming radiations determine the amount of energy received at the surface of the Earth. This forcing could vary in time due to a change in the solar activity or a change in the Earth-Sun distance. These two parameters vary at different timescales: at billion-scale, the energy coming from the sun gradually increase. At multi-millennial scale, the Earth-Sun distance varies due to gravitational interactions between the components of the solar system [Laskar et al., 2004]. At decadal timescale, the energy coming from the sun varies at a secondary order [Engels and Bas van Geel, 2012].
- (ii) The dynamic of the Earth's internal processes directly affects the surface climate through plate tectonic and volcanic activity [e.g. Armijo et al., 2015]. These processes act at million-year timescale, but could also punctually and temporary impact the climate at annual to multi decadal-scale in case of major volcanic eruption [e.g. Mann et al., 2021].
- (iii) The life itself could induced major climatic changes, as during the Great Oxydation Event at 2.2 Ga [Schirrmeister et al., 2013], or more recently with the anthropogenic induced climate change [IPCC report, AR6 WGI].

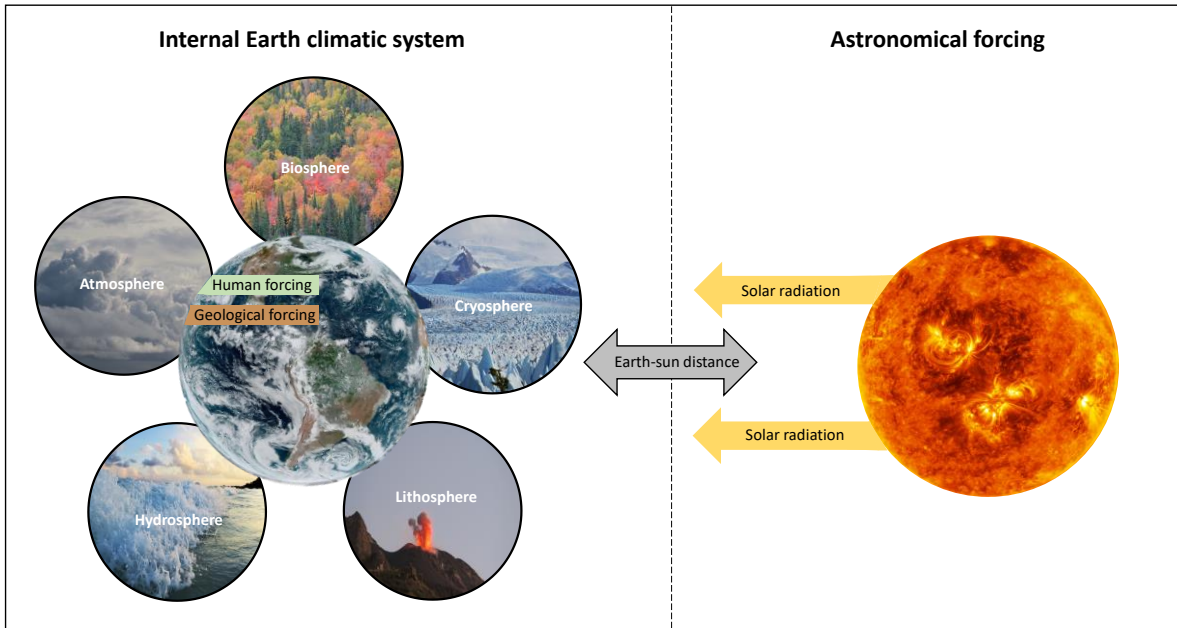


Fig. 1.1: Schematic view of the five realms of the Earth climate, and the associated forcings that drive Earth's climate.

The initial perturbation of the climate by an external forcing is then amplified or mitigated through negative and positive internal retroaction processes, due to the interactions at play between the different climatic realms (Fig. 1.2). The components of the internal Earth's system could react on a sub-annual to multi-millennial scale. For instance, the impact of a punctual climatic perturbation (e.g. a massive volcanic eruption) could pass onto the biosphere and the atmosphere in several years while its consequences could take centuries to millennia to pass on deep oceanic temperature and cryosphere extent (Fig. 1.2). The non-linearity of the climate thus complexifies the climatic response to an initial perturbation. This multi-timescale response of the internal climate system applies for the ongoing anthropogenic-induced climate perturbation. It is thus crucial to investigate the climatic variations not only at the observational timescale, that spanned the last few decades, but also at longer timescale i.e. ranging from centennial to multi-millennial timescales, to fully understand and quantify the future climatic response to the anthropogenic perturbation. *My PhD project fits into this context as its overarching goal is to investigate the natural climatic variations at centennial-to orbital- timescale and their link with past changes in the carbon cycle.*

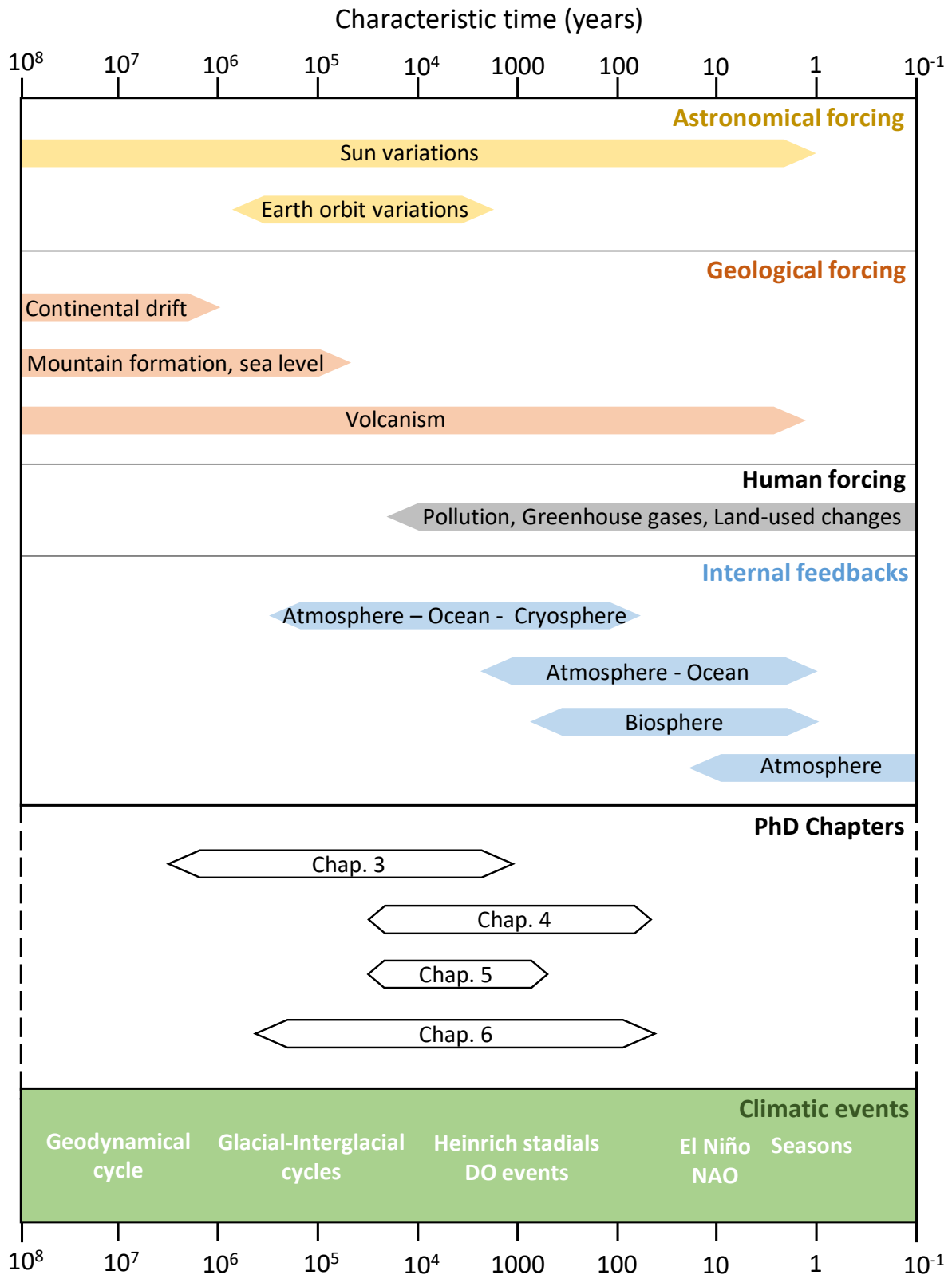


Fig. 1.2: External forcing, internal climate feedbacks, major climatic events and PhD chapters presented as a function of the characteristic timescale they tackle. DO events: Dansgaard-Oeschger Events. NAO: North-Atlantic Oscillation. Modified and adapted from Bard, leçon inaugurale du Collège de France, 2002.

1.1.2 Carbon cycle: sources and sinks from an atmospheric perspective

The climatic realms interact through other physical systems, among which the carbon cycle, that is intimately coupled with the evolution of the global temperature over the Earth's history. *The approach developed in this PhD will investigate both the Earth's climate and the carbon cycle variations, and the interactions at play between these two physical systems.*

Earth's carbon molecules are stored in multiple reservoirs that interact with each other (Fig. 1.3). Consequently, the amount of carbon is not fixed through time for a defined reservoir. The carbon cycle refers to these reservoirs and the associated interactions between them. In the framework of this PhD research, the approach is focused on the atmospheric carbon reservoir, as it is the main driver of the anthropogenic induced climate change [IPCC report, AR6 WGI]. The amount of carbon in the atmosphere will thus have a determinant impact on the global Earth's climate. Under this atmosphere-centred approach, a reservoir could be considered as a source/sink of carbon, if its net budget is negative/positive relatively to the atmosphere. The characterization of a reservoir as a source or a sink of carbon is thus highly dependent on the period and the timescale considered. The main carbon reservoirs are presented in Fig. 1.3 and are detailed below:

- The atmosphere: it contains carbon under the form of the CO_2 and CH_4 molecules. The estimated amount of carbon during the pre-industrial era in the atmosphere was ~ 600 Gigatons of Carbon (GtC).
- The ocean: it contains carbon under the form of dissolved inorganic carbon HCO_3^- . The estimated current amount of oceanic carbon is $\sim 39,000$ GtC, approximately 60 times more than in the atmosphere.
- The terrestrial biosphere: it contains carbon included in organic forms in soils and vegetation. The estimated current amount of carbon stored in the terrestrial biosphere is $\sim 2,000$ GtC, approximately three times more than in the atmosphere.
- The permafrost: it consists on perennially frozen ground containing trapped CO_2 and CH_4 greenhouse gases. The estimated current amount of carbon stored in the permafrost is $\sim 1,500$ GtC [Schuur et al., 2022].
- The geological reservoir: it contains carbon included in sedimentary rocks (CaCO_3 derivative minerals) and in organic matter (oil, gas and petrol). The estimated amount

of carbon in carbonate rock and in organic matter is $\sim 80,000,000$ GtC and $\sim 14,000$ GtC respectively, approximately 100,000 and 20 times more than in the atmosphere.

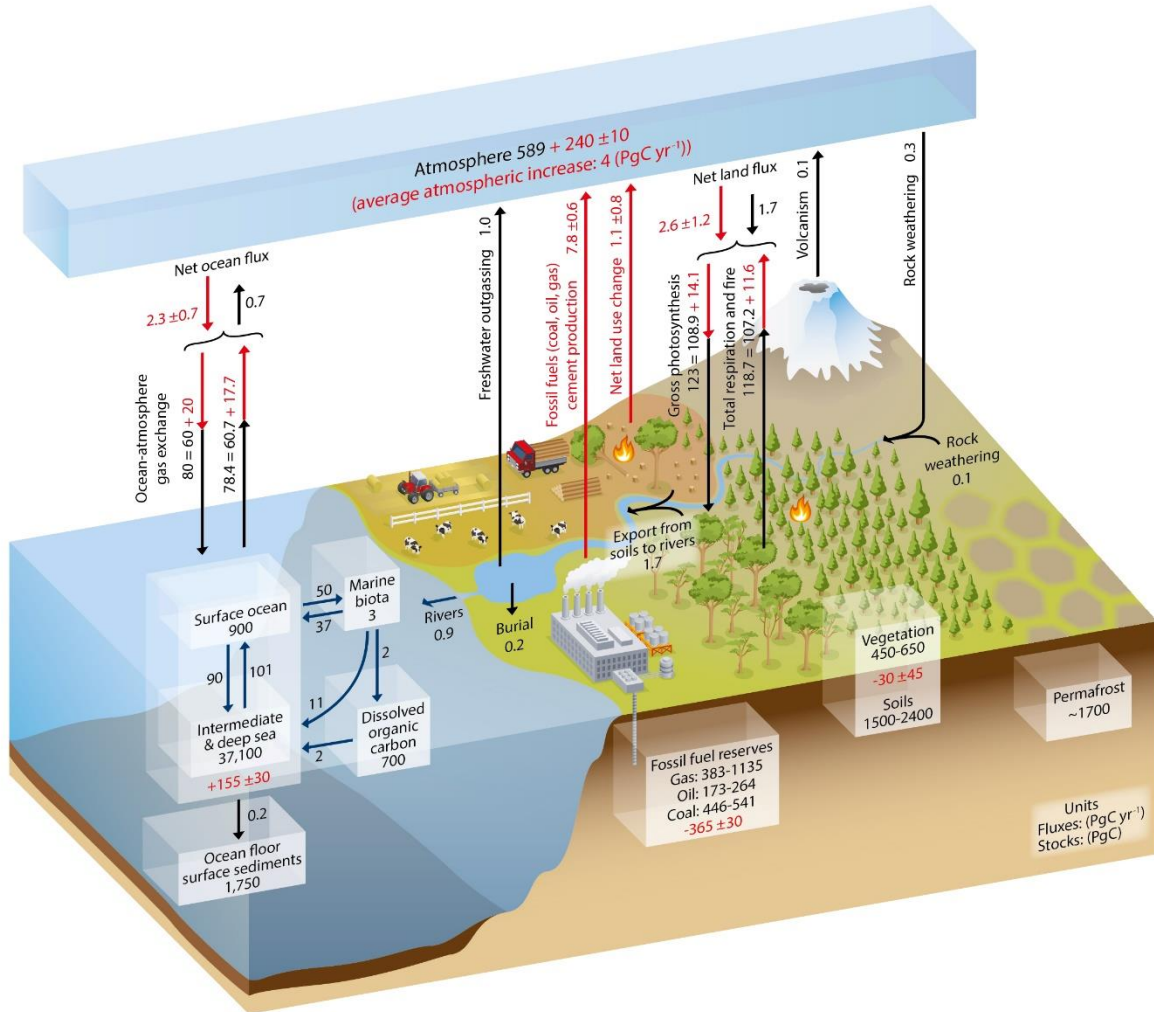


Fig. 1.3: Representation of the carbon cycle and the main carbon fluxes between the different reservoirs. The boxed numbers are reservoirs in petagrams of carbon (Pg C). Arrows represent annual exchange in Pg C per year. Black/red numbers and arrows represent preindustrial/anthropogenic reservoir masses and fluxes. The red numbers in the reservoirs denote cumulative changes of anthropogenic carbon for the industrial period. Uncertainties are reported as 90% confidence intervals. Taken from IPCC report, AR5 WGL.

The reservoirs exchange carbon through known physical mechanisms. Some of the main mechanisms at play in the atmosphere – carbon reservoir interactions are mentioned below (Fig. 1.4):

- ✦ Atmosphere – Terrestrial biosphere reservoir: respiration processes release carbon from the terrestrial biosphere to the atmosphere while photosynthesis takes carbon from the atmosphere to store it in the terrestrial biosphere reservoir.
- ✦ Atmosphere – Oceanic reservoir: when the partial pressure of CO₂ in the atmosphere is higher than the partial pressure of CO₂ in the local water, atmospheric carbon dioxide can dissolve into the ocean.
- ✦ Atmosphere – Geological reservoir: Erosion of carbonate rocks and volcanic activity release carbon from the geological reservoir to the atmosphere while erosion of silicate rocks stored carbon from the atmosphere to the geological reservoir.

The relative importance of the contribution of the different reservoirs to the exchange of atmosphere highly depends on the flux of carbon from this reservoir to the atmosphere, more than the size of the reservoir itself. For instance, the exchange between the lithospheric reservoir and atmosphere, apart from anthropogenic sourced contribution, is very low ($<0.3 \text{ GtC.yr}^{-1}$) while it is by far the most extended reservoir ($\sim 80,000,000 \text{ GtC}$). At a million-year time scale, this reservoir could have a significant influence on the atmospheric CO₂ concentrations.

Thus, the impact of a reservoir on the amount of carbon release in the atmosphere should be considered under the scope of: (i) the amount of exchange between the reservoirs, i.e. the speed of reactivity of the reservoir to an external perturbation (ii) the duration timescale at which this mechanism applies. It is also important to mention that a decreasing net flux of a sink reservoir and an increasing net flux of a source reservoir have the same consequence, i.e. an increase of the amount of carbon in the atmosphere. Reversely, an increase of the net flux of a sink reservoir and a decreasing net flux of a source reservoir will decrease the amount of carbon in the atmosphere. *In the framework of this PhD work, the variations in atmospheric CO₂ concentrations are thus interpreted as the consequence of changes in the dynamics between the carbon reservoirs. Based on an approach combining model simulations and paleoclimatic datasets from natural archives, I will attempt to identify the carbon reservoir(s) involved in the reconstructed past climate and atmospheric CO₂ changes (Chapter 4, Chapter 6).*

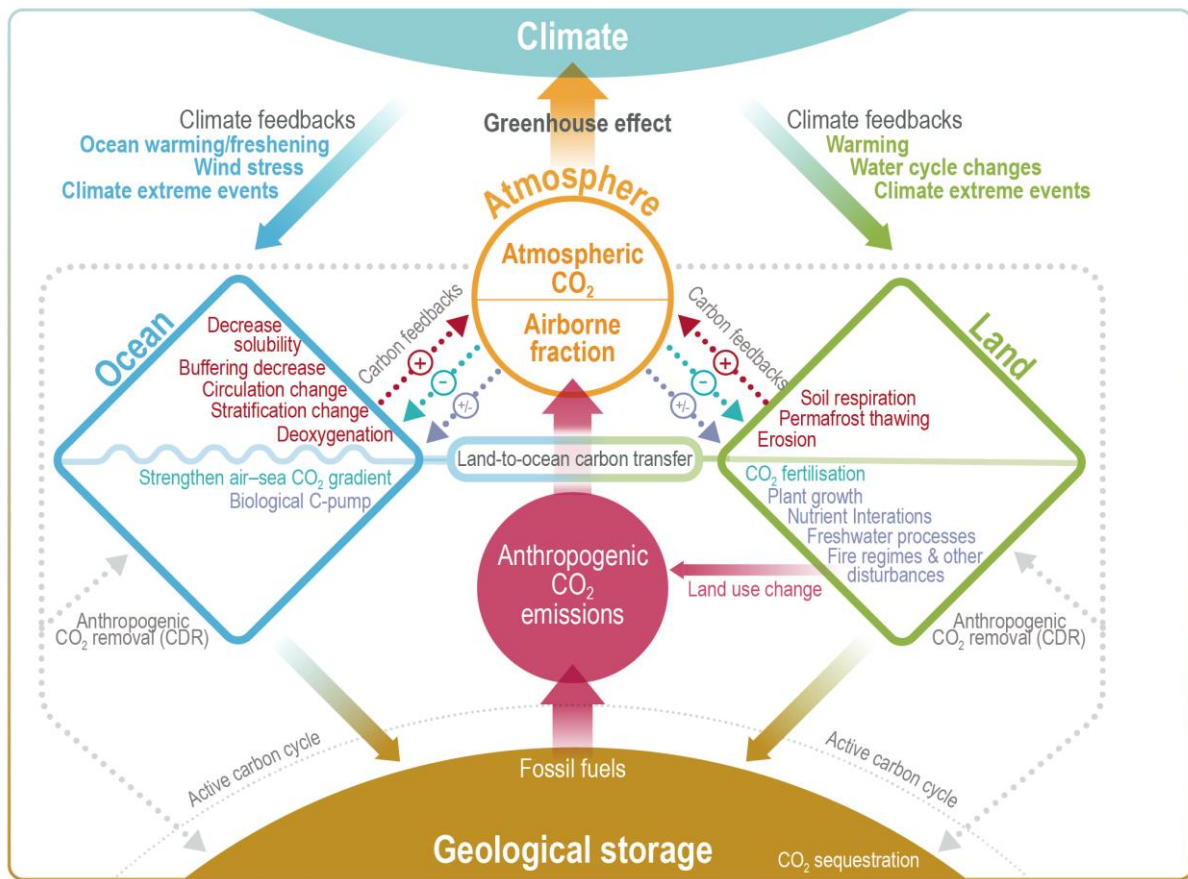


Fig. 1.4: CO₂-climate feedbacks processes and involved carbon reservoirs. Interactions between climate and land/ocean/atmosphere are represented in green/blue and orange. Negative and positive feedbacks between carbon reservoirs are represented by turquoise and red dotted arrows. Taken from the IPCC report, AR6 WGI.

1.1.3. Interactions between climate and carbon cycle

1.1.3.1 Impacts of a carbon cycle perturbation on climate:

The carbon is stored as CO₂ and CH₄ molecules in the atmosphere, that are two greenhouse gases. Their atmospheric concentration will influence the amount of infra-red radiations from the surface lost in space: the more the concentrations increase, the less the infra-red radiations from the surface are directly reemit in space. This greenhouse effect has thus for consequence to increase the global surface temperature of the Earth [Arrhenius, 1896]. With a null greenhouse gas concentration, the global temperature at the surface of Earth would be ~ -19°C. In other words, it would be ~ 35°C below the average temperature of the pre-industrial era [IPCC report, AR4 WGI]. By increasing the amount of carbon in the atmosphere, and thus the CO₂ and CH₄ concentrations, the Earth's climate moves towards warmer global surface temperature. A disturbance of the carbon cycle atmosphere reservoir will thus have for consequence to modify the global Earth's climate. In reaction to this perturbation, several

climate feedbacks will act on the different Earth carbon reservoir through mechanism such as global oceanic and land warming, climate extreme events and modification of the water cycle and wind circulations [IPCC report, AR6 WGI] (Fig. 1.4).

1.1.3.2 Impacts of climate changes on carbon reservoirs

The impact of a climate change on carbon cycle reservoirs is diverse and should be considered under the scope of each of these reservoirs. First, the oceanic reservoir is impacted by a change in the global temperature. The solubility of CO₂ in water decreases when the oceanic temperature increases. As a result, an increase of global temperature would provoke an immediate release of dissolved CO₂ into the atmosphere [Archer et al., 2004]. A change of air temperature also directly impacts the oceanic circulation and stratification [IPCC report, AR6 WGI]. For instance, the formation of sea ice in the Southern Ocean, that is highly dependent on the surface temperature conditions, modulates the intensity of CO₂-rich water upwelling from the deep ocean to the surface [e.g. Watson and Naveira Garabato, 2006; Fogwill et al., 2020]. These processes will modify the net flux of carbon from the ocean to the atmosphere, and thus create positive and/or negative retroactions of the original climate change.

In the land carbon reservoir, both precipitation and temperature affect the growth of terrestrial vegetation and the carbon storage in soils [e.g. Weltzin et al., 2003; Lin et al., 2010]. Depending on the latitude of the affected regions, an increase of temperature and/or precipitation could provoke a growth or a reduction of the terrestrial vegetation at decadal to centennial-scale, as well as increasing the erosion of the soil that destabilizes terrestrial vegetation [e.g. Bunn et al., 2007; Fletcher et al., 2010; Li et al., 2016]. For instance, the increase of temperature in the Northern High-latitudes would have for consequence to destabilize the permafrost, in which is stored large quantities of carbon as CO₂ and CH₄ greenhouse gases (~1,500 GtC) [Schuur et al., 2022].

Finally, changes in temperature and precipitation also act on the geological carbon reservoir through its impact on the erosion and alteration processes that are the dominant carbon cycle driver at multi-million-year scale. It could be considered at first order that increased precipitation and temperature will favoured erosion processes [Adams et al., 2020]. However, depending if this process affects carbonate or silicate rocks, the consequences will be opposite in net carbon flux with the atmosphere [Soulet et al., 2021; Zhang et al., 2021]. As for the terrestrial reservoir, the latitude will have a determining impact on erosion processes. A summary of these interactions for the CO₂ is represented in Fig. 1.4.

1.1.3.3 Multi-time scale characterisation of carbon cycle-climate interactions

Several feedbacks occur between carbon cycle and climate processes. Hence, a correlation between a climate change and carbon cycle variations does not allow to conclude on a specific causality relationship between the two systems. For instance, when a concomitant increase of temperature and atmospheric CO₂ concentrations is registered, processes involving a trigger from the climate or the carbon cycle could be invoked to explain the observed correlation. It underlines the crucial need to identify at high-resolution the phase relationship between the two mechanisms and/or quantified causality processes with physical models of different complexities. *Considering the large range of timescales at which occur these interactions, I developed during my PhD project a multi-timescale approach in order to (i) characterize this multi-scale variability of both carbon cycle and climate in the past and (ii) to determine across this range of timescale whether the carbon cycle-related processes act as a driver of climate changes, or rather as a positive feedback of an initial climatic perturbation.*

1.2. Paleoclimate: beyond the instrumental record

1.2.1 Interest of paleoclimatology

As developed in the previous sections, the variations of the carbon cycle and the climate and their interactions occur at multiple timescales. The greenhouse gas concentrations in the atmosphere are considered as a reliable tracer of the carbon cycle dynamic. Nevertheless, the oldest instrumental record of atmospheric greenhouse gas concentrations was initiated in 1958 with a continuous measurement of CO₂ concentrations [Keeling and Keeling, 2017]. If this record is key in monitoring the anthropogenic-induced increase of atmospheric greenhouse gas concentrations, a study of the interactions between climate and CO₂ concentrations based on the instrumental record is limited to 65 years back in time. Thus, it is impossible to explore these interactions at longer timescale, e.g. centennial-scale, millennial-scale or orbital-scale with an approach only based on instrumental monitoring.

The study of paleoclimates, that encompasses all the climates of the Earth's history, allows to explore the past climates at much longer timescales. The long-term past natural variations of the climate enable to contextualize the current ongoing warming and underline how unusual it is respectively to past natural variations [IPCC report, AR6 WGI, TS]. Also, a better understanding of the long-term interactions at play between the climate and the carbon cycle can help to constrain the future climatic trajectory beyond the end of the century, e.g. constraining climate sensitivity through different climates [IPCC report, AR6 WGI, TS; Tierney et al., 2020]. To do so, paleoclimate investigations rely on various natural archives (e.g. ice core, marine sediments, speleothems, pollens) that have recorded the past climate and carbon cycle variations [e.g. Petit et al., 1999; Lang and Wolff, 2011; Cheng et al., 2016; Sánchez Goñi et al., 2023]. Depending on the paleoarchive considered, it is possible to reconstruct climatic variables from the last centuries [e.g. Yao et al., 1997] to several million years [e.g. De Schepper et al., 2014], at sub-annual [e.g. Haines et al., 2016] to pluri-millennial scale resolution [e.g. Yamamoto et al., 2022]. In order to identify the processes responsible for the climate and carbon cycle changes reconstructed in the archives, the study of past climates also relies on simulations from Earth System Models (ESMs) that cover a large range of complexity [e.g. Stocker et al., 1992; Bouttes et al., 2016; Kageyama et al., 2021]. These models, can be used to investigate a large diversity of climate changes, both in terms of duration and amplitude. Especially, modelling the warm climates that occurred in the past to understand the physical

mechanisms at play during these periods is particularly relevant in the framework of the ongoing global warming [e.g. Masson et al., 1999; Yin and Berger, 2012; Sicard et al., 2022].

1.2.2. The Antarctic ice cores: a window on the past atmosphere

In this section 1.2.2., I introduce the Antarctic ice cores, as well as the paleoclimate models, that both have been extensively used in this PhD research.

1.2.2.1 Introduction

The ice core drilling sites are located in polar regions, i.e. the Greenland and Antarctic ice sheets, and in high-Alpine mountains. In the framework of this PhD project, I will focus on the Antarctic ice cores exclusively (Fig. 1.5). Antarctic ice cores are remarkable natural archives of the Earth's history. They result from the drilling of a site where the snow was accumulated progressively due to positive annual mass balance, providing invaluable continuous records of the past climate conditions and atmospheric composition.

The ice core archive is composed of two phases, the ice-phase, that results from the progressive compaction of the snow, and the gas-phase, that corresponds to the air trapped into the ice. Before its trapping, the atmosphere circulates into the firn, i.e. the porous layer at the surface of the ice sheet where the snow transforms progressively into ice. Both phases provide invaluable information on past Earth's climate. For instance, the water isotopes of the ice have allowed to reconstruct the Antarctic surface temperature variations [Jouzel et al., 1987; Masson-Delmotte et al., 2010] and the mid-latitude hydrological cycle [Vimeux et al., 1999; Landais et al., 2021] over the past 800 ka. Reversely, the gas-phase of an ice core represents a unique archive of the past atmosphere. A way to investigate the past carbon cycle variations is to measure atmospheric greenhouse gas concentrations in ice cores [Barnola et al., 1987; Fischer et al., 1999; Rhodes et al., 2015; Bauska et al., 2021]. *During my PhD project, I measured new CO_2 and CH_4 records to investigate the past dynamics of the carbon cycle* (Chapter 2).

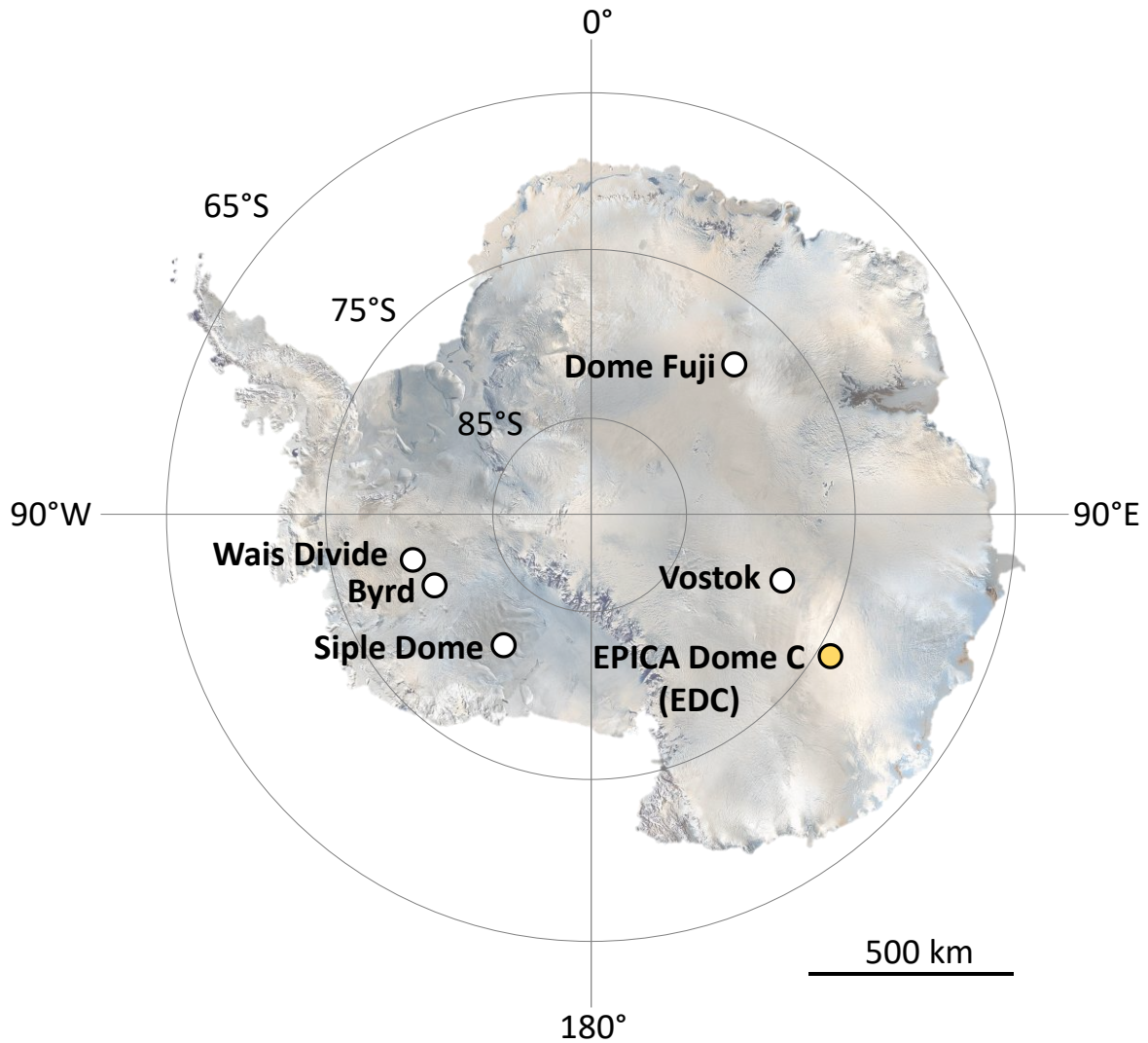


Fig. 1.5: Location of the Antarctic ice cores discussed in this study. The yellow dot corresponds to the EDC ice core on which have been measured the new datasets presented in the manuscript.

1.2.2.2 The EPICA Dome C (EDC) ice core

The EDC ice core was drilled in the framework of the European Project for Ice Coring in Antarctica (EPICA) from 1997 to 2003. The drilling site is located in the Eastern Antarctic plateau and is characterised by a very low accumulation rate ($\sim 2 \text{ cm.yr}^{-1}$, Cavitte et al. [2018]). This low-precipitation amount, combined with the high depth of the drilling (3260 m, Parrenin et al. [2007]) allow to provide the oldest continuous ice core records so far [Bazin et al., 2013; Bouchet et al., under review, see Appendices]. In particular, the EDC ice core offers reconstructions of Antarctic surface temperature and greenhouse gas concentrations over the past 800 ka [Jouzel et al., 2007; Bereiter et al., 2015; Nehrbass-Ahles et al., 2020; Shin et al., 2020], as well precious environmental and climate interpretation deduced from chemical and

impurities records [Wolff et al., 2006, 2023; Kaufmann et al., 2010; Lambert et al., 2012; Severi et al., 2023]. Twenty years later, this ice core is still extensively studied as it is the one of the three ice cores that provides records older than ~ 135 ka. The new measurements presented in *Chapter 2* have been performed on this ice core.

1.2.2.3 AICC2012 chronology and Δ age difference between air and ice

The current official chronology of reference of the EDC ice core is the Antarctic Ice Core Chronology 2012 (AICC2012) [Bazin et al., 2013; Veres et al., 2013]. It is a multi-site-based approach relying on an inverse dating method that combines glaciological modelling with absolute and stratigraphic age markers. Orbital age constraints measured in the gas-phase of ice core ($\delta^{18}\text{O}_{\text{atm}}$ of O_2 , O_2/N_2 ratios and total air content) have been also added to the age-scale [Bazin et al., 2013]. This chronology is independent from other archives and facilitates the inter comparison of records from the different ice core sites (NGRIP, TALDICE, EDML, Vostok and EDC). The average absolute age uncertainty of this chronology is 2.5 ka for the EDC ice core. A specificity of ice core chronologies is that they are composed of two age scales, one for the ice-phase, and the other for the gas-phase. This is due to the fact that at the surface of an ice sheet, the air can circulate into the firn column [Schwander et al., 1993]. This specificity has strong consequences for the ice core measurements: the air is younger than the surrounding ice at a same depth, due to this connection between the air and the surface atmosphere in the firn. This difference of age is called Δ age. In addition, it is possible to estimate a Δ depth, that corresponds to the difference depth between the air and the ice of the same age. These variables can be estimated with a firn densification model and by reconstructing the firn evolution through $\delta^{15}\text{N}$ of N_2 measurements [Capron et al., 2013; Bréant et al., 2017]. The uncertainty associated with this Δ age can reach up to several millennia in the AICC2012 chronology [Bazin et al., 2013], but will be reduced to ~ 600 years in the future AICC2023 chronology [Bouchet et al., under review, see Appendices]. The comparison between a gas-phase proxy and an ice-phase proxy measured on the EDC ice core will thus be associated with a multi-centennial scale uncertainty. *In this PhD work, the centennial-scale phasing between the carbon cycle and the climate will be investigated using exclusively gas-phase proxies in order to avoid the uncertainty associated with the Δ age* (Chapter 4).

1.2.3 Models in paleoclimate

Models are a complementary approach to data-based paleoclimatic reconstructions to investigate the physical mechanisms at play in the carbon cycle and the global climate. A large diversity of paleoclimate model has been developed [e.g. Paillard et al., 1998; Bouttes et al., 2016; Kageyama et al., 2021]. They differ in their computation time and the complexity of the modelled processes (Fig. 1.6). Depending on the scientific goal, a model of variable complexity will be used to perform paleoclimatic simulation.

Simple conceptual models aim to simplify complex climate systems into manageable components and processes. They focus on the most important factors that could impact climate, such as greenhouse gas concentrations, amount of incoming solar radiation, global ice volume, and the associated feedback mechanisms. These simplifications make them really efficient to investigate paleoclimate at million-year timescale. For these reasons, they have been used mainly to test hypothesis on mechanisms responsible for the occurrence of glacial-interglacial cycles [e.g. Calder, 1974; Paillard, 1998; Imbrie, 2011; Nyman and Ditlevsen, 2019].

The Earth system Models of Intermediate Complexity (EMICs) are extensively used in paleoclimate as they are a good compromise between more time-consuming models and non-spatialized conceptual models. Transient simulations over dozens of millennia could be performed with these models [e.g. Kessler et al., 2020]. They provide insights into regional climate pattern and are used to investigate specific climatic mechanisms, such as the impact of freshwater fluxes during the Termination I [Bouttes et al., 2023], the role of deep oceanic circulation in the outgassing of CO₂ during Heinrich events [Menviel et al., 2014], and the relative influence of carbon cycle and orbital forcings in the establishment of past climates [Yin and Berger, 2012].

The General Circulation Models (GCMs) are a more complex representation of the Earth's climate and carbon cycle systems compared to EMICs. The Paleoclimate Modeling Intercomparison Project (PMIP) has been initiated more than 30 years ago to compare the outputs of both EMIC and GCM models and evaluate their capacity to reproduce past climatic variations [Jousseume and Taylor, 1995]. Since then, many studies based on GCMs outputs-paleodata comparison from distinct paleo archives such as ice cores [Masson et al., 1999], marine sediments [Capron et al., 2014] or aquifer-based continental temperature [Bekaert et al., 2023] have been published. Transient simulations with these complex models required more computation resources and are thus more challenging. Nevertheless, some transient simulations

have been recently performed during the Termination I with GCMs [Bader et al., 2020; Kapsch et al., 2022; Zhang et al., 2023].

In the framework of my PhD and depending on the timescale considered, I have use (i) conceptual modelling to investigate glacial-interglacial cycles of the past 2 Ma (Chapter 3), and (ii) simulations from an EMIC to identify the potential source of carbon reacting at centennial-scale during millennial-scale climatic events (Chapter 6) (Fig. 1.6).

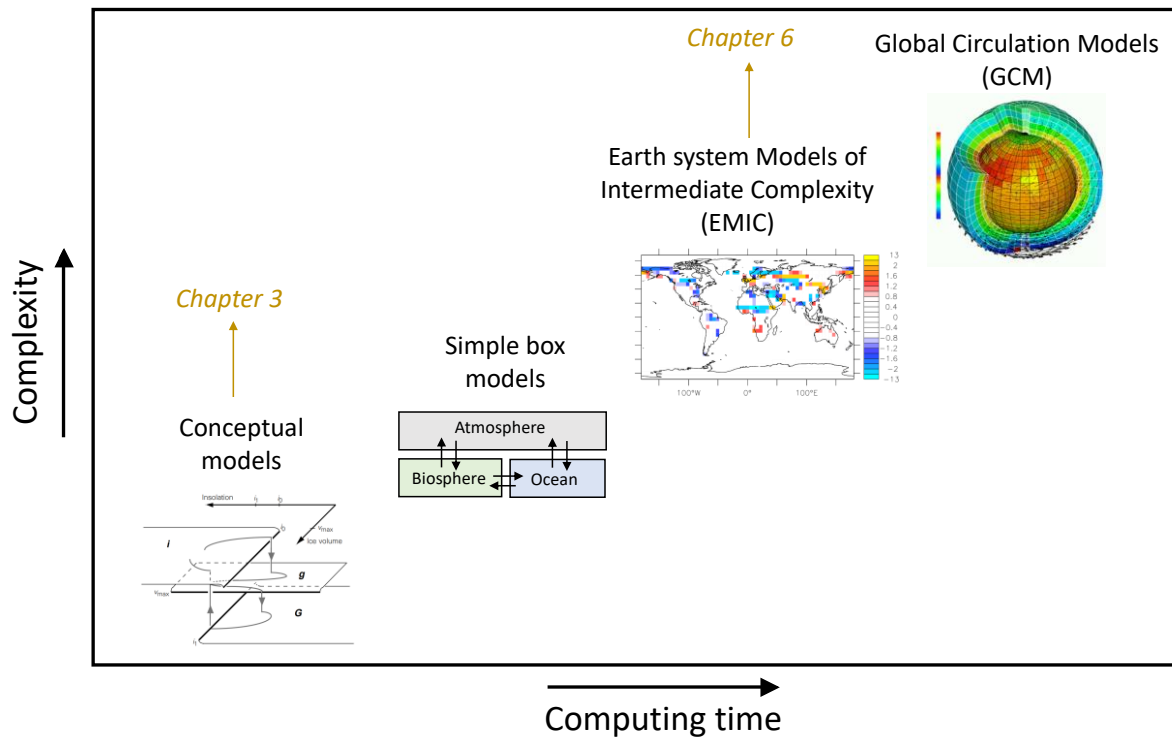


Fig. 1.6: Conceptual representation of the diversity of models used in paleoclimatology based on their complexity and computing time. Note that the reality is more a continuum than a series of categories. Illustration for conceptual model is from Paillard et al. [1998]. Illustration for GCM is from the LMD laboratory. Inspired from Bouttes, [2010]. *Chapter 3* and *Chapter 6* contains analysis performed with a conceptual model and an EMIC, respectively.

1.3. Climate and carbon cycle: a long-term perspective

After having introduced the main features of the Earth's climate and the carbon cycle, as well as paleoclimatology and its associated tools, I now contextualize the climate of the last 2 Ma in a global perspective, presenting the interactions between the carbon cycle and the climate at longer timescales.

1.3.1 Introduction

From an initial temperature of several thousand of degrees ~ 4.5 Ga ago, the Earth's global surface temperature has cooled until reaching the $50\text{-}0^\circ\text{C}$ interval 4 Ga ago [Krissansen-Totton et al., 2018]. During the past 4 Ga, the Earth's global surface temperature was maintained within this relatively narrow temperature range. Nevertheless, variation of dozens of degree of the Earth's global surface temperature has generated the alternance of extensively hot climate, characterized by an absence of ice at the surface of the Earth, to a nearly fully ice-covered Earth [Hoffman et al., 1998]. These variations are suspected to be driven by greenhouse gas concentrations in atmosphere, both responding to tectonic [Hoffman et al., 1998] and life forcing [Schirmer et al., 2013]. Depending on the timescale considered, the Earth's climate could thus be considered stable, or reversely, submitted to major variations. Before focusing on specific climatic periods, it is crucial to contextualize the development of the Pleistocene (2.58 – 0.01 Ma) climate and the global trend in which it fits.

1.3.2 Global overview of the climate-carbon cycle interactions of the past 56 Ma

There is 56 Ma ago, the Earth's temperature increased by $5\text{-}8^\circ\text{C}$ in 3-20 ka [Kennett and Stott, 1991; Gingerich, 2019]. This warming period, known as the Paleocene–Eocene Thermal Maximum (PETM), is thought to be the consequence of a large destabilization of the carbon cycle that led to an increase in global temperature (Fig. 1.7). At the end of this event, the global average temperature was $\sim 26^\circ\text{C}$ and the atmospheric CO_2 concentration was $\sim 1,500$ ppm [Rae et al., 2021] (Fig. 1.7). The PETM is an example of carbon cycle-driven climatic change. Since then, the global average temperature and the atmospheric CO_2 concentrations have followed a global decreasing trend. The weathering of silicate rocks is commonly identified as the main variable driving long-term trend in the carbon cycle [e.g. Urey 1952, Isson et al., 2020]. Recently, a study has pointed toward the change in the balance of weathering to CO_2 volcanic outgassing, and in a lesser extent the change in global temperature as the main driver of the CO_2 decline since the PETM [Rae et al., 2021]. The progressive decrease in global average

temperature is illustrated by the shift from the Eocene ice-free hot house to the emergence of glacial-interglacial cycles during the Pleistocene period [Westerhold et al., 2020] (Fig. 1.7).

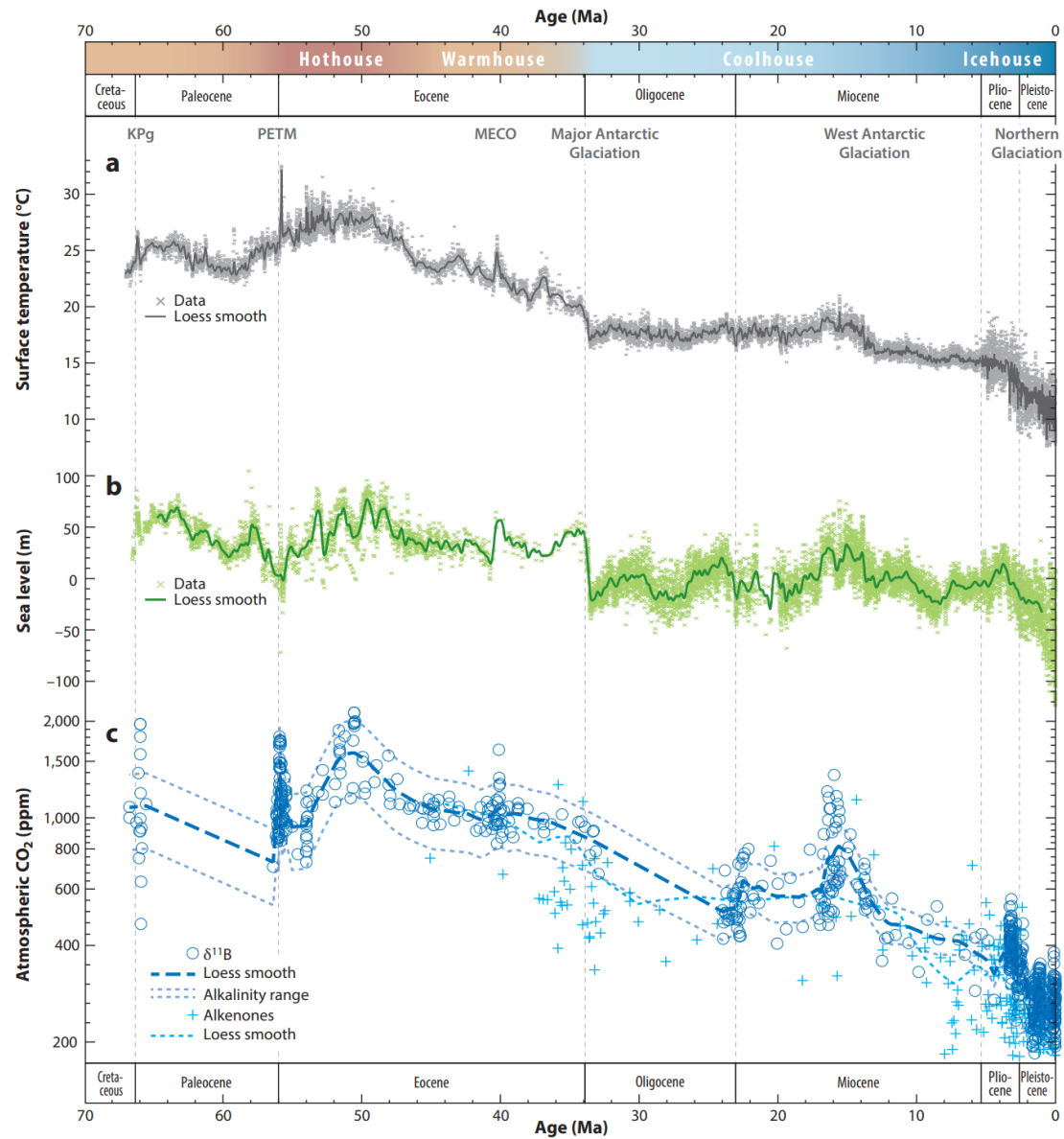


Fig. 1.7: CO₂ and global climate of the last 66 Ma. (a) Surface temperature estimated from the benthic $\delta^{18}\text{O}$ stack of Westerhold et al. (2020) (b) Sea level estimates from Miller et al. (2020) (c) Atmospheric CO₂ reconstructions from boron isotopes and alkenones. Note the superposition of climate variations occurring at various timescales (e.g. the gradual cooling over the past 56 Ma, the Miocene increase of CO₂ concentrations, or the glacial interglacial Pleistocene cyclicity). Taken from Rae et al. [2021].

1.3.3 Main features of the climate of the Pleistocene

While investigating the climate of the Pleistocene, it remains crucial to keep in mind a broader view not restricted to the past 2 Ma. The Pleistocene climate is the result of a gradual decrease in global surface temperature and atmospheric greenhouse gas concentrations for more

than 50 Ma, that led to the emergence of the climatic cycles. Although the linear decreasing trend is not anymore the dominant feature of the Pleistocene climate, the hypotheses of the existence and the influence of a background decreasing trend on Pleistocene climate have been suggested in previous studies [e.g. McClymont et al., 2013; Willeit et al., 2019].

The lower limit of the Pleistocene (2.58 Ma) was initially defined as the age of the older occurrence of glaciations registered in the sedimentary archive. The Pleistocene is characterized by an alternance between relatively warm period with ice restricted in the pole areas, i.e. interglacial period, and relatively cold period with ice extended on the Northern hemisphere continent, i.e. glacial period [Imbrie and Imbrie, 1980; Abe-Ouchi et al., 2013] (Fig. 1.8).

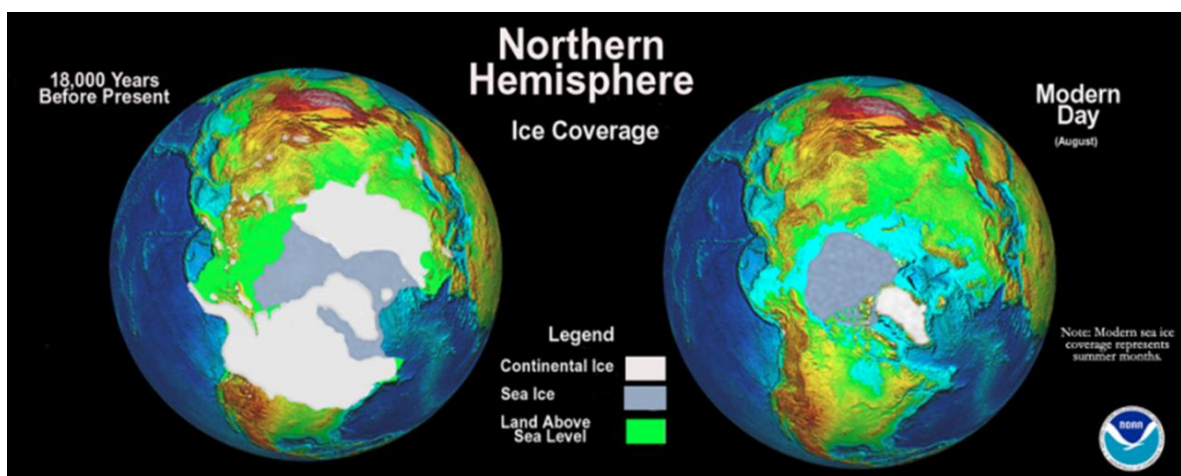


Fig. 1.8: Schematic representation of the continental ice extent and the associated variations in sea level from an interglacial (Modern day, right) and a glacial (Last Glacial Maximum, left) period of the late Pleistocene. Taken from NOAA online resources.

The cyclicity of the Pleistocene climate is registered in ice cores, marine sediments, and continental archives by both global and regional climatic proxy, and refers to the so-called glacial or climatic cycles. Although their definition is still debated, the interglacials could be defined as *warm, low ice extent (high sea level) end-members of the glacial-interglacial cycles* [Past Interglacial Working Group of PAGES, 2016]. Oppositely, the glacial could be defined as cold, high ice extent (low sea level) end-members of the glacial-interglacial cycles.

Interglacial and glacial periods can be considered as *climate states* in the perspective of the Earth's energy imbalance [IPCC report, AR6 WGI; Shackleton et al., 2023]. At the end of a glacial period, the Earth's energy imbalance is positive and the climate moves toward a transitory state commonly referred to as glacial terminations or deglaciations. On one hand, the term "termination" was originally defined as the time interval in the deglacial period that corresponds to a decrease in the foraminifera $\delta^{18}\text{O}$ record [Broecker and Van Donk, 1970]. On

the other hand, *deglaciation* is an older term referring to the retreat of an ice mass [Hershey et al., 1893; Alden, 1932]. In the context of glacial interglacial cycles, it refers to the progressive retreat of the Northern hemisphere ice sheets from their glacial to interglacial extent [Past Interglacial Working Group of PAGES, 2016]. The deglaciation process is thus reflected in the variations of the global ice volume. Since the response time of the cryosphere to a global climatic change may take several millennia [Shakun et al., 2015; Clark et al., 2016], the period covered by a “deglaciation” might not be strictly similar to the interval covered by a termination.

The term *termination* is now commonly used to a period of transition in all the properties that change during a glacial-interglacial transition [Denton et al., 2010; Landais et al., 2013; Past Interglacial Working Group of PAGES, 2016; Barker and Knorr, 2021]. In the manuscript, I will favour the use of the term *termination*. The use of the terms glacial, interglacial and termination will refer to their broad definition as described above.

The cyclicity of the Pleistocene climate is paced by changes in the amount and distribution of solar irradiance on the Earth’s surface [Berger, 1988]. The variations in Earth’s insolation are caused by the changes in three orbital parameters described by the Milankovitch cycles [Milankovitch, 1941] (Fig. 1.9) : (i) the variations in the eccentricity of the Earth’s ellipse around the sun (ii) the variations in the Earth’s precession axis (iii) the variations in the Earth’s obliquity. The first two parameters directly impact the Earth-Sun distance and thus the amount of solar irradiance, while the latest impacts the distribution of the insolation at the surface of the Earth. The orbital parameters vary among a dominant periodicity of 100, 41 and 23-19 ka for the eccentricity, obliquity and precession. They also vary in a lesser amplitude at others secondary periodicities that modulate their global variations. The summer insolation at the high-latitude of the Northern hemisphere would define the exact timing of the glaciation and deglaciation among the astronomical theory of climate of Milankovitch [1941]. The initial climate system response to the insolation variations is amplified through the ice sheet and carbon cycle dynamics that plays a major role in the amplitude of the climatic cycles [e.g. Ruddiman, 2006].

More than eighty years later, this theory is still dominant to explain this cyclicity, although additional complexities were progressively introduced [e.g. Paillard et al., 1998; Tzedakis et al., 2017].

Nevertheless, the observed climatic variations registered during glacial cycles are of larger amplitude than the expected climatic variations in response to the variation in insolation. The initial orbital pacing is thus amplified by retroactions mechanisms in the internal climatic

system of the Earth [Genthon et al., 1987]. More interestingly, the precession is the most impacting orbital parameter on the solar irradiance of the Earth. However, the observed dominant climate cycle periodicities are closer to the two other orbital parameters (~ 40 ka and ~ 100 ka). This non-linearity of the climate to the orbital parameter variations illustrates the major role play by the internal climatic retroactions in the shaping of Pleistocene climate.

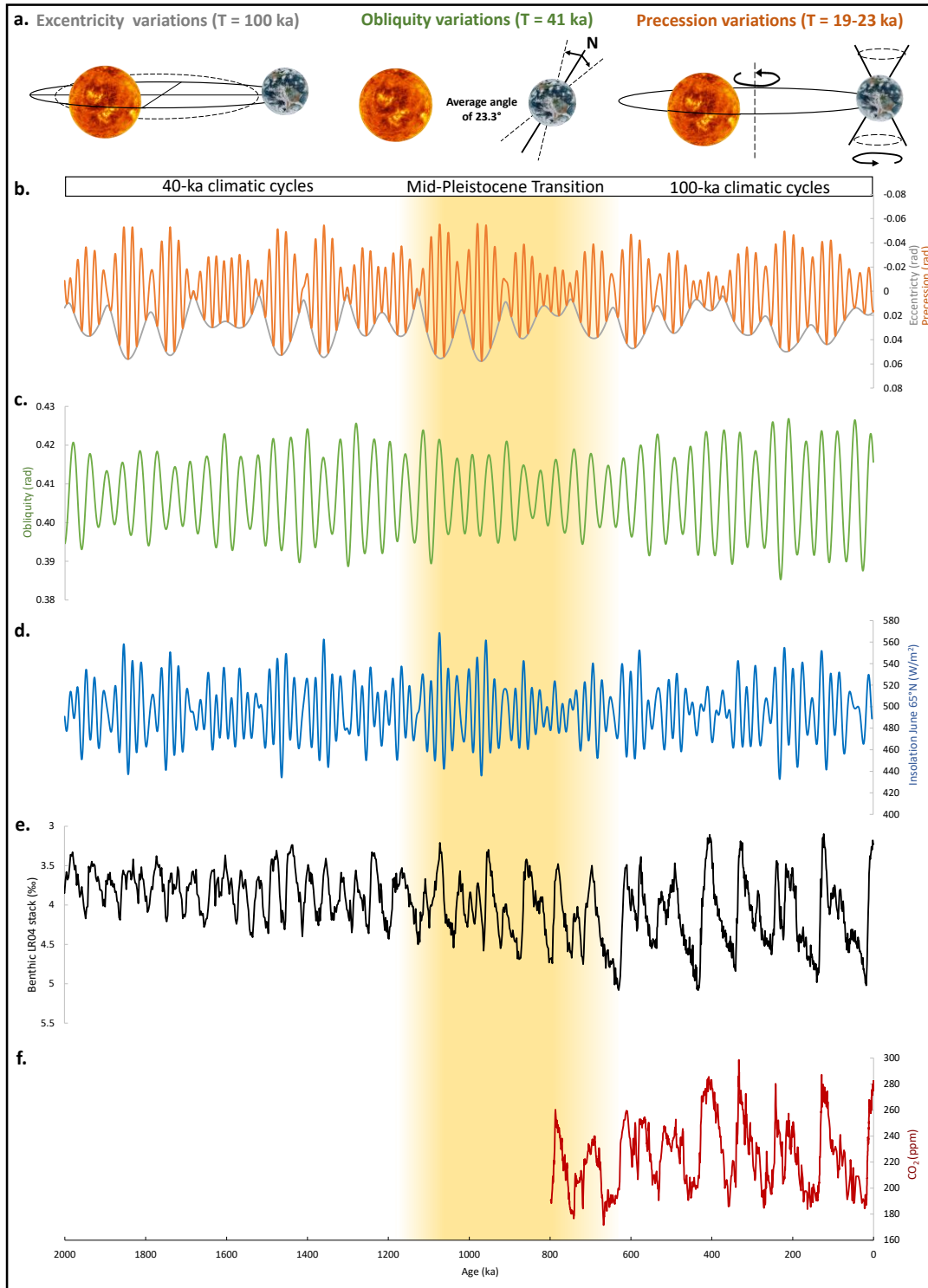


Fig. 1.9: Orbital and global climate forcing over the past 2 Ma. From top to bottom: a. Schematic representation of the three orbital forcing parameters. b Eccentricity and precession. c. Obliquity. d. Insolation June 65°N. e. Benthic LR04 stack (‰) [Lisiecki and Raymo, 2005]. f. Atmospheric CO₂ concentrations record from the ice core archive [Bereiter et al., 2015]. Yellow shaded area represents the approximate timing of the MPT.

1.3.4 The “Mid-Pleistocene Transition” problem

An emblematic example of the non-linearity of the Earth’s climate response to the orbital forcing is the so-called Mid-Pleistocene Transition (MPT). Somewhere between $\sim 1.2 - 0.8$ Ma, the periodicity of the climatic cycles has changed from ~ 40 ka to ~ 100 ka and in parallel, the amplitude of climatic cycles increased (Fig. 1.9). Before this transition, the Earth’s climate thus varied at a ~ 40 ka periodicity. A recent study has pointed the complexity of such cycles whose shape and amplitude could be driven by both precession and obliquity [Watanabe et al., 2023]. The authors propose that the larger amplitudes of obliquity and eccentricity during the 1.6-1.2 Ma period would help to establish a regular climatic cyclicity at 40 ka. Reversely, after the MPT, the average cyclicity shifted to ~ 100 ka. This approximate value has led to the eccentricity myth [Maslin et al., 2005] that would identify the eccentricity as the main driver of climatic cycles due to the similarity in the dominant periodicity. However, it is now suggested that the observed periodicity of climatic cycles during the last 800 ka is likely due to a combination of multiple skipped obliquity and/or precession cycles that led to ~ 80 and ~ 120 ka cycles [Huybers and Wunsch, 2005; Tzedakis et al., 2017; Hobart et al., 2023].

During the MPT, no significant change in the orbital parameter forcings is registered (Fig. 1.9). Then, why do the periodicity and amplitude of climatic cycles have changed? The carbon cycle has been proposed as a potential trigger for this transition [Chalk et al., 2017; Willeit et al., 2019]. However, no direct continuous record of atmospheric CO₂ concentrations is available yet throughout the MPT (Fig. 1.9). This example illustrates the complexity of the response of the internal climate system during the Pleistocene. *Understanding the mechanisms leading to the Pleistocene climate requires to investigate the internal climate retroactions triggered by the external orbital forcing. In this PhD work, I will investigate the relative role of the carbon cycle and orbital forcing on the establishment of the MPT* (Chapter 3).

1.4. Focus on the climate variations of the past 800 ka

Since the past 800 ka, the Earth's climate alternates between glacial and interglacial periods. Superimposed to this orbital-scale trend, variations of climate of lower amplitude complexifies the climatic signal at millennial to centennial-scale. Here I introduce the main specificities of the climate of the last 800 ka that I investigated in this PhD project.

1.4.1 Mechanisms during glacial terminations

The climate of the past 800 ka is composed of eight climatic cycles spanned by the EDC ice core (Fig. 1.10). This glacial-interglacial cyclicity and the associated terminations are referred to as orbital-scale climatic variability in this manuscript. The different climatic periods varying at orbital-scale have been named Marine Isotope Stage (MIS) from the $\delta^{18}\text{O}$ foraminifera record in core V28-238 [Shackleton and Opdyke, 1973] (Fig. 1.10). The climatic variations are asymmetric, as the glacial periods last several dozens of millennia whereas the interglacial duration does not exceed about 30 ka [Jouzel et al., 2007; Past Interglacial Working Group of PAGES, 2016]. These climatic cycles are characterized by a co-variation between Antarctic climate and greenhouse gas concentrations variations [Petit et al., 1999; Jouzel et al., 2007; Luthi et al., 2008]. The Mid-Brunhes event, at ~ 430 ka [Jansen et al., 1986; Lang and Wolff, 2011], initiates the establishment of the last four high-amplitude climatic cycles. These cycles are characterized by a larger amplitude, with sea level variations of ~ 100 m [Berends et al., 2021], CO_2 concentrations variations of up to 100 ppm [Bereiter et al., 2015], and an Antarctic warming of $4\text{-}10^\circ\text{C}$ [Jouzel et al., 2007; Buizert et al., 2021]. Nevertheless, the MIS 7 appears as an exception, registering relatively low sea level variation [Dutton et al., 2009] and a bi-phased warming [Desprat et al., 2006], thus setting itself apart from MIS 1, 9 and 11 [Lang and Wolff, 2011] (Fig. 1.10). The transitions occurring during these last four climatic cycles, i.e. the Termination I (TI), TII, TIII, TIV and TV are the most amplified climatic variations of the Pleistocene climate (Fig. 1.10). Our knowledge about the internal climate mechanisms at play during such major climatic transitions remains incomplete. Paleoclimatic records suggest a millennial-scale asynchronicity between the warming of the two hemispheres during the TI [Shakun et al., 2012]. This observation suggests a reduction of the Atlantic Meridional Overturning Circulation (AMOC) that consequently minimizes the cross-equatorial heat transport [Schmittner et al., 2003; Shakun et al., 2012]. This leading Southern Hemisphere warming at the onset of terminations have encouraged the hypothesis that the terminations are initially triggered by millennial-scale climatic variability that run out of

control, blurring the frontier between millennial-scale and orbital-scale variabilities [Wolff et al., 2009; Broecker et al., 2010; Barker and Knorr, 2021].

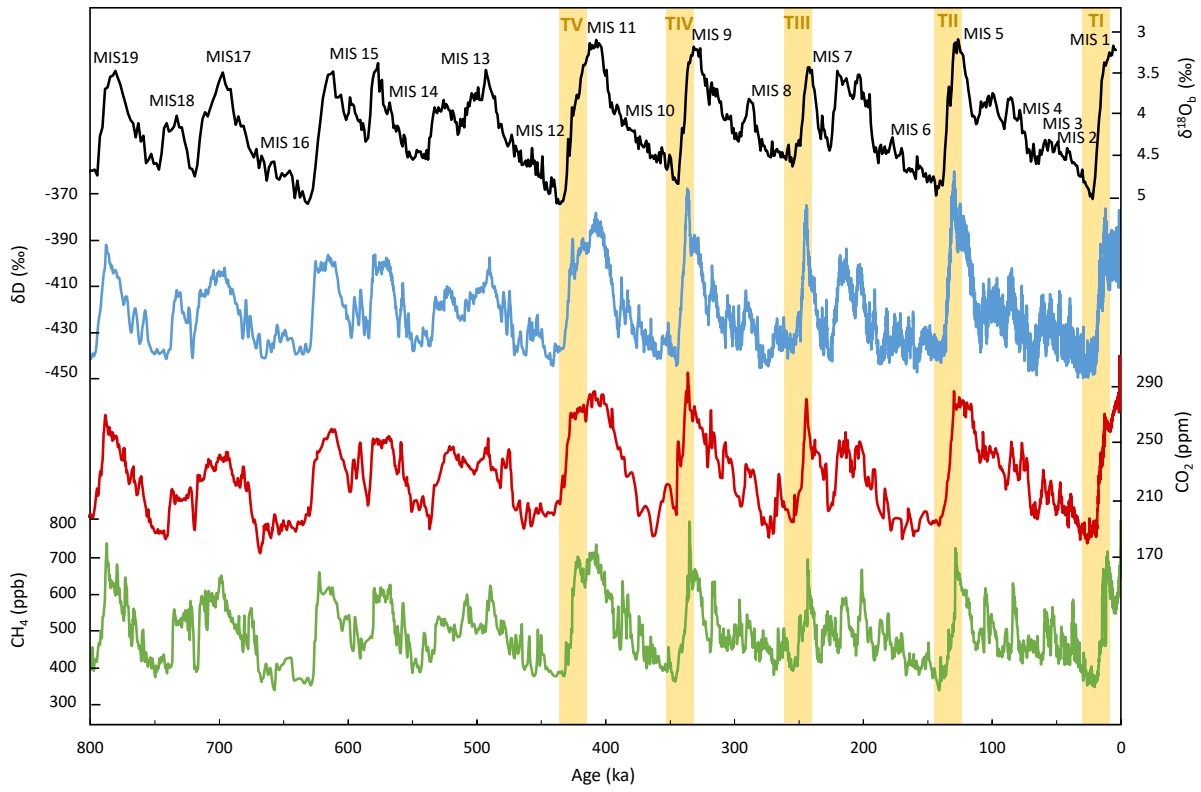


Fig. 1.10: Climate and carbon cycle records of the last 800 ka. From top to bottom: LR04 $\delta^{18}\text{O}_b$ stack [Lisiecki and Raymo, 2005] (black). EDC δD record [Jouzel et al., 2007] (blue), composite ice core CO_2 record [Bereiter et al., 2015] (red), composite ice core CH_4 record [Louergue et al., 2008] (green). δD , CO_2 and CH_4 record are on the AICC2012 chronology [Bazin et al., 2013; Veres et al., 2013]. Yellow shaded areas are the approximate highlight the last five terminations. MIS refers to Marine Isotope Stage.

Over the course of a termination, the progressive melting of ice sheets of the Northern Hemisphere modifies the albedo of continental surface and acts as a positive retroaction mechanism that amplify the initial warming [Abe-Ouchi et al., 2013]. The carbon cycle is also suspected to act as an active amplifier of the initial orbital forcing [Paillard, 2015]. Overturning circulation changes and variations in carbonate chemistry of the ocean would provoke the release of carbon from the Southern deep ocean to the atmosphere during terminations [Kohfeld and Ridgwell, 2009; Anderson et al., 2009; Sigman et al., 2010]. An impact of the low-latitude biosphere carbon reservoir was also suggested at the end of TII [Landais et al., 2013].

During these unstable periods, the temperature of the high-latitudes of the Southern Hemisphere registered an early warming in comparison to the Northern Hemisphere [Shakun et al., 2012]. Nevertheless, the role of carbon cycle during termination remains unclear,

especially because of the uncertainty in the phase relationship between atmospheric CO₂ concentrations and the Antarctic temperature change [Caillon et al., 2003; Pedro et al., 2012; Landais et al., 2013; Parrenin et al., 2013]

When investigating the role played by the carbon cycle in terminations, some of the biggest limitations are the resolution of the paleorecords and the Δ age uncertainty associated with the establishment of a sequence of climatic (ice-phase proxy) and carbon (gas-phase proxy) events. One objective of this PhD is to avoid this relative uncertainty by looking at the sequence of changes between the climate and atmospheric CO₂, focusing on records exclusively measured in the gas phase of the EDC ice core (Chapter 4).

1.4.2 Interglacials: benchmark periods for future climate

The last four interglacial periods (MIS 5, MIS 7e, MIS 9e, MIS 11) are characterized by global polar surface conditions similar to or warmer than the pre-industrial [Jouzel et al., 2007; Lang and Wolff, 2011; Capron et al., 2014]. They are also characterized by a wide diversity in term of duration and magnitude, due to different orbital forcings but also because of internal climate processes not fully understood yet [Yin and Berger, 2012; Bouttes et al., 2016; Hoffman et al., 2017]. The interglacials represent a unique opportunity to (i) investigate the effect of a warmer than pre-industrial climate on the different components of the Earth's system (ice sheets, oceanic circulations, carbon cycle) (ii) study the interactions between the carbon cycle and the climate under warmer than pre-industrial conditions and (iii) test the ability of climate models to spatially and temporally reproduce a warmer than pre-industrial climate. The intensity warming during interglacials are affected by a strong spatial heterogeneity, as revealed by both modelling and data approach [Yin and Berger, 2012; Capron et al., 2014]. A characterization of the warm interglacial climates thus requires a large spatial coverage, ideally from both continental and oceanic records.

Apart from the MIS 5 and MIS 11 for which the temporal and spatial patterns of warming have been characterized [Capron et al., 2014; Milker et al., 2015; Capron et al., 2017; Hoffman et al., 2017], no global synthesis of the warming during MIS 7 and MIS 9 have been published. During my PhD, I built the first multi-archive synthesis focusing on MIS 7 to temporally and spatially characterize the warming pattern and the regional similarity between carbon cycle and orbital forcings, and surface temperature evolutions (Chapter 5).

1.4.3 Millennial-scale climate variability

Millennial-scale climate variability was evidenced in numerous climate tracers from natural archives during glacial periods and terminations [Sánchez Goñi et al., 2002; Cheng et al., 2009; Fletcher et al., 2010; Wolff et al., 2010; Bauska et al., 2021]. Especially, during these millennial-scale event, the Southern hemisphere climate is characterized by a temperature increase of 1-3 °C in 1-2 ka, followed by a gradual temperature decrease [Barbante et al., 2006] (Fig. 1.11). These events have been called the Antarctic Isotopes Maximum (AIM) [Barbante et al., 2006; Landais et al., 2015]. The shape of these events is caused by the progressive slowdown of the AMOC, that no longer transports the heat from the Southern to the Northern hemisphere. Consequently, the heat slowly accumulates in the Southern Hemisphere. After several millennia, the resumption of the AMOC evacuates the heat from the Southern Hemisphere to the Northern Hemisphere. The Southern Hemisphere starts its cooling, while the Northern Hemisphere initiates its warming. This delay between the two hemispheres and the associated mechanism are called the bipolar seesaw [Broecker et al., 1998] and have been extensively studied with models [e.g. Stocker and Johnsen, 2003; Pedro et al., 2018]. Nevertheless, a synthesis analysis refining the relative dating of Northern and Southern hemisphere records have revealed some incoherency between the systematic application of this mechanism and the morphology of some AIM [Landais et al., 2015].

In the Northern Hemisphere, this millennial-scale climate variability is much more pronounced and is characterised by a succession of abrupt changes referred to as Dansgaard-Oeschger (DO) events [Dansgaard et al., 1993; Capron et al., 2021]. They are characterized by an alternance between the Greenland stadials, phases with full glacial conditions, and Greenland interstadials, defined by warmer conditions (Fig. 1.11). The Greenland stadial-interstadial transitions are characterized by a local surface temperature increase of up to 5-16°C in few decades [NGRIP community members, 2004; Kindler et al., 2014; Capron et al., 2021]. Continental records [e.g. Sánchez-Goñi et al., 2000; Genty et al., 2003], ice cores [Chappellaz et al., 1993], and marine sediments [Pedro et al., 2022] brought crucial information on their large spatial extent and their influence on global Earth's climate.

During the last glacial period, some Greenland stadials are associated with evidences of large iceberg discharges coming from the Laurentide ice sheet through the Hudson strait that have been registered in the Northern Atlantic Ice Rafted Debris (IRD) belt [Bond et al., 1992; Toucanne et al., 2022]. These events are called the Heinrich events. The Greenland Stadial during which is registered a Heinrich event is called a Heinrich Stadial (HS) [Barker et al.,

2009; Harrisson and Sánchez-Goñi, 2010; Hodell et al., 2017]. This discharge implies a massive input of freshwater in the North Atlantic related to a weakening of the AMOC. Heinrich events were initially defined for events occurring during the last glacial period. In the manuscript, I use the mention *Heinrich-like event* to refer to potential Heinrich event occurring before the last glacial period and evidenced in marine sediment cores of the North Atlantic. Also, the mention of *millennial-scale climate variability* refers to the AIM, DO events, or HS.

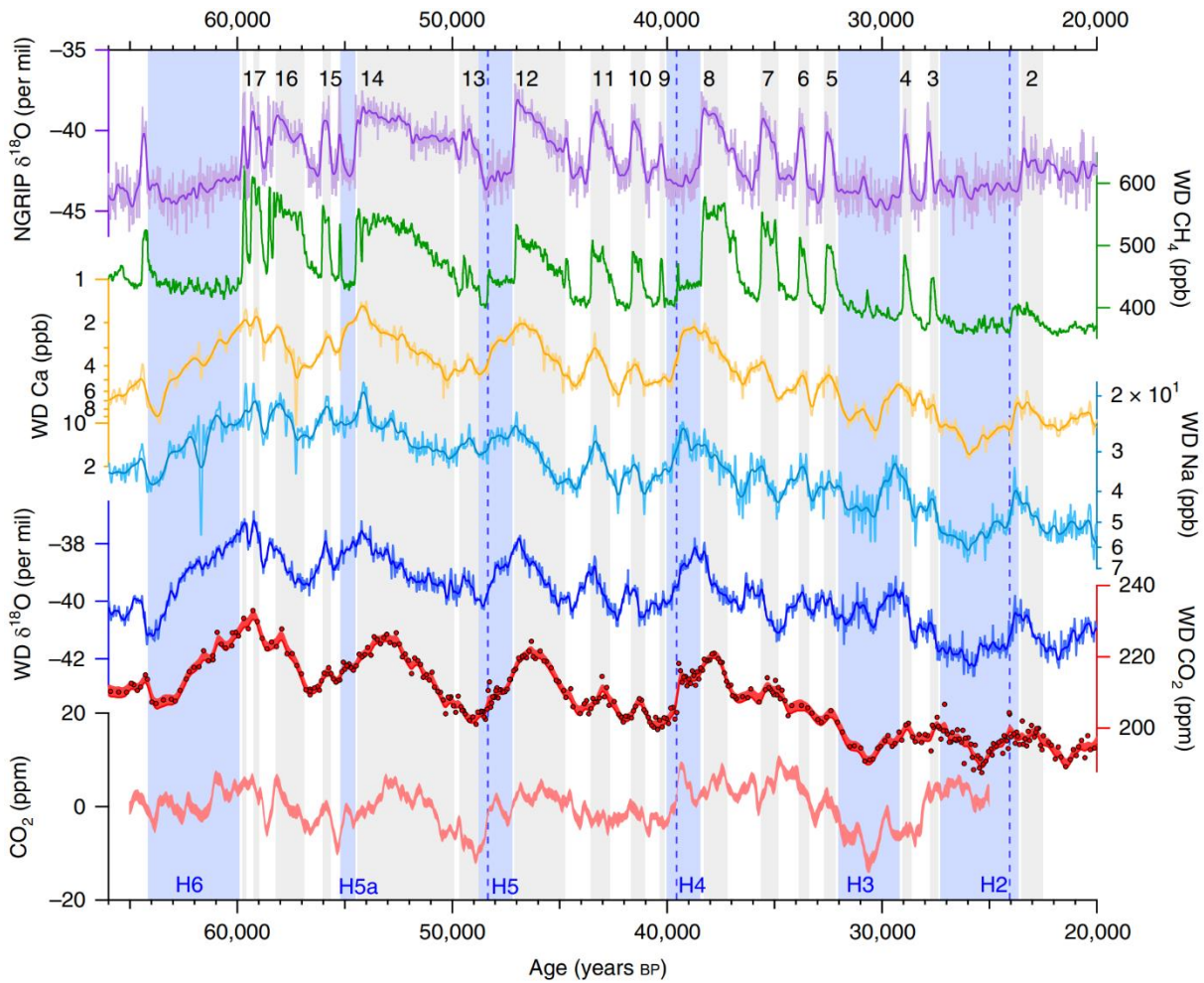


Fig. 1.11: Climate and carbon cycle records during the last glacial period. From top to bottom: NGRIP $\delta^{18}\text{O}$ [NGRIP project members, 2004], WAIS Divide CH_4 [Rhodes et al., 2015], $\log(\text{Ca})$ and $\log(\text{Na})$ [McConnell et al., 2017; Markle et al., 2018], WAIS Divide $\delta^{18}\text{O}$ [WAIS Divide project members, 2015], WAIS Divide CO_2 [Bauska et al., 2021] and residual variability in the CO_2 record not explained by a simple lagged (580 years) response to WAIS Divide $\delta^{18}\text{O}$ [Bauska et al., 2021]. Grey and blue bars indicate Greenland interstadials and Heinrich stadials. The dashed blue lines refer to the centennial-scale variability registered in the CO_2 record during HS5, HS4 and HS2. Taken from Bauska et al. [2021].

1.4.4 Centennial-scale climate variability

Improvements in experimental set-up, development of new tracers, and the drilling of high-resolution marine and ice cores have enabled the identification of sub-millennial scale variability in climate records and atmospheric CO₂ concentrations during the last 500 ka in ice core [Ahn et al., 2012; Marcott et al., 2014; Nehrbass-Ahles et al., 2020; Bauska et al., 2021], oceanic [Galaasen et al., 2014, 2020; Gray et al., 2018; Rae et al., 2018], and continental records [e.g. Kravchinsky et al., 2021] (Fig. 1.11). In this manuscript, the use of centennial-scale variability refers to any sub-millennial variations in climatic or carbon cycle records. The increase of atmospheric CO₂ concentrations of several ppm at centennial-scale are thought to be an abrupt response to the AMOC fluctuations occurring at millennial-scale climate variability [Marcott et al., 2014; Nehrbass-Ahles et al., 2020; Bauska et al., 2021]. *These centennial-scale variations of atmospheric CO₂ concentrations are still understudied due to the difficulty to obtain very highly-resolved and low-noise records from paleoclimate archives. Such records are key to improve our understanding of carbon cycle variations at sub-millennial-scale. These events are of particular interest in the context of the anthropogenic-induced climatic perturbation. In this PhD project, I will use the new greenhouse gas records presented in Chapter 2 and combined them to published records to investigate the impact of the background conditions on the occurrence of the centennial-scale events registered in the carbon cycle (Chapter 6).*

1.4.5 Interplay of multi-timescale climatic and carbon cycle variations

Centennial-scale and millennial-scale carbon cycle and climatic changes are superimposed onto the dominant orbital-scale variability (Fig. 1.12) [Marcott et al., 2014; Nehrbass-Ahles et al., 2020; Barker and Knorr, 2021; Bauska et al., 2021]. The understanding of climatic variations and its interactions with the carbon cycle thus requires to investigate the mechanisms at play between the different timescales. This overlap also suggests potential connections between the occurrence of the timescales. It is the case during the TI, when both centennial-scale and millennial-scale events are registered in the atmospheric CO₂ concentrations over the course of the termination (Fig. 1.12). For instance, if the indirect role of the orbital background on millennial-scale climatic variability have been evidenced (i.e. the dominance of glacial millennial-scale variability compared to the interglacial one) [Jouzel et al., 2007], large uncertainty remains on (i) the impact of the long-term climatic trend on the Pleistocene climate (section 1.3.) (ii) the role played by millennial-scale climatic variations in

the glacial terminations (iii) the potential influence of the orbital background on centennial-scale variability of the carbon cycle.

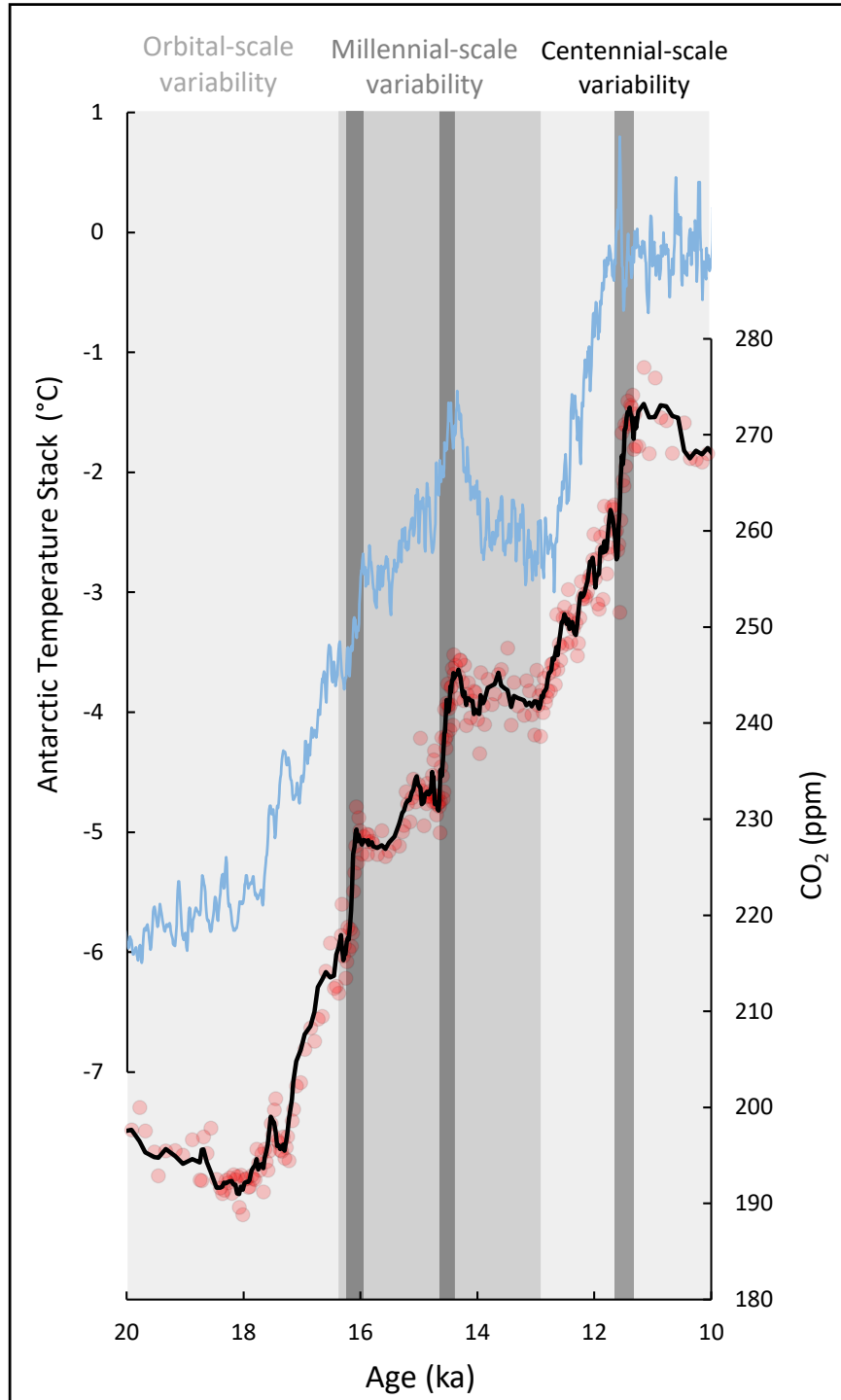


Fig. 1.12: Example of the interplay between the centennial-, millennial- and orbital-scale changes in the atmospheric CO₂ record during TI. Top: Antarctic temperature stack (blue curve) [Buizert et al., 2018]. Bottom: WAIS Divide CO₂ record during TI [Marcott et al., 2014]. The black curve is a moving mean of the raw CO₂ record (red light dots). Dark grey, grey and light grey areas refer to the centennial-scale, millennial-scale and orbital-scale variability respectively evidenced in the atmospheric CO₂ concentrations during TI.

1.5. PhD objectives

The aim of my PhD project is *to characterize the role of the changes in the carbon cycle on the climatic variations of the past 2 Ma and to understand the interplay between their orbital-, millennial- and centennial- scale interactions*, using an integrative approach combining experimental analyses performed on the EDC ice core, model simulations and paleo-data compilation. To tackle this objective, my work addresses the following research questions:

- What are the roles of the carbon cycle and the orbital forcing in triggering the MPT? (*Chapter 3*)
- What are the orbital-to-millennial-scale interactions between the carbon cycle and the Antarctic climate during glacial terminations? (*Chapter 4*)
- What is the spatio-temporal pattern of the warming during an interglacial period and how does it relate to orbital and carbon cycle forcings? (*Chapter 5*)
- Is there a link between the orbital background and the centennial-scale changes in the carbon cycle? (*Chapter 6*)

Chapter 2

Experimental analyses of CO₂ and CH₄ concentrations in the EPICA Dome C ice core

Chapter 2 is a methodological chapter providing an overview of the experimental techniques in place at IGE for extracting the air from ice samples and measuring the CO₂ and CH₄ concentrations. I performed CO₂ and CH₄ analyses on the EDC samples from January to December 2021 and in October 2022, respectively. The new records will be published in *Legrain et al., in revision (Chapter 6)*. After a brief overview of the experimental procedures which have already been described in details in previous PhD theses [Louergue, 2007; Shin, 2019], I focus here on the correction and uncertainty computations carried out during the post-measurement process. A comparison of the new measurements with the published Vostok, Dome Fuji (CO₂) and EDC (CH₄) records is also presented.

Chapter 2 aims at:

- 🔧 Contextualizing and introducing the ball mill CO₂ and the melt-refreeze CH₄ extraction systems at IGE and the associated measurement systems.
- 🔧 Providing a detailed procedure for corrections and uncertainties computations.
- 🔧 Comparing new CO₂ and CH₄ measurements with previously existing records.

Results:

- 🔧 203 new CO₂ measurements were performed on the EDC ice core covering the 260 – 190 ka period, leading to a 340 yrs temporal resolution attached to the new CO₂ record.
- 🔧 18 new CH₄ measurements were performed on the EDC ice core during the 255 – 250 and 210 – 200 ka intervals.

Data availability:

- 🔧 The new CO₂ and CH₄ records will be available on PANGEA once published.

2.1. Greenhouse gas extraction from ice cores: diversity and heterogeneity of methods

Ice cores are the only natural archives that provide a direct and continuous temporal preservation of the past atmosphere. In particular, greenhouse gas concentrations can be measured directly in the air bubbles trapped in the ice. Despite this advantage, physical [Schwander and Stauffer, 1984; Craig et al., 1988; Fourteau et al., 2017] and chemical [Delmas et al., 1980; Campen et al., 2003] processes during the formation of the ice and the storage could alter the original atmospheric signal. In the following section, I detailed the historical development and the main extraction techniques used for CO₂ and CH₄ measurement. Table 2.1 presents the key information of the extraction and measurement methods, such as the weight of ice required, the precision of the measurement system, the extraction efficiency and the number of samples measured per day.

2.1.1 Extraction methods for CO₂ measurements

At the beginning of ice core science, measuring CO₂ concentrations in ice cores appeared unfeasible due to the in-situ production of CO₂ in Greenland and non-polar ice cores [Coachman et al., 1956; Scholanders et al., 1956; Raynaud and Delmas, 1977]. However, a significant breakthrough occurred in 1980 with two key studies that successfully reconstructed CO₂ concentrations in Antarctic ice cores throughout the last glacial period [Delmas et al., 1980; Berner et al., 1980]. Extracting the air from the ice is the most challenging step in determining the atmospheric concentrations in past greenhouse gases. These pioneering studies have proposed dry extraction [Delmas et al., 1980] and a wet extraction [Berner et al., 1980] systems for the measurement of atmospheric CO₂ concentrations. Most of the current measurement systems are derived from these two methods (Table 2.1):

- (i) The advantage of the dry-extraction system is the absence of exchange between a gas phase and a water phase, as the ice is maintained in its solid form during the crushing process. Dry extraction systems employ various ice crushing methods to extract the air trapped within. At IGE in Grenoble, a ball mill system, inherited from the method of Delmas et al. [1980], is used (see section 2.2. for more details). The Bern University in Switzerland, the Oregon State University in the USA and the Seoul National University use a needle cracker methodology that crushes the ice using steel pins within a cooled vacuum chamber to release the trapped air [Ahn et al., 2009]. Additionally, the Bern university

also employ a Centrifugal Ice Microtome system that disintegrated the sample by slicing the ice within a cooled vacuum chamber, where magnetic bearings eliminated any friction [Bereiter et al., 2013].

- (ii) The wet extraction system has been developed at the Japanese National Institute of Polar Research (NIPR). The extraction system consists in melting the ice to collect the air released [Kawamura et al., 2003]. The advantage of this method is the ability to measure in parallel CO₂, CH₄, N₂O, air isotopes and total air content with the same extraction process [Kawamura et al., 2003]. However, the interaction between the air and the water and the induced partially solubilization of CO₂ in the water phase requires post measurement correction to reconstruct the original atmospheric CO₂ concentration.

More recently, the Bern university have developed a third extraction system based on ice sublimation [Schmitt et al., 2011]. This system has been recently improved in order to reduce the amount of ice required by the system [Mächler et al., 2023].

Having a variety of extraction methods is crucial in increasing confidence in past CO₂ records. Intercomparing studies demonstrate that methodology processes only have a limited effect on absolute CO₂ concentrations, typically inferior to 10 ppm [Bereiter et al., 2015; Shin et al., 2020].

Table 2.1: : Examples of extraction methods used for discrete measurements of atmospheric CO₂ and CH₄ concentrations. Modified from Shin, [2019].

Extraction method	Wet extraction		Sublimation extraction	Dry extraction			
				Ball mill	Needle cracker	Centrifugal Ice microtome	
Laboratory	NIPR	IGE	Bern	IGE	Bern	OSU/SNU	Bern
Greenhouse gas	CO ₂	CH ₄	CO ₂	CO ₂	CO ₂	CO ₂	CO ₂
Sample size	300g	45g	30g	40g	7g	8-15g	3-15g
Extraction efficiency	100%	100%	100%	62% (bubbles) 52% (clathrates)	70% (bubbles) 50% (clathrates)	85% (bubbles) 80% (clathrates)	95% (bubbles) 90% (clathrates)
Sample cadency (per day)	4	24	1	4	12-20	6	20
Number of replicates	No	No	1-2	1	4	7	3
Standard deviation (ppm)	~1.5 ppm	~5 ppb	~2 ppm	~1 ppm	~2.5 ppm	~1 ppm	~1 ppm
Detailed reference	Kawamura et al., [2003]	Raynaud et al., [1988]	Eggelston et al., [2016]; Schmitt et al., [2011]	Lorantou [2008]; Shin et al., [2020]	Lüthi et al., [2008]; Indermühle et al., [1999]	Ahn and Brook [2014]; Ahn et al., [2009]	Nehrbass-Ahles [2017], Silva [2022]

2.1.2 Extraction methods for CH₄ measurements

CH₄ concentration measurement is performed using a wet extraction system. Contrary to the CO₂, the CH₄ is not soluble in the water and thus the CH₄ concentrations do not required to be corrected from a loss of signal in the liquid-phase. The first measurements of atmospheric CH₄ in an ice core were performed by Robbins et al. [1973] in both Antarctic and Greenland ice cores providing a CH₄ record covering the last ~ 2,500 years. Progressively, the atmospheric CH₄ record has been extended back in time and the temporal resolution was increased [e.g. Craig et al., 1982; Chappellaz et al., 1990; Loulergue et al., 2008]. In addition to discrete analysis methods, the CH₄ is now also measured using continuous measurement methods (Continuous Flow Analysis, CFA), which involves gradually melting sections of the ice core [Rhodes et al., 2013, 2015; Fourteau, 2019].

2.2. Measurements of CO₂ concentrations at IGE

2.2.1 Context

The CO₂ experimental set-up for discrete measurements was built at IGE over 40 years ago [Delmas et al., 1980]. It relies on a dry-extraction methodology coupled with a gas chromatographer (details are provided in Section 2.2.2). The main principle of the extraction and measurement system have remained the same for more than 40 years, while successive improvements were performed over this time [Barnola, 1984; Barnola et al., 1987; Petit et al., 1999; Shin, 2019]. Recently, Shin, [2019] reported significant progress in the accuracy of the current measurement system. *In the framework of my PhD, one of the objectives is to take advantage of the recent improvements made in the CO₂ measurement and extraction systems to produce the first high-resolution CO₂ record over the 260-190 ka period in the Antarctic EDC ice core in order to provide new constraints on the carbon cycle-climate interactions over MIS 7 and TIII.*

At the start of my PhD, the CO₂ experimental set-up had not been used at IGE for over two years, and it was necessary to recalibrate the measurement device and conduct test measurements. This was done to ensure the accuracy of CO₂ measurements and to comprehensively assess the various source of uncertainties associated with the measurements. Firstly, a brief description of the experimental CO₂ line is presented in Section 2.2.2. Then, Section 2.2.3 will focus on the procedure used to quantify uncertainties. In Section 2.2.4, a comparison will be presented between the new EDC CO₂ record and the existing Vostok and Dome Fuji CO₂ records measured over the 260-190 ka period [Fischer et al., 1999; Petit et al., 1999; Kawamura et al., 2003, 2007].

2.2.2 CO₂ experimental set-up at IGE

A full description of the CO₂ experimental set-up at IGE is developed in Shin, [2019]. Here, I provide a summary of the measurement system, which consists of two main steps:

- ❧ Extraction process: the aim of this step is to separate the air, which contains the CO₂ signal, from the ice, which is considered as a source of contamination due to potential water vapor release [Shin, 2019]. An ice sample of ~ 40 g is introduced into the ice chamber, which is a leak-proof stainless-steel container of 150 cm³. Five 8 mm and three 12 mm stainless steel balls are then added to the sample [Barnola, 1984]. After connecting the ice chamber to the vacuum line, the cell valve is opened, and the

chamber undergoes a pumping process for approximately 20 minutes to remove the surrounding air. Simultaneously, the ice chamber is immersed in an ethanol bath at -70°C (Fig 2.1). Then, the ice chamber is moved to the cold room and is fixed onto a vertical crusher, that crushes the ice at a speed of 100 cycles per minute. This crushing process is a source of contamination that can vary between the four ice chambers used, as identified in Shin, [2019] and discussed in details in Section 2.2.3.

✂ Measurement process: the aim of this step is to determine the CO₂ concentration in the air sample extracted during the previous step. To do so, the ice chamber is connected to the extraction line (Fig 2.1). The air sample is sent to a Gas Chromatograph (GC) to separate the CO₂ from other gases. The GC is a device used for qualitative and quantitative analysis of multi-component gases. In this case, it separates CO₂ from air (N₂, O₂ and Ar) in a column that contains a stationary phase that interact with gases among their affinity. The air components are transported by the carrier gas to a Thermal Conductivity Detector (TCD) while CO₂ is converted to CH₄ and sent to a Flame Ionization Detector (FID). The concentration of CO₂ is determined by calibrating the FID response with varying amounts of a standard gas injected into the GC column. Five separate injections of the gas sample are made at distinct pressures to determine the final CO₂ concentration. The standard deviation of these five injections represent the internal error of the measurement process that is considered to be the most significant source uncertainty of the complete measurement system (Section 2.2.3.2).

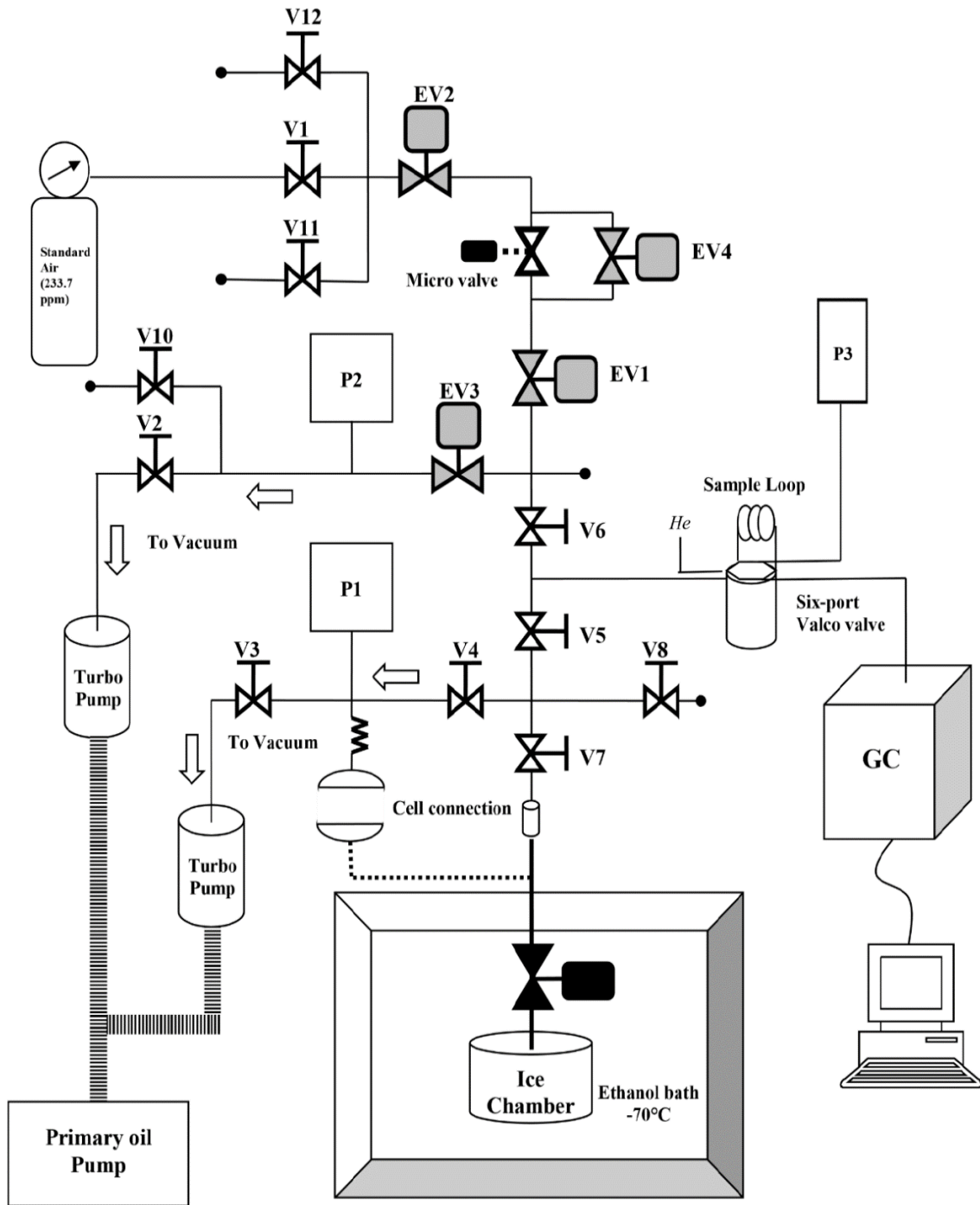


Fig 2.1: Schematic diagram showing the dry extraction line at IGE. Arrows indicate the direction of the gas flow toward vacuum. V and EV indicate manual Valve and Electronic Valve respectively. P indicates pressure gauges. GC indicates Gas Chromatograph This scheme is from Shin, [2019].

2.2.3. Corrections and source of uncertainties

I identified and quantify four main sources of uncertainties in this study of which two are associated with post-measurement correction applied on the measured CO₂ concentrations.

The average total uncertainty for the CO₂ concentrations for the EDC CO₂ dataset over the 260-190 ka period is 1.3 ppm. The Table 2.2 summarizes the uncertainty of the four sources of uncertainties.

Table 2.2: Sources of uncertainty associated with the CO₂ extraction and measurement processes. The average total standard deviation is obtained by performing the quadratic sum of the uncertainty of each of the four identified processes.

Source of uncertainty	Associated uncertainty (ppm)
Calibration process (<i>section 2.2.3.1</i>)	0.3
Internal variability (<i>section 2.2.3.2</i>)	1.0
Blank correction (<i>section 2.2.3.3</i>)	0.6
Gravitational correction (<i>section 2.2.3.4</i>)	0.4
Average total std.dev (<i>section 2.2.3.5</i>)	1.3

2.2.3.1 Calibration of the Air Liquid standard

Several bottles of international standards are available at IGE. These standards have been produced to perform inter-calibration between laboratories. Their accurate concentration and the associated uncertainty have been determined and are used as reference. However, due to their high cost and scarcity, they are not used regularly as standard in the CO₂ measurement system. At IGE, the reference standard used is an Air liquid bottle with a theoretical concentration of 230 ppm. This bottle is an industrial production that could not directly be used as a standard of reference. To be used as standard in the CO₂ measurement line, the accurate CO₂ concentration of this bottle and the associated uncertainty is first determined by using the international standards that are certified by the Commonwealth Scientific and Industrial Research Organisation and National Oceanic and Atmospheric Administration. The international standards are used to calibrate the Air Liquid bottle. To calibrate the Air liquid standard with international standards, the Air liquid is considered as a sample and the international standards as the standard of reference in the measurement process described in Shin, [2019]. Finally, the Air liquid standard that has been calibrated with the international standard is used routinely for CO₂ ice sample measurements as the standard of reference.

Two different international standards are used to calibrate the Air Liquid standard: CSIRO1677 (260.26 ±0.2 ppm) and JB03097 (241.24 ±0.015 ppm). In early 2021, I performed calibrations with the JB03097 and CSIRO1677 standards to determine the CO₂ concentration of the Air Liquid standard to be 229.5 ±0.3 ppm (1σ standard error, Fig. 2.2). This uncertainty of 0.3 ppm on the concentration of the standard is applied to all samples measured on the

experimental set-up. The only way to reduce this uncertainty would be to use an international standard directly, such as the JB3097 standard with a 0.015 ppm uncertainty on the CO₂ concentrations.

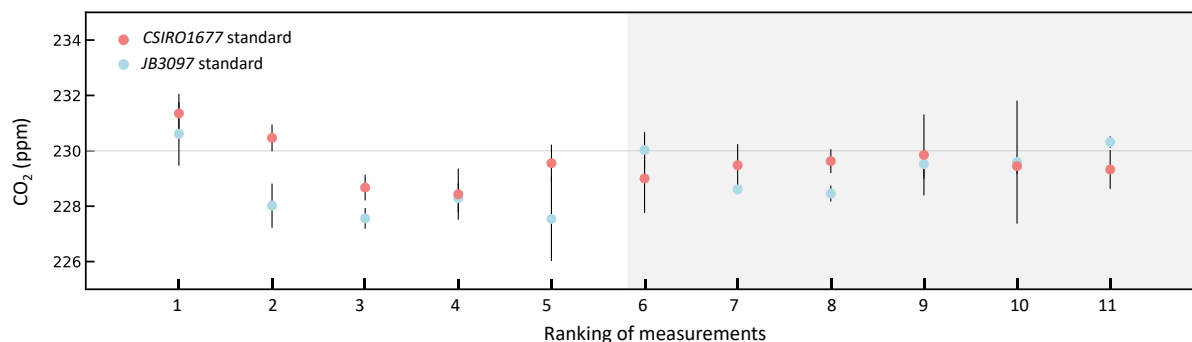


Fig. 2.2: Calibration of the Air Liquid bottle CO₂ concentration performed with the CSIRO1677 and JB3097 international standards in January and February 2021 (blue and red dots, 1 σ standard deviation). The grey shaded area corresponds to the last six measurements performed with the CSIRO1677 and JB3097 international standards that are used for the final calibration of the Air Liquid bottle. These six measurements correspond to the onset of the relatively stability in the measurements after an initial phase of restart of the experimental set-up.

2.2.3.2 Internal variability revealed by the five successive injections

Each air sample extracted from a single ice sample is injected five time at different pressure levels in the GC (Fig. 2.3). The aim of this step is to evaluate the reproducibility of the measurements and the sensibility of the measured concentrations to the injected pressure. For the EDC CO₂ dataset over the 260-190 ka period, the average standard deviation of the five injections is 1.0 ppm. This value corresponds to the internal uncertainty associated with the measurement system.

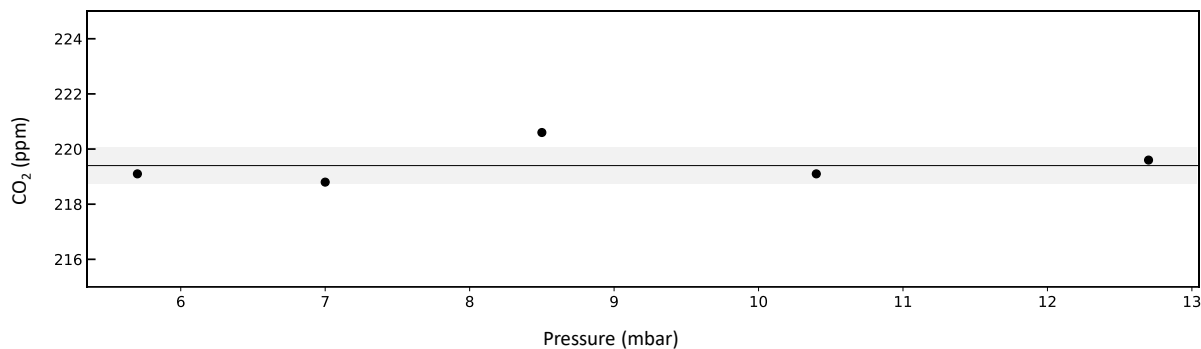


Fig. 2.3: Example of the five successive injections of the EDC4245B1 sample. Dark grey line is the average CO₂ concentration of the five injections (219.4 ppm) and the grey area represent the $\pm 1\sigma$ interval determined as the standard deviation of the five injections (0.6 ppm for the EDC4245B1 sample).

2.2.3.3 Ice crushing process and blank correction

The ice crushing process that involves steel balls and an ice chamber can result in the release of CO_2 molecules, that are naturally included in the porosity of the ice chamber, due to collisions between the components [Shin, 2019]. To minimize such contamination, Shin, [2019] includes a step in the measurement procedure that involves storing the balls and the ice chamber in a CO_2 -free atmosphere between two consecutive measurements. Despite this precaution, the crushing process is still responsible for artificially increasing past atmospheric CO_2 concentrations by several ppm [Shin, 2019]. In order to quantify this contamination, blank tests are conducted using bubble-free ice to mimic the process of ice sample measurement. The CO_2 concentrations of the standard gas is measured before and after the crushing process. The deviation of the standard gas CO_2 concentration measured from its theoretical value is considered as the contamination due to the crushing process (Fig. 2.4). The final CO_2 concentration of the ice samples are thus corrected from this value [Shin, 2019]. Each ice chamber (C1, C2, C4 and C5) has its own correction factor which is applied to its corresponding CO_2 ice samples, to correct it for the contamination induced by the crushing process. The correction factor applied on samples is recomputed each month. The correction factor applied for a measured sample corresponds to the average correction factor of the pre-dating and post-dating blank measurement. The correction associated with one ice chamber is thus variable through time. The variations of the contamination induced by the crushing process through time for a single cell could be explained by: (i) the irregularly use of the ice chamber (ii) variations in the number of hits of the stainless ball during the crushing process (iii) and potential residual gas of the bubble-free ice. The average standard deviation of the contamination for a single cell is 0.7 ppm (Table 2.3).

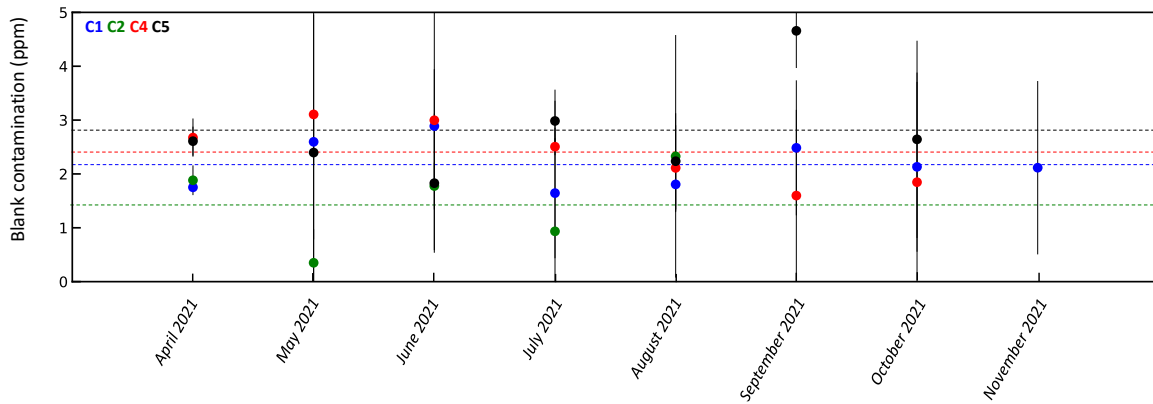


Fig. 2.4: Blank measurements performed in 2021. Blue, green, red and black dots correspond to blank measurements performed on the ice chamber C1, C2, C4 and C5 respectively. Dashed coloured lines correspond to the average correction during the period of measurements. Vostok data from the Petit et al. [1999] have been corrected *a posteriori* from this average value for the corresponding cell (Section 2.2.4.2).

For the dataset presented in this study, the average correction of concentrations subtracted to the raw concentrations blank is 2.6 ± 0.9 ppm (1σ standard deviation), ranging from 1.0 to 5.4 ppm (Fig. 2.5). The uncertainty associated with blank correction is computed as the standard deviation of the two blank measurements, that predate and postdate the sample measurement, and is used to correct CO₂ concentrations of the sample. The average uncertainty associated with crushing process is 0.6 ppm.

Table 2.3: Standard deviation of the correction factor measurements for each ice chamber.

Ice chamber	Standard deviation of the correction factor (ppm)
C1	0.4
C2	0.8
C4	0.6
C5	0.9

2.2.3.4 Gravitational correction

In this section, I use the $\delta^{15}\text{N}$ EDC new data measured in Grisart, [2022] over the 260-190 ka interval. Heavier molecules in the atmosphere are over-represented in the deepest part of the firn column [Craig et al., 1988]. This leads to an enrichment of heavier molecules in the air trapped in bubbles at the base of the firn. CO₂ concentrations thus need to be corrected from this gravitational effect. The deviation in CO₂ concentrations associated with the gravitational effect is computed using the following equation [Craig et al., 1988]:

$$[\text{CO}_2]_{\text{corr.grav.}} = (1 - \delta^{15}\text{N}_{\text{measured}} \times (M_{\text{CO}_2} - M_{\text{air}})) \times [\text{CO}_2]_{\text{measured}} \quad (1)$$

Where $[\text{CO}_2]_{\text{corr.grav}}$ is the final CO₂ concentration value corrected from gravitational effect, M is the molecular weight, $[\text{CO}_2]_{\text{measured}}$ is the CO₂ concentrations measured in the CO₂ line, and $\delta^{15}\text{N}_{\text{measured}}$ is the $\delta^{15}\text{N}$ of N₂ from the gas phase at the similar depth than the $[\text{CO}_2]_{\text{measured}}$. As $\delta^{15}\text{N}$ value were not systematically available at the exact depth of a CO₂ samples, $\delta^{15}\text{N}$ value have been interpolated linearly between the two bracketing $\delta^{15}\text{N}$ samples. The uncertainty associated with this correction is mainly composed of the uncertainty on the $\delta^{15}\text{N}$ value. The average gravitational correction in the dataset presented here is -1.4 ppm, ranging from -0.9 to

-2.1 ppm (Fig. 2.5). The uncertainty associated with gravitational correction is 0.4 ppm on average.

2.2.3.5 Final computation of CO₂ uncertainties

For each sample analysed the final uncertainty attached to the CO₂ measurement is obtained performing the quadratic sum of the four previously described uncertainties:

$$\sigma([\text{CO}_2]) = \sqrt{\sigma([\text{CO}_2])_{\text{five.inj}}^2 + \sigma([\text{CO}_2])_{\text{blank.corr}}^2 + \sigma([\text{CO}_2])_{\text{grav.corr}}^2 + \sigma([\text{CO}_2])_{\text{std}}^2}$$

with $\sigma([\text{CO}_2])_{\text{std}}$, $\sigma([\text{CO}_2])_{\text{five.inj}}$, $\sigma([\text{CO}_2])_{\text{blank.corr}}$, $\sigma([\text{CO}_2])_{\text{grav.corr}}$, the uncertainty associated with the standard calibration (section 2.2.3.1), the five injections (section 2.2.3.2), the blank correction (section 2.2.3.3) and the gravitational correction (section 2.2.3.4), respectively. Raw and corrected CO₂ data are shown in Fig. 2.5. and on average, the final uncertainty of the dataset is 1.3 ppm.

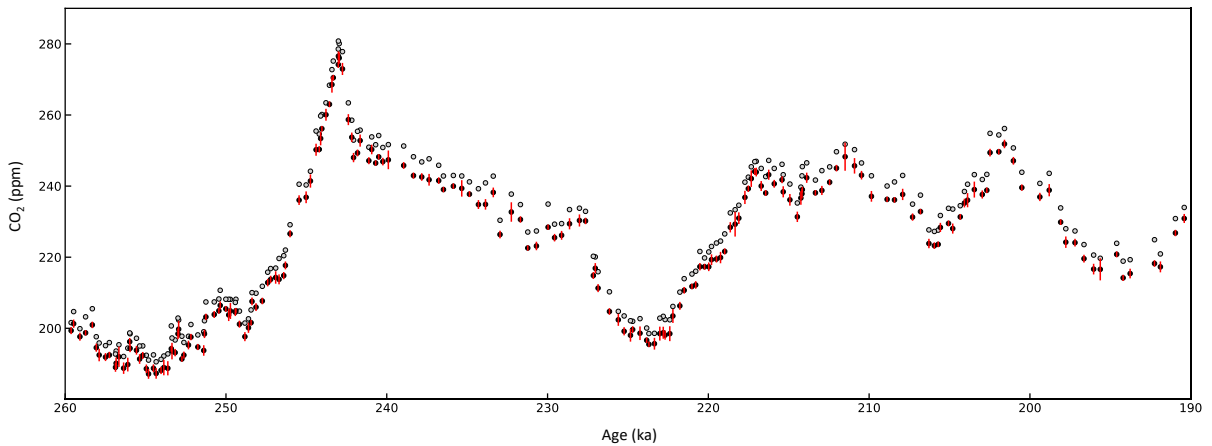


Fig. 2.5: Raw and corrected CO₂ measurements covering the 260-190 ka time-period. CO₂ measurements without gravitational and blank correction (grey dots). CO₂ measurements with gravitational and blank correction, and the associated uncertainty (black dots and red lines). Both records are plotted on the AICC2012 gas timescale [Bazin et al., 2013].

2.2.4. Comparison with previous atmospheric CO₂ records measured in ice core

2.2.4.1 Global overview

The 260-190 ka interval is covered by three Antarctic ice cores: EDC [Jouzel et al., 2007], Vostok [Petit et al., 1999] and Dome F [Kawamura et al., 2003]. While my study provides the first measurement of atmospheric CO₂ concentration in the EDC ice core over this specific period, atmospheric CO₂ records have been measured on both Dome F and Vostok [Fischer et al., 1999; Petit et al., 1999; Kawamura et al., 2003, 2007] (Fig. 2.6).

The Dome Fuji record mostly relies on wet-extraction based measurements. The high-solubility of CO₂ in the water phase induced a correction of ~4 ppm of the concentrations. However, no clear uncertainty associated with this correction is developed in the source papers and the uncertainty of the absolute value of the record is thus not quantified [Kawamura et al., 2003]. Still, four dry-extraction based measurements performed during the 260-190 ka period seem to validate the corrected absolute values of CO₂ concentrations measured by the wet extraction technique. While this record has an average resolution of 1.5 ka over the 260-190 ka period, it reproduced well the orbital-scale variations of CO₂ concentrations observed in the EDC and Vostok record (Fig. 2.6).

The Vostok CO₂ records were measured at IGE [Petit et al., 1999] and Scripps [Fischer et al., 1999] laboratories. The Scripps record is the most resolved record over the 260-211 ka interval compared to the Vostok IGE record (600 years instead of 860 years). However, this record is associated with a larger uncertainty (average standard deviation of 3.5 ppm) compared to the IGE record (approximate standard deviation of 2-3 ppm, [Petit et al. 1999]). In addition, the IGE record includes the entire period spanned by the TIII and MIS 7 (260-190 ka) contrary to the one from Fischer et al. [1999] (260-211 ka). The Petit et al. [1999] record is thus considered as the record of reference for this period, and is the one included in the atmospheric CO₂ composite record of the last 800 ka [Bereiter et al., 2015].

Finally, the new EDC record presented in this study has the advantage to provide a continuous record based on a dry-extraction method, highly resolved (340 years in average), and associated with low uncertainty (1.3 ppm in average) over the 260-190 ka period (Fig. 2.6). Especially, the gain in resolution could be exploited to study sub-millennial-scale (*Chapter 4, Chapter 6*) variability of the carbon cycle. The new EDC record also confirms the reliability of previous Dome Fuji and Vostok records in reproducing the orbital-scale variations of

atmospheric CO₂ concentrations over this period, while an apparent shift in the absolute concentrations value have been identified (Fig. 2.6).

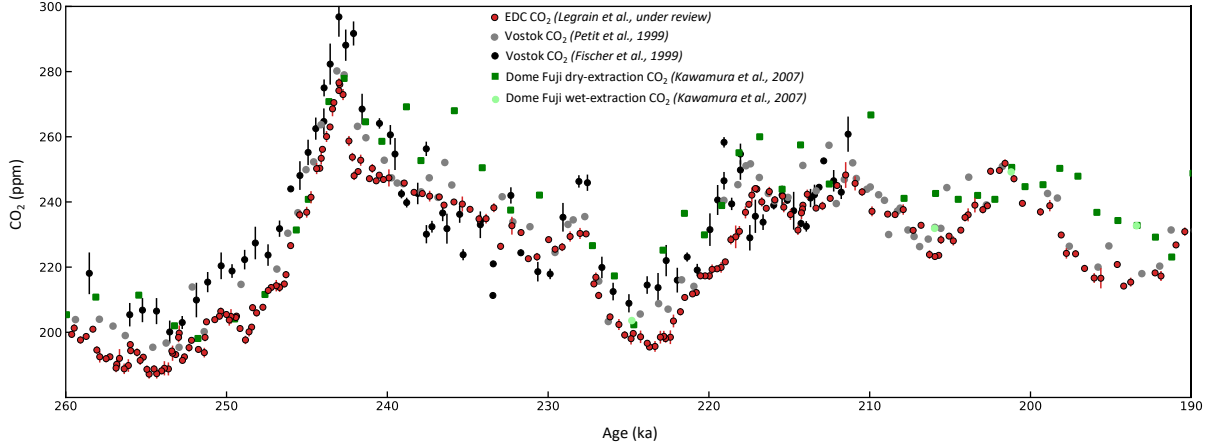


Fig. 2.6: Atmospheric CO₂ measurements covering the 260-190 ka time-period. EDC CO₂ measurement (red dots, Legrain et al., in revision), Vostok CO₂ measurements (grey and black dots, Petit et al., 1999; Fischer et al., 1999), Dome Fuji wet and dry CO₂ measurements (dark green squares and light green dots, Kawamura et al., 2003, 2007). EDC and Vostok records are plotted on the AICC2012 gas timescale [Bazin et al., 2013]. Dome Fuji record is plotted on the DFO-2006 gas timescale [Kawamura et al., 2007]. The uncertainty associated with each data point is not provided in the Dome Fuji [Kawamura et al., 2007] and Vostok record from [Petit et al., 1999].

2.2.4.2 Comparison with the Vostok CO₂ record measured at IGE [Petit et al., 1999]

In the 1990s, a CO₂ record associated with an average temporal resolution of 900 years was measured at the IGE on the Vostok ice core covering the interval 260-190 ka [Petit et al., 1999]. Because the atmosphere mixing time is typically one year, CO₂ concentrations are expected to be similar independently from a given drilling site. In addition, both records have been measured with a similar experimental set-up. Therefore, the Vostok CO₂ record measured at IGE should provide similar concentrations than the one measured in the EDC ice core in this study. Both records are presented on the AICC2012 gas timescale [Bazin et al., 2013] in Fig. 2.7.

I measured an offset of 5.5 ± 5.4 ppm on average between the original Vostok record and the new EDC record over the studied time interval (Fig. 2.7). Such offset is not significantly different to the one observed during the 190 – 135 ka period of 4.6 ± 3.0 ppm [Shin et al., 2020]. In the Vostok record, the effect of the crushing process on CO₂ concentrations as well as the gravitational fractionation in the firn was assumed to be negligible [Petit et al., 1999]. After applying the blank correction and the gravitational correction using the $\delta^{15}\text{N}$ record over the

260-190 ka [Breant et al., 2019, Grisart, 2022], the offset between the EDC and Vostok record is reduced to 1.4 ± 5.4 ppm (Fig. 2.7). Considering the large standard deviation of this offset, these results show that after *a posteriori* correction, no significant offset remains between the Vostok and the EDC records.

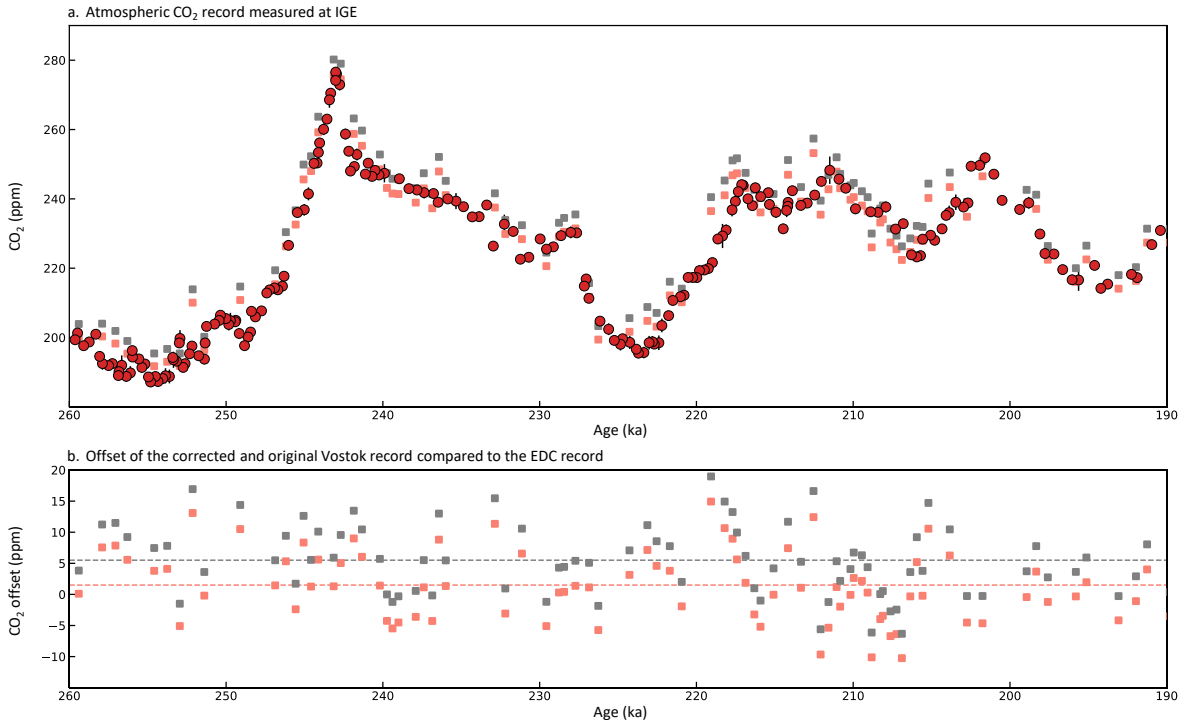


Fig. 2.7: Published and new CO₂ measurements covering the 260-190 ka time-period. a. New CO₂ measurements performed on the EDC ice core (red dots) [Legrain et al., in revision]. Published CO₂ data from the Vostok ice core (grey squares) [Petit et al., 1999] and Vostok CO₂ data corrected including gravitational and blank corrections (red square, this study). All records are plotted on the AICC2012 gas timescale [Bazin et al., 2013]. b. Difference between the original/corrected Vostok CO₂ record and the EDC CO₂ record (grey/pink square). Grey/ pink dashed lines represent the average offset of the original/corrected Vostok record compare to the EDC CO₂ record.

It is important to note that the blank correction of the CO₂ Vostok record is performed *a posteriori* as no estimation of contamination due to the crushing process was measured in the past. To do so, I assume a constant contamination through time from ice chambers used for CO₂ measurement. Vostok CO₂ concentrations were thus corrected from the average contamination value from the ice chamber it was measured (Fig. 2.7, coloured dashed lines). This hypothesize of a constant contamination through time that may not be strictly exact, leading to a secondary order uncertainty associated with this correction.

To further investigate the potential offset existing between the Vostok and EDC atmospheric CO₂ concentrations, I measured 20 new Vostok ice samples covering the 260-190

ka period at IGE in 2021. The measurement process is exactly the same as for the EDC samples, including gravitational and blank corrections. Since the measured published in Petit et al. [1999], the extraction and measurement system have remained similar [Petit et al., 1999; Shin et al., 2020]. Hence, the new Vostok measurements are expected to agree with the published Vostok record. The nine measurements performed during the 250-190 ka interval are in good agreement with the corrected Vostok and the EDC CO₂ record (Fig. 2.8). Such result confirms that the original offset between EDC and Vostok records [Shin et al., 2020] is mainly due to the recent corrections related to the crushing process and the gravitational effect that I applied on the EDC record. However, the concentrations across the 260-250 ka period, measured on 11 samples, are more intriguing. The new Vostok CO₂ concentrations are higher by 3-4ppm than the EDC ones and even than the corrected Vostok CO₂ data from Petit et al. [1999]. The origin of this offset could potentially be explained by a combination of the poor quality of the ice sample and the storage conditions of the newly measured ice samples. Indeed, the measured samples have been stored at -20°C for more than 40 yrs and some were affected by cracks and presented suspicious areas of potential melting refreezing. A most exhaustive campaign of Vostok CO₂ measurements would be very useful to be more conclusive on this existing offset across the interval 260-250 ka between the new Vostok data and the EDC and published Vostok records.

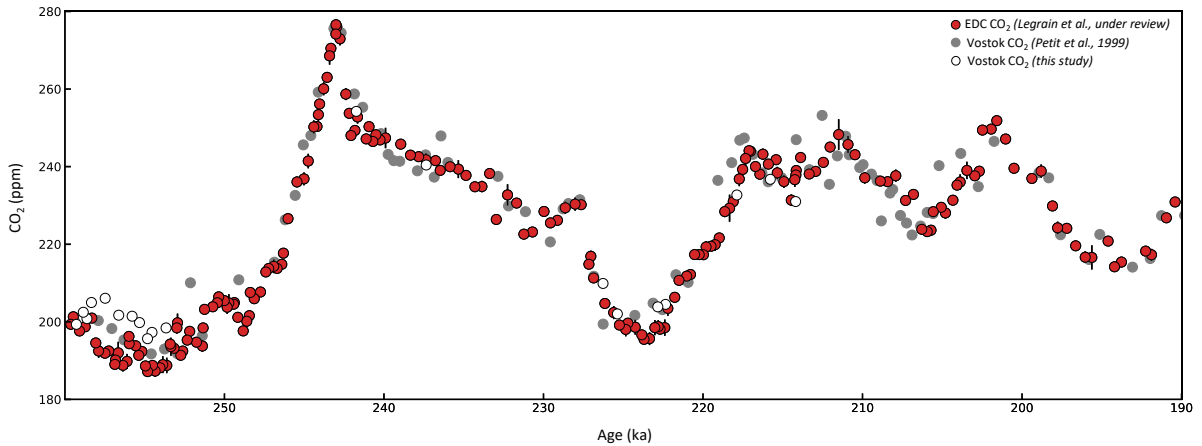


Fig. 2.8: New CO₂ measurements performed on the EDC/Vostok ice cores (red/white dots, this study). Vostok CO₂ record from Petit et al. [1999] corrected *a posteriori* from gravitational and crushing process contamination (grey dots). All records are plotted on the AICC2012 gas timescale [Bazin et al., 2013].

2.3. Measurements of CH₄ concentrations at IGE

2.3.1 Context

The discrete CH₄ measurement system was built at IGE over 40 years ago [Raynaud et al., 1982]. This system has notably played a crucial role in reconstructing the first atmospheric CH₄ variations over the last glacial-interglacial cycle and providing a continuous CH₄ record in the EDC ice core [Chappellaz et al., 1990; Louergue et al., 2008]. In 1999, a semi-automatic control system was implemented through a LabView program and a National Instruments material. Since then, the measurement system was not modified except for the post-treatment of raw results [Bellier, 2004]. A complete description of the system of measurement is available in [Louergue, 2007]. In October 2018, the computer that housed the LabView program crashed as well as the controlling National Instrument card making the measurement system inoperable.

The CH₄ concentrations are crucial in the characterization of centennial-scale CO₂ variations. In this purpose, the study investigating centennial-scale CO₂ changes across the past 500 ka developed in *Chapter 6* required a comparison with a centennial-scale resolved CH₄ record over specific time intervals. Due to the low resolution of the existing CH₄ record over targeted intervals, additional CH₄ measurements were necessary. The short term needs to increase the CH₄ resolution profile in the framework of this PhD project, coupled with the strong interest of the IGE gas team in having an operational CH₄ discrete measurement experimental set-up were two strong motivations to fix the CH₄ discrete measurement system. From May 2021, I led this initiative with the technical support of Axel Wohleber, PhD student at IGE, for the electro-technical and LabView coding aspects. I performed 18 new CH₄ measurement on the EDC ice core using the new fixed system.

2.3.2 CH₄ measurement system at IGE

A full description of the CH₄ measurement system at IGE is developed in Louergue, [2007]. The measurement process, using a GC, follows similar principles to those for the CO₂ concentrations measurements. As for the CO₂ measurement, standard calibration and blank measurements are performed in parallel to the sample measurements. I propose here to focus on describing the method for the air extraction from the ice.

The wet extraction technique is based on a melt-refreeze technic that separate the air, which contains the CH₄, from the ice. This part of the measurement process is semi-automatically controlled by a LabView program [Bordes, 1999]. An ice sample of ~45 g is

introduced into a glass cell. The twelve glass cells containing one ice sample each, are connected to the extraction line to initiate the pumping process and put all the samples under vacuum. During this process, the glass cells are immersed in a -60°C ethanol bath to maintain the sample into the ice-phase. After stopping the pumping process, the samples are melted to release the air into the glass cell. When the ice is completely melted, the fusion process is stopped to avoid the formation of water vapour, and the liquid sample is refrozen to extract the last air bubbles trapped into the liquid phase. The air sample is then injected into the GC.

2.3.3 Updating the experimental system for discrete CH₄ concentration analysis in ice samples

The primary goal of restarting the CH₄ measurement system goes beyond simply getting it operational again: it also aims to ensure its long-term viability by incorporating more modern supports compare to the ones used previously and that became outdated. The LabView program was initially coded in a 1999 LabView version and the computer was run in Windows 1998. The decision was taken to associate a Windows 10 computer to the line with a LabView 2015 license version. Incompatibilities between the 1999 LabView program and the LabView 2015 version required an update of the code. While carrying out this update, a new interface was created, transitioning from a purely linear structure to a step-based structure that can be activated or not. The objective is to facilitate the testing of the different steps of the procedure and also to make it easier to perform blank measurements and standard calibrations.

The second part of the measurement system that needed a replacement was the National Instrument acquisition card. Originally, this card was used to transfer the pressure and the temperature signal to the LabView program. This card was replaced by an Arduino card as the measurement line does not require the complexity of a National Instrument system. Twelve temperatures indicators, one from each cell, and one pressure indicator have been connected to this card (Fig. 2.9).

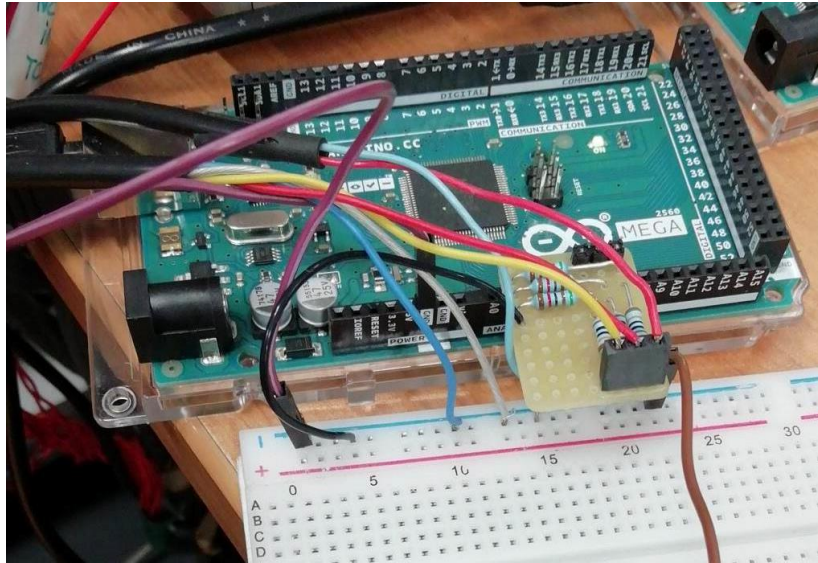


Fig. 2.9: New Arduino card and associated electronic connections.

2.3.4 Comparison of new vs old CH₄ measurement

The modifications only concerned the controlling part of the line and automation of the handling. They were thus no reason to suspect an offset between the new and the previous measurements. The 18 new measurements were performed following the exact procedure described in Loulergue et al., [2008].

A time interval of the EDC CH₄ record composed of previously measured [Loulergue et al., 2008] and 15 of the newly measured CH₄ samples is presented in Fig. 2.10. The good agreement between the old and new measurements gives confidence in the reliability of the new measurement system. Notably, the offset between an old and a new sample taken from a depth difference of 5 cm (corresponding to an age difference of 6 yrs at ~201.6 ka) is of 5.8 ± 7.2 ppb. It is now established that the CH₄ discrete measurement line at IGE can once again operate on ice samples of 45 g at a maximum rate of 24 samples a day with an estimated uncertainty of ± 10 ppb [Loulergue et al., 2008].

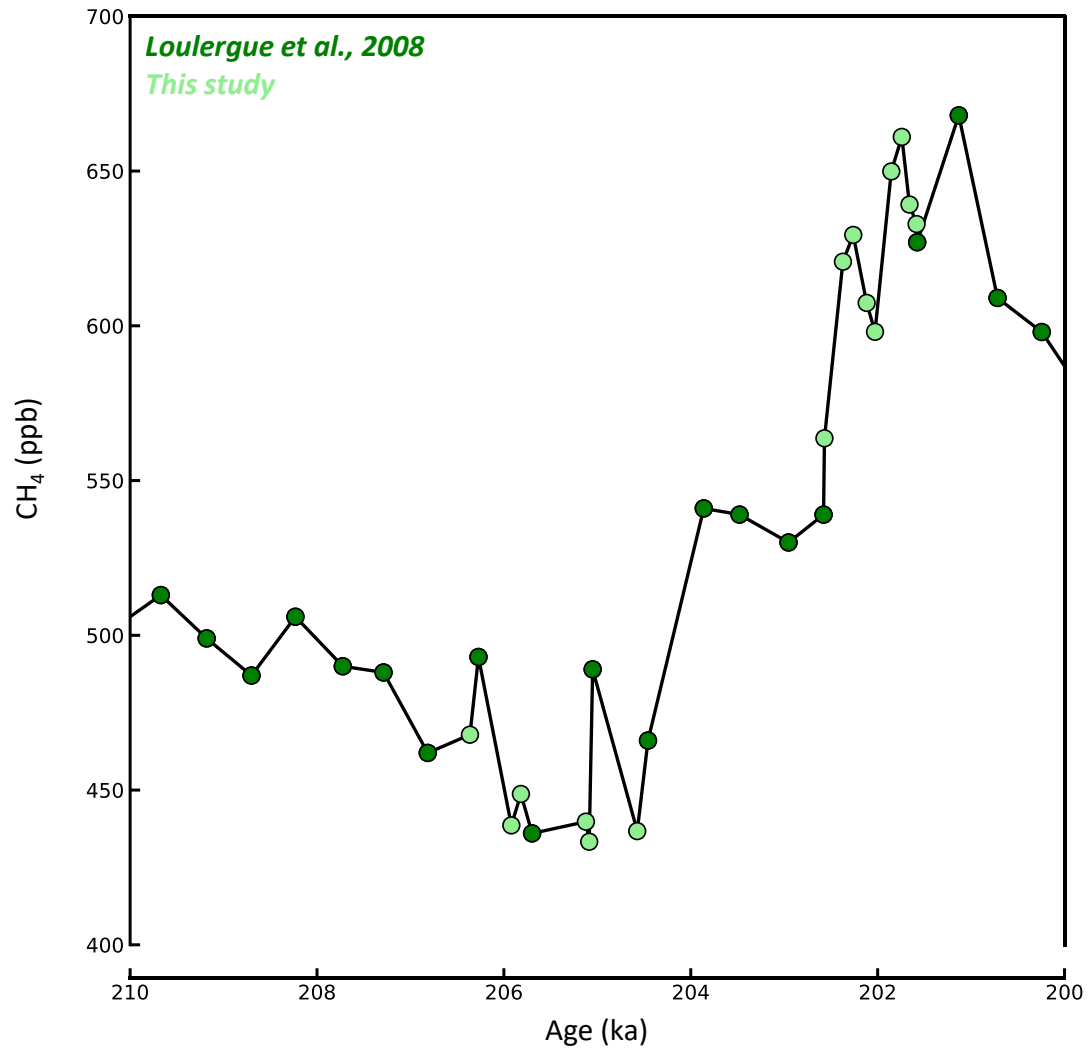


Fig. 2.10: Published and new CH_4 measurements covering the 210-200 ka time-period. a. New CH_4 measurements performed on the EDC ice core (light green dots, this study). Published CH_4 data from the EDC ice core (black green dots) [Loulergue et al., 2008]. Both records are plotted on the AICC2012 gas timescale [Bazin et al., 2013].

2.4. Perspectives

2.4.1 CO₂ measurement system

Using the IGE experimental system, I produced a new high-resolution CO₂ record with low experimental-noise variability. This system could be improved on two main points: (i) the sample weight is relatively high compare to the other laboratories (40 g, Table 2.1) (ii) the measurement cadence is relatively low (four samples/day). In addition, under the scope of the future Beyond EPICA-Oldest Ice (BE-OI) ice core that would provide very old but thin ice at its bottom, it is crucial to develop instruments that would be able to measure several variables in a single sample. To do so, the ANR BIOCOD, led by Roberto Grilli, aims to measure $\delta^{13}\text{C}$ of CO₂ in parallel to the CO₂ concentrations. This project will also replace the current extraction process, measurement line, and measurement system in order to reduce the size of ice samples and increase the measurement cadence. The first tests of this new measurement set-up have been initiated in 2023. The crushing process will remain similar, i.e. a ball mill system. However, the ice chamber and the stainless are currently being re-designed in order to extract more efficiency the air from smaller sample. These new ice chambers should also reduce the dead volume to increase the pressure of gas in the line. The measurement line will be designed to enable simultaneous measurement of several samples in parallel. Finally, the CO₂ concentrations and the isotopic composition of CO₂ will be measured by a laser spectrometer, as currently developed also at Oregon State University, Bern University and British Antarctic Survey laboratories.

2.4.2 CH₄ measurement system

The renewal of the CH₄ system allow to measured up to 24 samples of ~45 g per day. The short-term objective would be to convert the semi-automatic controlled using the LabView program into a Python code to restrain the compatibility problem through time that has caused the main difficulty when fixing the CH₄ experimental set-up of the renewal of the CH₄ system.

Also, while a CFA system has also been developed at IGE to measure CH₄ concentrations, the discrete measurement set-up is still very useful. While the CFA system is a very efficient system to obtain high-resolution records, it is associated with two main limitations: (i) absolute CH₄ concentrations measured with the CFA techniques are still debated [Fourteau et al., 2019] (ii) the use of CFA system requires a continuous stick of ice. For the oldest and most precious ice, such quantity of ice is not systematically available. Thus,

the discrete measurement system remains very complementary to the CFA system to provide CH₄ data for the absolute calibration of the CFA CH₄ record, and to be used when no continuous stick of ice is available. For instance, new CH₄ measurements will be performed using the discrete measurement system on EDC ice samples covering some specific periods of the 800-600 ka interval in 2024 in the framework of the new project Toward Beyond EPICA (ToBE) led by Frederic Parrenin (IGE) and funded by the French Research Agency (2023-2027).

Chapter 3

The role of the carbon cycle in triggering the Mid-Pleistocene Transition

In this first chapter of results, I focus on the orbital-scale variations of the climate and the potential interactions with the carbon cycle during the last 2 Ma. To do so, I explore the mechanisms at the origin of this transition using a conceptual model that aims to reproduce the global ice volume variations over the past 2 Ma. This chapter is composed of a published article in *Communications Earth & Environment* in March 2023, followed by complementary analyses and perspectives.

Chapter 3 aims at:

- 🔗 Investigating the role of the orbital variations in the trigger of the MPT.
- 🔗 Identifying the most relevant temporal structure (i.e. gradual or abrupt) of the mechanism of the internal forcing that triggers the MPT.

Methodology:

- 🔗 Development of a new conceptual model to fit paleodata-based global ice volume reconstructions over the past 2 Ma.

Highlights:

- 🔗 Over the past 2 Ma, the new conceptual model reproduces partially the change in amplitude and frequency of the glacial-interglacial cycles only with the orbital forcing.
- 🔗 The different simulations suggest that a gradual change in the internal climate system, e.g. an atmospheric CO₂ decrease throughout the Pleistocene, is more likely to have caused the MPT than an abrupt event.

Code availability:

- 🔗 The conceptual model used is available to download at https://github.com/EtienneLegrain/ConceptualModel_MPT_Legrain_etal.2023.git

3.1. Introduction

As illustrated in the introductory chapter, the MPT ($\sim 1.2 - 0.8$ Ma) is one of the most intriguing climate transitions that occurred during the Pleistocene. The shift from ~ 41 to ~ 100 ka cycles, is commonly not imputed to the orbital forcing, as no significant changes are observed in the obliquity, precessional and eccentricity signals at this period [Imbrie et al., 1993]. This transition is thus considered to be associated with a change in the internal forcing of the Earth's climate [Berends et al., 2021]. The diversity of physical mechanisms proposed as contributing causes of the MPT includes the cryosphere, lithospheric, oceanic and atmospheric realms (Fig 3.1). Here are given as examples the two main hypotheses proposed to have triggered the MPT:

(i) The atmospheric CO_2 concentrations decline throughout the Pleistocene (gradual mechanism): A close correlation have been founded between global climate and CO_2 concentrations during the last climatic cycles [Petit et al., 1999]. The gradual atmospheric CO_2 decreases is thus a potential trigger to have caused the establishment of 100 ka cycles during the MPT. Willeit et al., [2019] hypothesized a gradual volcanic outgassing decrease during the Pleistocene. This progressive decline of CO_2 concentrations would have caused to miss some potential terminations, leading to the occurrences of longer-than-40 ka climatic cycles. The absence of direct continuous atmospheric CO_2 measurements before the MPT make this assumption complicated to challenge (section 3.3.3.).

(ii) The regolith removal beneath the Laurentide ice sheet (abrupt mechanism): the removal of the thick sediment layer called regolith beneath ice sheets have been studied as a potential cause of the MPT [Clark and Pollard, 1998]. Indeed, the change of substratum from regolith to a high-friction crystalline Precambrian shield bedrock would have reduced the basal velocity of the ice sheet making it more stable. This would have allowed the build-up of larger ice sheets associated with longer glacial periods after the MPT [Clark et al., 2006]. Most studies testing this hypothesis are based on a prescribed regolith without morpho-geological and erosional constraints and categorize this regolith change as abrupt. Estimate of the subglacial erosion rates made unlikely the hypothesis of a gradual removal of regolith over the entire Pleistocene [Jamieson et al., 2008].

Testing those different mechanisms require physical models that simulate their impact on global Earth's climate [Berends et al., 2021]. However, the length of the studied time-period, commonly the last 2 Ma, restricts the use of complex modelling because of the computing time and resources [Berends et al., 2021]. Beyond their nature, the different mechanisms evoked to

explain the MPT can be classified in term of their temporal structure. Some of these mechanisms act over the entire Pleistocene. They are hereafter considered as “gradual” mechanisms. Others mechanisms are thought to occur during a specific time period of the MPT. They are hereafter considered as “abrupt” mechanisms (Fig 3.1).

Testing the relevance of the temporal structure of such mechanisms independently of their nature is commonly done with phenomenological conceptual models, that are not based on physical equations. A posteriori of the simulations, an analogy can be made with the published hypotheses based on the temporal structure criterion. The hypothesis of an absence of any specific temporal structure, i.e. purely externally forced model, can also be tested efficiently with such simple model. Conceptual modelling effort to modelled the global ice volume with an insolation forcing was initiated by Calder, [1974]. In this pioneering study, the global ice volume is supposed to vary linearly with insolation when specific insolation thresholds are overpassed. The results illustrate the ease of orbitally-driven conceptual model to reproduce the glacial-interglacial cyclicality of the 100 ka world. The next major advance was made by Paillard, [1998] who introduces the notion of equilibrium climate states in which the model switches among the global ice volume and orbital forcing values. The model was then extended by Parrenin and Paillard [2003, 2012] with distinct model formulation. These models have demonstrated the ability of a phenomenological approach to reproduce global ice volume variations of the last 1 million year, only considering the global ice volume itself and the input external forcing. More recently, such conceptual models have been extended across the MPT [Imbrie et al., 2011; Leloup et al., 2022].

My study takes place in a context of increasing modelling effort that aims to characterize and understand the underlying mechanisms behind this climatic transition. It consists on an improved version of the model of Parrenin and Paillard, [2012] that aimed to reproduced the global ice volume variations over the past 2 Ma. Fig 3.1 is a conceptual summary of the analysis performed in this chapter. In this study, I used an approach based on the temporal structure of the underlying mechanism behind the MPT to tackle the following questions:

- Is it possible to model the MPT solely by varying the external orbital forcing?
- What is the most relevant temporal structure for a triggering internal mechanism?
- Based on published hypothesis and the identified relevant temporal structure, what would be the most likely triggering mechanism of the MPT?

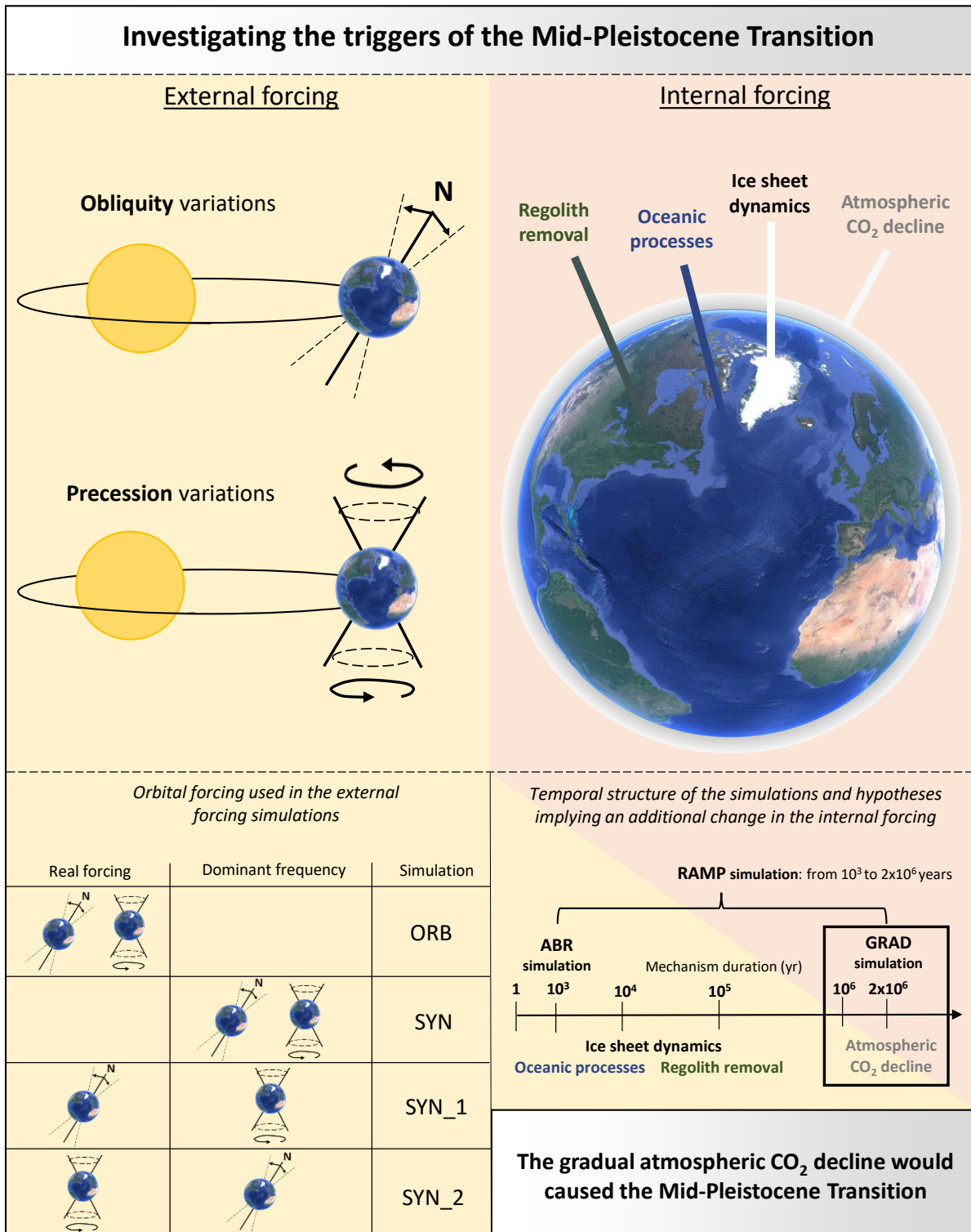


Fig 3.1: Conceptual summary of the analysis performed in Chapter 3. The yellow/red areas refer to the external/internal forcings. The left part presents the orbital forcing considered (top) and the simulations only based on this orbital forcing (ORB, SYN, SYN_1, SYN_2) (bottom). The distinction is made between simulations using the real orbital parameter forcing vs the synthetic orbital parameter forcing that is only composed of the dominant periodicity (~ 21 ka for precession and phase-shifted precession, ~ 41 ka for obliquity). The top right part illustrates the external forcings commonly invoked as potential triggers of the MPT. The bottom right part presents the hypothesis that combines a change in external and internal forcings. The black box indicates the most relevant simulation and its associated mechanism.

3.2. Publication: A gradual change is more likely to have caused the Mid-Pleistocene Transition than an abrupt event

Communications Earth & Environment

Legrain et al., 2023

A gradual change is more likely to have caused the Mid-Pleistocene Transition than an abrupt event

Etienne Legrain ¹✉, Frédéric Parrenin ¹ & Emilie Capron ¹

The Mid-Pleistocene Transition (~1.2–0.8 million years) corresponds to a time interval when high-amplitude ~100,000 years glacial-interglacial cycles replaced the more subdued ~40,000 years glacial-interglacial cycles. Whether it was triggered by physical processes affecting the climate system at a specific time interval or more gradually over the course of the Pleistocene, is still an open question. Here we use an original approach based on conceptual modelling to identify the temporal structure of the Mid-Pleistocene Transition controlling factors. By comparing our new simulations of global ice volume changes with existing paleo-reconstructions over the past 2 million years, we find that it is more relevant to simulate the Mid-Pleistocene Transition with a gradual-rather-than-abrupt change in the climate system. Our results support the hypothesis that a progressive decrease in atmospheric carbon dioxide concentrations throughout the Pleistocene played a key role in triggering this major climatic transition.

¹Université Grenoble Alpes, CNRS, IRD, Grenoble-INP, IGE, 38000 Grenoble, France. ✉email: etienne.legrain@univ-grenoble-alpes.fr

Changes in the Earth's orbit around the Sun, resulting in variations in the amount of received solar insolation on Earth, are responsible for the glacial–interglacial cycles observed throughout the Pleistocene^{1–4}. Somewhere between 1.2 and 0.8 million years (Ma), the glacial–interglacial cyclicity changed from low-amplitude ~40 thousand years (ka) cycles to the current high-amplitude ~100 ka cycles^{5–9}. What has triggered such change of periodicity during this time period, also referred to as the Mid-Pleistocene Transition (MPT), is one of the most intriguing and unsolved questions regarding Pleistocene climate.

While orbital forcing is unanimously recognized as the driver of the Pleistocene climatic cycles, no obvious variation of the main orbital parameters is observed over the MPT^{7,10,11}. Hence, internal causes in the Earth's climatic system have been proposed to explain this major transition from a ~40 ka to a ~100 ka cycle world. Based on the description of these physical mechanisms^{8,12,13}, we propose to divide them into two main groups, one group including what we will refer to hereafter as abrupt mechanisms, and one group gathering more gradual mechanisms.

Hypotheses associated with an abrupt change refer to mechanisms involving a threshold from which a change is observed and the system could not turn back. It is assumed that such mechanisms do not take place during the whole Pleistocene but are specific to the time interval necessary to trigger the transition. Two hypotheses have been investigated so far:

- (i) The MPT would result from the junction of the previously separated Laurentide and Cordillera ice sheets. This junction would provoke a threshold response of the ice-sheet volume^{14,15}. The merging of these two ice sheets during glaciations would have led to a rapid increase in global ice volume without any change in the climatic forcing¹⁴ while their separation during deglaciations would have accelerated their retreat¹⁵. Such a mechanism, dependent on the North American topography, was likely not triggered during the Early Pleistocene as the ice sheet never reached the required size¹⁴.
- (ii) The removal of the thick sediment layer called regolith beneath ice sheets is also mentioned as a possible cause of the MPT. Indeed, the change of substratum from regolith to a high-friction crystalline Precambrian shield bedrock would have reduced the basal velocity of the ice sheet making it more stable. This would have allowed the build-up of larger ice sheets associated with longer glacial periods after the MPT^{13,16,17}. Most studies testing this hypothesis are based on a prescribed regolith without morphological and erosional constraints and categorize this regolith change as abrupt. Estimates of the subglacial erosion rates made unlikely the hypothesis of a gradual removal of regolith over the entire Pleistocene¹⁸.

Hypotheses involving a gradual mechanism correspond to a progressive increase or decrease of a physical climatic parameter throughout the whole Pleistocene. One of the most frequently proposed parameters is the global atmospheric CO₂ concentration, which would have decreased progressively over the Pleistocene^{16,17,19,20}. This hypothesis remains challenging to test. Indeed, continuous atmospheric CO₂ records inferred from Antarctic ice cores only go as far back as 0.8 Ma²¹. Prior to 0.8 Ma, atmospheric CO₂ records have been derived from blue ice^{22,23}, continental sediments²⁴, or marine sediments^{25–27}. However, they are discontinuous, attached to large uncertainty and/or poorly resolved. Still, in the current existing CO₂ records, no decrease over the Pleistocene is found except when only considering the minimum values of atmospheric CO₂ reached at the end of glacial periods^{23,25,26}.

Others studies invoke the role of changes in the Arctic sea ice extent as a mechanism explaining the ~100 ka cycles of the Late Pleistocene^{28,29}. A large extent of sea ice would have caused a positive feedback retroaction and maintains the climate of the Earth under full glacial conditions. This mechanism is directly linked to the ocean surface temperature. Under a given temperature threshold temperature, Arctic sea ice would grow up^{28,29}. A gradual and continuous drop in Arctic temperature would hence be mandatory to explain the appearance of 100 ka only during the Late Pleistocene²¹.

A different approach based on more explicit modelling is used to investigate the potential causes of the MPT^{30–32}. This more physical approach allows us to test scenario that involves a change in the physics of the ice sheet itself before and after the MPT. This bifurcation of the terrestrial parameters of the ice sheets is suspected to play a role in the MPT³¹.

Several models reproduce successfully the MPT using these different hypotheses^{16,19,30–34}. However, it remains difficult to evaluate and compare their relevance as they do not always test the same physical mechanism. Also, they cover a wide range of complexity, going from simple conceptual models to multi-dimensional ice models, including or not carbon cycle feedbacks²⁰. Hence, the controlling factors of the MPT remain one of the biggest unknowns in paleoclimate sciences, and in particular, the role played by atmospheric CO₂ changes. In this context and under the umbrella of the International Partnership on Ice Core Sciences (IPICS), the international ice-core community is currently conducting several ice core drilling projects aiming at recovering a continuous Antarctic ice core to provide the first direct atmospheric CO₂ reconstructions across the MPT³⁵. It is crucial to conduct in parallel new modelling studies investigating the physical processes at the origin of the MPT.

In our study, we use a conceptual model to reproduce the global ice volume variations over the past 2 Ma. Instead of focusing on the nature of the triggering mechanism, we propose to consider its temporal structure as the determining criterion, regardless of the underlying physics. Hence, we investigate whether the MPT was triggered by physical processes affecting the climate system at a specific time interval or alternatively, more gradually over the course of the Pleistocene. Conceptual models have already proven their efficiency in modelling the Pleistocene climate before and after the MPT^{19,36–38}. The advantage of such simple models is that they enable clear identification of the influence of each new input when added to the initial version of the model. For instance, ref. ³⁹ evaluate the influence of different insolation forcing on reproducing the global ice volume changes over the Pleistocene. A family of conceptual models only consider the orbital forcing to reproduce global ice volume changes over Pleistocene^{36–38}. Two of these models apply a prescribed insolation as input^{36,37} while others are forced using a linear combination of the three orbital variables³⁸. They successfully reproduce the triggering of deglaciation over the past 1 Ma. Especially, the model of ref. ³⁸ pointed out the different roles of obliquity and precession during specific Terminations. To simulate global ice volume variations, these conceptual models are all fitted to a reference curve derived from paleo-reconstruction using a number of model parameters.

These model parameters allow to modulate the relative influence of the three orbital parameters and the ice volume itself on the resulting global ice volume computation. They also influence the glaciation and deglaciation thresholds which control in the model, the switch from a “glaciation” state to a “deglaciation” one, and reversely. Conceptual models forced only with orbital forcing reproduce the glacial–interglacial global ice volume variations over the past 1 Ma in term of amplitude and

frequency^{19,37,38}. However, the change in the amplitude and frequency of glacial–interglacial cycles during the MPT cannot be simulated unless the model parameters are changed^{19,39}. Note that ref. ³⁶ reproduce the change in frequency without changing the model parameters. However, they use a detrended benthic foraminifera $\delta^{18}\text{O}$ stack⁴⁰ as a reference curve for global ice volume changes. Hence, this prevents discussing the change in amplitude of the glacial–interglacial cycles during the MPT³⁶.

Ref. ³⁸ successfully reproduce the global ice volume for the last 1 Ma, only based on orbital forcing. The model switches between two states, glaciation and deglaciation, following a threshold mechanism related to the orbital forcing and the modelled global ice volume itself. However, when the model is run over the past 2 Ma, the MPT cannot be reproduced without changing model parameters. Such limitation could reveal the impossibility of reproducing the MPT with these model equations when considering only the orbital forcing. Or, alternatively, it could highlight the inefficiency of the method used in the study to find a combination of parameters allowing to reproduce of the MPT.

Here we use a zero-dimensional conceptual model that calculates changes in global ice volume over time as a function of orbital forcing. Terminations are achieved by introducing a strongly negative term into the mass balance once a certain ice volume threshold is crossed. This new conceptual model is derived from the conceptual model of ref. ³⁸. Our model differs in the exploration of the parameter space as we developed a more efficient inverse method to find the best-fit parameters (see the “Methods” section). Also, our new model reproduces global ice volume variation over the past 2 Ma. We enlarge the simulated time interval compared to previous studies in order to integrate the entire period of the MPT (~1.2–0.8 Ma) as well as multiple pre-MPT 40 ka glacial–interglacial cycles. We thus test the hypothesis of two modes of climate before and after the MPT and our results should be considered under this hypothesis. Alternative simple models have developed another approach implying a change of climate physics through the MPT^{30,31}.

Different forcing hypotheses for the MPT are tested using three simulations performed with our conceptual model in order to compare the relevance of each mechanism:

- (i) The ORB simulation uses only orbital forcing parameters as inputs.
- (ii) The ABR simulation is based on an internal abrupt forcing, in addition to the external forcing. The abrupt forcing is designed as such: the deglaciation threshold, which is the ice volume value that the model has to reach to initiate the deglaciation, differs before and after the timing of the MPT optimally determined by the inverse method. It conceptually reproduces an abrupt MPT as the deglaciation is facilitated before the MPT.
- (iii) The GRAD simulation is based on external forcing plus an internal gradual forcing. In this simulation, the gradual forcing is designed so the deglaciation threshold varies linearly over the last 2 Ma. This deglaciation threshold is thus different at each time step of the model. Contrary to the ABR simulation, no specific timing could be considered to represent the MPT.

In the following, we show that all three simulations reproduce the MPT as seen in the global ice volume reconstruction from ref. ⁴¹ with different degrees of success (see the “Methods” section). Based on our results, we investigate the relative role of internal versus external forcing in the triggering of MPT. Finally, we discuss our model results in the context of the different climate mechanisms proposed to explain the triggering of the MPT.

Results

The MPT in the ORB simulation. No modelling of the internal climate system is accounted for in the ORB simulation as reflected in the fact that the 13 model parameters being kept constant throughout the last 2 Ma (see the “Methods” section). Hence, the global ice volume variations modelled in the ORB simulation offer a basis to investigate the full role of the external forcing on the MPT (Fig. 1). To evaluate the degree of correlation

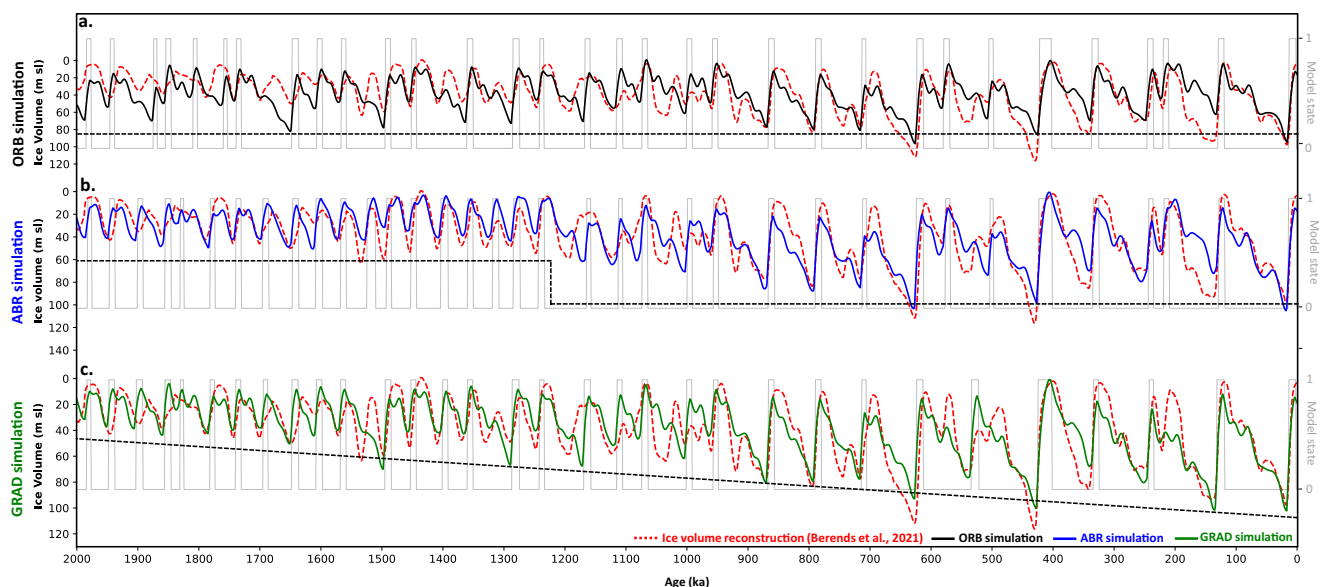


Fig. 1 Simulated and reconstructed global ice volume variations (in metre sea level equivalent, msl) over the last 2 Ma. The ORB (a, black curve), ABR (b, blue), and GRAD (c, green curve) simulations are superimposed onto the reconstructed global ice volume (red dashed curves) from ref. ⁴¹. For each simulation, the grey curve represents the state of the model, deglaciation (1) or glaciation (0) and the evolution of a key model parameter is indicated as a dashed black line. In the ORB simulation, the v_0 parameter is constant throughout the past 2 Ma (dashed black line). In the ABR simulation, the evolution of v_0 can be represented as a step change (dashed black line) between two different values. The optimal timing of the abrupt change in v_0 is at 1220 ka. In the GRAD simulation, the v_0 parameter linearly increases through time over the past 2 Ma.

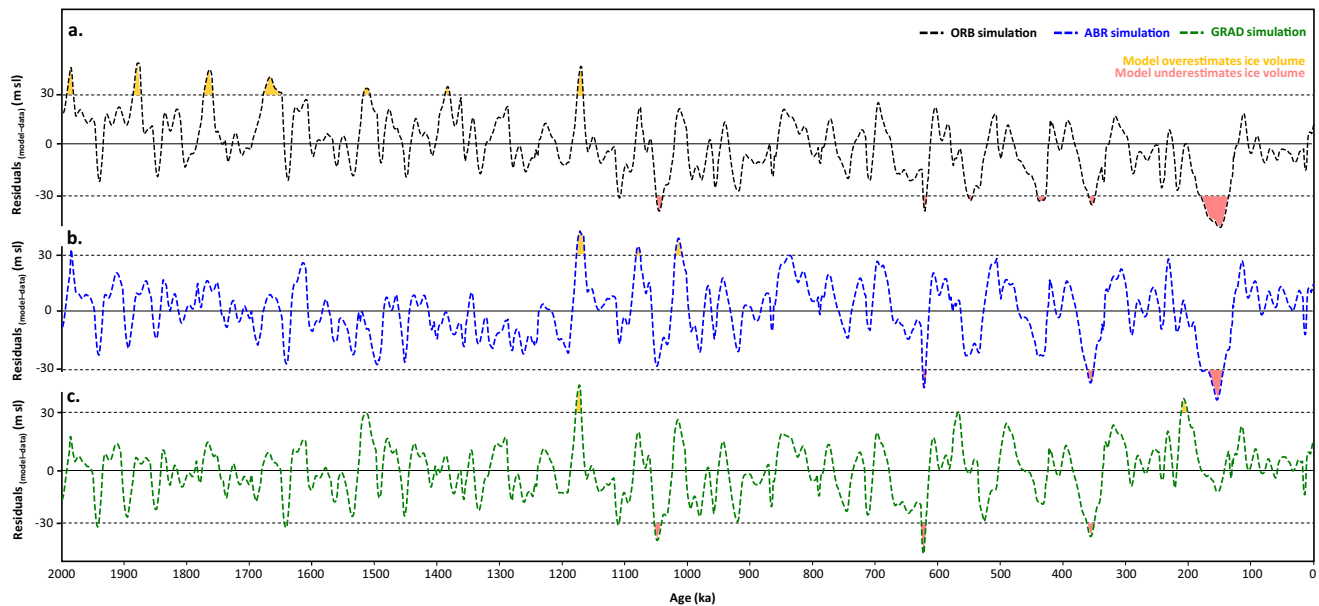


Fig. 2 Residuals between the modelled global ice volume and the reconstructed global ice volume changes. The reconstructed global ice volume is from ref. ⁴¹. ORB (a), ABR (b) and GRAD (c) simulations. Yellow and red areas are time intervals where the model-data deviation exceeds 30 m.

of the modelled global ice volume variations to the reconstructions, we calculate the average of the absolute values of the residuals over the past 2 Ma (Fig. 2). Residuals correspond to the difference between the modelled value and the observed value at the same time (see the “Methods” section). A positive or negative residual implies an underestimation or an overestimation respectively, of the modelled ice volume compared to the reconstructed ice volume changes. Average residuals for 400 ka windows were computed for each of the three simulations (Supplementary Table 1). These values are thus used to investigate the presence of any systematic biases in a specific time window. The modelled global ice volume from the ORB simulation is relatively well correlated with the global ice volume reconstruction for the last 2 Ma with an average absolute value of residuals of 18.1 m and a coefficient of determination R^2 equal to 0.44 (Fig. 1, Supplementary Fig. 1). The 11 terminations of the last 1 Ma are reproduced (Supplementary Fig. 2). All nine periods with residuals superior to 30 m correspond to a modelled global ice volume that is overestimated during interglacial periods (Fig. 2). Before 1 Ma, our model does not reproduce some existing Terminations, i.e. Termination (T) X, TXXII, whereas TIII is artificially doubled (Fig. 1; Supplementary Fig. 2).

The modelled deglaciations are the largest after 1 Ma with an amplitude higher than 70 m, whereas no modelled deglaciation has an amplitude of more than 70 m before 1 Ma (Supplementary Fig. 2). The model reduces the contrast of the amplitude changes before and after the MPT. The periodicity of the modelled deglaciation onsets increases gradually over the past 2 Ma. Residuals are respectively negative and positive before and after 1 Ma (Supplementary Table 1). Still, this is the first time that a simulation from a conceptual model using only orbital forcing can partially reproduce the MPT in terms of both amplitude and frequency without any changes in the model parameters. Two sensitivity tests were performed to confirm the robustness of the MPT transition modelled in the ORB simulation. First, a “model parameter sensitivity” test could demonstrate that it is reasonable to consider that the ORB simulation is mainly sensitive to the parameters controlling the switch from the glaciation to the deglaciation mode (Eq. (6), Supplementary Note 1, Supplementary Fig. 3). Second, a simulation run with a synthetic orbital

forcing was also performed. This synthetic forcing is an orbital forcing where all natural orbital frequencies except the dominant ones (41 ka for obliquity and 21 ka for precession and phase-shifted precession) are removed. The simulations show that ~100 ka cycles are not reproduced when using only the dominant forcing (Supplementary Note 1, Supplementary Fig. 4). This result highlights the important role played by the long-term orbital forcing in the MPT of the ORB simulation (SYN simulation, Supplementary Fig. 4).

The MPT in the ABR simulation. The ABR simulation accounts for both external and internal forcing. In the ABR simulation, the ν_0 parameter, which is the ice volume threshold value responsible for triggering deglaciation, varies abruptly at a specific time. This specific time is optimally inferred by our inverse method and corresponds to 1220 ka (see the “Methods” section for additional information). The modelled global ice volume is highly correlated with the reconstructed one from ref. ⁴¹ for the last 2 Ma. The average absolute value of residuals is 14.4 m and the coefficient of determination R^2 is equal to 0.64 (Fig. 1; Supplementary Figs. 1 and 5). Terminations over the past 2 Ma are all reproduced by the model. Over 1.2–1.6 Ma, the model mainly underestimates the global ice volume (Supplementary Table 1). In particular, the slightly higher global ice volume maxima from the paleo-reconstruction are not simulated (Fig. 2).

Our ABR simulation reproduces the MPT in terms of amplitude and frequency. However, it produces a systematic bias of overestimation before the MPT and underestimation after the MPT of glacial maxima (Supplementary Table 1). It is likely that a longer transition in the ν_0 parameter is required to avoid a systematic temporal bias between the simulated and the reconstructed ice volume changes.

Two additional ABR-type simulations were performed based on abrupt changes of the k_0 and α_g parameters in order to test the sensitivity of our results to the choice of the variable parameter (Supplementary Note 1, Supplementary Figs. 6, 7, Supplementary Table 2). These results have higher residual values (15.7 and 16.5 m) than the ABR simulation and they only reproduce partially the MPT (Supplementary Tables 5, 6). These

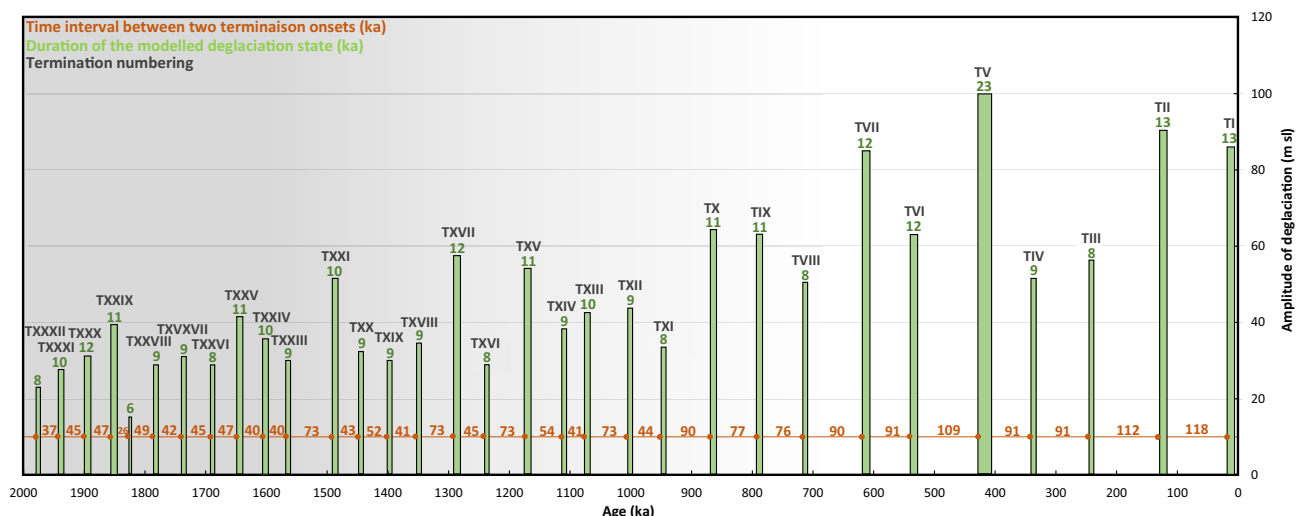


Fig. 3 Temporal structure of glacial-interglacial cycles simulated by the GRAD model. Each green stick corresponds to a deglaciation state. Height of the green stick represents the amplitude of the deglaciation in meter sea level equivalent. The width of each green stick and the associated green number indicate the duration of each of the deglaciation states. Grey roman numerals are termination names. Interval between two consecutive orange dots and the associated orange number corresponds to the time interval between two deglaciation onsets. Grey shaded area corresponds to a period of lower amplitude and higher frequency than the white area.

results confirm the relevance to consider the ν_0 parameter as the main driver of the MPT.

The MPT with the GRAD simulation. The GRAD simulation also aims at simulating the MPT using both external and internal forcing. However, the internal forcing is modelled by a gradual-rather-than-abrupt change to modulate how difficult it is to trigger a deglaciation. Here, the ν_0 parameter influencing the switch from glaciation to deglaciation mode linearly varies through time (see the “Methods” section). The average absolute value of residuals is 13.9 m and the coefficient of determination R^2 is equal to 0.67 (Fig. 1, Supplementary Fig. 1) which are, respectively, the lower and higher values of the three simulations. The GRAD simulation reproduces all but TXXII over the past 2 Ma (Fig. 3). No deglaciation has an amplitude superior to 60 m before 900 ka (Fig. 3). Compared to the ORB and ABR simulations, there is no systematic bias of overestimation or underestimation of global ice volume (Fig. 2). The residuals are centred around zero over the five sliding windows of 400 ka (Supplementary Table 1). To sum up, the GRAD simulation reproduces the MPT both in terms of amplitude and frequency while it has the smallest average residual of the three simulations (13.9 m). Finally, no systematic bias is identified over the past 2 Ma.

Such as for the ABR-type simulations, the sensitivity of the model results to other parameters was tested. Two additional GRAD-type simulations were performed based on the gradual change of the k_0 and α_g parameters (Supplementary Note 1, Supplementary Figs. 6, 7, Supplementary Table 2). These results have higher residual values (15.4 and 16.7 m) than the GRAD simulation and they only reproduce partially the MPT (Supplementary Tables 5, 6). Hence, for this set of simulations too, the results support the fact that it is relevant to consider the ν_0 parameter, i.e. the deglaciation threshold, as the main driver of the MPT.

Spectral analyses of the three simulations. Next, we perform spectral analyses on the modelled global ice volume curves from the three simulations to study the relative amplitude of the 100 and 40 ka signals before and after the MPT using the Discrete Fourier Translation (DFT) method with a Fast Fourier

Translation (FFT) algorithm⁴². The results of the spectral analysis of the three modelled global ice volume curves are compared to the results of the spectral analysis obtained on the global ice volume reconstruction (Fig. 4).

Performed over the last 1 Ma, the spectral analyses of the three global ice volume simulations highlight the dominant periodicities at 100 and 40 ka, as well as a third dominant periodicity at 23 ka, also registered in the global ice volume reconstruction. A higher power for the 100 ka peak compared to the 40 ka peak is observed for the GRAD simulation, which prevails also in the power spectrum for the ice volume reconstructions. This is different from the spectral analyses of the ABR and ORB global ice volume simulations that exhibit 100 and 40 ka peaks of similar power over the last 1 Ma. When performed over the 2–1 Ma time interval, the spectral analysis of the global ice volume reconstruction highlights a 40 ka peak and no peak at 100 ka. Such a pattern is well reproduced in the spectral analyses of the GRAD and ABR simulated global ice volume variations. In contrast, the power spectrum for the ORB simulated global ice volume underlines the existence of a peak at 200 ka in addition to the larger 40 ka peak (Fig. 4).

In summary, the spectral analyses of our modelled global ice volume reconstructions confirm that the three simulations reproduce the MPT with different degrees of success, with the GRAD simulation performing the best.

Quantifying the relevance of the simulations. When calculated over the past 2 Ma, the average residuals of the ORB, ABR and GRAD simulations are respectively 18.1, 14.4 and 13.9 m using 13, 15 and 14 parameters for each model (Supplementary Table 3). The GRAD simulation fits the best with the global ice volume reconstruction compared to the ABR simulation, while it also has less degree of freedom as fewer model parameters are used. Hence, the additional parameter of the GRAD simulation compared to the ORB simulation appears more relevant than the two parameters added in the ABR simulation. To investigate the relative relevance of the three simulations in a quantitative way, we use an objective criterion named the Bayesian Information Criterion (BIC; see Methods). The BIC enables quantifying the relevance of a model against another one^{43–45}. This criterion is

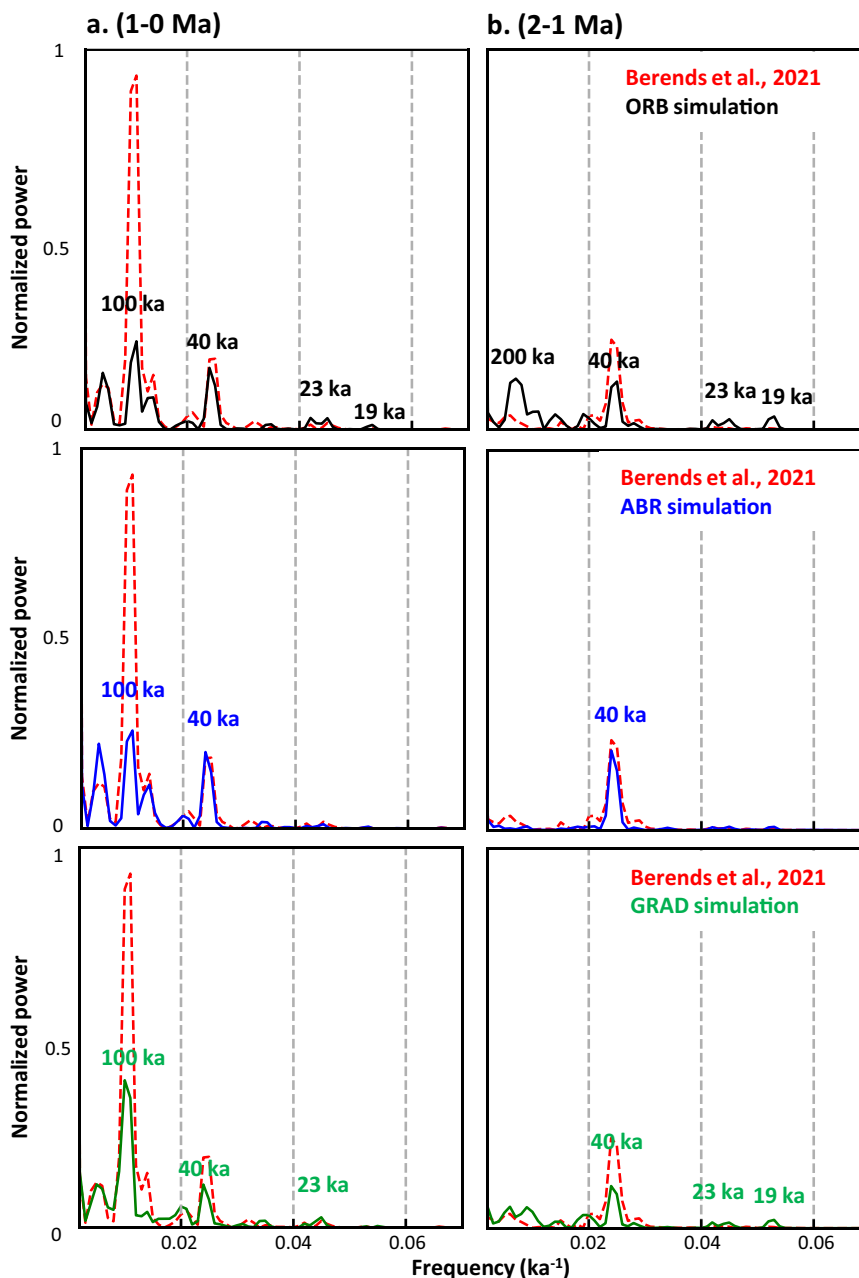


Fig. 4 Spectral analyses on the simulated and reconstructed global ice volume changes. Spectral analyses for the 1-0 Ma (a) and 2-1 Ma (b) time intervals for the ORB (dark), ABR (blue), and GRAD (green) simulations and the global ice volume reconstruction of ref. ⁴¹ (red).

based on the number of independent data, the number of parameters of the model, and the mean of residuals (see the “Methods” section). The ΔBIC_{ij} is the difference between the BIC of model j and the BIC of a model i . If this value is positive, it is an argument in favour of model j . Several degrees of confidence are expressed in function of the value of the positive number (see Methods). If the ΔBIC is superior to 10, the confidence is considered as very strong⁴⁶.

The ΔBIC calculated for the GRAD and ABR simulations against the ORB simulation are very strong, i.e. 61.7 and 49.6, respectively (Table 1). This result highlights the relevance of modelling an internal physical parameter of the Earth system in addition to the orbital forcing to fully reproduce the MPT. In addition, the ΔBIC of the GRAD simulation relative to the one of the ABR simulation is also strong i.e. 12.1 (Table 1), confirming

Table 1 BIC difference $\Delta BIC_{ij} = BIC_j - BIC_i$ for the ORB, GRAD and ABR simulations.

	Vs. ORB simulation	Vs. ABR simulation	Vs. GRAD simulation
ORB simulation	0	-	-
ABR simulation	49.6	0	-
GRAD simulation	61.7	12.1	0

The ΔBIC_{ij} criterion quantifies the evidence in favour of a model i (row) against a model j (column)⁴³. If the value is positive, it means that the model referred to in the row is more relevant than the model referred to in the column.

that using the GRAD simulation is more relevant than the ABR simulation.

Discussion

Previous studies exploring the cause of the MPT dismiss the hypothesis that this transition was solely driven by orbital forcing^{7,11,20,26,47}. They consider that the pre-MPT climate responds linearly to orbital forcing whereas the climate after the MPT is decoupled from orbital forcing through an internal mechanism of the Earth's climatic system^{48,49}. This hypothesis is also supported by an abrupt transition identified in several records from natural climatic archives^{8,12,13}. Also, the fact that up until now, no simple conceptual model could reproduce this transition using solely the orbital forcing as input was in favour of excluding orbital forcing as a potential driver of the MPT. Ref. ³⁶ modelled the MPT only with external forcing inputs and without changing parameters. However, the model is not compared to the original climatic signal. Instead, it is compared to a detrended version of the LR04 benthic foraminifera $\delta^{18}\text{O}$ composite curve⁵⁰. In their study, the signal between 2 and 1 Ma is normalized and centred on the mean and maximum amplitude of the signal of the last 1 Ma. This approach enables to study the model performance regarding the change in the frequency of glacial–interglacial cycles across the MPT and highlights that it is well simulated in their model. However, such a strategy prevents investigating the change in the amplitude of the glacial–interglacial cycles.

Our conceptual model is the first to reproduce at least partially the change in both the frequency and the amplitude of glacial–interglacial cycles observed in paleodata across the MPT without the inclusion of forcing from the internal climate system nor a change in model parameters (ORB simulation). Our sensitivity analysis shows that the most sensitive mechanism behind this simulation is the shift from glaciation to deglaciation mode, i.e. the trigger of the deglaciation (Supplementary Note 1, Supplementary Fig. 3, Supplementary Table 4). This result confirms the crucial role of the trigger of deglaciations in driving the Pleistocene climate.

Ref. ⁵¹ already shows that an internal component of the Earth system could be driven by variations at million-year scale of orbital parameters. A non-linear response to these million-year scale variations in orbital forcing may have played a role in this transition, as suggested by our SYN simulation and this would deserve future dedicated investigations (Supplementary Fig. 4). While the dominant frequencies (21 and 41 ka) are able to reproduce the pre-MPT climate, ~100 ka cycles appear to require a long-term modulation of external forcing. This long-term (hundreds of thousands to a million years) cyclicity in the orbital records might explain the minor role of orbital forcing in the previous studies focusing on the specific time period of the MPT. Still, we show that the ORB simulation globally overestimates and underestimates the amplitude of the glacial–interglacial cycles before and after the MPT respectively (Fig. 1, Supplementary Fig. 2). Thus, an internal component of the climate system is necessary to be coupled with this external forcing to fully explain the MPT.

In the GRAD and ABR simulations, the modulation of the deglaciation threshold conceptually includes a forcing from the internal climate system. The variation in the value of the deglaciation threshold across the MPT, either abruptly or gradually, implies that it becomes more difficult to initiate a deglaciation during the Late Pleistocene rather than the early Pleistocene. Although the nature of the change in the internal climate that is modelled by the change in the deglaciation threshold is not directly constrained by our conceptual model, we can rank the relevance of the different proposed mechanisms of MPT based on their temporal structure.

Erosion of the regolith beneath the Laurentide and Fennoscandian ice sheets is regularly invoked as a likely cause of the MPT^{7,13,16}. With such a hypothesis, the MPT would have begun at the time when all the regolith was removed. Indeed, ice sheets lied on hard crystalline bedrock, reducing basal velocity and allowing ice sheets to be thicker and more stable⁷. This hypothesis focuses on a specific time period for the transition to happen, which could be linked to the clear transition identified in some paleoclimatic records (ref. ⁸: 900 ka; ref. ¹³: between 950 and 860 ka). This mechanism also implies a direct response to the climate, where a binary change will provoke an abrupt transition. However, our results show that despite a major improvement in the model performance when adding a threshold occurring at a specific time, this solution is less relevant than adding a gradual trend to the initial orbital forcing.

The hypothesis of a gradual forcing in the internal climatic system to explain the MPT has been investigated before. For instance, changes in the atmospheric CO_2 concentrations have been proposed as a possible driver of the MPT^{16,19,20,25}. Indeed, a progressive decrease of the atmospheric CO_2 concentrations would have for consequence to gradually cool the Earth²⁰. Ref. ¹⁶ propose that the atmospheric CO_2 is a possible driver of the MPT using a model coupling climate, ice sheets and carbon cycle. However, they show that an additional mechanism, i.e. the regolith removal, is necessary to fully describe the MPT. A characteristic of this study is the fact that the CO_2 trend over the Pleistocene is not constrained by CO_2 data but is only suggested by the linear decrease of an unspecified parameter. Ref. ²⁶ investigates the role of CO_2 in the MPT, but more as a consequence rather than as a possible trigger of the MPT. In fact, they proposed that a change in the ice sheet dynamics would cause an increase in dustiness. This would lead to a fertilization of the Southern Ocean and a consequent decrease in global CO_2 concentrations.

The scarcity of atmospheric CO_2 reconstructions from natural archives before 800 ka makes the assumption of an atmospheric CO_2 concentration decrease throughout the Pleistocene challenging to test. Still, existing CO_2 reconstructions from Boron isotopes of marine sediment cores reach values superior to 400 ppm during the late Pliocene (2.3–3.3 Ma). This corresponds to CO_2 concentrations higher than CO_2 measured in the ice core for the last 800 ka⁵². During the Pleistocene, available data suggest relatively constant CO_2 levels characterizing interglacials prior, during and after the MPT while during glacial maxima, a gradually decreasing trend in CO_2 levels is observed through time^{23,25,26}. As our model is in favour of a gradual change, we hypothesize that an atmospheric CO_2 decrease during glacial times would be enough to provoke a gradually increasing stability of ice sheets during the glacial period, making them less sensitive to insolation variation after the MPT. The ease of the deglaciation trigger would be progressively reduced. Under these conditions, each obliquity cycle would not lead to deglaciation as in the pre-MPT world. Some obliquity cycles would be missed and deglaciations would be triggered through a specific obliquity and precession configuration, generating artificially ~100 ka cycles. The decreasing parameter in our gradual conceptual model could be linked to atmospheric CO_2 . This would create a stochastic and non-linear post-MPT climate, contrary to the obliquity-driven pre-MPT climate.

To conclude, our study tests conceptual hypotheses (e.g. external or internal forcing, abrupt or gradual mechanism) regarding the causes of the MPT and evaluates their efficiency to reproduce global ice volume reconstructions over the past 2 Ma. While our phenomenological model is clearly in favour of a gradual trigger of the MPT, the involvement of a change in atmospheric CO_2 concentrations remains a hypothesis that

requires direct testing. In particular, it would be very valuable and complementary that alternative physical-based approaches relying on more complex⁵³ or more explicit³¹ modelling investigate further our findings so it is possible to provide a direct identification of the physical mechanism behind the equations. With the deep drilling of a new ice core in Antarctica, the on-going European Beyond EPICA–Oldest Ice project aims to provide new climate and environmental records back to 1.5 Ma, and in particular the first continuous millennial-scale atmospheric CO₂ record throughout the MPT^{54,55}. The climate and environmental records from this new ice core should provide key information to progress on our understanding of the mechanisms responsible for the MPT. Understanding the carbon cycle–climate interactions during this major climatic transition from the past will tighten the constraints on the response of the Earth system over long time-scales to future greenhouse gas emissions.

Methods

Conceptual model formulation. The model used in our study is similar in the formulation to the previously published conceptual model of Quaternary climate of ref. 38. These conceptual models aim to reproduce the global ice volume v , i.e. sea level variations with only orbital forcing parameters as input^{19,37–39}. A linear combination of three orbital parameters $Esi \sim e \sin \omega$ (precession, ω the precession angle taken from the vernal equinox), $Eco \sim e \cos \omega$ (phase-shifted precession) and $Ob \sim \varepsilon$ (obliquity) could represent insolation at most latitudes and season³.

The model is composed of two states, the glaciation state “g” and the deglaciation state “d” which represent the climatic system. Two linear equations thus represent the climatic system:

$$g : \frac{dv}{dt} = -\alpha_{Esi} Esi_{tr}(t) - \alpha_{Eco} Eco_{tr}(t) - \alpha_O Ob(t) + \alpha_g \quad (1)$$

$$d : \frac{dv}{dt} = -\alpha_{Esi} Esi_{tr}(t) - \alpha_{Eco} Eco_{tr}(t) - \alpha_O Ob(t) + \alpha_d - \frac{v}{\tau_d} \quad (2)$$

where τ_d is the relaxation time in ka, α_{Esi} , α_{Eco} and α_O are constant parameters in $m \text{ ka}^{-1}$ which allow to give relative weight to the three orbital forcings. α_d and α_g are the speed of deglaciation and glaciation, respectively, in $m \text{ ka}^{-1}$. “Ob” is obliquity normalized to zero mean and unit variance and Esi and Eco are, respectively, calculated from Esi and Eco the precession parameters normalized to zero mean and unit variance using a truncation function:

$$\text{if } x \leq 0 : f(x) = x + \sqrt{4a^2 + x^2} - 2a \quad (3)$$

$$\text{if } x > 0 : f(x) = x \quad (4)$$

where a is a constant with $a = 1.06587$ from ref. 37. This truncation is similar to the one used by ref. 19.

The model can switch from one state to another if a threshold ice volume is exceeded by a linear combination of the 3 orbital parameters (plus ice volume for g to d transition):

$$g \text{ to } d : k_{Esi} Esi(t) + k_{Eco} Eco(t) + k_{Ob} Ob(t) + v > v_0 \quad (5)$$

(and $k_{Esi} Esi(t) + k_{Eco} Eco(t) + k_{Ob} Ob(t) \geq v_1$)

$$d \text{ to } g : k_{Esi} Esi(t) + k_{Eco} Eco(t) + k_{Ob} Ob(t) < v_1 \quad (6)$$

(and $k_{Esi} Esi(t) + k_{Eco} Eco(t) + k_{Ob} Ob(t) + v \leq v_0$)

With v_0 the ice volume above which the model switches to the deglaciation mode and v_1 the ice volume below which the model switches to the glaciation mode. These two parameters represent a limiting value that defines the range in which the ice volume is allowed to vary during the simulation. The physical interpretation of these parameters is that they represent the maximum and minimum size of the ice sheet under full glacial and deglacial conditions.

This initial version of the conceptual model, is similar in the equations formulation to the one of ref. 37, is the so-called ORB simulation in the following study.

Variants of the orbital conceptual model. In order to test the internal forcing climatic hypothesis, we develop two variants of the ORB simulation: (i) the ABR simulation and (ii) the GRAD simulation. These models are similar to the ORB simulation, except for the formulation of the g to d transition.

(i) For the ABR simulation, we use a distinct value of v_0 depending if we are after or before a threshold age T

If $t > T$:

$$v_0 = v_{0b} \quad (7)$$

If $t < T$:

$$v_0 = v_{0a} \quad (8)$$

where t is the discretized time, v_{0a} and v_{0b} are two values of v_0 determined from our inverse method.

(ii) For the GRAD simulation, we add a parameter C to the v_0 parameter which drops continuously the ice volume threshold along the time period of the model.

$$v_0(t) = v_0(t=0) + Ct \quad (9)$$

where t is the discretized time.

Finally, orbital, gradual and abrupt models are, respectively, composed of 13, 14 and 15 parameters (Supplementary Table 3). We solve the evolution of v over the last 2 Ma using a Runge–Kutta 4th order method with a time step of 1000 yr for the 3 models.

Use of the global ice volume reconstruction from Berends et al. (2021)⁴¹. We fit the model to the global ice volume reconstruction of ref. 41 which is based on the LR04 marine benthic foraminifera $\delta^{18}\text{O}$ stack⁵⁰. The use of this global ice volume reconstruction as a reference could induce two main biases in the model–data comparison. Firstly, ref. 41 deconvolute the initial isotopic signal of the LR04 stack, which is influenced by both global ice volume and deep-ocean temperature. The global ice volume quantification is obtained through a coupled model of the Northern Hemisphere ice sheets and ocean temperatures⁴¹. Secondly, the chronology of the LR04 stack is partially built using an orbital tuning-based dating method⁵⁰. However, the use of a global ice volume reconstruction instead of an isotopic record allows to provide dimensional and quantified model–data deviation in terms of sea level equivalent. Additionally, the isotopic signal from distinct oceanic basin has shown asynchronous variations at the onset of deglaciations^{56,57}. Such asynchronicity is also observed during the MPT, due to the diversity of statistical tools used to analyse the data and to the criterion used to determine the onset of MPT^{7,20}.

Note that we also fit the model to the global ice volume reconstruction from refs. 16,58. These ice volume reconstructions exhibit some differences from the more recent one from ref. 41, in particular, the amplitude of glacial–interglacial cycles appears larger. Using these two alternative records does not impact the conclusions of our study, i.e. the GRAD simulation is still the most appropriate to reproduce the MPT. We are aware of the limitations associated with a modelled reconstruction based on stacked benthic $\delta^{18}\text{O}$ records but it has the advantage to provide information at a global scale, i.e. the global ice volume changes. Indeed, other paleorecords covering the MPT are mainly interpreted as representative of local climate and/or environmental changes⁸.

Model fit to the global ice volume reconstructions using a Monte Carlo method.

As in ref. 37, we use a random walk based on the Metropolis algorithm^{59,60} to select the most probable experiments. In this study, we improve the selection of the best-fit parameters using a random walk with N walkers with the eemc python module⁶¹. The previously developed methodology³⁷ is a simplified case of this method with one walker. Our method allows to optimize the selection of the best parameters as it is more efficient to explore the parameter space⁶¹. For each model, we perform 100,000 experiments using a random walk at 30 walkers and we extracted the best-fit vectors of parameters for each model (Supplementary Table 3).

Model comparison method. In order to evaluate the relative relevance of each of the three simulations, we compare them using the Bayesian Information Criterion (BIC). This criterion quantifies the evidence in favour of a model against another model^{43,44}. It is expressed as following:

$$\text{BIC} = -2\ln L(\theta) + K \ln N \quad (10)$$

where N is the number of independent data points, K the number of model parameters and $\ln L(\theta)$ is the maximum log-likelihood, defined here as the χ^2 . We estimate N as 200, which corresponds to one independent data point every 10 ka, i.e. approximately at each ice volume extremum.

To compare directly two models, we compute the ΔBIC_{ij} , which is the BIC difference between two models:

$$\Delta\text{BIC}_{ij} = \text{BIC}_j - \text{BIC}_i \quad (11)$$

The ΔBIC could be directly interpreted as following: the evidence of the dominance of the relevance of the model j over model i is weak if $0 < \Delta\text{BIC}_{ij} < 2$, positive if $2 < \Delta\text{BIC}_{ij} < 6$, strong if $6 < \Delta\text{BIC}_{ij} < 10$, and very strong if $\Delta\text{BIC}_{ij} > 10$ (42).

Calculating the average residuals between simulated and reconstructed ice volume change. Here we investigate the influence of the high degree of freedom of our model on the ability of the three simulations to fit the reconstructed global ice volume. To do so, we quantify the residuals for our three simulations and also

perform an additional “test” simulation. The average residuals correspond to the average difference between simulated and reconstructed global ice volume. The average standard deviation of the ice volume reconstruction is 24.8 m. If our model was the simplest possible with no degree of freedom, i.e. a constant value of ice volume, the residual model data would thus be 24.8 m. In comparison, residuals for the ORB, ABR and GRAD simulations are, respectively, 18.1, 14.4, and 13.9 m. One could question if the ability of our model to represent the MPT is only due to the high degree of freedom of our model (from 13 to 15 parameters) and the sinusoidal nature of the input forcing. To test this, we evaluate if the ORB residual value of 18.1 m represents a significant improvement compared to the 24.8 m estimate. We run a “test” simulation over the past 2 Ma using the orbital forcing parameters corresponding to the 4–2 Ma interval. By using such “inappropriate” forcing we obtain a residual value of 20.4 m. This illustrates that the inverse method used in our model can reduce the model-data mismatch by about 4 m. However, the orbital forcing from the correct period (2–0 Ma) is required to further reduce the residual value to 18.1 m. This result illustrates that the significant reduction of the model-data mismatch in the ORB simulation is due to the use of the orbital forcing corresponding to the appropriate time period (2–0 Ma) period rather than the high degree of freedom of our model.

Reporting summary. Further information on research design is available in the Nature Portfolio Reporting Summary linked to this article.

Data availability

The data used to run the model and the model outputs are available at https://github.com/EtienneLegrain/ConceptualModel_MPT_Legrain_etal.2023.git.

Code availability

The conceptual model used is available to download at https://github.com/EtienneLegrain/ConceptualModel_MPT_Legrain_etal.2023.git.

Received: 6 September 2022; Accepted: 13 March 2023;

Published online: 23 March 2023

References

- Milankovitch, M. M. Canon of insolation and the Iceage problem. *Koniglich Serbische Akad. Beogr. Special Publ.* **132**, 1–633 (1941).
- Berger, A. Long-term variations of daily insolation and Quaternary climatic changes. *J. Atmos. Sci.* **35**, 2362–2367 (1978).
- Loutre, M. F. *Paramètres orbitaux et cycles diurne et saisonnier des insolutions*. Doctoral dissertation, UCL-Université Catholique de Louvain (1993).
- Laskar, J. et al. A long-term numerical solution for the insolation quantities of the Earth. *Astron. Astrophys.* **428**, 261–285 (2004).
- Shackleton, N. J. & Opdyke, N. D. Oxygen isotope and palaeomagnetic evidence for early Northern Hemisphere glaciation. *Nature* **270**, 216–219 (1977).
- Medina-Elizalde, M. & Lea, D. W. The mid-Pleistocene transition in the tropical. *Pac. Sci.* **310**, 1009–1012 (2005).
- Clark, P. U. et al. The middle Pleistocene transition: characteristics, mechanisms, and implications for long-term changes in atmospheric pCO₂. *Quat. Sci. Rev.* **25**, 3150–3184 (2006).
- Elderfield, H. et al. Evolution of ocean temperature and ice volume through the mid-Pleistocene climate transition. *Science* **337**, 704–709 (2012).
- Past Interglacials Working Group of PAGES. Interglacials of the last 800,000 years. *Rev. Geophys.* **54**, 162–219 (2016).
- Imbrie, J. et al. On the structure and origin of major glaciation cycles. 2. The 100,000-year cycle. *Paleoceanography* **8**, 699–735 (1993).
- Lisiecki, L. E. Links between eccentricity forcing and the 100,000-year glacial cycle. *Nat. Geosci.* **3**, 349–352 (2010).
- Ford, H. L., Sosdian, S. M., Rosenthal, Y. & Raymo, M. E. Gradual and abrupt changes during the Mid-Pleistocene transition. *Quat. Sci. Rev.* **148**, 222–233 (2016).
- Yehudai, M. et al. Evidence for a Northern Hemispheric trigger of the 100,000-y glacial cyclicity. *Proc. Natl Acad. Sci. USA* **118**, e2020260118 (2021).
- Bintanja, R. & Van de Wal, R. S. W. North American ice-sheet dynamics and the onset of 100,000-year glacial cycles. *Nature* **454**, 869–872 (2008).
- Gregoire, L. J., Payne, A. J. & Valdes, P. J. Deglacial rapid sea level rises caused by ice-sheet saddle collapses. *Nat. Lett.* **487**, 219–222 (2012).
- Willeit, M., Ganopolski, A., Calov, R. & Brovkin, V. Mid-Pleistocene transition in glacial cycles explained by declining CO₂ and regolith removal. *Sci. Adv.* **5**, eaav7337 (2019).
- Raymo, M. E. The timing of major climate terminations. *Paleoceanography* **12**, 577–585 (1997).
- Jamieson, S. S., Hulton, N. R. & Hagdorn, M. Modelling landscape evolution under ice sheets. *Geomorphology* **97**, 91–108 (2008).
- Paillard, D. The timing of Pleistocene glaciations from a simple multiple-state climate model. *Nature* **391**, 378–381 (1998).
- Berends, C. J., Köhler, P., Lourens, L. J. & van de Wal, R. S. W. On the cause of the mid-Pleistocene transition. *Rev. Geophys.* **59**, e2020RG000727 (2021).
- Bereiter, B. et al. Revision of the EPICA Dome C CO₂ record from 800 to 600 kyr before present. *Geophys. Res. Lett.* **42**, 542–549 (2015).
- Higgins, J. A. et al. Atmospheric composition 1 million years ago from blue ice in the Allan Hills, Antarctica. *Proc. Natl Acad. Sci. USA* **112**, 6887–6891 (2015).
- Yan, Y. et al. Two-million-year-old snapshots of atmospheric gases from Antarctic ice. *Nature* **574**, 663–666 (2019).
- Da, J., Zhang, Y. G., Li, G., Meng, X. & Ji, J. Low CO₂ levels of the entire Pleistocene epoch. *Nat. Commun.* **10**, 1–9 (2019).
- Hönisch, B., Hemming, N. G., Archer, D., Siddall, M. & McManus, J. F. Atmospheric carbon dioxide concentration across the mid-Pleistocene transition. *Science* **324**, 1551–1554 (2009).
- Chalk, T. B. et al. Causes of ice age intensification across the Mid-Pleistocene Transition. *Proc. Natl Acad. Sci. USA* **114**, 13114–13119 (2017).
- Yamamoto, M. et al. Increased interglacial atmospheric CO₂ levels followed the mid-Pleistocene Transition. *Nat. Geosci.* **15**, 307–313 (2022).
- Gildor, H. & Tziperman, E. Sea ice as the glacial cycles’ climate switch: role of seasonal and orbital forcing. *Paleoceanography* **15**, 605–615 (2000).
- Gildor, H. & Tziperman, E. A sea ice climate switch mechanism for the 100-ka glacial cycles. *J. Geophys. Res.: Oceans* **106**, 9117–9133 (2001).
- Nyman, K. H. & Ditlevsen, P. D. The middle Pleistocene transition by frequency locking and slow ramping of internal period. *Clim. Dyn.* **53**, 3023–3038 (2019).
- Verbitsky, M. Y., Crucifix, M. & Volobuev, D. M. A theory of Pleistocene glacial rhythmicity. *Earth Syst. Dyn.* **9**, 1025–1043 (2018).
- Verbitsky, M. Y. & Crucifix, M. ESD Ideas: The Pecllet number is a cornerstone of the orbital and millennial Pleistocene variability. *Earth Syst. Dyn.* **12**, 63–67 (2021).
- De Boer, B., Lourens, L. J. & Van De Wal, R. S. ent 400,000-year variability of Antarctic ice volume and the carbon cycle is revealed throughout the Plio-Pleistocene. *Nat. Commun.* **5**, 1–8 (2014).
- Daruka, I. & Ditlevsen, P. D. A conceptual model for glacial cycles and the middle Pleistocene transition. *Clim. Dyn.* **46**, 29–40 (2016).
- Dahl-Jensen, D. Drilling for the oldest ice. *Nat. Geosci.* **11**, 703–704 (2018).
- Imbrie, J. Z., Imbrie-Moore, A. & Lisiecki, L. E. A phase-space model for Pleistocene ice volume. *Earth Planet. Sci. Lett.* **307**, 94–102 (2011).
- Parrenin, F. & Paillard, D. Amplitude and phase of glacial cycles from a conceptual model. *Earth Planet. Sci. Lett.* **214**, 243–250 (2003).
- Parrenin, F. & Paillard, D. Terminations VI and VIII (~530 and ~720 kyr BP) tell us the importance of obliquity and precession in the triggering of deglaciations. *Clim. Past* **8**, 2031–2037 (2012).
- Leloup, G. & Paillard, D. Influence of the choice of insolation forcing on the results of a conceptual glacial cycle model. *Clim. Past* **18**, 547–558 (2022).
- Lisiecki, L. E. & Raymo, M. E. Plio–Pleistocene climate evolution: trends and transitions in glacial cycle dynamics. *Quat. Sci. Rev.* **26**, 56–69 (2007).
- Berends, C. J., De Boer, B. & Van De Wal, R. S. Reconstructing the evolution of ice sheets, sea level, and atmospheric CO₂ during the past 3.6 million years. *Clim. Past* **17**, 361–377 (2021).
- Rao, K. R., Kim, D. N., & Hwang, J. J. Fast Fourier transform: algorithms and applications, Vol. 32 (Springer, Dordrecht, 2010).
- Kass, R. E. & Raftery, A. E. Bayes factors. *J. Am. Stat. Assoc.* **90**, 773–795 (1995).
- Mitsui, T. & Crucifix, M. Influence of external forcings on abrupt millennial-scale climate changes: a statistical modelling study. *Clim. Dyn.* **48**, 2729–2749 (2017).
- Mitsui, T., Tzedakis, P. C. & Wolff, E. W. Insolation evolution and ice volume legacies determine interglacial and glacial intensity. *Clim. Past* **18**, 1983–1996 (2022).
- Raftery, A. E. Bayesian model selection in social research. *Sociol. Methodol.* **25**, 111–163 (1995).
- Maslin, M. A., & Ridgwell, A. J. Mid-Pleistocene revolution and the ‘eccentricity myth’. *Geol. Soc. Lond. Spec. Publ.* **247**, 19–34 (2005).
- Imbrie, J. et al. On the structure and origin of major glaciation cycles 1. Linear responses to Milankovitch forcing. *Paleoceanography* **7**, 701–738 (1992).
- Maslin, M. A. & Brierley, C. M. The role of orbital forcing in the Early Middle Pleistocene Transition. *Quat. Int.* **389**, 47–55 (2015).
- Lisiecki, L. E. & Raymo, M. E. A Pliocene–Pleistocene stack of 57 globally distributed benthic $\delta^{18}O$ records. *Paleoceanography* **20**, PA1003 (2005).
- Paillard, D. The Plio-Pleistocene climatic evolution as a consequence of orbital forcing on the carbon cycle. *Clim. Past* **13**, 1259–1267 (2017).

52. Martínez-Botí, M. A. et al. Plio-Pleistocene climate sensitivity evaluated using high-resolution CO₂ records. *Nature* **518**, 49–54 (2015).
53. Abe-Ouchi, A. et al. Insolation-driven 100,000-year glacial cycles and hysteresis of ice-sheet volume. *Nature* **500**, 190–193 (2013).
54. Fischer, H. et al. Where to find 1.5 million yr old ice for the IPICS “Oldest-Ice” ice core. *Clim. Past* **9**, 2489–2505 (2013).
55. Parrenin, F. et al. Is there 1.5-million-year-old ice near Dome C, Antarctica? *Cryosphere* **11**, 2427–2437 (2017).
56. Skinner, L. C. & Shackleton, N. J. An Atlantic lead over Pacific deep-water change across Termination I: implications for the application of the marine isotope stage stratigraphy. *Quat. Sci. Rev.* **24**, 571–580 (2005).
57. Stern, J. V. & Lisiecki, L. E. Termination I timing in radiocarbon-dated regional benthic $\delta^{18}O$ stacks. *Paleoceanography* **29**, 1127–1142 (2014).
58. Bintanja, R., Van De Wal, R. S. & Oerlemans, J. Modelled atmospheric temperatures and global sea levels over the past million years. *Nature* **437**, 125–128 (2005).
59. Metropolis, N., Rosenbluth, A. W., Rosenbluth, M. N., Teller, A. H. & Teller, E. Equation of state calculations by fast computing machines. *J. Chem. Phys.* **21**, 1087–1092 (1953).
60. Hastings, W. K. Monte Carlo sampling methods using Markov chains and their applications. *Biometrika* **57**, 97–109 (1970).
61. Foreman-Mackey, D., Hogg, D. W., Lang, D. & Goodman, J. emcee: the MCMC hammer. *Publ. Astron. Soc. Pac.* **125**, 306 (2013).

Acknowledgements

We thank Didier Paillard, Gaëlle Leloup, and Dominique Raynaud for their very insightful comments on this article. We thank Michel Crucifix for his help in the modelling work. We thank the two reviewers Tijn Berends and Mikhail Verbitsky for their insightful comments that significantly improve the final version of the manuscript. This study is an outcome of the Make Our Planet Great Again HOTCLIM project, it received the financial support from the French National Research Agency under the “Programme d’Investissements d’Avenir” (ANR-19-MPGA-0001). This publication was also generated in the frame of the Beyond EPICA Oldest Ice Core (BE-OI) project. The BE-OI project has received funding from the European Union’s Horizon 2020 research and innovation programme under grant agreement no. 815384 (Oldest Ice Core). It is supported by national partners and funding agencies in Belgium, Denmark, France, Germany, Italy, Norway, Sweden (through the Crafoord Foundation), and Switzerland, The Netherlands and the United Kingdom. Logistic support is mainly provided by ENEA and IPEV through the Concordia Station system. The opinions expressed and arguments employed herein do not necessarily reflect the official views of the European Union

funding agency or other national funding bodies. This is Beyond EPICA publication number 31.

Author contributions

F.P. and E.L. designed research; E.L., F.P. and E.C. performed research; E.L. wrote a draft of the paper, with subsequent inputs from E.C. and F.P.

Competing interests

The authors declare no competing interests.

Additional information

Supplementary information The online version contains supplementary material available at <https://doi.org/10.1038/s43247-023-00754-0>.

Correspondence and requests for materials should be addressed to Etienne Legrain.

Peer review information *Communications Earth & Environment* thanks C.J. Berends and Mikhail Verbitsky for their contribution to the peer review of this work. Primary Handling Editors: Rachael Rhodes and Aliénor Lavergne.

Reprints and permission information is available at <http://www.nature.com/reprints>

Publisher’s note Springer Nature remains neutral with regard to jurisdictional claims in published maps and institutional affiliations.



Open Access This article is licensed under a Creative Commons Attribution 4.0 International License, which permits use, sharing, adaptation, distribution and reproduction in any medium or format, as long as you give appropriate credit to the original author(s) and the source, provide a link to the Creative Commons license, and indicate if changes were made. The images or other third party material in this article are included in the article’s Creative Commons license, unless indicated otherwise in a credit line to the material. If material is not included in the article’s Creative Commons license and your intended use is not permitted by statutory regulation or exceeds the permitted use, you will need to obtain permission directly from the copyright holder. To view a copy of this license, visit <http://creativecommons.org/licenses/by/4.0/>.

© The Author(s) 2023

Supplementary Information to:

A gradual change is more likely to have caused the Mid-Pleistocene Transition than an abrupt event

Etienne Legrain^{1*}, Frédéric Parrenin¹, Emilie Capron¹

1 Univ. Grenoble Alpes, CNRS, IRD, Grenoble-INP, IGE, 38000, Grenoble, France

*Corresponding author: etienne.legrain@univ-grenoble-alpes.fr

Supplementary Note 1

Evaluating the robustness of the results from the ORB simulation

Testing the sensitivity to changes in model parameter values

We performed a sensitivity test to evaluate how our results from the ORB simulation are sensitive to small changes in the values of the parameters. For that, we deviate by +/- 20% of its original value the value taken in the best simulation, for each model parameter (Supplementary Table 2, Supplementary Figure 3). When proceeding as such for a given parameter, all the other ones of the simulation remain constant. The co-variance of parameter in the estimation of model sensitivity to parameters is thus not considered. We then run the simulations at a step of 0.01% of resolution and compute residuals for each of these simulations. Results are presented in Supplementary Figure 3. The discontinuous aspect of residuals change is due to the binary structure of the model, based on a glaciation (g) and a deglaciation mode (d). Every added, removed, or displaced g-to-d or d-to-g change will provoke an abrupt jump in the residuals value. We thus decided to consider the percentage of the values that result in an acceptably low residual interval, rather than to limit our analysis to the very local variability near the optimum value. We fixed this threshold at 10% above the best residual value from the ORB simulation. We applied this threshold value because we consider that above this value, the MPT is no longer reproduced by the model. Based on this threshold, we compute the percentage of simulations within the $\pm 20\%$ range of parameter change, that reproduces the MPT. Results are presented in Supplementary Table 4. The four most impacting parameters are the four parameters defining the deglaciation equation of the model, i.e. kO , $v0$, $kEco$ and $kEsi$. Among these four parameters, three of them are specific to an orbital forcing while the $v0$ parameter is a general deglaciation threshold which apply to the entire system. These are strong arguments in favour of using the $v0$ parameter to simulate

a gradual or abrupt change in the MPT. Also, this result confirms the robustness of the results obtained in the ORB simulation.

Testing the role of long-term modulation of orbital frequencies on the model results with the SYN simulation

Here we want to investigate the potential role of long-term orbital frequency in the ability of the ORB simulation to partially simulate the MPT. For that, we define an extreme case study where all natural orbital frequencies except the dominant ones (41 kyr for obliquity and 21kyr for precession and phase-shifted precession) are removed. The SYN simulation is based on the exact same model equations than the ORB simulation. However, the input forcings of the two models are different. While the ORB simulation is forced by reconstructed external forcing from Ref. 4, the SYN simulation is forced by a synthetic signal based on dominant frequencies of the ORB simulation forcings (Supplementary Figure 4). The three orbital forcings of the SYN simulation have the same mean and standard deviation than the ones of the ORB simulation. However, they vary only as a function of their dominant frequency: 21 kyr for the precession and phase shifted precession, and 41 kyr for the obliquity. The SYN simulation was run following the same methodology as the ORB, GRAD and ABR simulation (see methods), the SYN global ice volume simulation corresponds to the optimal fit from 100 000 experiments. The average. The average of absolute value of residuals between the simulated and reconstructed global ice volume of the SYN simulation is 19.7 m (against 18.1 m for the ORB simulation). Globally, the SYN simulation is able to reproduce the 41 kyr cyclicity of the pre MPT world, even if the model does not simulate any deglaciations over this period (Supplementary Figure 4). However, the SYN simulation do not reproduce any 100 kyr cycles after the MPT. In the SYN simulation, the model reinforced the influence of the obliquity over precession forcing by reducing the α_{Esi}/α_O and α_{Eco}/α_O ratios compared to the others simulations (Supplementary Table 2). The model generates thus more easily the 40kyr obliquity-driven cycles than the more complex 100 kyr cycles. This result suggests that the pre MPT climate is dominated by the most prominent frequency of the orbital forcing while the post MPT climate appears to require long-term modulation of orbital frequencies.

Evaluating the sensitivity of the ABR and GRAD simulations to the choice of the MPT-driven model parameter

Here we test the sensitivity of our main result (i.e., a gradual rather than abrupt mechanism triggers the MPT) to our initial hypothesis of a v_0 -driven MPT. We investigate the hypothesis of an αg -driven MPT and an kO -driven MPT. For that, we performed four additional simulations based on the abrupt or gradual change of the αg and kO parameter.

First, the k_0 parameter was chosen since our sensitivity test presented in the section above highlights that even a small change in its value could have a strong impact on the model results from the ORB simulation (Supplementary Figure 7).

The two simulations, called ABR k_0 and GRAD k_0 are similar to the ORB simulation, except for the formulation of the g to d transition.

(i) For the ABR k_0 simulation, we use a distinct value of k_0 between after or before a threshold age T_{k_0} :

If $t > T$:

$$k_0 = k_{0a}$$

If $t < T$:

$$k_0 = k_{0b}$$

(ii) For the GRAD k_0 simulation, we add a parameter C_{k_0} to the k_0 parameter which drop continuously the ice volume threshold along the time period of the model.

$$k_0(t) = k_0(t=0) + C_{k_0} C \times t$$

Where t is the discretized time.

Second, the α_g parameter is the most impacting parameter that belongs to the glacial mode (eq.1) (Supplementary Table 4, Supplementary Figures 3,6). We consider the glacial mode as one of the potential drivers of the MPT in our model as the MPT in the reconstruction of ice volume is characterized by an increase of the ice sheet size during glacial periods. Thus, we simulate an α_g -driven MPT.

The two simulations, called ABR α_g and GRAD α_g are similar to the ORB simulation, except for the formulation of the g mode.

(i) For the ABR α_g simulation, we use a distinct value of α_g depending if we are after or before a threshold age T_{k_0} :

If $t > T$:

$$\alpha_g = \alpha_{ga}$$

If $t < T$:

$$\alpha_g = \alpha_{gb}$$

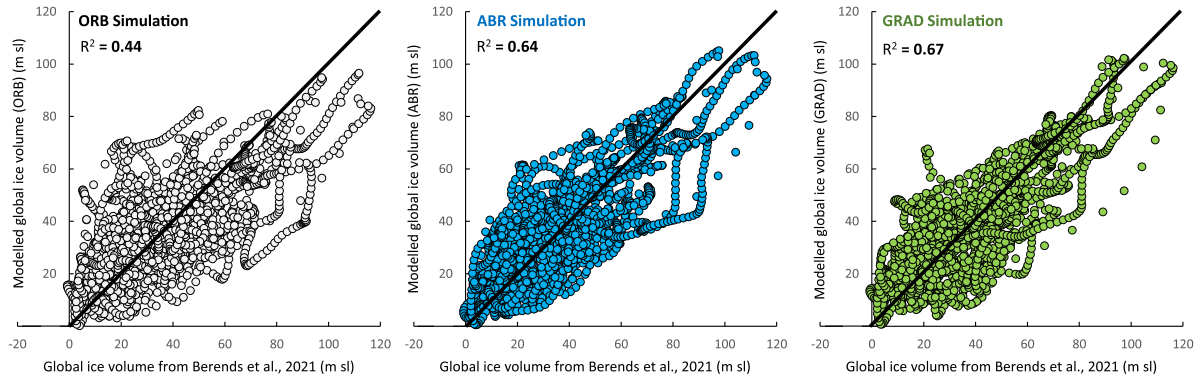
(ii) For the GRAD α_g simulation, we add a parameter C_{α_g} to the α_g parameter which drop continuously the ice volume threshold along the time period of the model.

$$\alpha_g(t) = \alpha_g(t=0) + C_{\alpha_g} \times t$$

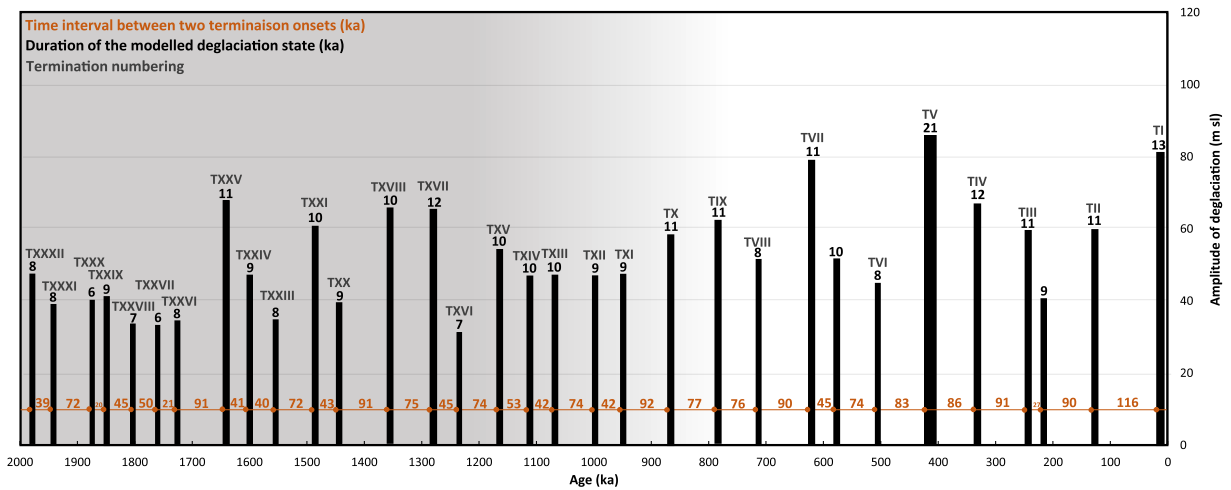
Where t is the discretized time.

To investigate the robustness of these additional results, we compute the Δ BIC criterion of the gradual versus abrupt simulations for these two series of parameters^{44,45}. Results are shown in Supplementary Tables 5 and 6. The evidence of the GRADkO against the ABRkO is *very strong* (12.1)⁴⁷. The evidence of the GRAD α_g against the ABR α_g is *positive* (3.0)⁴⁷. Those results reinforce our overall conclusion that a gradual mechanism is more relevant than an abrupt mechanism to explain the MPT, as already inferred from the main GRAD and ABR simulations.

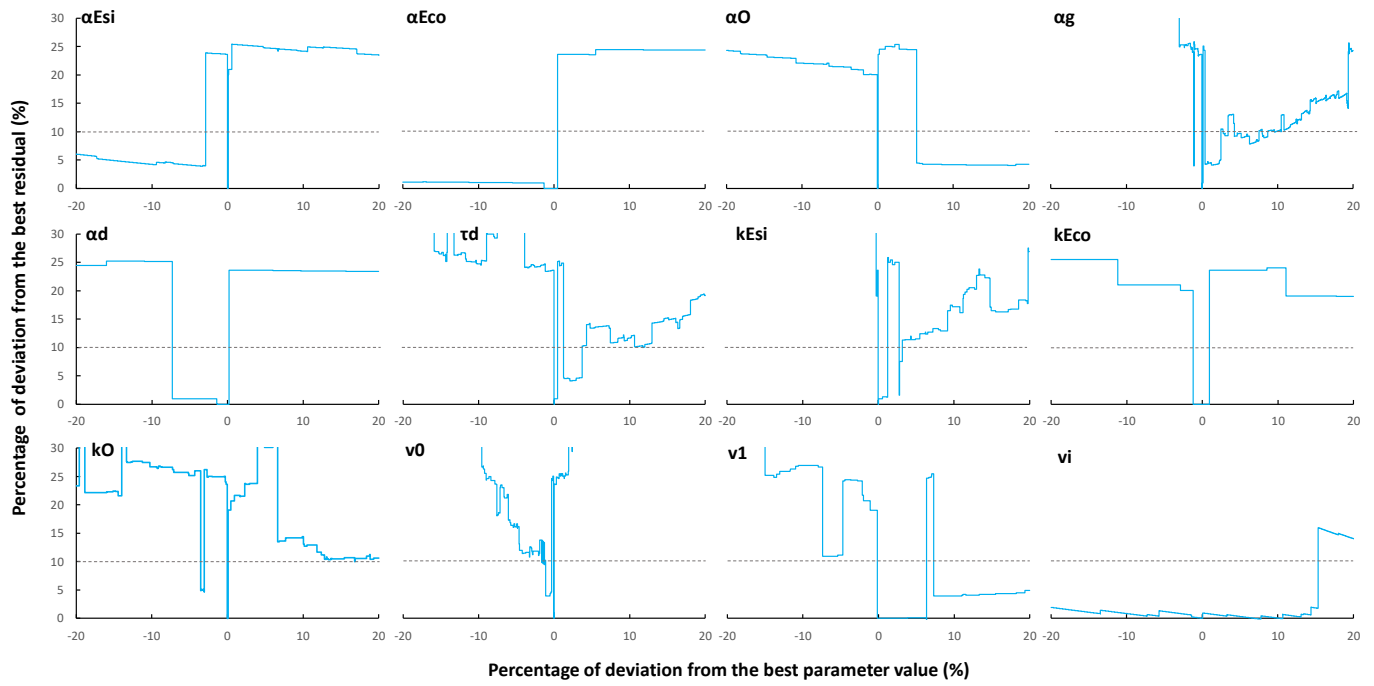
Supplementary Figures



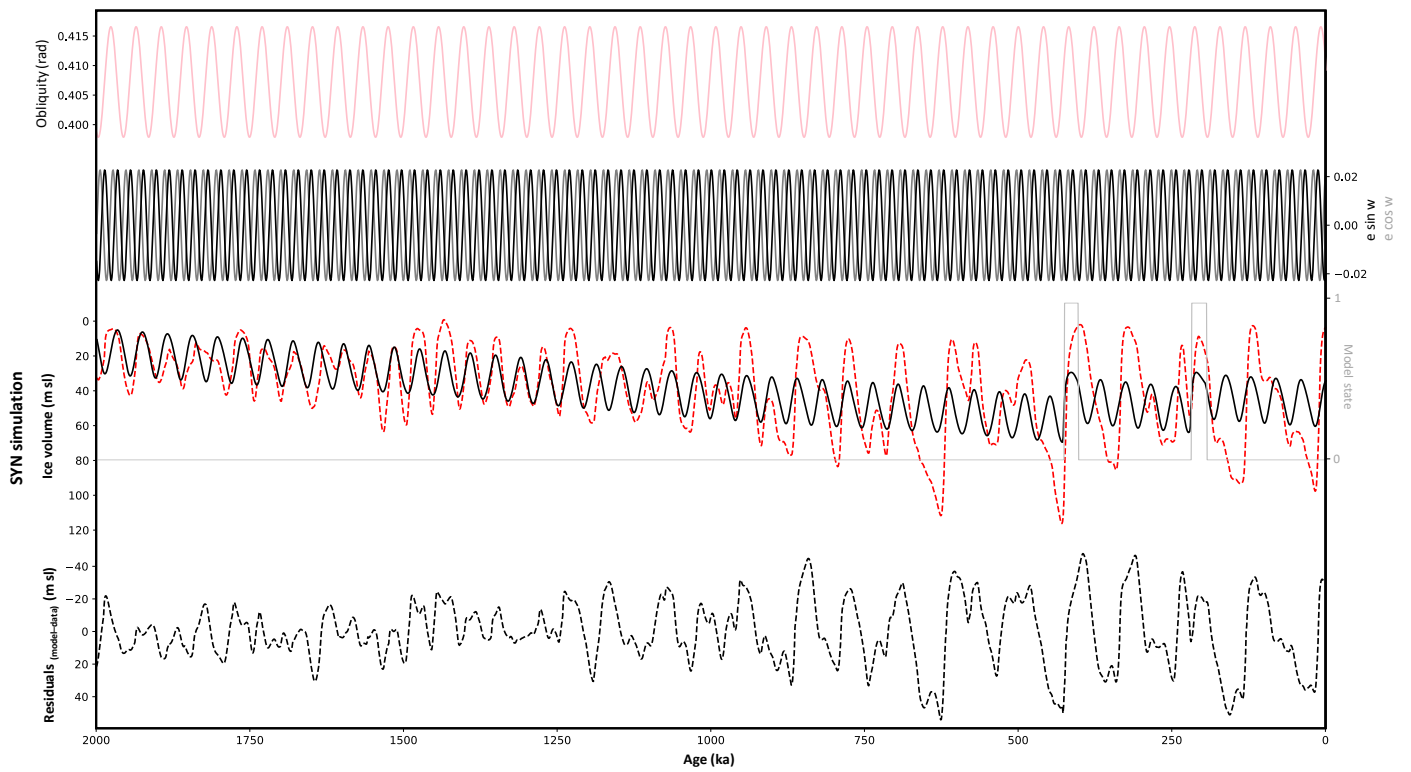
Supplementary Figure 1: Scatter plots of simulated global ice volume versus reconstructed global ice volume from ref. ⁴² and computation of the coefficient of determination (R^2). We interpolated the two dataset every 1 ka. A 1:1 line is added on each graph in black.



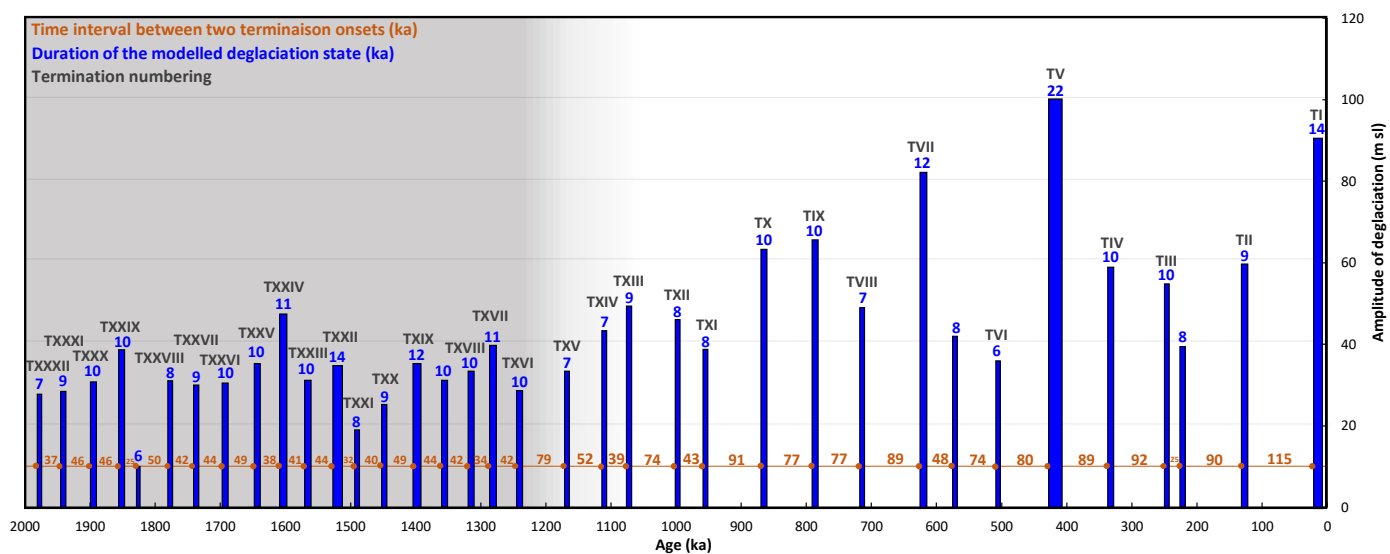
Supplementary Figure 2: Temporal structure of glacial-interglacial cycles in the ORB simulation. Each black stick corresponds to a deglaciation state. Height of the black stick represents the amplitude of the deglaciation in meter sea level equivalent. The width of each black stick and the associated black number indicate the duration of each deglaciation. Grey roman numerals are termination names. Interval between two consecutive orange dots and associated orange number corresponds to the time interval between two deglaciation onsets. Grey shaded area corresponds to a period of lower amplitude and higher frequency of glacial-interglacial cycles than during the white area.



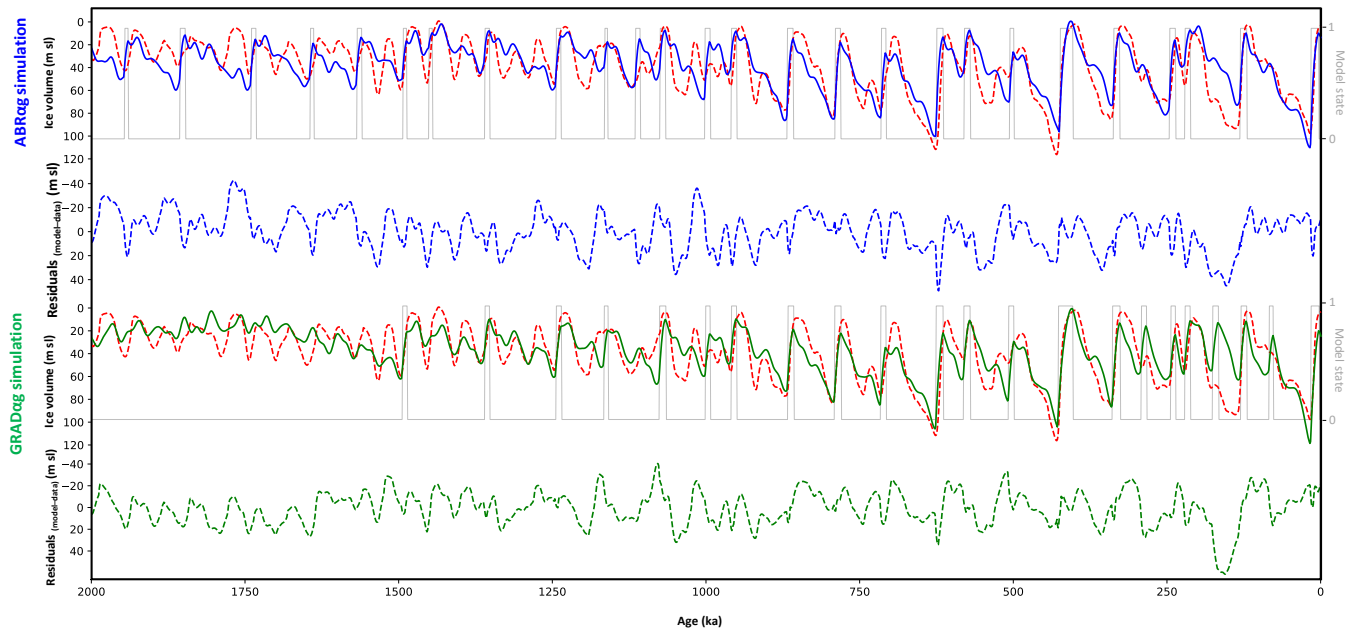
Supplementary Figure 3: Sensitivity test of the ORB simulation. For each of the ORB simulation parameter, we vary the parameter value in a $\pm 20\%$ range from its best value and compute the simulation residuals. Dashed lines represent an increase of residuals of 10%, which is an approximation of the threshold from which the MPT is no longer reproduced by the ORB simulation.



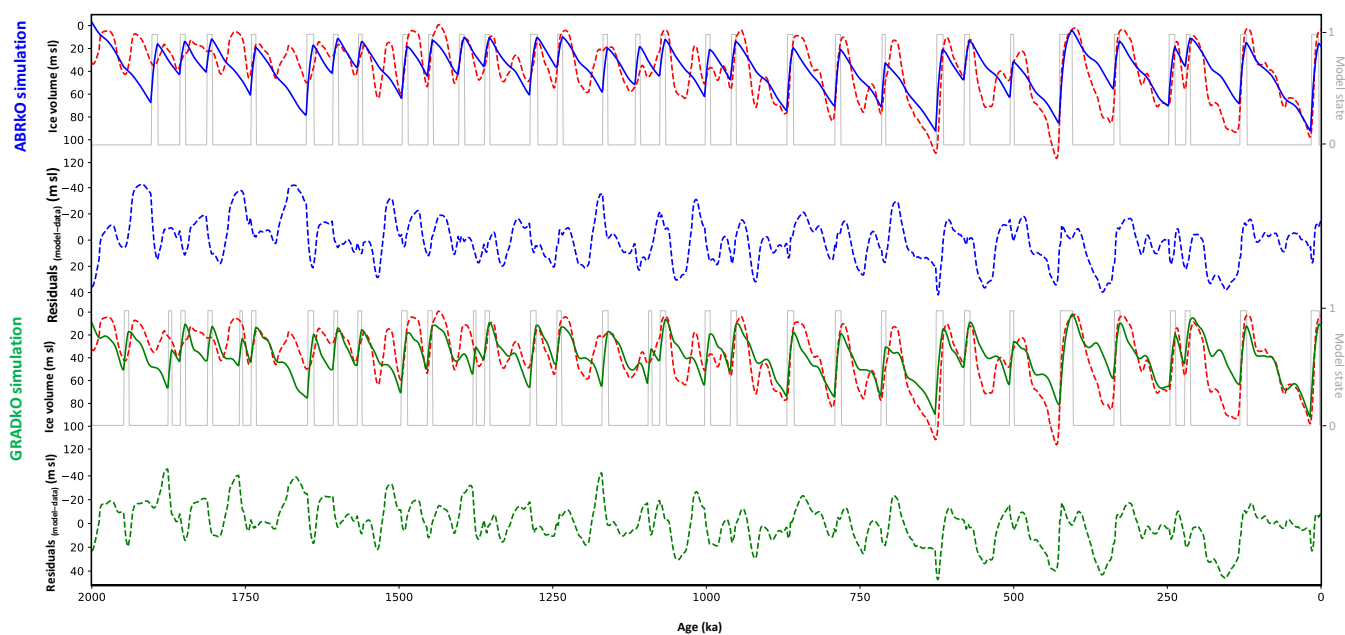
Supplementary Figure 4: Forcing and results from the SYN simulation. From top to bottom: synthetic signal of the three dominant frequency of obliquity (red) precession (black) and phased shifted precession (grey) used as forcing in the SYN simulation. Simulated (black) and reconstructed (red dashed curve, from ref. ⁴²) global ice volume variations (in meter sea level equivalent, m sl) over the last 2 Ma. The grey curve represents the state of the model, deglaciation (1) or glaciation (0). Residuals between the modelled global ice volume changes in the SYN simulation and the reconstructed global ice volume changes over the last 2 Ma.



Supplementary Figure 5: Temporal structure of glacial-interglacial cycles in the ABR simulation. Each blue stick corresponds to a deglaciation state. Height of the blue stick represents the amplitude of the deglaciation in meter sea level equivalent. The width of each blue stick and the associated blue number indicate the duration of each deglaciation. Grey roman numerals are termination names. Interval between two consecutive orange dots and associated orange number corresponds to the time interval between two deglaciation onsets. Grey shaded area corresponds to a period of lower amplitude and higher frequency of glacial-interglacial cycles than during the white area.



Supplementary Figure 6: Results from the GRADag and ABRag simulations. From top to bottom. ABRag simulation (blue) and reconstructed (red dashed curve, from ref. ⁴²) global ice volume variations (in meter sea level equivalent, m sl) over the last 2 Ma. The grey curve represents the state of the model, deglaciation (1) or glaciation (0). Residuals between the ABRag simulation and the reconstructed global ice volume changes over the last 2 Ma. GRADag simulation (green) and reconstructed (red dashed curve, from ref. ⁴¹) global ice volume variations (in meter sea level equivalent, m sl) over the last 2 Ma. The grey curve represents the state of the model, deglaciation (1) or glaciation (0). Residuals between the GRADag simulation and the reconstructed global ice volume changes over the last 2 Ma.



Supplementary Figure 7: GRADkO and ABRkO simulations. From top to bottom. ABRkO simulation (blue) and reconstructed (red dashed curve, from ref. ⁴²) global ice volume variations (in meter sea level equivalent, m sl) over the last 2 Ma. The grey curve represents the state of the model, deglaciation (1) or glaciation (0). Residuals between the ABRkO simulation and the reconstructed global ice volume changes over the last 2 Ma. GRADkO simulation (green) and reconstructed (red dashed curve, from ref. ⁴²) global ice volume variations (in meter sea level equivalent, m sl) over the last 2 Ma. The grey curve represents the state of the model, deglaciation (1) or glaciation (0). Residuals between the GRADkO modelled global ice volume and the reconstructed global ice volume over the last 2 Ma.

Supplementary Tables

Supplementary Table 1: Calculated residuals for each of the three global ice volume simulations relatively to the global ice volume reconstruction from ref. ⁴². A positive and a negative value mean that the model underestimates or overestimates, respectively, the global ice volume. Results are separated into five temporal windows of 400 ka.

	Time interval (ka)				
	0-400	400-800	800-1200	1200-1600	1600-2000
ORB simulation	10.3	6.2	3.7	-5.1	-13.8
ABR simulation	2.3	-0.7	-4.9	8.0	-2.7
GRAD simulation	-3.8	2.4	2.7	0.6	1.2

Supplementary Table 2: Parameters of the best run of each of the five additional simulations. The letter g refers to the glacial state.

	ABR_g simulation	GRAD_g simulation	ABR_{kO} simulation	GRAD_{kO} simulation	SYN simulation
α_{Esi} (m ka ⁻¹)	0.2904	0.5941	0.0348	0.2998	0.0300
α_{Eco} (m ka ⁻¹)	0.7353	0.2728	-0.0524	-0.2619	-0.1887
α_{O} (m ka ⁻¹)	0.5515	0.7960	0.1911	0.5987	1.3953
α_{g} (m ka ⁻¹)	0.8446	1.2585	0.7169	0.6733	0.0226
α_{d} (m ka ⁻¹)	-0.0136	-0.0080	-0.0049	-0.1459	14.1983
$\log(\tau_{\text{d}}/12 \text{ ka})$	5.9536	9.2166	7.6306	8.8945	2.3460
κ_{Esi} (m)	38.3525	25.4954	23.5932	25.5876	1.7955
κ_{Eco} (m)	-0.7094	-1.0686	-0.3358	-0.0572	-7.4895
κ_{O} (m)	15.5057	10.5257	12.1931	10.6505	11.1633
v_0 (m)	108.6964	93.3106	90.2714	89.8271	80.4311
v_1 (m)	4.5631	1.0932	6.4303	-0.4059	-4.0279
v_{init} (m)	23.4360	26.4092	-3.1123	9.4348	10.6978
Sinit	g	g	g	g	g
$C\alpha_{\text{g}}$ (m ka ⁻²)		0.00072			
$C\kappa_{\text{O}}$ (m ka ⁻¹)				0.0003	
α_{gb} (m ka ⁻¹)	0.3919	/			
k_{Ob} (m ka ⁻¹)			21.2581		
$t_{\text{MPT}\alpha_{\text{g}}}$ (ka)					
$t_{\text{MPT}\kappa_{\text{O}}}$ (ka)	1168.3311	/	1232.5194		

Supplementary Table 3 Parameters of the best run for each of the three simulations. ORB, ABR and GRAD simulations have respectively 13, 15 and 14 parameters. The letter g refers to the glacial state.

	ORB simulation	ABR simulation	GRAD simulation
α_{Esi} (m ka ⁻¹)	1.1398	0.2836	0.7266
α_{Eco} (m ka ⁻¹)	0.1788	0.6118	0.4498
α_{O} (m ka ⁻¹)	0.6811	0.7982	0.5299
α_{g} (m ka ⁻¹)	0.6546	0.7286	0.7059
α_{d} (m ka ⁻¹)	-0.1127	-0.0158	-0.0314
$\log(\tau_{\text{d}}/12 \text{ ka})$	8.5631	8.2346	7.5953
κ_{Esi} (m)	23.1714	20.9612	17.0326
κ_{Eco} (m)	-0.5175	-0.4549	-1.2318
κ_{O} (m)	12.3815	11.8480	8.1124
ν_{O} (m)	83.6019	98.0708	107.2550
ν_{1} (m)	7.4686	4.1636	3.4285
ν_{init} (m)	52.2861	23.7566	16.1543
Sinit	g	g	g
C (m ka ⁻¹)	/	/	0.0310
ν_{Ob} (m)	/	61.7859	/
t_{MPT} (ka)	/	1219.8969	/

Supplementary Table 4: Sensitivity test results of the ORB simulation. For each parameter, the second column represent the percentage of simulations, within the $\pm 20\%$ range of the best value , for which the increase of residuals of ORB simulation do not exceed 10%, which is an approximate threshold from which the MPT is no longer reproduced by the ORB simulation

Parameter	Percentage of simulations under 10% of residuals deviation (%)
α_{Esi}	43.1
α_{Eco}	51.1
α_O	37.5
α_g	17.7
α_d	18.7
τ_d	7.4
κ_{Esi}	4.2
κ_{Eco}	5.3
κ_O	1.5
v_0	2.3
v_1	48.1
v_{init}	88.4

Supplementary Table 5: BIC difference $\Delta BIC_{ij} = BIC_j - BIC_i$ for the αg simulations. This parameter quantifies the evidence in favour of a model i (row) against a model j (column)⁴⁴. If the value is positive, it means that the model referred to in the row is more relevant than the model referred to in the column.

	vs.ORB simulation	vs. ABR αg simulation	vs. GRAD αg simulation
ORB simulation	0	/	/
ABR αg simulation	29.3	0	/
GRAD αg simulation	38.4	9.2	0

Supplementary Table 6: BIC difference $\Delta BIC_{ij} = BIC_j - BIC_i$ for the kO simulations. This parameter quantifies the evidence in favour of a model i (row) against a model j (column)⁴⁴. If the value is positive, it means that the model referred to in the row is more relevant than the model referred to in the column.

	vs. ORB simulation	vs. ABRkO simulation	vs. GRADkO simulation
ORB simulation	0	/	/
ABRkO simulation	16.1	0	/
GRADkO simulation	19.2	3.0	0

3.3. Complementary analyses

Three main conclusions can be drawn from this study. First, the MPT is qualitatively reproduced using a simulation based on external forcing changes only. The ability of the ORB simulation to simulate the MPT without any change in the internal forcing is largely due to the long-term frequency of the orbital forcing, as revealed by the SYN simulation. Further analyses are required to identify the exact role of obliquity and precession long-term frequencies in the triggering of the MPT. Second, based on the GRAD and ABR simulations, I show that a gradual-rather-than-abrupt change in the internal climate system have caused the MPT. These simulations represent two extreme cases in terms of mechanism duration, as the change occurs in 2 Ma in the GRAD simulation and 1 ka in the ABR simulation. Consequently, they do not explore the relevance of temporal duration mechanism between 2 Ma and 1 ka. Further analyses are thus required to investigate intermediate scenarios. Third, the most relevant triggering hypothesis, based on its temporal structure, is the gradual decrease of atmospheric CO₂ concentrations through Pleistocene. A state-of-the-art of the available pre-MPT CO₂ records and CO₂ modelling attempt is necessary to confirm the validity of such hypothesis.

Consequently, three main questions have raised from this study are tackled in the following sections:

- What is the influence of long-term astronomical frequencies in the trigger of the MPT? (section 3.3.1.)
- Is the best hypothesis a compromise between the GRAD and the ABR simulations? (section 3.3.2.)
- Is the gradual atmospheric CO₂ decrease across the Pleistocene a credible hypothesis? (section 3.3.3.)

3.3.1. Role of the long-term frequencies of the orbital forcing in the triggering of the MPT

Previous conceptual models applied an arbitrary change in the model parameters to reproduce the MPT [Paillard et al., 1998; Leloup et al., 2022]. Another intermediate approach is to keep the model parameters constant, as in the ORB simulation, and to fit the simulated global ice volume to a detrended version of the reconstructed global ice volume [Imbrie et al.,

2011]. This detrended version removed the variation in amplitude before and after the MPT as registered in the original data-based reconstruction. The model of Imbrie et al. [2011] is able to reproduce the change in frequency, but not in amplitude, of the MPT. In both approaches, the MPT signature in the global ice volume is not simulated only due to the orbital forcing and requires additional complexification of the model [Paillard et al., 1998] or simplification of the climatic signal [Imbrie et al., 2011]. A somewhat surprising result from this study is the ability of the model to partially fit the global ice volume reconstruction from Berends et al., [2021] only forced by the orbital background conditions. Indeed, in the ORB simulation, the model parameters remain constant over the past 2 Ma, implying that the variations of amplitude and frequency in the simulated global ice volume are only due to the input forcing of the model, i.e. the orbital forcing.

The ability of the ORB simulation to reproduce partially the MPT questions the impact of the orbital forcing in the triggering of the MPT. The relative importance of the dominant orbital frequencies vs. the long-term frequency of the obliquity and precession is investigated with the SYN simulation. This simulation (Supplementary Materials, section 3.2.) is similar to the ORB simulation but uses a synthetic orbital forcing only composed of the dominant frequencies of the obliquity (41 ka) and precession (21 ka). The inability of this simulation to simulate the MPT identify the long-term frequencies of the orbital forcing as essential to produce high-amplitude climatic cycles. This result suggests to explore more in details the role of long-term orbital frequency in the trigger of the MPT.

Here I investigate the relative role of long-term obliquity vs. precession frequencies in the ability of the model to reproduce the MPT. For that, two additional simulations are performed, the SYN_1 and SYN_2 simulations. The SYN_1 simulation uses the real obliquity forcing and the 21-ka synthetic precessional forcing as input (Fig 3.2). The SYN_2 simulation uses the real precessional forcing and the 41-ka synthetic obliquity forcing as input (Fig 3.3). Both simulations thus represent an intermediate forcing between the ones used in the SYN and ORB simulations. Apart from this change in the input orbital parameters, these two simulations are similar to the ORB and SYN simulations.

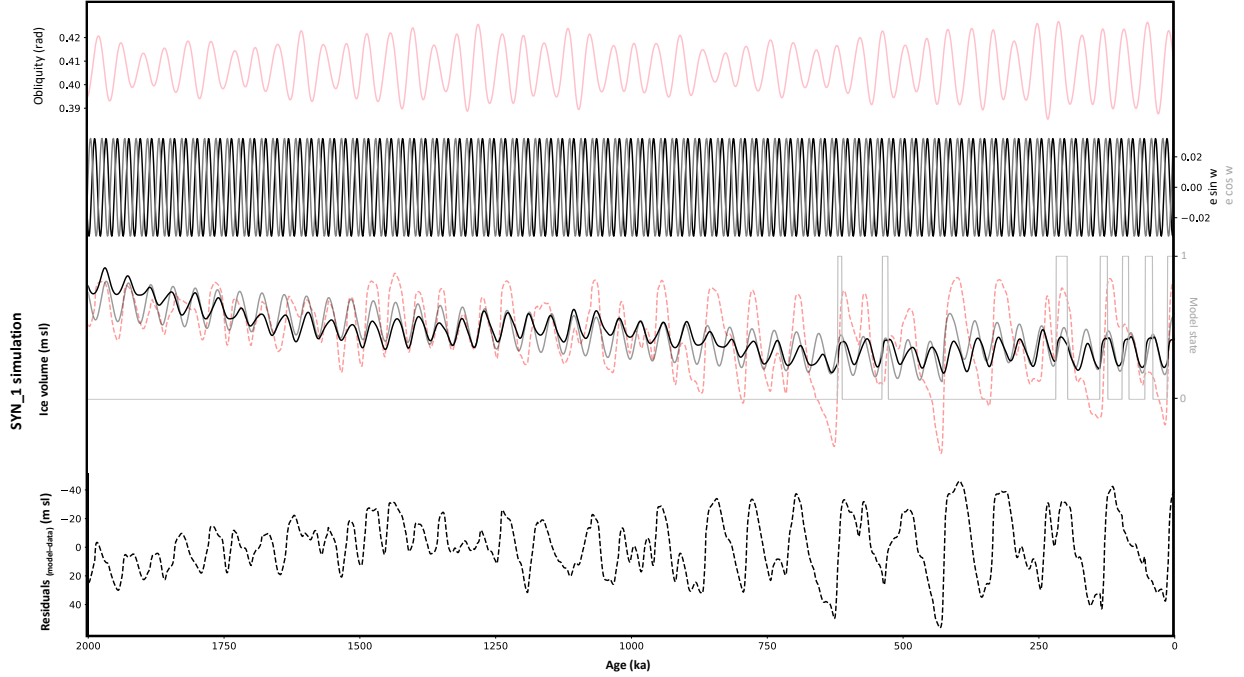


Fig 3.2: Forcing and results from the SYN_1 simulation. From top to bottom: real signal of the dominant of obliquity (red). Synthetic signal of precession (black) and phased shifted precession (grey). SYN_1 simulation (black), SYN simulation (light grey) and reconstructed (red dashed curve, [Berends et al., 2021]) global ice volume variations (in meter sea level equivalent, m sl) over the last 2 Ma. The grey curve represents the state of the model, deglaciation (1) or glaciation (0). Residuals between the modelled global ice volume changes in the SYN_1 simulation and the reconstructed global ice volume changes over the last 2 Ma.

In the SYN_1 simulation, the addition of the real obliquity forcing compared to the SYN simulation does not improve the ability of the model to reproduce the MPT (Fig 3.2). The average of residuals of the obtain optimal fit of the SYN_1 simulation is very closed to the one obtained for the SYN simulation. In particular, the model is still unable to switch from the glaciation to deglaciation mode before ~ 650 ka. This result underlines the role of long-term frequency of precession in the ability of our model to produce climatic cycles.

In the SYN_2 simulation, the addition of the real precession forcing compared to the SYN simulation strongly improves the ability of the model to reproduce high-amplitude climatic cycles (Fig 3.3). The SYN_2 simulation better fits the reconstructed ice volume than the SYN_1 simulation (average of residuals of 18.9 and 20.0 m sl, respectively). However, the MPT is not reproduced with the SYN_2 simulation, as it produces cycles of similar amplitude during the 2.0 – 1.6 Ma and 0.6 – 0.1 Ma periods.

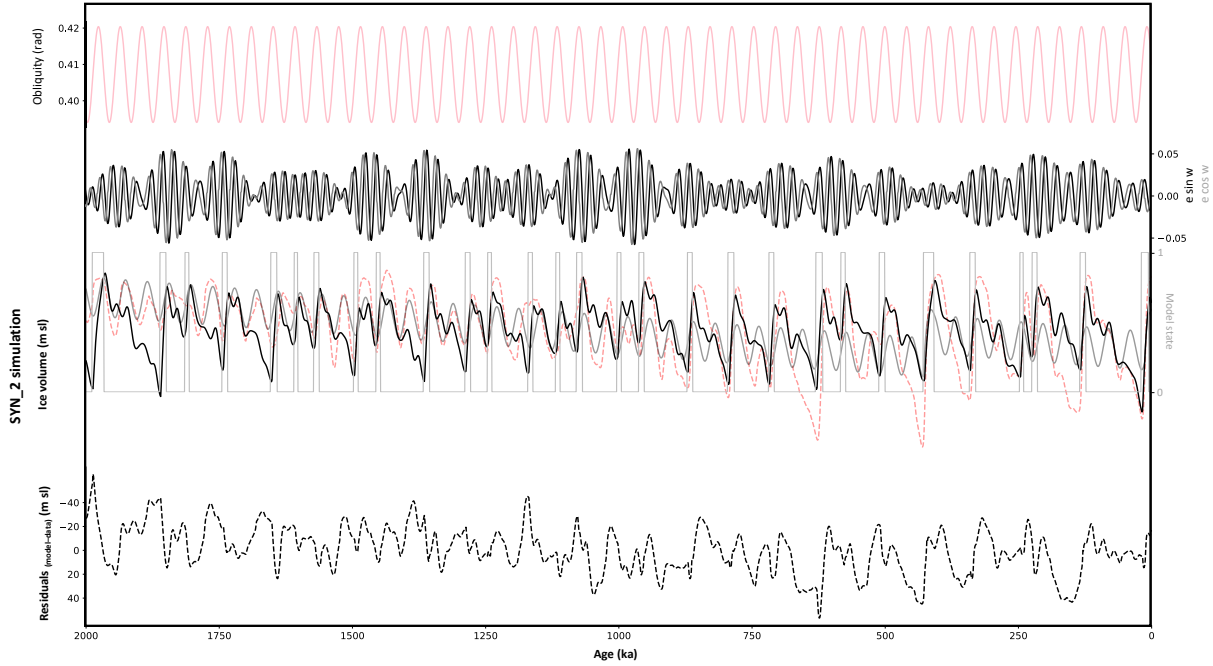


Fig 3.3: Forcing and results from the SYN_2 simulation. From top to bottom: synthetic signal of the dominant frequency of obliquity (red). Real signal of precession (black) and phased shifted precession (grey). SYN_2 simulation (black), SYN simulation (light grey) and reconstructed (red dashed curve, [Berends et al., 2021]) global ice volume variations (in meter sea level equivalent, m sl) over the last 2 Ma. The grey curve represents the state of the model, deglaciation (1) or glaciation (0). Residuals between the modelled global ice volume changes in the SYN_2 simulation and the reconstructed global ice volume changes over the last 2 Ma.

From these results, I can identify the long-term frequency of the precessional forcing as a requirement to produce climatic cycles with the model, whether they belong to the 41 ka- or the 100 ka- world. Reversely, the establishment of realistic climatic cycles seems independent from the long-term frequency of the obliquity. One possible cause of this observation is the strong modulation of precession by the eccentricity [Berger and Loutre, 1991]. The standard deviation of the precessional signal is more than doubled compared to the one of the obliquity signal (0.023 against 0.009 rads). A synthetic signal of precession only composed of a 21-ka periodicity is probably an oversimplification of the complex precessional signal.

An analysis of the difference between the modelled ice volume of the ORB vs. SYN_2 simulation identifies three main periods of mismatch during the past 1 Ma (Fig 3.4): the glacial periods MIS 16 and MIS 12, and an interglacial period, MIS 7. During these time intervals, the amplitude of the global ice volume with the SYN_2 simulation is smaller by at least 10 m sl or more compared to the ORB simulated global ice volume.

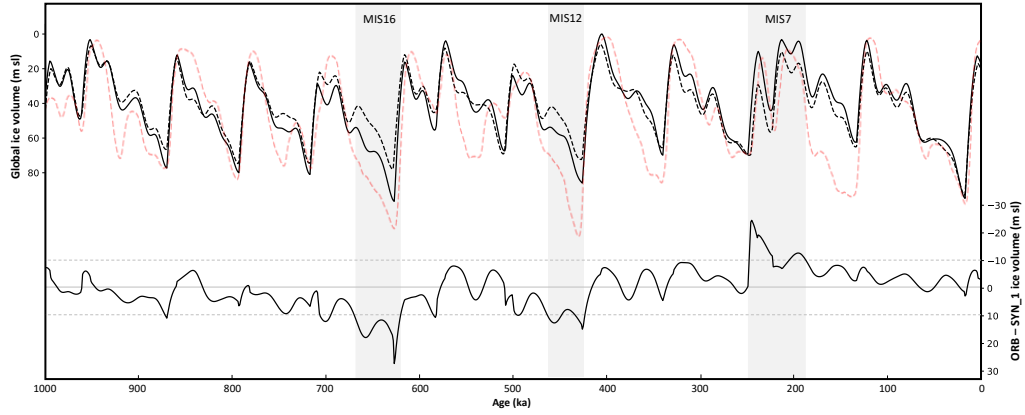


Fig 3.4: Comparison of the ORB vs SYN_2 simulation. Top: modelled global ice volume from the ORB (black line) and SYN_2 (black dashed line) simulations. Bottom: reconstructed (red dashed curve, [Berends et al., 2021]) global ice volume variations (in meter sea level equivalent, m sl) over the last 2 Ma. Difference between the modelled ice volume variations from the ORB – SYN_2 simulation (black curve). Vertical grey areas are time intervals where the absolute difference (ORB – SYN_2) is superior to 10 m.

The only difference between the ORB vs. SYN_2 simulation is the absence in the latter of the long-term frequencies of obliquity in the input forcing. Although the long-term frequency of the precession seems to be a determining factor for the establishment of climatic cycles, the long-term frequency of the obliquity seems to act as a second-order amplifier that accentuates the amplitude of ~ 100 ka climatic cycles. These results suggest to investigate more in details the role played by the long-term frequency obliquity in the establishment of ~ 100 ka cycles during the MPT. A progressive approach would be necessary to untangle the relative influence of the long-term orbital frequencies in the ability of the model to reproduce the MPT. For instance, the long-term frequency of the precession could be added successively until observing a significant change in amplitude before and after the MPT in the climatic cycles, as observed in the ORB simulation.

3.3.2. The RAMP simulation: an intermediate between the ABR and GRAD simulations

The ABR and GRAD simulations represent two end-members in term of mechanism duration, i.e. 1 ka and 2 Ma. The climatic hypothesis associated with potential triggers of the MPT are related to the GRAD or the ABR simulations depending on their temporal structure duration. If the temporal duration is closer to the GRAD simulation, the hypothesis is considered to be represented by this simulation. If not, the hypothesis is considered to be represented by the ABR simulation. This binary approach allows to investigate two extreme

cases. Especially, the abrupt oceanic processes [Yehudai et al., 2021] and the more gradual atmospheric CO₂ decrease [Chalk et al., 2017] are well described by the two simulations. However, they have some limitations in representing hypotheses implying mechanisms assumed to last dozen to hundred of thousand years. For instance, the hypotheses related to ice sheet dynamics [Bintanja and van de Wal, 2008], regolith removal [Clark et al., 1998], or moisture transportation [Sánchez-Goñi et al., 2023] are associated to the ABR simulation in our approach because the order of magnitude of their duration is far from the two million years of the GRAD simulation. However, one could question the classification of such processes as abrupt. Another type of temporal structure closer to some of the proposed mechanisms for the MPT can be investigated more realistically. It would represent an intermediary between the GRAD and the ABR simulations. Hence, I propose here to develop an additional simulation, hereafter the RAMP simulation. The RAMP simulation allows for a gradual change during a specific time window between two intervals characterised by stable states across the past 2 Ma. In other words, while the GRAD simulation systematically applied this gradual change over the past 2 Ma, the inverse method of the RAMP simulation determines what is the best time period within the past 2 Ma to apply a gradual change.

The RAMP simulation is similar to the ORB simulation, except for the formulation of the g to d transition. In the ramp simulation, the v_0 value vary depending if it is younger, older, or between threshold ages T_1 and T_2 :

If $t > T_2$:

$$(3.1) \quad v_0 = v_{0b}$$

If $t < T_1$:

$$(3.2) \quad v_0 = v_{0a}$$

If $T_1 < t < T_2$:

$$(3.3) \quad v_0(t) = v_0(t = 0) + Ct$$

with C a constant which drops continuously the ice volume threshold along the time period between ages T_1 and T_2 , and t the discretized time. The RAMP simulation is composed of 16 parameters. The model solves the evolution of v over the last 2 Ma using a Runge–Kutta 4th order method with a time step of 1,000 years as in the other simulations.

Note that the GRAD simulation corresponds to a special case of the RAMP simulation for $T_1 = 0$ and $T_2 = 2000$ and the ABR simulation is a special case of the RAMP simulation for $T_1 = T_2$.

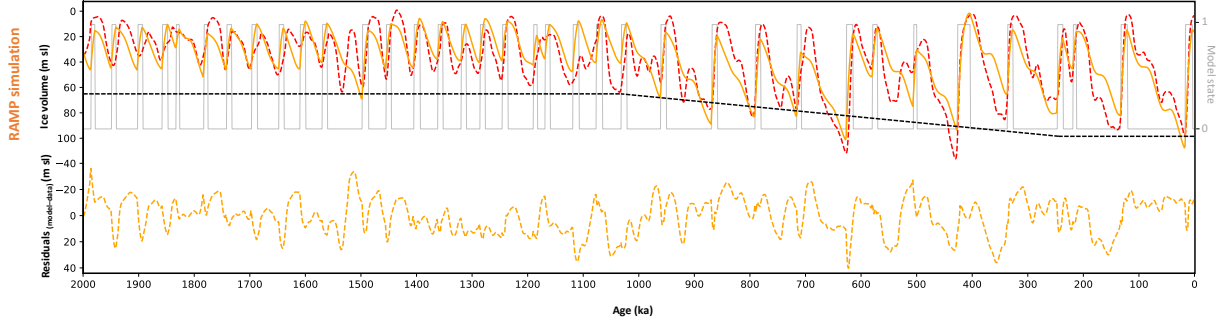


Fig 3.5: RAMP simulation. Top: RAMP simulation (orange) and reconstructed (red dashed curve from Berends et al. (2021)) global ice volume variations (in meter sea level equivalent, m sl) over the last 2 Ma. The grey curve represents the state of the model, deglaciation (1) or glaciation (0). Residuals between the RAMP simulation and the reconstructed global ice volume changes over the last 2 Ma. The optimal timing of the transition in the RAMP simulation is between 1026 and 249 ka.

The optimal specific time window of a gradual change inferred by the inverse method is between 1026 and 249 ka (Fig 3.5). The late timing of the end of the transition is quite intriguing as it is commonly considered that the MPT is completed around ~ 650 ka with the apparition of the first high-amplitude climatic cycles [Berends et al., 2021]. The probable explanation is the occurrence of two pronounced glacial periods at ~ 630 and 440 ka in the global ice volume reconstruction [Berends et al. 2021]. Due to these pronounced glacial periods, the intensity of global ice volume minima is considered to be constant by the model only after these periods, extending the period of transition until ~ 300 ka. The optimal duration of ~ 800 ka of the transition confirms the RAMP simulation as an intermediate simulation between the two n-members ABR and GRAD simulations.

Table 3.1: BIC difference $\Delta BIC_{ij} = BIC_j - BIC_i$ for the ORB, ABR, RAMP and GRAD simulations. The ΔBIC_{ij} criterion quantifies the evidence in favour of a model i (row) against a model j (column)⁴⁴. If the value is positive, it means that the model referred to in the row is more relevant than the model referred to in the column.

	vs.ORB simulation	vs. ABR simulation	vs. RAMP simulation	vs. GRAD simulation
ORB simulation	0	/	/	/
ABR simulation	49.6	0	/	/
RAMP simulation	56.4	6.7	0	/
GRAD simulation	61.7	12.1	5.3	0

The average absolute value of residuals is 13.5 m, slightly better than the ABR (14.4 m) and GRAD (13.9 m) simulations. Nevertheless, this result was expected as the RAMP simulation is a complexification of the GRAD and ABR simulations (i.e. the GRAD and ABR simulations are a special case of the RAMP simulation). The relevance of the RAMP simulation against the three main other simulations is investigated with the BIC criterion. This criterion aims to quantify the evidence in favour of a model against another model, based on the number of model parameters and the residuals between the model and the data [Raftery, 1995]. The relevance of the RAMP simulation against the ABR simulation is strong [Raftery, 1995] (Table 3.1). Reversely, the relevance of the GRAD simulation against the RAMP simulation is strong [Kass and Raftery, 1995]. The increased complexity of the RAMP simulation (16 parameters against 14) not allows a significant reduction of the residuals compared to the GRAD simulation. The RAMP simulation thus does not provide more relevant result than the GRAD simulation. This additional analysis confirms that a gradual change over at least the past 2 Ma seems more relevant than an abrupt event or even a gradual change that occurred in a specific time window. These results confirm the GRAD simulation as the most relevant approach to simulate the MPT. A decreasing parameter over the Pleistocene would thus be the best candidate to have caused the MPT among this conceptual approach.

3.3.3. The gradual atmospheric CO₂ decrease across the Pleistocene as a trigger of the MPT

Our modelling results identify a gradual mechanism in the internal climate as the most probable temporal structure that would have triggered the MPT. This gradual trend could be hypothesized as a gradual cooling over the Pleistocene [Berends et al., 2021]. However, this gradual cooling would be the consequence of an underlying mechanism and not a spontaneous mechanism. Direct analyses of CO₂ concentrations in ice cores have revealed the close coupling between atmospheric CO₂ and temperature during the last glacial-interglacial cycles [Barnola et al., 1987; Petit et al., 1999; Lüthi et al., 2008]. A change in the carbon cycle that would have caused a gradual cooling of the Earth during the Pleistocene is thus the natural candidate to be the gradual mechanism. Both an increasing volcanic CO₂ outgassing and an increased weathering are invoked as causes of a potential CO₂ concentration decreasing trend through the MPT. Here I propose a review of the existing CO₂ data from natural archives and modelling efforts to discuss further this hypothesis.

Atmospheric CO₂ is directly measured in air bubbles trapped in ice cores. The current continuous CO₂ record spanned the past 800 ka [Bereiter et al., 2015]. Consequently, the MPT and pre-MPT atmospheric CO₂ concentrations are not constrained by direct continuous measurements. Only three punctual sets of direct CO₂ measurements between 2 and 1 Ma have been published recently in blue ice samples from the Allan Hills [Yan et al., 2019]. The scenario of a progressive decrease of atmospheric CO₂ concentrations over the past 2 Ma could thus not be confronted to a continuous CO₂ record directly measured in ice cores. Before 800 ka, the atmospheric CO₂ concentrations are estimated using proxy-based reconstruction. Three main proxies provide highly resolved CO₂ estimates through the MPT: (i) boron-isotopes based reconstruction, using the close coupling between oceanic pH and dissolved CO₂ concentrations [Hönisch et al., 2005; Chalk et al., 2017; Dyez et al., 2018], (ii) phytoplankton carbon-isotopes based reconstruction, using the dependence of isotopic fractionation of algae from the amount of dissolved CO₂ in the water [Bae et al., 2015; Pagani et al., 2010], (iii) and leaf wax carbon-isotopes based reconstructions, using the co-variation between $\delta^{13}\text{C}$ from leaf wax and atmospheric CO₂ concentrations [Yamamoto et al., 2022].

No change in the global CO₂ concentrations before and after the MPT is observed in these three proxies [Berends et al., 2021]. However, they reveal contrasting results in the identification of the atmospheric CO₂ concentration trends during specifically interglacial or glacial periods over the last 2 Ma (Fig. 3.6). Phytoplankton and boron-isotopes based reconstructions show a gradual decrease of glacial minima CO₂ concentrations across the MPT [Chalk et al., 2017]. However, the poor correlation between phytoplankton-based and ice core CO₂ concentrations over the past 800 ka suggests to consider with caution the variations revealed by this proxy (Fig. 3.6a). Reversely, the leaf-wax based CO₂ reconstruction identified stable glacial CO₂ minima while interglacial CO₂ concentrations increase gradually over the past 1.5 Ma [Yamamoto et al., 2022] (Fig. 3.6a). The opposite trends observed in the proxy-based CO₂ reconstruction do not provide clear answers regarding the long-term evolution of the CO₂ concentration across the Pleistocene.

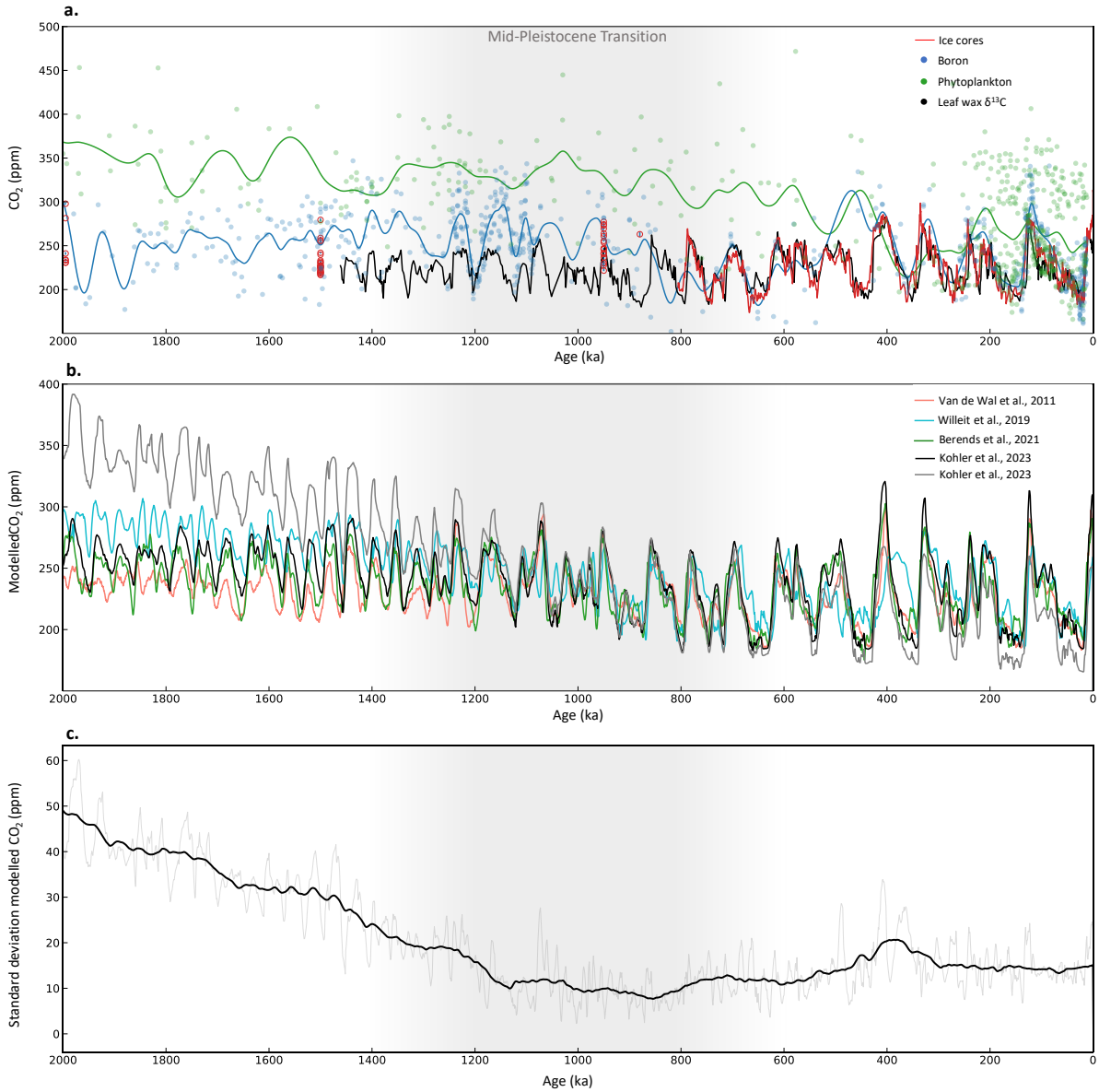


Fig. 3.6: Reconstructed and modelled atmospheric CO₂ concentrations over the past 2 Ma. a. Reconstructed CO₂ concentrations from ice cores, red lines [Bereiter et al., 2015] and red circles [Yan et al., 2019], boron-isotopes, blue dots (compilation from <https://www.paleo-co2.org/>, Hoenisch, [2021]), phytoplankton carbon-isotopes, green dots (compilation from <https://www.paleo-co2.org/>, Hoenisch, [2021]) and leaf wax carbon-isotopes, black line [Yamamoto et al., 2022]. Blue and green dots are 100-ka moving average for the boron- and phytoplankton-CO₂ based records. b. Modelled CO₂ concentrations from Van de Wal et al., [2011] (pink), Willeit et al., [2019] (blue), Berends et al., [2021] (green), Köhler et al., [2023] (grey and black). The grey and black curve correspond to the two extreme scenarios of CO₂ concentrations modelling of the study of Köhler et al., [2023]. c. Standard deviation of the five modelled CO₂ records (light grey). The black line is a 100-ka moving average. The vertical grey shaded area corresponds to the approximate duration of the MPT.

Modelling effort based on an inverse method of the LR04 $\delta^{18}\text{O}$ benthic stack [Van de Wal et al., 2011; Berends et al., 2021; Köhler et al., 2023] and carbon cycle models [Willeit et al., 2019; Köhler et al., 2023] simulates the atmospheric CO₂ concentrations through and before the MPT (Fig. 3.6b). Inverse modelling approaches aim to reproduce the benthic $\delta^{18}\text{O}$ paleo

reconstruction and deduced other physical variables based on empirical relationships between factors like surface temperatures and atmospheric CO₂ concentrations. This simple method reconstructs simultaneously temperature, ice volume and CO₂, allowing to study the lead-lag relationships between the reconstructed parameters. A different approach implies carbon cycle models that could be coupled or not to ice-sheet models. These models are forced by the orbital parameters variations and are based on assumptions on the volcanic CO₂ release through time. These models are very useful to test the carbon cycle response to different volcanic CO₂ release scenario [Willeit et al., 2019; Köhler et al., 2023].

Inverse method-based and carbon cycle models are in good agreement over the past 1 Ma (average standard deviation of the three model of ~10 ppm, Fig. 3.6c). During the early Pleistocene, the standard deviation is increased by a factor four. It reveals the large uncertainties remaining on the atmospheric CO₂ concentrations during this period (Fig. 3.6). The models that used an inverse method are based on empirical relationships and assumption between several physical variables (e.g. global surface temperatures, benthic $\delta^{18}\text{O}$, atmospheric CO₂). They are very sensitive on this parametrization which may explain the difference observed between the different inverse method-based models [Berends et al., 2021]. In addition, the observed decreasing trend of atmospheric CO₂ concentration in the carbon cycle model is forced by the input scenario of volcanic CO₂ outgassing, which is not constrained by paleo-reconstruction. The two simulations of the BICYCLE model illustrate well the wide range of possible atmospheric CO₂ concentrations scenario depending on the input decrease in volcanic CO₂ outgassing [Köhler et al., 2023].

The proxy-dependence of reconstructed CO₂ concentrations and the modelling approach-dependence of simulated CO₂ concentrations explains the wide range of reconstructed and simulated atmospheric CO₂ concentrations before 1 Ma. The International Partnership on Ice Core Sciences (IPICS) has initiated the Oldest Ice challenge that aim to drill ice core covering the MPT period [Dahl-Jensen et al., 2018]. Continuous Antarctic ice cores will provide the first direct atmospheric CO₂ reconstructions across the MPT. These new records will help to constrain the pre-MPT atmospheric CO₂ concentrations, allowing modelling to explore and discriminate the physical mechanism behind this transition.

3.4. Perspectives

The ease with which one can modify the conceptual model I have developed (e.g. GRAD, ABR and ORB simulations only differs from one single equation) and the speed of computing time (e.g. the order of magnitude is one day for a simulation associated with 100,000 experiments and 30 walkers) allows to explore and test numerous hypotheses efficiently.

The section 3.3.1. goes beyond the results published in March 2023 in *Communications Earth & Environment* [Legrain et al., 2023]. It investigates the relative contributions of long-term precession and orbital frequencies in the gradual establishment of the 100-kyr climatic cycles. This approach was already explored with the complete forcing in the paper of Parrenin and Paillard, [2012]. Further detailed analyses could be led in the future to determine which specific long-term frequency in the obliquity and precession, in addition to the 41-ka and 21-ka periodicities, are decisive in the occurrence of the MPT. For that, the progressive addition of 100-ka and 400-ka precession periodicities could provide more details on the importance of modulation frequency of the precession parameter in the establishment of glacial-interglacial cycles. The removal of long-term frequencies in the GRAD simulation would also provide interesting results on the relative influence of internal trend vs long-term orbital frequency on the establishment of 100 ka cycles.

The new RAMP simulation proposed in section 3.3.2. is an example of more complex formulation of the n-members hypothesis formulated in the GRAD and ABR simulations that imply a stationarity-linearity-stationarity scheme. Other simulations could (i) explore a two or three segments shape that varies linearly or (ii) test an exponential pattern of the change during a specific time window. For this family of simulations, the BIC criterion remains decisive to evaluate the relevance of the gain induced by increasing the complexity of the model. The section 3.3.3. also underlined the importance of obtaining precise atmospheric CO₂ concentration reconstructions across the MPT in order to better constraint the physical models and test the hypothesis of a role of the carbon cycle in triggering the MPT.

Lastly, the conceptual modelling approach is commonly applied on global ice volume reconstructions [Paillard et al., 1998; Parrenin and Paillard, 2003; Imbrie et al., 2011; Leloup et al., 2022]. This variable is a global indicator of glacial-interglacial climate variability that relies on data-based reconstructions covering the past 2 Ma [Berends et al., 2021b]. However, conceptual modelling could also be used in a predictive approach for time periods not constrained by paleodata. A previous study from Paillard and Parrenin, [2004] has demonstrated the efficiency of two-state conceptual models to investigate the carbon cycle

variability. Similar conceptual modelling of the atmospheric CO₂ record over the last 2 Ma using the model presented in this chapter could be developed to provide a direct modelled estimate of atmospheric CO₂ concentrations across and before the MPT.

Synthesis

In this chapter, I present the results published in *Communications Earth & Environment* in March 2023 and the associated complementary analyses. The triggering mechanism at the origin of the MPT is investigated through a simple conceptual model used to fit the reconstructed global ice volume. Based on these results, I underline the major role played by the orbital forcing in this transition. In addition, additional simulations show that a slight modification in the orbital forcing prevents the occurrence of the MPT in the conceptual model. Hence, while a change in the internal climate system is required to fully complete the MPT, I propose that the specific non-dominant frequencies of the orbital context over the past 2 Ma are essential in the occurrence of the MPT. In other words, the orbital forcing plays a key role in the establishment of 100 ka climatic cycles.

In addition, I propose that a gradual change occurring over the past 2 Ma is more likely to have caused the MPT than an abrupt event. Considering the temporal structure of the investigated mechanisms, the results point toward the gradual decrease of glacial CO₂ concentrations over the past 2 Ma as the underlying mechanism that triggered the MPT. Evidence of such decrease in the data remain unclear [Chalk et al., 2017; Berends et al., 2021; Yamamoto et al., 2022]. Under the umbrella of the IPICS Oldest Ice Challenge, the on-going international drilling projects should provide continuous ice cores covering the MPT in the next decade. Direct measurements of atmospheric CO₂ concentrations should help confirming or rejecting the hypothesis of a major role played by the carbon cycle in the triggering of the MPT.

Chapter 4

Interactions between the Antarctic climate and the carbon cycle during glacial terminations

In this chapter, I propose to quantify the evolution of the phase relationship between the Antarctic climate and the carbon cycle during major climatic transitions of the Pleistocene, i.e. the glacial terminations. To do so, I use the new CO₂ record presented in *Chapter 2* and new measurements of $\delta^{15}\text{N}$ of N₂ performed on the EDC ice core at LSCE (by F. Prié, A. Grisart and A. Landais). This chapter is composed of an article in preparation, followed by some perspectives.

Chapter 4 aims at:

- Quantifying the evolution of the Antarctic climate- CO₂ phasing over the past five glacial terminations in order to better understand the evolution of this coupling during these major climatic transitions.

Methodology:

- Use of new measurements of 44 CO₂ samples over Termination III and of 37 $\delta^{15}\text{N}$ samples over Terminations IV and V performed on the EDC ice core.
- Multi-method approach for the phasing quantification using least square correlation, piecewise linear function and Monte Carlo analysis.

Highlights:

- At the end of four of the past five terminations, the atmospheric CO₂ increase significantly lags the Antarctic warming by several centuries.
- Such multi centennial-scale asynchronous pattern observed on TI, TII, TIII and TV, already described during the millennial-scale variability of the last glacial period, suggests that terminations are ultimately ended by a millennial-scale variability occurring under favourable orbital conditions.
- A low-latitude sink of carbon is likely to be responsible of the initiation of atmospheric CO₂ decrease at the end of a termination.

Data availability:

- The new $\delta^{15}\text{N}$ records will be available on PANGEA once published.

4.1. Introduction

In 1987, the first atmospheric CO₂ concentration record spanning a complete glacial-interglacial cycle was published [Barnola et al., 1987]. In this pioneering paper, the authors evidenced a correlation between atmospheric CO₂ and Antarctic temperature during the last climatic cycle. Based on this result, they conclude their study as following: “ *Such a high correlation would be expected if CO₂ plays an important role in forcing the climate* ”. One approach to investigate the role of atmospheric CO₂ in the global climate is to focus on periods of major climatic transitions. The most amplified variations of the Pleistocene are registered during the transition from glacial-to-interglacial climate, i.e. the glacial terminations. While it is now established that orbital forcing drives at first order the glacial-interglacial cyclicity of the Pleistocene climate, large uncertainty remains on the internal amplifier of the initial orbital signal [Hays et al., 1976; Parrenin and Paillard, 2012; Tzedakis et al., 2017]. In the study from Shakun et al. [2012], the authors evidenced a lag of global temperature on average respectively to the atmospheric CO₂ concentrations variations during the last deglaciation. This observation supports the importance of atmospheric CO₂ as an amplifier of the orbital forcing. Nevertheless, the relationship between the high-latitudes of Southern Hemisphere temperature and the atmospheric CO₂ concentrations reveal potential regional early warming preceding the CO₂ concentration rise [Shakun et al., 2012]. Identify the evolution of the phasing between the Antarctic temperature and the atmospheric CO₂ concentrations during different glacial terminations would allow to investigate the interactions at play between these two variables at multi-centennial to multi-millennial scale. Three theoretical cases could occur: (i) in case of a lead of the atmospheric CO₂ concentrations increase over the Antarctic climate variations, it would suggest that the carbon cycle firstly responds to the orbital forcing and then consequently induces a delayed climatic variations in Antarctica (ii) in case of a lead of Antarctic climate over CO₂, it would suggest that the carbon cycle is disturbed by the climate change in the Southern Hemisphere and would act with a delay as an amplifier of the initial climate response. (iii) The case of an observed synchronicity of the change in the two records could reveal a real climatic synchronicity, but also can be artificially caused by the noise associated with some records. This noise would prevent to lower the uncertainty associated with the phasing identification method, and thus produce results highlighting a non-significative phasing potentially interpreted as a synchronicity.

In 1991, a new study refined the analysis of Antarctic climate - atmospheric CO₂ phasing focused on the last two glacial terminations [Barnola et al., 1991]. The authors conclude

that at the onset of glacial terminations, the atmospheric CO₂ concentration increases in phase or lags by less than 1,000 years the Antarctic climate warming [Barnola et al., 1991]. In the framework of this study, the case of a lead of atmospheric CO₂ over the Antarctic temperature is thus excluded. Nevertheless, the methodology used in the phasing analysis has revealed three major limitations associated with the phasing approach: (i) the resolution of the records is determinant to identify potential sub-millennial scale phasing (ii) the method of identification of the slope changes could not be limited to a visual inspection of the curves (iii) the temperature-proxy (water isotopes of ice) is an ice-phase proxy, while the atmospheric CO₂ concentrations are directly measured into the gas-phase of the ice core. The resulting Δ age uncertainty associated with the comparison of the two records can reached up to thousands of years in East Antarctic the ice cores [Bazin et al., 2013].

During the following decades, many studies have investigated this phasing during the last three terminations, using more resolved records and more complex statistical methods for the signal analysis [e.g. Fischer et al., 1999; Monnin et al., 2001; Caillon et al., 2003, Ahn et al., 2004; Pedro et al., 2012; Landais et al., 2013; Parrenin et al., 2013; Chowdhry Beeman et al., 2019]. Two studies performed on TII and TIII have also use new proxies ($\delta^{15}\text{N}$ and $\delta^{40}\text{Ar}$) of surface Antarctic climate variability from the gas-phase of the ice core to bypass the uncertainty associated with the Δ age [Caillon et al., 2003; Landais et al., 2013]. All these studies have evidenced two main features of the phasing: (i) it is unlikely that atmospheric CO₂ increase leads over Antarctic warming at the onset of a termination (ii) the phasing could evolve during a termination. Apart from these similarities, these studies have produced a large heterogeneity of results for a same termination, spanning from a synchronous to a millennial-scale lead of Antarctic temperature over atmospheric CO₂ [e.g. Ahn et al., 2004; Parrenin et al., 2013; Chowdhry Beeman et al., 2019], but also between terminations revealing constant to variable phasing [Caillon et al., 2003; Parrenin et al., 2013]. However, it appears challenging to distinguish the real climate phasing from a result bias by the use of a specific approach. The observed large heterogeneity of results questions the influence of the methodological and proxy choices on the identification of the phase relationship between the atmospheric CO₂ concentration and the Antarctic climate across terminations.

The study presented in this chapter takes place in a context of recent publication of multi-centennial scale records of both Antarctic climate-proxy and atmospheric CO₂ records, and after three decades of phasing analyses [Dreyfus et al., 2010; Landais et al., 2013; Parrenin et al., 2013; Nehrbass-Ahles et al., 2020; Legrain et al., in revision]. Fig. 4.1 is a conceptual summary of the analysis performed in this chapter. The purpose of the presented study is to

investigate the evolution of Antarctic climate-CO₂ phasing throughout the past five terminations. The approach used consider three different statistical methods to quantify the phasing between two variables [Caillon et al., 2003; Parrenin et al., 2013; Chowdhry Beeman et al., 2019] in order to distinguish the method-induced results from the significant phasing results during glacial terminations. This study will also rely on $\delta^{15}\text{N}$ records, a gas-phase proxy of the surface Antarctic climate, in order to avoid any uncertainty due to the Δage , as in Landais et al. [2013].

Based on this approach, I will tackle the following questions:

- Is it possible to identify an Antarctic climate – atmospheric CO₂ phasing that is not dependent on the methodology used?
- What are the interactions at play between carbon cycle and climate during a Termination?

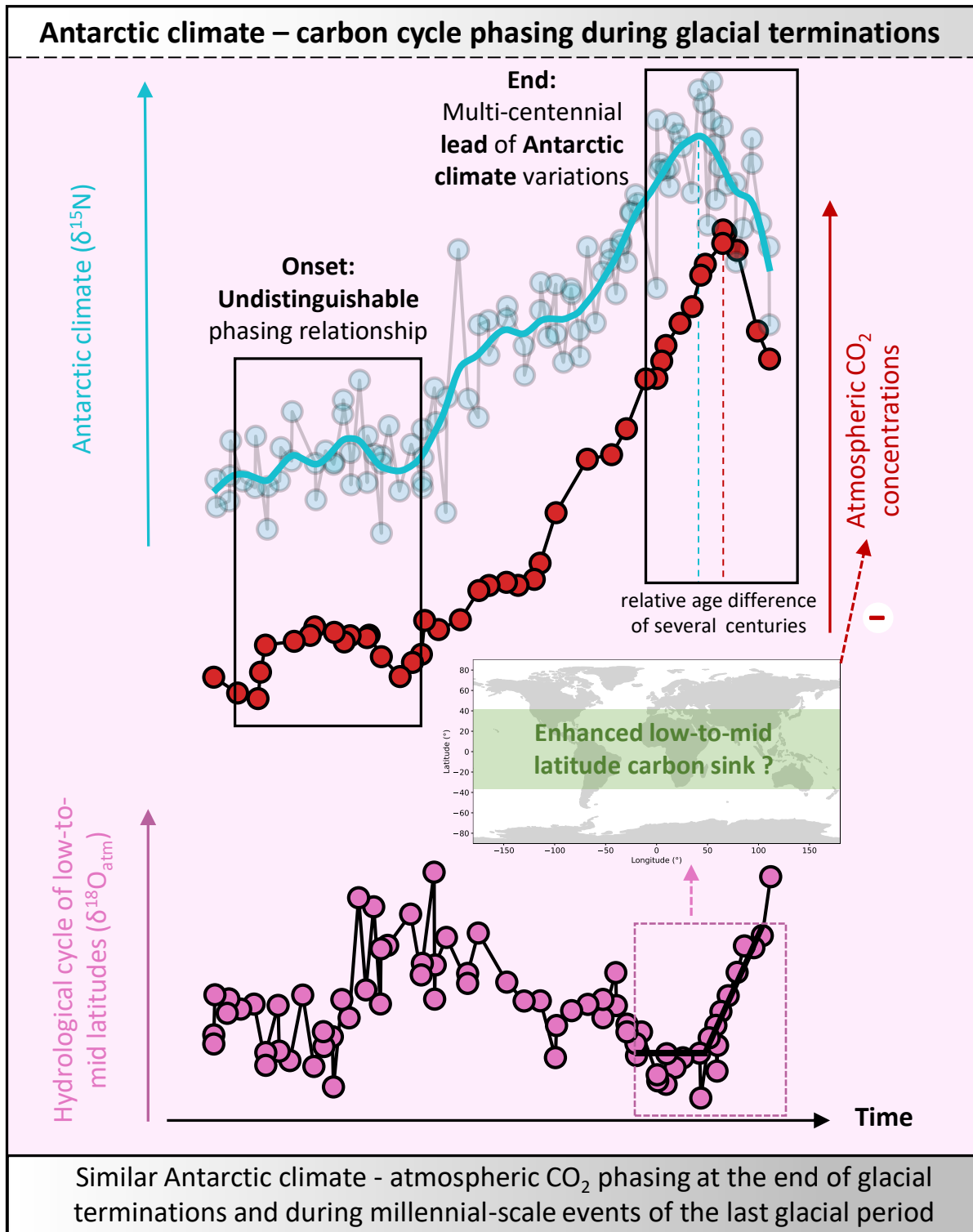


Fig. 4.1: Conceptual summary of the analysis performed in Chapter 4. The blue, red and pink curves represent the morphology of the $\delta^{15}\text{N}$, atmospheric CO_2 and $\delta^{18}\text{O}_{\text{atm}}$ records from TIII, taken as an example of the proxy variations during terminations. The black rectangles represent respectively the end and the onset of the termination. The pink dashed rectangle represents the period of $\delta^{18}\text{O}_{\text{atm}}$ associated with a potential enhancement of the low-to-mid latitude carbon sink. The - sign indicates the negative effect of the low-to-mid latitude carbon sink on the atmospheric CO_2 concentrations. The x-axis and y-axis are deliberately purely qualitative to emphasize the conceptual and representative aspect of this schematic.

4.2. Publication: Evolution of the Antarctic climate-atmospheric CO₂ phasing over the past five glacial terminations (in prep)

Legrain et al., in prep

1 **Evolution of the Antarctic climate-atmospheric CO₂ phasing over the past five glacial**
2 **terminations (in preparation)**

3 Legrain et al.,

4 **Abstract**

5 The phasing between Antarctic climate and atmospheric CO₂ can be quantified across glacial
6 terminations to refine the processes responsible for carbon cycle changes during global warming
7 transitions. Previous studies have revealed heterogeneous results across the past three glacial
8 terminations. However, they rely on reconstructions of varying temporal resolutions, from West or
9 East Antarctic ice cores, on climate proxies measured either on the ice or the gas phase, as well as on
10 several statistical methods. These method-related differences prevent unambiguous climatic
11 interpretations. Here, we quantify the phasing evolution between Antarctic climate and atmospheric
12 CO₂ across the past five glacial terminations using new and existing records from the EPICA Dome C
13 ice core of atmospheric CO₂ and the isotopic composition of nitrogen ($\delta^{15}\text{N}$), used as a gas-phase
14 Antarctic surface climate proxy. Our analysis comparing three statistical methods reveal that the
15 phasing at the termination onsets depends on the considered methodology and termination.
16 Reversely, a multi-centennial lag of the atmospheric CO₂ increase over the Antarctic climate change
17 appears as a pervasive climatic feature at the end of terminations. Our complementary multi-proxy
18 analysis suggests that such Antarctic climate-CO₂ pattern ending terminations exhibits similarities with
19 the last glacial millennial-scale variability. We propose that glacial terminations are ultimately ended
20 by a millennial-scale event occurring under favourable orbital conditions and that the decoupling
21 between the carbon cycle and the Antarctic climate is due to the development of a mid-to-low
22 northern latitude carbon sink constraining the exact timing of atmospheric CO₂ decrease at the end of
23 glacial terminations.

24 **Significance**

25 Glacial terminations represent the largest global warming transitions of the Quaternary. We
26 quantify the evolution of the Antarctic climate-atmospheric CO₂ phasing over the past five glacial
27 terminations with several statistical methods. While the phase relationship at the onset of
28 terminations seems method-dependent, the multi-centennial lag of atmospheric CO₂ decrease over
29 the Antarctic climate change is a recurrent climatic feature at the end of terminations. We interpret
30 this lag as a consequence of a millennial-scale event leading to the end of the terminations. Especially,
31 we propose that the development of a mid-to-low latitude sink of carbon of the Northern Hemisphere
32 was responsible for initiating the decrease of atmospheric CO₂ concentrations at the end of glacial
33 terminations.

34 Introduction

35 Glacial cycles of the Pleistocene are paced by small periodic variations in the astronomical
36 forcing (Milankovitch, 1941; Shackleton and Opdyke, 1977; Pisias and Moore, 1981; Tzedakis et al.,
37 2017). During this epoch, the most prominent climatic changes are the transitions from a glacial state
38 to an interglacial state, also known as glacial terminations (Past Interglacials Working Group of PAGES,
39 2016). The timing of occurrences of these major climatic transitions is driven by insolation forcing,
40 itself determined by the orbital variations of the Earth (e.g. Tzedakis et al., 2017). How the relatively
41 small variations in insolation forcing translate into these major climatic variations remains unclear.
42 During a Termination, the warming is initiated in the Southern Hemisphere, with an Antarctic
43 temperature increase of 4-7°C (Petit et al., 1999; Shakun et al., 2012; Buizert et al., 2021) and it is
44 systematically coupled with an atmospheric CO₂ concentration increase of 60-100 ppm (Barnola et al.,
45 1987; Petit et al., 1999; Marcott et al., 2014). The atmospheric CO₂ concentrations are controlled by
46 sinks and sources of carbon in the Earth System that act on centennial-to orbital timescales. The
47 oceanic reservoir through changes in oceanic circulation, especially in the Southern Ocean, and the
48 continental biosphere that is sensitive to changes in surface climatic conditions are the two main active
49 drivers of atmospheric CO₂ concentrations during the Pleistocene (Petit et al., 1999; Nehrbass-Ahles
50 et al., 2020; Bauska et al., 2021). A millennial-scale variability superimposed onto the orbital-scale
51 changes has also been identified during some of the past terminations in both Antarctic temperature
52 and atmospheric CO₂ records (Jouzel et al., 2007; Marcott et al., 2014; Legrain et al., in revision). This
53 millennial-scale variability is superimposed on the linear increase of Antarctic temperature and
54 atmospheric CO₂ (Parrenin et al., 2013) and is even suspected to play a role in the termination
55 occurrences itself (Wolff et al., 2009; Barker et al., 2021). The close coupling between atmospheric CO₂
56 and the warming in Antarctic temperature question: what is the role of carbon cycle in glacial
57 terminations ? Does the carbon cycle act as a driver or as an amplifier of the Antarctic warming ?
58 Determine which of Antarctic climate or carbon cycle first reacts at the onset of a termination would
59 allow to establish a causality link between these two drivers and propose a sequence of changes
60 starting from the initial insolation variations to the resulting observed major climatic transitions.
61 During the past three decades, efforts have been led to produce high-resolution atmospheric CO₂
62 (Bereiter et al., 2015; Nehrbass-Ahles et al., 2020; Bauska et al., 2021; Legrain et al. in revision) and
63 surface Antarctic temperature records (Jouzel et al., 2007; Buizert et al., 2018). In addition, numerous
64 statistical approaches for lead-lag analysis have been developed to investigate the phasing between
65 carbon cycle and surface Antarctic climate across the last three terminations and the 650-430 ka
66 interval (e.g. Caillon et al., 2003; Siegenthaler et al., 2005; Pedro et al., 2012; Parrenin et al., 2013;
67 Landais et al., 2013; Chowdhry Beeman et al., 2019).

68 The phasing between atmospheric CO₂ and Antarctic temperature during Termination I (TI)
69 was studied in several ice cores and using distinct statistical methodologies (e.g. Barnola et al., 1991;
70 Monnin et al., 2001; Ahn et al., 2004; Pedro et al., 2012; Parrenin et al., 2013; Chowdhry Beeman et
71 al., 2019) (Table 1). With time, temporal resolution of both atmospheric CO₂ and Antarctic temperature
72 records increased and more complex statistical methods have been developed while all these studies
73 rely on the water isotopes composition of ice as a proxy for surface Antarctic temperature (Lorius et
74 al., 1985; Jouzel et al., 1987). However, analysing the phasing between atmospheric CO₂ and Antarctic
75 temperature, which are measured in the gas phase on one hand and on the ice phase on the other
76 hand is subject to uncertainties associated with the relative age difference between ice and air at a
77 same depth level (the so-called delta age). To circumvent this issue, some studies used ice cores drilled
78 at sites characterised by high accumulation rate to minimize the uncertainties related to the delta age
79 (Ahn et al., 2004; Pedro et al., 2012). Another one developed an independent proxy of ice-gas age
80 difference (Parrenin et al., 2013). The studies investigating the Antarctic temperature/CO₂ phasing
81 across the entire TI suggest that Antarctic temperature-CO₂ lag range from -56 up to 410 years)(Monin
82 et al., 2001; Ahn et al., 2004; Pedro et al., 2012). Reversely, studies focusing on the end and onset of
83 terminations reveals an Antarctic temperature-CO₂ lag from 337 up to 1000 years and from
84 synchronous up to 1000 years, respectively (Fischer et al., 1999; Monin et al., 2001; Parrenin et al.,
85 2013; Chowdhry Beeman et al., 2019) (Table 1). The Antarctic temperature-CO₂ phase relationships
86 across TII and TIII were investigated originally using water isotopes as Antarctic temperature proxy
87 (Barnola et al., 1991; Fischer et al., 1999). However, these studies only rely on a visual identification of
88 the phasing and the uncertainties related to the delta age are too large to identify significant sub-
89 millennial phasing. In order to circumvent the delta-age-related uncertainties, TII and TIII were
90 investigated then using the isotopic composition of nitrogen ($\delta^{15}\text{N}$) as a proxy of Antarctic climate since
91 it is measured directly in the gas-phase of the EDC and Vostok ice cores (Caillon et al., 2003; Landais et
92 al., 2013)(Table 1). Indeed, the $\delta^{15}\text{N}$ is considered to reflect variations in the firnification processes,
93 which is strongly related with surface climate conditions in the East Antarctic plateau (Dreyfus et al.,
94 2010; Landais et al., 2013; Breant et al., 2019). Using such approach, a 800 ± 200 years lag of
95 atmospheric CO₂ over Antarctic temperature was calculated during TIII. However, the statistical
96 methodology used only provides a single phasing value calculated for the entire time interval covered
97 by the termination. In other words, this approach does not allow exploring potential phasing changes
98 across the termination (Caillon et al., 2003; Table 1). During TII, an analysis based on a ramp fitting
99 method revealed a two-step phasing, including a synchronous rise of CO₂ and Antarctic surface
100 temperature at the onset of the termination and a multi-centennial lag of CO₂ at the end of the
101 termination (Landais et al., 2013). While these studies are both based on air-isotopes Antarctic
102 temperature proxy and East Antarctic ice cores, they differ by the statistical approach of lead-lag

103 quantification applied (see Methods). Here, we argue that such heterogeneous and spread results
104 obtained from one study to the other can be attributed to the temporal resolution of the paleoclimatic
105 records and differences in the statistical approaches used to infer the phasing. Another source for this
106 heterogeneity is also likely related to the fact that the water isotopic records inferred from ice cores
107 drilled in different parts of Antarctica can also be reflect asynchronous regional climatic changes (WAIS
108 Divide community members 2013). For instance, the Siple Dome ice core was retrieved at a coastal
109 site from West Antarctica (Brook et al. 2005) while the EDC ice core was drilled on the high plateau in
110 East Antarctica (Stauffer et al., 2004).

111 These phasing studies allowed to make progress on the mechanisms at play during
112 terminations. The near-synchronous to sub-millennial lag of atmospheric CO₂ vs Antarctic temperature
113 during terminations has confirmed the Southern Ocean as the main source of carbon at orbital-scale
114 and millennial-scale (Monnin et al., 2001; Pedro et al., 2012; Parrenin et al., 2013). Interpreting the
115 phasing at a specific period of the Termination, e.g. onset or end, is more subject to discussion.
116 Especially, the observed lag of CO₂ during TIII in comparison to the two last terminations and the
117 variability of phasing results during TI question the reliability of this approach. Indeed, a critical
118 question emerges from the successive lead/lag studies: does the observed differences in the phasing
119 between Antarctic Temperature and atmospheric CO₂ concentrations during the last three
120 terminations represent a real climatic signal, or could they be due to the heterogeneity of methods
121 used?

122 To address this question, a systematic evaluation of the phasing between atmospheric CO₂ and
123 Antarctic climate during terminations based on the same ice core, statistical method, and Antarctic
124 climate proxy is necessary. Also, due to the diversity in term of structure that is associated with glacial
125 terminations as observed in paleoclimatic archives (Past Interglacials Working Group of PAGES, 2016),
126 an extension of the Antarctic climate-CO₂ phasing study beyond the last three terminations would
127 provide useful insights. Here we combine new and recently published sub-millennial-scale $\delta^{15}\text{N}$ of N₂
128 and atmospheric CO₂ records to analyse the Antarctic climate-CO₂ phasing over the last five
129 terminations (Dreyfus et al., 2010; Landais et al., 2013; Bréant et al., 2019; Nehrbass-Ahles et al., 2020;
130 Legrain et al., under review; Bouchet et al., under review). These analyses, the first conducted over TIV
131 and TV, are performed using records from the same ice core (EDC) and a similar Antarctic climate proxy
132 ($\delta^{15}\text{N}$ of N₂). In addition, we based our approach on a multiple methods of phasing identification that
133 are representative of the large diversity of phasing method used (Caillon et al., 2003; Parrenin et al.,
134 2013; Chowdhry Beeman et al., 2019; Supplementary information). Based on this original approach,
135 we are now able to distinguish the climatic pervasive pattern of terminations from the approach-
136 dependent results. Finally, the results are integrated in a broader context including others

137 paleoclimate records to explore the climatic implications of our results on the evolution of the
138 Antarctic climate-CO₂ phase relationship over the past five glacial terminations.

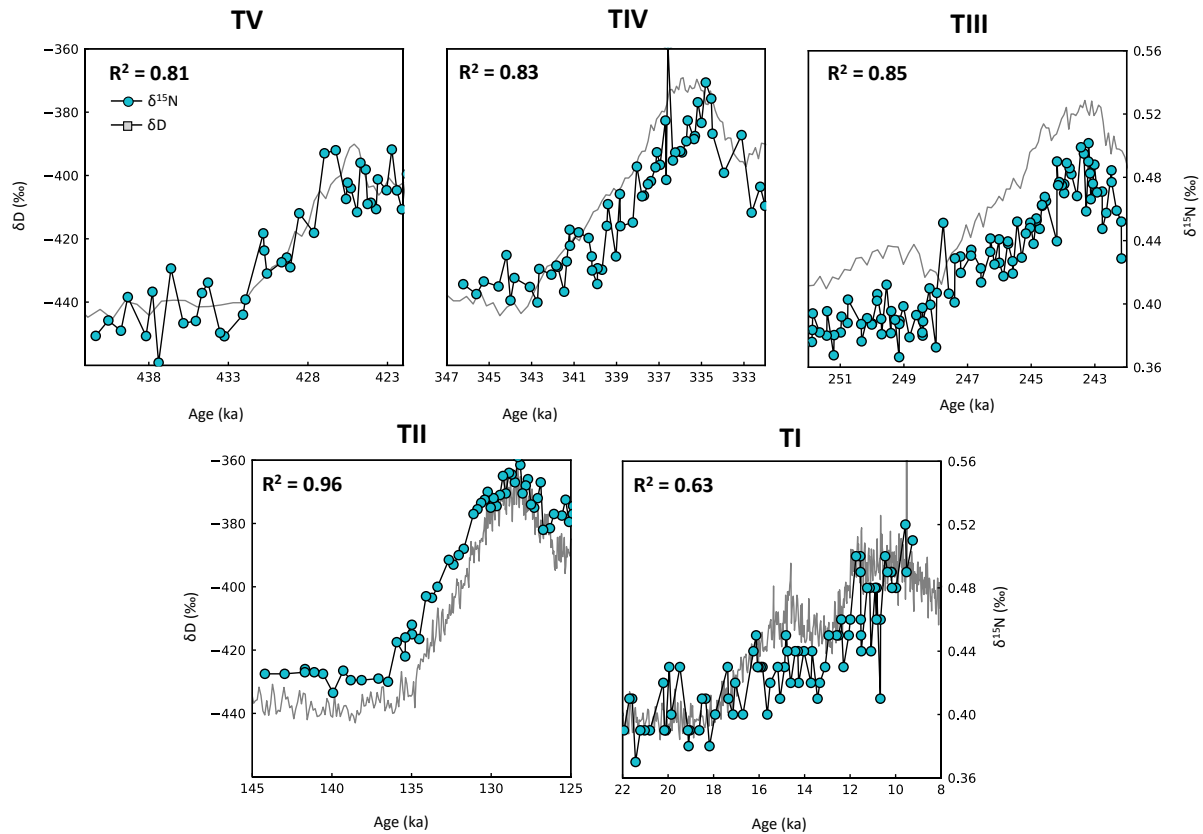
139

140 **Results**

141 ***δ¹⁵N records across TIV and TV***

142 We measured 37 new δ¹⁵N samples on the Antarctic EPICA Dome C (EDC) ice core over TIV and
143 TV using the melt-refreeze extraction system coupled with a mass spectrometer at LSCE. A complete
144 description of the methodology of measurement is available in Bréant et al. (2019). Combining these
145 new measurements with published ones (Bouchet et al., under review), the average temporal
146 resolution over TIV and TV is 200 and 480 years, respectively. Measurements are associated with an
147 uncertainty of 0.01‰. As during the last three terminations, δ¹⁵N increase during from the onset to
148 the end of TIV and TV by ~0.10-0.15‰. The amplitude of change is similar to the one registered during
149 the last three terminations (Dreyfus et al., 2010; Landais et al., 2013; Bréant et al., 2019). The increase
150 occurs in parallel to the δD record, an ice-phase proxy of Antarctic temperature (Jouzel et al., 2007).
151 The correlation found between δD and δ¹⁵N over the TII, TIII, TIV and TV terminations is very strong
152 (R² > 0.8; Fig. 1; Supplementary materials). The coefficient of determination R² is down to 0.6 during
153 TI. The δ¹⁵N during TI is very noisy and this is probably related to the fact that the measured ice samples
154 were of poor quality, presenting multiple cracks. Indeed, TI falls within an interval of the EDC core
155 characterised by brittle ice (Dreyfus et al., 2010). Based on these results, we propose here to use the
156 δ¹⁵N as an Antarctic surface climate proxy during glacial terminations following Dreyfus et al., 2010;
157 Landais et al., 2013; Bréant et al., 2019.

158



159

160 **Fig. 1: Comparison of $\delta^{15}\text{N}$ and δD records from the EDC ice core.** The $\delta^{15}\text{N}$ record (blue dots black line, Dreyfus et al., 2010;
 161 Landais et al., 2013; Bréant et al., 2019; Bouchet et al., under review; this study) and the δD (grey square, Jouzel et al., 2007)
 162 on the AICC2012 timescale. The correlation between the two records is quantified using the coefficient of determination R^2 .

163

164 ***Phasing between Antarctic climate and atmospheric CO_2***

165 In this section, the phasing between Antarctic climate and CO_2 concentrations over the past
 166 five terminations is quantified using three distinct methods from Caillon et al., 2003; Parrenin et al.,
 167 2013 and Chowdhry Beeman et al., 2019. First, the method of Caillon et al., 2003 calculates an average
 168 phasing between Antarctic climate and atmospheric CO_2 across the entire Termination, preventing the
 169 investigation of whether the phasing has evolved through time (Fischer et al., 1999; Monnin et al.,
 170 2001; Ahn et al., 2004; Pedro et al., 2012, see Supplementary Materials). Second, Parrenin et al. (2013)
 171 developed a method based on a piecewise linear function to quantify the phasing between Antarctic
 172 climate and atmospheric CO_2 concentrations at multiple stages during TI. Hence, they could investigate
 173 the evolution of the Antarctic climate- CO_2 phasing across this termination. Third, the method of
 174 Chowdhry Beeman et al. (2019) also uses a piecewise linear function to distinguish the phasing at
 175 various stages of the Termination. Nevertheless, instead of providing a single “best fit” such as in
 176 Parrenin et al. 2013, it analyses the ensemble of fits accepted by the routine providing probabilistic
 177 locators of changes in slope (Chowdhry Beeman et al., 2019). Methodologies are described in details

178 in the original papers (Caillon et al., 2003; Parrenin et al., 2013 and Chowdhry Beeman et al., 2019)
179 and are also discussed in the section Methods and in the Supplementary Materials.

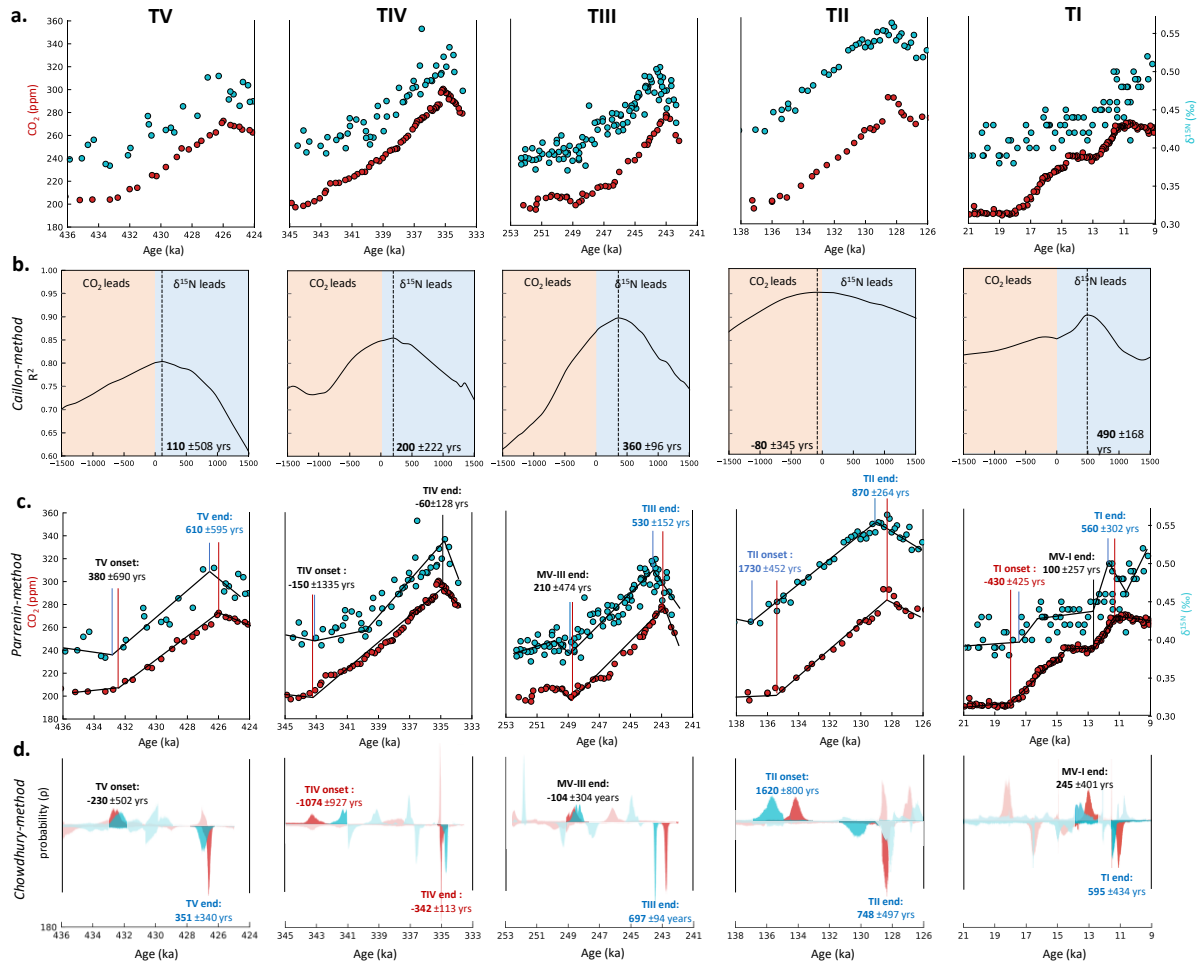
180 Figure 2 presents our new analyses of the Antarctic climate-CO₂ phase relationship across the
181 past five terminations (all results are given with the 1 σ uncertainty). Based on the approach from
182 Caillon et al. (2003), our results show that on average, the Antarctic climate significantly leads the
183 atmospheric CO₂ concentrations by 490 \pm 168 and 360 \pm 96 years during TI and TIII respectively (Table
184 1). However, no significant phase relationship can be significantly identified during TII, TIV and TV (-80
185 \pm 345, 200 \pm 222, 110 \pm 508 years).

186 Following the approach of Parrenin et al. (2013), the onsets of TIV and TV do not exhibit
187 significant asynchronicity between the Antarctic climate and atmospheric CO₂ increases: -150 \pm 1335
188 and 380 \pm 690 years respectively. In opposite, atmospheric CO₂ leads Antarctic climate at the onset of
189 TI (-430 \pm 425 years) and lag Antarctic climate at the onset of TII (1730 \pm 452 years) (Figs. 2 and 3). The
190 millennial-scale variability at the onset of TIII prevents a clear identification of the start of the
191 termination in both records. The results for the termination onsets obtained with the Chowdhry
192 Beeman et al., 2019 method are different as a significant (-1074 \pm 927 years) lag of the Antarctic climate
193 over the CO₂ is identified at the onset of TIV. Reversely, the onset of Antarctic climate variations during
194 TI could not be identified (Fig. 2, Table 1).

195 Looking now at the results at the end of TI, TII, TIII and TV, our analysis using the Parrenin et
196 al., 2013 method reveals a systematic lag of CO₂ over Antarctic climate of 560 \pm 302, 870 \pm 264, 530
197 \pm 152, 610 \pm 595 years (Figs 2 and 3). Similarly, our results based on the Chowdhry Beeman et al., 2019
198 method identify a CO₂ lag over Antarctic climate of 595 \pm 434, 748 \pm 497, 697 \pm 94, 351 \pm 340 years at
199 the end TI, TII, TIII and TV, respectively. The only exception occurs at the end of TIV, while Parrenin et
200 al., 2013 reveals a near synchronous decrease (-60 \pm 128 years) and the Chowdhry Beeman et al., 2019
201 method a slight lead of atmospheric CO₂ over Antarctic climate of -342 \pm 113 years (Table 1).

202 Beyond the end and the onset of terminations, other breakpoints are revealed by the Parrenin
203 et al. (2013) and the Chowdhry Beeman et al. (2019) methods. Some of these breakpoints are
204 associated to the low-resolution of the signal (see Supplementary Information). We thus decided to
205 only interpret the breakpoint associated with the millennial-scale variability in both records and with
206 both methods, and, in the case of TI, already discussed in previous studies. The millennial-scale
207 variability that occurs during the TI and TIII end synchronously in both records with the Parrenin et al.,
208 2013 method (100 \pm 257 and 210 \pm 474 years respectively) and the Chowdhry Beeman et al., 2019
209 method (245 \pm 401 and -104 \pm 304 years) (Table 1).

210



211

212 **Fig. 2: Phasing analysis of the $\delta^{15}\text{N}$ and atmospheric CO_2 records during the past five terminations.** a. Blue and red curves
 213 are respectively the $\delta^{15}\text{N}$ (Dreyfus et al., 2010; Bréant et al., 2019; Bouchet et al., under review; this study) and atmospheric
 214 CO_2 records from the EDC ice core on the AICC2012 timescale (Bazin et al., 2013; Veres et al., 2013). b. Quantification of the
 215 average phasing over the entire termination following the method from Caillon et al., 2003. The vertical dash line corresponds
 216 to the time shift that needs to be made between the two datasets to obtain the best correlation (R^2). c. Quantification of the
 217 phasing at different stages of the termination (end, onset, end of millennial-variability) using the method from Parrenin et
 218 al., 2013. The only interpreted changes are the ones marked with vertical lines. Blue and red text represent a lead of $\delta^{15}\text{N}$
 219 and CO_2 , respectively, while a black text represents no significant lag of one of the parameters. d. Quantification of the
 220 phasing at different stages of the termination (end, onset, end of millennial-variability) using the method from Chowdhry
 221 Beeman et al., 2019. Blue and red curves are the normalized histograms of probable changes for $\delta^{15}\text{N}$ and atmospheric CO_2 ,
 222 respectively. Histograms are downward-oriented when the rate of change decreases and upward-oriented when it increases.
 223 The only interpreted changes are the ones marked with plain colours. Blue and red text represent a lead of $\delta^{15}\text{N}$ and CO_2 ,
 224 respectively, while a black text represents no significant lag of one of the parameters. MV: Millennial-scale variability

225

226

227

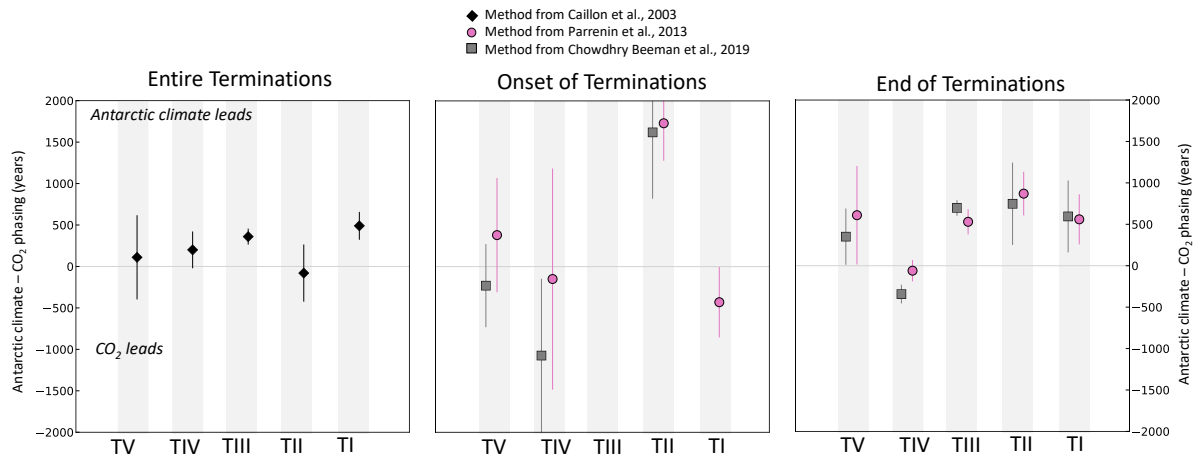
228 **Discussion**

229 The analyses performed with the Parrenin et al. (2013) and Chowdhry Beeman et al. (2019)
230 methods have revealed an evolution of the Antarctic climate-CO₂ phasing during terminations: among
231 a single Termination, the phasing could differ between the onset and the end of the Termination.
232 Accordingly, the method from Caillon et al. (2003) oversimplified the phasing results and is not
233 discussed further in this section.

234 ***Antarctic climate-CO₂ phasing at the onset of terminations***

235 Quantifying the Antarctic climate- CO₂ phasing at the onset of terminations can help
236 deciphering whether the carbon cycle act as a trigger of the climatic transition that firstly respond to
237 the orbital forcing or rather as an amplifier. Previous studies have provided conclusions that either
238 demonstrates a synchronous rise of both parameters, or a multi-centennial lag of atmospheric CO₂
239 over Antarctic climate (Table 1). Here our approach has allowed to investigate this phasing without
240 any bias due to the use of different ice core sites, Antarctic climate proxies and statistical methods of
241 phasing identification. Especially, we identify that the phasing at the onset of a termination is highly
242 dependent of the statistical method used. For instance, our results applying the Parrenin et al., 2013
243 method reveal a millennial-scale lead of Antarctic climate over atmospheric CO₂ at the onset of TII
244 while the study of Landais et al., 2013, that used the Ramp Fit method (Mudelsee, 1999), propose a
245 synchronous increase. This heterogeneity can also be observed by comparing studies focusing on TI
246 that are based on ice-phase Antarctic climate proxy, but from different ice core sites (Ahn et al., 2004;
247 Parrenin et al., 2013).

248 We consider it is challenging to quantify precisely the phasing at the onset of a termination
249 because of two main reasons. First, the onset of a termination is characterized by a relatively slow rate
250 of increase in both CO₂ and $\delta^{15}\text{N}$ records, making it hard to distinguished proxy-induced or
251 measurement-induced variability from the real climatic increase. Second, the onset of a termination
252 occurred in a full glacial condition, characterized by a larger short-term variability than during
253 interglacial periods (Jouzel et al., 2007). Third, the occurrence of large millennial-scale events (such as
254 Antarctic Isotopes Maximum, AIM), nearly synchronous to the onset of the termination (e.g. during
255 TIII) makes it challenging to identify precisely the timing of the onsets in the proxies.



256

257 **Fig. 3: Quantification of the Antarctic climate-CO₂ phasing during the different stages of the past five terminations. Left:**
 258 phasing along the termination using the Caillon et al., 2003 methodology (black diamonds). **Middle:** Phasing results at the
 259 onset of the terminations using the method from Parrenin et al., 2013 (pink circles) and the one from Chowdhry Beeman et
 260 al., 2019 (grey squares). **Right:** Phasing results at the end of the terminations using the method from Parrenin et al., 2013
 261 (pink circles) and the one from Chowdhry Beeman et al., 2019 (grey squares). At the onset of TIII (both methods) and TI
 262 (Chowdhry Beeman-method), the statistical methods do not converge to provide a timing of slope change for at least of one
 263 the two records. For the three panels, a positive value implies a lead of Antarctic climate over atmospheric CO₂.

264

265 ***Antarctic climate-CO₂ phasing at the end of terminations***

266 Our analysis shows that the multi-centennial scale lead of the Antarctic climate over
 267 atmospheric CO₂ observed at the end of TI, TII, TIII and TV does not depend on the method used. It
 268 was previously evidenced during TI and TII with a different climatic proxy for TI and with the Rampfit
 269 statistical methodology for TII (Mudelsee, 1999; Landais et al., 2013; Parrenin et al., 2013; Chowdhry
 270 Beeman et al., 2019). Here we confirm these results for the last two terminations and evidence a
 271 similar pattern at the end of TIII and TV, making the multi-centennial lag of atmospheric CO₂ over
 272 Antarctic temperature a pervasive pattern of four of the five past terminations. Towards the end of a
 273 termination, the atmospheric CO₂ and δ¹⁵N signal undergoes an abrupt increase followed by a decrease
 274 (Fig. 2). This morphology probably explains why it is easier to quantify the phasing at the end of a
 275 termination compared to its onset. Indeed, the associated change in slope can be easily detected
 276 through statistical method due to its abruptness.

277 The only exception of the five past terminations occurred during the end of TIV. The multi-
 278 phasing method of analysis could be biased due to the superimposition of climate variabilities at
 279 different timescales. The end of this termination is characterised by an increase rate of 26.2 ±17.6 ppm
 280 per century and an amplitude of 15.8 ±1.1 ppm in the CO₂ record which is the fastest and most
 281 amplified centennial-scale event in the atmospheric CO₂ record of the last 500 ka (Nehrbass-Ahles et

282 al., 2020; Legrain et al. under review). This event is not associated with any counterparts in the water
283 isotopic record from Antarctica (Jouzel et al., 2007; Fig. 1). We hypothesise that this event would have
284 provoked an early maximum in CO₂ concentrations that consequently disturb the CO₂ - Antarctic
285 temperature phasing at the end of the Termination.

286 ***The end of glacial terminations as millennial-scale variabilities***

287 Here we discuss the observed multi-centennial-scale lag of atmospheric CO₂ over Antarctic
288 climate at the end of Termination. Interestingly, such multi-centennial scale lag of atmospheric CO₂
289 over Antarctic temperature has been identified during Antarctic Isotopes Maximum (AIM) in the WAIS
290 Divide record during the last glacial period (Bauska et al., 2021). The lag observed during AIM is of
291 similar amplitude to the one identified at the end of terminations (Fig. 2) (~500 years).

292 A millennial-scale mode of variability characterized by centennial-scale increase of CH₄
293 concentrations of at least 50 ppb is registered during the last glacial period in the ice core record
294 (Rhodes et al., 2015; Bauska et al., 2021). This variability in CH₄ concentrations can be attributed to a
295 shift of Intertropical Convergence Zone (ITCZ) and subsequent release of CH₄ from Northern
296 Hemisphere wetlands (Rhodes et al., 2015). Similarly, the end of the past five terminations is
297 characterized by a sharp increase in CH₄ concentrations of at least 100 ppb (Fig. 4). Thus, our results
298 suggest that the end of terminations could be considered as an millennial-scale variability.

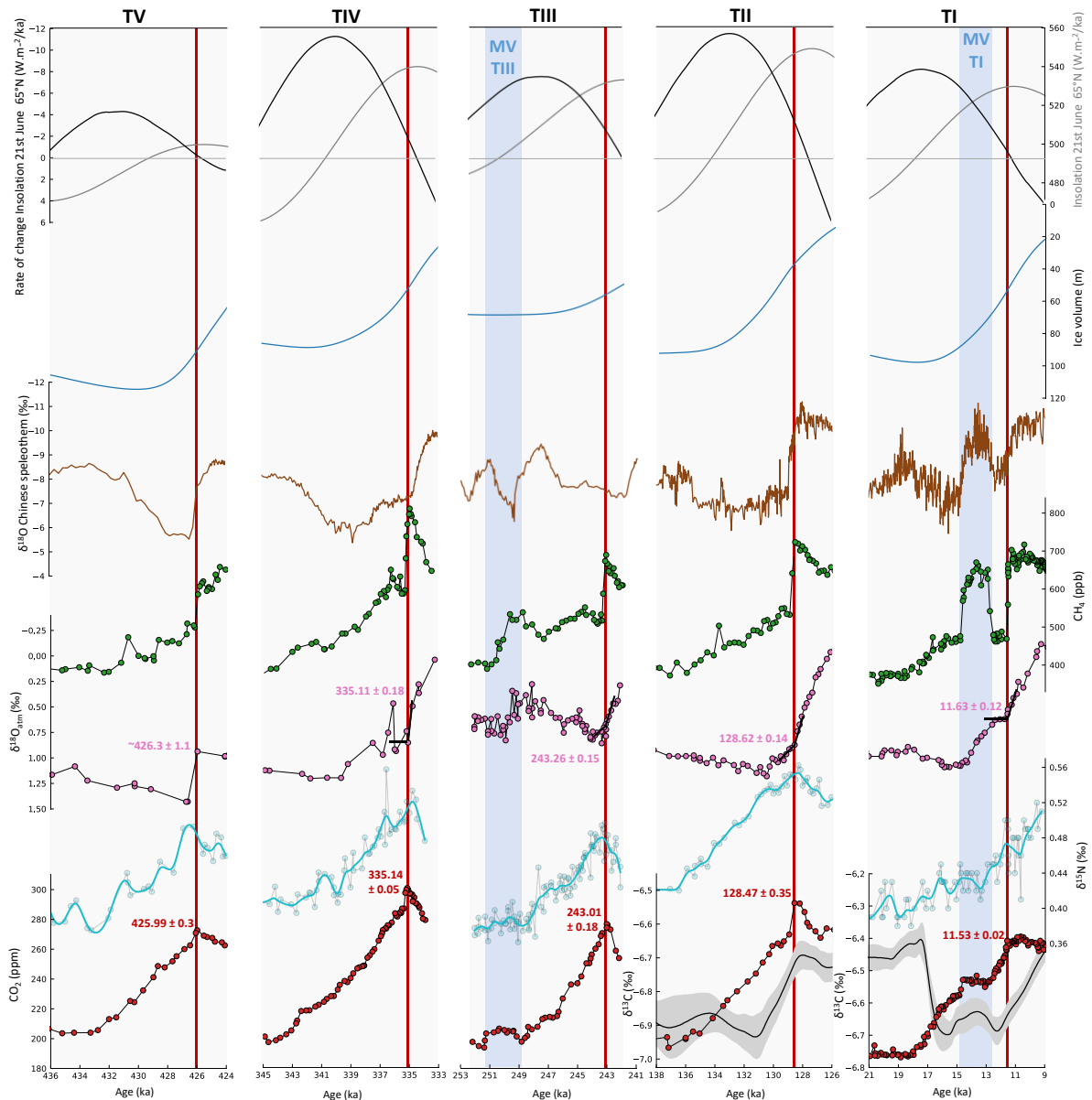
299 Wolff et al. (2009) proposed that the onset of terminations is initiated by a Southern
300 Hemisphere millennial-scale variability that does not propagate to the Northern Hemisphere. They
301 argue that the terminations are ended by the delayed response in the North hemisphere to the initial
302 Southern Hemisphere perturbation. Thus, they hypothesize the terminations as a potential single
303 millennial-scale event, that initiate the warming in the Southern hemisphere, and, after several
304 millennia of muted bipolar see-saw, the initial heat is finally propagated to the Northern Hemisphere,
305 causing the end of the Termination.

306 However, the occurrence of millennial-scale variability in the course of TI and TIII does not
307 argue in favour of considering a termination as a single delayed millennial-scale event (Fig. 4). It reveals
308 that the delayed response of Northern Hemisphere to the Southern warming can occurs before the
309 end of the Termination. This delayed Northern Hemisphere propagation of the Southern warming thus
310 not systematically trigger the end of the Termination.

311 Especially, Antarctic warming and atmospheric CO₂ concentrations continue to rise after the
312 end of the millennial-scale variability during TI and TIII. The millennial-scale variabilities occurring
313 during TI and TIII are ended by synchronous changes in the Antarctic climate and atmospheric CO₂,

314 indicating a different dominant mechanism than during the end of terminations and the last glacial
315 period. In addition, we observe that the onset of the atmospheric CO₂ decrease at the end of a
316 termination occurs under a relatively stable orbital forcing (Fig. 4). In particular the millennial-scale
317 climate variabilities we highlight at the end of TI, TII, TIII and TV occur under a rate of change of the
318 65°N 21st June Insolation lower than 3 W.m⁻².ka⁻¹. Reversely, this average rate of change in the 65°N
319 21st June Insolation during the millennial-scale variabilities occurring in the middle of TI and TIII are
320 higher, at 6.2 and -4.8 W.m².ka⁻¹ respectively (Fig. 4). Hence, we propose that at this stage of the
321 Termination, the impact of the orbital forcing is dominant over the millennial-scale variability
322 explaining the continuing atmospheric CO₂ and Antarctic temperature increase after the millennial-
323 scale variability occurring during TI and TIII. Also, we argue that in opposite, the occurrence of a
324 millennial-scale variability in a low-forcing orbital context could end a Termination. Our results
325 highlight the importance of the orbital context during millennial-scale variations in determining
326 whether the orbital- or millennial-scale processes affecting the carbon cycle will be dominant.

327



328

329 **Fig. 4: Sequence of events of climatic records over the past five terminations.** From top to bottom: Insolation 65°N 21st
 330 June (grey) and associated rate of change (black). Horizontal light grey lines illustrate a null rate of change. Global ice volume
 331 reconstruction (Berends et al., 2021). $\delta^{18}\text{O}$ composite of the Chinese speleothem (Cheng et al., 2019). Gas-phase proxies
 332 measured on the EDC ice core: CH_4 (green) (Loulergue et al., 2008; Rhodes et al., 2015), $\delta^{18}\text{O}_{\text{atm}}$ (pink) (Extier et al., 2018),
 333 $\delta^{15}\text{N}$ (blue) (Dreyfus et al., 2010; Landais et al., 2013; Breant et al., 2019; this study) and CO_2 (red) (Landais et al., 2013;
 334 Marcott et al., 2014; Nehrbass-Ahles et al., 2020; Legrain et al., under review) records displayed on the AICC2012 timescale
 335 (Veres et al., 2013; Bazin et al., 2013). Blue line is a smoothing spline of the $\delta^{15}\text{N}$ used to highlight the global trend of the $\delta^{15}\text{N}$
 336 record. Red vertical lines indicate the CO_2 concentration maxima recorded during the terminations. Black lines were inferred
 337 following the Parrenin et al. (2013) method and illustrate the change in rate of $\delta^{18}\text{O}_{\text{atm}}$ variations that coincides with the CO_2
 338 concentration peaks. Vertical blue areas highlight the millennial-scale variability occurring during terminations.

339

340

341 ***Atmospheric CO₂ sink at the end of terminations***

342 In this section we investigate processes constraining the timing of the atmospheric CO₂
343 concentrations decrease at the end of a Termination. For that, we investigate the sequence of events
344 observed at the end of terminations in several paleoclimate records. First, our analysis is based on the
345 atmospheric CH₄ (Spahni et al., 2005; Loulergue et al., 2008) and the $\delta^{18}\text{O}_{\text{atm}}$ of O₂ (Dreyfus et al, 2007;
346 Landais et al., 2013; Bazin et al., 2016; Extier et al., 2018), measured on the same gas phase of the EDC
347 ice core as $\delta^{15}\text{N}$ and CO₂ (Fig. 4). In particular, the $\delta^{18}\text{O}_{\text{atm}}$ is interpreted as a complex tracer integrating
348 changes in global sea level, hydrological cycle and biosphere productivity (Bender et al., 1994; Landais
349 et al., 2010, 2013). Over the past 800 ka, strong similarities are observed between $\delta^{18}\text{O}_{\text{atm}}$ and Chinese
350 speleothem calcite $\delta^{18}\text{O}$ tracking the East Asian monsoon change at millennial and orbital scale (Wang
351 et al., 2008; Extier et al., 2018). This correlation suggests that the low-to-mid latitude hydrological cycle
352 of the Northern hemisphere is thought to be the dominant driver of $\delta^{18}\text{O}_{\text{atm}}$ variations at these
353 timescales. A decrease of the $\delta^{18}\text{O}_{\text{atm}}$ signal is identified at the end of TI, TIII, TIV and TV (Fig. 4). The
354 timing of variation of the decreasing rate of $\delta^{18}\text{O}_{\text{atm}}$ is precisely determined using the Parrenin et al.,
355 2013 method for TI, TII, TIII and TIV. As the $\delta^{18}\text{O}_{\text{atm}}$ during TV is poorly resolved, the method of Parrenin
356 et al., 2013 could not be applied and the timing of change as well as the associated uncertainty is
357 visually estimated. The phasing between $\delta^{18}\text{O}_{\text{atm}}$ and atmospheric CO₂ is 100 ± 122 , 150 ± 377 , 250 ± 234 ,
358 -30 ± 187 , 300 ± 1100 years, 1σ , for the TI, TII, TIII, TIV and TV, respectively, a positive value indicating a
359 lead of $\delta^{18}\text{O}_{\text{atm}}$ over CO₂. Our analysis reveals that the change in $\delta^{18}\text{O}_{\text{atm}}$ rate of decrease coincides at
360 centennial scale with the peak of CO₂ concentrations at the end of a termination for the past five
361 terminations, although a potential centennial-scale lead of $\delta^{18}\text{O}_{\text{atm}}$ over atmospheric CO₂ could not be
362 fully excluded for TIII (Fig. 4).

363 In addition, the end of the past five terminations is characterized by a sharp increase in CH₄
364 concentrations of at least 100 ppm. This abrupt CH₄ release is interpreted as reflecting a perturbation
365 of the low-to-mid latitude of Northern Hemisphere continental CH₄ sources (Loulergue et al., 2008;
366 Rhodes et al., 2015).

367 The $\delta^{13}\text{C}$ -CO₂ record is available for the last two terminations (Lourantou et al., 2010; Schmitt
368 et al., 2012; Schneider et al., 2013; Bauska et al., 2016). At the end of terminations, strong differences
369 are observed between the two terminations: the $\delta^{13}\text{C}$ -CO₂ signature rise after reaching the Antarctic
370 temperature and CO₂ peak during TI while it remains quite stable during the ~5 ka following the end
371 of TII (Fig. 4). Disentangle the $\delta^{13}\text{C}$ -CO₂ sources and sinks at the exact timing of the end of termination
372 required carbon cycle method as performed during the last glacial and TI (Bauska et al., 2016; Bauska
373 et al., 2021).

374 The Chinese speleothem $\delta^{18}\text{O}$ record also provides interesting insights to understand the
375 Northern latitude carbon cycle dynamics as they track the variations in the hydrological cycle of the
376 Asian monsoon (Cheng et al., 2009). This record also registered a peak around the period of CO_2
377 maximum concentrations although the relative age uncertainty associated with different timescales
378 makes it difficult to discuss the synchronicity of these events at centennial-scale (Cheng et al., 2016)
379 (Fig. 4).

380 Based on these observations, we propose that the decline in atmospheric CO_2 concentrations
381 at the end of termination is due to the enhancement of a continental CO_2 sink at the mid-to-low
382 latitude of the North hemisphere, as inferred from the $\delta^{18}\text{O}_{\text{atm}}$ and CH_4 variations. The AMOC
383 strengthening observed at the end of terminations (Carlson, 2008) would cause the development of
384 this sink (Landais et al., 2013). The dynamics of CO_2 atmospheric concentrations at the end of a
385 termination would be therefore the result of changes in the carbon cycle dynamics of Northern
386 hemisphere. As a consequence, the late decrease in atmospheric CO_2 concentrations is decoupled
387 from the Antarctic surface climate, which is cooling several hundreds of years before the atmospheric
388 CO_2 concentration starts to decrease at the end of terminations.

389

390 **Conclusions**

391 Based on several statistical approaches, we identify a robust multi-centennial lag of
392 atmospheric CO_2 over the Antarctic climate at the end of T1, T2, T3 and T4. We highlight the similarity
393 of this Antarctic climate- CO_2 pattern with the one existing between these two properties during the
394 millennial-scale climate variability characterising the last glacial period. We show that the strength of
395 the orbital forcing, tracked by the rate of change of the 65°N 21st June Insolation, is determinant for
396 the millennial-scale variability to cause the end of the termination, highlighting the close interplay
397 between millennial-scale climate variability and the orbital forcing to shape glacial terminations.
398 Lastly, the exact timing of the atmospheric CO_2 decline at the end of a termination is synchronous with
399 an enhancement of a low-to-mid latitude carbon sink. At the end of a Termination, the carbon cycle is
400 thus driven by Northern Hemisphere and low latitude processes, explaining the observed decoupling
401 between local Antarctic climate change and global atmospheric CO_2 concentrations. Further modelling
402 effort should be conducted (i) to test quantitatively how the orbital forcing modulates the ability of a
403 millennial-scale variability to end a glacial termination and (ii) to perform a quantitative evaluation of
404 the mid-to-low latitude sink responsible for the CO_2 decline (iii) extend the carbon isotopes record on
405 terminations older than T2 and perform carbon cycle modelling to identify sources and sinks of carbons
406 at the end of these terminations.

407 **Table 1: Compilation of studies investigating the phasing between atmospheric CO₂ and Antarctic**
 408 **climate over the past five terminations. MV: Millennial-scale Variability. C: Caillon, P :Parrenin, CB :**
 409 **Chowdhury Beeman.**

Reference	Termination I Raynaud et al., 1999	Fisher et al., 1999	Mann et al., 2001	Ahn et al., 2004	Peterson et al., 2012	Parrenin et al., 2013	Chowdhury et al., 2019	This study
Ice core	Dome C	Taylor dome / Byrd	EDC	Siple dome	Byrd Dome / Siple dome CO ₂	EDC CO ₂ Antarctic temperature stack	Was Duvie CO ₂ Antarctic temperature stack	EDC
Antarctic climate proxy	Water isotopes based	Water isotopes based	Water isotopes based	Water isotopes based	Water isotopes based	Water isotopes based	Water isotopes based	Air isotopes based (δ ¹⁵ N)
Statistical method	Visual inspection	Visual inspection	Linear fit (onset) and R ² correlation (global)	R ² correlation applied on derivative and smoothed records	R ² correlation with Monte Carlo analysis	Piecewise linear fit	Bayesian analysis with piecewise linear fit	R ² correlation / piecewise linear fit / Bayesian analysis with piecewise linear fit
Major results (f > 0, Antarctic climate leads CO ₂)	Global Synchronous	Onset: ~1000 yrs MV: 300-500 yrs End: 600 - 1000 yrs	Onset: 800-600 yrs Global: ~410 yrs	Global: ~150-400 yrs	Global: ~5.6 to 381 yrs	Onset: 10-1610 yrs MV onset: 6130 yrs MV end: 501320 yrs End: 500-290 yrs	Onset: 12.7-715 yrs MV onset: 730-167 yrs MV end: 211-117 yrs End: 337-629 yrs	Onset: 480-425 yrs MV onset: 320-197 yrs MV end: 560-302 yrs CB method: Onset: undetermined MV end: 245-401 yrs End: 595-434 yrs
Reference	Termination II							
Ice core	Barnold et al., 1991	Caillon et al., 2013	Fischer et al., 1999	This study				
Antarctic climate proxy	Water isotopes based	Air isotopes based (δ ¹⁵ N)	Water isotopes based	Air isotopes based (δ ¹⁵ N)				
Statistical method	Visual inspection	Ramp fit	Visual inspection	R ² correlation / piecewise linear fit / Bayesian analysis with piecewise linear fit				
Major results (f > 0, Antarctic climate leads CO ₂)	Onset: less than 1000 yrs	Onset: synchronous Mid-slope: 900-332.5 yrs	Onset: undetermined End: 400-200 yrs	Global: ~80-1345 yrs Onset: 870-264 yrs CB method: Onset: 1620 ± 800 yrs End: 748-497 yrs				
Reference	Termination III							
Ice core	Fischer et al., 1999	Caillon et al., 2003	This study					
Antarctic climate proxy	Vostok	Water isotopes based (δ ¹⁸ O)	EDC					
Statistical method	Water isotopes based	Air isotopes based (δ ¹⁸ O)	R ² correlation / piecewise linear fit / Bayesian analysis with piecewise linear fit					
Major results (f > 0, Antarctic climate leads CO ₂)	Onset: undetermined End: 600-200 yrs	Global: 800-2200 yrs	Global: 360-195 yrs Panel method: Onset: undetermined MV end: 40-172 yrs End: 530-152 yrs CB method: Onset: undetermined MV end: -104-2304 yrs End: 697-494 yrs					
Reference	Termination IV							
Ice core	This study							
Antarctic climate proxy	Air isotopes based (δ ¹⁵ N)							
Statistical method	R ² correlation / piecewise linear fit / Bayesian analysis with piecewise linear fit							
Major results (f > 0, Antarctic climate leads CO ₂)	Global: ~220-2222 yrs Panel method: Onset: 60-1335 yrs End: 60-128 yrs CB method: Onset: -1074-4927 yrs End: -342-113 yrs							
Reference	Termination V							
Ice core	This study							
Antarctic climate proxy	Air isotopes based (δ ¹⁵ N)							
Statistical method	R ² correlation / piecewise linear fit / Bayesian analysis with piecewise linear fit							
Major results (f > 0, Antarctic climate leads CO ₂)	Global: 110-2508 yrs Panel method: Onset: 80-450 yrs End: 610-595 yrs CB method: Onset: -230 ± 502 yrs End: 351-1340 yrs							

410 **Methods**

411 *EDC $\delta^{15}\text{N}$ measurements*

412 One serie of measurements of $\delta^{15}\text{N}$ of N_2 have been performed along TIV and TV on the EDC
413 ice core at LSCE using a semi-automated wet extraction line (Fig. 1). The air is extraction using is a melt
414 refreeze air extraction technique and is then analysed on a dual inlet Delta 220 V plus (Thermo Electron
415 Corporation) mass spectrometer (see Capron et al., 2010 for the detailed analytical procedure). Results
416 are expressed as an anomaly to atmospheric air. The results have been corrected from chemical
417 interferences of $\delta\text{O}_2/\text{N}_2$ and CO_2 (Landais et al., 2003). 37 duplicate samples were measured at the
418 depth interval of 2580.9 – 2609.5 m and 2776.8 – 2793.2 m corresponding to the time intervals 334.5-
419 344.0 ka and 423.6-439.3 ka on the AICC2012 time scale. The final average temporal resolution over
420 TIV and TV is 200 and 480 years respectively.

421 *Statistical methods to analyse the Antarctic climate- CO_2 phasing*

422 In the present study, the evolution of the timing of $\delta^{15}\text{N}$ vs CO_2 changes across the past five
423 terminations has been investigated using EDC ice core records. Since both records are measured in the
424 air-phase of the ice core, there is no inherent relative age uncertainty between them. However, we
425 argue that the choice of the methodology of phasing quantification could impact the results. Hence,
426 we propose in this study to use and compare three different statistical approaches.

427 (i) *Method from Caillon et al. (2003)*. This approach is a statistical method based on least
428 squares. It operates under the assumption of a constant phasing between two curves
429 throughout a defined time window (e.g. time interval covering the entire glacial
430 termination). In this method, one of the two curves are shifted from a minimum to an
431 extremum time value, with a step defined by the user. At each step, the sum of the square
432 of the residuals is computed. The fit that corresponds to the highest value for the
433 coefficient of determination R^2 is considered as the best solution and the corresponding
434 age shift represents the relative lag of the moving record over the fixed one. In this study,
435 we performed the R^2 computation between -1500 and +1500 years from the original
436 agescale at a time step of 10 years. Results are shown in Fig. 2b. Two sources of
437 uncertainties are attached to our results. . First, an uncertainty originates from the
438 temporal resolution of the $\delta^{15}\text{N}$ record, which is the less resolved record compared to the
439 CO_2 record (Fig. 4). Second, we consider an uncertainty related to the fact that not all the
440 variability is captured by a simple shift of the two curves. To do so, we propose to multiply
441 the optimal lag by $1-R^2$. To express the total uncertainties, we performed the quadratic
442 sum of the two described uncertainties.

443 (ii) *Method from Parrenin et al. (2013)*. The LinearFit code is a piecewise linear function that
444 enables the investigation of the phasing at specific break points in a given dataset. The
445 number of break points n in the linear function is determined arbitrary by the user. Starting
446 from an initial position of the n break points determined by the user, the function explores
447 the entire temporal range of the time series to find their optimal locations. The best fit
448 associated with the position of the n break points is quantified using a cost function that
449 minimizes the total sum of residuals (Fig. 2c). The uncertainty associated with each break
450 point is evaluated by calculating the standard deviation of the residuals of the data value
451 to a first best n points linear function (Parrenin et al., 2013). This function provides the
452 single best fit solution that has been identified.

453 (iii) *Method from Chowdhry Beeman et al. (2019)*. They developed a method for detecting
454 break points in paleorecords building upon the approach of Parrenin et al. (2013).
455 However, they enhanced the methodology by employing a Bayesian analysis to explore
456 the parameter space and to estimate the likely timing of these changes. The key technique
457 used in this method is the Metropolis-Hastings algorithm that is a Markov chain Monte
458 Carlo method (Foreman-Mackey et al., 2013). The notable advantage of this approach is
459 that it does not rely on a pre-determined number of points for the linear function. This
460 flexibility eliminates the need for the user to make subjective choices as the inverse
461 method of the model itself determines objectively the number of slope breaks. Eventually,
462 the method generates an ensemble of fits accepted by the routine, which are then
463 depicted as histograms (Fig. 2d). These histograms are used as probabilistic indicators of
464 the locations where changes in slope occur within the records. The uncertainty attached
465 to the break point locations is obtained by fitting the histogram to a normal distribution,
466 which allows to quantify the uncertainty at a 1σ level. A detailed description of the code
467 can be found in Chowdhry Beeman et al. (2019).

468

469

470

471

472

473

474

475 **Supplementary Materials**

476 *On the use of $\delta^{15}\text{N}$ as a surface Antarctic climate proxy at the EDC site*

477

478 The water isotopes present in the ice-phase of Antarctic ice cores have been widely used as
479 proxies of Antarctic surface temperature (Jouzel et al., 2007; Buizert et al., 2018). The aim of this study
480 is to compare the Antarctic climate with atmospheric CO_2 variations measured in the gas-phase of ice
481 cores. However, the age of the air bubbles trapped in the ice is always younger than the age of the
482 surrounding ice matrix. Consequently, a difference of age (Δage) exists between ice and gas at the
483 same depth. The uncertainty associated with this Δage depends on the ability to reconstruct the
484 evolution through time of the Lock-in-Depth, which is the depth at which air is trapped in the ice
485 (Parrenin et al., 2013). This uncertainty that can reached up to 20% of the delta age itself is an
486 important limiting factor when comparing the timing of changes between ice-phase and gas-phase
487 proxies. To overcome this challenge, three approaches can be used:

488 (i) The LID is constrained using the variations of the $\delta^{15}\text{N}$ records coupled with a firn
489 densification model (eg. Parrenin et al. 2013). The LID is then converted into a
490 difference of depth (Δdepth) using a modeled vertical thinning function and
491 assuming a constant firn average density. The methodology of phasing
492 identification between ice-phase and gas-phase proxy has been essentially used
493 during the TI (Parrenin et al., 2013; Chowdhry Beeman et al., 2019) and during the
494 last glacial period (Bauska et al., 2021).

495 (ii) The use of a high-accumulation site (typically Siple Dome: $10\text{-}20\text{ cm.yr}^{-1}$; Hamilton,
496 2002) reduces the uncertainty on Δage , as a Δdepth value would correspond to a
497 smaller Δage value for a high accumulation site. Consequently, using ice-core
498 records from high-accumulation sites, the Antarctic climate- CO_2 phasing could be
499 investigated using an ice-phase temperature proxy across TI (Ahn et al., 2004;
500 Pedro et al., 2012).

501 (iii) The air isotopes of the gas-phase of ice cores, especially $\delta^{15}\text{N}$ and $\delta^{40}\text{Ar}$, are
502 affected by two main processes: the thermal fractionation and the gravitational
503 fractionation (Severinghaus et al., 1998). This last fractionation would dominant
504 in the East Antarctic plateau (Dreyfus et al., 2010; Bréant et al., 2019). Thus, the
505 isotopic variations reflect the changes in the firnification process. It depends to
506 the surface temperature and the accumulation process (Bréant et al., 2019). In the
507 East Antarctic Plateau, this process was directly correlated to surface air
508 temperature variations (Caillon et al., 2003; Dreyfus et al., 2010; Landais et al.,

509 2013). Changes in air isotopes have thus been used in investigating the phasing
510 between Antarctic surface temperature and atmospheric CO₂ during TII in the EDC
511 ice core (Landais et al., 2013) and TIII in the Vostok ice core (Caillon et al., 2003).

512 In our study, we focus on the EDC site from the East Antarctic plateau that is characterized by
513 an average accumulation rate of 1-5 cm/yr (Bréant et al., 2019). We investigate the phasing during
514 terminations during ages as old as ~440 ka. Given the limitations associated with the low-accumulation
515 nature of the EDC site and the age range of our study, the Δ age is associated with an uncertainty of
516 several centuries that would prevent us discussing phasing between Antarctic climate and atmospheric
517 CO₂ (Bazin et al., 2013). Hence, we propose here to follow the strategy of Landais et al. (2013) and
518 Caillon et al. (2003). It has been demonstrated that the $\delta^{15}\text{N}$ variations at the EDC site would be a
519 combine signal of both accumulation and temperature processes (Bréant et al., 2019). In addition, it is
520 likely that accumulation processes are directly linked with temperature changes in the East Antarctic
521 plateau (Parrenin et al., 2007; Loulergue et al., 2007; Bréant et al., 2019). As a consequence, we
522 consider here the $\delta^{15}\text{N}$ as a proxy of the Antarctic climate variations (accounting for both the surface
523 temperature and accumulation rate changes) rather than a purely temperature-driven proxy.

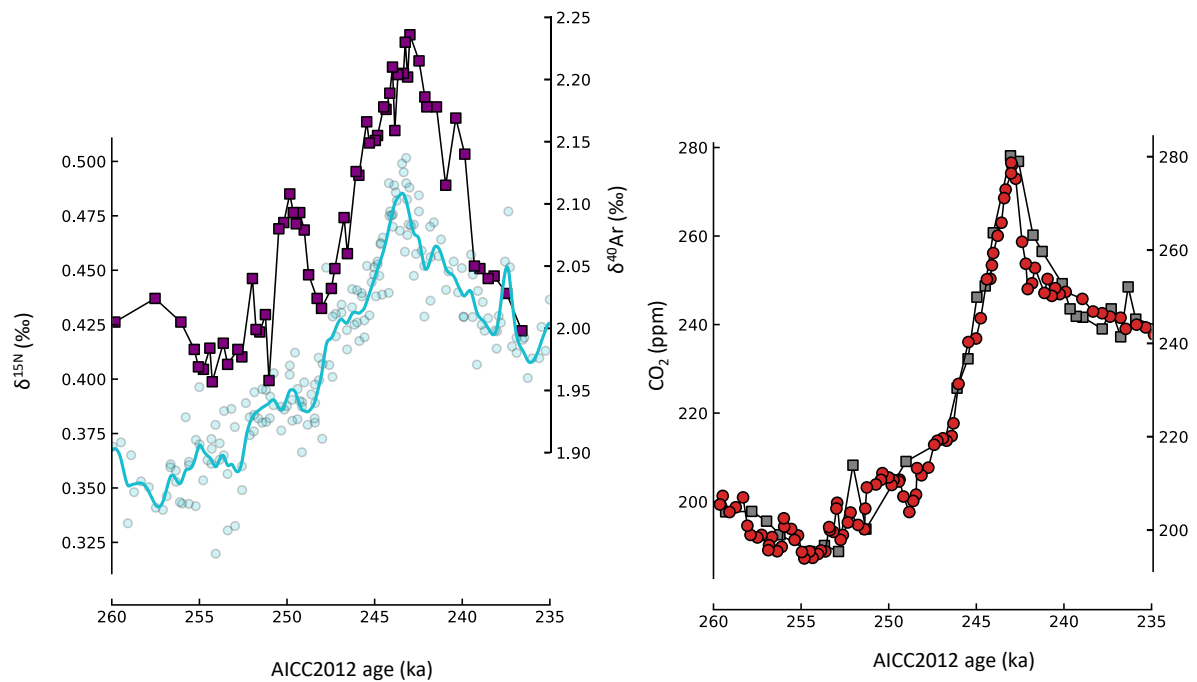
524 The strong correlation ($R^2 > 0.8$ apart from TI) observed between the δD and $\delta^{15}\text{N}$ confirms the
525 $\delta^{15}\text{N}$ during the last five terminations as a reliable proxy for Antarctic climate changes. The lower R^2
526 during TI ($R^2=0.63$) can be explained by the fact that this period falls with a depth interval where the
527 EDC ice is brittle, leading to a degraded quality of the $\delta^{15}\text{N}$ data affected by the presence of multiple
528 cracks in the ice samples.. For the TI period, reliable quantification of the phasing between Antarctic
529 temperature and CO₂ concentrations have been established through water isotopes-based
530 temperature reconstruction (Parrenin et al., 2013; Chowdhry Beeman et al., 2019). Our results during
531 TI, i.e. a lag of atmospheric CO₂ over Antarctic climate variations at the end of the termination and the
532 synchronous end of the Antarctic Cold Reversal, are consistent with those of Parrenin et al. (2013) and
533 Chowdhry Beeman et al. (2019).

534 The hypothesis of a delayed response of $\delta^{15}\text{N}$ to changes in temperature or accumulation at
535 the surface cannot be excluded. Indeed, it could be caused by the response time in the firn to surface
536 climatic changes. In the context of our study, we evidenced in particular a multi-centennial lead of
537 Antarctic climate changes over CO₂ concentrations at the end of the terminations. If the response of
538 $\delta^{15}\text{N}$ is indeed delayed compared to the real climate signal, this implies that the estimated lead of
539 Antarctic climate changes is likely a minimal value and may be even larger. Reversely, an anticipated
540 response of the neve compared to surface climatic changes seems physically very unlikely.

541

543

544 The phasing between the Antarctic climate and atmospheric CO_2 during TIII was initially
545 investigated based on Vostok ice core records (Caillon et al., 2003). The Antarctic climate proxy used
546 was the $\delta^{40}\text{Ar}$, which is driven by the same physical processes in the firn column that controls the $\delta^{15}\text{N}$
547 variations (Severinghaus et al., 1998). The EDC $\delta^{15}\text{N}$ and Vostok $\delta^{40}\text{Ar}$ records appear visually correlated
548 in their global trend, as they both increase during the deglaciation (Figure S1). In addition, the peak
549 associated with the end of termination occurs synchronously at centennial-scale. The major visual
550 difference between the two records is the most pronounced bump in the $\delta^{40}\text{Ar}$ record during the
551 millennial-scale variability occurring at ~ 250 ka. Regarding the CO_2 records, the morphology of the two
552 records are similar, with a synchronous maximum of concentrations reached at the end of TIII.
553 However, the very low resolution at the onset of TIII in the Vostok record does not allow to identify
554 the millennial-scale variability observed in the EDC CO_2 record (Fig. S1). This global similarity combined
555 with a difference in resolution and in sub-orbital-scale variability observed in the record explains the
556 qualitative similarity in the observed CO_2 lag over Antarctic climate using the Caillon et al., (2003)
557 method. However, differences in the lag of CO_2 concentration values are observed: 800 ± 200 years
558 using the Vostok records and 360 ± 96 years using the EDC records. When using a statistical approach
559 allowing an evolution of the Antarctic climate- CO_2 phasing through the glacial termination, the results
560 reveal that the end of millennial variability occurs synchronously, during the first part of the
561 Termination, while the end of the termination is characterized by a significant lag of atmospheric CO_2
562 over Antarctic climate. Hence, TIII is a good case-study to illustrate the importance in the choice of the
563 methodology to determine the Antarctic climate- CO_2 phasing during past deglaciations.



564

565 Fig. S1: Comparison of the records used in the phasing analysis from this study and the from Caillon et al., 2003. Left: EDC
 566 $\delta^{15}\text{N}$ record (blue dots, Breant et al., 2019). Vostok $\delta^{40}\text{Ar}$ record (purple squares, Caillon et al., 2003). Right: EDC CO_2 record
 567 (red dots, Legrain et al., under review). Vostok CO_2 record (grey squares, Caillon et al., 2003). All records are plotted on the
 568 AICC2012 gas timescale (Bazin et al., 2013).

569

570 *Statistical methods to quantify the Antarctic climate- CO_2 phasing during past terminations*

571

572 Various methods have been used to constrain the phasing between the Antarctic climate and
 573 the atmospheric CO_2 concentrations during glacial terminations (Barnola et al., 1991; Fischer et al.,
 574 1999; Monnin et al., 2001; Mudelsee, 2001; Caillon et al., 2003, Ahn et al., 2004; Pedro et al., 2012;
 575 Landais et al., 2013; Parrenin et al., 2013; Schneider et al., 2013; Chowdhry Beeman et al., 2019).

576 One family of statistical methods relies on the assumption that the phasing is constant along
 577 a glacial termination. Under this assumption, a simple answer could be provided for each Termination.
 578 An example is the study of Caillon et al. (2003) that evidenced a constant lag of 800 ± 200 years of
 579 atmospheric CO_2 over Antarctic temperature during the entire TIII. Following this study, more complex
 580 approaches have been investigated on TI and TII questioning this result (Landais et al., 2013; Parrenin
 581 et al., 2013; Chowdhry Beemand et al., 2019). However, the hypothetical specificity of TIII could not be
 582 excluded from inter-termination comparison (Parrenin et al., 2013). Our analysis here reveals that the
 583 phasing of TIII is more complex than a constant lag of atmospheric CO_2 over Antarctic climate (Caillon
 584 et al., 2003; Fig. 2). Nevertheless, we consider that this type of methods can provide a good estimate

585 of the approximate phasing. This is why we propose to apply the methodology from Caillon et al. (2003)
586 to the past five terminations.

587 The second family of statistical method implies piecewise linear function that allows to
588 investigate the temporal evolution of the Antarctic climate-CO₂ phasing at different periods of a
589 Termination. As these methods focus on shorter time windows, they require the use of relatively high-
590 resolution records, explaining why these more complex methods have not been used initially (Barnola
591 et al., 1991; Mudelsee, 2001; Caillon et al., 2003). TII has been studied based on a rampfitting method
592 (Landais et al., 2013). The Rampfit tool (Mudelsee, 1999) find the best fit between and the record and
593 a constant-linear-constant piecewise function. It thus allows to identify phasing during two periods of
594 the Termination, e.g. the onset and the end of a Termination. However, this approach has two main
595 limitations: (i) The ramp is fitted between what are assumed to be two stable states. But for most
596 terminations the pre and post termination records are not characterised by stable values, (ii) the
597 breakpoints are by definition limited to two. Such model is thus not adapted for the glacial
598 terminations affected by millennial-scale variability as they do not exhibit the morphology of a simple
599 ramp (e.g. TI, TIII). In addition, the rampfitting tool is very sensitive to the time window considered for
600 the search of the ramp fit, which in turns influences strongly the timing of of the identified breakpoints
601 characterising the onset and the end of the ramp across the Termination. The Linearfit fit function
602 from Parrenin et al. (2013) is an improved version of Rampfit that solved the two mains problems: (i)
603 all segments of the function are linear function (ii) more than two breakpoints are allowed and the
604 number of breakpoints is fixed by the user after a visual inspection of the considered glacial
605 termination. Thus, we propose here to use this model rather than the Rampfit approach in our study.

606 Finally, a recent study has developed a more rigorous statistical tool based on Metropolis
607 Algorithm (Chowdhry Beeman et al., 2019). This method provides more complex estimate of
608 uncertainty, and the number of breakpoints is not fixed by the user. We consider that this method is
609 the most reliable for the highly resolved records of TI used in the source study (Chowdhry Beeman et
610 al., 2019). However, the convergence of such method requires noiseless and highly-resolved records.
611 We thus considered that this method is not superior to the method of Parrenin et al. (2013) for TII, TIII,
612 TIV and TV, where the records are less resolved than during TI. Reversely, we consider that a
613 complementary use of Parrenin et al. (2013) method and Chowdhry Beeman et al. (2019) particularly
614 efficient for the older glacial terminations.

615 Based on our results, we would recommend the combine use of several methods to distinguish
616 method-dependent results from pervasive climatic signal. And even with this recommendation, the
617 quantified phase relationships with different statistical methods should be carefully interpreted, taking
618 into account the fact that the methods are sensitive to (i) the dataset on which it is implied: for

619 instance, heterogeneity reveal at the onset of TI between the Parrenin et al., 2013 and Chowdry
620 Beeman et al. (2019) are mainly due to the use of EDC CO₂ record vs WAIS Divide CO₂ record (ii) the
621 time windows considered for the search of the optimal fit (iii) the chosen complexity of such a fit
622 (especially for Parrenin et al., 2013; Chowdry Beeman et al., 2019). A visual inspection of the results is
623 systematically necessary to identify the potential aberrant results produced by objective
624 methodologies.

625

626 *On the use of smoothed $\delta^{15}\text{N}$ records*

627

628 In Antarctic, the $\delta^{15}\text{N}$ records are noisier compared to the δD records due to the complexity of
629 processes governing the $\delta^{15}\text{N}$ variations (Bréant et al., 2019). As discussed in the last section, the use
630 of the Chowdhry Beeman et al. (2019) method and, in a smaller extent the one from Parrenin et al.
631 (2013), require low-noise records to converge. Hence, in order to use efficiently the method of
632 Chowdhry Beeman et al. (2019), we applied a Savitzky-Golay filter with an approximate cutoff
633 periodicity of 500 years to the $\delta^{15}\text{N}$ record. Chowdhry Beeman et al. (2019) demonstrated that
634 smoothing the data does not significantly impact the final results of the study. When using the Parrenin
635 et al. (2013) methodology, only the $\delta^{15}\text{N}$ TI was smoothed.

636

637

638

639

640

641

642

643

644

645

646

647

648

649

650

651 **References**

- 652 Ahn, J., Wahlen, M., Deck, B. L., Brook, E. J., Mayewski, P. A., Taylor, K. C., & White, J. W. (2004). A
653 record of atmospheric CO₂ during the last 40,000 years from the Siple Dome, Antarctica ice
654 core. *Journal of Geophysical Research: Atmospheres*, 109(D13).
- 655 Barker, S., & Knorr, G. (2021). Millennial scale feedbacks determine the shape and rapidity of glacial
656 termination. *Nature Communications*, 12(1), 2273.
- 657 Barnola, J. M., Raynaud, D. Y. S. N., Korotkevich, Y. S., & Lorius, C. (1987). Vostok ice core provides
658 160,000-year record of atmospheric CO₂. *Nature*, 329(6138), 408-414.
- 659 Barnola, J. M., Pimienta, P., Raynaud, D., & Korotkevich, Y. S. (1991). CO₂-climate relationship as
660 deduced from the Vostok ice core: A re-examination based on new measurements and on a re-
661 evaluation of the air dating. *Tellus B*, 43(2), 83-90.
- 662 Bauska, T. K., Baggenstos, D., Brook, E. J., Mix, A. C., Marcott, S. A., Petrenko, V. V., ... & Lee, J. E.
663 (2016). Carbon isotopes characterize rapid changes in atmospheric carbon dioxide during the last
664 deglaciation. *Proceedings of the National Academy of Sciences*, 113(13), 3465-3470.
- 665 Bauska, T. K., Marcott, S. A., & Brook, E. J. (2021). Abrupt changes in the global carbon cycle during
666 the last glacial period. *Nature Geoscience*, 14(2), 91-96.
- 667 Bazin, L., Landais, A., Capron, E., Masson-Delmotte, V., Ritz, C., Picard, G., ... & Prié, F. (2016). Phase
668 relationships between orbital forcing and the composition of air trapped in Antarctic ice
669 cores. *Climate of the Past*, 12(3), 729-748.
- 670 Bender, M., Sowers, T., & Labeyrie, L. (1994). The Dole effect and its variations during the last
671 130,000 years as measured in the Vostok ice core. *Global Biogeochemical Cycles*, 8(3), 363-376.
- 672 Bereiter, B., Eggleston, S., Schmitt, J., Nehrbass-Ahles, C., Stocker, T. F., Fischer, H., ... & Chappellaz, J.
673 (2015). Revision of the EPICA Dome C CO₂ record from 800 to 600 kyr before present. *Geophysical
674 Research Letters*, 42(2), 542-549.
- 675 Bouchet, M., Landais, A., Grisart, A., Parrenin, F., Prié, F., Jacob, R., ... & Yang, G. M. (under review).
676 The AICC2023 chronological framework and associated timescale for the EPICA Dome C ice
677 core. *EGUsphere*, 2023, 1-39.
- 678 Bréant, C., Landais, A., Orsi, A., Martinerie, P., Extier, T., Prié, F., ... & Leuenberger, M. (2019).
679 Unveiling the anatomy of Termination 3 using water and air isotopes in the Dome C ice core, East
680 Antarctica. *Quaternary Science Reviews*, 211, 156-165.
- 681 Brook, E. J., White, J. W., Schilla, A. S., Bender, M. L., Barnett, B., Severinghaus, J. P., ... & Steig, E. J.
682 (2005). Timing of millennial-scale climate change at Siple Dome, West Antarctica, during the last
683 glacial period. *Quaternary Science Reviews*, 24(12-13), 1333-1343.
- 684 Buizert, C., Sigl, M., Severi, M., Markle, B. R., Wettstein, J. J., McConnell, J. R., ... & Steig, E. J. (2018).
685 Abrupt ice-age shifts in southern westerly winds and Antarctic climate forced from the
686 north. *Nature*, 563(7733), 681-685.
- 687 Buizert, C., Fudge, T. J., Roberts, W. H., Steig, E. J., Sherriff-Tadano, S., Ritz, C., ... & Schwander, J.
688 (2021). Antarctic surface temperature and elevation during the Last Glacial
689 Maximum. *Science*, 372(6546), 1097-1101.

690 Caillon, N., Severinghaus, J. P., Jouzel, J., Barnola, J. M., Kang, J., & Lipenkov, V. Y. (2003). Timing of
691 atmospheric CO₂ and Antarctic temperature changes across Termination III. *Science*, 299(5613),
692 1728-1731.

693 Capron, E., Landais, A., Lemieux-Dudon, B., Schilt, A., Masson-Delmotte, V., Buiron, D., ... & Oerter, H.
694 (2010). Synchronising EDML and NorthGRIP ice cores using $\delta^{18}\text{O}$ of atmospheric oxygen ($\delta^{18}\text{O}_{\text{atm}}$)
695 and CH₄ measurements over MIS5 (80–123 kyr). *Quaternary Science Reviews*, 29(1-2), 222-234.

696 Carlson, A. E., Stoner, J. S., Donnelly, J. P., & Hillaire-Marcel, C. (2008). Response of the southern
697 Greenland Ice Sheet during the last two deglaciations. *Geology*, 36(5), 359-362.

698 Cheng, H., Edwards, R. L., Broecker, W. S., Denton, G. H., Kong, X., Wang, Y., ... & Wang, X. (2009). Ice
699 age terminations. *science*, 326(5950), 248-252.

700 Chowdhry Beeman, J., Gest, L., Parrenin, F., Raynaud, D., Fudge, T. J., Buizert, C., & Brook, E. J. (2019).
701 Antarctic temperature and CO₂: near-synchrony yet variable phasing during the last
702 deglaciation. *Climate of the Past*, 15(3), 913-926.

703 Dreyfus, G. B., Parrenin, F., Lemieux-Dudon, B., Durand, G., Masson-Delmotte, V., Jouzel, J., ... &
704 Leuenberger, M. (2007). Anomalous flow below 2700 m in the EPICA Dome C ice core detected using
705 $\delta^{18}\text{O}$ of atmospheric oxygen measurements. *Climate of the Past*, 3(2), 341-353.

706 Dreyfus, G. B., Jouzel, J., Bender, M. L., Landais, A., Masson-Delmotte, V., & Leuenberger, M. (2010).
707 Firn processes and $\delta^{15}\text{N}$: potential for a gas-phase climate proxy. *Quaternary Science Reviews*, 29(1-
708 2), 28-42.

709 Extier, T., Landais, A., Bréant, C., Prié, F., Bazin, L., Dreyfus, G., ... & Leuenberger, M. (2018). On the
710 use of $\delta^{18}\text{O}_{\text{atm}}$ for ice core dating. *Quaternary science reviews*, 185, 244-257.

711 Fischer, H., Wahlen, M., Smith, J., Mastroianni, D., & Deck, B. (1999). Ice core records of atmospheric
712 CO₂ around the last three glacial terminations. *Science*, 283(5408), 1712-1714.

713 Jouzel, J., Lorius, C., Petit, J. R., Genthon, C., Barkov, N. I., Kotlyakov, V. M., & Petrov, V. M. (1987).
714 Vostok ice core: a continuous isotope temperature record over the last climatic cycle (160,000
715 years). *Nature*, 329(6138), 403-408.

716 Jouzel, J., Masson-Delmotte, V., Cattani, O., Dreyfus, G., Falourd, S., Hoffmann, G., ... & Wolff, E. W.
717 (2007). Orbital and millennial Antarctic climate variability over the past 800,000
718 years. *science*, 317(5839), 793-796.

719 Landais, A., Chappellaz, J., Delmotte, M., Jouzel, J., Blunier, T., Bourg, C., ... & Steffensen, J. P. (2003).
720 A tentative reconstruction of the last interglacial and glacial inception in Greenland based on new gas
721 measurements in the Greenland Ice Core Project (GRIP) ice core. *Journal of Geophysical Research:*
722 *Atmospheres*, 108(D18).

723 Landais, A., Dreyfus, G., Capron, E., Masson-Delmotte, V., Sanchez-Goñi, M. F., Desprat, S., ... &
724 Johnsen, S. (2010). What drives the millennial and orbital variations of $\delta^{18}\text{O}_{\text{atm}}$?. *Quaternary*
725 *Science Reviews*, 29(1-2), 235-246.

726 Landais, A., Dreyfus, G., Capron, E., Jouzel, J., Masson-Delmotte, V., Roche, D. M., ... & Teste, G.
727 (2013). Two-phase change in CO₂, Antarctic temperature and global climate during Termination
728 II. *Nature geoscience*, 6(12), 1062-1065.

729 Legrain, E., Capron, E., Menviel, L., et al., (in revision). High obliquity favours centennial-scale
730 variations in the carbon cycle.

731 Lorius, C., Jouzel, J., Ritz, C., Merlivat, L., Barkov, N. I., Korotkevich, Y. S., & Kotlyakov, V. M. (1985). A
732 150,000-year climatic record from Antarctic ice. *Nature*, 316(6029), 591-596.

733 Loulergue, L., Parrenin, F., Blunier, T., Barnola, J. M., Spahni, R., Schilt, A., ... & Chappellaz, J. (2007).
734 New constraints on the gas age-ice age difference along the EPICA ice cores, 0–50 kyr. *Climate of the*
735 *Past*, 3(3), 527-540.

736 Loulergue, L., Schilt, A., Spahni, R., Masson-Delmotte, V., Blunier, T., Lemieux, B., ... & Chappellaz, J.
737 (2008). Orbital and millennial-scale features of atmospheric CH₄ over the past 800,000
738 years. *Nature*, 453(7193), 383-386.

739 Lourantou, A., Chappellaz, J., Barnola, J. M., Masson-Delmotte, V., & Raynaud, D. (2010). Changes in
740 atmospheric CO₂ and its carbon isotopic ratio during the penultimate deglaciation. *Quaternary*
741 *Science Reviews*, 29(17-18), 1983-1992.

742 Marcott, S. A., Bauska, T. K., Buizert, C., Steig, E. J., Rosen, J. L., Cuffey, K. M., ... & Brook, E. J. (2014).
743 Centennial-scale changes in the global carbon cycle during the last deglaciation. *Nature*, 514(7524),
744 616-619.

745 Milankovitch, M. M. (1941). Canon of insolation and the iceage problem. *Koniglich Serbische*
746 *Akademie Beograd Special Publication*, 132.

747 Monnin, E., Indermühle, A., Dällenbach, A., Flückiger, J., Stauffer, B., Stocker, T. F., ... & Barnola, J. M.
748 (2001). Atmospheric CO₂ concentrations over the last glacial termination. *Science*, 291(5501), 112-
749 114.

750 Mudelsee, M. (1999). RAMPFIT—a Fortran 77 program for ramp function regression.

751 Mudelsee, M. (2001). The phase relations among atmospheric CO₂ content, temperature and global
752 ice volume over the past 420 ka. *Quaternary Science Reviews*, 20(4), 583-589.

753 Nehrbass-Ahles, C., Shin, J., Schmitt, J., Bereiter, B., Joos, F., Schilt, A., ... & Stocker, T. F. (2020).
754 Abrupt CO₂ release to the atmosphere under glacial and early interglacial climate
755 conditions. *Science*, 369(6506), 1000-1005.

756 Parrenin, F., Barnola, J. M., Beer, J., Blunier, T., Castellano, E., Chappellaz, J., ... & Wolff, E. (2007). The
757 EDC3 chronology for the EPICA Dome C ice core. *Climate of the Past*, 3(3), 485-497.

758 Parrenin, F., Masson-Delmotte, V., Köhler, P., Raynaud, D., Paillard, D., Schwander, J., ... & Jouzel, J.
759 (2013). Synchronous change of atmospheric CO₂ and Antarctic temperature during the last deglacial
760 warming. *Science*, 339(6123), 1060-1063.

761 Past Interglacials Working Group of PAGES. (2016). Interglacials of the last 800,000 years. *Reviews of*
762 *Geophysics*, 54(1), 162-219.

763 Pedro, J. B., Rasmussen, S. O., & Van Ommen, T. D. (2012). Tightened constraints on the time-lag
764 between Antarctic temperature and CO₂ during the last deglaciation. *Climate of the Past*, 8(4), 1213-
765 1221.

766 Petit, J. R., Jouzel, J., Raynaud, D., Barkov, N. I., Barnola, J. M., Basile, I., ... & Stievenard, M. (1999).
767 Climate and atmospheric history of the past 420,000 years from the Vostok ice core,
768 Antarctica. *Nature*, 399(6735), 429-436.

769 Piasias, N. G., & Moore Jr, T. C. (1981). The evolution of Pleistocene climate: a time series
770 approach. *Earth and Planetary Science Letters*, 52(2), 450-458.

771 Rhodes, R. H., Brook, E. J., Chiang, J. C., Blunier, T., Maselli, O. J., McConnell, J. R., ... & Severinghaus,
772 J. P. (2015). Enhanced tropical methane production in response to iceberg discharge in the North
773 Atlantic. *Science*, 348(6238), 1016-1019.

774 Schmitt, J., Schneider, R., Elsig, J., Leuenberger, D., Laurantou, A., Chappellaz, J., ... & Fischer, H.
775 (2012). Carbon isotope constraints on the deglacial CO₂ rise from ice cores. *Science*, 336(6082), 711-
776 714.

777 Schneider, R., Schmitt, J., Köhler, P., Joos, F., & Fischer, H. (2013). A reconstruction of atmospheric
778 carbon dioxide and its stable carbon isotopic composition from the penultimate glacial maximum to
779 the last glacial inception. *Climate of the Past*, 9(6), 2507-2523.

780 Severinghaus, J. P., Sowers, T., Brook, E. J., Alley, R. B., & Bender, M. L. (1998). Timing of abrupt
781 climate change at the end of the Younger Dryas interval from thermally fractionated gases in polar
782 ice. *Nature*, 391(6663), 141-146.

783 Shackleton, N. J., & Opdyke, N. D. (1977). Oxygen isotope and palaeomagnetic evidence for early
784 Northern Hemisphere glaciation. *Nature*, 270(5634), 216-219.

785 Shakun, J. D., Clark, P. U., He, F., Marcott, S. A., Mix, A. C., Liu, Z., ... & Bard, E. (2012). Global warming
786 preceded by increasing carbon dioxide concentrations during the last
787 deglaciation. *Nature*, 484(7392), 49-54.

788 Siegenthaler, U., Stocker, T. F., Monnin, E., Luthi, D., Schwander, J., Stauffer, B., ... & Jouzel, J. (2005).
789 Stable carbon cycle climate relationship during the Late Pleistocene. *Science*, 310(5752), 1313-1317.

790 Spahni, R., Chappellaz, J., Stocker, T. F., Loulergue, L., Hausammann, G., Kawamura, K., ... & Jouzel, J.
791 (2005). Atmospheric methane and nitrous oxide of the late Pleistocene from Antarctic ice
792 cores. *Science*, 310(5752), 1317-1321.

793 Stauffer, B., Flückiger, J., Wolff, E., & Barnes, P. (2004). The EPICA deep ice cores: first results and
794 perspectives. *Annals of Glaciology*, 39, 93-100.

795 Tzedakis, P. C., Crucifix, M., Mitsui, T., & Wolff, E. W. (2017). A simple rule to determine which
796 insolation cycles lead to interglacials. *Nature*, 542(7642), 427-432.

797 Veres, D., Bazin, L., Landais, A., Toyé Mahamadou Kele, H., Lemieux-Dudon, B., Parrenin, F., ... &
798 Wolff, E. W. (2013). The Antarctic ice core chronology (AICC2012): an optimized multi-parameter and
799 multi-site dating approach for the last 120 thousand years. *Climate of the Past*, 9(4), 1733-1748.

800 WAIS Divide Project Members (2013). Onset of deglacial warming in West Antarctica driven by local
801 orbital forcing. *Nature*, 2013, vol. 500, no 7463, p. 440-444.

802 Wang, Y., Cheng, H., Edwards, R. L., Kong, X., Shao, X., Chen, S., ... & An, Z. (2008). Millennial-and
803 orbital-scale changes in the East Asian monsoon over the past 224,000 years. *Nature*, 451(7182),
804 1090-1093.

805 Wolff, E. W., Fischer, H., & Röthlisberger, R. (2009). Glacial terminations as southern warmings
806 without northern control. *Nature Geoscience*, 2(3), 206-209.

807

808

4.3. Perspectives

The analysis I have performed in this chapter has revealed how challenging it is to identify the onset of a termination in both CO₂ and $\delta^{15}\text{N}$ records. Regarding the CO₂ records, it would be crucial to increase the resolution during the specific time interval of suspected onset of termination, especially for TII and TV. Nevertheless, the imprinted millennial-scale variability observed at the onset TIII and maybe even TIV may still prevent to identify clearly the onset of a termination regardless of the reachable resolution.

The use of the $\delta^{15}\text{N}$ record as a proxy of Antarctic climate proxy was motivated by the absence of relative age uncertainty between this record and the atmospheric CO₂ concentration record. Nevertheless, some of these $\delta^{15}\text{N}$ records are affected by low-amplitude and high frequency variability that cannot be simply explained by the Antarctic surface climate variations. While this variability affects only at second order the record, a better understanding of the driven mechanisms of $\delta^{15}\text{N}$ at the EDC site is necessary to reinforce the confidence on the interpretation made of this proxy. Hence, experimental and theoretical work should be led in the future to better understand and identify the processes affecting $\delta^{15}\text{N}$ beyond its first-order climatic imprint. Collaborators at LSCE and IGE are currently investigating this topic, in particular in the framework of the PhD of Marie Bouchet, supervised by Amaëlle Landais and Frédéric Parrenin. In addition, effort to increase the resolution of the EDC $\delta^{15}\text{N}$ record during TV, but also during older terminations, would provide valuable insights to also characterize the interactions between carbon cycle and past climatic variations of East Antarctica during these time intervals.

My analysis of the sequence of events at play at the end of past terminations have revealed a sub-centennial scale synchronicity between atmospheric CO₂ decrease and a change in $\delta^{18}\text{O}_{\text{atm}}$ signal. I interpret this result as reflecting the enhancement of a low-latitude sink of carbon that would initiate the onset of the CO₂ decrease. While the interpretation of this change in $\delta^{18}\text{O}_{\text{atm}}$ signal and the associated qualitative impact on the carbon cycle is supported by previous studies [Landais et al., 2010, 2013; Extier et al., 2018], a physical quantification of such mechanism is required. The implementation of the $\delta^{18}\text{O}_{\text{atm}}$ signal in the model of intermediate complexity iLOVECLIM currently developed at LSCE will allow to perform simulations that could test the quantitative impact on the carbon cycle of the observed change in the $\delta^{18}\text{O}_{\text{atm}}$. It will also help to identify regionally the carbon sinks at the origin of this observed atmospheric CO₂ decrease at the end of the Termination.

Lastly, the BE-OI project should provide old ice spanning the pre-MPT world (~before 0.8 Ma). While the main motivation is to constrain the absolute atmospheric CO₂ level during the pre- and syn- MPT world (~ 1.5 – 0.8 Ma), it would also be interesting to use these high-resolution records to investigate the phasing during this period. Some changes in the internal climate and potentially their interactions with the carbon cycle are expected to occur across this transition [Legrain et al., 2023]. It would thus be interesting to identify if the Antarctic climate – atmospheric CO₂ phasing is identical to the one of the post-MPT world, characterized in this chapter. Nevertheless, due to the probable very low-resolution at the bottom of the future Beyond EPICA ice core, analyses at sub-millennial-scale of pre- and syn-MPT climate and CO₂ records require the development of measurement system using very low-quantity of ice [Mächler et al., 2023].

Synthesis

In this chapter, I investigate the role of the carbon cycle and the processes responsible for its variations during the largest climatic transitions of the Pleistocene, by quantifying the evolution of the phasing between Antarctic climate and atmospheric CO₂ concentrations across the past five terminations. To do so, I use new and recently published high-resolution CO₂ and δ¹⁵N records from the EDC ice core. Previous studies have investigated this phasing across the past three terminations revealing significantly different results from one study to another. Nevertheless, the use of different ice cores, statistical methods and proxies for the Antarctic climate makes it difficult to distinguish whether the heterogeneity is method-induced or whether it reflects climatic differences. My approach is based on the use of three statistical methods, in order to distinguish method-dependent results from robust phasing patterns. My analyses evidence that the phasing at the onset of terminations varies depending on the methodology used and the termination considered. Reversely, a significant multi-centennial lag of the atmospheric CO₂ decrease over the Antarctic climate cooling is observed at the end of four of the past five terminations. A phasing of similar temporal scale has been described previously during the millennial-scale events over the last glacial period. Following the theory developed by Wolff et al. [2009], I propose that terminations are ultimately ended by millennial-scale events. Nevertheless, the occurrence of millennial-scale variabilities over the course of the TI and TIII reveals the complexity of interactions between orbital-scale and millennial-scale variability. I suggest that millennial-scale variability could either temporarily stop or definitely achieve the termination process depending of the orbital context under which they occur. Finally, an analysis of the sequence of events including additional paleoclimatic proxies at the end of terminations suggests the enhancement of a mid-to-low latitude carbon sink may constrain the exact timing of atmospheric CO₂ decrease at the end of terminations. Further modelling efforts as well as new climatic records on the oldest terminations (TIII, TIV and TV) are needed to test my interpretation and quantify the consequences at multi-centennial scale of the enhancement of a mid-to-low latitude carbon sink on atmospheric CO₂ concentrations.

Chapter 5

Spatio-temporal climatic variability at millennial-to-orbital scale during MIS 7

In this chapter, I investigate the spatio-temporal pattern of surface temperature changes during the MIS 7 and the Termination III. To do so, I produce the first multi-archive synthesis of surface temperature records covering the 260-190 ka period and I compare them to the pre-industrial climate as well as to global climatic and external variables. This chapter is composed of an article in preparation, followed by several perspectives.

Chapter 5 aims at:

- ✦ Characterizing the spatio-temporal pattern of surface temperature changes during MIS 7 and Termination III.

Methodology:

- ✦ Global-scale compilation of surface air temperature from 3 ice cores and sea surface temperatures from 38 marine sediments cores.
- ✦ Definition of a common temporal framework and quantitative estimates of the associated uncertainties for the compiled surface temperature records.
- ✦ Time slices at 246, 242, 218, 215 and 200 ka of surface temperature anomalies relative to pre-industrial ones.

Highlights:

- ✦ The intensities of warming during MIS 7e and MIS 7a-7c are similar in magnitude apart in the southern high latitudes.
- ✦ The southern high-latitude region was warmer than pre-industrial during MIS 7e.
- ✦ Based on a strong obliquity imprint on surface temperature records and the relatively low amplitude of the warming during MIS 7, I propose that the MIS 7 owns specificities that resemble those associated with the pre-MPT interglacials.

Data availability:

- ✦ Meta-data of the synthesis are available upon request and the raw records are available online in paleoclimate databases or in the source papers.

5.1. Introduction

The Marine Isotope Stage 7 (MIS 7, ~245-190 ka) occurs under a very distinct orbital configuration and consequent spatial insolation pattern compared to the other post Mid-Brunhes Event interglacials, i.e. MIS 1, 5, 9 and 11. Especially, the precession and obliquity registered their maximum amplitude of the last 800 ka. So far, MIS 7 has not been the focus of many scientific studies. Nevertheless, the study of this interglacial would allow to investigate the climatic responses under strong orbital forcing variability.

The morphology of paleoclimatic records between 260-190 ka is characterized by an alternance of glacial and interglacial conditions (see Fig. 1 in the chapter draft, section 5.2.): (i) the TIII (around ~250 ka) is a termination composed of a three-phase sequence similarly to TI [Cheng et al., 2009; Bréant et al., 2019]. Following this termination, the MIS 7e is commonly considered as the strict interglacial period (Past Interglacial Working Group of PAGES, 2016). It is characterized by an overshoot registered in both atmospheric CO₂ concentrations [Legrain et al., in revision] and Antarctic water isotopic records [Jouzel et al., 2007]. The MIS 7e is interrupted to a back to full glacial conditions during MIS 7d. Consequently, MIS 7e is the shortest interglacial period occurring after the Mid-Brunhes Event regardless of the definition used [Past Interglacial Working Group of PAGES, 2016]. This back-to-full glacial condition is abruptly ended by the second Termination TIII-A around ~220 ka. At the end of TIII-A, the climate goes back to warmer conditions during MIS 7c. This period is ended by a brief and not intense cold period MIS 7b. Finally, the climate reaches a third warm period known as MIS 7a, before gradually moving to the glacial stage MIS 6 at around 190 ka. In the following, the end of this sequence will be referred to as MIS 7a-7c as many surface temperature records do not allow to distinguish unambiguously MIS 7c from MIS 7a. This variability of the climate during MIS 7 at orbital-scale is unique in the past five interglacials and it thus deserves a special attention.

This work takes place in the context of increasing number of high-resolution paleoclimatic records spanning the 260-190 ka interval over the past two decades. Benefiting from this community effort, I present here the first multi-archive synthesis of surface temperature records spanning the 260-190 ka interval. Fig 5.1 is a conceptual summary of the analysis performed in this chapter.

Based on this new surface temperature synthesis, I will tackle the following questions:

- What is the relative and spatial intensity of the warm phases occurring during MIS 7?
- How warm is the MIS 7 in comparison to the pre-industrial climate?
- What is the relative influence of the different background and orbital variables on the particular pattern of MIS 7 surface temperatures?

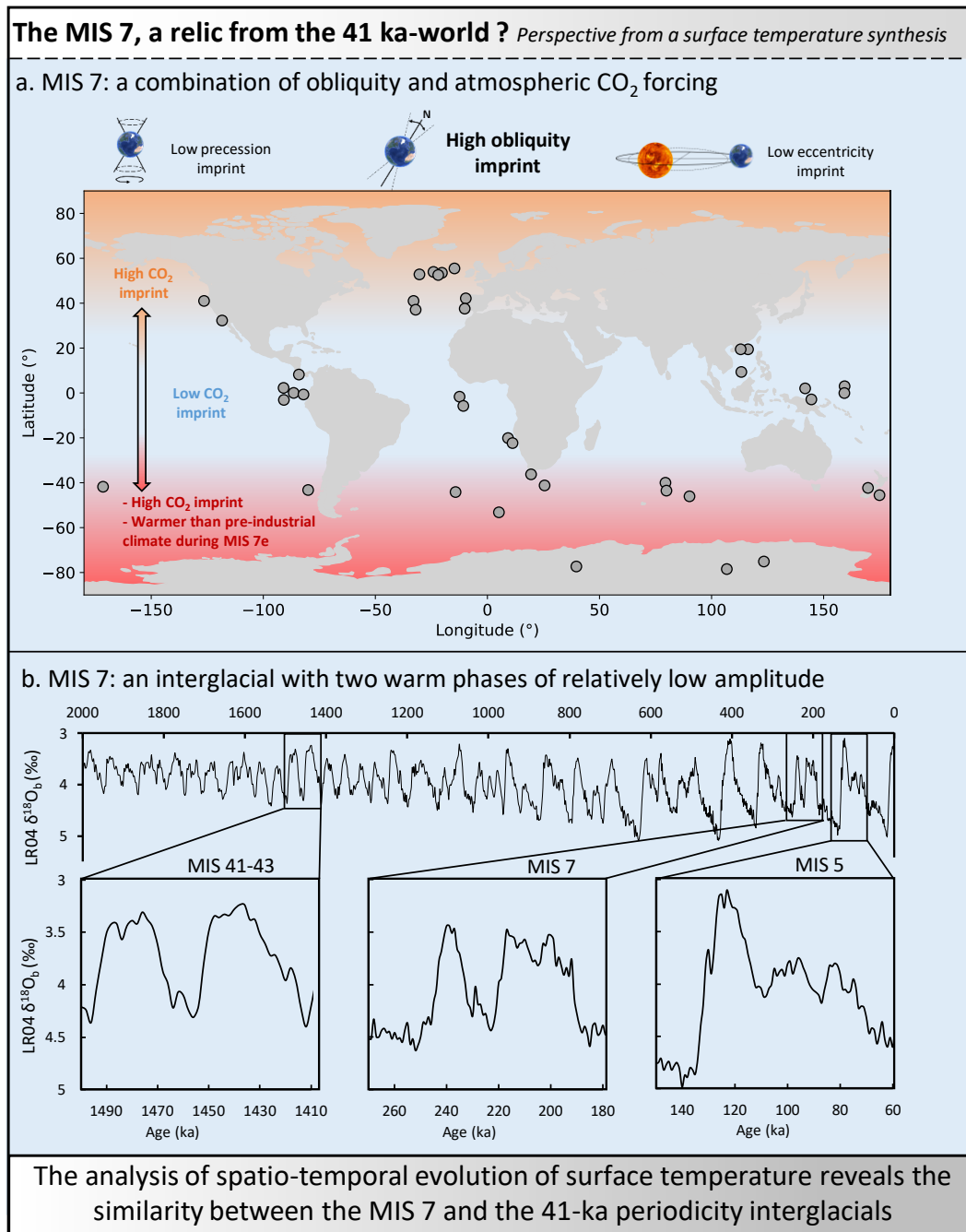


Fig 5.1: Conceptual summary of the analysis performed in Chapter 5. a. The grey dots on the map represent the compiled surface temperature records included in the new multi-archive synthesis. The orange area represents the Northern high-latitudes, where the surface temperature record is strongly correlated ($R^2 = 0.54$) with atmospheric CO₂ concentrations. Similarly, the red area represents the Southern high-latitudes, where the surface temperature records are strongly correlated with atmospheric CO₂ concentrations ($R^2 = 0.51$) and where a warmer-than-pre-industrial climate has been registered at 242 ka. The light blue area represents the tropics, where a low CO₂ imprint on surface temperature records have been recorded. On top of the map the relative similarity in morphology between the different orbital parameters and the surface temperature records is represented. b. The LR04 benthic $\delta^{18}\text{O}_b$ stack from Lisiecki and Raymo [2004] is represented over the past 2 Ma with zooms on three specific periods including MIS 7, MIS 41-43 and MIS 5. MIS 41-43 and MIS 5 have been chosen as “typical” examples of the interglacials from the 41 kyr-world and 100-kyr world, although each period registered internal variability in their interglacial patterns. These examples are taken to illustrate the global difference of amplitude and frequency of interglacial occurring before the MPT (e.g. MIS 41-43) and after the MPT (e.g. MIS 5), although the diversity of interglacials is much more complex. Vertical and horizontal scales are similar to facilitate the comparison. Note the higher similarity of the MIS 7 with the MIS41-43 than with the MIS5 in term of amplitude and peak frequency.

5.2. Publication: Spatio-temporal pattern of surface temperature changes during Marine Isotopic Stage 7 (in prep)

Legrain et al., in prep

1 **Spatio-temporal pattern of surface temperature changes during the MIS 7 (in preparation)**

2 *Legrain et al.,*

3

4 **Abstract**

5 The Marine Isotope Stage 7 (MIS 7, ~245-190 ka), exhibits an unusual morphology compare to
6 the other interglacials of the late Pleistocene. It is characterized by a large climatic variability composed
7 of two warm stages separated by a short period going back to full glacial conditions. While previous
8 studies have extensively investigated the spatio-temporal variability of climate during the current and
9 the last interglacials, a spatio-temporal picture of the MIS 7 is not available yet mainly due to the
10 scarcity of paleoclimatic records and the dating uncertainties associated to their chronologies. Here
11 we compiled three surface air temperature records from Antarctic ice cores and 38 sea surface
12 temperature (SST) records from marine sediments records located at low and high latitudes. To
13 compare these records, we align them on a global temporal framework, the AICC2012 reference
14 chronology, and we quantify the attached uncertainty accounting for both the uncertainty associated
15 with the surface temperature reconstruction methods and the one associated with the dating.

16 Our multi-archive synthesis spanning the 260-190 ka interval reveals that the intensities of the
17 two warm periods during MIS 7 are of similar amplitude except in the southern high latitudes. In
18 addition, comparing five climate time slices at 246, 242, 218, 215 and 200 ka to the climatological mean
19 from 1854 to 1883, we point out that the tropics and the Northern hemisphere have remained cooler
20 or similar to the pre-industrial temperatures during the whole interglacial. Reversely, the southern
21 high latitudes exhibit surface temperatures warmer than during the pre-industrial during MIS 7e
22 compared to MIS 7c-7a. The evolution of the compiled surface temperature records is compared with
23 variables illustrating the climatic and orbital background across MIS 7. This comparison evidences a
24 high correlation with obliquity records, revealing a stronger imprint of the obliquity forcing on surface
25 temperature records compared to precession, eccentricity and insolation forcings. The imprint of
26 atmospheric CO₂ concentration changes is also registered, mostly in the high-latitude surface
27 temperature records.

28 We suggest that the surface temperature patterns across MIS 7 were driven by both obliquity
29 and atmospheric CO₂ concentrations forcing. Especially, we propose that the exceptional amplitude of
30 the obliquity signal during MIS 7 would favour the occurrence of a relatively cold interglacial occurring
31 in two warm phases. We also observe that the delay between the two warm phases is close to the 40-
32 ka periodicity of the glacial-interglacial cycles occurring before the Mid-Pleistocene Transition. The

33 occurrence of such interglacial, in the middle of the more amplified interglacials of the late Pleistocene,
34 suggests a lingering influence of the 41 ka-world drivers during this period.

35

36 **Main text**

37 **1. Introduction**

38 Interglacial periods of the Pleistocene span a large diversity in term of external orbital forcing,
39 ice distribution, atmospheric greenhouse gas concentrations and global and regional climatic patterns
40 (Tzedakis et al., 2009; Lang and Wolff, 2011). These complexities allow to investigate mechanisms at
41 play in the establishment of warm climates under very distinct boundary conditions. The current
42 (Holocene) and the last (Marine Isotope Stage 5, MIS 5) Interglacials, as well as their preceding
43 Terminations I and II have been extensively studied thanks to the large amount of very highly resolved
44 records covering these periods (Shakun et al., 2012; Capron et al., 2014; Hoffman et al. 2017). Previous
45 investigation of these interglacial climates has evidenced crucial paleoclimatic mechanisms at play
46 during interglacial periods for sea ice expansion (e.g. Masson-Delmotte et al., 2011; Steinsland et al.,
47 2023), deep oceanic circulation (e.g. Oppo et al., 2006; Luo et al., 2018), sub-orbital scale variability
48 (e.g. Frogley et al., 1999; Wang et al., 2018) and regional amplitude of surface temperature change
49 (Hoffman et al., 2017). Both the Holocene and the Last Interglacial are considered as long and relatively
50 stable interglacials, and thus not reflects the diversity of interglacials (Past Interglacials Working Group
51 of PAGES, 2016). Consequently, the analysis of climate processes beyond the Last Interglacial period
52 could bring complementary information due to the different context of occurrences of these warm
53 periods. The investigation of older interglacials and their associated terminations is more challenging
54 due to the scarcity of high-resolution records and challenging dating, but it represents a research
55 priority for the paleoclimate community (Capron et al., 2019).

56 An extreme combination of boundary conditions occurs during the Termination III (TIII) (~255-
57 245 ka) and the following MIS 7 (Fig. S1). This period is characterised by the largest changes in the 65°N
58 summer insolation in the context of the past 800 ka (Laskar et al., 2004). Also, the lowest obliquity
59 values of the past 2 Ma are reached near after the end of TIII and the short MIS 7e, during MIS 7d
60 (Laskar et al., 2004). Under this context, the climate switches back to full glacial conditions during MIS
61 7d as evidenced in the Antarctic temperature reconstruction and the atmospheric CO₂ concentrations
62 that reached levels close to those prevailing at the onset of TIII (Petit et al., 1999; Jouzel et al., 2007;
63 Legrain et al., under review) (Fig. 1). This climatic sequence is also registered in marine and continental
64 local proxies (e.g. Desprat et al., 2006; Martrat et al., 2007; Roucoux et al., 2008; Wendt et al., 2021).

65 Following this glacial minimum, a second termination (i.e., TIII-A) occurs around ~218 ka leading to the
66 following MIS 7c. The amplitude of TIII-A recorded in both Antarctic surface temperature and
67 atmospheric CO₂ concentration records is smaller than the amplitude of TIII in, while pollen-based and
68 biogenic silicate-based climate reconstructions registered climatic amplitude similar to or superior
69 than TIII during TIII-A (Prokopenko et al., 2006; Roucoux et al., 2006). This period is ended by a brief
70 and not intense period, the MIS 7b. Finally, the climatic reaches a third warm period known as MIS 7a,
71 before gradually moving to the glacial stage MIS6 at around 190 ka. The end of this sequence will be
72 referred to as MIS 7c-7a in this article as many surface temperature records do not allow to distinguish
73 between the MIS 7c and MIS 7a.

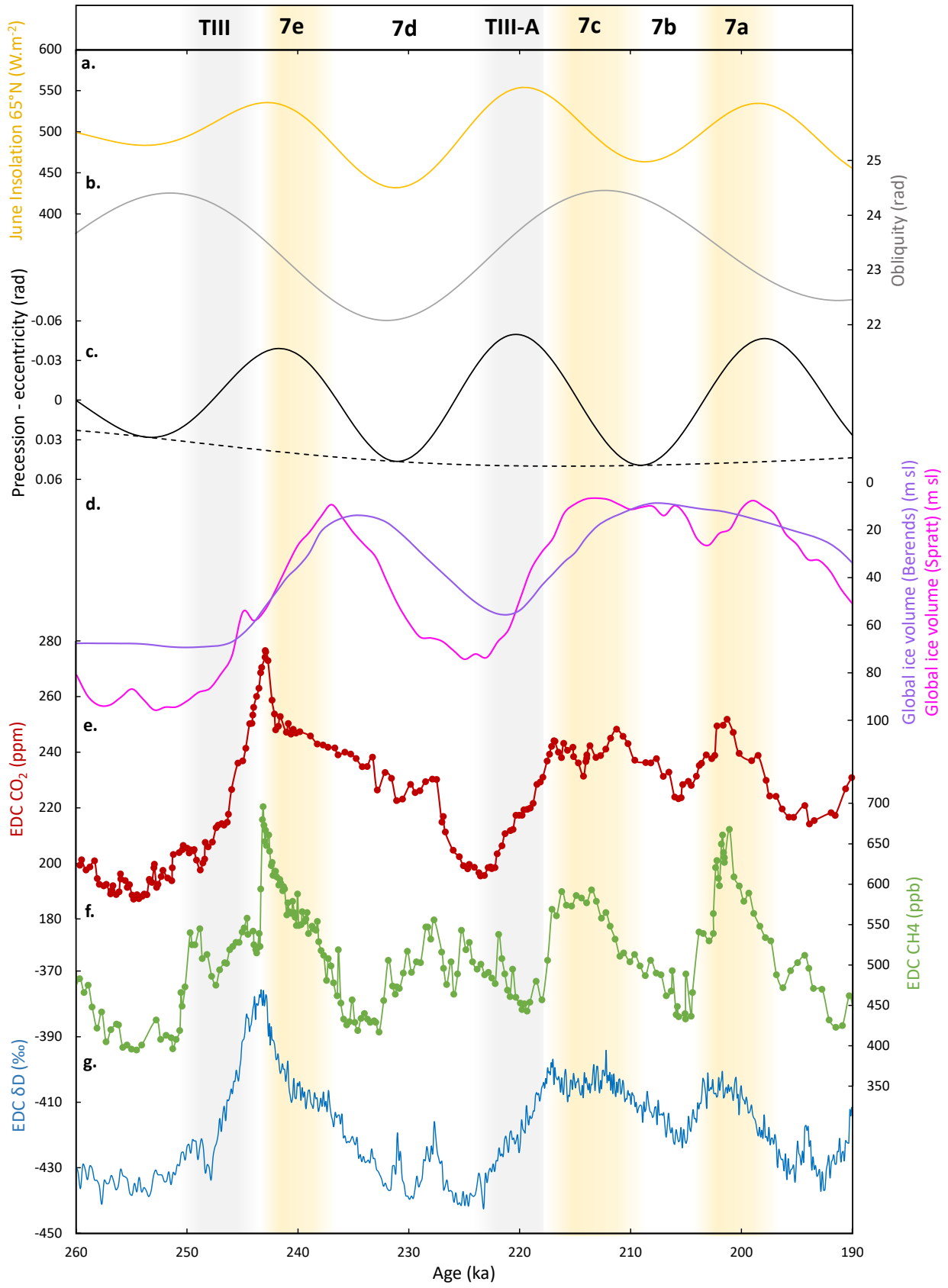
74 Due to all of these complexities, the MIS 7c-7a can be considered or not as an interglacial
75 period depending on definition chosen to define an interglacial period (Past Interglacials Working
76 Group of PAGES, 2016). Considering this particular structure of the climatic and environmental
77 changes, MIS 7 represents a great study case to investigate the response of the climate at regional
78 scale and its link with both external orbital forcing and carbon cycle.

79 Estimates of global ice volume changes are relatively uncertain during the MIS 8 - MIS 7e- MIS
80 7d – 7c-7a sequence (Lea et al., 2002; Siddall et al., 2003; Dutton et al., 2009; Lisiecki and Raymo,
81 2016). Simple conceptual models forced by orbital parameters have difficulties reproducing the
82 different ice volume data-based reconstructions and they only partially mimic this complex sequence
83 of climatic changes (Imbrie et al., 2011; Parrenin and Paillard, 2012; Legrain et al., 2023). Mechanisms
84 at play have been investigated based on more sophisticated physical models (Colleoni et al., 2014;
85 Ganopolski and Brovkin, 2017; Choudhury et al., 2020). The ability of such model to reproduce this
86 climatic sequence is limited to the comparison with integrative climatic variables such as global ice
87 volume reconstruction (Ganopolski and Brovkin, 2017; Choudhury et al., 2020). We can mention here
88 the interesting model-data latitudinal comparison performed by Colleoni et al. (2014) during the MIS
89 7 using the data synthesis from Lang and Wolff (2011). Nevertheless, all paleorecords used were
90 aligned on the LR04 chronology regardless of their geographical origin suggesting a synchronicity of
91 the benthic foraminifera $\delta^{18}\text{O}$ in the whole ocean, that is very unlikely (Lisiecki and Raymo, 2009). In
92 addition, the number of records used in this paleodata-model comparison is quantitatively restricted
93 (10 records).

94

95

96



99 Fig. 1 : Climatic and orbital records during the 260-190 ka interval. From top to bottom: a. June Insolation at 65°N. b. Obliquity.
100 c. Eccentricity and precession. d. Global ice volume in sea meter equivalent from Berends et al. (2021) (purple) and Spratt
101 and Lisiecki, 2016 (pink). e. Atmospheric CO₂ record from EDC (Legrain et al., under review). f. Atmospheric CH₄ record from
102 EDC (Loulergue et al., 2008; Legrain et al., under review). g. EDC dD record (Jouzel et al., 2007). Yellow shaded area highlights
103 MIS 7e, 7c and 7a. Note that depending on the definition used, MIS 7c and 7a are sometimes not considered as interglacial
104 periods (Past Interglacials Working Group of PAGES, 2016). White areas are the cold periods MIS 8, MIS 7d and MIS 7b. Grey
105 shaded areas highlight the TIII and TIII-A.

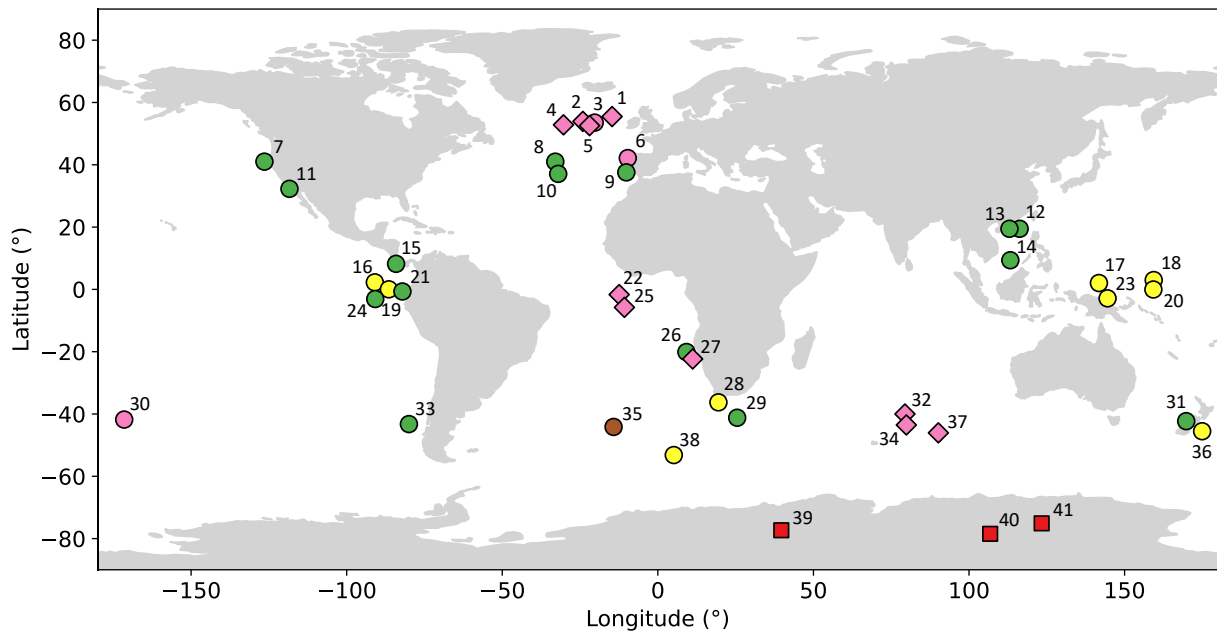
106

107 The diverse patterns observed in the different global and regional climatic proxies during the
108 MIS 7 and the identification of their forcing mechanisms require an approach that considers the spatio-
109 temporal variability of the warming. Such approach was already applied to the Last Interglacial based
110 on a multi-archive synthesis composed of marine sediments and ice cores records from the high-
111 latitude regions aligned on a common temporal framework (Capron et al., 2014). This study evidenced
112 a polar specificity of the warming, with an extended period of warm conditions but of lower amplitude
113 in the southern high latitudes compared to the northern high latitudes. A warmer than pre-industrial
114 climate in the high latitudes during the Last Interglacial was also evidenced (Capron et al., 2017). In
115 parallel, another study extended this analysis to the low latitude regions evidencing a less pronounced
116 warming in the tropical areas compared to the pre-industrial (Hoffman et al., 2017). Similar synthesis
117 spanning older interglacials are necessary to characterize the evolution of regional-scale surface
118 temperature to compare the climate of these periods and evidence differences and similarities
119 between past interglacials.

120 Here we present the first multi-archive synthesis gathering both high- and low- latitudes
121 surface temperature records aligned on a common temporal framework covering the TIII and the MIS
122 7 period. Based on this synthesis, we are able to (i) compare the spatial variations of the warming
123 intensity between TIII and TIII-A, and the intensities of MIS 7e and 7c-7a (ii) characterize the spatio-
124 temporal intensity of the warming during MIS 7e and MIS 7c-7a compared to the pre-industrial climate
125 (iii) evidence the similarities between regional temperature patterns and the background orbital and
126 climatic variables during MIS 7.

127

128



129

130 Fig. 2 : Location of marine sediment and ice core sites. The new data compilation contains surface air temperature records
 131 from Antarctic ice cores (red square) and annual (circle) and summer (diamond) SST reconstructions based on alkenones
 132 (green), faunal assemblages (pink), Mg/Ca (yellow), percentage of polar foraminifera species (brown). Numbers refer to
 133 record labels from Table S1.

134

135 2. Material and methods

136 2.1. Selection of paleoclimatic data sites

137 We first select sites with an average temporal resolution of surface temperature
 138 reconstruction better than 4 ka. Among this first selection of sites, we only keep those in which the
 139 typical morphology of the MIS 7 can be identified. In case of doubt, first-order identification of MIS 7
 140 morphology is checked with additional information, such as benthic and/or planktonic $\delta^{18}\text{O}$ records. In
 141 total, we select three records of continental surface air temperature deduced from water stable
 142 isotope records from Antarctic ice cores and 38 sea surface temperature (SSTs) records from marine
 143 sediments cores (Fig. 2). The data have been collected from the PANGEA and NOAA databases or
 144 provided directly by the authors when their dataset were not available online. Two additional datasets
 145 not published yet from the marine cores MD94-101 (SST record) and MD07-3077 ($\delta^{18}\text{O}_b$ record) have
 146 also been used (N. Vazquez Riveiros, pers. Com.). The data records have been compiled and analysed
 147 over the 260-190 ka period in order to include TIII and the whole MIS 7. The average resolution of the
 148 surface temperature records is 1.8 ± 1.1 ka. Table S1 compiles all details on the selected records.

149 2.1.1. Continental ice core records

150 The Vostok, Dome F and EPICA Dome C (EDC) Antarctic ice cores are the only ice cores records
151 extended as far back in time as 260 ka. These three ice cores are located on the East Antarctic plateau,
152 at elevations superior to 3000 m asl and latitudes south from 75°S. These three ice cores are thus not
153 representative of the whole potential diversity of surface temperature pattern in the polar regions.
154 Nevertheless, they represent the only available continuous paleo-archives at such high-latitudes
155 spanning the 260-190 ka period and thus provide precious information of the dynamics of the antarctic
156 climate.

157 We include the three antarctic surface temperature records inferred from water isotope
158 records (Petit et al., 1999; Jouzel et al., 2007, Kawamura et al., 2007; Landais et al., 2021). These
159 temperature reconstructions are based on present-day correlation between surface temperature and
160 water isotopic composition. Other factors could influence the isotopic composition of water molecules,
161 such as precipitation and origin of the moisture (Jouzel et al., 2003). Recently, the use of Antarctic
162 isotopes as paleothermometer has been challenged by an alternative methodology based on firn
163 properties (Buizert et al., 2021). Nevertheless, the water stable isotopes remain the more reliable
164 approach to reconstruct paleotemperature for the MIS 7 interval, with surface temperature associated
165 with a maximum 1σ uncertainty of $\pm 2^\circ\text{C}$ (Landais et al., 2021).

166 2.1.2. Marine sediments cores records

167 The marine sediment records gathered in this synthesis are located in the northern high latitudes
168 ($>40^\circ\text{N}$, 8 records), the southern high latitudes ($>40^\circ\text{S}$, 10 records) and from the mid-to-low latitudes
169 (between 40°N and 40°S , 20 records). They include SST reconstructions based on alkenone
170 unsaturation ratios (15 records), faunal assemblage transfer functions (14 records), foraminiferal
171 Mg/Ca ratios (9 records) and the percentage of the polar foraminifera species *Neogloboquadrina*
172 *pachyderma sinistral* (one record). 10 of these records represent summer SST and 28 records are
173 interpreted as annual SST, following the interpretation provided in the source papers (Table S1). When
174 available, we also compile benthic and planktonic foraminifera $\delta^{18}\text{O}$ records that will be used to define
175 the age scale of the record.

176

177 2.2. Definition of a common temporal framework between the ice and marine records

178 The original age models from the compiled records were build using multiple approaches,
179 including distinct paleoclimatic assumptions (Govin et al. 2015). A direct comparison of the records on
180 their original timescale can led to multi-millennia relative age uncertainty between the records. In
181 some of the oldest studies, uncertainties associated with the age scale is not quantified. Before

182 comparing these records, an effort to homogenize age models is thus required. In addition, the paleo
183 records from this synthesis comes from two different archives. We thus propose to align the surface
184 temperature records from both archives on a single reference chronology. For that purpose, we choose
185 to use the ice core chronology AICC2012 as the reference chronology (Bazin et al., 2013). It is a multi-
186 sites-based approach relying on an inverse dating method that combines glaciological modelling with
187 absolute and stratigraphic marker. Orbital age constraints measured in the gas-phase of ice core, i.e.
188 $\delta^{18}\text{O}_{\text{atm}}$, $\delta\text{O}_2/\text{N}_2$ and total air content, have been also added to the chronology. The absolute 1σ dating
189 uncertainty is ± 2.0 ka over the 260-190 ka period (Bazin et al., 2013).

190 2.2.1 Paleoclimatic hypotheses

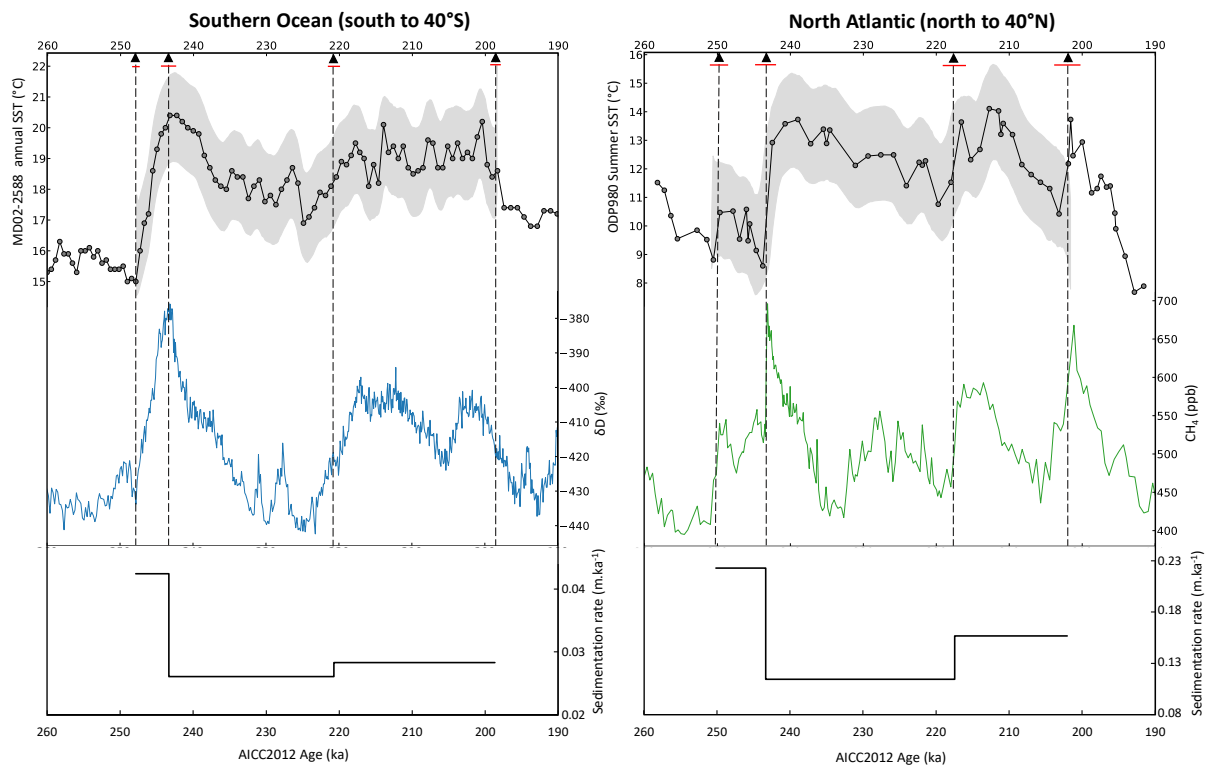
191 We follow the strategy of Govin et al. (2012) and Capron et al. (2014) to align high-latitude (poleward
192 to 40°) marine records onto the AICC2012 ice core chronology, and the one developed by Hoffman et
193 al. (2017) to extend our common temporal framework to the mid-to-low latitudes (between 40°N and
194 40°S). Our strategy relies on four main climatic hypotheses:

- 195 (i) To place the SST records south to 40°S onto AICC2012, we hypothesize that the Southern
196 Ocean surface temperature covaries with East Antarctic plateau surface temperature.
197 Such co-variation has been evidenced during the last glacial period and the TI that benefits
198 from independent radiocarbon dating for marine sediments (e.g. Waelbroeck et al., 1995;
199 Pahnke et al., 2003; Calvo et al., 2007). We thus align SST record from marine core located
200 south to 40°S onto the EDC deuterium record (δD , Jouzel et al., 2007) (Fig. 3).
- 201 (ii) To place the SST records north to 40°N onto AICC2012, we hypothesize that the abrupt
202 North-Atlantic surface temperature increases are synchronous with the rapid changes in
203 CH_4 recorded in the EDC ice core. Such co-variation during abrupt events was evidenced
204 during TI (e.g. Chappellaz et al., 1993; Severinghaus and Brook, 1999; Fluckiger et al., 2004;
205 Huber et al., 2006) and was already used in alignment strategy during the Last Interglacial
206 (Govin et al., 2012; Capron et al., 2014). We hypothesize that this link could be extended
207 to the large past abrupt CH_4 increases registered during TIII, TIII-A, and at the onset of MIS
208 7a (Fig. 3). We thus align SST record from marine core located north to 40°N in the North
209 Atlantic onto the abrupt CH_4 increases occurring during the 260-190 ka interval. We do
210 not use the Greenland synthetic curve (GLSC, Barker et al. (2011)) as in Hoffman et al.
211 (2017) because we consider that this curve is associated with stronger climatic assumption
212 than the CH_4 -based alignment. This curve relies on the hypothesis of a constant and
213 systematic bipolar see saw between the Northern and Southern hemispheres over the past
214 800 ka to extent the Greenland climate records beyond the last glacial-interglacial cycles

215 (Barker et al., 2011). Still, to evaluate the uncertainty associated with the use of a strategy
216 rather another, we align the North Atlantic cores on both CH₄ and GLSC (8 cores). The
217 average age difference is of 0.6 ±0.5 ka (Fig. S2).

218 (iii) To place the SST records from the low-to-mid latitudes (between 40°N and 40°S) onto
219 AICC2012, we hypothesize that the variations of $\delta^{18}\text{O}_b$ occurs synchronously within a single
220 water mass in an oceanic basin. Asynchronicity of benthic $\delta^{18}\text{O}$ ($\delta^{18}\text{O}_b$) changes from cores
221 of distinct oceanic basin could reach up to 4 ka during the terminations of the late
222 Pleistocene (Lisiecki and Raymo, 2009). Reversely, $\delta^{18}\text{O}_b$ variations are synchronous or
223 affected by sub-millennial scale lag within a single oceanic basin (Stern et al., 2014; Lisiecki
224 and Stern, 2016). Such approach was already used in the synthesis including low-latitude
225 records during the Last Interglacial (Hoffman et al., 2017). Thus, we select a reference core
226 for the North Atlantic, South Atlantic, and Pacific basin located north to 40°N or south to
227 40°S that was previously aligned onto AICC2012. And then, we perform intra-basin $\delta^{18}\text{O}_b$
228 alignment to extent the common temporal framework based on AICC2012 to the low
229 latitudes (Fig. 4).

230 (iv) To place SST records from the low-to-mid latitudes that do not have $\delta^{18}\text{O}_b$ records, we
231 hypothesize that planktonic $\delta^{18}\text{O}_p$ changes co-vary at very local-scale (typically < 2000 km).
232 We thus align a marine core already scaled on the AICC2012 chronology through $\delta^{18}\text{O}_b$
233 alignment with a new marine core through $\delta^{18}\text{O}_p$ records (Fig. 4). Such strategy has been
234 used for five marine cores of the synthesis. Planktonic $\delta^{18}\text{O}_p$ is a proxy that is very sensitive
235 to local evaporation, that is thought to reflect local climatic conditions at first order
236 (Emiliani, 1954; Mulitza et al., 2002). We first evaluate the relevance to perform such
237 alignment based on information provided in the source paper of each of the $\delta^{18}\text{O}_p$ records
238 and we compare the modern local climatic conditions at the surface of the two drilling
239 sites.



240

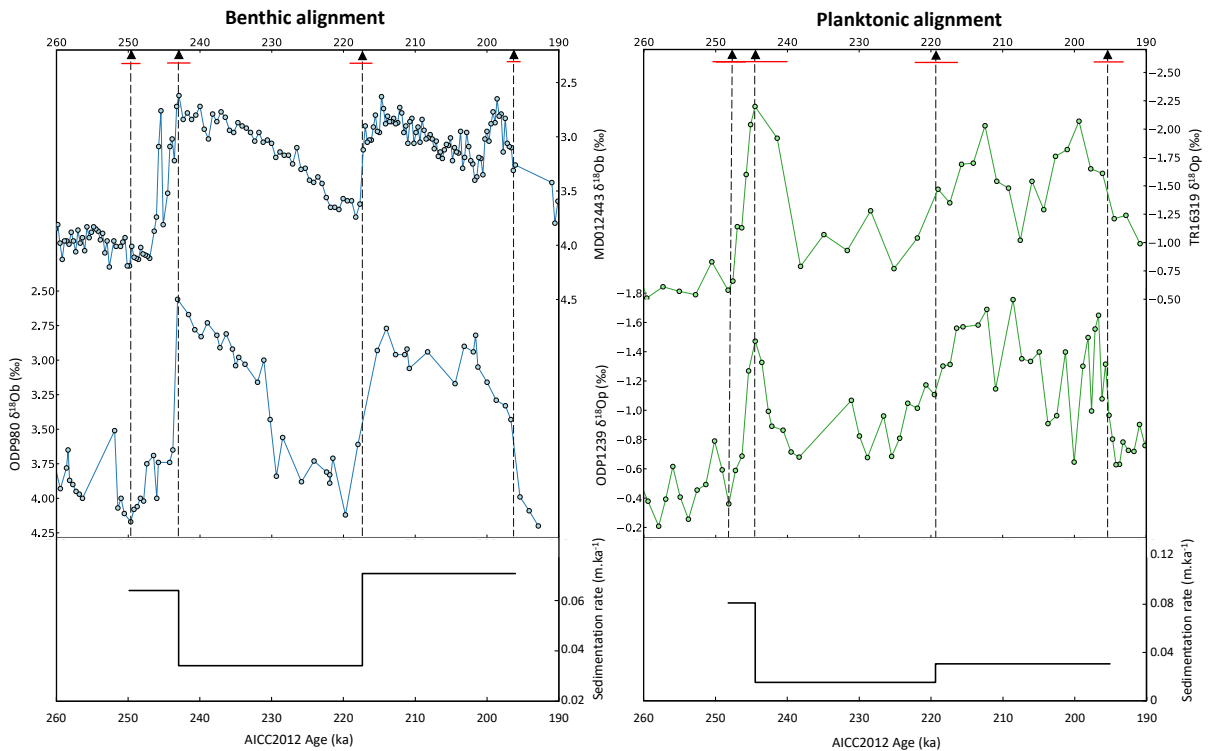
241 Fig. 3 : Example of alignment performed in the Southern Ocean (MD02-2588 core, left) and in the North Atlantic (ODP980
 242 core, right). Black triangles and vertical dotted lines highlight the tie-points between the marine core and the EDC δD record
 243 (left panel, blue curve, Jouzel et al., 2007) and the EDC CH_4 record (right panel, green curve, Loulergue et al., 2008). The
 244 resulting sedimentation rate variations is shown in black at the bottom of each panel. Grey shaded areas are the 1σ
 245 confidence intervals resulting from the Monte Carlo iterations. Red lines are the uncertainty associated with each tie point.

246

247 2.2.2 Alignment strategy

248 All alignments are performed with the AnalySeries 2.0 software (Paillard et al., 1996). The
 249 principle of the alignment relies on tie points visually determined by the user based on morphologic
 250 similarity between the two records. The model then performs a linear interpolation between the tie
 251 points to produce a new age-model for the entire dataset. No extrapolation beyond the younger and
 252 older tie points is performed. As each tie point represents a hypothesis on the sedimentation rate, we
 253 minimize as much as possible the number of tie points defined for each alignment. The coherency of
 254 the final alignments is evaluated with (i) the sedimentation rate changes calculated and provided by
 255 the software (ii) the use of independent variables not used in the alignment (e.g. $\delta^{18}O_b$ for SST
 256 alignments) (iii) several sequence of alignment for a same core performed independently to evaluate
 257 the tie points chosen as objectively as possible.

258



259

260 Fig. 4 : Example of alignment performed for low-latitude cores based on benthic $\delta^{18}\text{O}$ (blue, left panel) and planktonic $\delta^{18}\text{O}$
 261 (green, right panel). Example of the alignment of the MD012443 (left) and TR16319 core (right). Black triangles and vertical
 262 dotted lines highlight the tie-points between the marine core and the reference benthic and planktonic $\delta^{18}\text{O}$ record already
 263 aligned on the AICC2012 age scale. The resulting sedimentation rate variations is shown in black at the bottom of each panel.
 264 Red lines are the uncertainty associated with each tie point.

265

266 2.2.3 Uncertainty quantification

267 The uncertainty associated with the original SST reconstruction depends on (i) the proxy-
 268 measurement uncertainty (ii) the calibration used to convert the proxy into sea surface temperature.
 269 This total uncertainty is directly compiled from the sources studies and it ranges from 0.5 to 1.7 °C
 270 (Table S1).

271 The total uncertainty associated with the age-scale alignment depends on three main sources
 272 of uncertainties: (i) the uncertainty associated with the resolution of the correlated and reference
 273 records, (ii) the absolute age uncertainty associated with AICC2012 (iii) the morphological uncertainty.
 274 This last uncertainty refers to the tie-point approach of the alignment and aims to take into account
 275 the uncertainty of the choice of the tie-point location of the user. Typically, in case of a tie-point located
 276 at a peak maximum, an uncertainty is applied if the operator hesitates between one peak maximum
 277 and the following and/or the preceding one, and no independent variable (e.g. $\delta^{18}\text{O}_b$) allow to clearly
 278 identify the most probably peak. This uncertainty is by far the most important one when applied.

279 Nevertheless, it is only applied on the few tie-points for which no choice could be made between two
280 morphologies. The marine cores align on CH₄ record are also associated with another source of
281 uncertainty which is the uncertainty associated with the gas-ice age difference in AICC2012.
282 Uncertainties for each tie-point are presented in Table S2.

283 The final uncertainty associated with the SST value at a specific time will depend on both the
284 original SST uncertainty and the age-scale uncertainty. To evaluate this final uncertainty for each
285 surface temperature record, we perform a Monte-Carlo analysis involving 1,000 age model
286 simulations. In each iteration, we introduce random noise to the SST values, considering the
287 temperature reconstruction error. Additionally, we randomly determine the age of each tie-point
288 within the range of dating error (Table S2). Any iteration with potential age reversals was discarded.
289 Linear interpolation was used between tie-points to assign ages to each depth with SST values. We
290 present all SST records along with a non-parametric 1 σ confidence interval envelope after resampling
291 every 0.1 ka in Fig. 5.

292 The use of the Monte-Carlo program from Capron et al. (2014), applied on MIS 7 have revealed
293 some limits in the estimation of the global uncertainty envelope. First, edge inconsistencies have been
294 revealed at the temporal extremities of the records. Second, the smoothing process is probably not
295 adapted for the resolution and the structure of the MIS 7 records (Fig. 5). However, these
296 approximations do not affect the correlation analysis (section 2.5) and the comparison of relative
297 intensity between terminations (section 2.3) that are based on the raw SST records, and thus do not
298 concern the main results of this study. Nevertheless, the computation of time slice relies on the
299 smoothed curve of the program. The results from the two time slices at 246 and 200 ka, that are close
300 to the younger and older age of the period compiled in the records, could be affected at second order
301 by these biases and should be considered cautiously.

302

303 **2.3. Intensity comparison between TIII and TIII-A**

304 We perform a comparison between the amplitude of the temperature change in each record
305 during TIII and during TIII-A (Fig. 6, Table S3). To do so, the maximum and minimum values reach during
306 each termination are visually identified and collected for each SST and Antarctic surface temperature
307 records aligned on the AICC2012 chronology. The intensity of a termination is simply expressed as the
308 difference between the maximum and the minimum temperature at the onset and at the end of the
309 termination. We also perform a comparison between the maximum absolute temperature reach
310 during the MIS 7c-7a and the one reached during MIS 7e (Fig. 6, Table S3). The maximum values
311 reached during MIS 7c-7a and MIS 7e is also identified through a simple visual method. This maximum

312 value is systematically the same than the maximum value reached at the end of TIII, and often similar
313 to the maximum value reached at the end of TIII-A.

314 The maximum intensity of MIS 7c-7a and MIS 7e and the amplitude of temperature change
315 during TIII and TIII-A are compared in term of absolute temperature change in degree Celsius (°C) for
316 each site. Nevertheless, the tropics register a smaller absolute temperature change between glacial
317 and interglacial periods than the high-latitudes (Fig. 5). Consequently, a difference of maximum
318 temperature of 1°C between 7e and 7c could represent a minor difference compared to the maximum
319 amplitude of temperature change during MIS 7 in high-latitudes. This same 1°C value can nearly be the
320 maximum amplitude of temperature in the low-latitude during the whole MIS 7. The use of absolute
321 value thus could artificially reduce the relative difference of intensity when comparing the
322 terminations and the MIS 7e and MIS 7c-7a in the low-latitude in comparison to the high latitudes. To
323 investigate the influence of this potential bias on results from Fig. 6, we compute relative temperature
324 changes for terminations amplitude and MIS 7e and MIS 7c-7a maximum values compared to the total
325 amplitude of the record during the 260-190 ka period (results are expressed in percentage, Fig. S3).
326 The results shown not major difference between the absolute and relative temperature changes across
327 terminations and MIS 7e and 7c-7a (Fig. S3). We thus present the absolute temperature comparison in
328 the section presenting our results.

329

330 **2.4. Time slices of surface temperature anomalies relative to pre-industrial at 246, 242, 218, 215 and** 331 **200 ka**

332 In order to compare the intensity of warming during the MIS 7 relative to the pre-industrial
333 period, we build data-based time slices at 246, 242, 218, 215 and 200 ka (Figs 7 and 8, Table S3). The
334 dates of the time slices have been chosen to capture the temperature pattern at the onset of TIII (246
335 ka), during MIS 7e (242 ka), during MIS 7c (218 and 215 ka), and during MIS 7a in some records (200
336 ka). The surface temperature for each time slice is computed as the average of the 2 ka windows
337 centred on the time slice value and relies on the resampled SST records obtained in the Monte-Carlo
338 analysis (Fig. 5). The pre-industrial surface temperatures are extracted from the NOAA Extended
339 Reconstructed Sea Surface Temperature (SST) V4 (Huang et al., 2015) and are computed as the average
340 of the 1854-1883 period. Summer SST are defined as averaged July, August and September SST in the
341 Northern Hemisphere and as averaged January, February and March SST in the Southern Hemisphere.
342 Regarding the ice core records, the pre-industrial values are estimated as the past 2 ka temperature
343 average derived from the water isotopic composition of each ice core, following Landais et al. (2021).

344

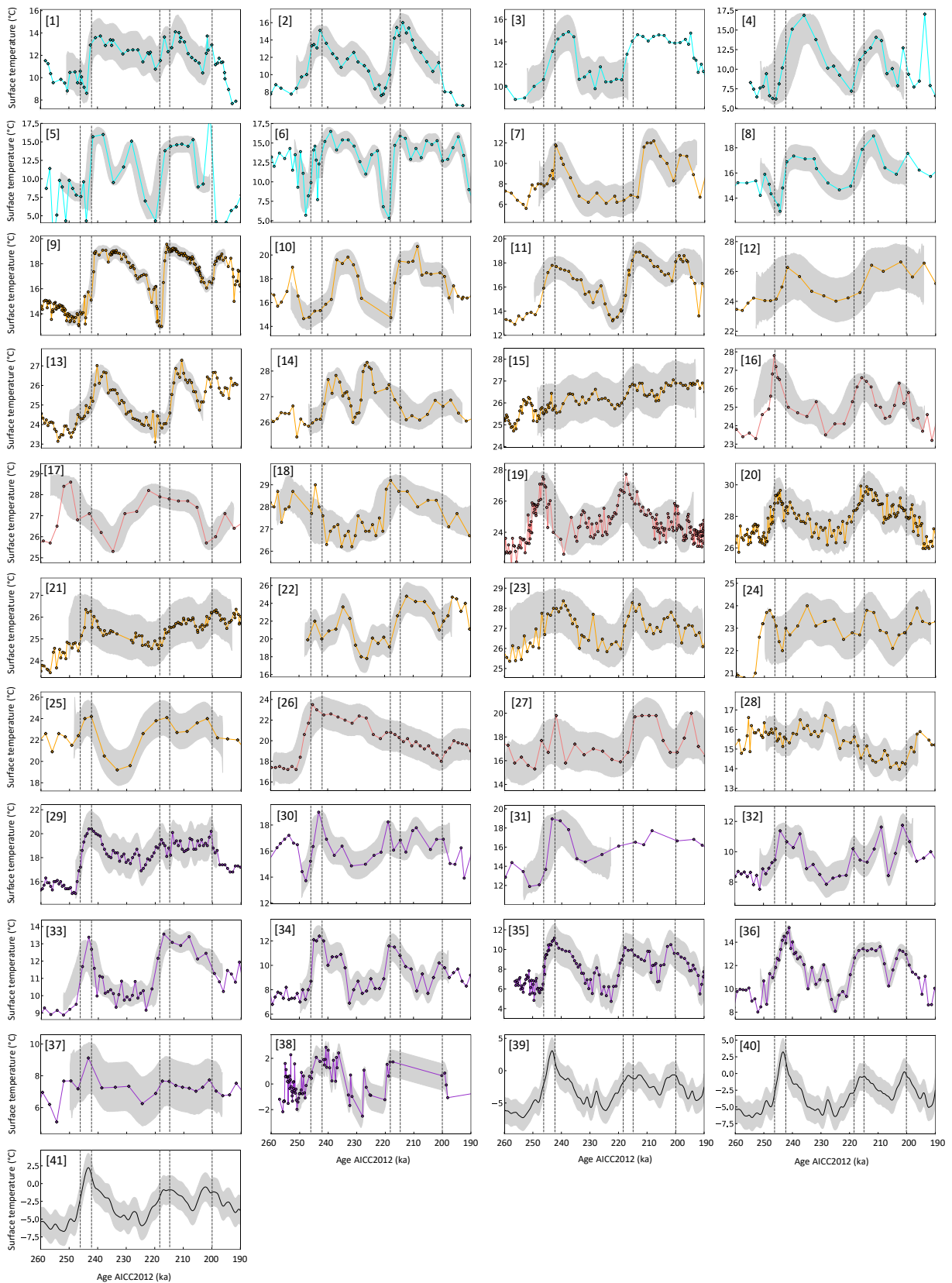
345 **2.5. Correlation between surface temperature records and background climatic and orbital variables**

346 We aim to compare the structure of the surface temperature records to the structure of
347 external climatic and orbital variables (Figs. 9 and 10, Table S4). To perform such comparison, we use
348 the R^2 metric that is computed for each surface temperature record– external variable couple over the
349 260-190 ka interval. This R^2 value thus represents the average degree of correlation of the evolution
350 of two independent records over the 260-190 ka interval. In order to take into account the absolute
351 age uncertainty of the AICC2012 timescale during MIS 7 (~2 ka, Bazin et al., 2013) and the resolution-
352 induced age uncertainty of our dataset (average resolution of 1.8 ka), we select the best R^2 between
353 the reference external record and the surface temperature record shifted between the ± 2 ka interval
354 (Fig. S4).

355

356

357



358
359

360 Fig. 5: Surface temperature records aligned on the AICC2012 timescale between 260 ka and 190 ka. Light blue and purple
 361 curves are the records aligned on the EDC CH₄ and δD record, respectively (see Fig. 3). Orange and light red curves are the
 362 records aligned through benthic and planktonic δ¹⁸O, respectively (see Fig. 4). Dots are annual air and sea surface

363 temperatures and diamonds are summer surface temperatures. Grey shaded areas are the 1σ confidence intervals inferred
364 from the Monte Carlo iterations. This envelope of uncertainty is represented only in the range of the younger and older tie-
365 point. Consequently, the SST records out of these intervals are not align robustly on the AICC2012 chronology and are not
366 used in the time slice computation. For instance, no tie-point could have been used for core [3] beyond 220 ka and
367 consequently this record is only scaled on the AICC2012 on the ~250-220 ka interval. Dashed black lines are the timing of the
368 five time slices at 246, 242, 218, 215 and 200 ka.

369

370 **3. Results**

371 The spatio-temporal evolution of the 41 synchronized surface temperature records allows to
372 identify major climatic features during the MIS 7 and the associated terminations.

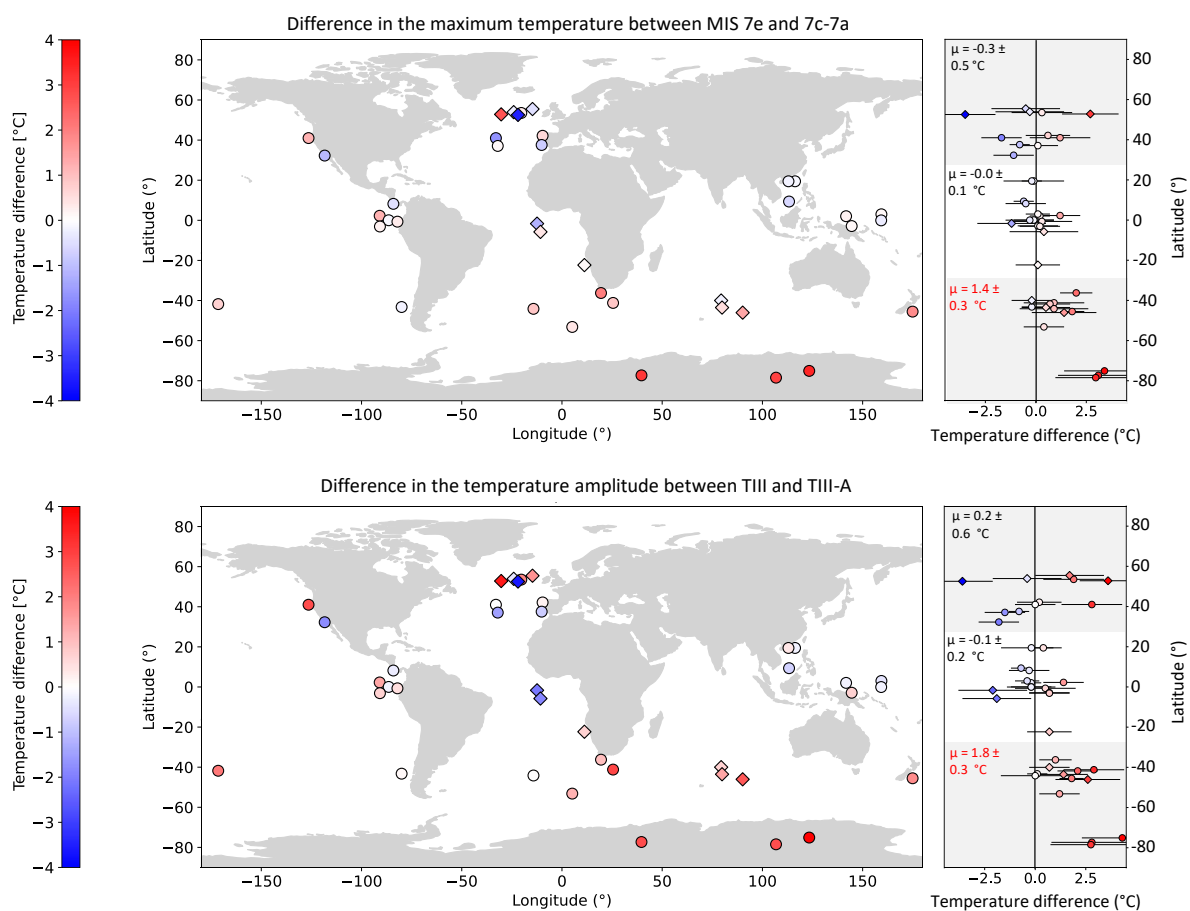
373 **3.1 Regional variability in the morphology of the MIS 7**

374 Our new climatic synthesis enables to highlight a large spatial variability in the relative
375 amplitude of the two terminations TIII and TIII-A. In the Southern Ocean and Antarctica, the TIII is
376 significantly more amplified than the TIII-A (average of 13 sites, difference of warming amplitude
377 during TIII vs TIII-A: $+1.8 \pm 0.3^\circ\text{C}$, standard error) (Fig. 6). In the tropical regions, terminations are of the
378 same amplitude (average of 16 sites, difference of warming amplitude during TIII vs TIII-A: $-0.1 \pm 0.2^\circ\text{C}$,
379 standard error). Those results appear robust and do not seem to be affected by significant variability
380 between the records. Reverse, the high dispersion of the results in the northern high latitudes
381 (standard error of 0.6°C based on 11 sites, ranging from -3.6 to $+3.6^\circ\text{C}$) reveals that the amplitude of
382 surface temperature changes could vary at local scale. For instance, the V27-116 marine core records
383 a more amplified temperature change during TIII ($3.6 \pm 1.4^\circ\text{C}$, standard deviation) while the SU90-39
384 marine core records a more amplified temperature change during TIII-A ($-3.6 \pm 1.5^\circ\text{C}$, standard
385 deviation). These two cores are distant of 600 km, and both SST reconstructions are based on
386 foraminifera assemblages and are interpreted as reflecting variations in summer SST. A similar
387 variability can be observed in the ODP1020 and ODP1012 marine cores, distant from 1200 km and
388 which provide annual alkenone-based SST records from the coastal North-East Pacific region. While
389 the ODP1020 marine core records a more amplified temperature change during TIII ($2.8 \pm 1.5^\circ\text{C}$,
390 standard deviation), the ODP1012 marine core records a more amplified temperature change during
391 TIII-A ($-1.8 \pm 1^\circ\text{C}$, standard deviation). Thus, this local-variability does not only affect annual or summer
392 SSTs records, or a specific proxy of SST. We thus consider that it reflects a real climate signal rather
393 than a bias induced by the methodology approach.

394 Similar patterns are founded when focusing on the difference of maximum temperature reached
395 between MIS 7e and MIS 7c-7a (Fig. 6). The MIS 7e is significantly more pronounced than MIS 7c-7a in

396 the high-latitudes of Southern hemisphere, including both SST and surface air temperature ($1.4 \pm 0.3^\circ\text{C}$,
 397 standard error) while they are of same amplitude in the tropics ($0.0 \pm 0.1^\circ\text{C}$, standard error). The same
 398 dispersion as described above for the termination amplitude is observed in the northern high latitudes
 399 regarding the relative intensity of the MIS 7e and MIS 7c-7a ($-0.3 \pm 0.5^\circ\text{C}$, standard error). Finally, our
 400 results also suggest a larger magnitude of warming difference during MIS 7e and 7c-a over the East
 401 Antarctic plateau than in the surrounding Southern Ocean ($3.2 \pm 0.2^\circ\text{C}$ vs $0.7 \pm 0.6^\circ\text{C}$). A similar contrast
 402 is registered in the amplitude of temperature between the terminations ($3.3 \pm 0.9^\circ\text{C}$ over the East
 403 Antarctic plateau and $1.8 \pm 1.1^\circ\text{C}$ in the Southern Ocean).

404



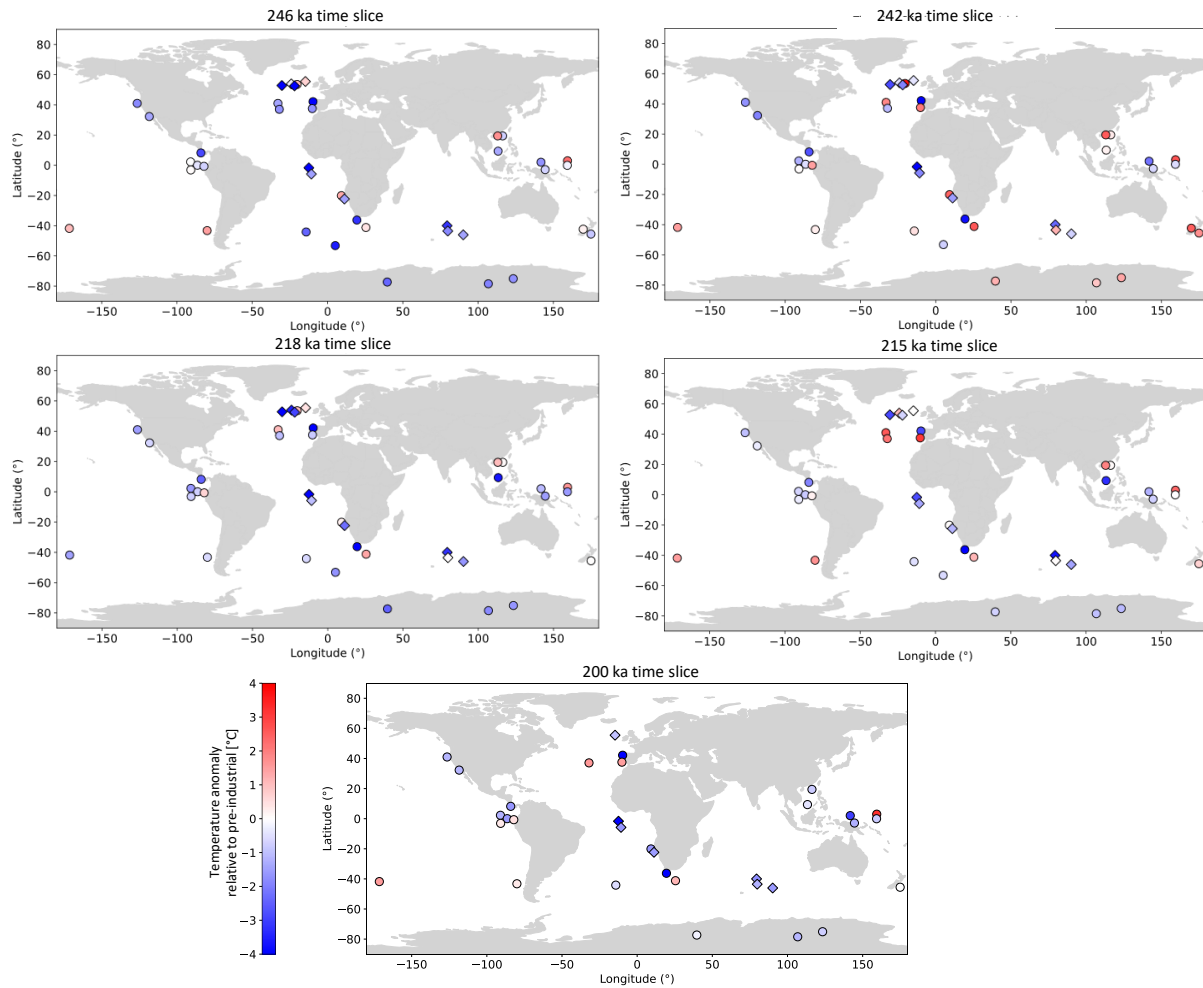
405

406 Fig. 6: Spatio-temporal warming pattern during MIS 7e, MIS 7c-7a, TIII and TIII-A. Top: Difference in the maximum
 407 temperature between MIS 7e and MIS 7c-7a. A positive (red) value mean that the maximum temperature was higher during
 408 MIS 7e compared to MIS 7c-7a. On top right, the same temperature difference is plotted as a function of latitude. Bottom:
 409 Difference in the temperature amplitude (defined as the difference between the maximum and the minimum values on each
 410 end of a termination) between TIII and TIII-A. A positive (red) value mean that the amplitude of temperature was larger during
 411 TIII compared to TIII-A. On top right, the same temperature difference is plotted as a function of latitude. Dots: annual surface
 412 temperature. Diamonds: summer surface temperature. μ sign refers to the average value, \pm the standard error.

413

414 3.2 Comparison of the MIS 7 climate with the pre-industrial one

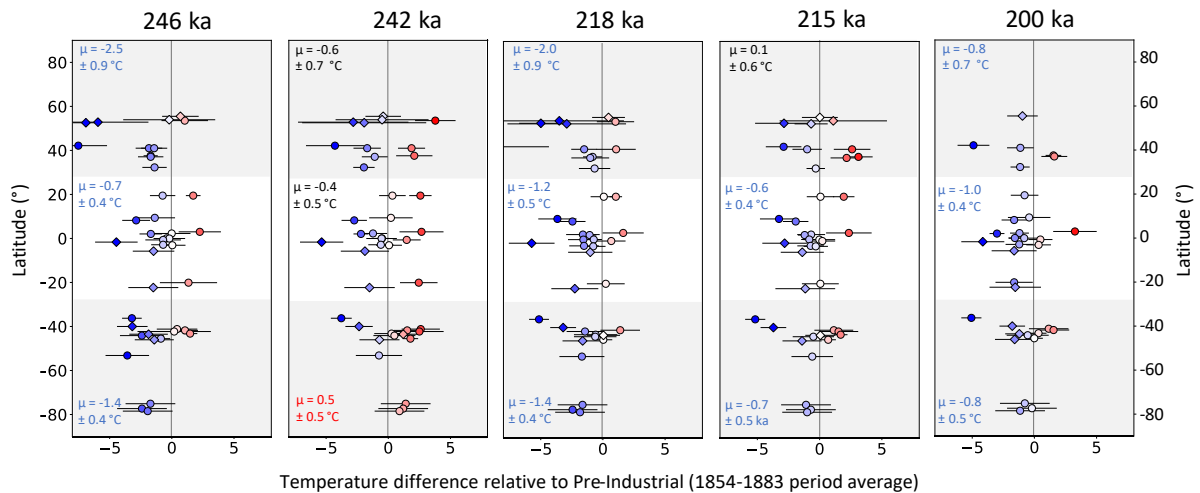
415 We now used the time slices computed at 246, 242, 218, 215 and 200 ka to compared the
416 climate of the MIS 7 to the pre-industrial climate. The southern mid to high-latitudes (south to 30°S)
417 were warmer than pre-industrial at 242 ka ($0.5 \pm 0.5^\circ\text{C}$, standard error). These warmer conditions are
418 amplified when focusing on site south of 40°S ($0.8 \pm 0.4^\circ\text{C}$, standard error). Reversely, this region is
419 significantly colder than pre-industrial at 246 ($-1.4 \pm 0.4^\circ\text{C}$), 218 ($-1.4 \pm 0.4^\circ\text{C}$), 215 ($-0.7 \pm 0.5^\circ\text{C}$) and 200
420 ($-0.8 \pm 0.5^\circ\text{C}$) ka (Figs. 7 and 8). At 246, 218, 215 and 200 ka, the tropics globally remain significantly
421 colder than the pre-industrial ($-0.7 \pm 0.4^\circ\text{C}$, $-1.7 \pm 0.4^\circ\text{C}$, $-0.6 \pm 0.4^\circ\text{C}$, $-1.0 \pm 0.4^\circ\text{C}$, standard error). At 242
422 ka, the quantified cooler trend is not significant ($-0.4 \pm 0.5^\circ\text{C}$, standard error). Behind these averaged
423 values, the temperature anomalies in the tropics reveal a large regional-scale variability. The cluster of
424 sites on the west and east sides of the Pacific Ocean reveals the variable pattern of temperature
425 anomalies at 242 ka and 215 ka at local-scale (Fig. 9c). Finally, the Northern hemisphere region is
426 significantly colder than the pre-industrial (246 ka: $-2.5 \pm 0.9^\circ\text{C}$, 218 ka: $-2.0 \pm 0.9^\circ\text{C}$, 200 ka: $-0.8 \pm 0.7^\circ\text{C}$,
427 standard error) apart in the 242 ka and the 215 ka time slices (242 ka: $-0.6 \pm 0.7^\circ\text{C}$, 215 ka: $0.1 \pm 0.6^\circ\text{C}$,
428 standard error). During the 260-190 ka period, the only region significantly warmer than during the
429 pre-industrial is thus the southern high latitudes around 242 ka.



430

431 Fig. 7: Temperature anomalies computed for the five time slices at 246 ka, 242 ka, 218 ka, 215 ka and 200 ka relatively to the
 432 pre-industrial period. A positive (red) value mean that the temperature was higher compared to the pre-industrial. SST
 433 anomalies are calculated relative to the annual sea surface temperature water temperature of the 1854-1883 period for the
 434 28 annual surface temperature records. The averaged July, August and September SST and the averaged January, February
 435 and March SST of the 1854-1883 period are used for SST anomalies computations for the Southern (6 records) and Northern
 436 (4 records) summer SST temperature records . 1854-1883 averages are derived from the ERSSTV4 reconstruction
 437 (<https://psl.noaa.gov/data/gridded/data.noaa.ersst.v4.html>). Antarctic surface air temperature anomalies are provided
 438 relative to the mean surface temperature of the past 2 ka from each ice core following Landais et al. (2021). Each time slice
 439 value corresponds to the ± 1 ka average centred on the time slice value name (e.g. average of 245-247 ka for the 246 ka time
 440 slice). Dots: annual surface temperature. Diamonds: summer surface temperature.

441



442

443 Fig. 8: Temperature anomalies computed for the five time slices at 246 ka, 242 ka, 218 ka, 215 ka and 200 ka relative to the
 444 pre-industrial period as a function of the latitude (see Fig. 9 caption for more details). Grey shaded areas refer to the extra-
 445 tropical area (poleward to 30° of latitude). Numbers are the zonal mean (from top to bottom: 90°N-30°N, 30°N-30°S, 30°S-
 446 90°S) of the temperature anomalies and their associated standard error. A blue/red indicates a colder/warmer time period
 447 compared to the pre-industrial. Uncertainty associated with each datapoint accounts for both the uncertainty of the dating
 448 and the uncertainty of the SST absolute value. Dots: annual surface temperature. Diamonds: summer surface temperature.

449

450 3.3 Correlation of the surface temperature records with variables illustrating the external and 451 climate background

452 In order to characterize the particular pattern of the evolution of surface temperature during
 453 MIS 7, we compare the structure of these records to other paleorecords representing the external and
 454 climate background during this period. We select the obliquity, precession, eccentricity and 65°N June
 455 Insolation to represent the orbital forcing (Laskar et al., 2004). In addition, we also compare our records
 456 to atmospheric CO₂ concentrations (Legrain et al., in revision) and two different reconstruction of
 457 global ice volume (Spratt and Lisiecki, 2016; Berends et al., 2021).

458 The surface temperature records are globally better correlated with the obliquity record
 459 (average $R^2 = 0.41$) than to the precession, eccentricity and June 65°N Insolation (average $R^2 = 0.15$, $R^2 = 0.26$, $R^2 = 0.26$). The obliquity-surface temperature records correlation can vary at local scale and do
 460 not show significant latitudinal trend (Fig. 9). The surface temperature records are also correlated with
 461 the EDC atmospheric CO₂ record (average $R^2 = 0.48$) (Fig. 10). The correlation with atmospheric CO₂
 462 reveals a latitudinal pattern as the northern and southern high latitudes depict a higher correlation ($R^2 = 0.53$) than the low latitudes ($R^2 = 0.41$) (Fig. 9). Especially, the correlation between surface
 463 temperature and atmospheric CO₂ concentration is strong ($R^2 > 0.50$) for 18 of the 24 surface
 464 temperature records poleward to 30°, against only 5 of the 16 surface temperature records located in
 465
 466

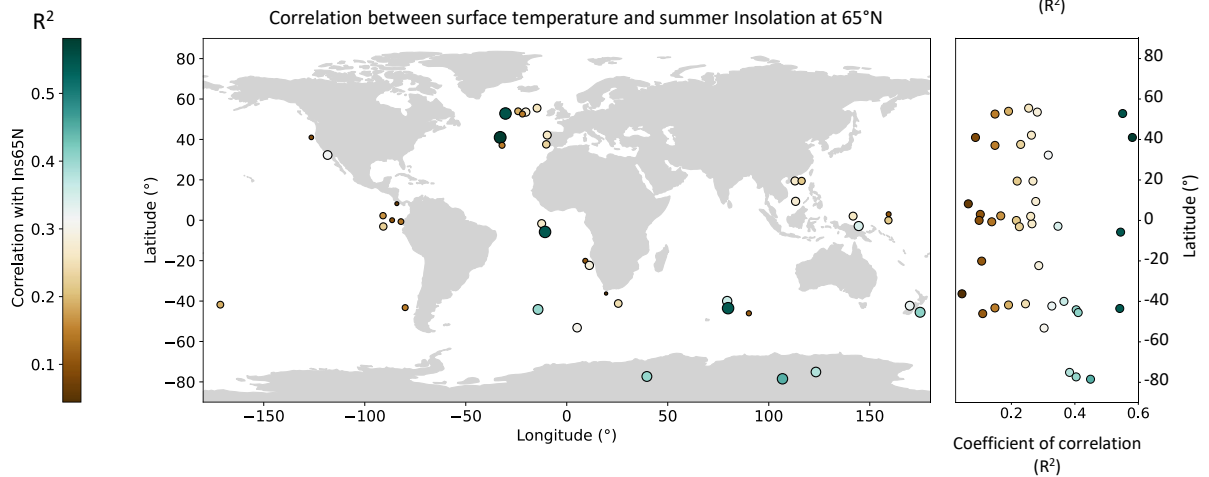
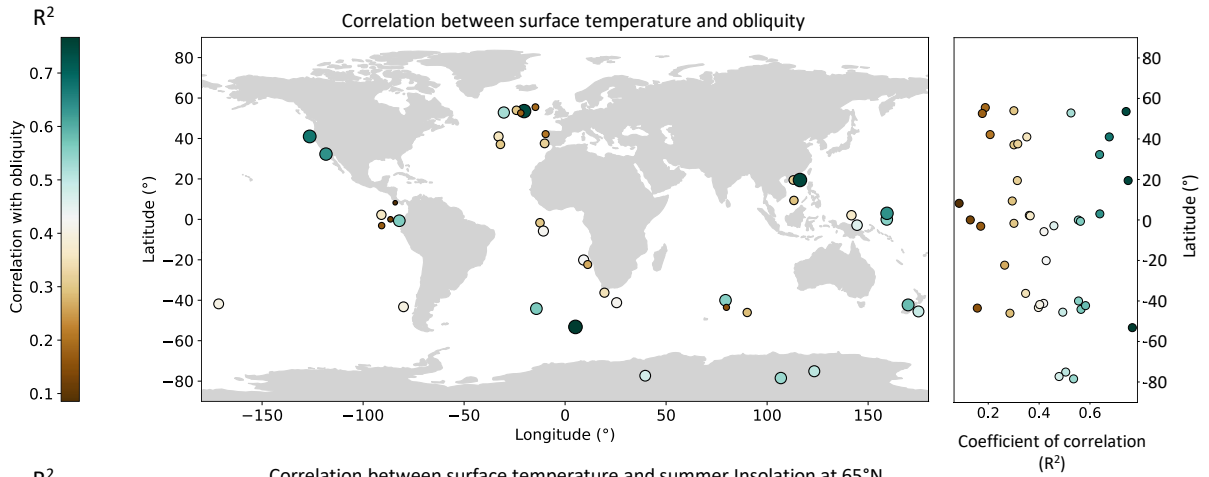
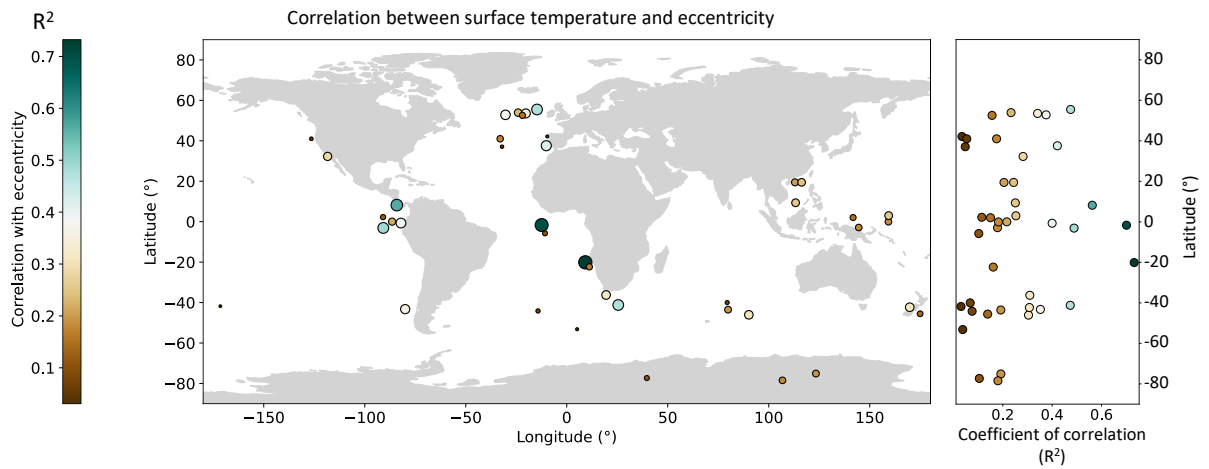
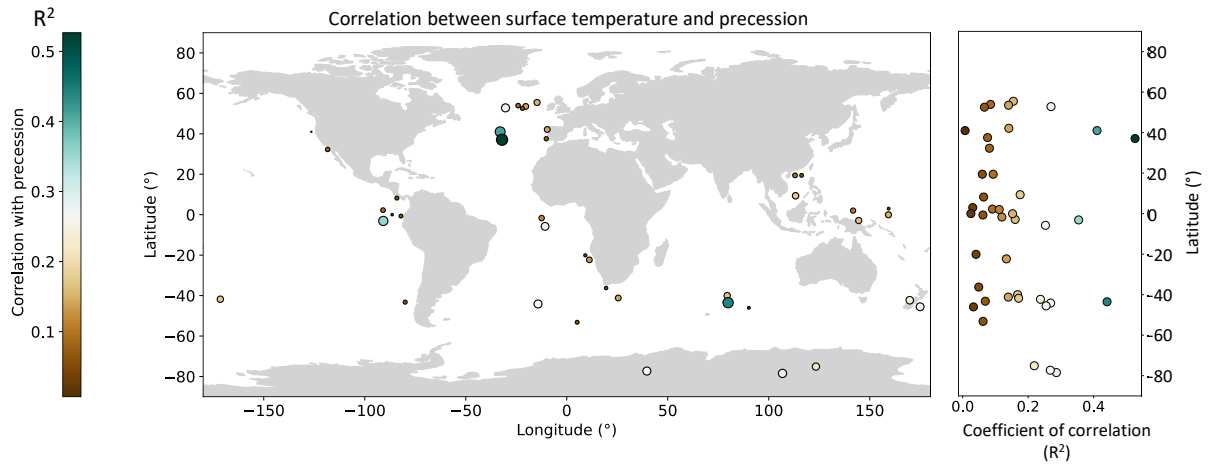
467 the tropical area. Interestingly, the comparison of the R^2 values obtained with the obliquity-surface
468 temperature and CO_2 -surface temperature correlations do not show any correlation ($R^2=0.09$) (Fig. S5).
469 This indicates that the sites highly correlated with atmospheric CO_2 are not specifically correlated with
470 the obliquity signal, and reversely.

471 Also, the surface temperature records are correlated to the global ice volume regardless of the
472 reconstruction used (from Berends et al. (2021): $R^2 = 0.49$, from Spratt and Lisiecki, 2016: $R^2 = 0.47$).
473 The global ice volume reconstruction from Berends et al. (2021) follow a latitudinal pattern of
474 correlation similar to those of atmospheric CO_2 , with a better correlation reached in the high-latitudes
475 compared to the tropics (average $R^2=0.53$ and $R^2=0.43$, respectively). This trend is less pronounced
476 when using the global ice volume reconstruction from Spratt and Lisiecki, 2016 (average $R^2=0.48$ and
477 $R^2=0.45$, respectively). The comparison of the R^2 values obtained with the ice volume-surface
478 temperature and CO_2 -surface temperature reveals a high correlation ($R^2=0.51$ and $R^2=0.55$ for Spratt
479 and Lisiecki, 2016 and Berends et al. (2021) respectively) (Fig. S5). This indicates that the surface
480 temperature sites correlated with atmospheric CO_2 are also correlated with global ice volume
481 reconstruction at first order.

482

483

484



486 Fig. 9: Comparison between the orbital forcing and the surface temperature records. From top to bottom: Correlation
487 between the precession, eccentricity, obliquity, and June 65°N Insolation records (Laskar et al., 2004) and the surface
488 temperature records. Side panels on the right of each map are the R^2 values represented as a function of latitude. Green and
489 brown dots are relative markers of high and low R^2 values that refers to the relative correlation scale provided on the left.
490 The size of the dots are absolute markers of R^2 values to facilitate the comparison between the four panels and the panels
491 from Fig. 10.

492

493 **4. Discussion**

494 **4.1 Potential and limits of our first MIS 7 spatio-temporal data synthesis**

495 This synthesis gathers SST records inferred from multiple proxies (Table S1). Comparison of
496 SST records derived from different proxies should be led carefully as seasonal bias could affect the
497 absolute value of surface temperature proxies, both in the tropics and high-latitudes (MARGO project
498 members, 2009; Leduc et al., 2010, 2017; Bova et al., 2021). However, such bias especially affects the
499 absolute estimates of SST (Leduc et al., 2010; Capron et al., 2014). In our approach, we perform
500 comparison of the relative amplitudes of temperature changes within a record, that do not involve any
501 consideration of absolute SST values. Potentially more problematic, the time slice computation and
502 their comparison to the pre-industrial climate involve the use of absolute SST estimates. Nevertheless,
503 the major result of this pre-industrial comparison, i.e. the establishment of a warmer-than-pre-
504 industrial climate in the Southern latitudes around 242 ka, is supported by SST records from different
505 proxies (i.e. SST record [30] based on Foraminiferal assemblages , SST record [31]: Alkenone , [36]:
506 Mg/Ca ratio, Fig. 2). In addition, surface air temperature records from the three ice cores confirm this
507 result.

508 Also, we compile here both sea surface temperature records considered as reflecting the
509 summer (10 records) or the annual temperature (28 records), following the interpretation proposed in
510 their original paper. Recent debates have questioned the real climatic signal reflected by these records,
511 i.e. a seasonal vs annual signature (Bova et al., 2021). The records interpreted as summer SST do not
512 register a distinct amplitude signal (Figs. 5,6) nor differences in the comparison with the pre-industrial
513 climate (Figs. 7,8), than the records considered as reflecting the annual surface temperature. In
514 addition, the scarcity of the records during MIS 7 do not allow to base this synthesis on a single SST
515 proxy. As discussed above, we consider than the main results from this study are not dependent from
516 this approach.

517 As we go back in time, the quantity of high-resolution records decreases. Consequently, the number
518 of highly-resolved records during MIS 7 is inferior to the Last Interglacial, and even more so to the

519 Holocene. In this synthesis, the resolution of the records is better than <4 ka, that is the same high-
520 pass filter as in Hoffman et al. (2017), but twice the value from Capron et al. (2014). In addition, the
521 median resolution is 1.7 ka, that is superior to the 1.1 ka median resolution from Hoffman et al. (2017).
522 The choice of including records resolved from 2 ka up to 4 ka of resolution is the consequence of the
523 compromise between the quantity of records, that is necessary to assess statistically-robust results,
524 and the quality of records, to extract climatic information from the uncertainty induced by low-
525 resolution records. Nevertheless, the noise induced by the low-resolution of records is taken into
526 account in the computation of the final uncertainty (Fig. 5). We arbitrarily consider here that 4 ka
527 constitute a maximum threshold above which the uncertainty associated with records alignment
528 would prevent to distinguish climatic signal from the surrounding noise, but under which paleoclimatic
529 information could be identified.

530 Lastly, the use of a compilation of multiple climate records allows to investigate the spatial
531 pattern of warming evolution during MIS 7. Nevertheless, 41 local surface temperature records could
532 not capture the whole complexity of spatial heterogeneity of climate changes. Especially, the central
533 Pacific and the Indian ocean are not represented in this synthesis, as well as the mid-to-low latitudes
534 continental sites. Thus, all the results described in this study should be considered in the framework
535 of the heterogenous spatial distribution of the synthesis.

536

537

538

539

540

541

542

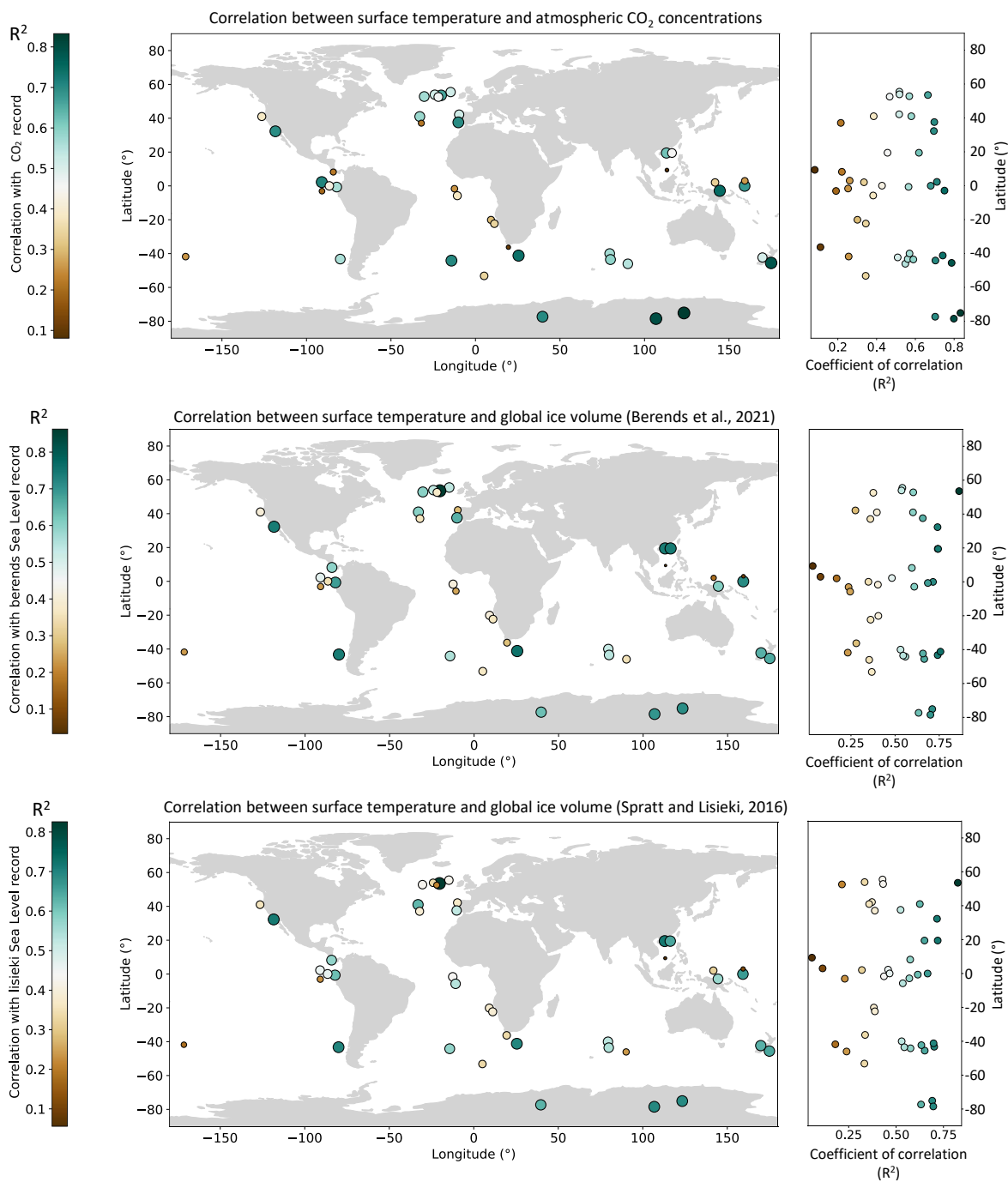
543

544

545

546

547



550 Fig. 10: Comparison between the atmospheric CO₂ concentrations and global ice volume, and the surface temperature
 551 records. Top left: Correlation between the atmospheric CO₂ concentrations and the surface temperature records. Middle left:
 552 Correlation between the global ice volume reconstruction from Berends et al. (2021) and the surface temperature records.
 553 Low left: Correlation between the global ice volume reconstruction from Spratt and Lisiecki (2016) and the surface
 554 temperature records. Side panels on the right of each map are the R^2 values represented as a function of latitude. Green and
 555 brown dots are relative markers of high and low correlations values that refers to their relative correlation scale. The size of
 556 the dots are absolute markers of high and low correlation values, to facilitate the comparison between the three panels and
 557 the panels from Fig. 9.

558 **4.2 Relative amplitude of the warmth during MIS 7**

559 Our study based on 41 surface temperature records reveals an additional warmth during MIS
560 7e compared to MIS 7c-7a restricted to the southern high latitudes. Similarly to the Southern high-
561 latitude surface temperature, the asymmetric pattern between MIS 7e and MIS 7c-7a is registered in
562 the atmospheric CO₂ concentrations record (Kawamura et al., 2007; Legrain et al., under review). This
563 observed overshoot in CO₂ concentrations is thought to be linked to a slowdown followed by a
564 resumption of the Atlantic Meridional Oceanic Circulation (Ganopolski and Brovkin, 2017). The
565 temporary slowdown in the AMOC would have for consequence to accumulate the heat in the high-
566 latitudes of Southern hemisphere (Pedro et al., 2018). This hypothesis of similarity between
567 atmospheric CO₂ and Antarctic temperature is supported with our results indicating a similar
568 asymmetric pattern between MIS 7e and MIS 7c-7a in both southern high latitudes and atmospheric
569 CO₂ concentrations. More globally, our results also suggest that the dynamics of atmospheric CO₂
570 concentrations is more related to the high-latitudes rather than the tropics during the entire MIS 7.
571 When moving northward of 40°S, MIS 7e and MIS 7c-7a are undistinguishable in terms of their intensity
572 (Fig. 6). The tropical and northern climatic similarity between the two warm periods is also observed
573 in local palynological (Desprat et al., 2006; Roucoux et al., 2008) and speleothem (Bard et al.,
574 2011; Cheng et al., 2016; Wendt et al., 2021) records from European and Asian continental areas.

575 One of the questions resulting from these observations is: why this warmth excess at the end
576 of TIII has not propagated northward? A part of the answer probably lies in the duration of MIS 7e,
577 which is the shorter interglacial peak of the past 800 ka (Past Interglacials Working Group of PAGES,
578 2016). The relative influence of atmospheric CO₂ concentrations vs insolation forcing has been tested
579 over the past five interglacials (Yin and Berger, 2012) and more specifically during the MIS 7
580 (Choudhury et al., 2020). These analyses suggest that the warming associated with the relatively high
581 CO₂ concentrations during MIS 7e is counter-balanced by the insolation-induced cooling. Especially,
582 the study from Choudhury et al. (2020) reveals the predominant role of orbital forcing in shaping the
583 MIS 7e-7d-7c sequence. During this period, around ~ 232 ka, obliquity reached its lowest value of the
584 past 2 Ma (22.1°) (Laskar et al., 2004) (Fig. S1). Consequently, the lowest 65°N June insolation value of
585 the past 800 ka is registered at the same period, inducing an orbital-induced cooling during the stage
586 7d, counterbalancing the high atmospheric CO₂ concentrations (Yin and Berger, 2012).

587

588 **4.3 External drivers of the surface temperature pattern during MIS 7**

589 Our analysis reveals similarities between the structure of the atmospheric CO₂ concentrations
590 and global ice volume with the surface temperature patterns. Such results were expected as these

591 variables are closely related to climatic variations during the last glacial-interglacial cycles (Manabe
592 and Broccoli, 1985; Barnola et al., 1987; Genthon et al., 1987; Clark et al., 1999; Jouzel et al., 2007).
593 Nevertheless, the relative comparison of these results with orbital forcing reveal interesting specificity
594 of the mechanism at play during MIS 7. From the precession, eccentricity, June 65°N Insolation and
595 obliquity records, the latter is by far the orbital variable that is the most correlated with the surface
596 temperature evolution during MIS 7, at level similar to the atmospheric CO₂ concentrations and global
597 ice volume (Fig. 9). This high-correlation between surface temperature pattern and obliquity compared
598 to other orbital parameters is intriguing, as a previous study focusing on the influence of orbital
599 parameters on surface temperature in conditions similar to MIS 13 to MIS 11 pointed toward a
600 dominant precessional control of SSTs pattern (Wu et al., 2020). A recent study illustrates how the
601 large variations in obliquity have helped to establish the ~41 ka frequency climatic cycles during the
602 1.6-1.2 Ma interval (Watanabe et al., 2023). The obliquity amplitude reached during the MIS 7 is even
603 higher than the one during the 1.6-1.2 Ma period (Fig. S1).

604 This orbital imprint highlights the specificity of the MIS 7: while occurring after the Mid-
605 Brunhes Event that established the predominance of extended and warm ~100 ka climatic cycles, the
606 MIS 7 structure appears more related to the structure of the interglacials occurring before the Mid-
607 Pleistocene Transition (MPT) (~1.2-0.8 Ma), characterized by less amplified ~41 ka glacial-interglacial
608 cycles (Berends et al., 2021). Especially, the start of the two glacial inceptions occurring right after the
609 MIS 7e and 7a-7c are separated by ~40 ka (Fig. 1). Nevertheless, the MIS 7 takes place in a context of
610 globally high atmospheric CO₂ concentrations and extended continental ice sheets typical of the late
611 Pleistocene (Abe-Ouchi et al., 2013). Our results suggest that the surface temperature patterns are
612 also closely coupled with global ice volume and atmospheric CO₂ concentrations and global ice volume.
613 During TIII, both of these climate variables registered high-amplitude variations (60-90 m sl equivalent,
614 and ~90 ppm), that are intermediate values between the typical amplitude of pre- and post- MPT
615 terminations (Abe-Ouchi et al., 2013; Watanabe et al., 2023). We suggest that the pattern of MIS 7
616 would be the consequence of a trade-off between an orbital forcing similar to the one during the 1.6-
617 1.2 ka period, and the high-level of atmospheric CO₂ concentrations combined with the large extent of
618 ice sheets typical from the post Mid-Brunhes Event. We speculate that during the MIS 7, a potential
619 threshold in the orbital forcing could have been reached allowing to restore partially and temporarily
620 the pre-MPT climate cycle structure, which is not visible during the MIS1 , 5, 9 and 11.

621

622

623

624 **4.4 Comparison with pre-industrial and future modelling**

625 The MIS 7 is globally colder than, or of similar intensity to, the pre-industrial regardless the
626 considered time slice. The only regional exceptions are the southern high latitudes as previously
627 discussed. The MIS 7 thus represents an anomaly in its warming intensity compared to the MIS 5, and
628 probably to the MIS 9 and MIS 11 based on Antarctic surface temperature records (Jouzel et al., 2007).
629 Such particularity has already been pointed out by syntheses focusing on the diversity of past
630 interglacials (Tzedakis et al., 2009; Lang and Wolff, 2011). Evidence of the occurrence of globally cooler
631 than-pre-industrial interglacial inferred from our multi-archive synthesis reveals the unique
632 opportunity to (i) investigate and quantify physical mechanisms at play during this period (ii) evaluate
633 the ability of spatialized models to reproduce a different interglacial type from the already well
634 investigated MIS 1 and MIS 5. Especially, simulating and understanding the processes associated with
635 the relative regional intensities of MIS 7e and MIS 7c-7a represents a stimulating challenge for the
636 palaeomodeling community.

637

638 **5. Conclusions**

639 We present here a multi-archive synthesis of surface temperature records spanning the TIII
640 and the MIS 7 (260-190 ka). We aligned on the AICC2012 ice chronology 41 air and sea surface
641 temperature records from ice and marine sediment cores with a temporal resolution better than 4 ka.
642 This is the first attempt to reconstruct the spatial evolution of surface temperature across the MIS 7.
643 We have evidenced key features of the MIS 7 among which (i) a global symmetric intensity of warming
644 between the two warm periods (7e and 7a-7c) and their associated terminations (TIII and TIII-A) at the
645 exception of the southern high latitudes that experienced a more pronounced TIII and associated MIS
646 7e, (ii) a similarity between high-latitude temperature records evolution and atmospheric CO₂
647 concentrations, and (iii) an imprint of the obliquity forcing on the surface temperature evolution during
648 MIS 7, leading us to suggest that the specific structure of this interglacial could result from a
649 combination of highly-amplified atmospheric CO₂ concentrations and global ice volume variations, and
650 an exceptionally high variability in the orbital forcing.

651 Additionally, we provide a spatio-temporal picture of the evolution of the surface
652 temperatures during the MIS 7 with five time slices calculated for 246, 242, 218, 215 and 200 ka. Our
653 comparison with the pre-industrial climate reveals that the MIS 7 remains colder or of similar intensity
654 than pre-industrial climate apart in the southern high latitudes during MIS 7e. Here we have focused
655 on the interpretation of the paleo-surface temperature records and their spatial and temporal

656 evolution. Nevertheless, this work encourages future model-data comparison during the MIS 7 as
657 performed for the Last Interglacial (e.g. Capron et al., 2014; Stone et al. 2016; Otto-Bliesner et al. 2020).

658

659

660

661

662

663

664

665

666

667

668

669

670

671

672

673

674

675

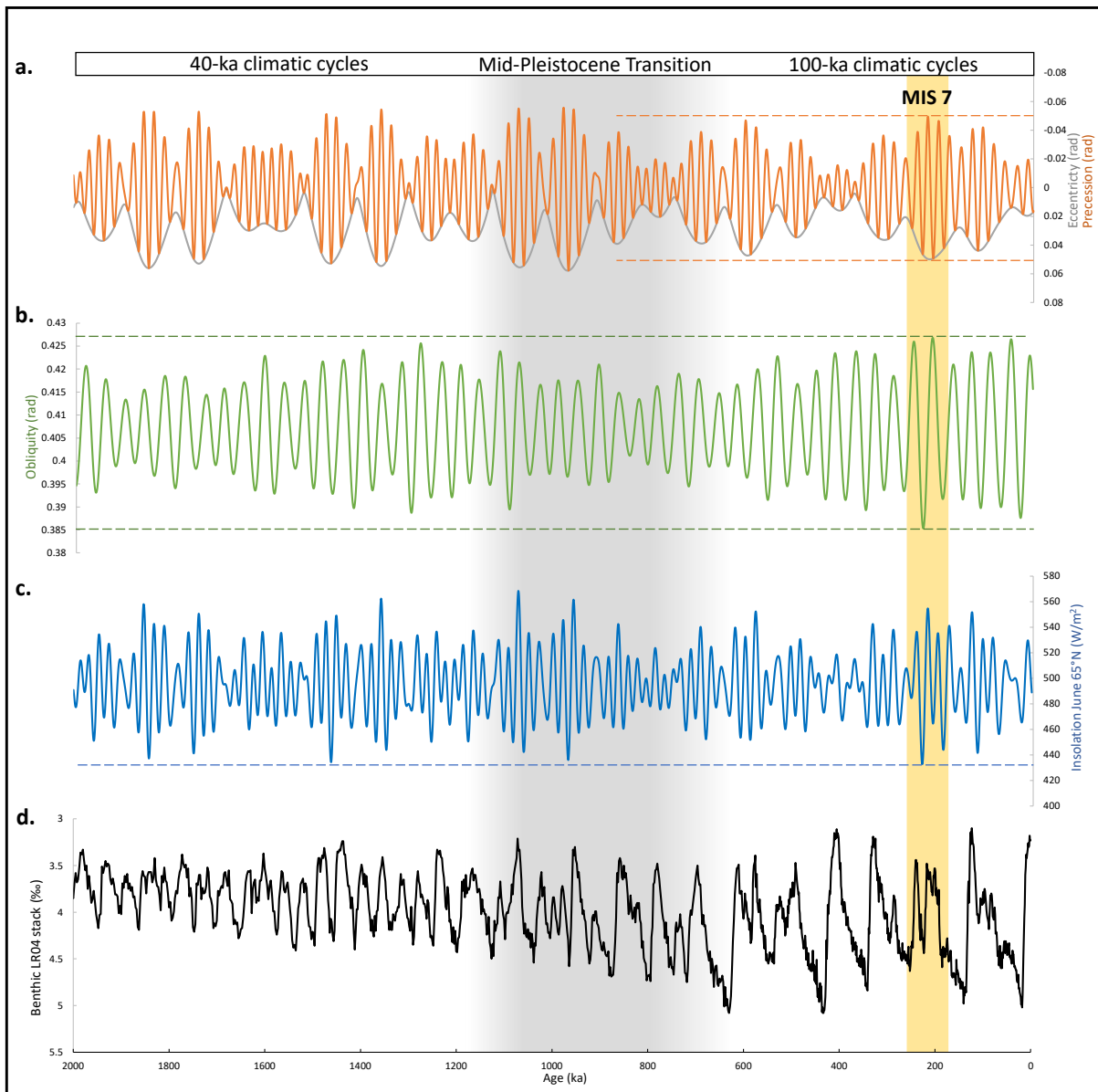
676

677

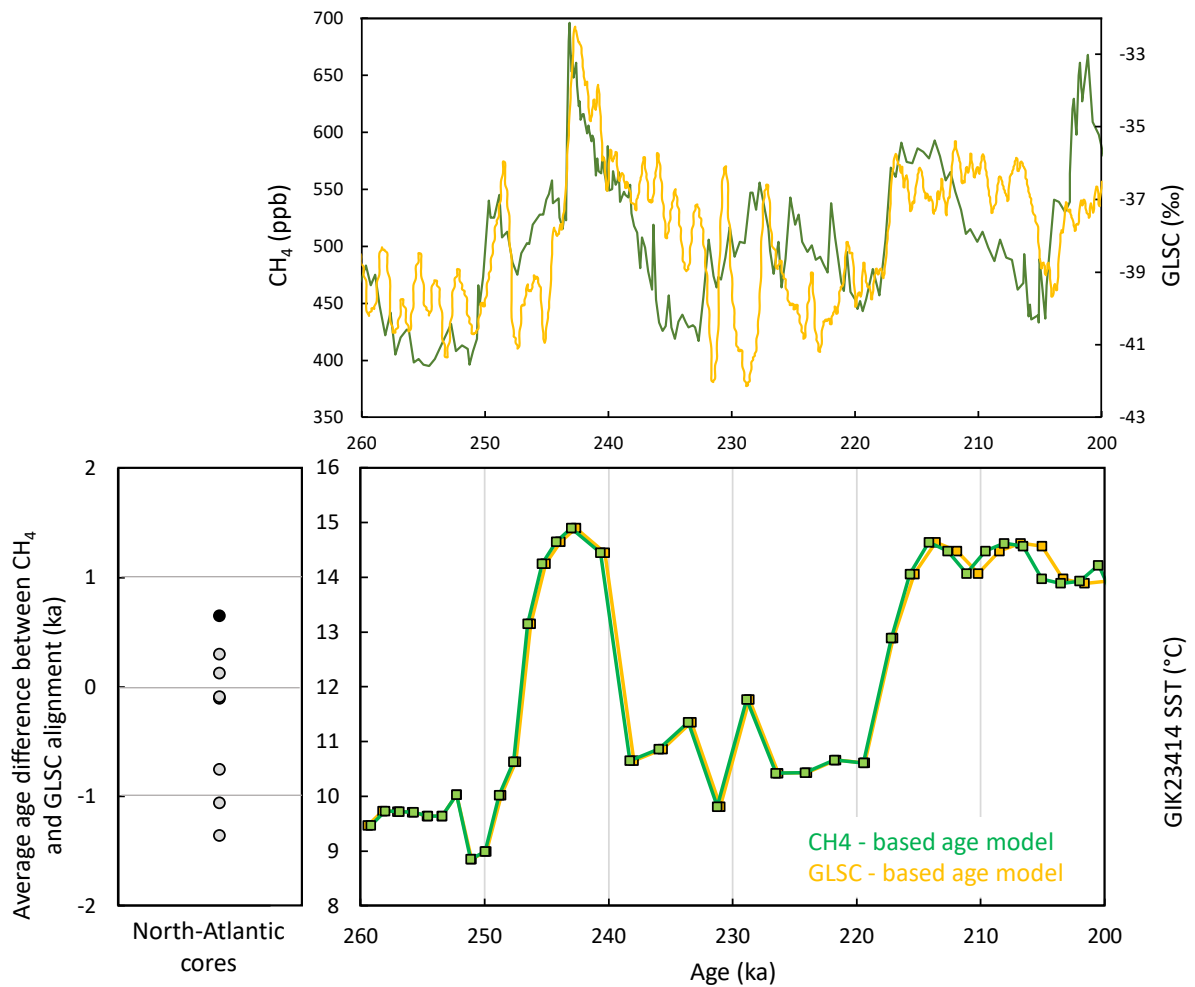
678

679

680



684 Fig. S1 : MIS 7 in the context of the past 2 Ma. From top to bottom: a Eccentricity and precession record. 685 686 c. Insolation June 65°N. d. Benthic LR04 stack (‰) (Lisieki and Raymo, 2005). Yellow shaded area indicates the MIS 7. Grey 687 shaded area represents the approximate timing of the Mid-Pleistocene Transition. The dashed horizontal lines underlined 688 the occurrence of the maximum or minimum orbital value of the period duration represented by the horizontal extent of the 689 minimum and maximum precession value of the past 800 ka, green: minimum and maximum obliquity value of the past 2 Ma, black: minimum June Insolation 65°N value of the past 2 Ma.



690

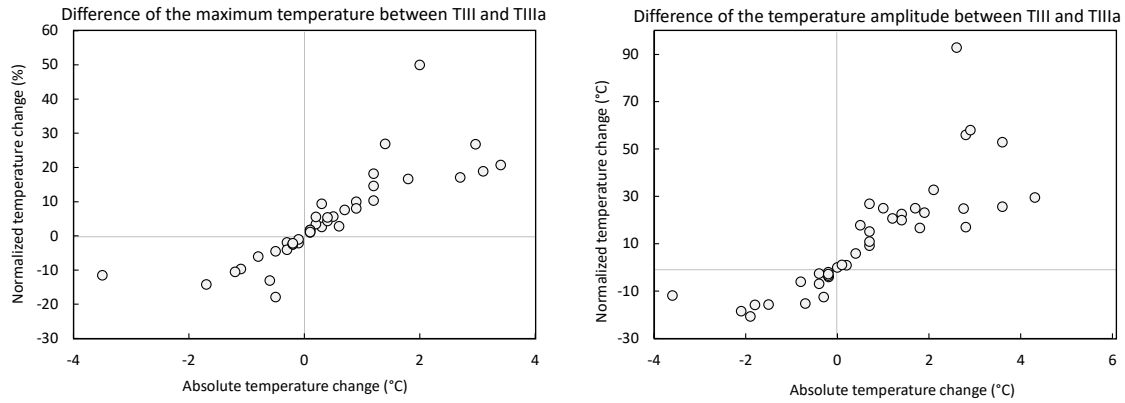
691 Fig. S2 : Comparison of the use of GLSC vs. CH₄ as reference to align high-latitude North-Atlantic cores. Top: GLSC (yellow)
 692 and CH₄ (green) records on the AICC2012 age scale (Bazin et al., 2013). Bottom left: average age difference between the two
 693 approaches for the eight cores. The black dot corresponds to the analysis performed on GIK23414 SST age model. Bottom
 694 right: Example of the GIK23414 SST record scaled on CH₄ (green curve) or GLSC (yellow curve). The average absolute age
 695 difference is 670 years. Overall, the absolute difference is 550 years on average for the eight North-Atlantic cores.

696

697

698

699



700

701 Fig. S3 : Comparison of the use of normalised vs. absolute relative temperature change to characterize the relative TIII and
 702 TIII-A amplitude (left) and relative MIS 7e – MIS 7c-7a maximum temperature for the 41 compiled surface temperature. The
 703 normalised temperature has been computed by normalising the temperature range of a specific period to the minimum and
 704 maximum value of temperature in the 260-190 ka interval. For instance, if the TIII registered an amplitude of warming of 5°C
 705 corresponding to 25-20°C, and these values corresponds to the maximum and minimum temperature value of the 260-190
 706 ka period, the normalised value will be 100%. If, for the same core, the amplitude registered during TIII-A is 3°C, the
 707 normalised value will be 60%. Finally, the relative normalised temperature change would thus be 40% (100%-60%) and the
 708 absolute value would be 2°C (5°C – 3°C). Note that if the amplitude of the temperature change during TIII and TIII-A is
 709 respectively 1°C and 0.6°C , and the amplitude of change during TIII still corresponds to the maximum and minimum
 710 temperature value of the 260-190 ka period, the absolute relative temperature change would be different (0.4°C) while the
 711 normalised relative temperature change would be similar (40%). Please note the high-correlation of both plot ($R^2 = 0.7$).

712

713

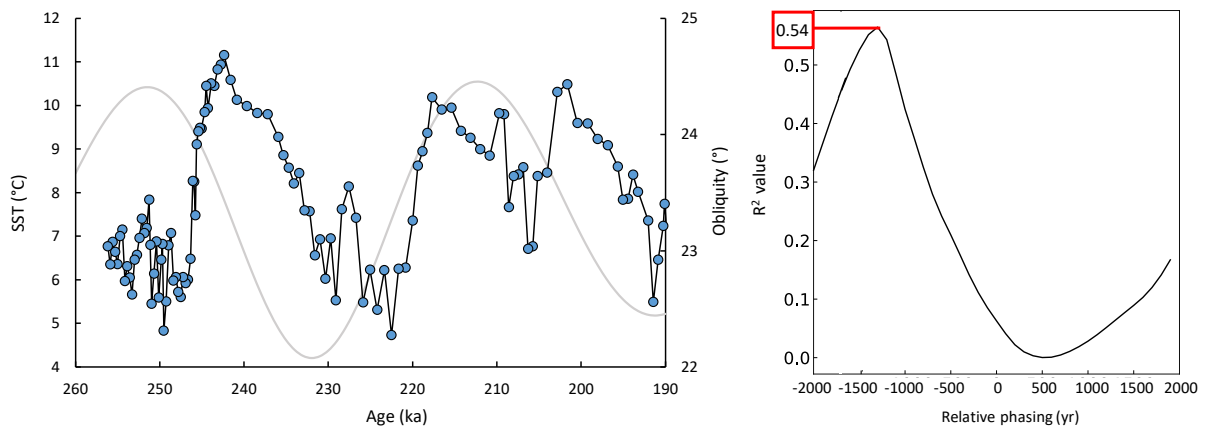
714

715

716

717

718



719

720 Fig. S4: Example of correlation computed over the -2000 / +2000 relative age windows at a time step of 100 years for the
 721 MD07-3077 core compared to the obliquity record. Left: MD07-3077 SST record (blue dots and black line) and obliquity record
 722 (grey line). Right: correlation analysis over the -2000/+2000 windows. The best value is $R^2 = 0.54$.

723

724

725

726

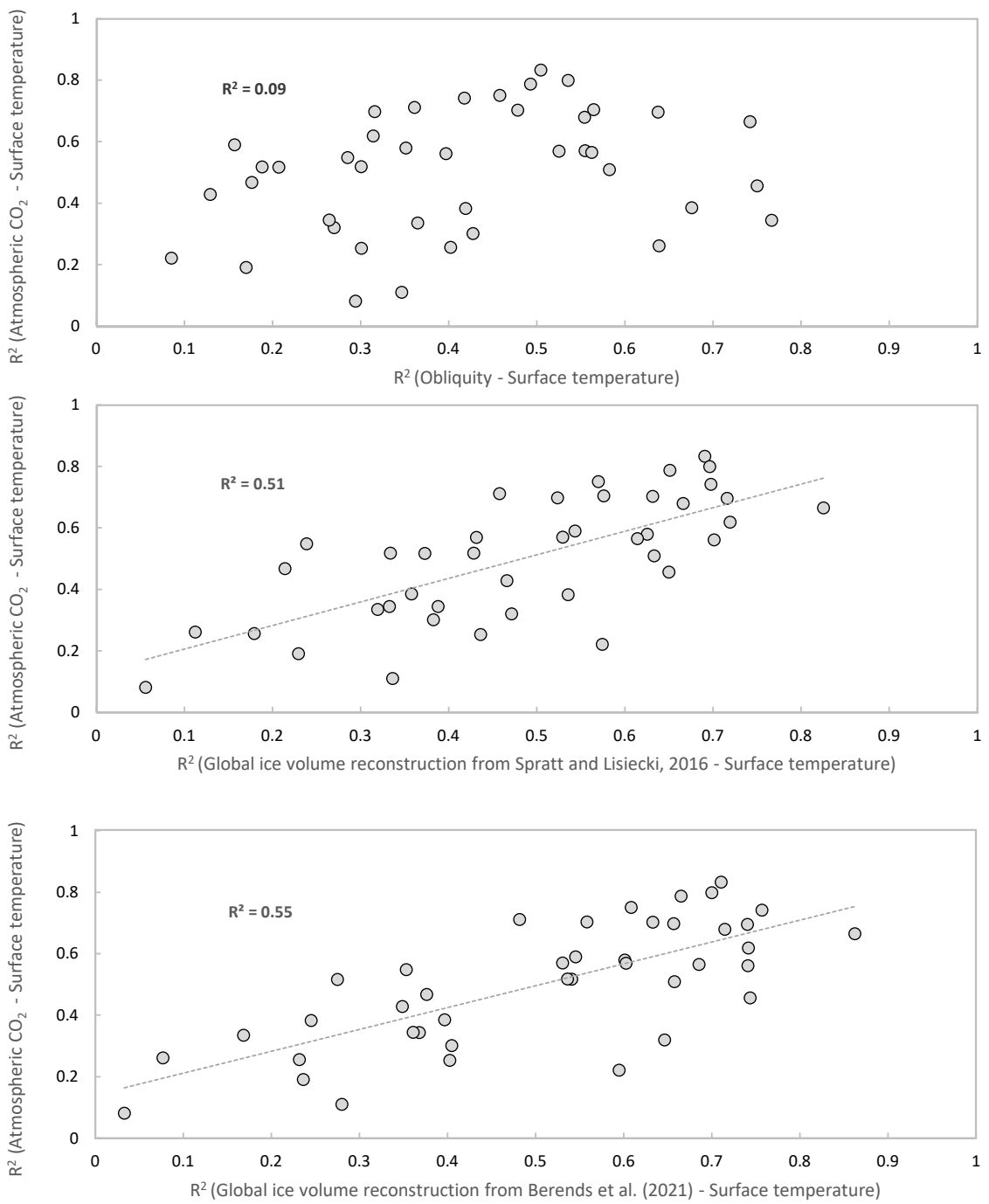
727

728

729

730

731



732

733

734 Fig. S5: Comparison of the correlation between global variables (atmospheric CO₂, obliquity, global ice volume) respectively
 735 to the local surface temperature records.

736

737

738 **Supplementary Tables**

739

740 Supplementary Tables are available upon request. If you are interested in, please send an email to:

741 etienne.legrain@univ-grenoble-alpes.fr or emilie.capron@univ-grenoble-alpes.fr

742

743

744

745

746

747

748

749

750

751

752

753

754

755

756

757

758

759

760

761

762

763 **References**

- 764 Abe-Ouchi, A., Saito, F., Kawamura, K., Raymo, M. E., Okuno, J. I., Takahashi, K., & Blatter, H. (2013).
765 Insolation-driven 100,000-year glacial cycles and hysteresis of ice-sheet volume. *nature*, 500(7461),
766 190-193.
- 767 Barker, S., Knorr, G., Edwards, R. L., Parrenin, F., Putnam, A. E., Skinner, L. C., ... & Ziegler, M. (2011).
768 800,000 years of abrupt climate variability. *science*, 334(6054), 347-351.
- 769 Barnola, J. M., Raynaud, D. Y. S. N., Korotkevich, Y. S., & Lorius, C. (1987). Vostok ice core provides
770 160,000-year record of atmospheric CO₂. *Nature*, 329(6138), 408-414.
- 771 Bazin, L., Landais, A., Lemieux-Dudon, B., Toyé Mahamadou Kele, H., Veres, D., Parrenin, F., ... & Wolff,
772 E. (2013). An optimized multi-proxy, multi-site Antarctic ice and gas orbital chronology (AICC2012):
773 120–800 ka. *Climate of the Past*, 9(4), 1715-1731.
- 774 Berends, C. J., De Boer, B., & Van De Wal, R. S. (2021). Reconstructing the evolution of ice sheets, sea
775 level, and atmospheric CO₂ during the past 3.6 million years. *Climate of the Past*, 17(1), 361-377.
- 776 Bova, S., Rosenthal, Y., Liu, Z., Godad, S. P., & Yan, M. (2021). Seasonal origin of the thermal maxima
777 at the Holocene and the last interglacial. *Nature*, 589(7843), 548-553.
- 778 Buizert, C., Fudge, T. J., Roberts, W. H., Steig, E. J., Sherriff-Tadano, S., Ritz, C., ... & Schwander, J. (2021).
779 Antarctic surface temperature and elevation during the Last Glacial Maximum. *Science*, 372(6546),
780 1097-1101.
- 781 Calvo, E., Pelejero, C., De Deckker, P., & Logan, G. A. (2007). Antarctic deglacial pattern in a 30 kyr
782 record of sea surface temperature offshore South Australia. *Geophysical Research Letters*, 34(13).
- 783 Capron, E., Govin, A., Stone, E. J., Masson-Delmotte, V., Mulitza, S., Otto-Bliesner, B., ... & Wolff, E. W.
784 (2014). Temporal and spatial structure of multi-millennial temperature changes at high latitudes during
785 the Last Interglacial. *Quaternary Science Reviews*, 103, 116-133.
- 786 Capron, E., Govin, A., Feng, R., Otto-Bliesner, B. L., & Wolff, E. W. (2017). Critical evaluation of climate
787 syntheses to benchmark CMIP6/PMIP4 127 ka Last Interglacial simulations in the high-latitude
788 regions. *Quaternary Science Reviews*, 168, 137-150.
- 789 Capron, E., Rovere, A., Austermann, J., Axford, Y., Barlow, N. L., Carlson, A. E., ... & Wolff, E. W. (2019).
790 Challenges and research priorities to understand interactions between climate, ice sheets and global
791 mean sea level during past interglacials. *Quaternary Science Reviews*, 219, 308-311.

792 Chappellaz, J. A., Fung, I. Y., & Thompson, A. M. (1993). The atmospheric CH₄ increase since the Last
793 Glacial Maximum. *Tellus B: Chemical and Physical Meteorology*, 45(3), 228-241.

794 Choudhury, D., Timmermann, A., Schloesser, F., Heinemann, M., & Pollard, D. (2020). Simulating
795 Marine Isotope Stage 7 with a coupled climate–ice sheet model. *Climate of the Past*, 16(6), 2183-2201.

796 Clark, P. U., Alley, R. B., & Pollard, D. (1999). Northern Hemisphere ice-sheet influences on global
797 climate change. *Science*, 286(5442), 1104-1111.

798 Colleoni, F., Masina, S., Cherchi, A., Navarra, A., Ritz, C., Peyaud, V., & Otto-Bliesner, B. (2014).
799 Modeling Northern Hemisphere ice-sheet distribution during MIS 5 and MIS 7 glacial
800 inceptions. *Climate of the Past*, 10(1), 269-291.

801 Desprat, S., Goñi, M. F. S., Turon, J. L., Duprat, J., Malaizé, B., & Peypouquet, J. P. (2006). Climatic
802 variability of Marine Isotope Stage 7: direct land–sea–ice correlation from a multiproxy analysis of a
803 north-western Iberian margin deep-sea core. *Quaternary Science Reviews*, 25(9-10), 1010-1026.

804 Dutton, A., Bard, E., Antonioli, F., Esat, T. M., Lambeck, K., & McCulloch, M. T. (2009). Phasing and
805 amplitude of sea-level and climate change during the penultimate interglacial. *Nature
806 Geoscience*, 2(5), 355-359.

807 Emiliani, C., 1954. Depth habitat of some species of pelagic foraminifera as indicated by oxygen isotope
808 ratio. *Am. J.Sci.* 252, 149-158.

809 Flückiger, J., Blunier, T., Stauffer, B., Chappellaz, J., Spahni, R., Kawamura, K., ... & Dahl-Jensen, D.
810 (2004). N₂O and CH₄ variations during the last glacial epoch: Insight into global processes. *Global
811 Biogeochemical Cycles*, 18(1).

812 Frogley, M. R., Tzedakis, P. C., & Heaton, T. H. E. (1999). Climate variability in northwest Greece during
813 the last interglacial. *Science*, 285(5435), 1886-1889.

814 Ganopolski, A., & Brovkin, V. (2017). Simulation of climate, ice sheets and CO₂ evolution during the
815 last four glacial cycles with an Earth system model of intermediate complexity. *Climate of the
816 Past*, 13(12), 1695-1716.

817 Genthon, G., Barnola, J. M., Raynaud, D., Lorius, C., Jouzel, J., Barkov, N. I., ... & Kotlyakov, V. M. (1987).
818 Vostok ice core: climatic response to CO₂ and orbital forcing changes over the last climatic
819 cycle. *Nature*, 329(6138), 414-418.

820 Govin, A., Braconnot, P., Capron, E., Cortijo, E., Duplessy, J. C., Jansen, E., ... & Waelbroeck, C. (2012).
821 Persistent influence of ice sheet melting on high northern latitude climate during the early Last
822 Interglacial. *Climate of the Past*, 8(2), 483-507.

823 Govin, A., Capron, É., Tzedakis, P. C., Verheyden, S., Ghaleb, B., Hillaire-Marcel, C., ... & Zahn, R. (2015).
824 Sequence of events from the onset to the demise of the Last Interglacial: Evaluating strengths and
825 limitations of chronologies used in climatic archives. *Quaternary Science Reviews*, 129, 1-36.

826 Hoffman, J. S., Clark, P. U., Parnell, A. C., & He, F. (2017). Regional and global sea-surface temperatures
827 during the last interglaciation. *Science*, 355(6322), 276-279.

828 Huang, B., Banzon, V. F., Freeman, E., Lawrimore, J., Liu, W., Peterson, T. C., ... & Zhang, H. M. (2015).
829 Extended reconstructed sea surface temperature version 4 (ERSST. v4). Part I: Upgrades and
830 intercomparisons. *Journal of climate*, 28(3), 911-930.

831 Huber, C., Leuenberger, M., Spahni, R., Flückiger, J., Schwander, J., Stocker, T. F., ... & Jouzel, J. (2006).
832 Isotope calibrated Greenland temperature record over Marine Isotope Stage 3 and its relation to
833 CH₄. *Earth and Planetary Science Letters*, 243(3-4), 504-519.

834 Imbrie, J. Z., Imbrie-Moore, A., & Lisiecki, L. E. (2011). A phase-space model for Pleistocene ice
835 volume. *Earth and Planetary Science Letters*, 307(1-2), 94-102.

836 Jouzel, J., Vimeux, F., Cailion, N., Delaygue, G., Hoffmann, G., Masson-Delmotte, V., & Parrenin, F.
837 (2003). Magnitude of isotope/temperature scaling for interpretation of central Antarctic ice
838 cores. *Journal of Geophysical Research: Atmospheres*, 108(D12).

839 Jouzel, J., Masson-Delmotte, V., Cattani, O., Dreyfus, G., Falourd, S., Hoffmann, G., ... & Wolff, E. W.
840 (2007). Orbital and millennial Antarctic climate variability over the past 800,000
841 years. *science*, 317(5839), 793-796.

842 Kawamura, K., Parrenin, F., Lisiecki, L., Uemura, R., Vimeux, F., Severinghaus, J. P., ... & Watanabe, O.
843 (2007). Northern Hemisphere forcing of climatic cycles in Antarctica over the past 360,000
844 years. *Nature*, 448(7156), 912-916.

845 Landais, A., Stenni, B., Masson-Delmotte, V., Jouzel, J., Cauquoin, A., Fourré, E., ... & Grisart, A. (2021).
846 Interglacial Antarctic–Southern Ocean climate decoupling due to moisture source area shifts. *Nature*
847 *Geoscience*, 14(12), 918-923.

848 Lang, N., & Wolff, E. W. (2011). Interglacial and glacial variability from the last 800 ka in marine, ice
849 and terrestrial archives. *Climate of the Past*, 7(2), 361-380.

850 Laskar, J., Robutel, P., Joutel, F., Gastineau, M., Correia, A. C., & Levrard, B. (2004). A long-term
851 numerical solution for the insolation quantities of the Earth. *Astronomy & Astrophysics*, 428(1), 261-
852 285.

853 Lea, D. W. (2002). The glacial tropical Pacific--not just a west side story. *Science*, 297(5579), 202-203.

854 Leduc, G., Schneider, R., Kim, J. H., & Lohmann, G. (2010). Holocene and Eemian sea surface
855 temperature trends as revealed by alkenone and Mg/Ca paleothermometry. *Quaternary Science*
856 *Reviews*, 29(7-8), 989-1004.

857 Leduc, G., Garidel-Thoron, T. D., Kaiser, J., Bolton, C., & Contoux, C. (2017). Databases for sea surface
858 paleotemperature based on geochemical proxies from marine sediments: implications for model-data
859 comparisons. *Quaternaire. Revue de l'Association française pour l'étude du Quaternaire*, 28(2), 201-
860 216.

861 Legrain, E., Parrenin, F., & Capron, E. (2023). A gradual change is more likely to have caused the Mid-
862 Pleistocene Transition than an abrupt event. *Communications Earth & Environment*, 4(1), 90.

863 Legrain, E., Capron, E., Menviel, L., et al., (in revision). High obliquity favours centennial-scale variations
864 in the carbon cycle.

865 Lisiecki, L. E., & Raymo, M. E. (2005). A Pliocene-Pleistocene stack of 57 globally distributed benthic
866 $\delta^{18}\text{O}$ records. *Paleoceanography*, 20(1).

867 Lisiecki, L. E., & Raymo, M. E. (2009). Diachronous benthic $\delta^{18}\text{O}$ responses during late Pleistocene
868 terminations. *Paleoceanography*, 24(3).

869 Lisiecki, L. E., & Stern, J. V. (2016). Regional and global benthic $\delta^{18}\text{O}$ stacks for the last glacial
870 cycle. *Paleoceanography*, 31(10), 1368-1394.

871 Luo, Y., Tjiputra, J., Guo, C., Zhang, Z., & Lippold, J. (2018). Atlantic deep water circulation during the
872 last interglacial. *Scientific Reports*, 8(1), 4401.

873 Manabe, S., & Broccoli, A. J. (1985). The influence of continental ice sheets on the climate of an ice
874 age. *Journal of Geophysical Research: Atmospheres*, 90(D1), 2167-2190.

875 Martrat, B., Grimalt, J. O., Shackleton, N. J., de Abreu, L., Hutterli, M. A., & Stocker, T. F. (2007). Four
876 climate cycles of recurring deep and surface water destabilizations on the Iberian
877 margin. *Science*, 317(5837), 502-507.

878 Masson-Delmotte, V., Buiron, D., Ekaykin, A., Frezzotti, M., Gallée, H., Jouzel, J., ... & Vimeux, F. (2011).
879 A comparison of the present and last interglacial periods in six Antarctic ice cores. *Climate of the*
880 *Past*, 7(2), 397-423.

881 Mulitza, S., Boltovskoy, D., Donner, B., Meggers, H., Paul, A., & Wefer, G. (2003). Temperature: $\delta^{18}\text{O}$
882 relationships of planktonic foraminifera collected from surface waters. *Palaeogeography,*
883 *Palaeoclimatology, Palaeoecology*, 202(1-2), 143-152.

884 Oppo, D. W., McManus, J. F., & Cullen, J. L. (2006). Evolution and demise of the Last Interglacial warmth
885 in the subpolar North Atlantic. *Quaternary Science Reviews*, 25(23-24), 3268-3277.

886 Otto-Bliesner, B. L., Brady, E. C., Tomas, R. A., Albani, S., Bartlein, P. J., Mahowald, N. M., ... & Sommers,
887 A. N. (2020). A comparison of the CMIP6 midHolocene and lig127k simulations in
888 CESM2. *Paleoceanography and Paleoclimatology*, 35(11), e2020PA003957.

889 Pahnke, K., Zahn, R., Elderfield, H., & Schulz, M. (2003). 340,000-year centennial-scale marine record
890 of Southern Hemisphere climatic oscillation. *Science*, 301(5635), 948-952.

891 Paillard, D., Labeyrie, L. D., & Yiou, P. (1996). AnalySeries 1.0: a Macintosh software for the analysis of
892 geophysical time-series. *Eos*, 77(39), 379.

893 Parrenin, F., & Paillard, D. (2012). Terminations VI and VIII (~ 530 and ~ 720 kyr BP) tell us the
894 importance of obliquity and precession in the triggering of deglaciations. *Climate of the Past*, 8(6),
895 2031-2037.

896 Past Interglacials Working Group of PAGES. (2016). Interglacials of the last 800,000 years. *Reviews of*
897 *Geophysics*, 54(1), 162-219.

898 Pedro, J. B., Jochum, M., Buizert, C., He, F., Barker, S., & Rasmussen, S. O. (2018). Beyond the bipolar
899 seesaw: Toward a process understanding of interhemispheric coupling. *Quaternary Science*
900 *Reviews*, 192, 27-46.

901 Petit, J. R., Jouzel, J., Raynaud, D., Barkov, N. I., Barnola, J. M., Basile, I., ... & Stievenard, M. (1999).
902 Climate and atmospheric history of the past 420,000 years from the Vostok ice core,
903 Antarctica. *Nature*, 399(6735), 429-436.

904 Prokopenko, A. A., Hinnov, L. A., Williams, D. F., & Kuzmin, M. I. (2006). Orbital forcing of continental
905 climate during the Pleistocene: a complete astronomically tuned climatic record from Lake Baikal, SE
906 Siberia. *Quaternary Science Reviews*, 25(23-24), 3431-3457.

907 Roucoux, K. H., Tzedakis, P. C., Frogley, M. R., Lawson, I. T., & Preece, R. C. (2008). Vegetation history
908 of the marine isotope stage 7 interglacial complex at Ioannina, NW Greece. *Quaternary Science*
909 *Reviews*, 27(13-14), 1378-1395.

910 Severinghaus, J. P., & Brook, E. J. (1999). Abrupt climate change at the end of the last glacial period
911 inferred from trapped air in polar ice. *Science*, 286(5441), 930-934.

912 Shakun, J. D., Clark, P. U., He, F., Marcott, S. A., Mix, A. C., Liu, Z., ... & Bard, E. (2012). Global warming
913 preceded by increasing carbon dioxide concentrations during the last deglaciation. *Nature*, 484(7392),
914 49-54.

915 Siddall, M., Rohling, E. J., Almogi-Labin, A., Hemleben, C., Meischner, D., Schmelzer, I., & Smeed, D. A.
916 (2003). Sea-level fluctuations during the last glacial cycle. *Nature*, 423(6942), 853-858.

917 Spratt, R. M., & Lisiecki, L. E. (2016). A Late Pleistocene sea level stack. *Climate of the Past*, 12(4), 1079-
918 1092.

919 Steinsland, K., Grant, D. M., Ninnemann, U. S., Fahl, K., Stein, R., & De Schepper, S. (2023). Sea ice
920 variability in the North Atlantic subpolar gyre throughout the last interglacial. *Quaternary Science*
921 *Reviews*, 313, 108198

922 Stern, J. V. (2014). *Regional Benthic Foraminiferal Oxygen Isotope Stacks for the Last Glacial*
923 *Cycle* (Doctoral dissertation, University of California, Santa Barbara).

924 Stone, E. J., Capron, E., Lunt, D. J., Payne, A. J., Singarayer, J. S., Valdes, P. J., & Wolff, E. W. (2016).
925 Impact of meltwater on high-latitude early Last Interglacial climate. *Climate of the Past*, 12(9), 1919-
926 1932.

927 Tzedakis, P. C., Raynaud, D., McManus, J. F., Berger, A., Brovkin, V., & Kiefer, T. (2009). Interglacial
928 diversity. *Nature Geoscience*, 2(11), 751-755.

929 Waelbroeck, C., Jouzel, J., Labeyrie, L., Lorius, C., Labracherie, M., Stiévenard, M., & Barkov, N. I.
930 (1995). A comparison of the Vostok ice deuterium record and series from Southern Ocean core MD 88-
931 770 over the last two glacial-interglacial cycles. *Climate Dynamics*, 12, 113-123.

932

933 Wang, Y., Jia, J., Liu, H., Lu, C., Xia, D., & Lu, H. (2018). The magnetic susceptibility recorded millennial-
934 scale variability in central Asia during last glacial and interglacial. *Geophysical Journal International*,
935 215(3), 1781-1788

- 936 Watanabe, Y., Abe-Ouchi, A., Saito, F., Kino, K., O'ishi, R., Ito, T., ... & Chan, W. L. (2023). Astronomical
937 forcing shaped the timing of early Pleistocene glacial cycles. *Communications Earth &*
938 *Environment*, 4(1), 113.
- 939 Wendt, K. A., Li, X., Edwards, R. L., Cheng, H., & Spötl, C. (2021). Precise timing of MIS 7 substages from
940 the Austrian Alps. *Climate of the Past*, 17(4), 1443-1454.
- 941 Wu, Z., Yin, Q., Guo, Z., & Berger, A. (2020). Hemisphere differences in response of sea surface
942 temperature and sea ice to precession and obliquity. *Global and Planetary Change*, 192, 103223.
- 943 Yin, Q. Z., & Berger, A. (2012). Individual contribution of insolation and CO₂ to the interglacial climates
944 of the past 800,000 years. *Climate dynamics*, 38, 709-724.

5.3. Perspectives

The multi-archive synthesis presented in this chapter is the first spanning the MIS 7. For this reason, I have focused the analysis on the spatio-temporal pattern of surface temperature that have not been described before, apart from local studies. While including both marine (38) and continental (3) records, this synthesis lacks in characterizing the mid-to-low-latitude climatic evolution on land. The inclusion of pollen and speleothems records previously aligned onto the AICC2012 timescale would improve the spatial coverage of this study. The alignment of such continental records on a common temporal framework is nevertheless very challenging, as demonstrated by an on-going effort across the Last Interglacial [Bazin et al., 2019, QUIGS meeting].

Multi-archive synthesis outputs are highly dependent on the common temporal framework used to align paleoclimatic records. The dating uncertainty of the compiled surfaced temperature records can be improved, using a more accurate chronology of reference. An on-going work will propose a new chronology of reference for ice cores that includes new absolute and relative age markers that consequently reduced the absolute age uncertainty of the chronology compared to AICC2012 (AICC2023, Bouchet et al. [under review], see Appendices). In addition, another strategy relies on the alignment of marine and ice core records directly on absolute age-scale dated by tephra or paleomagnetic constrains [Bazin et al., 2019]. Nevertheless, this methodology of alignment requires absolutely dated layers in marine sediments and ice cores, that is not yet available for all climatic periods.

Beyond this study, the multi-archive synthesis of the MIS 7 surface temperature can be used in a model-data comparison exercise to (i) test with physics-based tools climate forcing and feedbacks hypothesized from the data and (ii) to evaluate how well ESM, also used for future projections, simulate warm climates [Stone et al., 2016; Otto-Bliesner et al., 2021]. Such exercise was already done for the Last Interglacial [Govin et al., 2012; Capron et al., 2014, 2017; Hoffman et al., 2017]. Interestingly, the simulation of the MIS 7 requires very specific combination of model parameters to be simulated from non-spatialized and spatialized models [e.g. Parrenin and Paillard, 2012; Colleoni et al., 2014]. The identification of regional areas on which spatialized model reconstruction registered the most deviation compared to the data reconstruction could provide key information on the physical and climatic mechanisms required to model the complexity of the MIS 7. Simulations performed with EMIC over the MIS 7 have already been published [Yin et Berger 2012; Bouttes et al., 2016] and will allow a future model-

data comparison as it has been done for the Last Interglacial [Govin et al., 2012; Capron et al., 2014, 2017]

Interglacial surface temperature syntheses have been already published for the Holocene and the Last Interglacial [e.g. Shakun et al., 2012; Capron et al., 2014; Hoffman et al., 2017; Bova et al., 2021]. This study is included in a broader project led by Emilie Capron (MOPGA HOTCLIM, Characterisation & Dynamics of Past Warm Climates, 2020-2026) that aims to build such climate synthesis for MIS 9. The construction of the MIS 9 synthesis has been initiated in 2023 by Claire Coutelle, a Master student that I co-supervised together with Emilie Capron. Once the MIS 9 climate synthesis will be finalised, it will be interesting to lead a study comparing the results founded in the past four interglacials. Such multi-interglacial approach could look in particular into: (i) the spatial variability of relative interglacial intensity (ii) the impact of the different orbital context on the spatio-temporal evolution of the surface temperature patterns, and (iii) the ability of a single set of model parameters to reproduce the climate diversity of the past four interglacials.

Synthesis

In this chapter, I present the building and the results from a multi-archive synthesis characterizing the spatial evolution of surface temperature during MIS 7 and the preceding TIII. Based on this synthesis, I evidence the latitudinal-scale variability of the relative intensity between MIS 7e and 7a-7c. MIS 7e is warmer in the Southern latitudes compared to MIS 7a-7c, following the amplitude changes observed in atmospheric CO₂ concentrations and Antarctic temperature records. Reversely, the low and northern latitudes registered equivalent surface temperature levels during MIS 7e and MIS 7a-7c. Second, the southern high latitudes exhibit local surface temperatures warmer than the pre-industrial during MIS 7e. Third, the high-latitude temperature records in both hemispheres are better correlated with the atmospheric CO₂ concentrations and global ice volume estimates than the ones from the low latitude regions. Lastly, correlation analyses between orbital records and surface temperature patterns highlight the strong imprint of obliquity in shaping the temperature evolution during the MIS 7. Based on this strong obliquity imprint and the relatively low amplitude of the warming during MIS 7, I propose that the MIS 7 owns specificities that resemble those associated with the pre-MPT interglacials.

This synthesis is included in a more global effort to characterize the interglacial climates during the past 500 ka through the MOPGA HOTCLIM project. While my study has focused on the spatio-temporal pattern of data-based paleotemperature records, future work should (i) compare the results with spatialized outputs from Earth System Model and (ii) compare the spatio-temporal climate evolution during the MIS 7 with those during other interglacials to improve our understanding of the forcings, the climate system response and the impacts during warm periods of the past.

Chapter 6

Centennial-scale variations in the carbon cycle over the past 500,000 years

In this last chapter of results, I investigate the centennial-scale variations in the carbon cycle based on the combination of new and published CO₂ and CH₄ records from the Antarctic EDC ice core together with climatic and carbon cycle simulations from an Earth system model of intermediary complexity. A strong influence of the long-term orbital variations on centennial-scale variations in the carbon cycle is underlined during the last 500 ka. This chapter is composed of an article currently in revision for *Nature*, followed by perspectives.

Chapter 6 aims at:

- Investigating the occurrence of centennial-scale variations in the carbon cycle during the 260-190 ka period.
- Understanding the causes of these centennial-scale variations over the past 500 ka.

Methodology:

- New measurements of 203 CO₂ samples and 18 CH₄ samples on the EDC ice core over the 260-190 ka period.
- Climatic and carbon cycle simulations performed with an Earth system model of intermediary complexity (collaboration with Laurie Menviel, University of New South Wales, Australia).

Highlights:

- Statistical analysis reveals that centennial-scale variations of CO₂ occurred under a high-obliquity context across the past 500 ka.
- The new simulations of carbon cycle point to the terrestrial vegetation as the variable carbon source sensitive to a high-obliquity context at centennial-scale.

Data availability:

- The new CO₂ and CH₄ records and the outputs of the simulations will be available on PANGEA once published.

6.1. Introduction

Centennial-scale increases of atmospheric CO₂ concentrations have been described for the first time by Ahn et al. [2012] in the Siple Dome ice core during TI. This result was confirmed two years later by Marcott et al. [2014] based high-resolution records from the West Antarctic Ice Sheet (WAIS) Divide ice core (WDC). They identified three rapid CO₂ changes characterized by a ~10-15 ppm increases in less than two centuries over the same period. The major specificity of these CO₂ events is that they have no equivalent in the stable water isotope profile measured on the WDC ice core, suggesting that the centennial-scale changes in the carbon cycle are decoupled to Antarctic climate variations [Marcott et al., 2014]. This result was unexpected given the strong covariance between atmospheric CO₂ and Antarctic temperature at millennial- and orbital-scale during TI [e.g. Schmitt et al., 2012; Parrenin et al., 2013] and beyond [Jouzel et al., 2007; Bereiter et al., 2015]. Later, this mode of variability was identified as a pervasive pattern of the carbon cycle during both glacial [Bauska et al., 2021], interglacial and deglacial [Nehrbass-Ahles et al., 2020] periods.

The Northern Hemisphere variability, through its impacts on the AMOC, has been identified as a potential cause of the centennial-scale variations of the carbon cycle. The first family of these events, referred to as Carbon Dioxide Jumps + (CDJ+) in Nehrbass-Ahles et al., [2020], occurs synchronously with DO-like events. The invigoration of AMOC during a DO-like events would provoke an abrupt release of carbon at centennial-scale from Southern Ocean and/or terrestrial vegetation [Rae et al., 2018; Bauska et al., 2021; Nehrbass-Ahles et al., 2020]. These CDJs+ are associated with synchronous major CH₄ concentrations increase of more than 50 ppb and up to 250 ppb [Nehrbass-Ahles et al., 2020]. The second family of these events occurs during HS [Marcott et al., 2014] and are named CDJ- [Nehrbass-Ahles et al., 2020]. CDJ- are thought to be the consequence of the collapse of the AMOC during extensive cold periods of the Northern Hemisphere [Nehrbass-Ahles et al., 2020]. The Southern Ocean and/or the terrestrial vegetation are suspected as potential sources of carbon during CDJ. The CDJ- are associated with smaller CH₄ release in the atmosphere than those synchronous to CDJ+ during the TI and the last glacial period, while no CH₄ release in the atmosphere are detected further back in time during CDJ- events [Nehrbass-Ahles et al., 2020]. Nevertheless, not all of the DO-like or HS led to centennial-scale CO₂ increases [Bauska et al., 2021]. Until now, the relatively low number of identified CDJs did not allow to investigate potential favourable context of occurrences of these events, apart from their identified link with the Northern Hemisphere millennial-scale variability.

The study presented in this chapter takes place in a context of international efforts to increase resolution of the CO₂ records over the past 500 ka [Nehrbass-Ahles et al., 2020; Shin et al., 2020; Bauska et al., 2021; Silva, 2022]. Fig. 6.1 is a conceptual summary of the analysis performed in this chapter.

Combining the new CO₂ record I measured and these recently published high-resolution CO₂ records, I will tackle the following questions:

- What are the processes responsible for the non-linear centennial-scale response of the carbon cycle to the Northern Hemisphere millennial-scale climate variability?
- Does the background orbital context impact the occurrence of centennial-scale events?
- What are the carbon sources involved in this abrupt carbon cycle variation?

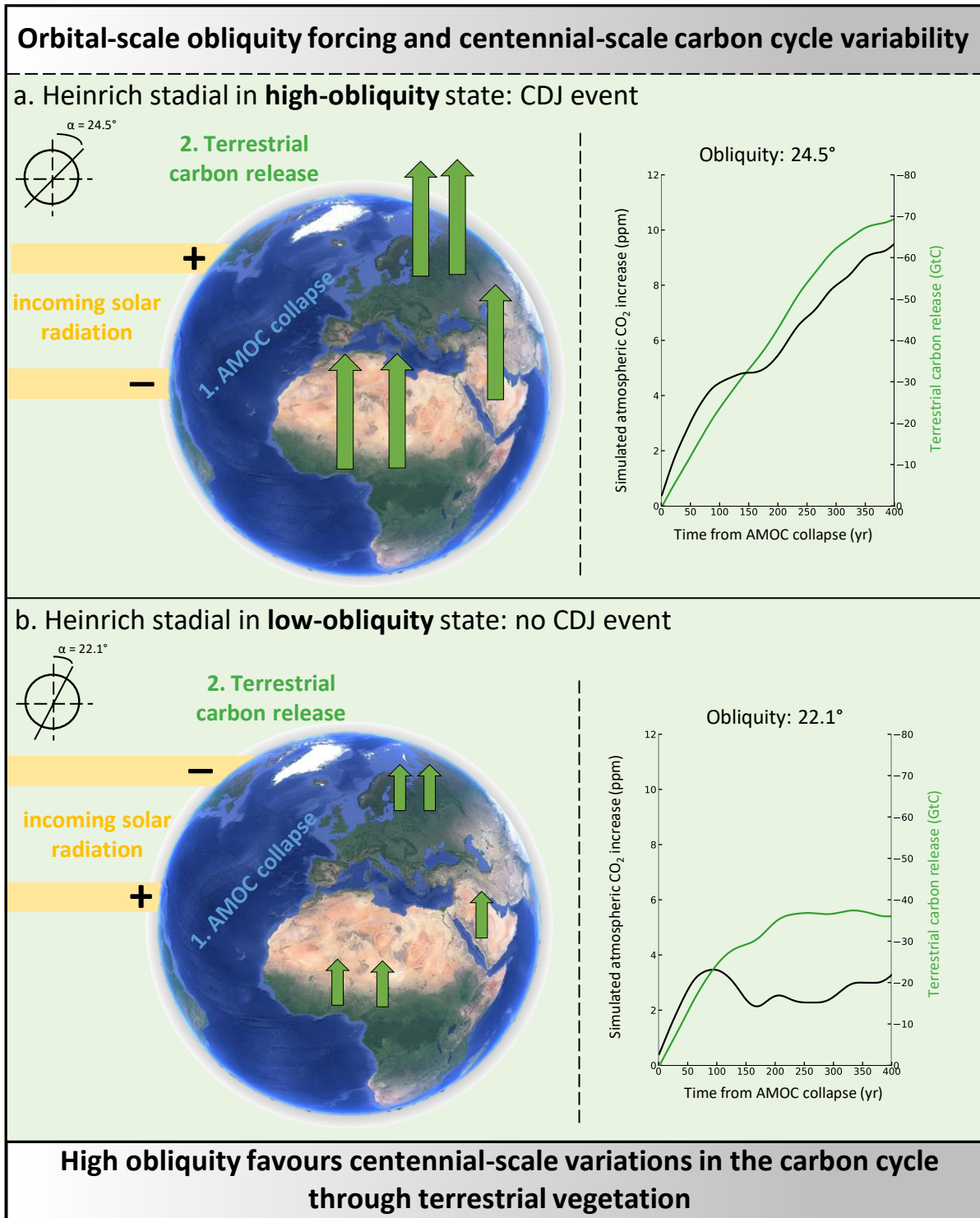


Fig. 6.1: Conceptual summary of the analysis performed in Chapter 6. The top/bottom panel presents the consequence of a Heinrich Stadial occurring during (a) high and (b) low-obliquity states. The yellow shaded area represents the incoming forcing at the surface of Earth. The + and - sign refers to an increased/decreased incoming insolation at this latitude compare to the other obliquity state. Green arrows represent the area where the terrestrial carbon release in atmosphere is sensitive to the obliquity state as inferred from the LOVECLIM simulations (see Section 6.2.). The right panel represents the evolution from the AMOC collapse of the simulated atmospheric CO₂ concentrations and terrestrial carbon release in the HighObl (top) and LowObl (bottom) simulations performed under high (top) and low (bottom) obliquity with the LOVECLIM model. Details of the study is available in Legrain et al. [in revision].

6.2. Publication: High obliquity favours centennial-scale variations in the carbon cycle (in revision)

Legrain et al., in revision for Nature

1 High obliquity favours centennial-scale variations in the carbon cycle

2 Etienne Legrain^{1*}, Emilie Capron¹, Laurie Menviel^{2,3}, Axel Wohleber¹, Frédéric Parrenin¹, Grégory
3 Teste¹, Amaëlle Landais⁴, Marie Bouchet⁴, Roberto Grilli¹, Christoph Nehrbass-Ahles^{5,6}, Lucas Silva⁷,
4 Hubertus Fischer⁷, Thomas F. Stocker⁷

5 *1 Université Grenoble Alpes, CNRS, IRD, Grenoble INP, IGE, Grenoble, France*

6 *2 Climate Change Research Centre, University of New South Wales, Sydney, Australia*

7 *3 The Australian Centre for Excellence in Antarctic Science, University of Tasmania, Hobart, Tasmania*
8 *7001, Australia*

9 *4 Laboratoire des Sciences du Climat et de l'Environnement, LSCE/IPSL, CEA-CNRS-UVSQ, Université*
10 *Paris-Saclay, Gif-sur-Yvette, France*

11 *5 Department of Earth Sciences, University of Cambridge, Cambridge, UK*

12 *6 National Physical Laboratory, Teddington, UK*

13 *7 Climate and Environmental Physics, Physics Institute, and Oeschger Centre for Climate Change*
14 *Research, University of Bern, Bern, Switzerland*

15 **Corresponding author: etienne.legrain@univ-grenoble-alpes.fr*

16

17 **Abstract**

18 Centennial-scale releases of atmospheric carbon dioxide (Carbon Dioxide Jumps, CDJs) are identified
19 during deglacial¹, glacial^{2,3} and interglacial⁴ periods and linked to the Northern Hemisphere abrupt
20 climate variability^{1,3,4}. However, the limited number of identified CDJs prevents investigating the role
21 of orbital background conditions on the different components of the global carbon cycle that may lead
22 to such rapid atmospheric CO₂ releases. Here, we present a new high-resolution CO₂ record measured
23 on an Antarctic ice core between 260 and 190 thousand years ago which reveals seven new CDJs. 18
24 of the 20 CDJs identified over the past 500 thousand years occurred under a context of high obliquity.
25 New simulations performed with an Earth system model of intermediate complexity point toward both
26 the continental biosphere and the Southern Ocean as the two main carbon sources during these rapid
27 events. Notably, the continental biosphere appears to be the obliquity-dependent CO₂ source for CDJs
28 connected to Heinrich events. For the first time, we demonstrate that the long-term external forcing
29 directly impacts past abrupt atmospheric CO₂ variations. Hence, the current high obliquity phase could
30 enhance variations within the carbon cycle in case of a major oceanic circulation disruption due to
31 anthropogenic disturbances, generating additional atmospheric CO₂ release from natural sources.

32

33

34 **Main text**

35 Understanding the mechanisms of natural centennial-scale changes in the carbon cycle is a major
36 challenge under the ongoing anthropogenic CO₂-driven climate change. Recent efforts to produce
37 high-resolution atmospheric CO₂ records from Antarctic ice cores demonstrated the pervasive
38 character of centennial-scale atmospheric CO₂ increases (Carbon Dioxide Jumps, CDJs) in the global
39 climate system over the last 500 ka (thousand years before present)⁴. These CDJs consist of an
40 atmospheric CO₂ increase of varying magnitude, from ~5 ppm up to ~ 16 ppm, that occurs in a few of
41 centuries at estimated rates of up to 26 ppm/century in the atmosphere⁴. Unlike the orbital- and
42 millennial-scale carbon cycle variations^{5,6}, this abrupt variability is decoupled from Antarctic surface
43 temperature changes^{1,4}. Two types of Northern Hemisphere (NH) climatic events are associated with
44 the centennial-scale CO₂ changes: (i) the so-called Dansgaard-Oeschger (DO) events are identified in
45 Greenland ice cores, and characterized by a local surface temperature increase of 5 to 16°C in less than
46 a century during the last glacial period^{7,8}. (ii) the Heinrich stadials (HS) are identified as cold phases in
47 Greenland during which Heinrich events occurred, as reflected in the occurrence of Ice Rafted Debris
48 (IRD) in North Atlantic sediment cores⁹. The CDJs that occurred during a DO event (hereafter CDJ+)⁴
49 are associated with an increase in atmospheric methane (CH₄) concentrations larger than 50 ppb^{10,11}.
50 The CDJs that occurred during an HS (hereafter CDJ-)⁴ are not associated with any major CH₄ increase⁴.
51 Proposed hypotheses to explain how these rapid atmospheric CO₂ increases relate to DO events or HS
52 involve both terrestrial^{3,10,12} and marine CO₂ sources^{13–15} but overall, the underlying mechanisms
53 remain poorly understood (Supplementary Materials). In addition, some of the DO-like events and HS
54 occurring under glacial and early interglacial conditions^{3,4} may not leave a detectable CDJ imprint in
55 ice-core records. Hence, the centennial-scale CO₂ variability may not respond linearly to the Northern
56 Hemisphere abrupt climate variability.

57 Here, we argue that the orbital-scale climatic background conditions modulate the intensity of the
58 centennial-scale carbon cycle response to the Northern Hemisphere climatic perturbations. To test this
59 hypothesis, we extend the time frame covered by high-resolution atmospheric CO₂ reconstructions to
60 allow the identification of additional potential CDJs under varying orbital configurations. Then, we
61 investigate the impact of orbital-scale changes in the climatic background on centennial-scale CO₂
62 increases through new simulations performed with an Earth system model of intermediate complexity.

63 **New sub-millennial-scale atmospheric CO₂ record**

64 We measured 203 new samples on the Antarctic EPICA Dome C (EDC) ice core over the 260 – 190 ka
65 interval using the dry-extraction system coupled to a gas chromatograph at the Institute of
66 Environmental Geosciences (IGE, Grenoble, France; ^{6,16}; see methods). Our new CO₂ record is in general

67 agreement with previously published data⁵, but we increase the mean temporal resolution by a factor
68 of three to an average of 340 years (Fig. 1, Supplementary Fig. 1). Owing to the high-resolution data,
69 we identify seven previously unidentified periods of centennial-scale CO₂ release to the atmosphere.
70 These CDJs have been identified using the detection methodology described in ref. ⁴. In summary, we
71 first remove the orbital-scale (i.e. deglaciation and glaciation) and millennial-scale (i.e. Antarctic
72 Isotope Maximum events) imprint in the CO₂ record using cubic smoothing splines¹⁷. Second, we
73 calculate the rate of change of the detrended CO₂ record and third, we apply the threshold of 1.5
74 ppm/century from ref. ⁴ to identify CDJs (see methods; Supplementary Figs. 2, 3). We identify two CDJ+
75 associated with atmospheric CH₄ increases higher than 50 ppb in less than 300 years (Supplementary
76 Fig. 3), and five CDJ- that are not associated with a detectable increase in atmospheric CH₄ in the ice
77 core record. Five CDJs took place under either glacial or deglaciation conditions¹⁸ (CDJ-8.1, CDJ-8.2,
78 CDJ-TIII, CDJ+7e, CDJ-7c; Supplementary Fig. 5). Also, two CDJs occurred during interglacial conditions
79 (CDJ-7b, CDJ+7a) when Northern Hemisphere ice sheets had shrunk to a size approaching the Holocene
80 value, confirming the occurrence of CDJs during periods of relatively small global ice sheet volume^{4,19}
81 (Supplementary Fig. 5). Hence, combining published and newly-described events we find 20 CDJs
82 occurring under a wide range of climatic and orbital boundary conditions over the past 500 ka (Fig. 2,
83 Supplementary Fig. 6, Supplementary Table 4).

84

85

86

87

88

89

90

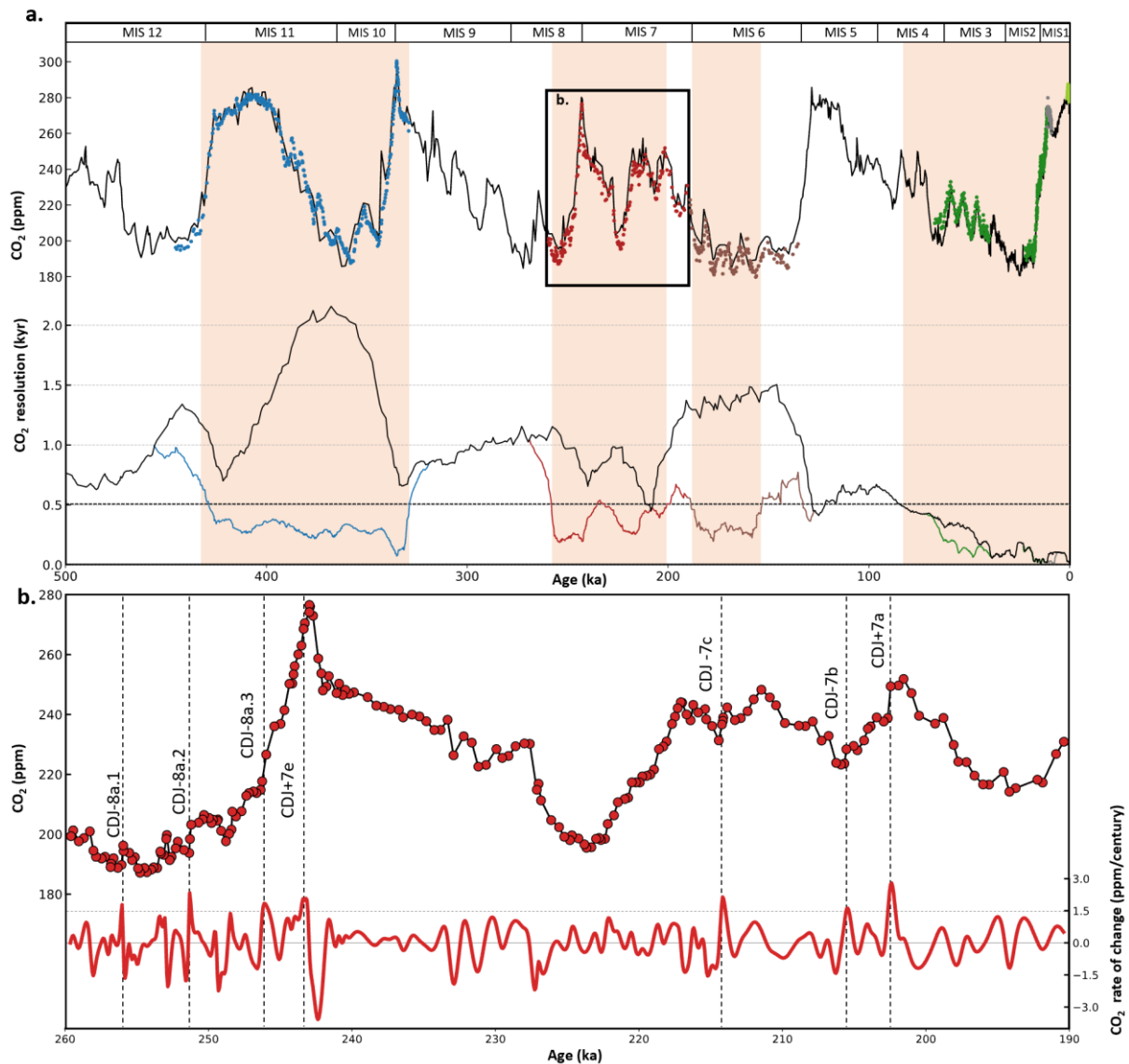
91

92

93

94

95



96

97 **Fig. 1: Improvement of the ice-core atmospheric CO₂ record resolution since the composite CO₂ record from**
 98 **ref. ⁴⁹ over the last 500 ka. a. Top:** High-resolution records are represented in blue⁴, red (this study), brown¹⁶,
 99 green³, grey⁵², and light-green dots⁵¹, plotted on their published age scale. They are superimposed on the
 100 composite CO₂ record⁴⁹ (black line). Bottom: Temporal resolutions of all records computed as the running mean
 101 of 20 data points (colour codes similar to top panel). Data are not corrected for potential offsets due to the use
 102 of different experimental setups. Vertical red bands indicate periods where the ice-core CO₂ record is associated
 103 with a temporal resolution better than 500 years. **b. Top:** Zoom on our new EDC CO₂ record between 260-190 ka
 104 (red dots, black line). Vertical black dashed lines indicate the newly identified CDJs (see methods, supplementary
 105 materials). Bottom: CO₂ rates of change from the detrended CO₂ record for the smoothing spline (1 kyr cutoff
 106 period)⁴. Vertical back dashed lines indicate the timing of the identified CDJs. A centennial-scale CO₂ release is
 107 identified when the rate is higher than 1.5ppm/century (dashed horizontal grey line)⁴. MIS: Marine Isotope Stage.

108

109

110

111 **Carbon cycle variability and obliquity state**

112 The sources and mechanisms behind centennial-scale release of atmospheric CO₂ have been previously
113 investigated based on carbon isotope measurements on Antarctic ice and carbon cycle modelling^{3,20}.
114 Two main hypotheses have been discussed: (i) the role of a terrestrial carbon source from the
115 continental biosphere due to a shift in the intertropical convergence zone^{1,3} and (ii) an increase of
116 upwelling activity in the Southern Ocean and/or the North Pacific Ocean possibly due to enhanced
117 intensity of winds^{13,14}. However, the role played by long-term forcing on the centennial-scale CO₂
118 variability has not yet been assessed.

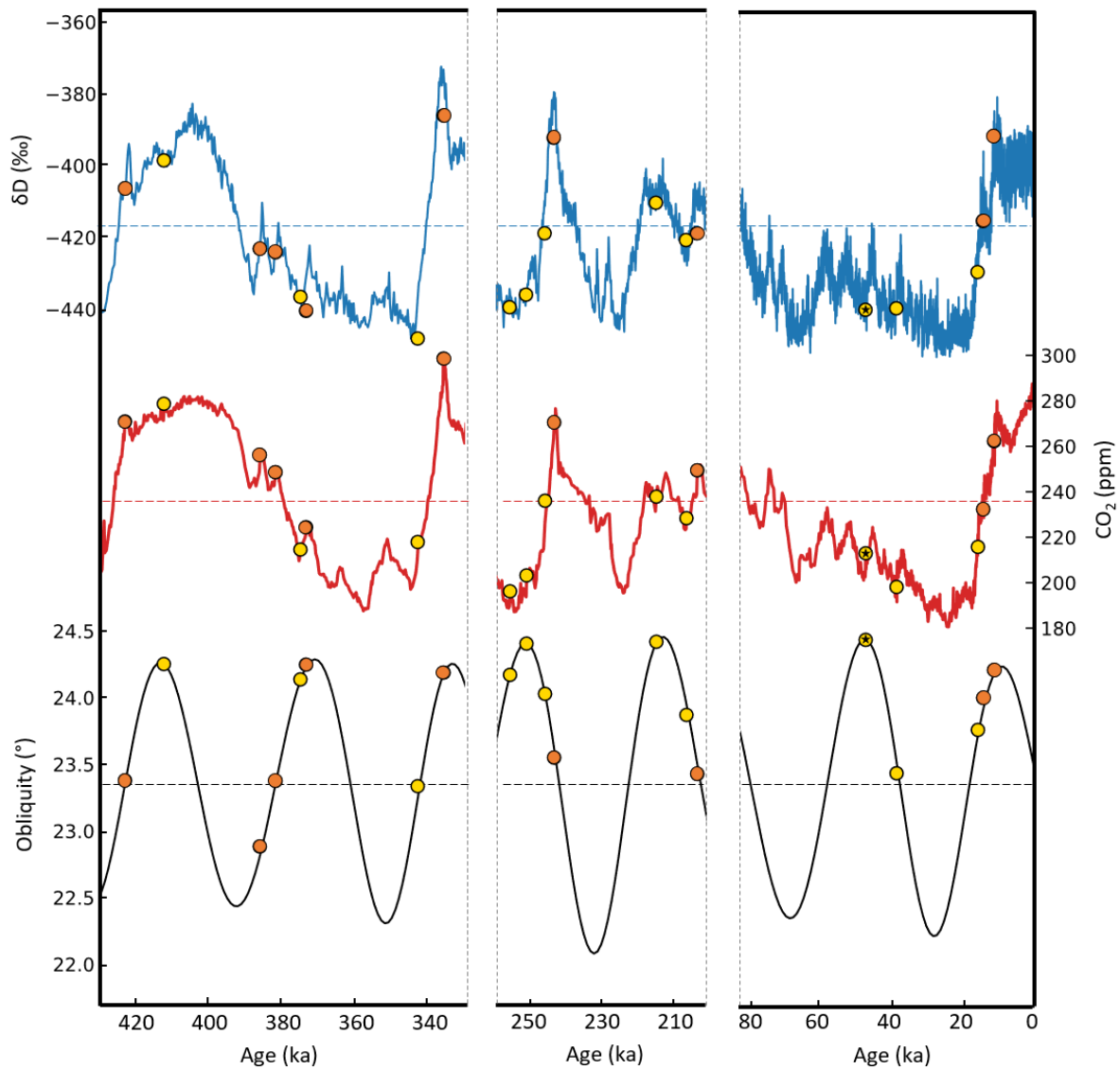
119 Here we investigate the potential role of the long-term forcing, e.g. the global ice volume and the
120 orbital forcing, on the occurrence of CDJs. We show that 18 of the 20 CDJs occurred at times above the
121 average obliquity value (23.33°) of the 12 obliquity cycles of the last 500 ka (Fig. 2; Supplementary Fig.
122 5). We note that all seven obliquity maxima between 416 and 9 ka covered by high-resolution data
123 that allows the identification of abrupt changes are associated with CDJ occurrences. Reversely, only
124 one out of the five obliquity minima are linked to a CDJ (Fig. 2). We investigate the hypothesis of a
125 coincidental origin of this specific pattern of CDJs relative to obliquity changes performing a statistical
126 chi-square test (see Methods). According to our analysis, the null hypothesis that centennial-scale
127 release of CO₂ is independent of the obliquity state can be rejected with 95% confidence ($p < 0.05$). Vice
128 versa, the occurrence of CDJs appears decoupled from the changes in precession, eccentricity, and
129 global ice volume (Supplementary Fig. 5; Supplementary Table 1). Note that our results are
130 independent from the ice-core gas chronology used to display the CO₂ record²¹⁻²⁴ and the choice in the
131 orbital parameter datasets^{25,26} (Supplementary Materials, Supplementary Fig. 7).

132 Obliquity plays a major role in triggering deglaciations²⁷ and its imprint is recorded in both terrestrial
133 and marine records during the late Pleistocene²⁸. Recently, it was suggested that a low obliquity phase
134 could induce a meridional temperature gradient that provokes CO₂ outgassing from the Southern
135 Ocean at multi-millennial scales²⁹. In parallel, our results suggest that these low-obliquity periods are
136 not associated with major abrupt atmospheric CO₂ changes at centennial-scale (Fig. 2). These
137 observations question the mechanisms put forward to explain the multi-millennial scale CO₂
138 outgassing²⁹ to also cause the CDJ carbon cycle muting at centennial-scale under similar low-obliquity
139 phasing.

140

141

142



143

144 **Fig. 2: Climatic and obliquity states for centennial-scale releases of atmospheric CO_2 during the three periods**
 145 **associated with high-resolution ice-core CO_2 records.** Top to bottom: EDC Deuterium record (δD)⁶⁶ on the
 146 AICC2012 timescale (blue line). Atmospheric CO_2 high-resolution records on the AICC2012 time scale^{21,22} for the
 147 500-67 ka interval, on the WD2014^{67,68} time scale for the 67-12 ka interval, and on several original timescales for
 148 the 12-0 ka interval (this study; refs. ^{3,4,49,51,52}; red line). Obliquity²⁶ (black). Horizontal dashed lines indicate the
 149 average value for each considered proxy record over the last 500 ka. Yellow and orange dots indicate the value
 150 of the record during the occurrence of CDJ- and CDJ+, respectively¹⁻⁴. The CDJ- identified during HS5 (~49ka) and
 151 simulated with LOVECLIM is identified with black stars.

152

153

154

155

156

157 **Modelling assessment of centennial-scale CO₂ sources**

158 We investigate the impact of obliquity changes on centennial-scale carbon cycle increases occurring
159 during a HS, i.e. CDJ-, and the potential associated mechanisms. To do so, we perform a suite of
160 sensitivity experiments to mimic the carbon cycle response to a HS under both high and low obliquity
161 boundary conditions with the Earth System Model LOVECLIM³⁰. We find that HS5 is the most
162 appropriate HS to use as a case study since the corresponding CDJ occurs during a period characterised
163 by the highest obliquity value (24.3°).

164 We perform four simulations under 49 ka boundary conditions, i.e., with realistic orbital parameters,
165 including an obliquity of 24.3°, as well as an estimate of northern hemispheric ice-sheet extent,
166 topography and associated albedo²⁶ (Methods, Supplementary Table 2). We also perform four
167 simulations under the same boundary conditions except for obliquity, where peak 24.3° was replaced
168 with an artificially low obliquity of 22.1°, i.e. the lowest value of the last 500 ka (Supplementary Table
169 2). In all experiments, an idealized Heinrich Event is simulated by adding a 0.3 Sverdrups (Sv)
170 freshwater in the North Atlantic during 1000 years, to induce an Atlantic Meridional Overturning
171 Circulation (AMOC) shutdown.

172 The simulation conducted under 49 ka climatic conditions (*HighObl*) reveals a centennial-scale
173 response of the carbon cycle to the induced freshwater perturbation (Fig. 3a), characterised by a
174 ~9.5ppm increase in atmospheric CO₂ over the first 400 years of the simulation (Fig. 3a, Fig. 3c,
175 Supplementary Table 2). A similar simulation performed under low obliquity (*LowObl*), only leads to a
176 ~3.3 ppm CO₂ increase over the first 400 years following the freshwater perturbation (Fig. 3c,
177 Supplementary Table 2). In both experiments, the CO₂ increase is due to a terrestrial carbon release
178 brought about by climatic changes induced by the AMOC weakening (Fig. 3d, Supplementary Fig. 8a).
179 However, surface air temperature is cooler under low obliquity, particularly in the Northern
180 Hemisphere (-1.4 °C north of 20°N), thus impacting the precipitation patterns (Fig. 4a). The decrease
181 of precipitation and the lower temperature observed over the Northern high-latitude generated by
182 the freshwater input leads to a smaller terrestrial carbon reservoir under low obliquity (-105 Gigatons
183 of carbon, GtC; Fig. 4b) compared to high obliquity. As a result, the global terrestrial carbon release is
184 smaller under low obliquity conditions (Fig. 4c).

185 To investigate the role of terrestrial carbon release, two freshwater experiments are performed in
186 which carbon fluxes between the continental biosphere and the atmosphere are suppressed. Under
187 such conditions, neither the experiment performed under high obliquity (*HighObl_noVeg*) nor the one
188 performed under low obliquity (*LowObl_NoVeg*) produce a centennial-scale CO₂ event (i.e. ~0 ppm CO₂
189 change at year 400, Fig. 3c, Supplementary Fig. 10, Supplementary Table 2). Those results highlight

190 that the obliquity no longer has an influence on the centennial-scale CO₂ variability if the continental
191 biosphere is muted. They point to the continental biosphere as the variable source of carbon at
192 centennial-scale for CDJ- events, which appears strongly controlled by the Earth's obliquity.

193 A stronger upwelling in the Southern Ocean, potentially resulting from enhanced Southern
194 Hemisphere Westerlies (SHW) has been suggested as a process leading to CDJ¹⁴ whereas an AMOC
195 weakening leads to enhanced stratification in the Southern Ocean in LOVECLIM³¹. Thus, the robustness
196 of the modelled responses was tested by conducting two additional simulations with an imposed ~
197 40% increase of the SHW windstress, one under 49 ka conditions (*HighObl_SHW*) and one under low
198 obliquity conditions (*LowObl_SHW*) (Supplementary Table 2). This leads to a stronger CO₂ release
199 during both high and low obliquity conditions. However, the difference in total CO₂ release between
200 high and low obliquity conditions persists and again only exists if the terrestrial biosphere exchanges
201 CO₂ with the atmosphere. These results reinforce the idea that the SHW play a key role in centennial-
202 scale carbon cycle increases (Fig. 3a, Supplementary Table 2). However, the fact that larger CO₂
203 changes are simulated when terrestrial vegetation and enhanced SHW (*HighObl_SHW* and
204 *LowObl_SHW*) are considered, strongly suggests that the terrestrial biosphere reservoir is the main
205 source of the higher carbon release during high obliquity conditions for CDJ- events.

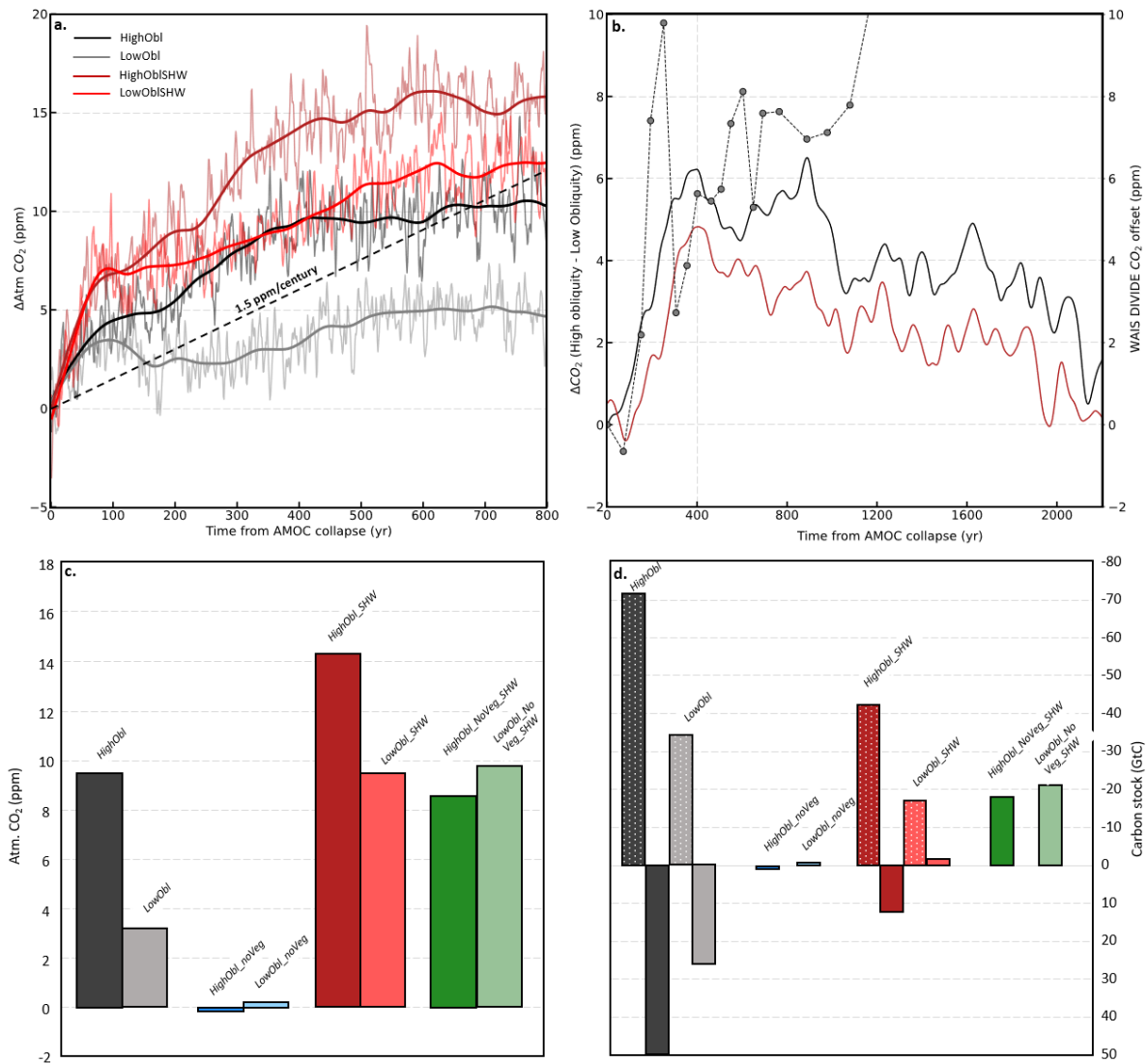
206 Now, we compare the centennial-scale atmospheric CO₂ variations recorded in the WAIS Divide ice
207 core across HS 5 (~49 ka) and those modelled in the LOVECLIM simulations that include terrestrial
208 carbon fluxes. In particular, we look at the CO₂ difference between the high- and low-obliquity
209 simulations (ΔCO_2 , Fig. 3b). ΔCO_2 increases at centennial-scale and reaches a maximum around year
210 400. In terms of magnitude, this ΔCO_2 partially explains the recorded centennial-scale variability in the
211 WAIS Divide CO₂ record (Fig. 3b). This comparison illustrates a similar temporal structure between the
212 measured and simulated CO₂ changes. After year 1000, the WAIS Divide CO₂ changes are decoupled
213 from the variations of the simulated ΔCO_2 , revealing a change in the dynamics of the carbon cycle from
214 centennial-scale to millennial-scale most likely not related to obliquity state (Fig. 3b). While this model-
215 data comparison is limited by the modelling design, it supports our hypothesis that the orbital-scale
216 obliquity changes influence centennial-scale carbon cycle variations through the terrestrial carbon
217 reservoir.

218

219

220

221



222

223 **Fig. 3 Simulated carbon cycle response to an AMOC shutdown.** **a.** Evolution of atmospheric CO₂ for the four
 224 simulations including an interactive terrestrial carbon as a function of time from the AMOC collapse. The dashed
 225 grey line corresponds to a 1.5 ppm/century CO₂ increase, which is also the threshold used to identify CDJ events
 226 in the ice-core CO₂ record. Bold lines are smoothing spline filters. **b.** ΔCO₂ between *HighObl* – *LowObl* (black line)
 227 and *HighObl_SHW* – *LowObl_SHW* (red line). A positive value means that the CO₂ anomaly due to the perturbation
 228 is higher under high-obliquity phase. Grey dots with dashed line correspond to the atmospheric CO₂ record from
 229 the WAIS ice core during HS5, the HS that is simulated in the present study. **c.** Paired coloured bars correspond
 230 to the atmospheric CO₂ offset values 400 years after the freshwater perturbation for simulations using the
 231 obliquity value at 49 ka (left, 24.3°) and a prescribed low-obliquity value (right, 22.1°). Words in *italic* refer to
 232 simulation names. **d.** Same simulation results as in panel c but with carbon stock in GtC. Negative carbon anomaly
 233 represents a carbon release from that reservoir into the atmosphere. Plain coloured bars represent the oceanic
 234 carbon stock and coloured bars with white dots represent the terrestrial carbon stock. Colors refer to the same
 235 simulation as in c. The year 400 snapshot represents the period with the largest atmospheric CO₂ difference
 236 between the high and low obliquity simulations and corresponds to a time period where most of the CO₂
 237 response to the freshwater forcing has occurred.

238

239

240

241 **Drivers of centennial-scale atmospheric CO₂ increases**

242 Previous studies have demonstrated acidification of the Southern Ocean^{14,15,32,33} and of the North
243 Pacific¹³ at the exact timing of CDJ+ 2a.2 and CDJ- 2a.1 during the last deglaciation. This would be
244 consistent with enhanced upwelling of carbon-rich deep waters in the Southern Ocean, brought about
245 by stronger SHW. Consequently, enhanced CO₂ outgassing in the Southern Ocean resulting from
246 stronger or poleward shifted SHW could have also contributed to CDJ+¹⁴. Our modelling results show
247 that variations in SHW can act as a key driver of centennial-scale carbon cycle. However, the SHW
248 changes resulting from an AMOC shutdown could also be modulated by obliquity. Hence, we cannot
249 exclude the hypothesis that the Southern Ocean is an obliquity-dependant source of CO₂ and
250 additional simulations investigating the link between the SHW and obliquity should be performed with
251 alternative models (Supplementary Materials).

252 Our simulations indicate that the continental biosphere provides an additional source of carbon to the
253 atmosphere during CDJ- events, as already inferred by modelling or carbon-isotope approaches^{3,34-36}
254 and reveals the obliquity-dependence of this carbon source at centennial-scale. Especially, the region
255 between 8°N and 40°N appears as the additional source of terrestrial carbon under a high-obliquity
256 phase (Fig. 4c). Previous studies revealed an orbital and millennial time-scale control of obliquity on
257 vegetation changes based on pollen³⁷⁻³⁹ and sediment records^{28,40}, as well as through modelling
258 approaches⁴¹. This obliquity control modulates the carbon stock available to be released during
259 centennial-scale increases through the extent and type of vegetation. In the low-latitude regions, the
260 induced shifts in the Inter Tropical Convergence Zone and changes in latitudinal insolation gradients⁴¹
261 cause an obliquity-pacing vegetation change especially for subtropical biomes and tree coverage^{37,38,40}.
262 In the mid-latitudes regions, obliquity and precession forcing seems to be the main driver of the Asian
263 monsoon system and hence of the induced summer precipitation that controls the vegetation
264 coverage in the area²⁸. At higher latitudes, the predominance of trees and shrubs over grasses and
265 herbs is favoured under high obliquity due to lower local ice extent³⁹. Our study suggests that the
266 expansion of continental biomass in the high latitudes and the change of vegetation at low latitudes in
267 high obliquity phases could thus provide a large amount of carbon to be released during CDJ- (Fig. 3d).
268 In principle, this additional carbon is also available for an enhanced terrestrial carbon release during
269 CDJ+ under high obliquity conditions. However, our model experiments by design only test the
270 terrestrial release during an AMOC shutdown (Henrich event, hence equivalent to CDJ- events) and
271 not for a resumption of the AMOC into interstadial conditions (CDJ+ events). With respect to the
272 opposite latitudinal shift of the ITCZ in both cases, a similar obliquity dependence on the terrestrial
273 biosphere carbon release is possible but not necessary and additional model experiments need to be
274 performed to corroborate the influence of obliquity also for CDJ+ events. To conclude, our study

275 confirms a joined contribution of terrestrial and oceanic carbon release at least during CDJ- events and
276 points toward the terrestrial carbon reservoir as the variable sensitive to obliquity in this centennial-
277 scale response.

278 Under the conditions of the 100 kyr glacial-interglacial cycles during the last 600 ka, a strong imprint
279 of both obliquity³⁷⁻⁴¹ and precession⁴²⁻⁴⁴ was demonstrated for regional variability of vegetation and
280 climate. However, our CDJ compilation reveals no direct correlation between precession and CDJ
281 occurrences over the past 500 ka (Supplementary Fig. 5), and our new simulations confirm the
282 quantitative impact of obliquity on centennial-scale variability of terrestrial carbon fluxes during CDJ-
283 (Fig. 4). Future simulations investigating the precession influence on centennial-scale CO₂ release
284 would be useful to investigate the potential role of precession changes in driving CDJs.

285 Our results reinforce the importance of producing carbon isotope and oceanic pH records during CDJ
286 periods to confirm the processes leading to the atmospheric CO₂ increase during centennial-scale
287 events. In addition, further modelling studies of both CDJ+ and CDJ- events should be conducted to
288 confirm the pervasive character of the identified mechanism. Here we show that past centennial-scale
289 increases of atmospheric CO₂ concentrations were associated with an AMOC disruption during high-
290 obliquity phases. Six of the past CDJs occurred under the same obliquity value than the current one
291 ($\pm 5\%$ of the range of the obliquity value variability of the last 500 ka). While a 15% weakening of the
292 AMOC since the mid-twentieth century has been estimated⁴⁵, large uncertainties remain on the
293 potential occurrence of a large AMOC disruption at multi-centennial-scale in the future^{46,47}. If such
294 AMOC disruption occurs, the current relatively high-obliquity phase is favourable to a strong release
295 of carbon which could be superimposed on the anthropogenic-sourced perturbation.

296

297

298

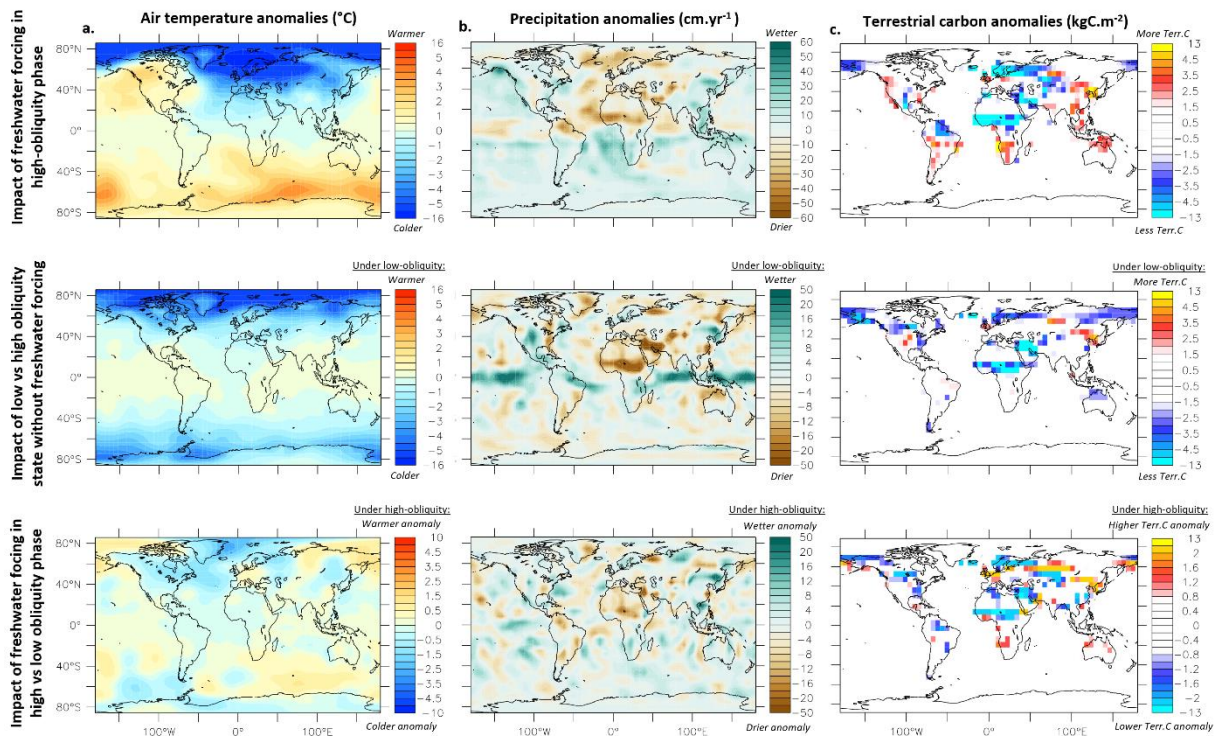
299

300

301

302

303



304

305 **Fig. 4. Impacts of the freshwater forcing and the obliquity state on the climatic conditions and terrestrial**
 306 **carbon stock. a. Air temperature anomalies resulting from (top) a freshwater forcing under a high obliquity phase**
 307 **vs. no freshwater forcing under a high obliquity phase (*HighObl* – *HighOblCTR*), (middle) a low obliquity phase**
 308 **without a freshwater forcing vs. a high obliquity phase without a freshwater forcing (*LowOblCTR* – *HighOblCTR*)**
 309 **and (bottom) the impact of the freshwater forcing in a high vs. low obliquity phase (*HighObl* - *HighOblCTR*) –**
 310 **(*LowObl* - *LowOblCTR*) on air temperatures. b. Same as (a) for precipitation anomalies. c. Same as (a) for the**
 311 **terrestrial carbon anomalies.**

312

313

314

315

316

317

318

319

320

321

322

323 **Acknowledgments**

324 This study is an outcome of the Make Our Planet Great Again HOTCLIM project, it received the financial
325 support from the French National Research Agency under the “Programme d’Investissements
326 d’Avenir” (ANR-19-MPGA-0001). This publication was also generated in the frame of the Beyond EPICA
327 Oldest Ice Core (BE-OI) project. The BE-OI project has received funding from the European Union’s
328 Horizon 2020 research and innovation programme under grant agreement no. 815384 (Oldest Ice
329 Core). It is supported by national partners and funding agencies in Belgium, Denmark, France,
330 Germany, Italy, Norway, Sweden (through the Crafoord Foundation), and Switzerland, The
331 Netherlands and the United Kingdom. Logistic support is mainly provided by ENEA and IPEV through
332 the Concordia Station system. The opinions expressed and arguments employed herein do not
333 necessarily reflect the official views of the European Union funding agency or other national funding
334 bodies. This is Beyond EPICA publication number XX. LM acknowledges funding from the Australian
335 Research Council (ARC) grants FT180100606 and SR200100008. The research leading to these results
336 has received funding from the French National Research Agency (ANR HUM117 and ANR NEANDROOT),
337 and the European Research Council under the European Union Horizon 2020 Programme (ERC ICORDA,
338 grant number 817493). TFS and HF gratefully acknowledge funding by the Swiss National Science
339 Foundation (grants 200020_200492 and 200020_200328, respectively).

340 **Data availability**

341 The data used in this study and the model outputs are available to download at – *a link to the PANGEA*
342 *repository will be available before publication* -

343

344 **Material and methods**

345 **Atmospheric CO₂ measurements on the EDC ice core**

346 Atmospheric CO₂ measurements on the EDC ice core have been performed at Institut des Geosciences
347 de l’Environnement (IGE) using the ball mill dry extraction system coupled with a gas chromatography
348 analyser^{5,16}. A total of 203 new depth levels have been measured between 2043.8 and 2360.6 m
349 corresponding to the time period from 259.4 to 190.4 ka on the AICC2012 gas timescale²¹ (Fig. 1). Each
350 data point corresponds to air extracted from a single ice sample of 40 g and the resulting CO₂ amount
351 fraction is the average of five successive injections made at different pressure levels in the gas
352 chromatograph. The average standard deviation of the five injections is 0.9 ppm. 30 injections of a
353 standard gas (synthetic air from Air Liquide) containing 229.5 ± 0.3 ppm of CO₂ in dry air, which was
354 referenced to two primary standards (241.24 ± 0.015 ppm from NOAA, JB03097, and 260.26 ± 0.2 ppm

355 from CSIRO, CSIRO1677), are used to calibrate the gas chromatograph. First, we correct our data for
356 the crushing process CO₂ contamination that is estimated to be on average of 2.6 ±0.9 ppm (1σ
357 standard deviation), ranging from 1.0 to 5.4 ppm. This correction is necessary as some CO₂ is released
358 from the CO₂ extraction chamber during the crushing process, which is contaminating our extracted
359 air from the ice sample. Blank tests are conducted by measuring the CO₂ concentration of a standard
360 gas of known amount fraction and crushing artificial gas-free ice. The difference between the
361 measured and expected CO₂ amount fraction is attributed to the crushing process itself. The additional
362 CO₂ amount fraction is then converted into CO₂ levels to normalize the correction to the volume of
363 injected gas. Blank measurements were performed for every ten measured samples for each of the
364 four extraction cells. Following the procedure of ref.¹⁶, the new CO₂ data are then corrected for
365 gravitational fractionation occurring in the firn. For that we use a record of the isotopic composition
366 of nitrogen in the trapped air covering our studied time interval ($\delta^{15}\text{N}$ of N₂)⁴⁸ (not shown here). The
367 average correction is -1.4 ±0.3 ppm (1σ standard deviation), ranging from -0.9 to -2.1 ppm. The average
368 overall propagated uncertainty of the CO₂ amount fractions is 1.3 ppm. This uncertainty includes the
369 uncertainty related to the five injections (one standard deviation), the uncertainty of the measurement
370 system as determined by standard gas over blank ice measurements (one standard deviation), and the
371 uncertainty associated with and the correction for gravitational settling based on $\delta^{15}\text{N}$ corrections

372 Over the 260-190 ka time interval, the existing composite CO₂ record⁴⁹ includes data measured on the
373 Vostok ice core, associated with a temporal resolution of ~ 0.85 ka⁵ (Supplementary Fig. 1). The
374 comparison between our new EDC and the Vostok CO₂ records reveals an offset already observed in
375 ref. ¹⁶ which have been measured using an earlier version of the Ball Mill extraction system. Especially,
376 the Vostok CO₂ concentrations are slightly higher by 5.5 ppm on average. This offset can be explained
377 by the fact that the Vostok CO₂ measurements were not corrected for the gravitational fractionation
378 and no blank correction was applied⁵. When we apply these two corrections on the Vostok CO₂ record,
379 the observed offset is reduced to ~1.5 ppm which is within the uncertainty boundaries of 3 ppm⁵
380 (Supplementary Fig. 1).

381 **High resolution CO₂ data compilation**

382 In addition to this study, four multi-centennial-scale resolved atmospheric CO₂ datasets have been
383 published since the atmospheric CO₂ composite record from ref. ⁴⁹ was compiled.
384 If we add the duration of all periods with a resolution better than 0.5 ka, we obtain a cumulative
385 duration of 275 ka (vertical red areas, Fig. 1) covering 429 to 329 ka⁴, 258 to 200 ka (this study), 188 to
386 153 ka¹⁶, and 84 to 0 ka^{3,50-54}. In the case of ref. ¹⁶, the probable experimental-induced noise and
387 fractionation effects during the bubble enclosure process in the ice core⁵⁵ do not allow to distinguish

388 natural centennial-scale variability from measurement-induced noise. The point to point variability
389 registered during some periods of the record (186-183 ka; 170-168 ka) confirms that any interpretation
390 of centennial-scale variability during this period needs to take carefully this higher variability into
391 account. For these reasons, we do not investigate the potential presence of CDJs in the high-resolution
392 CO₂ record from ref. ¹⁶. As a result, the periods associated with both high resolution and low
393 measurement-induced variability correspond to a cumulative time interval of 239 ka over the last 500
394 ka. We consider that apart from the 429-329 ka, 258-200 ka and the 84-0 ka periods (Fig. 2), potential
395 CDJs occurrences are not identifiable due to insufficient temporal resolution and larger uncertainty
396 associated with the Vostok data. In addition, ice older than 500 ka is affected by strong thinning and
397 higher resolution CO₂ measurements should be performed in the future, in particular taking advantage
398 of new semi-continuous analytical techniques⁵⁶. Data presented in Fig. 1 are plotted as published and
399 no corrections have been applied. However, this does not affect the results of our study as we focus
400 our analysis on the relative and not absolute variations of CO₂ amount fractions. These periods
401 associated with sub-millennial-scale CO₂ resolution allow to identify centennial scale abrupt variability
402 of atmospheric CO₂ when associated with low measurement-induced noise (Fig. 2).

403 **Atmospheric CH₄ measurements on the EDC ice core**

404 CDJ+ have been linked to atmospheric CH₄ releases of more than 50 ppb⁴ in the ice core record.
405 However, their identification requires multi-centennial scale resolution of the CH₄ record. Three of the
406 new CDJs identified in this study show a potential CH₄ variability but the associated resolution (> 0.5
407 ka) was not good enough to validate the occurrence of a synchronous CH₄ increase. The existing CH₄
408 EDC record for Marine Isotopic Stage (MIS) 8a – 6e is based on measurements performed on the IGE
409 and the University of Bern experimental setups⁵⁷. We perform 18 new measurements on the time
410 interval of the CDJs 7a, 7b and 8.2, in order to detect a potential CH₄ rise associated with these events.
411 These CH₄ measurements on the EDC ice core were performed at IGE using a melt-refreezing extraction
412 method coupled with a gas chromatography analyser. The method used for the analysis of these
413 samples is identical to that described in ref. ⁵⁷. Each sample represents ~40 g of ice from which the air
414 is extracted with a melt-refreezing method. The air is then analysed with a gas chromatograph. 15
415 injections of a single standard gas (synthetic air from Air Liquide) containing 498.1 ± 2.7 ppb of CH₄ in
416 dry air, which was referenced to one primary standard 393.9 ± 2.6 ppb from CSIRO, CSIRO1657), are
417 used to calibrate the gas chromatograph. The average CH₄ analytical uncertainty is 5 ppb (1 sigma). We
418 do not correct the concentration for gravitational enrichment to avoid an offset with the previously
419 published record from ref.⁴³. Corrections would be ~3 ppb on average, less than 1% of the CH₄
420 concentrations signal⁵⁷. A total of 18 new depth levels have been measured focusing on the depth

421 interval where centennial-scale atmospheric CO₂ releases have been identified. All samples are
422 corrected for blank contributions using gas-free ice. All CH₄ data are shown in Supplementary Fig. 1.

423 **Identification of the centennial-scale CO₂ events**

424 In order to identify the presence of CDJs in our new CO₂ record between 260 and 190 ka, we follow
425 the method developed by ref. ⁴. We can summarize this methodology as follows: first, we remove the
426 orbital- and millennial-scale trend in the CO₂ record using smoothing splines with a cut-off frequency
427 ranging from 6 to 14 ka to evaluate the best detrending method. The aim is to find a good compromise
428 between removing multi-millennial- to orbital-scale trends while preserving the centennial scale
429 variability (Supplementary Fig. 2). Then, a second series of splines ranging from 0.4 to 1.2 ka is applied
430 on the detrended CO₂ record in order to obtain equidistant records aiming at smoothing out
431 measurement uncertainty while still preserving the centennial scale variability. Third, the rate of
432 change of the final residual CO₂ record is computed (Supplementary Figs. 2,3). To identify a CDJ, we
433 apply the threshold of 1.5 ppm/century as in ref. ⁴.

434 Outside the 260-190 ka interval, we compile the CDJs already identified in previous studies^{1,3,4}. Thus,
435 this CDJ compilation covering the last 500 ka includes CDJ events identified with different methods.
436 The approach from ref. ¹ is based on the analysis of the raw curve of CO₂ concentrations without any
437 corrections to remove the orbital- or the millennial-scale trends. Such approach is appropriate to
438 identify the centennial-scale atmospheric CO₂ changes of the last termination as the record is very
439 highly resolved (<0.1 ka). In addition, the centennial-scale variability is of such magnitude (~12 ppm)
440 that it excludes any error of identification. Recently, ref. ³ developed a new approach for the
441 identification of the centennial-scale atmospheric CO₂ variability, using the δD record measured on the
442 ice. Based on the assumption that this local surface temperature proxy does not include centennial-
443 scale climate variability during the intervals of interest¹, they use the δD as a filter for identifying
444 centennial-scale CO₂ release. The first step is to estimate a constant dephasing of CO₂ versus δD in
445 order to align the two records. Then, by subtracting a normalised δD curve to the CO₂ record, they
446 obtain a residual CO₂ signal. This method is well adapted to identify centennial-scale CO₂ release during
447 the last glacial period, where millennial-scale variability is the dominant climatic pattern. However,
448 many studies have pointed out the fact that the dephasing between Antarctic water isotopes and CO₂
449 is not constant during deglaciations⁵⁸⁻⁶⁰. In addition, a decoupling of δD and CO₂ variations is also
450 registered at the end of the interglacials²⁹. The coupling between δD and CO₂ during the 260-190 ka
451 interval, which is mainly composed of a deglaciation and an interglacial period, is thus not trivial.
452 Hence, for this time interval dominated by the high amplitude orbital variability, we consider that the

453 method of ref. ⁴ based on smoothing spline is the most adapted for the identification of the centennial-
454 scale atmospheric CO₂ releases.

455 We apply the ref. ⁴ methodology to the most recent period (84-0 ka) where the methodology of ref. ³
456 was originally used to identify potential CDJs. Four of the five CDJs are also identified with the ref. ⁴-
457 method (not shown here) and no additional CDJs are revealed. As previously discussed, the
458 methodology from ref. ³ seems more appropriate for glacial periods where millennial-scale variability
459 appears to be the dominant climatic pattern. We propose to keep the method used by ref. ³ as a
460 reference for the 84-0 ka period. The diversity of methodologies used for the identification of
461 centennial-scale CO₂ release underlines that the main result of the study, i.e. the influence of the
462 obliquity on the occurrence of such events, is not dependent on the choice of the CDJ detection
463 method.

464 Centennial-scale variability in a recent atmospheric CO₂ record measured on the Taylor glacier ice has
465 been observed during the Marine Isotope Stage 5-4 transition⁶¹. However, the short time interval
466 covered by the high-resolution CO₂ record (~13 ka) and the absence of water isotopes measurements
467 in the Taylor glacier prevent to apply the CDJ methodology identification from ref. ⁴ or from ref. ³. Since
468 the centennial-scale part of the identified atmospheric CO₂ increase of ~7 ppm cannot be decoupled
469 from the potential millennial-scale variability observed in water isotopes from the EDC ice core during
470 the same period, we do not include this potential abrupt event in our compilation.

471 **Chi-square test**

472 We apply a statistical method to investigate the potential role of the Earth's obliquity in the centennial-
473 scale atmospheric CO₂ variability. The Chi-square method allows to test the null hypothesis that a
474 distribution of a parameter (centennial-scale variability occurrences) versus another (obliquity value)
475 is independent. For that, we separate the centennial-scale events in two categories dependent on
476 whether they occur in the context of an obliquity value above or under the average obliquity of the 12
477 obliquity cycles of last 500 ka (corresponding to the mean obliquity value of the 494.5-9.5 ka period,
478 i.e. 23.33°).

479 For that, we compute:

$$480 \quad X = \frac{(\textit{observed} - \textit{expected})^2}{\textit{expected}}$$

481 With *observed* the number of centennial-scale events occurring above the average obliquity value of
482 the 12 obliquity cycles of the last 500 ka, here 18, and *expected* the theoretical value expected under
483 the null hypothesis. The theoretical value would be 10 (i.e. half of the total number of detected CDJs)

484 if the studied period would contain as high obliquity than low obliquity period. However, only 44.6 %
485 of the studied period is above the average obliquity value taken as reference (23.33). The theoretical
486 value is thus 8.96. We found:

$$487 \quad X = 5.37$$

488 This value is higher than $\alpha_{0.05}$, the risk at 5% to accept the null hypothesis even if it is wrong, which is
489 3.84 for a degree of freedom of 1.

490 We can thus reject the null hypothesis that the distribution of centennial-scale CO₂ events is
491 independent of the obliquity state with a confidence level of 95%. In order to test the sensitivity of the
492 chosen threshold (here the average obliquity value of the 12 obliquity cycles of the last 500 ka), we
493 performed a chi-square test for the interval of obliquity values (22.7 -23.9°) systematically reached
494 during each obliquity cycle over the last 500 ka (Supplementary Fig. 11). Our analysis reinforces the
495 observation of missing CDJ during low-obliquity periods.

496 We also apply the Chi-square test for the Earth's precession and eccentricity parameters using the
497 mean values of the last 500 ka (Supplementary Table 1). The null hypothesis of an independence of
498 centennial-scale CO₂ events from precession and eccentricity context could not be rejected at a
499 confidence level of 95%.

500 **Experimental design of carbon cycle modelling**

501 To understand the processes that could lead to a different response of the carbon cycle during an
502 AMOC shutdown as a function of obliquity, numerical experiments are performed with the Earth
503 system model LOVECLIM²⁵. LOVECLIM includes a free surface primitive equation ocean model with a
504 horizontal resolution of 3°x3° and 20 unevenly spaced vertical levels, a dynamic/thermodynamic sea-
505 ice model, a quasi-geostrophic T21 atmospheric model, a dynamic global vegetation model (DGVM)
506 and a marine carbon cycle model. The DGVM used, VECODE (Vegetation Continuous Description
507 model), simulates the vegetation structure, and associated terrestrial carbon reservoirs³⁰.

508 The initial 49ka state was derived from a transient experiment that started at 140 ka. The penultimate
509 deglaciation (140-120ka) followed the PMIP4 protocol⁶², with the model being forced by changes in
510 orbital parameters⁶³, atmospheric greenhouse gases⁶⁴ and changes in continental ice-sheets⁶². That
511 simulation was continued between 120 and 49 ka forced with estimates of changes in continental ice-
512 sheets from an offline simulation⁶⁵. The Bering strait was gradually closed at 70 ka, and kept closed
513 until the early Holocene.

514 From that initial state at 49 ka, the model was run for 3000 years with prognostic atmospheric CO₂
515 concentration and under constant 49 ka boundary conditions (HighOblCTR). This experiment was run
516 for another 1000 years to serve as control run for the 49 ka experiments.

517 From the initial transient state, another experiment was run under 49 ka boundary conditions but with
518 an obliquity of 22.1°. This experiment was first run for 4000 years with a constant atmospheric CO₂
519 concentration of 204 ppm, after which the CO₂ was prognostic for 2000 years (LowOblCTR).

520 From these control runs (HighOblCTR and LowOblCTR), two meltwater experiments were
521 performed (HighObl and LowObl) by adding 0.3 Sv of meltwater into the North Atlantic (60-10°W, 50-
522 60°N) for 1000 years thus leading to an AMOC shutdown in ~300 years. The meltwater flux was then
523 stopped for 800 years, after which a negative meltwater flux was added to the North Atlantic (-0.1 Sv)
524 for 400 years so that the AMOC would recover.

525 Two experiments with similar forcing to HighObl and LowObl but with a 37 to 40% increase of the
526 westerly wind stress over the Southern Ocean from year 0 to 1800 (HighObl_SHW and LowObl_SHW)
527 were also performed.

528 Finally, two experiments similar to HighObl and LowObl, and two experiments similar to HighObl_SHW
529 and LowObl_SHW were performed, in which the terrestrial carbon fluxes did not impact atmospheric
530 CO₂ (HighObl_NoVeg, LowObl_NoVeg, HighObl_NoVeg_SHW and LowObl_NoVeg_SHW). Note that for
531 these experiments, the model was first run for 2000 years without any meltwater so that the
532 atmospheric CO₂ concentration would equilibrate.

533

534

535

536

537

538

539

540

541

542

- 544 1. Marcott, S. A. *et al.* Centennial-scale changes in the global carbon cycle during the last
545 deglaciation. *Nature* **514**, 616–619 (2014).
- 546 2. Ahn, J., Brook, E. J., Schmittner, A. & Kreutz, K. Abrupt change in atmospheric CO₂ during the last
547 ice age. *Geophys. Res. Lett.* **39**, (2012).
- 548 3. Bauska, T. K., Marcott, S. A. & Brook, E. J. Abrupt changes in the global carbon cycle during the
549 last glacial period. *Nat. Geosci.* **14**, 91–96 (2021).
- 550 4. Nehrbass-Ahles, C. *et al.* Abrupt CO₂ release to the atmosphere under glacial and early
551 interglacial climate conditions. *Science* **369**, 1000–1005 (2020).
- 552 5. Petit, J. R. *et al.* Climate and atmospheric history of the past 420,000 years from the Vostok ice
553 core, Antarctica. **399**, 10 (1999).
- 554 6. Lüthi, D. *et al.* High-resolution carbon dioxide concentration record 650,000–800,000 years
555 before present. *Nature* **453**, 379–382 (2008).
- 556 7. Capron, E. *et al.* The anatomy of past abrupt warmings recorded in Greenland ice. *Nat Commun*
557 **12**, 2106 (2021).
- 558 8. North Greenland Ice Core Project members. High-resolution record of Northern Hemisphere
559 climate extending into the last interglacial period. *Nature* **431**, 147–151 (2004).
- 560 9. Ruddiman, W. F. Late Quaternary deposition of ice-rafted sand in the subpolar North Atlantic (lat
561 40° to 65°N). *Geol Soc America Bull* **88**, 1813 (1977).
- 562 10. Rhodes, R. H. *et al.* Enhanced tropical methane production in response to iceberg discharge in
563 the North Atlantic. *Science* **348**, 1016–1019 (2015).
- 564 11. Huber, C. *et al.* Isotope calibrated Greenland temperature record over Marine Isotope Stage 3
565 and its relation to CH₄. *Earth and Planetary Science Letters* **243**, 504–519 (2006).
- 566 12. Bauska, T. K. *et al.* Carbon isotopes characterize rapid changes in atmospheric carbon dioxide
567 during the last deglaciation. *Proc. Natl. Acad. Sci. U.S.A.* **113**, 3465–3470 (2016).
- 568 13. Gray, W. R. *et al.* Deglacial upwelling, productivity and CO₂ outgassing in the North Pacific
569 Ocean. *Nature Geosci* **11**, 340–344 (2018).
- 570 14. Rae, J. W. B. *et al.* CO₂ storage and release in the deep Southern Ocean on millennial to
571 centennial timescales. *Nature* **562**, 569–573 (2018).
- 572 15. Ronge, T. A. *et al.* Southern Ocean contribution to both steps in deglacial atmospheric CO₂ rise.
573 *Sci Rep* **11**, 22117 (2021).
- 574 16. Shin, J. *et al.* Millennial-scale atmospheric CO₂ variations during the
575 Marine Isotope Stage 6 period (190–135 ka). *Clim. Past* **16**, 2203–2219 (2020).
- 576 17. Enting, I. G. On the use of smoothing splines to filter CO₂ data. *J. Geophys. Res.* **92**, 10977 (1987).
- 577 18. Past Interglacials Working Group of PAGES. Interglacials of the last 800,000 years. *Rev. Geophys.*
578 **54**, 162–219 (2016).
- 579 19. Berends, C. J., de Boer, B. & van de Wal, R. S. W. Reconstructing the evolution of ice sheets, sea
580 level, and atmospheric CO₂ during the past 3.6 million years. *Clim. Past*
581 **17**, 361–377 (2021).
- 582 20. Bauska, T. K. *et al.* Controls on Millennial-Scale Atmospheric CO₂ Variability During the Last
583 Glacial Period. *Geophys. Res. Lett.* **45**, 7731–7740 (2018).
- 584 21. Bazin, L. *et al.* An optimized multi-proxy, multi-site Antarctic ice and gas orbital chronology
585 (AICC2012): 120–800 ka. *Clim. Past* **9**, 1715–1731 (2013).

- 586 22. Veres, D. *et al.* The Antarctic ice core chronology (AICC2012): an optimized multi-parameter and
587 multi-site dating approach for the last 120 thousand years. *Clim. Past* **9**, 1733–1748 (2013).
- 588 23. Barker, S. *et al.* 800,000 Years of Abrupt Climate Variability. *Science* **334**, 347–351 (2011).
- 589 24. Extier, T. *et al.* On the use of $\delta^{18}\text{O}_{\text{atm}}$ for ice core dating. *Quaternary Science Reviews* **185**, 244–
590 257 (2018).
- 591 25. Berger, A. & Loutre, M. F. Insolation values for the climate of the last 10 million years.
592 *Quaternary Science Reviews* **10**, 297–317 (1991).
- 593 26. Laskar, J. *et al.* A long-term numerical solution for the insolation quantities of the Earth. *A&A*
594 **428**, 261–285 (2004).
- 595 27. Parrenin, F. & Paillard, D. Terminations VI and VIII (~ 530 and ~ 720 kyr BP) tell us the
596 importance of obliquity and precession in the triggering of deglaciations. *Clim. Past* **8**, 2031–2037
597 (2012).
- 598 28. Li, T. *et al.* Continued obliquity pacing of East Asian summer precipitation after the mid-
599 Pleistocene transition. *Earth and Planetary Science Letters* **457**, 181–190 (2017).
- 600 29. Ai, X. E. *et al.* Southern Ocean upwelling, Earth’s obliquity, and glacial-interglacial atmospheric
601 CO_2 change. *Science* **370**, 1348–1352 (2020).
- 602 30. Goosse, H. *et al.* Description of the Earth system model of intermediate complexity LOVECLIM
603 version 1.2. *Geosci. Model Dev.* **3**, 603–633 (2010).
- 604 31. Menviel, L., England, M. H., Meissner, K. J., Mouchet, A. & Yu, J. Atlantic-Pacific seesaw and its
605 role in outgassing CO_2 during Heinrich events: Heinrich CO_2 . *Paleoceanography* **29**, 58–70
606 (2014).
- 607 32. Li, T. *et al.* Rapid shifts in circulation and biogeochemistry of the Southern Ocean during deglacial
608 carbon cycle events. *Sci. Adv.* **6**, eabb3807 (2020).
- 609 33. Anderson, R. F. *et al.* Wind-Driven Upwelling in the Southern Ocean and the Deglacial Rise in
610 Atmospheric CO_2 . *Science* **323**, 1443–1448 (2009).
- 611 34. Schmitt, J. *et al.* Carbon Isotope Constraints on the Deglacial CO_2 Rise from Ice Cores. *Science*
612 **336**, 711–714 (2012).
- 613 35. Jeltsch-Thömmes, A. & Joos, F. Modeling the evolution of pulse-like perturbations in atmospheric
614 carbon and carbon isotopes: the role of weathering–sedimentation imbalances. *Clim. Past* **16**,
615 423–451 (2020).
- 616 36. Bozbiyik, A., Steinacher, M., Joos, F., Stocker, T. F. & Menviel, L. Fingerprints of changes in the
617 terrestrial carbon cycle in response to large reorganizations in ocean circulation. *Clim. Past* **7**,
618 319–338 (2011).
- 619 37. Bogotá-A, R. G. *et al.* Rapid climate change from north Andean Lake Fúquene pollen records
620 driven by obliquity: implications for a basin-wide biostratigraphic zonation for the last 284 ka.
621 *Quaternary Science Reviews* **30**, 3321–3337 (2011).
- 622 38. Dupont, L. Orbital scale vegetation change in Africa. *Quaternary Science Reviews* **30**, 3589–3602
623 (2011).
- 624 39. Zech, W. *et al.* Obliquity forcing of Quaternary glaciation and environmental changes in NE
625 Siberia. *Quaternary International* **234**, 133–145 (2011).
- 626 40. Ferreira, J. Q. *et al.* Changes in obliquity drive tree cover shifts in eastern tropical South America.
627 *Quaternary Science Reviews* **279**, 107402 (2022).
- 628 41. Bosmans, J. H. C., Hilgen, F. J., Tuenter, E. & Lourens, L. J. Obliquity forcing of low-latitude
629 climate. *Clim. Past* **11**, 1335–1346 (2015).

- 630 42. Joannin, S., Bassinot, F., Nebout, N. C., Peyron, O. & Beaudouin, C. Vegetation response to
631 obliquity and precession forcing during the Mid-Pleistocene Transition in Western
632 Mediterranean region (ODP site 976). *Quaternary Science Reviews* **30**, 280–297 (2011).
- 633 43. Denison, S. M., Maslin, M. A., Boot, C., Pancost, R. D. & Ettwein, V. J. Precession-forced changes
634 in South West African vegetation during Marine Isotope Stages 101–100 (~2.56–2.51 Ma).
635 *Palaeogeography, Palaeoclimatology, Palaeoecology* **220**, 375–386 (2005).
- 636 44. Claussen, M., Fohlmeister, J., Ganopolski, A. & Brovkin, V. Vegetation dynamics amplifies
637 precessional forcing. *Geophys. Res. Lett.* **33**, L09709 (2006).
- 638 45. Caesar, L., Rahmstorf, S., Robinson, A., Feulner, G. & Saba, V. Observed fingerprint of a
639 weakening Atlantic Ocean overturning circulation. *Nature* **556**, 191–196 (2018).
- 640 46. Lenton, T. M. *et al.* Climate tipping points — too risky to bet against. *Nature* **575**, 592–595
641 (2019).
- 642 47. He, F. & Clark, P. U. Freshwater forcing of the Atlantic Meridional Overturning Circulation
643 revisited. *Nat. Clim. Chang.* **12**, 449–454 (2022).
- 644 48. Bréant, C. *et al.* Unveiling the anatomy of Termination 3 using water and air isotopes in the
645 Dome C ice core, East Antarctica. *Quaternary Science Reviews* **211**, 156–165 (2019).
- 646 49. Bereiter, B. *et al.* Revision of the EPICA Dome C CO₂ record from 800 to 600 kyr before present:
647 Analytical bias in the EDC CO₂ record. *Geophys. Res. Lett.* **42**, 542–549 (2015).
- 648 50. Rubino, M. *et al.* Revised records of atmospheric trace gases CO₂, CH₄, N₂O, and
649 $\delta^{13}C-CO_2$ over the last 2000
650 years from Law Dome, Antarctica. *Earth Syst. Sci. Data* **11**, 473–492 (2019).
- 651 51. Bauska, T. K. *et al.* Links between atmospheric carbon dioxide, the land carbon reservoir and
652 climate over the past millennium. *Nature Geosci* **8**, 383–387 (2015).
- 653 52. Shin, J. *et al.* Millennial variations in atmospheric CO₂ during the early Holocene (11.7–7.4 ka).
654 *Clim. Past* **18**, 2063–2075 (2022).
- 655 53. Ahn, J. & Brook, E. J. Siple Dome ice reveals two modes of millennial CO₂ change during the last
656 ice age. *Nat Commun* **5**, 3723 (2014).
- 657 54. Bereiter, B. *et al.* Mode change of millennial CO₂ variability during the last glacial cycle
658 associated with a bipolar marine carbon seesaw. *Proc. Natl. Acad. Sci. U.S.A.* **109**, 9755–9760
659 (2012).
- 660 55. Lüthi, D. *et al.* CO₂ and O₂/N₂ variations in and just below the bubble-clathrate transformation
661 zone of Antarctic ice cores. *Earth and Planetary Science Letters* **297**, 226–233 (2010).
- 662 56. Mächler, L. *et al.* Laser-induced sublimation extraction for centimeter-resolution multi-species
663 greenhouse gas analysis on ice cores. *Atmos. Meas. Tech.* **16**, 355–372 (2023).
- 664 57. Louergue, L. *et al.* Orbital and millennial-scale features of atmospheric CH₄ over the past
665 800,000 years. *Nature* **453**, 383–386 (2008).
- 666 58. Parrenin, F. *et al.* Synchronous Change of Atmospheric CO₂ and Antarctic Temperature During
667 the Last Deglacial Warming. *Science* **339**, 1060–1063 (2013).
- 668 59. Chowdhry Beeman, J. *et al.* Antarctic temperature and CO₂: near-
669 synchrony yet variable phasing during the last deglaciation. *Clim. Past* **15**, 913–926 (2019).
- 670 60. Landais, A. *et al.* Two-phase change in CO₂, Antarctic temperature and global climate during
671 Termination II. *Nature Geosci* **6**, 1062–1065 (2013).
- 672 61. Menking, J. A. Multiple carbon cycle mechanisms associated with the glaciation of Marine
673 Isotope Stage 4. *Nature Communications* (2022).
- 674

- 675 62. Menviel, L. *et al.* The penultimate deglaciation: protocol for Paleoclimate Modelling
676 Intercomparison Project (PMIP) phase 4 transient numerical simulations between 140 and 127
677 ka, version 1.0. *Geosci. Model Dev.* **12**, 3649–3685 (2019).
- 678 63. Berger, A. L. Long-Term Variations of Caloric Insolation Resulting from the Earth’s Orbital
679 Elements. *Quat. res.* **9**, 139–167 (1978).
- 680 64. Köhler, P., Nehrbass-Ahles, C., Schmitt, J., Stocker, T. F. & Fischer, H. A 156 kyr smoothed history
681 of the atmospheric greenhouse gases CO₂, CH₄,
682 and N₂O and their radiative forcing. *Earth Syst. Sci. Data* **9**, 363–387
683 (2017).
- 684 65. Abe-Ouchi, A. *et al.* Insolation-driven 100,000-year glacial cycles and hysteresis of ice-sheet
685 volume. *Nature* **500**, 190–193 (2013).
- 686 66. Jouzel, J. *et al.* Orbital and Millennial Antarctic Climate Variability over the Past 800,000 Years.
687 *Science* **317**, 793–796 (2007).
- 688 67. Buizert, C. *et al.* The WAIS Divide deep ice core WD2014 chronology – Part 1: Methane
689 synchronization (68–31 ka BP) and the gas age–ice age difference. *Clim. Past* **11**, 153–173 (2015).
- 690 68. Sigl, M. *et al.* The WAIS Divide deep ice core WD2014 chronology – Part 2: Annual-layer counting
691 (0–31 ka BP). *Clim. Past* (2016).
- 692
- 693

1 **Supplementary Information to:**

2

3 **High obliquity favours centennial-scale variations in the carbon cycle**

4 Etienne Legrain^{1*}, Emilie Capron¹, Laurie Menviel^{2,3}, Axel Wohleber¹, Frédéric Parrenin¹, Grégory
5 Teste¹, Amaëlle Landais⁴, Marie Bouchet⁴, Roberto Grilli¹, Christoph Nehrbass-Ahles^{5,6}, Lucas Silva⁷,
6 Hubertus Fischer⁷, Thomas F. Stocker⁷

7 *1 Université Grenoble Alpes, CNRS, IRD, Grenoble INP, IGE, Grenoble, France*

8 *2 Climate Change Research Centre, University of New South Wales, Sydney, Australia*

9 *3 The Australian Centre for Excellence in Antarctic Science, University of Tasmania, Hobart, Tasmania*
10 *7001, Australia*

11 *4 Laboratoire des Sciences du Climat et de l'Environnement, LSCE/IPSL, CEA-CNRS-UVSQ, Université*
12 *Paris-Saclay, Gif-sur-Yvette, France*

13 *5 Department of Earth Sciences, University of Cambridge, Cambridge, UK*

14 *6 National Physical Laboratory, Teddington, UK*

15 *7 Climate and Environmental Physics, Physics Institute, and Oeschger Centre for Climate Change*
16 *Research, University of Bern, Bern, Switzerland*

17 **Corresponding author: etienne.legrain@univ-grenoble-alpes.fr*

18

19 **Supplementary Note 1**

20 **Orbital- to millennial-scale variability of the CO₂ new record**

21 Our CO₂ record represents a substantial improvement in temporal resolution compared to the existing
22 millennial-scale CO₂ record measured on the Vostok ice core over the 260-190 ka time interval¹
23 (Supplementary Fig. 1).

24 At orbital-scale, our new dataset reveals that the Termination III (TIII) (~248-242 ka) is much more
25 pronounced than the so-called TIIIa² (~223 -217 ka), with a global CO₂ rise of 79 and 48 ppm,
26 respectively. This morphology is similar to the Antarctic temperature record from the EDC core³.
27 Between 241 and 227 ka, the progressively decreasing plateau of CO₂ concentrations seems decoupled
28 from East Antarctic surface temperature. Such decoupling was already described during MIS 5⁴ and
29 more globally during the low obliquity period of the past 800 ka⁵. This pattern, probably linked to the
30 dynamics of the Southern Ocean under low-obliquity phase⁶, is confirmed by our new CO₂ record
31 during the period of lowest obliquity of the past 800 ka.

32 At millennial-scale, we identify a high-variability period between 251.4 and 248.9 ka at the onset of
33 TIII. This millennial-scale variability was not observed in the previous Vostok CO₂ record, probably due
34 to the lack of resolution over this period¹. However, this event was already described in the Antarctic
35 site temperature² and speleothem δ¹⁸O records⁷. Such two-phase deglaciation visible in the CO₂ record
36 was also observed during TI and contrasts with the more linear terminations such as TII.

37 **Context of occurrences of the identified CDJs**

38 We identified nine CDJ+ that occurred synchronously to a large atmospheric CH₄ increase and are a
39 potential consequence of a DO-like event (Supplementary Fig. 4 and 12). Oceanic circulation changes
40 associated with some DO events induced a centennial-scale response of the carbon-cycle characterized
41 by a 5 to 10 ppm CO₂ increase as measured in Antarctic ice cores⁸⁻¹⁰. This response is due to major
42 climatic perturbations in the Northern Hemisphere and the tropics, including a northward shift of the
43 Intertropical Convergence Zone (ITCZ) that induced the formation of new tropical wetlands¹¹.

44 Reversely, nine of them are considered as CDJ- as they are associated with a potential HS without
45 major CH₄ increase (Supplementary Fig. 4 and 12). HS are associated with a massive freshwater input
46 in the North Atlantic that induced an extended reduction in the strength of the AMOC^{12,13}. The HS are
47 thought to cause a moderate increase of CH₄ of less than 50 ppb⁹. However, the punctual absence of
48 atmospheric CH₄ variations during CDJs was already observed in older parts of the EDC ice core¹⁰. It
49 could be explained by the gas diffusion in the deepest part of the ice core or by the insufficient
50 resolution of the CH₄ record (Supplementary Fig. 1), which is also limited by the width of the gas age
51 distribution in the ice core samples¹⁰.

52 CDJ+ 11a.4 is the only event occurring under a low-obliquity period. It is associated with one of the
53 highest CH₄ abrupt increases of the last 500 ka (174 ppb at 387 ka) (Supplementary Fig. 12), suggesting
54 that the associated DO-like event strongly impacted the carbon cycle at that period. Under these
55 particular conditions, the low-obliquity might not have been sufficient to mitigate the destabilization
56 of atmospheric CO₂ at centennial-scale. A CDJ event could hence occur even under a low-obliquity
57 period due to the intensity of the initial perturbation in the carbon cycle.

58 **Impact of the choice of ice core chronologies on absolute CDJ dating**

59 In this study, we display our ice-core record onto the AICC2012 chronology^{14,15} which is the chronology
60 of reference for the EDC ice core. This chronology is mainly based on orbital dating with the use of
61 δ¹⁸O_{atm}, δO₂/N₂ and total air content records. The average uncertainty over the last 500 ka is 2.0 ± 1.6
62 ka for the AICC2012 gas chronology. The period of highest uncertainty, excluding the last meters of the
63 ice core, occurs over the 440-350 ka period reaching up to ~4 ka. This large uncertainty could be

64 explained by the relatively low-eccentricity during this period that made the identification of orbital-
65 scale morphology in the $\delta^{18}\text{O}_{\text{atm}}$, $\delta\text{O}_2/\text{N}_2$ and total air content records difficult. Alternatively, two other
66 EDC ice core age-scales have been published: Speleo-age¹⁶ and $\delta^{18}\text{O}_{\text{calcite}}$ chronology¹⁷. Both rely on the
67 assumption of a strong covariation of the $\delta^{18}\text{O}$ record from East-Asian speleothems with the $\delta^{18}\text{O}_{\text{atm}}$
68 measured in the gas phase of the EDC ice core. While the Speleo-age is purely based on speleothem
69 records for dating, the $\delta^{18}\text{O}_{\text{calcite}}$ chronology is a compromise between AICC2012 age markers and
70 speleothem-based alignment. The largest age difference between chronologies is found during the
71 440-350 ka period, reaching ~ 4 ka¹⁷. This 4-ka age difference could lead to a change of up to 0.5° in the
72 obliquity at a same depth level of the ice core. This large dating uncertainty over this interval is
73 illustrated in Supplementary Fig. 14. Despite this multi-millennial-scale discrepancy between the three
74 chronologies, the chi-square test led to the rejection of the null hypothesis: (i) for AICC2012 and
75 $\delta^{18}\text{O}_{\text{calcite}}$ chronologies, the null hypothesis of an independence of CDJ occurrence from the obliquity
76 state could be rejected at 95% of confidence. (ii) for the Speleo-age chronology, the chi-square test
77 rejects this null hypothesis at 90% of confidence (Supplementary Table 3). We also test the influence
78 of the choice of the orbital parameter data sets by comparing the one from ref. ¹⁸ and from ref. ¹⁹
79 (Supplementary Fig. 7). The results confirms the absence of a dating-dependence of our results, as 19
80 of the 20 CDJ occurred above the mean obliquity value of the 12 obliquity cycles of the last 500 ka
81 when the astronomical solution from ref. ¹⁹ is considered.

82 **Climate boundary conditions for the occurrence of centennial-scale CO_2 increases**

83 Here we explore the potential influence of the orbital-scale climate forcing on the occurrence of CDJs.
84 We have not found evidence of a link between the eccentricity and precession on the occurrence of
85 centennial-scale variability (Supplementary Fig. 5). The influence of the global climate state
86 (interglacial, glacial, or deglacial) have also been investigated through global ice volume. CDJs occurred
87 under warm, cold or transitional climate periods, as long as continental ice sheets were still large
88 enough to allow for some freshwater forcing of the AMOC. Most of the identified events in previous
89 studies occurred during periods of polar ice sheet instability⁸⁻¹⁰. The only exception is for the CDJs
90 occurring during MIS 11c¹⁰ (CDJ-11c) which occurred in a context of already quite reduced continental
91 ice volume.

92 The occurrence of CDJ+ 11a.4¹⁰ during a low-obliquity phase questions the link between the magnitude
93 of the original climatic perturbation that leads to a CDJ and the obliquity state. Hence, we investigate
94 the potential influence of the magnitude of the Heinrich-like and DO-like events on the occurrence or
95 absence of a CDJ (Supplementary Fig. 12). First, we focus on the CDJ+ associated with DO-like events
96 and a large atmospheric CH_4 release. To do so, we identified 30 CH_4 increases higher than 50 ppb during

97 the period of possible identification of centennial-scale CO₂ release. We assume that above this
98 threshold, such abrupt CH₄ increases are a potential marker of a DO-like event. Nine of them occurred
99 synchronously with the CDJs²⁰ (results are presented in Supplementary Fig. 12). We show that at first
100 order, some events of low/high magnitude (i.e. small/high CH₄ increase) that occurred under a very
101 high/low obliquity phase could lead to a CDJ. More specifically, the only CDJ occurring under low
102 obliquity is associated with a large CH₄ release in the atmosphere (175 ppb). This result may illustrate
103 that the control of the obliquity state on the carbon cycle could be limited when an extreme climate
104 perturbation occurred. Under low obliquity, a very intense initial disruption of the carbon cycle
105 alongside an increase in CH₄ levels greater than 50 ppb, likely related to strong tropical precipitation
106 changes, could possibly generate a CDJ.

107 The second type of CDJ is associated with HS¹⁰. We investigate the potential link between the
108 magnitude of the HS and the occurrence of a CDJ. To do so, we based our analysis on the IRD record
109 from the North Atlantic ODP 980 core. We assume that above 15% of IRD content, i.e. the percentage
110 of sediment grains larger than 150µm that are detrital in the sediment fraction, the occurrence of these
111 IRD could track the potential occurrence of a Heinrich-like events. This threshold value corresponds to
112 the lowest IRD percentage registered for the last glacial period during a Heinrich event observed in the
113 ODP980 marine sediment core²¹. This methodology includes two main limitations. First, the dating
114 uncertainty between the chronologies makes it difficult to robustly match the CDJs and a potential
115 related IRD peak. Second, the IRD signal is from a single location and cannot be considered as
116 representative of the North Atlantic IRD signal.

117 In total, 18 of these potential Heinrich-like events have been identified during the period of possible
118 identification of centennial-scale CO₂ release (Supplementary Fig. 12), and nine of them occurred
119 simultaneously, within error limits, to a CDJ- event. Eight out of these nine potential Heinrich-like
120 events occurred while obliquity was above 23.35°, seemingly independent from their individual
121 magnitude in the ODP 980 IRD record.

122 **Climatic impact of a low obliquity state**

123 A low obliquity state in experiment *LowObICTR* leads to colder conditions at both northern and
124 southern high latitudes compared to the control 49ka experiment (Fig. 4a). The mean air temperature
125 anomaly is -4.2°C north of 60°N (Supplementary Fig. 9). The cooling extends to the middle latitudes,
126 particularly over the continental areas. The high-latitude cooling is associated with a 7 % and 9 %
127 increase in annual mean sea-ice cover in the Northern Hemisphere and the Southern Ocean,
128 respectively. The resulting enhanced temperature gradient between the poles and the tropics impacts
129 the hydrological cycle, shifting the ITCZ as well as inducing drier conditions at mid to high latitudes (Fig.

130 4b). These climatic changes impact the vegetation and soil carbon, with widespread decrease of the
131 terrestrial carbon content, but more particularly in the northern high latitudes, the Sahel Zone and the
132 Middle East. As a result, the terrestrial carbon reservoir is 105 GtC (7%) lower in *LowObICTR* than in
133 *HighObICTR*.

134 **Climatic response to a North Atlantic meltwater input**

135 The meltwater addition of 0.3 SV into the North Atlantic leads to an AMOC shutdown in ~300 years in
136 all experiments. The AMOC stays completely off during the duration of the meltwater pulse (i.e. until
137 year 1000), after which it slightly increases to 5 Sv, before abruptly recovering between years 1800
138 and 2000 as salt is added to the North Atlantic. The AMOC shutdown leads to a reduced meridional
139 oceanic heat transport to the North Atlantic, and therefore to a 7°C reduction in Sea Surface
140 Temperatures (SST), as well as sea-ice advance, in the North Atlantic¹³. This leads to an atmospheric
141 cooling over most regions north of the equator apart from the north-eastern Pacific (Fig. 4a). The
142 warming over the north-eastern Pacific is due to enhanced North Pacific Intermediate Water
143 formation^{22,23}.

144 The reduced meridional oceanic heat transport to the North Atlantic leads to an SST increase in the
145 South Atlantic, which spreads to the Southern Ocean through the Antarctic circumpolar current in ~150
146 years (+1.6°C, zonal average over 45-60°S). These temperature changes impact the hydrological cycle
147 (Fig. 4b, Supplementary Fig. 9), with notably drier conditions over Europe, North Africa and the western
148 part of Asia. In addition, a southward shift of the Intertropical convergence zone is simulated, thus
149 leading to drier conditions in the northern tropics and wetter conditions in the southern tropics¹³.

150 **Vegetation and carbon cycle response to an AMOC shutdown**

151 These climatic changes impact the vegetation cover and the soil carbon, with a reduction of carbon
152 stored in most of the northern hemisphere, particularly at high northern latitudes (-53 GtC, for
153 *HighObl*) and in the northern tropics (-53 GtC, for *HighObl*), while there is an increase in the southern
154 tropics (+35 GtC, for *HighObl*). Overall, there is a 70 GtC loss from the terrestrial biosphere in *HighObl*,
155 mostly occurring during the first 400 years of the simulation (Supplementary Fig. 8).

156 Since the climate is colder and the precipitation pattern altered in the control experiment under a low
157 obliquity state, the terrestrial carbon reservoir is 105 GtC lower (Fig. 4). As a result, the terrestrial
158 biosphere only loses 34 GtC in *LowObl*.

159 A previous study has shown that the AMOC shutdown and associated changes in oceanic circulation
160 lead to a large reorganisation of dissolved inorganic carbon (DIC) concentration in the ocean²⁴. Due to
161 the reduction of the North Atlantic Deep Water transport, the carbon content in the Atlantic basin

162 (north of 35°S) increases by 250 GtC in *HighObl*, and 245 GtC in *LowObl* (Supplementary Figure 13). If
163 the terrestrial carbon fluxes are muted, the ocean does not have to buffer the terrestrial carbon
164 decrease, and therefore the Atlantic Ocean carbon reservoir increases slightly less (238 GtC in
165 *HighObl_NoVeg* and 236 GtC in *LowObl_NoVeg*).

166 Due to slightly higher stratification and increased DIC within the Atlantic water masses, the Southern
167 Ocean carbon reservoir increases by 60 GtC in *HighObl* and 42 GtC in *LowObl* (Supplementary Fig. 13).
168 However, as the North Pacific Intermediate Water flow increases to up to 30 Sv, there is large carbon
169 decrease in the Pacific basin (-270 GtC in *HighObl* and -282 GtC in *LowObl*) (Supplementary Fig. 13).

170 If the terrestrial carbon fluxes are muted, the Southern Ocean carbon increase is reduced (+40 GtC in
171 *HighObl_NoVeg* and +37 GtC in *LowObl_NoVeg*), while the decrease in the Pacific basin is enhanced (-
172 294 GtC in *HighObl_NoVeg* and -284 GtC in *LowObl_NoVeg*).

173 In the experiments where a strengthening of the SH westerlies is imposed, enhanced upwelling of DIC-
174 rich deep waters leads to a CO₂ outgassing in the Southern Ocean. The stronger ventilation in the
175 Southern Ocean reduces the DIC concentration in the Southern Ocean and within Antarctic
176 intermediate waters²⁵ (Supplementary Figure 14). As a result, due to the competing effects of the
177 AMOC shutdown and stronger SHW, the carbon reservoir increase is reduced in the Southern Ocean
178 (20 GtC in *HighObl_SHW* and 4 GtC in *LowObl_SHW*), and in the Atlantic (i.e. 238 GtC in *HighObl_SHW*
179 and 235 GtC for *LowObl_SHW*). The loss of carbon from the South Pacific is also accentuated, while it
180 is attenuated in the North Pacific due to the increased southern sourced waters. As a result, there is
181 an accentuated loss of carbon from the Pacific in *HighObl_SHW* (-282 GtC), while the loss of carbon is
182 attenuated in *LowObl_SHW* (-252 GtC) (Supplementary Fig. 14).

183

184

185

186

187

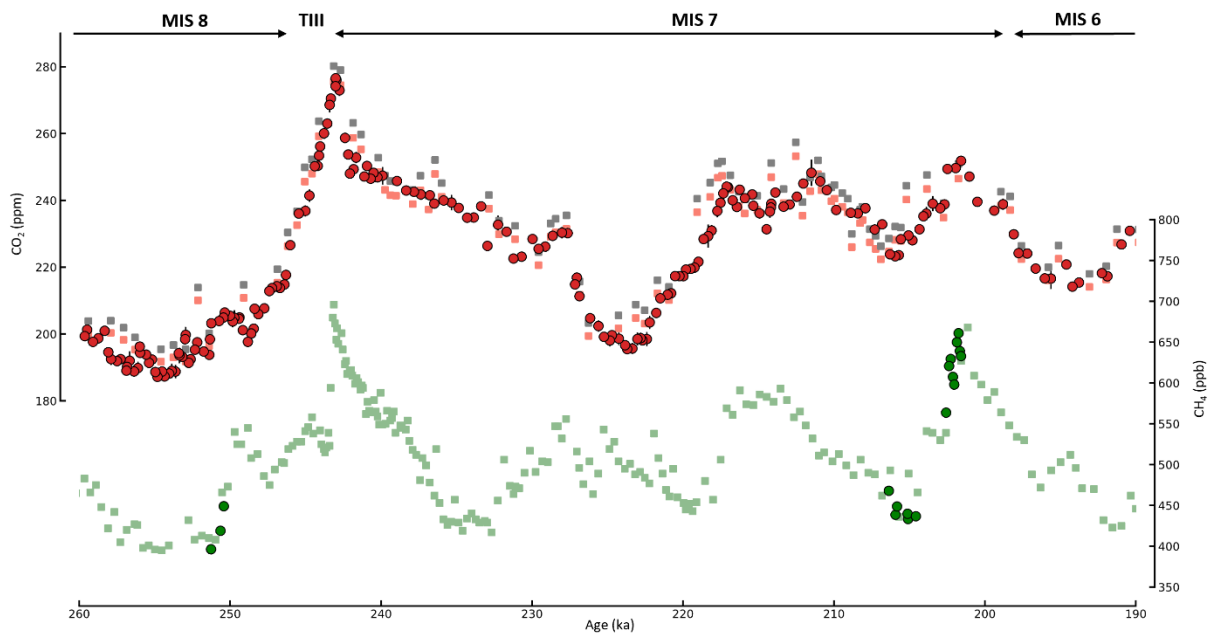
188

189

190

191 **Supplementary Figures**

192



193

194 **Supplementary Fig. 1: Published and new CO₂ and CH₄ measurements covering the 260-190 ka time-period.**
195 (Top panel) New CO₂ measurements on the EDC ice core (red dots, this study). Published CO₂ data from the
196 Vostok ice core¹ (grey squares) and Vostok CO₂ data corrected including gravitational and blank corrections (red
197 square, this study). All records are plotted on the AICC2012 gas timescale¹⁴. (Bottom panel) New (green dots, this
198 study) and published^{20,26} (green squares) CH₄ records from the EDC ice core.

199

200

201

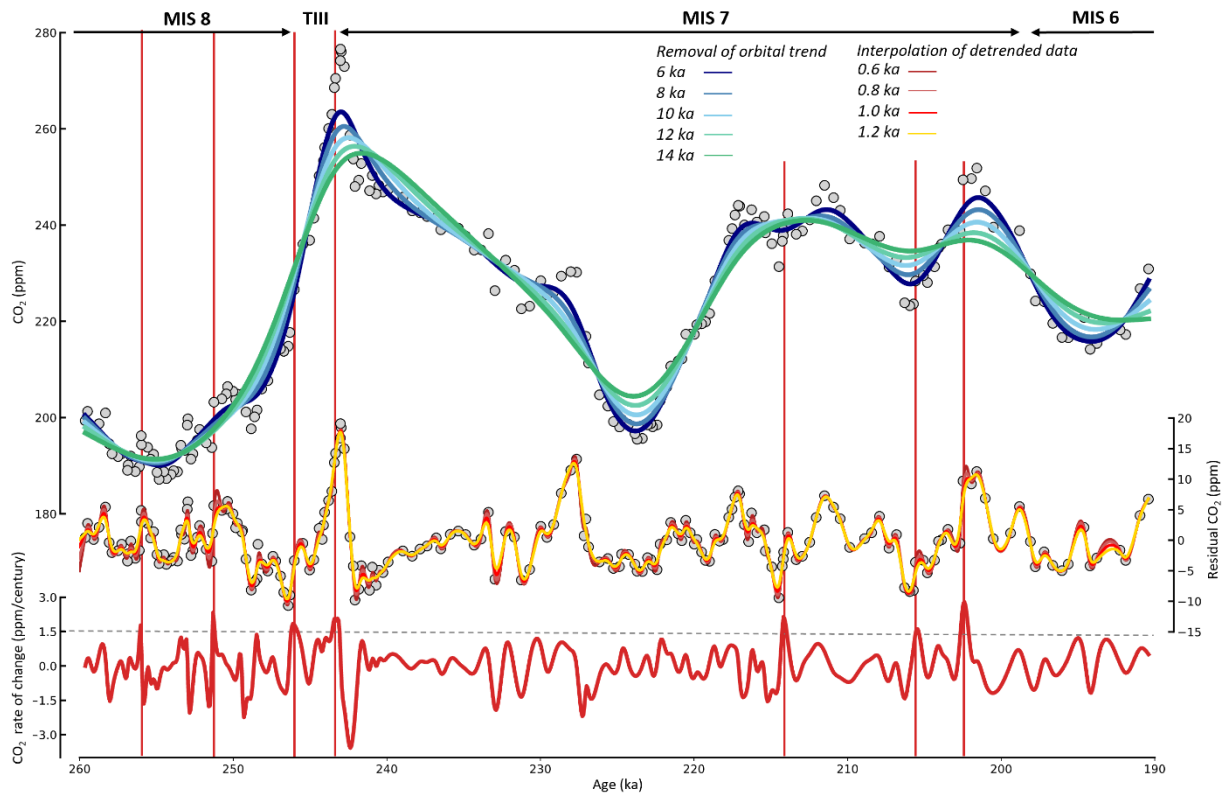
202

203

204

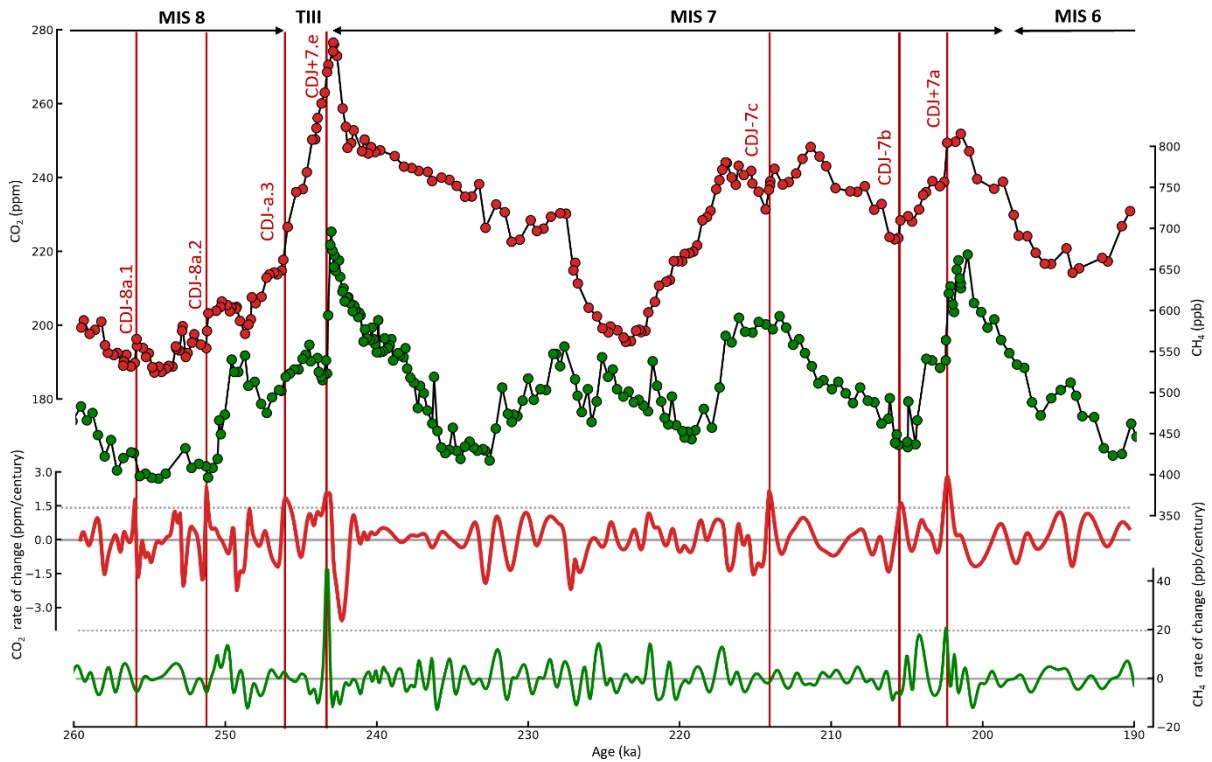
205

206



207

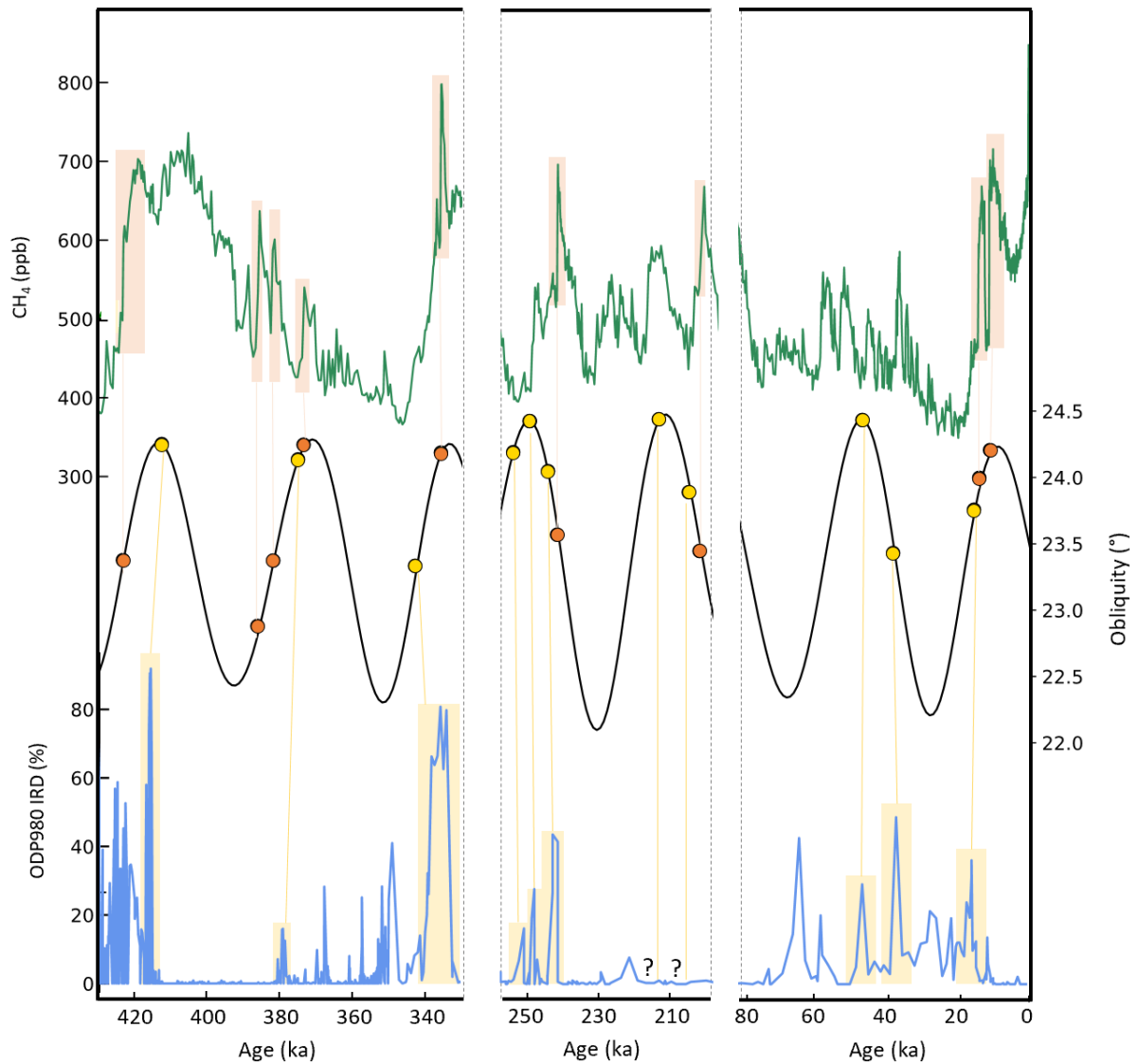
208 **Supplementary Fig. 2: Calculation of the CO₂ rate of change across the 260-190 ka interval based on the new**
 209 **EDC CO₂ record.** Top: Removal of orbital- to multi-millennial-scale trends from the EDC CO₂ record (grey dots,
 210 this study) using five different smoothing splines²⁷ with cut-off periods (i.e., degrees of smoothing) ranging from
 211 6 to 14 kyr. Middle: Detrended EDC CO₂ record after subtraction of the 10 kyr spline. A second set of five
 212 smoothing splines with cut-off periods ranging from 0.6 to 1.2 kyr is applied to the different detrended data sets.
 213 Bottom panel: Resulting rates of change of the detrended CO₂ record for the 1.0 kyr smoothing spline¹⁰. Vertical
 214 red lines indicate the timing of the identified CDJs. A centennial-scale CO₂ release is identified when the rate is
 215 higher than 1.5ppm/century (dashed horizontal line)¹⁰.



216

217 **Supplementary Fig. 3: Identification of centennial-scale CDJs between 260 and 190 ka.** Top: EDC CO₂ record on
 218 (red dots, this study). Middle: EDC CH₄ record (green dots, this study and ref. ^{20,26}). Bottom: Resulting rates of
 219 change of the detrended CO₂ and CH₄ records for the 1.0 ka smoothing spline. Vertical red lines indicate the
 220 timing of the identified CDJs. A centennial-scale CO₂ release is identified when the rate is higher than 1.5
 221 ppm/century (dashed horizontal line)¹⁰ and is considered to be associated with a significant CH₄ increase (CDJ+)
 222 when the CH₄ rate of change is higher than 20 ppb/century. All records are on the AICC2012 timescale¹⁴.

223

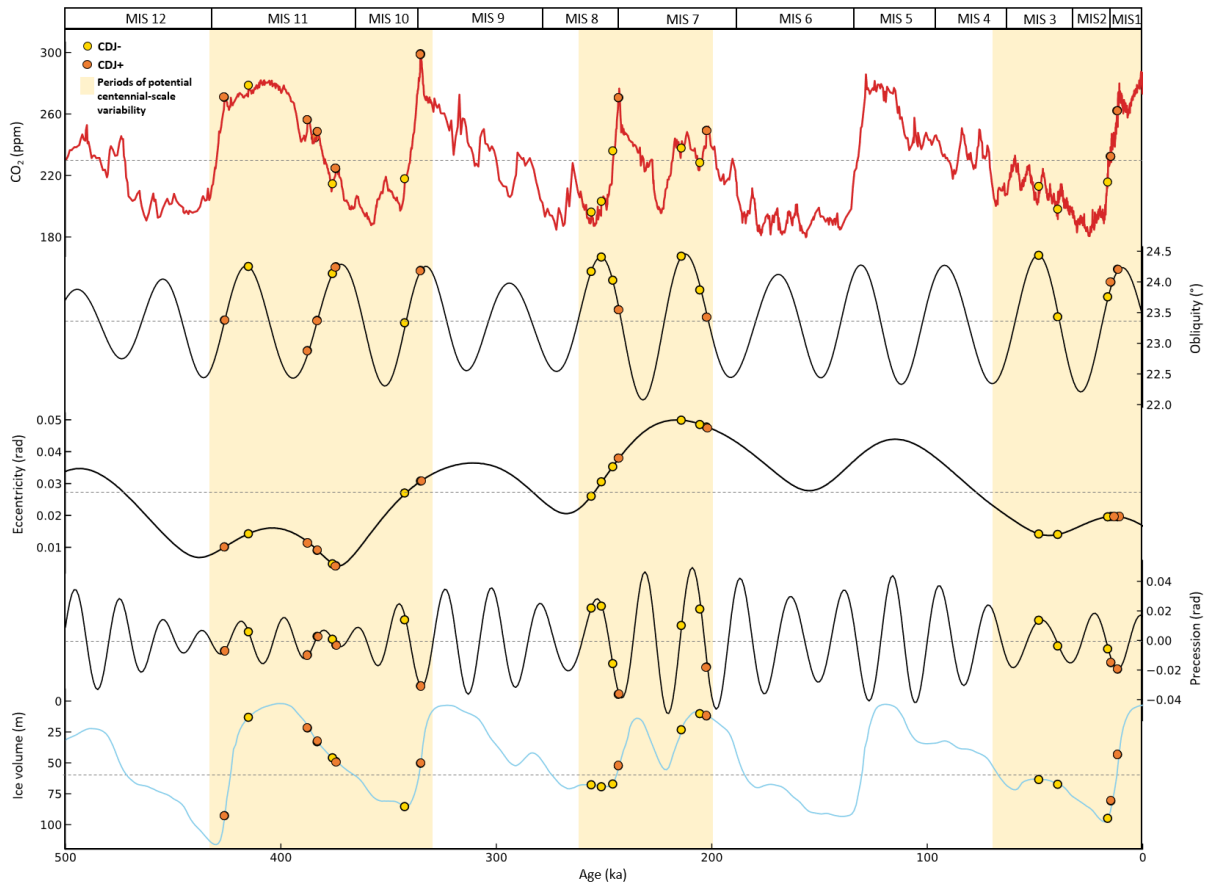


224

225

226 **Supplementary Fig. 4 Identification of DO-like and Heinrich-like events associated with CDJs over the last 500**
 227 **ka.** Top to bottom: atmospheric CH₄ record from the EDC ice core²⁰ (top, green). Obliquity (middle, black). Dots
 228 represent CDJs associated with Heinrich-like (blue) and DO-like events (green)^{8–10,28}. IRD record from the marine
 229 sediment core ODP 980 on its original timescale²¹ (bottom, blue). Yellow shaded areas correspond to Heinrich-
 230 like or DO-like events potentially associated with a CDJ. Question marks on the IRD record are when no IRD
 231 signature that we could associate to Heinrich-like events could be found.

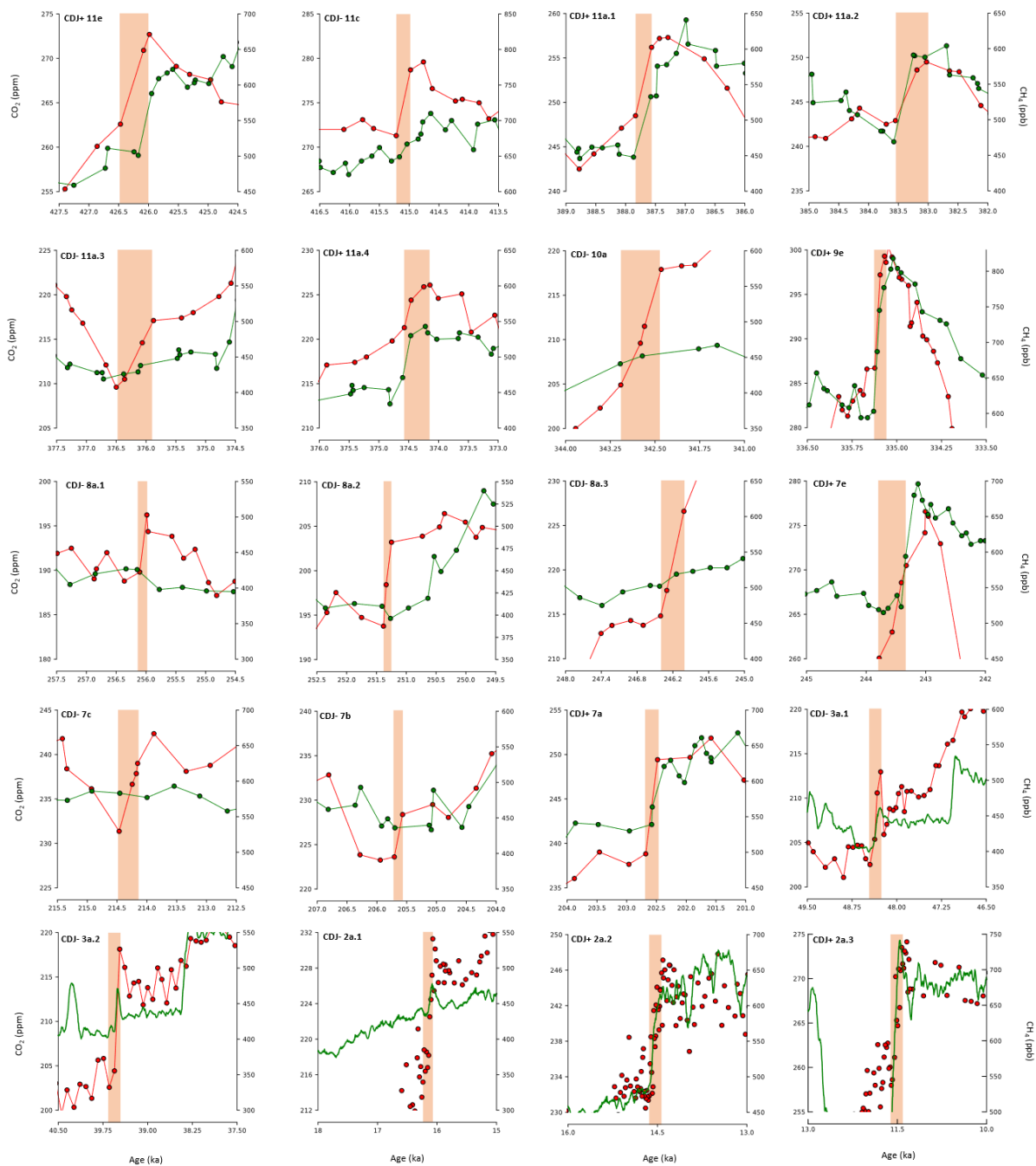
232



233

234 **Supplementary Fig. 5: Orbital-scale climatic background of occurrences of the CDJs.** From top to bottom: EDC
 235 CO₂ record (red, this study and refs.^{9,10,29–32}). Obliquity (black). Eccentricity (black). Precession (black). Global ice
 236 volume reconstruction³³ (blue). Yellow and orange dots indicate the timing of the CDJ- and CDJ+ occurrences in
 237 the context of the superimposed curve. From top to bottom Yellow bars represent the time intervals where the
 238 temporal resolution and the measurement-induced noise of the ice-core CO₂ records allow for the potential
 239 identification of abrupt changes.

240



241

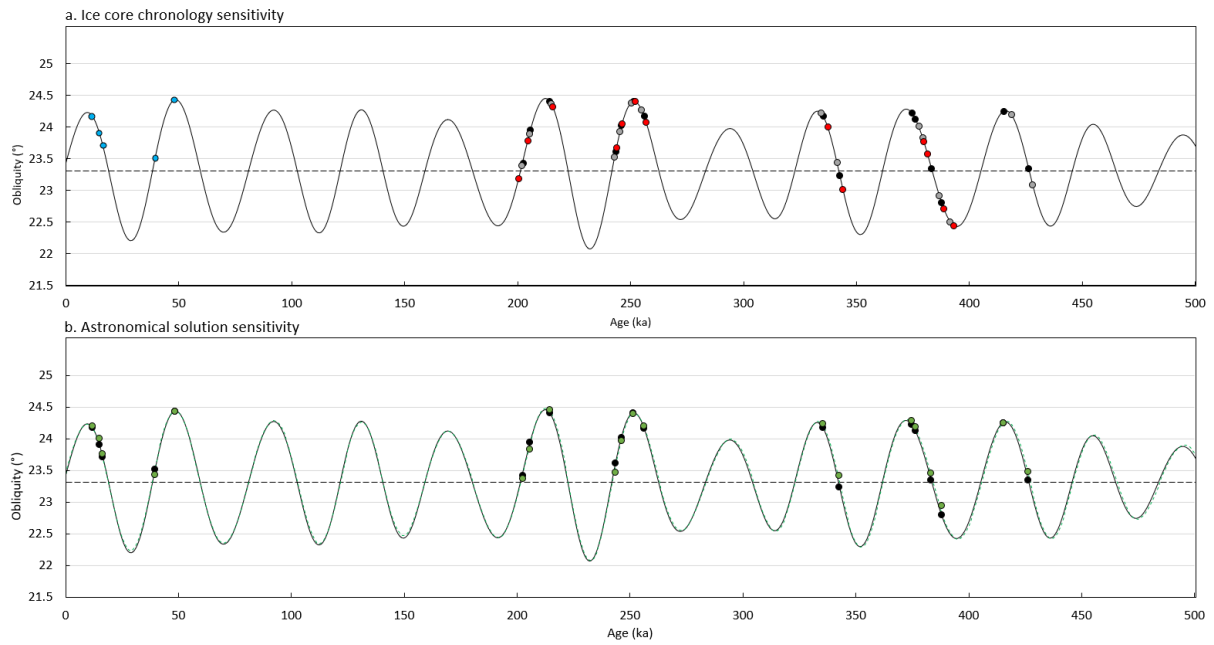
242

243 **Supplementary Fig.6: Detailed view of the 20 CDJs from the current and previously published studies.** EDC CO₂
 244 (red line and dots) and CH₄ (green line and dots) records on the AICC2012 gas timescale^{14,15} (older than 67 ka)
 245 and WD2014^{34,35} (younger than 67 ka) timescale (red dots). Vertical red bars correspond to periods associated
 246 with a CDJ.

247

248

249



250

251 **Supplementary Fig. 7: Testing the sensitivity of the relationship between the CDJs and the obliquity**
 252 **values to the choice of the ice-core gas chronology and of the astronomical solution. a. :** Dots
 253 correspond to CDJ occurrences put respectively on the WD2014³⁴ (blue), AICC2012¹⁴ (black), $\delta^{18}\text{O}_{\text{calcite}}$
 254 ¹⁷ (grey) and Speleo-age¹⁶(red) ice core chronologies. **b.** Dots correspond to CDJ occurrences computed
 255 with the astronomical solution of Ref. ¹⁹ (black) and Ref. ¹⁸ (green), respectively. The ice core timescale
 256 used is AICC2012 between 500 and 67 ka and WD2014 for the CDJs between 67 and 0 ka.

257

258

259

260

261

262

263

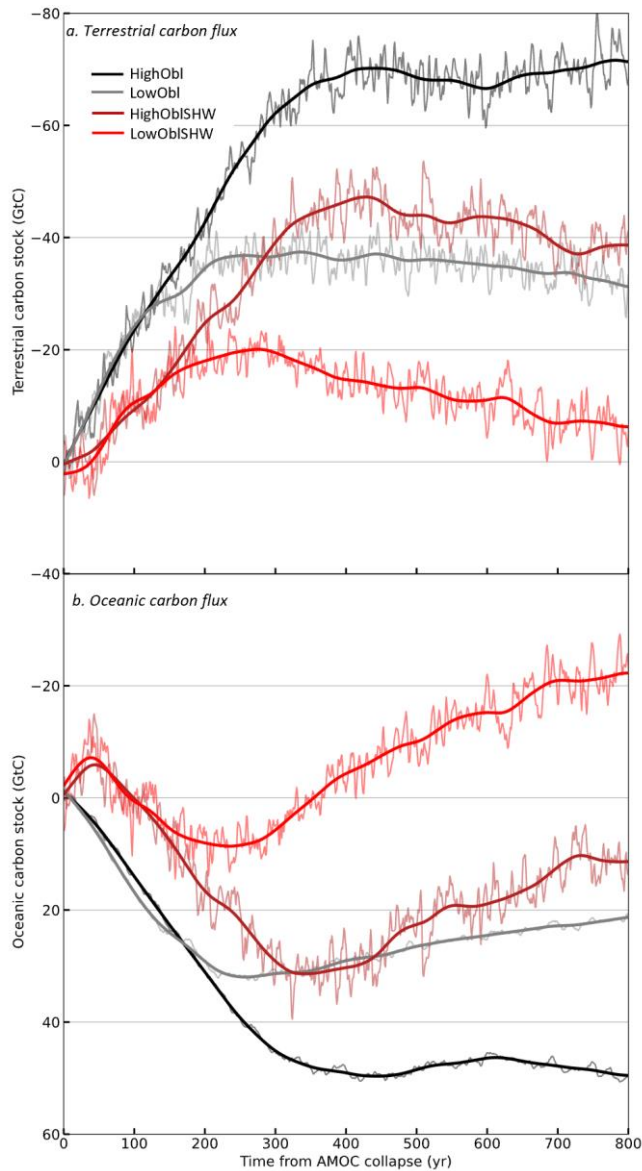
264

265

266

267

268



269

270

271 **Supplementary Fig. 8: Terrestrial and oceanic carbon changes in carbon reservoirs during HS 5 under high and**
 272 **low obliquity phase.** a. Terrestrial carbon stock (in GtC) from the start of the simulation until 0.8 ka. *HighObI* and
 273 *LowObI* are performed under the obliquity at 49 ka (24.3°) and artificially low obliquity forcing (22.1°),
 274 respectively. *HighObI_SHW* and *LowObI_SHW* are similar to the previous two simulations with enhanced strength
 275 of Southern Hemisphere Winds (+20%). Bold lines are smoothing splines filters. b. Similar to a. but for oceanic
 276 carbon stock. The Y axis is reverse to show that a decrease in the terrestrial carbon leads to an atmospheric CO₂
 277 increase.

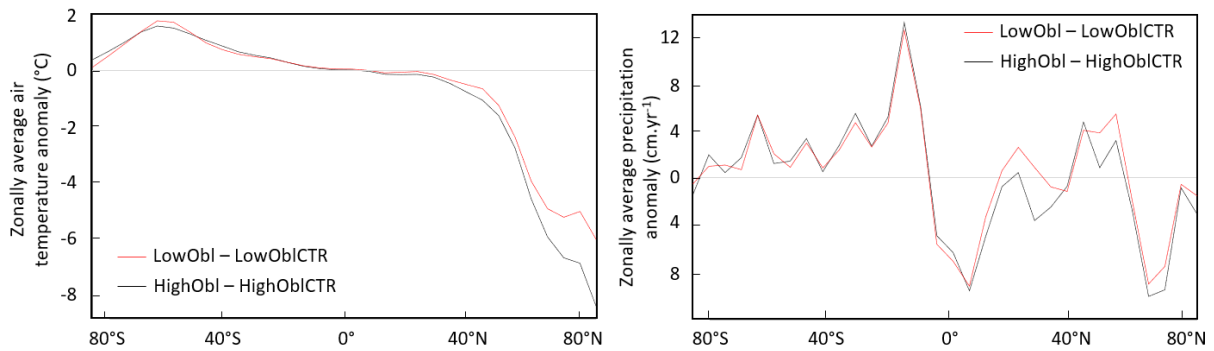
278

279

280

281

282

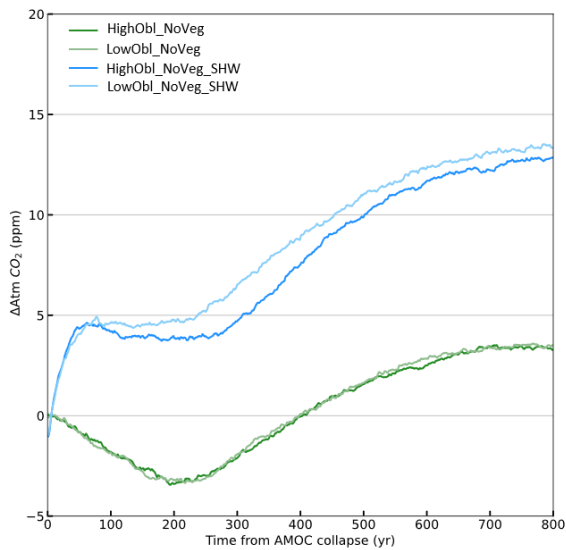


283

284 **Supplementary Fig. 9:** Zonally averaged (left) air temperature anomaly (°C) and (right) precipitation anomaly
285 (cm/yr) for (black) *HighObI* compared to *HighObICTR* and (red) *LowObI* compared *LowObICTR* in the LOVECLIM
286 model.

287

288



289

290

291 **Supplementary Fig. 10: Simulating centennial-scale CO₂ changes during HS5 under high and low obliquity**
292 **without terrestrial carbon fluxes.** Simulated CO₂ anomalies magnitude (ppm) for the first 800 years of the
293 simulation. *HighObI_NoVeg* and *LowObI_NoVeg* are performed under the obliquity at 49 ka (24.3°) and artificially
294 low obliquity forcing (22.1°), respectively. *HighObI_NoVeg_SHW* and *LowObI_NoVeg_SHW* are similar to the
295 previous two simulations with stronger Southern Hemisphere windstress (+40%).

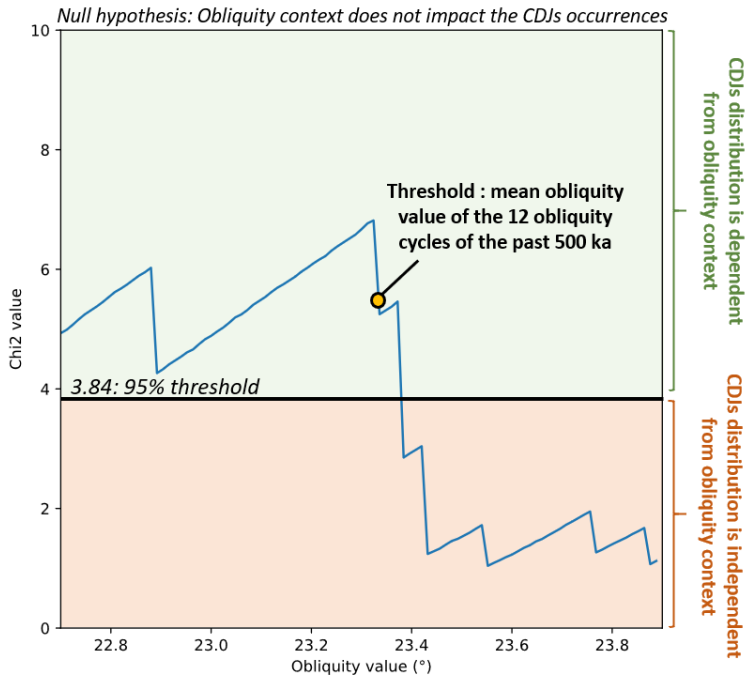
296

297

298

299

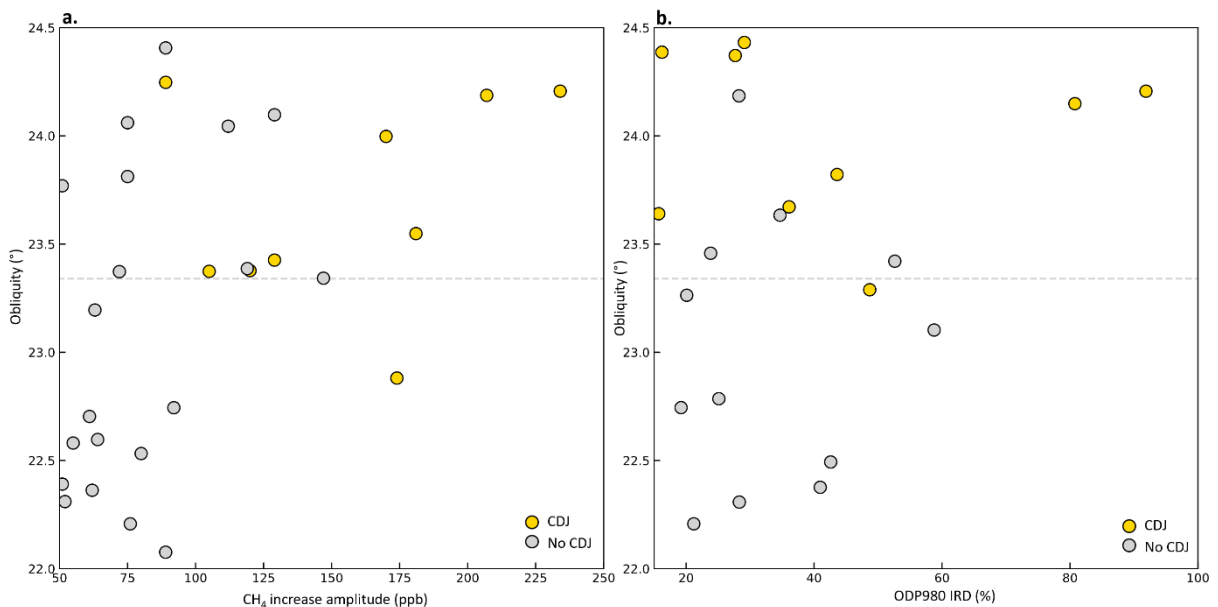
300



301

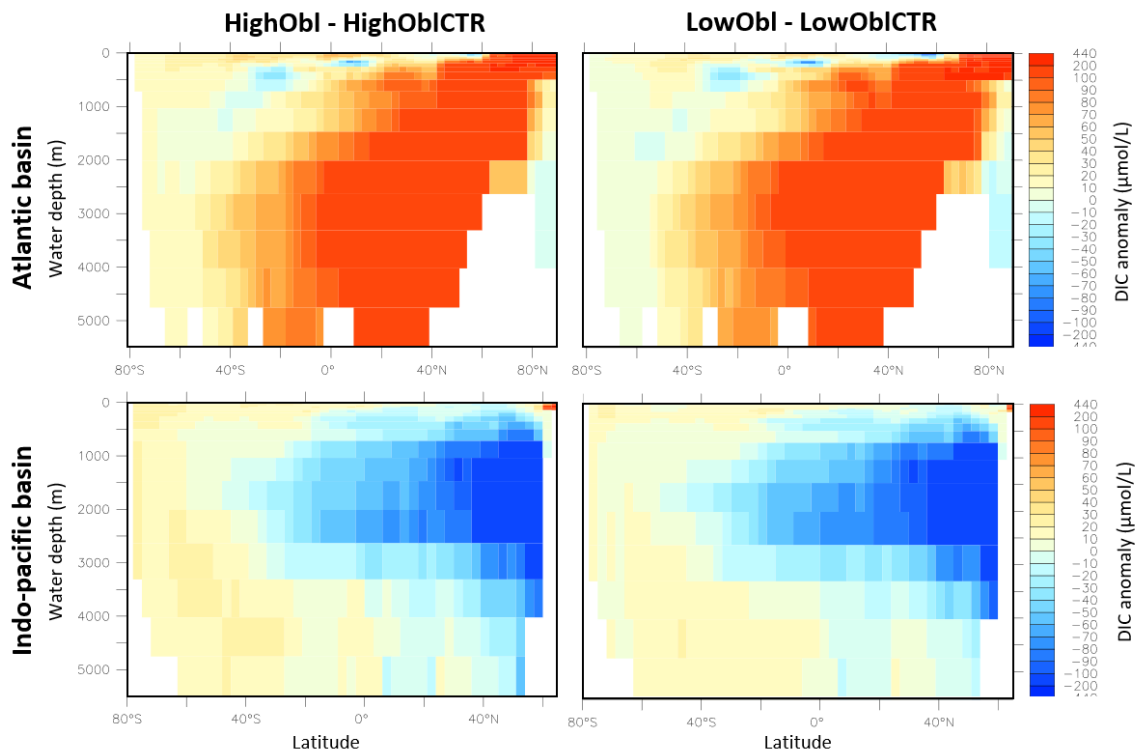
302 **Supplementary Fig. 11: Sensitivity of the Chi-square test to the threshold obliquity value.** The null hypothesis
 303 is rejected at 95% of confidence when the Chi-square value (blue curve) is higher than 3.84. The expected value
 304 varies with the threshold of obliquity chosen (x-axis).

305



306

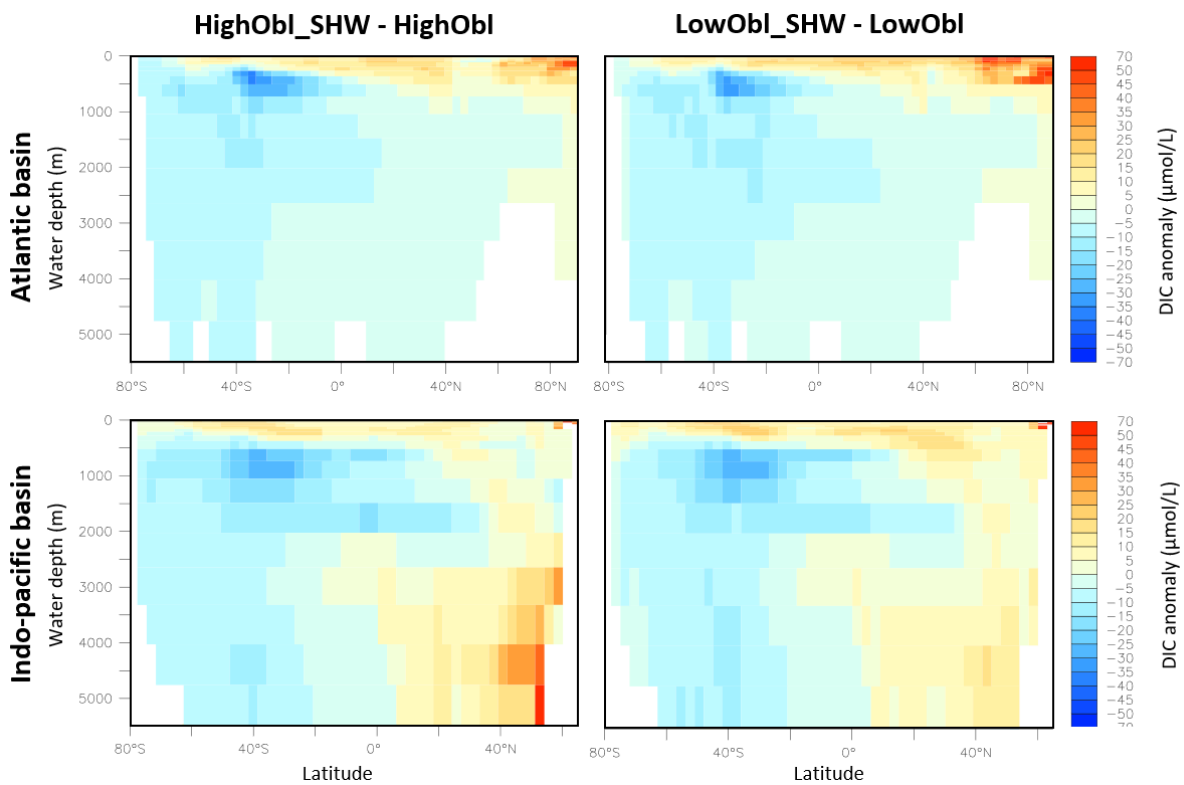
307 **Supplementary Fig. 12: Potential Heinrich-like events, DO-like events and associated CDJs during the past 500**
 308 **ka. a.** Dots correspond to centennial-scale CH₄ increases of more than 50 ppb. Yellow (grey) are potential DO-
 309 like events potentially (not) associated with CDJs, respectively. The grey dashed line corresponds to the average
 310 obliquity value (23.33°) of the 12 obliquity cycles of the last 500 ka. **b.** Dots correspond to sediment samples with
 311 more than 15% of IRD recorded in the ODP 980 located in the IRD North Atlantic belt²¹ that could be associated
 312 with potential Heinrich-like events.



313

314 **Supplementary Fig. 13:** DIC anomaly ($\mu\text{mol/L}$) averaged over (top) the Atlantic and (bottom) the Indo-Pacific
 315 basin for (left) *HighObl* compared to *HighObICTR* and (right) *LowObl* compared to *LowObI*.

316



317

318 **Supplementary Fig. 14:** DIC anomaly ($\mu\text{mol/L}$) averaged over (top) the Atlantic and (bottom) the Indo-Pacific
 319 basin for (left) *HighObl_SHW* compared to *HighObl* and (right) *LowObl_SHW* compared to *LowObl*.

320 **Supplementary Tables**

321 Supplementary Table 1: Chi-square test at one degree of freedom and 5% of significance of the
 322 following hypothesis: *CDJ occurrences are independent from the average value of the last 500ka of the*
 323 *tested parameter*. This hypothesis could be rejected at 95% of confidence only for obliquity.

324

Tested parameter	X ² test results
Obliquity	5.3 > 3.84
Precession	0.1 < 3.84
Eccentricity	0.4 < 3.84
Sea level	0.1 < 3.84
CO ₂	0.1 < 3.84

325

326

327 Supplementary Table 2: Description of the different LOVECLIM simulations and corresponding
 328 modelled ΔCO₂ in ppm at year 400.

329

<i>Simulation name</i>	<i>Details</i>	ΔCO ₂ (ppm)
<i>HighObl</i>	<i>49 ka Boundary conditions</i>	9.5
<i>LowObl</i>	<i>Similar to above under low obliquity phase</i>	3.3
<i>HighObl_NoVeg</i>	<i>No carbon flux between the terrestrial biosphere and atmosphere</i>	-0.1
<i>LowObl_NoVeg</i>	<i>Similar to above under low obliquity phase</i>	0.2
<i>HighObl_SHW</i>	<i>Enhanced Southern Hemisphere Winds (+20%)</i>	14.2
<i>LowObl_SHW</i>	<i>Similar to above under low obliquity phase</i>	9.4
<i>HighObl_NoVeg_SHW</i>	<i>No carbon flux between the terrestrial biosphere and atmosphere and enhanced Southern Hemisphere Winds (+20%)</i>	8.5
<i>LowObl_NoVeg_SHW</i>	<i>Similar to above under low obliquity phase</i>	9.8

330

331

332

333

334

335

336

337

338

339 Supplementary Table 3: Chi-square test at one degree of freedom for the different tested chronology
 340 of the following null hypothesis: *CDJ occurrences are independent from the average value of the 12*
 341 *obliquity cycles of the last 500ka*. This hypothesis could be rejected at the 95% confidence level (3.8)
 342 for AICC2012¹⁴ and $\delta^{18}\text{O}_{\text{calcite}}$ chronology¹⁷, and at the 90% confidence level (2.7) for the Speleo-age
 343 chronology¹⁶.

344

Considered chronology	X ² test results
AICC2012	5.37 > 3.8
$\delta^{18}\text{O}_{\text{calcite}}$	3.93 > 3.8
Speleo-age	2.71 > 2.7

345

346

347

348

349

350 Supplementary Table 4: CDJs of the past 500 ka. Ages of CDJ are from the AICC2012^{14,15} chronology
 351 except for the five youngest CDJs that are on the WD2014^{34,35} chronology. Obliquity value is from ref.
 352 ¹⁸.

CDJ name	CDJ age (ka)	age uncertainty (1 σ) (ka)	Obliquity value (°)	Reference
CDJ+2a.3	11.8	0.1	24.18	<i>Marcott et al. (2014)</i>
CDJ+2a.2	14.7	0.2	23.92	<i>Marcott et al. (2014)</i>
CDJ-2a.1	16.3	0.2	23.72	<i>Marcott et al. (2014)</i>
CDJ-3a.2	39.4	0.4	23.48	<i>Ahn et al. (2012)</i>
CDJ-3a.1	48.4	0.4	24.44	<i>Bauska et al. (2021)</i>
CDJ+7a	202.6	2.0	23.50	<i>This study</i>
CDJ-7b	205.6	2.1	23.95	<i>This study</i>
CDJ-7c	214.3	2.3	24.40	<i>This study</i>
CDJ+7e	243.5	2.1	23.62	<i>This study</i>
CDJ-8a.3	246.2	2.3	24.04	<i>This study</i>
CDJ-8a.2	251.3	2.8	24.41	<i>This study</i>
CDJ-8a.1	256.0	2.9	24.17	<i>This study</i>
CDJ+9e	335.3	2.5	24.17	<i>Nehrbass-Ahles et al. (2020)</i>
CDJ-10a	342.5	3.1	23.25	<i>Nehrbass-Ahles et al. (2020)</i>
CDJ+11a.4	374.5	4.8	24.23	<i>Nehrbass-Ahles et al. (2020)</i>
CDJ-11a.3	376.1	4.7	24.13	<i>Nehrbass-Ahles et al. (2020)</i>
CDJ+11a.2	383.3	4.2	23.36	<i>Nehrbass-Ahles et al. (2020)</i>
CDJ+11a.1	387.7	3.9	22.82	<i>Nehrbass-Ahles et al. (2020)</i>
CDJ-11c	415.1	3.6	24.25	<i>Nehrbass-Ahles et al. (2020)</i>
CDJ+11e	426.2	3.6	23.37	<i>Nehrbass-Ahles et al. (2020)</i>

353

354

355 **References**

- 356 1. Petit, J. R. *et al.* Climate and atmospheric history of the past 420,000 years from the Vostok ice
357 core, Antarctica. **399**, 10 (1999).
- 358 2. Bréant, C. *et al.* Unveiling the anatomy of Termination 3 using water and air isotopes in the
359 Dome C ice core, East Antarctica. *Quaternary Science Reviews* **211**, 156–165 (2019).
- 360 3. Landais, A. *et al.* Interglacial Antarctic–Southern Ocean climate decoupling due to moisture
361 source area shifts. *Nat. Geosci.* **14**, 918–923 (2021).
- 362 4. Landais, A. *et al.* Two-phase change in CO₂, Antarctic temperature and global climate during
363 Termination II. *Nature Geosci* **6**, 1062–1065 (2013).
- 364 5. Uemura, R. *et al.* Asynchrony between Antarctic temperature and CO₂ associated with obliquity
365 over the past 720,000 years. *Nat Commun* **9**, 961 (2018).
- 366 6. Ai, X. E. *et al.* Southern Ocean upwelling, Earth’s obliquity, and glacial-interglacial atmospheric
367 CO₂ change. *Science* **370**, 1348–1352 (2020).
- 368 7. Cheng, H. *et al.* Ice Age Terminations. *Science* **326**, 248–252 (2009).
- 369 8. Marcott, S. A. *et al.* Centennial-scale changes in the global carbon cycle during the last
370 deglaciation. *Nature* **514**, 616–619 (2014).
- 371 9. Bauska, T. K., Marcott, S. A. & Brook, E. J. Abrupt changes in the global carbon cycle during the
372 last glacial period. *Nat. Geosci.* **14**, 91–96 (2021).
- 373 10. Nehrbass-Ahles, C. *et al.* Abrupt CO₂ release to the atmosphere under glacial and early
374 interglacial climate conditions. *Science* **369**, 1000–1005 (2020).
- 375 11. Rhodes, R. H. *et al.* Enhanced tropical methane production in response to iceberg discharge in
376 the North Atlantic. *Science* **348**, 1016–1019 (2015).
- 377 12. Henry, L. G. *et al.* North Atlantic ocean circulation and abrupt climate change during the last
378 glaciation. *Science* **353**, 470–474 (2016).
- 379 13. Menviel, L. C., Skinner, L. C., Tarasov, L. & Tzedakis, P. C. An ice–climate oscillatory framework for
380 Dansgaard–Oeschger cycles. *Nat Rev Earth Environ* **1**, 677–693 (2020).
- 381 14. Bazin, L. *et al.* An optimized multi-proxy, multi-site Antarctic ice and gas orbital chronology
382 (AICC2012): 120–800 ka. *Clim. Past* **9**, 1715–1731 (2013).
- 383 15. Veres, D. *et al.* The Antarctic ice core chronology (AICC2012): an optimized multi-parameter and
384 multi-site dating approach for the last 120 thousand years. *Clim. Past* **9**, 1733–1748 (2013).
- 385 16. Barker, S. *et al.* 800,000 Years of Abrupt Climate Variability. *Science* **334**, 347–351 (2011).
- 386 17. Extier, T. *et al.* On the use of $\delta^{18}\text{O}_{\text{atm}}$ for ice core dating. *Quaternary Science Reviews* **185**, 244–
387 257 (2018).
- 388 18. Laskar, J. *et al.* A long-term numerical solution for the insolation quantities of the Earth. *A&A*
389 **428**, 261–285 (2004).
- 390 19. Berger, A. & Loutre, M. F. Insolation values for the climate of the last 10 million years.
391 *Quaternary Science Reviews* **10**, 297–317 (1991).
- 392 20. Louergue, L. *et al.* Orbital and millennial-scale features of atmospheric CH₄ over the past
393 800,000 years. *Nature* **453**, 383–386 (2008).
- 394 21. McManus, J. F., Oppo, D. W. & Cullen, J. L. A 0.5-Million-Year Record of Millennial-Scale Climate
395 Variability in the North Atlantic. *Science* **283**, 971–975 (1999).
- 396 22. Okazaki, Y. *et al.* Deepwater Formation in the North Pacific During the Last Glacial Termination.
397 *Science* **329**, 200–204 (2010).

- 398 23. Menviel, L. *et al.* Removing the North Pacific halocline: Effects on global climate, ocean
399 circulation and the carbon cycle. *Deep Sea Research Part II: Topical Studies in Oceanography* **61–**
400 **64**, 106–113 (2012).
- 401 24. Menviel, L., England, M. H., Meissner, K. J., Mouchet, A. & Yu, J. Atlantic-Pacific seesaw and its
402 role in outgassing CO₂ during Heinrich events: Heinrich CO₂. *Paleoceanography* **29**, 58–70
403 (2014).
- 404 25. Menviel, L. *et al.* Southern Hemisphere westerlies as a driver of the early deglacial atmospheric
405 CO₂ rise. *Nat Commun* **9**, 2503 (2018).
- 406 26. Spahni, R. *et al.* Atmospheric Methane and Nitrous Oxide of the Late Pleistocene from Antarctic
407 Ice Cores. *Science* **310**, 1317–1321 (2005).
- 408 27. Enting, I. G. On the use of smoothing splines to filter CO₂ data. *J. Geophys. Res.* **92**, 10977 (1987).
- 409 28. Ahn, J., Brook, E. J., Schmittner, A. & Kreutz, K. Abrupt change in atmospheric CO₂ during the last
410 ice age. *Geophys. Res. Lett.* **39**, (2012).
- 411 29. Bereiter, B. *et al.* Revision of the EPICA Dome C CO₂ record from 800 to 600 kyr before present:
412 Analytical bias in the EDC CO₂ record. *Geophys. Res. Lett.* **42**, 542–549 (2015).
- 413 30. Shin, J. *et al.* Millennial-scale atmospheric CO₂ variations during the
414 Marine Isotope Stage 6 period (190–135 ka). *Clim. Past* **16**, 2203–2219 (2020).
- 415 31. Shin, J. *et al.* Millennial variations in atmospheric CO₂ during the early Holocene (11.7–7.4 ka).
416 *Clim. Past* **18**, 2063–2075 (2022).
- 417 32. Bauska, T. K. *et al.* Links between atmospheric carbon dioxide, the land carbon reservoir and
418 climate over the past millennium. *Nature Geosci* **8**, 383–387 (2015).
- 419 33. Berends, C. J., de Boer, B. & van de Wal, R. S. W. Reconstructing the evolution of ice sheets, sea
420 level, and atmospheric CO₂ during the past 3.6 million years. *Clim. Past*
421 **17**, 361–377 (2021).
- 422 34. Buizert, C. *et al.* The WAIS Divide deep ice core WD2014 chronology – Part 1: Methane
423 synchronization (68–31 ka BP) and the gas age–ice age difference. *Clim. Past* **11**, 153–173 (2015).
- 424 35. Sigl, M. *et al.* The WAIS Divide deep ice core WD2014 chronology – Part 2: Annual-layer counting
425 (0–31 ka BP). *Clim. Past* (2016).
- 426

6.3. Perspectives

This study provides new evidences of centennial-scale CO₂ increases over MIS 7 and the preceding termination (260-190 ka). Combining my new dataset with recently published high-resolution CO₂ record over the last 500,000 years, I established a link between the centennial-scale variations in the carbon cycle and a high-obliquity context. Four main points that rely on these results require further attention.

- (i) Since the last atmospheric CO₂ composite curve in 2015 [Bereiter et al., 2015], large efforts have been undertaken to provide a sub-millennial-scale CO₂ record from Antarctic ice cores [Nehrbass-Ahles et al., 2020; Shin et al., 2020; Bauska et al., 2021; Menking et al., 2022; Shin et al., 2022; Silva, 2022; Legrain et al., in revision]. New measurements are also planned covering the MIS 8 period (330-260 ka, EDC Gas consortium discussions). When ice sample across this period will be measured, sub-millennial resolved atmospheric CO₂ record will be available from the last glacial period to the past 500 ka in the EDC ice core. A new composite curve could thus be produced in the coming decade integrating (i) these high-resolution EDC records, (ii) previous millennial-scale resolved record covering the 500-800 ka period [Bereiter et al., 2015] and (iii) high-resolution records from high-accumulation Antarctic ice core covering the last glacial cycle [Marcott et al., 2014; Bauska et al., 2021].
- (ii) Mechanisms explaining the dependence of the centennial-scale variations of CO₂ concentrations associated with HS to obliquity have been identified through simulations performed with the Earth System Model of intermediate complexity LOVECLIM. These simulations point to the continental vegetation as the obliquity-dependent source of carbon at centennial-scale. However, the dependence of the centennial-scale CO₂ variations associated with DO-like events were not investigated through these simulations. Further modelling efforts could reproduce the same simulations scheme as performed during the HS5 modelling but focusing on a specific DO event. For instance, the DO event happening around 11.7 ka (referred to as DO 0; Kindler et al. [2014]), ending TI, occurs under a very high obliquity context. The impact of such event on the carbon cycle, performed under real and artificially low obliquity phase could help to confirm the continental vegetation as being also the obliquity-dependence source of carbon that varies at centennial-scale during a DO event.

- (iii) In addition, while the data analysis has revealed a strong dependency of centennial-scale variations of carbon cycle to the obliquity context through the continental vegetation variations, no precessional influence has been identified in the data. Nevertheless, this orbital parameter is likely having a strong influence on the carbon cycle variability and especially the dynamics of continental vegetation at low latitude [Claussen et al., 2006; Joanin et al., 2011]. Future modelling studies should explore the impact of a low and high precession scenario associated with a modelled HS and/or DO event to confirm the non-dependence of centennial-scale variations of carbon cycle to the precessional context as observed in the data.
- (iv) Complementary to the modelling approach, high-resolution carbon isotopes records would allow to explore the mechanisms at play during these centennial-scale CO₂ events. Such records are available during the last glacial cycle and the TII [Schmitt et al., 2012 ; Schneider et al., 2013; Bauska et al., 2018; Menking et al., 2022]. Centennial-scale resolved carbon isotopes records during the last glacial cycle revealed a significant negative excursion during CDJ- and no significant change during CDJ+ [Bauska et al., 2018; Bauska et al., 2021]. A systematic measurement of carbon isotopes during the already identified CDJs could help to confirm the probable different origin of carbon during the two types of CDJs events suggested by these preliminary carbon isotopes results. Such measurement will become available at IGE in the coming years with the development of a new laser spectrometer (see section 2.4.1).

Synthesis

In this chapter, I present the results from an article currently in revision for *Nature*. Based on a new high-resolution CO₂ record over the 260 – 190 ka period, I identify seven centennial-scale releases of atmospheric CO₂ (CDJs) measured in the Antarctic EDC ice core. To provide a comprehensive understanding of the centennial-scale variability in the carbon cycle, I analyse the high-resolution atmospheric CO₂ records of the past 500,000 years. In particular, 18 out of the 20 CDJs identified occurred during periods of high obliquity, suggesting an influence of orbital background conditions on rapid atmospheric CO₂ releases. To explore the potential sources of these rapid CO₂ increases, I analysed simulations of an Earth system model of intermediate complexity (LOVECLIM) performed by Laurie Menviel (University of New South Wales, Australia). The simulations aimed to reproduce the CDJ associated with HS 5 event under both real and artificially low obliquity phases. The results suggest that during a Heinrich stadial, both the continental biosphere and the Southern Ocean act as primary carbon sources contributing to CDJ occurrences. In addition, only the continental biosphere appears to be an obliquity-dependent CO₂ source during centennial-scale events. This study highlights the potential impact of long-term external forcing on past abrupt CO₂ variations. Notably, it suggests that the current high obliquity phase could amplify variations in atmospheric CO₂ concentrations at centennial-scale in case of a disruption in the oceanic circulation due to anthropogenic disturbances. Further simulations investigating the influence of obliquity on the centennial-scale atmospheric CO₂ event associated with a DO event and exploring the impact of precession on centennial-scale variations in the carbon cycle would provide valuable insights. Furthermore, this study is part of a broader global effort that aimed at producing high-resolution records throughout the period covered by the Antarctic ice cores. The development of a multi-ice core based composite CO₂ record would significantly increase the resolution of the current CO₂ composite curve [Bereiter et al., 2015].

Chapter 7

Conclusions and perspectives

In Chapter 7, I provide a point-by-point synthesis of the main findings of my research work in the light of the questions formulated in the introductory chapter. In parallel, I developed the main perspectives for future research arising from my results. Finally, I conclude this chapter with a broader discussion of the global outcomes of my PhD work.

7.1. Conclusions and perspectives

🔗 What are the roles of the carbon cycle and the orbital forcing in triggering the MPT?

(Chapter 3)

Main results: My conceptual modelling approach has revealed the coupling between the orbital forcing and a gradual trend in the internal climate over the past 2 Ma as the most probable scenario to have caused the MPT. Reversely, an abrupt event occurring at millennial-scale does not appear to be particularly relevant. Based on the temporal duration of the involved mechanism, I propose that the gradual trend across the past 2 Ma could be carried by the atmospheric CO₂ concentrations. No continuous and direct measurement of atmospheric CO₂ concentrations is available across the past 2 Ma to test this hypothesis. Nevertheless, proxy-based CO₂ reconstructions illustrate either a gradual trend in glacial [Chalk et al., 2017] or interglacial [Yamamoto et al. 2022] CO₂ concentrations. Physical modelling has pointed that the forcing induced by a CO₂ concentration decrease would be quantitatively enough to be responsible at least partly for the MPT [Willeit et al., 2019]. In addition, my results underline the importance of the orbital forcing in triggering the MPT. While this forcing is not sufficient by itself, it appears to play an essential role in triggering the MPT. Especially, the low-frequencies of obliquity and precession modulation appear to have played a key role in amplifying the climatic cycles through the MPT.

Perspectives: *First, the on-going BE-OI project aims to provide a continuous ice archive as old as 1.5 Ma. Hence, it will provide hopefully the required very old ice to test the hypothesis of a decline of atmospheric CO₂ concentrations through the MPT. Second, the results from this part of my PhD project have stimulated a new conceptual modelling study starting in October 2023 at IGE by Felix Pollak, a new PhD student supervised by Frédéric Parrenin. While my study focused on the simulation of global ice volume reconstruction, this new project will attempt to reconstruct the atmospheric CO₂ concentrations and potentially other global variables such as the mean ocean temperature and the CH₄ concentrations across the MPT following the theoretical background from Parrenin and Paillard, [2004] and using the inverse method I developed in Legrain et al. [2023].*

- 🔗 What are the orbital-to-millennial-scale interactions between the carbon cycle and the Antarctic climate during glacial terminations? (*Chapter 4*)

Main results: I have performed phasing analyses to investigate the interactions between atmospheric CO₂ concentrations and Antarctic climate over the past five terminations. To do so, I used high-resolution $\delta^{15}\text{N}$ and atmospheric CO₂ records from the EDC ice core. The phase relationship analyses I have performed over the past five terminations evidences a multi-centennial scale lag of the atmospheric CO₂ concentrations decrease over the Antarctic climate cooling at the end of the terminations. This delay, similar to the one observed during the millennial-scale variability of the last glacial period, suggests that terminations are ultimately ended by millennial-scale events. The occurrence of millennial-scale events in the course of the TI and TIII underlines the importance of the orbital context to determine whether this millennial-scale variability will eventually end the termination or will only bring it to a temporary pause. The analysis of the sequence of events at play at the end of termination also reveals a sub-centennial-scale synchronicity between the onset of atmospheric CO₂ concentrations decrease and an abrupt change in the $\delta^{18}\text{O}_{\text{atm}}$ of O₂ and CH₄ records. This result suggests that the enhancement of a mid-to-low latitude carbon sink may constrain the exact timing of atmospheric CO₂ concentration decrease at the end of terminations.

Perspectives: *First, the inter-comparison of the results performed with different methods has revealed the incapacity to identify a clear phasing signal at the onset of terminations due to the high sub-orbital scale variability during glacial period and the low-amplitude variability of the $\delta^{15}\text{N}$ of N₂ record. Experimental and theoretical work should be led to better understand the processes affecting $\delta^{15}\text{N}$ beyond its first-order climatic imprint. Collaborators at LSCE and IGE are currently investigating this topic, in particular in the framework of the PhD of Marie Bouchet, supervised by Amaëlle Landais and Frédéric Parrenin. Second, the apparent synchronicity of $\delta^{18}\text{O}_{\text{atm}}$ variations and atmospheric CO₂ decrease at the end of termination deserves more attention. Further work is necessary to fully and quantitatively understand the processes driving the observed variations of $\delta^{18}\text{O}_{\text{atm}}$. The LSCE is currently investigating the question of the drivers of the $\delta^{18}\text{O}_{\text{atm}}$ signal and the associated physical processes in the framework of the PhD projects of Clémence Paul and Nicolas Bienville, supervised by Amaëlle Landais. Third, a quantification of the observed processes at play during terminations based on an EMIC including isotopes modelling (e.g. the iLOVECLIM model) would bring key information, focusing on the impact of sources and sinks of carbon variations on the modulation of the $\delta^{18}\text{O}_{\text{atm}}$ signal at the end of terminations.*

- 🔗 What is the spatio-temporal pattern of the warming during an interglacial period and how does it relate to orbital and carbon cycle forcings? (*Chapter 5*)

Main results: The multi-archive surface temperature synthesis across the MIS 7 enables to evidence for the first time key climatic features for this time period among which (i) all regions of the globe registered a similar intensity of warming between the two warm periods (MIS 7e and MIS 7a-7c) and their associated terminations (TIII and TIII-A) at the exception of the high-latitudes of the Southern hemisphere, that evidenced a more pronounced TIII and associated MIS 7e (ii) a morphological similarity of the high-latitude temperature records and atmospheric CO₂ concentrations (iii) a strong imprint of the obliquity forcing on the surface temperature evolution during MIS 7, which suggests a parallel between the MIS 7 and the pre-MPT interglacials (iv) a not warmer than pre-industrial climate during MIS 7, apart in the southern high-latitudes during MIS 7e. These results suggest that the MIS 7 climate evolution was influenced by a combination of a very specific orbital forcing, similar to the one of the 1.6-1.2 ka period, and the high levels of atmospheric CO₂ concentrations typical of the post-MPT interglacials.

Perspectives: *First, this study developed paleoclimatic interpretations inferred from data-based surface temperature reconstruction aligned on a common temporal framework. In addition, I produced time slices (i) to facilitate the comparisons between the data-based surface temperature reconstruction and the existing simulations at equilibrium that includes MIS 7 and (ii) to motivate further modelling-based investigation of this period. Such model-data comparison will provide key information on the ability of the climate models to reproduce surface temperature evolution in the context of intense orbital forcing variability. This work is part of a broader project (HOTCLIM, led by Emilie Capron) that aims to characterize the spatio-temporal evolution of interglacial climates during the past 500 ka. In addition to this MIS 7 study, a MIS 9 synthesis will be achieved by Nathan Stevenard who will start a Post-Doctoral position at IGE in 2024 in collaboration with Emilie Capron. A model-data comparison will be performed in collaboration with Nathaëlle Bouttes from the LSCE using LOVECLIM simulations over the MIS 7 and MIS 9. The building of these syntheses and the model-data comparison exercises should provide a unique opportunity to investigate the similarities and differences of the surface temperature patterns under very distinct background orbital conditions. Especially, advances on our understanding of past interglacials dynamics should be made by performing a comparison of the different interglacial climates focusing on: (i) the spatial variability of the relative interglacial intensity, (ii) the impact of the different orbital contexts on the evolution of the surface temperature, and (iii) the ability of a single set of model parameters to reproduce the diversity of climates during the past four interglacials.*

- 🔗 Is there a link between the orbital-scale climatic background and the centennial-scale changes in the carbon cycle? (*Chapter 6*)

Main results: I provide the first atmospheric CO₂ record measured on the EDC ice core spanning the 260-190 ka period. This record is composed of 201 new data points leading to a temporal resolution of 340 years. The temporal resolution is thus improved by a factor three compared to the Vostok atmospheric CO₂ record that is used over this time period in the current CO₂ composite record. This high-resolution record has allowed to investigate the sub-millennial-scale variability of atmospheric CO₂ concentrations. Based on my new multi-centennial scale record and previously-published ones for other time intervals, I evidence that 18 of the 20 centennial-scale increases of atmospheric CO₂ over the past 500 ka occur in a context of high-obliquity values. New simulations performed with the LOVECLIM model reveals that both the Southern Ocean and the continental biosphere act as sources of carbon during these abrupt CO₂ changes. Nevertheless, only the continental biosphere appears to be an obliquity-dependent CO₂ source. These results suggest for the first time an influence of orbital background conditions on abrupt carbon releases.

Perspectives: *First, my results reinforce the importance of producing carbon isotope and oceanic pH records during periods of centennial-scale variability of CO₂ concentrations to confirm the processes leading to the atmospheric CO₂ increase during centennial-scale events. A project at IGE led by Roberto Grilli is on-going to develop a new laser spectrometer for the combined analysis of ice core samples for CO₂ concentration and its isotopic signature, the $\delta^{13}C$. Second, the modelling work performed in the framework of this study focuses on the centennial-scale variations of CO₂ associated with HS, representing about half of the 20 identified events. The other abrupt CO₂ changes are associated with DO events. While modelling the global impact of DO events remains challenging, future simulations focusing on the influence of the obliquity context on the sources of carbon during DO events will be performed by the end of the year by Laurie Menviel with the LOVECLIM model. Lastly, this new CO₂ record is part of the effort of the ice core groups from the Bern and Grenoble universities to produce sub-millennial atmospheric CO₂ concentrations from the EDC ice core over the past 800 ka. High-resolution records are currently measured at Bern University over MIS 5 and MIS 8 [Silva, 2022; L. Silva, comm. Pers]. Since the last atmospheric CO₂ composite curve from Bereiter et al. [2015], an intense production of sub-millennial resolved CO₂ records have been initiated [Shin et al., 2020; Nehrbass-Ahlès et al., 2020; Bauska et al., 2021; Menking et al., 2022; Shin et al., 2022; Silva, 2022; Legrain et al., in revision]. Hence, the publication of a new atmospheric CO₂ composite curve at a sub-millennial resolution in the coming years would represent a valuable update.*

7.2. Concluding remarks

My PhD research has been based on a multi-method (experimental, modelling, statistical) approach applied on various timescales (centennial-, millennial-, orbital-scales) in order to characterize the carbon cycle and climate interactions during the past 2 Ma. Beyond the diversity of research angles, two main pervasive features of the Pleistocene climate have emerged that I discuss here as a final conclusion of this manuscript.

On the role of the orbital forcing. All the paleoclimatic studies presented in this manuscript have for objective to investigate the coupling between the climate and the carbon cycle. Nevertheless, regardless of the timescale considered, a pervasive influence of the orbital background conditions has been evidenced (i) on the establishment of the MPT (*Chapter 3*), (ii) on the millennial-scale variability at the end of glacial terminations (*Chapter 4*), (iii) on the surface temperature patterns during the MIS 7 (~245-190 ka) (*Chapter 5*), and (iv) on the occurrences and amplitude of centennial-scale carbon cycle variability (*Chapter 6*). While it is established that the climate of the Pleistocene is primary driven by the orbital forcing, the recurrence of its impact on the carbon cycle, the climate, and their interactions at sub-orbital scale have been highlighted in my PhD research. The climate of the Pleistocene is commonly summarised as composed of two main periods: the pre-MPT 41 ka “world”, corresponding to the obliquity periodicity, and the post-MPT 100 ka “world”, that responds non-linearly to the combination of the orbital forcings. My PhD results suggest that the impact of the obliquity forcing is pervasive in the post-MPT world, at orbital and sub-orbital scale, on (i) the magnitude of centennial-scale carbon cycle variations, (ii) the specific shape of the MIS 7 and (iii) on the amplification of the post-MPT climatic cycles through its long-term frequency.

On the interplay between timescales and temporal periods. This study is restricted to the climate of the past 2 Ma, and, within this manuscript, the different chapters are focused on specific time periods that are investigated at different timescales. Nevertheless, an interplay between the different periods and timescales considered have been evidenced: (i) the MPT, while occurring somewhere between 1.2-0.8 Ma, is likely influence by a long-term gradual trend in the internal climate and should be considered on the global scope of the establishment of the Pleistocene climate (*Chapter 3*). (ii) An interplay between the millennial-scale variability and the glacial terminations has been suggested (*Chapter 4*). (iii) The investigation of the MIS 7 has underlined similarities in amplitude and periodicity with interglacials occurring before the MPT (~1.6-1.2 Ma) (*Chapter 5*). (iv) The orbital context directly impacts the amplitude of the carbon cycle variations at centennial-scale, while their variations are itself driven by

millennial-scale events (*Chapter 6*). The interplay between the climatic variations occurring at different timescales appears thus as a main characteristic of the Pleistocene climate.

Hence, my results have underlined two main characteristics of the interactions and variations of the carbon cycle and the climate during the Pleistocene:

- ✦ The pervasive role of the orbital forcing in the climate and the carbon cycle variations regardless of the timescale considered.
- ✦ An interplay between the processes acting at different timescales on the carbon cycle-climate interactions.

General references

- Abe-Ouchi, A., Saito, F., Kawamura, K., Raymo, M. E., Okuno, J. I., Takahashi, K., & Blatter, H. (2013). Insolation-driven 100,000-year glacial cycles and hysteresis of ice-sheet volume. *nature*, *500*(7461), 190-193.
- Adams, B. A., Whipple, K. X., Forte, A. M., Heimsath, A. M., & Hodges, K. V. (2020). Climate controls on erosion in tectonically active landscapes. *Science Advances*, *6*(42), eaaz3166.
- Ahn, J., Wahlen, M., Deck, B. L., Brook, E. J., Mayewski, P. A., Taylor, K. C., & White, J. W. (2004). A record of atmospheric CO₂ during the last 40,000 years from the Siple Dome, Antarctica ice core. *Journal of Geophysical Research: Atmospheres*, *109*(D13).
- Ahn, J., Brook, E. J., & Howell, K. (2009). A high-precision method for measurement of paleoatmospheric CO₂ in small polar ice samples. *Journal of Glaciology*, *55*(191), 499-506.
- Ahn, J., Brook, E. J., Mitchell, L., Rosen, J., McConnell, J. R., Taylor, K., ... & Rubino, M. (2012). Atmospheric CO₂ over the last 1000 years: A high-resolution record from the West Antarctic Ice Sheet (WAIS) Divide ice core. *Global Biogeochemical Cycles*, *26*(2).
- Alden, W. C. (1932). Glacial geology of the central states (No. 26). US Government Printing Office.
- Anderson, R. F., Ali, S., Bradtmiller, L. I., Nielsen, S. H. H., Fleisher, M. Q., Anderson, B. E., & Burckle, L. H. (2009). Wind-driven upwelling in the Southern Ocean and the deglacial rise in atmospheric CO₂. *science*, *323*(5920), 1443-1448.
- Archer, D., Martin, P., Buffett, B., Brovkin, V., Rahmstorf, S., & Ganopolski, A. (2004). The importance of ocean temperature to global biogeochemistry. *Earth and Planetary Science Letters*, *222*(2), 333-348.
- Armijo, R., Lacassin, R., Coudurier-Curveur, A., & Carrizo, D. (2015). Coupled tectonic evolution of Andean orogeny and global climate. *Earth-Science Reviews*, *143*, 1-35.
- Arrhenius, S. (1896). XXXI. On the influence of carbonic acid in the air upon the temperature of the ground. *The London, Edinburgh, and Dublin Philosophical Magazine and Journal of Science*, *41*(251), 237-276.
- Bader, J., Jungclaus, J., Krivova, N., Lorenz, S., Maycock, A., Raddatz, T., ... & Claussen, M. (2020). Global temperature modes shed light on the Holocene temperature conundrum. *Nature Communications*, *11*(1), 4726.

- Barbante, C., Barnola, J. M., Becagli, S., Beer, J., Bigler, M., Boutron, C., ... & Wolff, E. (2006). One-to-one coupling of glacial climate variability in Greenland and Antarctica. *Nature*, *444*(7116), 195-198.
- Barker, S., Diz, P., Vautravers, M. J., Pike, J., Knorr, G., Hall, I. R., & Broecker, W. S. (2009). Interhemispheric Atlantic seesaw response during the last deglaciation. *Nature*, *457*(7233), 1097-1102.
- Barker, S., & Knorr, G. (2021). Millennial scale feedbacks determine the shape and rapidity of glacial termination. *Nature Communications*, *12*(1), 2273.
- Barnola, J. M. (1984). *Etude des variations passées du CO₂ atmosphérique à partir de l'analyse de l'air piégé dans la glace: détermination du niveau pré-industriel, description de la transition âge glaciaire-holocène* (Doctoral dissertation, Université Scientifique et Médicale de Grenoble).
- Barnola, J. M., Raynaud, D. Y. S. N., Korotkevich, Y. S., & Lorius, C. (1987). Vostok ice core provides 160,000-year record of atmospheric CO₂. *Nature*, *329*(6138), 408-414.
- Barnola, J. M., Pimienta, P., Raynaud, D., & Korotkevich, Y. S. (1991). CO₂-climate relationship as deduced from the Vostok ice core: A re-examination based on new measurements and on a re-evaluation of the air dating. *Tellus B*, *43*(2), 83-90.
- Bauska, T. K., Brook, E. J., Marcott, S. A., Baggenstos, D., Shackleton, S., Severinghaus, J. P., & Petrenko, V. V. (2018). Controls on millennial-scale atmospheric CO₂ variability during the last glacial period. *Geophysical Research Letters*, *45*(15), 7731-7740.
- Bauska, T. K., Marcott, S. A., & Brook, E. J. (2021). Abrupt changes in the global carbon cycle during the last glacial period. *Nature Geoscience*, *14*(2), 91-96.
- Bazin, L., Landais, A., Lemieux-Dudon, B., Toyé Mahamadou Kele, H., Veres, D., Parrenin, F., ... & Wolff, E. (2013). An optimized multi-proxy, multi-site Antarctic ice and gas orbital chronology (AICC2012): 120–800 ka. *Climate of the Past*, *9*(4), 1715-1731.
- Bazin et al., (2019). Last Interglacial temperature changes at 127 ka in North Atlantic using a new coherent chronological framework based on tephra and paleomagnetic constraints. PAGES-QUIGS workshop on “Warm extremes – Marine isotope stage 5e and its relevance to the future”, Cambridge UK.
- Bekaert, D. V., Blard, P. H., Raoult, Y., Pik, R., Kipfer, R., Seltzer, A. M., ... & Marty, B. (2023). Last glacial maximum cooling of 9° C in continental Europe from a 40 kyr-long noble gas paleothermometry record. *Quaternary Science Reviews*, *310*, 108123..
- Bellier, B. (2004). *Etude des variations du cycle du carbone au cours de l'Holocène à partir de l'analyse couplée CO₂-CH₄ piégés dans les glaces polaires* (Doctoral dissertation, Université Joseph-Fourier-Grenoble I).
- Bereiter, B., Stocker, T. F., & Fischer, H. (2013). A centrifugal ice microtome for measurements of atmospheric CO₂ on air trapped in polar ice cores. *Atmospheric Measurement Techniques*, *6*(2), 251-262.

- Bereiter, B., Eggleston, S., Schmitt, J., Nehrbass-Ahles, C., Stocker, T. F., Fischer, H., ... & Chappellaz, J. (2015). Revision of the EPICA Dome C CO₂ record from 800 to 600 kyr before present. *Geophysical Research Letters*, *42*(2), 542-549.
- Berends, C. J., Köhler, P., Lourens, L. J., & Van de Wal, R. S. W. (2021). On the cause of the Mid-Pleistocene transition.
- Berends, C. J., De Boer, B., & Van De Wal, R. S. (2021b). Reconstructing the evolution of ice sheets, sea level, and atmospheric CO₂ during the past 3.6 million years. *Climate of the Past*, *17*(1), 361-377.
- Berger, A. (1988). Milankovitch theory and climate. *Reviews of geophysics*, *26*(4), 624-657.
- Berner, W., Oeschger, H., & Stauffer, B. (1980). Information on the CO₂ cycle from ice core studies. *Radiocarbon*, *22*(2), 227-235.
- Bintanja, R., & Van de Wal, R. S. W. (2008). North American ice-sheet dynamics and the onset of 100,000-year glacial cycles. *Nature*, *454*(7206), 869-872.
- Bond, G., Heinrich, H., Broecker, W., Labeyrie, L., McManus, J., Andrews, J., ... & Ivy, S. (1992). Evidence for massive discharges of icebergs into the North Atlantic ocean during the last glacial period. *Nature*, *360*(6401), 245-249.
- Bordes, C. (1999). Automatisation de l'extraction du méthane des glaces polaires. Grenoble, Stage de DEA, LGGE.
- Bouchet, M., Landais, A., Grisart, A., Parrenin, F., Prié, F., Jacob, R., ... & Yang, G. M. (under review). The AICC2023 chronological framework and associated timescale for the EPICA Dome C ice core. *EGUsphere*, *2023*, 1-39.
- Bouttes, N. (2010). *L'évolution du cycle du carbone au cours du Quaternaire* (Doctoral dissertation, Paris 6).
- Bouttes, N., Swingedouw, D., Roche, D. M., Sanchez-Goni, M. F., & Crosta, X. (2016). Response of the carbon cycle to the different orbital configurations of the last 9 interglacials. *Clim. Past*.
- Bouttes, N., Lhardy, F., Quiquet, A., Paillard, D., Goosse, H., & Roche, D. M. (2023). Deglacial climate changes as forced by different ice sheet reconstructions. *Climate of the Past*, *19*(5), 1027-1042.
- Bova, S., Rosenthal, Y., Liu, Z., Godad, S. P., & Yan, M. (2021). Seasonal origin of the thermal maxima at the Holocene and the last interglacial. *Nature*, *589*(7843), 548-553.
- Bréant, C., Martinerie, P., Orsi, A., Arnaud, L., & Landais, A. (2017). Modelling firn thickness evolution during the last deglaciation: constraints on sensitivity to temperature and impurities. *Climate of the Past*, *13*(7), 833-853.
- Bréant, C., Landais, A., Orsi, A., Martinerie, P., Extier, T., Prié, F., ... & Leuenberger, M. (2019). Unveiling the anatomy of Termination 3 using water and air isotopes in the Dome C ice core, East Antarctica. *Quaternary Science Reviews*, *211*, 156-165.

- Broecker, W. S., & Van Donk, J. (1970). Insolation changes, ice volumes, and the O18 record in deep-sea cores. *Reviews of Geophysics*, 8(1), 169-198.
- Broecker, W. S. (1998). Paleocean circulation during the last deglaciation: a bipolar seesaw?. *Paleoceanography*, 13(2), 119-121.
- Broecker, W. S., Denton, G. H., Edwards, R. L., Cheng, H., Alley, R. B., & Putnam, A. E. (2010). Putting the Younger Dryas cold event into context. *Quaternary Science Reviews*, 29(9-10), 1078-1081.
- Buizert, C., Sigl, M., Severi, M., Markle, B. R., Wettstein, J. J., McConnell, J. R., ... & Steig, E. J. (2018). Abrupt ice-age shifts in southern westerly winds and Antarctic climate forced from the north. *Nature*, 563(7733), 681-685.
- Buizert, C., Fudge, T. J., Roberts, W. H., Steig, E. J., Sherriff-Tadano, S., Ritz, C., ... & Schwander, J. (2021). Antarctic surface temperature and elevation during the Last Glacial Maximum. *Science*, 372(6546), 1097-1101.
- Bunn, A. G., Goetz, S. J., Kimball, J. S., & Zhang, K. (2007). Northern high-latitude ecosystems respond to climate change. *Eos, Transactions American Geophysical Union*, 88(34), 333-335.
- Caillon, N., Severinghaus, J. P., Jouzel, J., Barnola, J. M., Kang, J., & Lipenkov, V. Y. (2003). Timing of atmospheric CO₂ and Antarctic temperature changes across Termination III. *Science*, 299(5613), 1728-1731.
- Calder, N. (1974). Arithmetic of ice ages. *Nature*, 252(5480), 216-218.
- Campen, R. K., Sowers, T., & Alley, R. B. (2003). Evidence of microbial consortia metabolizing within a low-latitude mountain glacier. *Geology*, 31(3), 231-234.
- Capron, E., Landais, A., Buiron, D., Cauquoin, A., Chappellaz, J., Debret, M., ... & Prié, F. (2013). Glacial-interglacial dynamics of Antarctic firn columns: comparison between simulations and ice core air- δ 15 N measurements. *Climate of the Past*, 9(3), 983-999.
- Capron, E., Govin, A., Stone, E. J., Masson-Delmotte, V., Mulitza, S., Otto-Bliesner, B., ... & Wolff, E. W. (2014). Temporal and spatial structure of multi-millennial temperature changes at high latitudes during the Last Interglacial. *Quaternary Science Reviews*, 103, 116-133.
- Capron, E., Govin, A., Feng, R., Otto-Bliesner, B. L., & Wolff, E. W. (2017). Critical evaluation of climate syntheses to benchmark CMIP6/PMIP4 127 ka Last Interglacial simulations in the high-latitude regions. *Quaternary Science Reviews*, 168, 137-150.
- Capron, E., Rasmussen, S. O., Popp, T. J., Erhardt, T., Fischer, H., Landais, A., ... & White, J. W. C. (2021). The anatomy of past abrupt warmings recorded in Greenland ice. *Nature Communications*, 12(1), 2106.
- Cavitte, M. G., Parrenin, F., Ritz, C., Young, D. A., Van Liefferinge, B., Blankenship, D. D., ... & Roberts, J. L. (2018). Accumulation patterns around Dome C, East Antarctica, in the last 73 kyr. *The Cryosphere*, 12(4), 1401-1414.

- Chalk, T. B., Hain, M. P., Foster, G. L., Rohling, E. J., Sexton, P. F., Badger, M. P., ... & Wilson, P. A. (2017). Causes of ice age intensification across the Mid-Pleistocene Transition. *Proceedings of the National Academy of Sciences*, *114*(50), 13114-13119.
- Chappellaz, J., Barnola, J. M., Raynaud, D., Korotkevich, Y. S., & Lorius, C. (1990). Ice-core record of atmospheric methane over the past 160,000 years. *Nature*, *345*(6271), 127-131.
- Chappellaz, J., Blunier, T., Raynaud, D., Barnola, J. M., Schwander, J., & Stauffert, B. (1993). Synchronous changes in atmospheric CH₄ and Greenland climate between 40 and 8 kyr BP. *Nature*, *366*(6454), 443-445.
- Cheng, H., Edwards, R. L., Broecker, W. S., Denton, G. H., Kong, X., Wang, Y., ... & Wang, X. (2009). Ice age terminations. *science*, *326*(5950), 248-252.
- Cheng, H., Edwards, R. L., Sinha, A., Spötl, C., Yi, L., Chen, S., ... & Zhang, H. (2016). The Asian monsoon over the past 640,000 years and ice age terminations. *nature*, *534*(7609), 640-646.
- Chowdhry Beeman, J., Gest, L., Parrenin, F., Raynaud, D., Fudge, T. J., Buizert, C., & Brook, E. J. (2019). Antarctic temperature and CO₂: near-synchrony yet variable phasing during the last deglaciation. *Climate of the Past*, *15*(3), 913-926.
- Clark, P. U., & Pollard, D. (1998). Origin of the middle Pleistocene transition by ice sheet erosion of regolith. *Paleoceanography*, *13*(1), 1-9.
- Clark, P. U., Archer, D., Pollard, D., Blum, J. D., Rial, J. A., Brovkin, V., ... & Roy, M. (2006). The middle Pleistocene transition: characteristics, mechanisms, and implications for long-term changes in atmospheric pCO₂. *Quaternary Science Reviews*, *25*(23-24), 3150-3184.
- Clark, P. U., Shakun, J. D., Marcott, S. A., Mix, A. C., Eby, M., Kulp, S., ... & Plattner, G. K. (2016). Consequences of twenty-first-century policy for multi-millennial climate and sea-level change. *Nature climate change*, *6*(4), 360-369.
- Claussen, M., Fohlmeister, J., Ganopolski, A., & Brovkin, V. (2006). Vegetation dynamics amplifies precessional forcing. *Geophysical Research Letters*, *33*(9).
- Coachman, L. K., Hemmingsen, E., & Scholander, P. F. (1956). Gas enclosures in a temperate glacier. *Tellus*, *8*(4), 415-423.
- Colleoni, F., Masina, S., Cherchi, A., & Iovino, D. (2014). Impact of orbital parameters and greenhouse gas on the climate of MIS 7 and MIS 5 glacial inception. *Journal of climate*, *27*(23), 8918-8933.
- Craig, H., & Chou, C. C. (1982). Methane: The record in polar ice cores. *Geophysical Research Letters*, *9*(11), 1221-1224.
- Craig, H., Horibe, Y., & Sowers, T. (1988). Gravitational separation of gases and isotopes in polar ice caps. *Science*, *242*(4886), 1675-1678.
- Dahl-Jensen, D. (2018). Drilling for the oldest ice. *Nature Geoscience*, *11*(10), 703-704.

- Dansgaard, W., Johnsen, S. J., Clausen, H. B., Dahl-Jensen, D., Gundestrup, N. S., Hammer, C. U., ... & Bond, G. (1993). Evidence for general instability of past climate from a 250-kyr ice-core record. *nature*, *364*(6434), 218-220.
- De Schepper, S., Gibbard, P. L., Salzmann, U., & Ehlers, J. (2014). A global synthesis of the marine and terrestrial evidence for glaciation during the Pliocene Epoch. *Earth-Science Reviews*, *135*, 83-102.
- Delmas, R. J., Ascencio, J. M., & Legrand, M. (1980). Polar ice evidence that atmospheric CO₂ 20,000 yr BP was 50% of present. *Nature*, *284*(5752), 155-157.
- Denton, G. H., Anderson, R. F., Toggweiler, J. R., Edwards, R. L., Schaefer, J. M., & Putnam, A. E. (2010). The last glacial termination. *science*, *328*(5986), 1652-1656.
- Desprat, S., Goñi, M. F. S., Turon, J. L., Duprat, J., Malaizé, B., & Peyrouquet, J. P. (2006). Climatic variability of Marine Isotope Stage 7: direct land–sea–ice correlation from a multiproxy analysis of a north-western Iberian margin deep-sea core. *Quaternary Science Reviews*, *25*(9-10), 1010-1026.
- Dutton, A., Bard, E., Antonioli, F., Esat, T. M., Lambeck, K., & McCulloch, M. T. (2009). Phasing and amplitude of sea-level and climate change during the penultimate interglacial. *Nature Geoscience*, *2*(5), 355-359.
- Dyez, K. A., Hönisch, B., & Schmidt, G. A. (2018). Early Pleistocene obliquity-scale pCO₂ variability at ~ 1.5 million years ago. *Paleoceanography and Paleoclimatology*, *33*(11), 1270-1291.
- Engels, S., & van Geel, B. (2012). The effects of changing solar activity on climate: contributions from palaeoclimatological studies. *Journal of Space Weather and Space Climate*, *2*, A09.
- Extier, T., Landais, A., Bréant, C., Prié, F., Bazin, L., Dreyfus, G., ... & Leuenberger, M. (2018). On the use of $\delta^{18}\text{O}_{\text{atm}}$ for ice core dating. *Quaternary science reviews*, *185*, 244-257.
- Fischer, H., Wahlen, M., Smith, J., Mastroianni, D., & Deck, B. (1999). Ice core records of atmospheric CO₂ around the last three glacial terminations. *Science*, *283*(5408), 1712-1714.
- Fischer, H., Meissner, K. J., Mix, A. C., Abram, N. J., Austermann, J., Brovkin, V., ... & Zhou, L. (2018). Paleoclimate constraints on a future warmer world. *Nature Geoscience*, *1*.
- Fletcher, W. J., Goni, M. F. S., Allen, J. R., Cheddadi, R., Combourieu-Nebout, N., Huntley, B., ... & Tzedakis, P. C. (2010). Millennial-scale variability during the last glacial in vegetation records from Europe. *Quaternary Science Reviews*, *29*(21-22), 2839-2864.
- Fogwill, C. J., Turney, C. S. M., Menviel, L., Baker, A., Weber, M. E., Ellis, B., ... & Cooper, A. (2020). Southern Ocean carbon sink enhanced by sea-ice feedbacks at the Antarctic Cold Reversal. *Nature Geoscience*, *13*(7), 489-497.

- Forster, P. M., Smith, C. J., Walsh, T., Lamb, W. F., Lamboll, R., Hauser, M., ... & Zhai, P. (2023). Indicators of Global Climate Change 2022: annual update of large-scale indicators of the state of the climate system and human influence. *Earth System Science Data*, *15*(6), 2295-2327.
- Fourteau, K., Faïn, X., Martinerie, P., Landais, A., Ekaykin, A. A., Lipenkov, V. Y., & Chappellaz, J. (2017). Analytical constraints on layered gas trapping and smoothing of atmospheric variability in ice under low-accumulation conditions. *Climate of the Past*, *13*(12), 1815-1830.
- Fourteau, K., Martinerie, P., Faïn, X., Schaller, C. F., Tuckwell, R., Löwe, H., ... & Lipenkov, V. Y. (2019). High-resolution methane concentrations measurements of the Lock-In firn and ice core (108–200m depth), PANGAEA.
- Galaasen, E. V., Ninnemann, U. S., Irvah, N., Kleiven, H. K. F., Rosenthal, Y., Kissel, C., & Hodell, D. A. (2014). Rapid reductions in North Atlantic Deep Water during the peak of the last interglacial period. *Science*, *343*(6175), 1129-1132.
- Galaasen, E. V., Ninnemann, U. S., Kessler, A., Irvah, N., Rosenthal, Y., Tjiputra, J., ... & Hodell, D. A. (2020). Interglacial instability of North Atlantic deep water ventilation. *Science*, *367*(6485), 1485-1489.
- Genthon, G., Barnola, J. M., Raynaud, D., Lorius, C., Jouzel, J., Barkov, N. I., ... & Kotlyakov, V. M. (1987). Vostok ice core: climatic response to CO₂ and orbital forcing changes over the last climatic cycle. *Nature*, *329*(6138), 414-418.
- Genty, D., Blamart, D., Ouahdi, R., Gilmour, M., Baker, A., Jouzel, J., & Van-Exter, S. (2003). Precise dating of Dansgaard–Oeschger climate oscillations in western Europe from stalagmite data. *Nature*, *421*(6925), 833-837.
- Gingerich, P. D. (2019). Temporal scaling of carbon emission and accumulation rates: modern anthropogenic emissions compared to estimates of PETM onset accumulation. *Paleoceanography and Paleoclimatology*, *34*(3), 329-335.
- Govin, A., Braconnot, P., Capron, E., Cortijo, E., Duplessy, J. C., Jansen, E., ... & Waelbroeck, C. (2012). Persistent influence of ice sheet melting on high northern latitude climate during the early Last Interglacial. *Climate of the Past*, *8*(2), 483-507.
- Gray, W. R., Rae, J. W., Wills, R. C., Shevenell, A. E., Taylor, B., Burke, A., ... & Lear, C. H. (2018). Deglacial upwelling, productivity and CO₂ outgassing in the North Pacific Ocean. *Nature Geoscience*, *11*(5), 340-344.
- Grisart, A. (2023). *Étude à haute résolution des cycles hydrologiques et climatiques à partir d'une carotte de glace d'Antarctique avec un focus sur les déglaciations* (Doctoral dissertation, Université Paris-Saclay).
- Haines, S. A., Mayewski, P. A., Kurbatov, A. V., Maasch, K. A., Sneed, S. B., Spaulding, N. E., ... & Bohleber, P. D. (2016). Ultra-high resolution snapshots of three multi-decadal periods in an Antarctic ice core. *Journal of Glaciology*, *62*(231), 31-36.

- Harrison, S. P., & Goñi, M. S. (2010). Global patterns of vegetation response to millennial-scale variability and rapid climate change during the last glacial period. *Quaternary Science Reviews*, *29*(21-22), 2957-2980.
- Hays, J. D., Imbrie, J., & Shackleton, N. J. (1976). Variations in the Earth's Orbit: Pacemaker of the Ice Ages: For 500,000 years, major climatic changes have followed variations in obliquity and precession. *science*, *194*(4270), 1121-1132.
- Hershey, O. H. (1893). The Pleistocene rock gorges of northwestern Illinois: Am. The American Geologist, *12*, 314.
- Hobart, B., Lisiecki, L. E., Rand, D., Lee, T., & Lawrence, C. E. (2023). Late Pleistocene 100-kyr glacial cycles paced by precession forcing of summer insolation. *Nature Geoscience*, *16*(8), 717-722.
- Hodell, D. A., Nicholl, J. A., Bontognali, T. R., Danino, S., Dorador, J., Dowdeswell, J. A., ... & Röhl, U. (2017). Anatomy of Heinrich Layer 1 and its role in the last deglaciation. *Paleoceanography*, *32*(3), 284-303.
- Hoenisch, B. (2021). Paleo-CO2 data archive (Version 1)[Data set].
- Hoffman, P. F., Kaufman, A. J., Halverson, G. P., & Schrag, D. P. (1998). A Neoproterozoic snowball earth. *science*, *281*(5381), 1342-1346.
- Hoffman, J. S., Clark, P. U., Parnell, A. C., & He, F. (2017). Regional and global sea-surface temperatures during the last interglaciation. *Science*, *355*(6322), 276-279.
- Hönisch, B., & Hemming, N. G. (2005). Surface ocean pH response to variations in pCO₂ through two full glacial cycles. *Earth and Planetary Science Letters*, *236*(1-2), 305-314.
- Huybers, P., & Wunsch, C. (2005). Obliquity pacing of the late Pleistocene glacial terminations. *Nature*, *434*(7032), 491-494.
- Imbrie, J., & Imbrie, J. Z. (1980). Modeling the climatic response to orbital variations. *Science*, *207*(4434), 943-953.
- Imbrie, J., Berger, A., Boyle, E. A., Clemens, S. C., Duffy, A., Howard, W. R., ... & Toggweiler, J. R. (1993). On the structure and origin of major glaciation cycles 2. The 100,000-year cycle. *Paleoceanography*, *8*(6), 699-735.
- Imbrie, J. Z., Imbrie-Moore, A., & Lisiecki, L. E. (2011). A phase-space model for Pleistocene ice volume. *Earth and Planetary Science Letters*, *307*(1-2), 94-102.
- IPCC, 2007: Climate Change 2007: Synthesis Report. Contribution of Working Group I to the Fourth Assessment Report of the Intergovernmental Panel on Climate Change, 2007 Solomon, S., D. Qin, M. Manning, Z. Chen, M. Marquis, K.B. Averyt, M. Tignor and H.L. Miller (eds.) Cambridge University Press, Cambridge, United Kingdom and New York, NY, USA.
- IPCC, 2013: Climate Change 2013: The Physical Science Basis. Contribution of Working Group I to the Fifth Assessment Report of the Intergovernmental Panel on Climate Change [Stocker, T.F., D. Qin, G.-K. Plattner, M. Tignor, S.K. Allen, J. Boschung, A. Nauels, Y. Xia, V. Bex

and P.M. Midgley (eds.)). Cambridge University Press, Cambridge, United Kingdom and New York, NY, USA, 1535 pp.

IPCC, 2018: Summary for Policymakers. In: Global Warming of 1.5°C. An IPCC Special Report on the impacts of global warming of 1.5°C above pre-industrial levels and related global greenhouse gas emission pathways, in the context of strengthening the global response to the threat of climate change, sustainable development, and efforts to eradicate poverty [Masson-Delmotte, V., P. Zhai, H.-O. Pörtner, D. Roberts, J. Skea, P.R. Shukla, A. Pirani, W. Moufouma-Okia, C. Péan, R. Pidcock, S. Connors, J.B.R. Matthews, Y. Chen, X. Zhou, M.I. Gomis, E. Lonnoy, T. Maycock, M. Tignor, and T. Waterfield (eds.)]. Cambridge University Press, Cambridge, UK and New York, NY, USA, pp. 3-24, doi:10.1017/9781009157940.001.

IPCC, 2021: Climate Change 2021: The Physical Science Basis. Contribution of Working Group I to the Sixth Assessment Report of the Intergovernmental Panel on Climate Change [Masson-Delmotte, V., P. Zhai, A. Pirani, S.L. Connors, C. Péan, S. Berger, N. Caud, Y. Chen, L. Goldfarb, M.I. Gomis, M. Huang, K. Leitzell, E. Lonnoy, J.B.R. Matthews, T.K. Maycock, T. Waterfield, O. Yelekçi, R. Yu, and B. Zhou (eds.)]. Cambridge University Press, Cambridge, United Kingdom and New York, NY, USA, In press, doi:10.1017/9781009157896.

Isson, T. T., Planavsky, N. J., Coogan, L. A., Stewart, E. M., Ague, J. J., Bolton, E. W., ... & Kump, L. R. (2020). Evolution of the global carbon cycle and climate regulation on earth. *Global Biogeochemical Cycles*, *34*(2), e2018GB006061.

Jamieson, S. S., Hulton, N. R., & Hagdorn, M. (2008). Modelling landscape evolution under ice sheets. *Geomorphology*, *97*(1-2), 91-108.

Joannin, S., Bassinot, F., Nebout, N. C., Peyron, O., & Beaudouin, C. (2011). Vegetation response to obliquity and precession forcing during the Mid-Pleistocene Transition in Western Mediterranean region (ODP site 976). *Quaternary Science Reviews*, *30*(3-4), 280-297.

Joussaume, S., & Taylor, K. E. (1995). Status of the paleoclimate modeling intercomparison project (PMIP). *World Meteorological Organization-Publications-WMO TD*, 425-430.

Jouzel, J., Lorius, C., Petit, J. R., Genthon, C., Barkov, N. I., Kotlyakov, V. M., & Petrov, V. M. (1987). Vostok ice core: a continuous isotope temperature record over the last climatic cycle (160,000 years). *Nature*, *329*(6138), 403-408.

Jouzel, J., Masson-Delmotte, V., Cattani, O., Dreyfus, G., Falourd, S., Hoffmann, G., ... & Wolff, E. W. (2007). Orbital and millennial Antarctic climate variability over the past 800,000 years. *science*, *317*(5839), 793-796.

Kageyama, M., Harrison, S. P., Kapsch, M. L., Lofverstrom, M., Lora, J. M., Mikolajewicz, U., ... & Zhu, J. (2021). The PMIP4 Last Glacial Maximum experiments: preliminary results and comparison with the PMIP3 simulations. *Climate of the Past*, *17*(3), 1065-1089.

Kapsch, M. L., Mikolajewicz, U., Ziemann, F., & Schannwell, C. (2022). Ocean response in transient simulations of the last deglaciation dominated by underlying ice-sheet reconstruction and method of meltwater distribution. *Geophysical Research Letters*, *49*(3), e2021GL096767.

- Kass, R. E., & Raftery, A. E. (1995). Bayes factors. *Journal of the American Statistical Association*, *90*(430), 773-795.
- Kaufmann, P., Fundel, F., Fischer, H., Bigler, M., Ruth, U., Udisti, R., ... & Wagenbach, D. (2010). Ammonium and non-sea salt sulfate in the EPICA ice cores as indicator of biological activity in the Southern Ocean. *Quaternary Science Reviews*, *29*(1-2), 313-323.
- Kawamura, K., Nakazawa, T., Aoki, S., Sugawara, S., Fujii, Y., & Watanabe, O. (2003). Atmospheric CO₂ variations over the last three glacial/interglacial climatic cycles deduced from the Dome Fuji deep ice core, Antarctica using a wet extraction technique. *Tellus B: Chemical and Physical Meteorology*, *55*(2), 126-137.
- Kawamura, K., Parrenin, F., Lisiecki, L., Uemura, R., Vimeux, F., Severinghaus, J. P., ... & Watanabe, O. (2007). Northern Hemisphere forcing of climatic cycles in Antarctica over the past 360,000 years. *Nature*, *448*(7156), 912-916.
- Keeling, R. F., & Keeling, C. D. (2017). Atmospheric monthly in situ CO₂ data-mauna loa observatory, Hawaii. *Scripps CO₂ program data*.
- Kennett, J. P., & Stott, L. D. (1991). Abrupt deep-sea warming, palaeoceanographic changes and benthic extinctions at the end of the Palaeocene. *Nature*, *353*(6341), 225-229.
- Kessler, A., Bouttes, N., Roche, D. M., Ninnemann, U. S., Galaasen, E. V., & Tjiputra, J. (2020). Atlantic meridional overturning circulation and $\delta^{13}\text{C}$ variability during the last interglacial. *Paleoceanography and Paleoclimatology*, *35*(5), e2019PA003818.
- Kindler, P., Guillevic, M., Baumgartner, M., Schwander, J., Landais, A., & Leuenberger, M. (2014). Temperature reconstruction from 10 to 120 kyr b2k from the NGRIP ice core. *Climate of the Past*, *10*(2), 887-902.
- Kohfeld, K. E., & Ridgwell, A. (2009). Glacial-interglacial variability in atmospheric CO₂. *Surface ocean-lower atmosphere processes*, *187*, 251-286.
- Köhler, P. (2023). Atmospheric CO₂ concentration based on boron isotopes versus simulations of the global carbon cycle during the Plio-Pleistocene. *Paleoceanography and Paleoclimatology*, *38*(2), e2022PA004439.
- Kravchinsky, V. A., Zhang, R., Borowiecki, R., Tarasov, P. E., van der Baan, M., Anwar, T., ... & Müller, S. (2021). Centennial scale climate oscillations from southern Siberia in the Last Glacial Maximum. *Quaternary Science Reviews*, *270*, 107171.
- Krissansen-Totton, J., Arney, G. N., & Catling, D. C. (2018). Constraining the climate and ocean pH of the early Earth with a geological carbon cycle model. *Proceedings of the National Academy of Sciences*, *115*(16), 4105-4110.
- Lambert, F., Bigler, M., Steffensen, J. P., Hutterli, M., & Fischer, H. (2012). Centennial mineral dust variability in high-resolution ice core data from Dome C, Antarctica. *Climate of the Past*, *8*(2), 609-623.

- Landais, A., Dreyfus, G., Capron, E., Masson-Delmotte, V., Sanchez-Goñi, M. F., Desprat, S., ... & Johnsen, S. (2010). What drives the millennial and orbital variations of $\delta^{18}\text{O}_{\text{atm}}$? *Quaternary Science Reviews*, *29*(1-2), 235-246.
- Landais, A., Dreyfus, G., Capron, E., Jouzel, J., Masson-Delmotte, V., Roche, D. M., ... & Teste, G. (2013). Two-phase change in CO₂, Antarctic temperature and global climate during Termination II. *Nature geoscience*, *6*(12), 1062-1065.
- Landais, A., Masson-Delmotte, V., Stenni, B., Selmo, E., Roche, D. M., Jouzel, J., ... & Popp, T. (2015). A review of the bipolar see-saw from synchronized and high resolution ice core water stable isotope records from Greenland and East Antarctica. *Quaternary Science Reviews*, *114*, 18-32.
- Landais, A., Stenni, B., Masson-Delmotte, V., Jouzel, J., Cauquoin, A., Fourré, E., ... & Grisart, A. (2021). Interglacial Antarctic–Southern Ocean climate decoupling due to moisture source area shifts. *Nature Geoscience*, *14*(12), 918-923.
- Lang, N., & Wolff, E. W. (2011). Interglacial and glacial variability from the last 800 ka in marine, ice and terrestrial archives. *Climate of the Past*, *7*(2), 361-380.
- Laskar, J., Robutel, P., Joutel, F., Gastineau, M., Correia, A. C., & Levrard, B. (2004). A long-term numerical solution for the insolation quantities of the Earth. *Astronomy & Astrophysics*, *428*(1), 261-285.
- Legrain, E., Parrenin, F., & Capron, E. (2023). A gradual change is more likely to have caused the Mid-Pleistocene Transition than an abrupt event. *Communications Earth & Environment*, *4*(1), 90.
- Legrain, E., Capron, E., Menviel, L., et al., (in revision). High obliquity favours centennial-scale variations in the carbon cycle.
- Leloup, G., & Paillard, D. (2022). Influence of the choice of insolation forcing on the results of a conceptual glacial cycle model. *Climate of the Past*, *18*(3), 547-558.
- Li, Z., & Fang, H. (2016). Impacts of climate change on water erosion: A review. *Earth-Science Reviews*, *163*, 94-117.
- Lin, D., Xia, J., & Wan, S. (2010). Climate warming and biomass accumulation of terrestrial plants: a meta-analysis. *New Phytologist*, *188*(1), 187-198.
- Lisiecki, L. E., & Raymo, M. E. (2005). A Pliocene-Pleistocene stack of 57 globally distributed benthic $\delta^{18}\text{O}$ records. *Paleoceanography*, *20*(1).
- Louergue, L. (2007). *Contraintes chronologiques et biogéochimiques grâce au méthane dans la glace naturelle: une application aux forages du projet EPICA* (Doctoral dissertation, Université Joseph-Fourier-Grenoble I).
- Louergue, L., Schilt, A., Spahni, R., Masson-Delmotte, V., Blunier, T., Lemieux, B., ... & Chappellaz, J. (2008). Orbital and millennial-scale features of atmospheric CH₄ over the past 800,000 years. *Nature*, *453*(7193), 383-386.

- Lüthi, D., Le Floch, M., Bereiter, B., Blunier, T., Barnola, J. M., Siegenthaler, U., ... & Stocker, T. F. (2008). High-resolution carbon dioxide concentration record 650,000–800,000 years before present. *nature*, *453*(7193), 379-382.
- Mächler, L., Baggenstos, D., Krauss, F., Schmitt, J., Bereiter, B., Walther, R., ... & Fischer, H. (2023). Laser-induced sublimation extraction for centimeter-resolution multi-species greenhouse gas analysis on ice cores. *Atmospheric Measurement Techniques*, *16*(2), 355-372.
- Marcott, S. A., Bauska, T. K., Buizert, C., Steig, E. J., Rosen, J. L., Cuffey, K. M., ... & Brook, E. J. (2014). Centennial-scale changes in the global carbon cycle during the last deglaciation. *Nature*, *514*(7524), 616-619.
- Markle, B. R., Steig, E. J., Roe, G. H., Winckler, G., & McConnell, J. R. (2018). Concomitant variability in high-latitude aerosols, water isotopes and the hydrologic cycle. *Nature Geoscience*, *11*(11), 853-859.
- Mann, M. E., Steinman, B. A., Brouillette, D. J., & Miller, S. K. (2021). Multidecadal climate oscillations during the past millennium driven by volcanic forcing. *Science*, *371*(6533), 1014-1019.
- Maslin, M. A., & Ridgwell, A. J. (2005). Mid-Pleistocene revolution and the ‘eccentricity myth’. *Geological Society, London, Special Publications*, *247*(1), 19-34.
- Masson, V., Cheddadi, R., Braconnot, P., Joussaume, S., Texier, D., & PMIP participants. (1999). Mid-Holocene climate in Europe: what can we infer from PMIP model-data comparisons?. *Climate Dynamics*, *15*, 163-182.
- Masson-Delmotte, V., Stenni, B., Pol, K., Braconnot, P., Cattani, O., Falourd, S., ... & Otto-Bliesner, B. (2010). EPICA Dome C record of glacial and interglacial intensities. *Quaternary Science Reviews*, *29*(1-2), 113-128.
- McClymont, E. L., Sosdian, S. M., Rosell-Melé, A., & Rosenthal, Y. (2013). Pleistocene sea-surface temperature evolution: Early cooling, delayed glacial intensification, and implications for the mid-Pleistocene climate transition. *Earth-Science Reviews*, *123*, 173-193.
- McConnell, J. R., Burke, A., Dunbar, N. W., Köhler, P., Thomas, J. L., Arienzo, M. M., ... & Winckler, G. (2017). Synchronous volcanic eruptions and abrupt climate change ~ 17.7 ka plausibly linked by stratospheric ozone depletion. *Proceedings of the National Academy of Sciences*, *114*(38), 10035-10040.
- Menking, J. A., Shackleton, S. A., Bauska, T. K., Buffen, A. M., Brook, E. J., Barker, S., ... & Petrenko, V. V. (2022). Multiple carbon cycle mechanisms associated with the glaciation of Marine Isotope Stage 4. *Nature communications*, *13*(1), 5443.
- Menviel, L., England, M. H., Meissner, K. J., Mouchet, A., & Yu, J. (2014). Atlantic-Pacific seesaw and its role in outgassing CO₂ during Heinrich events. *Paleoceanography*, *29*(1), 58-70.
- Milker, Y., Rachmayani, R., Weinkauff, M. F., Prange, M., Raitzsch, M., Schulz, M., & Kučera, M. (2015). Global Synthesis of Sea-Surface Temperature Trends During Marine Isotope Stage 11. *Integrated Analysis of Interglacial Climate Dynamics (INTERDYNAMIC)*, 13-18.

- Miller, K. G., Browning, J. V., Schmelz, W. J., Kopp, R. E., Mountain, G. S., & Wright, J. D. (2020). Cenozoic sea-level and cryospheric evolution from deep-sea geochemical and continental margin records. *Science advances*, *6*(20), eaaz1346.
- Monnin, E., Indermühle, A., Dällenbach, A., Flückiger, J., Stauffer, B., Stocker, T. F., ... & Barnola, J. M. (2001). Atmospheric CO₂ concentrations over the last glacial termination. *Science*, *291*(5501), 112-114.
- Nehrbass-Ahles, C., Shin, J., Schmitt, J., Bereiter, B., Joos, F., Schilt, A., ... & Stocker, T. F. (2020). Abrupt CO₂ release to the atmosphere under glacial and early interglacial climate conditions. *Science*, *369*(6506), 1000-1005.
- NGRIP project members. High-resolution record of Northern Hemisphere climate extending into the last interglacial period. *Nature*, 2004, vol. 431, no 7005, p. 147-151.
- Nyman, K. H., & Ditlevsen, P. D. (2019). The middle Pleistocene transition by frequency locking and slow ramping of internal period. *Climate Dynamics*, *53*(5-6), 3023-3038.
- Otto-Bliesner, B. L., Brady, E. C., Zhao, A., Brierley, C. M., Axford, Y., Capron, E., ... & Zheng, W. (2021). Large-scale features of Last Interglacial climate: results from evaluating the lig127k simulations for the Coupled Model Intercomparison Project (CMIP6)–Paleoclimate Modeling Intercomparison Project (PMIP4). *Climate of the Past*, *17*(1), 63-94.
- Paillard, D. (1998). The timing of Pleistocene glaciations from a simple multiple-state climate model. *Nature*, *391*(6665), 378-381.
- Paillard, D. (2015). Quaternary glaciations: from observations to theories. *Quaternary Science Reviews*, *107*, 11-24.
- Parrenin, F., & Paillard, D. (2003). Amplitude and phase of glacial cycles from a conceptual model. *Earth and Planetary Science Letters*, *214*(1-2), 243-250.
- Parrenin, F., Barnola, J. M., Beer, J., Blunier, T., Castellano, E., Chappellaz, J., ... & Wolff, E. (2007). The EDC3 chronology for the EPICA Dome C ice core. *Climate of the Past*, *3*(3), 485-497.
- Parrenin, F., & Paillard, D. (2012). Terminations VI and VIII (~ 530 and ~ 720 kyr BP) tell us the importance of obliquity and precession in the triggering of deglaciations. *Climate of the Past*, *8*(6), 2031-2037.
- Parrenin, F., Masson-Delmotte, V., Köhler, P., Raynaud, D., Paillard, D., Schwander, J., ... & Jouzel, J. (2013). Synchronous change of atmospheric CO₂ and Antarctic temperature during the last deglacial warming. *Science*, *339*(6123), 1060-1063.
- Past Interglacials Working Group of PAGES. (2016). Interglacials of the last 800,000 years. *Reviews of Geophysics*, *54*(1), 162-219.
- Pedro, J. B., Rasmussen, S. O., & Van Ommen, T. D. (2012). Tightened constraints on the time-lag between Antarctic temperature and CO₂ during the last deglaciation. *Climate of the Past*, *8*(4), 1213-1221.

- Pedro, J. B., Jochum, M., Buizert, C., He, F., Barker, S., & Rasmussen, S. O. (2018). Beyond the bipolar seesaw: Toward a process understanding of interhemispheric coupling. *Quaternary Science Reviews*, *192*, 27-46.
- Pedro, J. B., Andersson, C., Vettoretti, G., Voelker, A. H. L., Waelbroeck, C., Dokken, T. M., ... & Nisancioglu, K. H. (2022). Dansgaard-Oeschger and Heinrich event temperature anomalies in the North Atlantic set by sea ice, frontal position and thermocline structure. *Quaternary Science Reviews*, *289*, 107599.
- Petit, J. R., Jouzel, J., Raynaud, D., Barkov, N. I., Barnola, J. M., Basile, I., ... & Stievenard, M. (1999). Climate and atmospheric history of the past 420,000 years from the Vostok ice core, Antarctica. *Nature*, *399*(6735), 429-436.
- Rae, J. W., Burke, A., Robinson, L. F., Adkins, J. F., Chen, T., Cole, C., ... & Taylor, B. J. (2018). CO₂ storage and release in the deep Southern Ocean on millennial to centennial timescales. *Nature*, *562*(7728), 569-573.
- Rae, J. W., Zhang, Y. G., Liu, X., Foster, G. L., Stoll, H. M., & Whiteford, R. D. (2021). Atmospheric CO₂ over the past 66 million years from marine archives. *Annual Review of Earth and Planetary Sciences*, *49*, 609-641.
- Raftery, A. E. (1995). Bayesian model selection in social research. *Sociological methodology*, 111-163.
- Raynaud, D., & Delmas, R. (1977). Composition des gaz contenus dans la glace polaire.
- Raynaud, D., Delmas, R., Ascencio, J. M., & Legrand, M. (1982). Gas extraction from polar ice cores: a critical issue for studying the evolution of atmospheric CO₂ and ice-sheet surface elevation. *Annals of Glaciology*, *3*, 265-268.
- Rhodes, R. H., Faïn, X., Stowasser, C., Blunier, T., Chappellaz, J., McConnell, J. R., ... & Brook, E. J. (2013). Continuous methane measurements from a late Holocene Greenland ice core: Atmospheric and in-situ signals. *Earth and Planetary Science Letters*, *368*, 9-19.
- Rhodes, R. H., Brook, E. J., Chiang, J. C., Blunier, T., Maselli, O. J., McConnell, J. R., ... & Severinghaus, J. P. (2015). Enhanced tropical methane production in response to iceberg discharge in the North Atlantic. *Science*, *348*(6238), 1016-1019.
- Robbins, R. C., Cavanagh, L. A., Salas, L. J., & Robinson, E. (1973). Analysis of ancient atmospheres. *Journal of Geophysical Research*, *78*(24), 5341-5344.
- Ruddiman, W. F. (2006). Orbital changes and climate. *Quaternary Science Reviews*, *25*(23-24), 3092-3112.
- Sánchez-Goñi, M. F., Turon, J. L., Eynaud, F., & Gendreau, S. (2000). European climatic response to millennial-scale changes in the atmosphere-ocean system during the Last Glacial period. *Quaternary Research*, *54*(3), 394-403.
- Sánchez Goñi, M. F., Cacho, I., Turon, J. L., Guiot, J., Sierro, F. J., Peyrouquet, J. P., ... & Shackleton, N. J. (2002). Synchronicity between marine and terrestrial responses to millennial

scale climatic variability during the last glacial period in the Mediterranean region. *Climate dynamics*, 19, 95-105.

Sánchez Goñi, M. F., Extier, T., Polanco-Martínez, J. M., Zorzi, C., Rodrigues, T., & Bahr, A. (2023). Moist and warm conditions in Eurasia during the last glacial of the Middle Pleistocene Transition. *Nature Communications*, 14(1), 2700.

Schirrmeister, B. E., de Vos, J. M., Antonelli, A., & Bagheri, H. C. (2013). Evolution of multicellularity coincided with increased diversification of cyanobacteria and the Great Oxidation Event. *Proceedings of the National Academy of Sciences*, 110(5), 1791-1796.

Schmitt, J., Schneider, R., & Fischer, H. (2011). A sublimation technique for high-precision measurements of $\delta^{13}\text{C}$ CO₂ and mixing ratios of CO₂ and N₂O from air trapped in ice cores. *Atmospheric Measurement Techniques*, 4(7), 1445-1461.

Schmitt, J., Schneider, R., Elsig, J., Leuenberger, D., Lourantou, A., Chappellaz, J., ... & Fischer, H. (2012). Carbon isotope constraints on the deglacial CO₂ rise from ice cores. *Science*, 336(6082), 711-714.

Schmittner, A., Saenko, O. A., & Weaver, A. J. (2003). Coupling of the hemispheres in observations and simulations of glacial climate change. *Quaternary Science Reviews*, 22(5-7), 659-671.

Schneider, R., Schmitt, J., Köhler, P., Joos, F., & Fischer, H. (2013). A reconstruction of atmospheric carbon dioxide and its stable carbon isotopic composition from the penultimate glacial maximum to the last glacial inception. *Climate of the Past*, 9(6), 2507-2523.

Scholander, P. F., Kanwisher, J. W., & Nutt, D. C. (1956). Gases in icebergs. *Science*, 123(3186), 104-105.

Schuur, E. A., Abbott, B. W., Commane, R., Ernakovich, J., Euskirchen, E., Hugelius, G., ... & Turetsky, M. (2022). Permafrost and climate change: Carbon cycle feedbacks from the warming Arctic. *Annual Review of Environment and Resources*, 47, 343-371.

Schwander, J., & Stauffer, B. (1984). Age difference between polar ice and the air trapped in its bubbles. *Nature*, 311(5981), 45-47.

Schwander, J., Barnola, J. M., Andrié, C., Leuenberger, M., Ludin, A., Raynaud, D., & Stauffer, B. (1993). The age of the air in the firn and the ice at Summit, Greenland. *Journal of Geophysical Research: Atmospheres*, 98(D2), 2831-2838.

Severi, M., Becagli, S., Caiazzo, L., Nardin, R., Toccafondi, A., & Traversi, R. (2023). The ²³⁹Pu nuclear fallout as recorded in an Antarctic ice core drilled at Dome C (East Antarctica). *Chemosphere*, 329, 138674.

Shackleton, N. J., & Opdyke, N. D. (1973). Oxygen isotope and palaeomagnetic stratigraphy of Equatorial Pacific core V28-238: Oxygen isotope temperatures and ice volumes on a 105 year and 106 year scale. *Quaternary research*, 3(1), 39-55.

Shackleton, S., Seltzer, A., Baggenstos, D., & Lisiecki, L. E. (2023). Benthic $\delta^{18}\text{O}$ records Earth's energy imbalance. *Nature Geoscience*, 1-6.

- Shakun, J. D., Clark, P. U., He, F., Marcott, S. A., Mix, A. C., Liu, Z., ... & Bard, E. (2012). Global warming preceded by increasing carbon dioxide concentrations during the last deglaciation. *Nature*, *484*(7392), 49-54.
- Shakun, J. D., Lea, D. W., Lisiecki, L. E., & Raymo, M. E. (2015). An 800-kyr record of global surface ocean $\delta^{18}\text{O}$ and implications for ice volume-temperature coupling. *Earth and Planetary Science Letters*, *426*, 58-68.
- Shin, J. (2019). *Variations atmosphériques du CO₂ à l'échelle millénaire durant le stade isotopique MIS 6* (Doctoral dissertation, Université Grenoble Alpes).
- Shin, J., Nehrbass-Ahles, C., Grilli, R., Chowdhry Beeman, J., Parrenin, F., Teste, G., ... & Chappellaz, J. (2020). Millennial-scale atmospheric CO₂ variations during the Marine Isotope Stage 6 period (190–135 ka). *Climate of the Past*, *16*(6), 2203-2219.
- Shin, J., Ahn, J., Chowdhry Beeman, J., Lee, H. G., Seo, J. M., & Brook, E. J. (2022). Millennial variations in atmospheric CO₂ during the early Holocene (11.7–7.4 ka). *Climate of the Past*, *18*(9), 2063-2075.
- Sicard, M., de Boer, A. M., & Sime, L. C. (2022). Last Interglacial Arctic sea ice as simulated by the latest generation of climate models. *Past Global Changes Magazine*, *30*(2), 92-93.
- Sigman, D. M., Hain, M. P., & Haug, G. H. (2010). The polar ocean and glacial cycles in atmospheric CO₂ concentration. *Nature*, *466*(7302), 47-55.
- Silva, 2022. High-resolution reconstruction of atmospheric CO₂ concentrations during the last interglacial based on the EDC ice core. PhD dissertation, University of Bern.
- Soulet, G., Hilton, R. G., Garnett, M. H., Roylands, T., Klotz, S., Croissant, T., ... & Le Bouteiller, C. (2021). Temperature control on CO₂ emissions from the weathering of sedimentary rocks. *Nature Geoscience*, *14*(9), 665-671.
- Stocker, T. F., Wright, D. G., & Broecker, W. S. (1992). The influence of high-latitude surface forcing on the global thermohaline circulation. *Paleoceanography*, *7*(5), 529-541.
- Stocker, T. F., & Johnsen, S. J. (2003). A minimum thermodynamic model for the bipolar seesaw. *Paleoceanography*, *18*(4).
- Stone, E. J., Capron, E., Lunt, D. J., Payne, A. J., Singarayer, J. S., Valdes, P. J., & Wolff, E. W. (2016). Impact of meltwater on high-latitude early Last Interglacial climate. *Climate of the Past*, *12*(9), 1919-1932.
- Tierney, J. E., Zhu, J., King, J., Malevich, S. B., Hakim, G. J., & Poulsen, C. J. (2020). Glacial cooling and climate sensitivity revisited. *Nature*, *584*(7822), 569-573.
- Toucanne, S., Naughton, F., Rodrigues, T., Vázquez-Riveiros, N., & Goñi, M. F. S. (2022). Abrupt (or millennial or suborbital) climatic variability: Heinrich events/stadials. In *European Glacial Landscapes* (pp. 181-187). Elsevier.
- Tzedakis, P. C., Crucifix, M., Mitsui, T., & Wolff, E. W. (2017). A simple rule to determine which insolation cycles lead to interglacials. *Nature*, *542*(7642), 427-432.

- Urey, H. C. (1952). On the early chemical history of the earth and the origin of life. *Proceedings of the National Academy of Sciences*, 38(4), 351-363.
- Van de Wal, R. S. W., De Boer, B., Lourens, L. J., Köhler, P., & Bintanja, R. (2011). Reconstruction of a continuous high-resolution CO₂ record over the past 20 million years. *Climate of the Past*, 7(4), 1459-1469.
- Veres, D., Bazin, L., Landais, A., Toyé Mahamadou Kele, H., Lemieux-Dudon, B., Parrenin, F., ... & Wolff, E. W. (2013). The Antarctic ice core chronology (AICC2012): an optimized multi-parameter and multi-site dating approach for the last 120 thousand years. *Climate of the Past*, 9(4), 1733-1748.
- Vimeux, F., Masson, V., Jouzel, J., Stievenard, M., & Petit, J. R. (1999). Glacial–interglacial changes in ocean surface conditions in the Southern Hemisphere. *Nature*, 398(6726), 410-413.
- Watanabe, Y., Abe-Ouchi, A., Saito, F., Kino, K., O’ishi, R., Ito, T., ... & Chan, W. L. (2023). Astronomical forcing shaped the timing of early Pleistocene glacial cycles. *Communications Earth & Environment*, 4(1), 113.
- Watson, A. J., & Naveira Garabato, A. C. (2006). The role of Southern Ocean mixing and upwelling in glacial-interglacial atmospheric CO₂ change. *Tellus B: Chemical and Physical Meteorology*, 58(1), 73-87.
- Weltzin, J. F., Loik, M. E., Schwinning, S., Williams, D. G., Fay, P. A., Haddad, B. M., ... & Zak, J. C. (2003). Assessing the response of terrestrial ecosystems to potential changes in precipitation. *Bioscience*, 53(10), 941-952.
- Westerhold, T., Marwan, N., Drury, A. J., Liebrand, D., Agnini, C., Anagnostou, E., ... & Zachos, J. C. (2020). An astronomically dated record of Earth’s climate and its predictability over the last 66 million years. *Science*, 369(6509), 1383-1387.
- Willeit, M., Ganopolski, A., Calov, R., & Brovkin, V. (2019). Mid-Pleistocene transition in glacial cycles explained by declining CO₂ and regolith removal. *Science Advances*, 5(4), eaav7337.
- Wolff, E. W., Fischer, H., Fundel, F., Ruth, U., Twarloh, B., Littot, G. C., ... & Gaspari, V. (2006). Southern Ocean sea-ice extent, productivity and iron flux over the past eight glacial cycles. *Nature*, 440(7083), 491-496.
- Wolff, E. W., Fischer, H., & Röthlisberger, R. (2009). Glacial terminations as southern warmings without northern control. *Nature Geoscience*, 2(3), 206-209.
- Wolff, E. W., Chappellaz, J., Blunier, T., Rasmussen, S. O., & Svensson, A. (2010). Millennial-scale variability during the last glacial: The ice core record. *Quaternary Science Reviews*, 29(21-22), 2828-2838.
- Wolff, E. W., Burke, A., Crick, L., Doyle, E. A., Innes, H. M., Mahony, S. H., ... & Sparks, R. S. J. (2023). Frequency of large volcanic eruptions over the past 200 000 years. *Climate of the Past*, 19(1), 23-33.

- Yamamoto, M., Clemens, S. C., Seki, O., Tsuchiya, Y., Huang, Y., O'ishi, R., & Abe-Ouchi, A. (2022). Increased interglacial atmospheric CO₂ levels followed the mid-Pleistocene Transition. *Nature Geoscience*, 15(4), 307-313.
- Yan, Y., Bender, M. L., Brook, E. J., Clifford, H. M., Kemeny, P. C., Kurbatov, A. V., ... & Higgins, J. A. (2019). Two-million-year-old snapshots of atmospheric gases from Antarctic ice. *Nature*, 574(7780), 663-666.
- Yao, T., Shi, Y., & Thompson, L. G. (1997). High resolution record of paleoclimate since the Little Ice Age from the Tibetan ice cores. *Quaternary International*, 37, 19-23.
- Yehudai, M., Kim, J., Pena, L. D., Jaume-Seguí, M., Knudson, K. P., Bolge, L., ... & Goldstein, S. L. (2021). Evidence for a Northern Hemispheric trigger of the 100,000-y glacial cyclicity. *Proceedings of the National Academy of Sciences*, 118(46), e2020260118.
- Yin, Q. Z., & Berger, A. (2010). Insolation and CO₂ contribution to the interglacial climate before and after the Mid-Brunhes Event. *Nature Geoscience*, 3(4), 243-246.
- Yin, Q. Z., & Berger, A. (2012). Individual contribution of insolation and CO₂ to the interglacial climates of the past 800,000 years. *Climate dynamics*, 38, 709-724.
- Zhang, S., Bai, X., Zhao, C., Tan, Q., Luo, G., Wang, J., ... & Xi, H. (2021). Global CO₂ consumption by silicate rock chemical weathering: its past and future. *Earth's Future*, 9(5), e2020EF001938.
- Zhang, H., Sjolte, J., Lu, Z., Liu, J., Sun, W., & Wan, L. (2023). Asymmetric changes in temperature in the Arctic during the Holocene based on a transient run with the Community Earth System Model (CESM). *Climate of the Past*, 19(3), 665-680.

Appendices

- ✦ Appendix A is a publication presenting the new chronology of reference for ice cores AICC2023 and is directly related to the PhD project.
- ✦ Appendices B, C and D are three papers related to the research project I carried out during my Master thesis and that I pursued in parallel of my PhD project.

Appendix A : Co-authorship : Bouchet, M., Landais, A., Grisart, A., Parrenin, F., Prié, F., Jacob, R., Fourré, E., Capron, E., Raynaud, D., Lipenkov, V. Y., Loutre, M.-F., Extier, T., Svensson, A., Legrain, E., Martinerie, P., Leuenberger, M., Jiang, W., Ritterbusch, F., Lu, Z.-T., and Yang, G.-M.: The Antarctic Ice Core Chronology 2023 (AICC2023) chronological framework and associated timescale for the European Project for Ice Coring in Antarctica (EPICA) Dome C ice core, *Clim. Past*, 19, 2257–2286, <https://doi.org/10.5194/cp-19-2257-2023>, 2023.

Appendix B : First-author publication : Legrain, E., Blard, P. H., & Charreau, J. (2022). Glacial equilibrium line–based relationship for paleoclimate reconstructions (Sierra Nevada, USA). *Quaternary Research*, 109, 183-194.

Appendix C : First-author publication: Legrain, E., Blard, P. H., Kageyama, M., Charreau, J., Leduc, G., Bourdin, S., & Bekaert, D. V. (2023). Moisture amplification of the high-altitude deglacial warming. *Quaternary Science Reviews*, 318, 108303.

Appendix D : Co-authorship : Bekaert, D. V., Blard, P. H., Raoult, Y., Pik, R., Kipfer, R., Seltzer, A. M., Legrain, E. & Marty, B. (2023). Last glacial maximum cooling of 9° C in continental Europe from a 40 kyr-long noble gas paleothermometry record. *Quaternary Science Reviews*, 310, 108123.

Appendix A : Co-atorship : Bouchet, M., Landais, A., Grisart, A., Parrenin, F., Prié, F., Jacob, R., Fourré, E., Capron, E., Raynaud, D., Lipenkov, V. Y., Loutre, M.-F., Extier, T., Svensson, A., Legrain, E., Martinerie, P., Leuenberger, M., Jiang, W., Ritterbusch, F., Lu, Z.-T., and Yang, G.-M.: The Antarctic Ice Core Chronology 2023 (AICC2023) chronological framework and associated timescale for the European Project for Ice Coring in Antarctica (EPICA) Dome C ice core, *Clim. Past*, 19, 2257–2286, <https://doi.org/10.5194/cp-19-2257-2023>, 2023.



The Antarctic Ice Core Chronology 2023 (AICC2023) chronological framework and associated timescale for the European Project for Ice Coring in Antarctica (EPICA) Dome C ice core

Marie Bouchet¹, Amaëlle Landais¹, Antoine Grisart¹, Frédéric Parrenin², Frédéric Prié¹, Roxanne Jacob¹,
Elise Fourné¹, Emilie Capron², Dominique Raynaud², Vladimir Ya Lipenkov³, Marie-France Loutre^{4,5},
Thomas Extier⁶, Anders Svensson⁷, Etienne Legrain², Patricia Martinerie², Markus Leuenberger⁸, Wei Jiang⁹,
Florian Ritterbusch⁹, Zheng-Tian Lu⁹, and Guo-Min Yang⁹

¹Laboratory for Sciences of Climate and Environment, LSCE-IPSL, CEA-CNRS-UVSQ,
University of Paris-Saclay, 91190 Gif-sur-Yvette, France

²Institute of Environmental Geosciences, CNRS, INRAE, IRD, Grenoble INP,
University of Grenoble Alpes, 38000 Grenoble, France

³Arctic and Antarctic Research Institute, 199397 St. Petersburg, Russia

⁴PAGES International Project Office, University of Bern, 3012 Bern, Switzerland

⁵Georges Lemaître Centre for Earth and Climate Research (TECLIM), Earth and Life Institute,
Catholic University of Louvain (UCL), 1348 Louvain-la-Neuve, Belgium

⁶EPOC, UMR 5805, CNRS, University of Bordeaux, 33600 Pessac, France

⁷Physics of Ice, Climate, and Earth, Niels Bohr Institute, University of Copenhagen, 2100 Copenhagen, Denmark

⁸Climate and Environmental Physics, Physics Institute, and Oeschger Centre for Climate Change Research,
University of Bern, 3012 Bern, Switzerland

⁹Department of Engineering and Applied Physics, Hefei National Laboratory,
University of Science and Technology of China, Hefei, 230026, China

Correspondence: Marie Bouchet (marie.bouchet@lsce.ipsl.fr)

Received: 22 May 2023 – Discussion started: 26 May 2023

Revised: 21 September 2023 – Accepted: 25 September 2023 – Published: 10 November 2023

Abstract. The EPICA (European Project for Ice Coring in Antarctica) Dome C (EDC) ice core drilling in East Antarctica reaches a depth of 3260 m. The reference EDC chronology, the AICC2012 (Antarctic Ice Core Chronology 2012), provides an age vs. depth relationship covering the last 800 kyr (thousands of years), with an absolute uncertainty rising up to 8000 years at the bottom of the ice core. The origins of this relatively large uncertainty are twofold: (1) the $\delta^{18}\text{O}_{\text{atm}}$, $\delta\text{O}_2/\text{N}_2$ and total air content (TAC) records are poorly resolved and show large gaps over the last 800 kyr, and (2) large uncertainties are associated with their orbital targets. Here, we present new highly resolved $\delta^{18}\text{O}_{\text{atm}}$, $\delta\text{O}_2/\text{N}_2$ and $\delta^{15}\text{N}$ measurements for the EDC ice core covering the last five glacial–interglacial transitions; a new low-

resolution TAC record over the period 440–800 ka BP (ka: 1000 years before 1950); and novel absolute ^{81}Kr ages. We have compiled chronological and glaciological information including novel orbital age markers from new data on the EDC ice core as well as accurate firn modeling estimates in a Bayesian dating tool to construct the new AICC2023 chronology. For the first time, three orbital tools are used simultaneously. Hence, it is possible to observe that they are consistent with each other and with the other age markers over most of the last 800 kyr (70 %). This, in turn, gives us confidence in the new AICC2023 chronology. The average uncertainty in the ice chronology is reduced from 1700 to 900 years in AICC2023 over the last 800 kyr (1σ). The new timescale diverges from AICC2012 and suggests age shifts

reaching 3800 years towards older ages over marine isotope stages (MISs) 5, 11 and 19. But the coherency between the new AICC2023 timescale and independent chronologies of other archives (Italian Lacustrine succession from Sulmona Basin, Dome Fuji ice core and northern Alpine speleothems) is improved by 1000 to 2000 years over these time intervals.

1 Introduction

1.1 Building age scales for deep polar ice cores

1.1.1 Motivation

Deep polar ice cores are unique archives of past climate, and their investigation is valuable to study mechanisms governing the Earth's climate variations. Precise chronologies are key to identifying the successions and lengths of climatic events, along with exploring phase relationships between the external forcing (changes in the Earth's orbit) and the diverse climatic responses (variations in temperature and atmospheric greenhouse gas concentrations). To date ice cores, we need to construct two separate chronologies: one for the ice and one for the younger air trapped in bubbles. Due to the thinning of horizontal ice layers as depth increases, a wide time span of paleoclimatic information is stored within the deepest part of the ice sheet. Therefore, many of the ice core community's ongoing efforts focus on improving deep-ice-core timescales for ice and gas phases, as well as extending them further back in time (Crotti et al., 2021; Oyabu et al., 2022). Ice cores drilled at sites characterized by a high accumulation rate of snow at the surface (10 to 30 cm a⁻¹) can be dated by counting ice layers deposited year after year (Svensson et al., 2008; Sigl et al., 2016). In contrast, East Antarctica sites are associated with very low accumulation rates (1 to 5 cm a⁻¹), which prevent annual layers from being identified and counted. As a consequence, chronologies of ice cores at low-accumulation sites are commonly established using ice flow and accumulation models (Nye, 1959; Schwander et al., 2001), then tied up with chronological and glaciological constraints (Veres et al., 2013; Bazin et al., 2013; Parrenin et al., 2017).

1.1.2 Glaciological modeling

Glaciological modeling has been historically used to date Greenlandic and Antarctic ice cores. A unidimensional ice flow model was first applied to the Camp Century ice core (Dansgaard and Johnsen, 1969) and later to other ice cores such as the ones drilled at EPICA (European Project for Ice Coring in Antarctica) Dome C (EDC) and Dome Fuji (EPICA Community Members, 2004; Parrenin et al., 2007a). First, water isotope (δD or $\delta^{18}O$) measurements provide estimates of past evolution of the accumulation rate of snow and temperature at the surface. Then, an ice flow model (Par-

renin et al., 2004) takes as inputs past accumulation together with a vertical velocity–depth profile through the ice sheet to determine the thinning of annual snow/ice layers in time and therefore the ice timescale. This approach is very sensitive to some poorly known parameters including boundary conditions such as bedrock topography, geothermal properties or subglacial sliding. For this reason, the glaciological modeling approach is complemented with chronological constraints (gas or ice age known at certain depth levels).

1.1.3 Chronological constraints derived from measurements

Chronological constraints obtained either by measurement of radionuclides or by synchronization to a curve of reference are established for both ice and gas timescales. For building long chronologies, some time constraints can be obtained from the ¹⁰Be series measured in ice. The ¹⁰Be cosmogenic nuclide is produced at different rates depending on the solar activity, and its arrival on Earth is modulated by the strength of the Earth's magnetic field (Yiou et al., 1997; Raisbeck et al., 2007; Heaton et al., 2021). Some links hence exist between ¹⁰Be flux and precisely dated magnetic events such as the Laschamp excursion, an abrupt decline in the geomagnetic field magnitude occurring at about 41 ka BP and visible as a positive excursion in the ¹⁰Be flux records in ice cores (Lascu et al., 2016; Raisbeck et al., 2017). ⁴⁰Ar measurements in the gas phase of Antarctic ice cores also provide dating constraints for old ice, especially for non-continuous stratigraphic sequences (Yan et al., 2019). ⁴⁰Ar is produced in solid earth by the radioactive decay of ⁴⁰K, leading to an increasing concentration of ⁴⁰Ar in the atmosphere at a rate of $0.066 \pm 0.006 \text{‰ Myr}^{-1}$ (Bender et al., 2008). Recently, the possibility of measuring ⁸¹Kr in ice samples of a few kilograms gave a new absolute dating tool for ice cores (Jiang et al., 2020). ⁸¹Kr is a radioactive isotope that is suitable for dating ice cores in the range from 0.03 to 1.3 Ma BP (Ma: million years before 1950), making it perfectly adapted for Antarctic ice core dating (Buizert et al., 2014; Crotti et al., 2021).

To further constrain the oldest ice core chronologies, the so-called “orbital dating” tools are also used. These tools consist of aligning some tracers measured in ice cores to the Earth orbital series, called targets, whose fluctuations in time are accurately calculated from the known variations in orbital parameters (Berger, 1978; Laskar et al., 2011). The synchronization of the orbital tracer with its target provides ice or gas age constraints. So far, three orbital dating tools have been developed: $\delta^{18}O$ of O₂ ($\delta^{18}O_{\text{atm}}$), $\delta O_2/N_2$ and total air content (TAC). The $\delta^{18}O_{\text{atm}}$ was typically aligned with the precession parameter (or with the 21 June insolation at 65° N) delayed by 5000 years because such a lag between $\delta^{18}O_{\text{atm}}$ and its orbital target was observed during the last deglaciation (Shackleton, 2000; Dreyfus et al., 2007). However, variations in the phasing between $\delta^{18}O_{\text{atm}}$ and preces-

sion have been suspected (Jouzel et al., 2002) and identified since (Bazin et al., 2016). In particular, millennial-scale events (as Heinrich-like events) occurring during deglaciations have been shown to delay the response of $\delta^{18}\text{O}_{\text{atm}}$ to orbital forcing (Extier et al., 2018a). Because there was a significant unpredictability in the lag between $\delta^{18}\text{O}_{\text{atm}}$ and its orbital target, a large uncertainty in the $\delta^{18}\text{O}_{\text{atm}}$ -based tie points (up to 6000 years) was assigned in the construction of the AICC2012 (Antarctic Ice Core Chronology 2012; Bazin et al., 2013). To improve the accuracy of the gas timescale, Extier et al. (2018a) rather aligned the variations in $\delta^{18}\text{O}_{\text{atm}}$ to the $\delta^{18}\text{O}_{\text{calcite}}$ recorded in absolute-dated East Asian speleothems between 640 and 100 ka BP. Indeed, the two records show similar orbital (related to the 21 July insolation at 65° N) and millennial variabilities, which may correspond to southward shifts in the Intertropical Convergence Zone (ITCZ) position, themselves linked to Heinrich-like events as supported by the modeling study of Reutenauer et al. (2015).

In parallel, Bender (2002) observed that the elemental ratio $\delta\text{O}_2/\text{N}_2$ of air trapped in the Vostok ice core appears to vary in phase with the 21 December insolation at 78° S (Vostok latitude) between 400 and 160 ka BP. Subsequent observations led Bender (2002) to assert that local summer solstice insolation affects near-surface snow metamorphism and that this imprint is preserved as snow densifies in the firn and, later on, affects the ratio $\delta\text{O}_2/\text{N}_2$ measured in air bubbles formed at the lock-in zone. Wiggle matching between $\delta\text{O}_2/\text{N}_2$ and local summer solstice insolation has been used to construct orbital timescales for the Dome Fuji, Vostok and EDC ice cores reaching back 360, 400 and 800 ka BP, respectively, with a chronological uncertainty for each $\delta\text{O}_2/\text{N}_2$ tie point estimated between 250 and 4000 years (Kawamura et al., 2007; Suwa and Bender, 2008; Bazin et al., 2013; Oyabu et al., 2022). Finally, Raynaud et al. (2007) found very similar spectral properties between the TAC record of EDC and the integrated summer insolation (ISI) at 75° S obtained by a summation over a year of all daily local insolation above a certain threshold over the last 440 kyr. As for $\delta\text{O}_2/\text{N}_2$, these similarities may be explained by the insolation imprint in near-surface snow well preserved down to the lock-in zone, where it could affect the air content in deep ice, although the physical mechanisms involved during the snow and firn densification for $\delta\text{O}_2/\text{N}_2$ and TAC are likely different (Lipenkov et al., 2011). Lately, Bazin et al. (2013) made use of TAC to constrain Vostok and EDC ice core chronologies back to 430 ka BP with an uncertainty for each TAC tie point varying between 3000 and 7000 years. Although these three orbital tools complement each other (TAC and $\delta\text{O}_2/\text{N}_2$ inferred ages agree within less than 1000 years between 390 and 160 ka BP for the Vostok ice core; Lipenkov et al., 2011), they hardly ever have been employed together. Plus, they are often associated with large uncertainties (reaching 7000 years), which lie in the choice of the appropriate orbital target, in its alignment with ice core records that can be ambiguous during pe-

riods of low eccentricity in the Earth's orbit (leading to low-amplitude insolation variations) and in the poor quality of the signals measured in the deepest section of the cores.

To connect ice and gas timescales, the estimation of the lock-in depth (LID), indicating the lowest depth where the air is trapped in enclosed bubbles, and diffusivity becomes effectively zero (Buizert et al., 2013), is used to calculate the ice–gas age difference. Measurements of $\delta^{15}\text{N}$ from N_2 yield a first estimate of this depth, and the LID can also be calculated with firn densification modeling (Goujon et al., 2003; Bréant et al., 2017).

For many years, each polar ice core was characterized by its singular timescale, which was not naturally consistent with other ice core timescales. To address this issue, other measurements provide relative dating constraints (stratigraphic links), improving the coherency between timescales of ice cores from both hemispheres. The synchronization of globally well-mixed atmospheric methane ice core records gives tie points with an accuracy of a few decades to several centuries (60–1500 years) (Lemieux-Dudon et al., 2010; Epifanio et al., 2020). Climate-independent events, such as large volcanic eruptions, can be observed in ice cores from Greenland and Antarctica via singular patterns of the distribution of sulfate. Identification of these deposits permits the precise synchronization of several ice cores (within 5 to 150 years) (Svensson et al., 2020).

1.1.4 Bayesian dating tools

In order to integrate stratigraphic matching, independent synchronization and absolute dating constraints as well as glaciological modeling to produce coherent ice core chronologies, researchers developed Bayesian dating tools such as Datiche (Lemieux-Dudon et al., 2010), IceChrono1 (Parrenin et al., 2015) and Paleochrono (Parrenin et al., 2021). These tools use an inverse method combining all chronological information to provide a coherent age scale for several ice cores. These probabilistic tools adjust prior estimates of ice and gas chronologies built with a glaciological model (background scenario) so that they respect chronological constraints.

Here we focus on the chronology of the EDC deep ice core. The EPICA project provided two cores in East Antarctica, including one at Dome C (EDC). The second (and final) drilling attempt at Dome C gave the 3260 m long EDC99 core, whose drilling was willingly stopped at 15 m above bedrock due to the expected presence of meltwater. EDC furnishes the oldest continuous ice core record so far, covering the last 800 kyr (EPICA Community Members, 2004; Jouzel et al., 2007).

1.2 The AICC2012 chronology

Bazin et al. (2013) and Veres et al. (2013) used the probabilistic dating tool Datiche to establish the coherent

AICC2012 chronology back to 800 ka BP for five ice cores, including EDC, Vostok, EPICA Dronning Maud Land ice core (EDML), North GRenland Ice core Project (NGRIP) and Talos Dome Ice core (TALDICE). To determine the EDC age scale, they used various orbital dating constraints including 39 tie points attached to a 6000-year uncertainty derived from $\delta^{18}\text{O}_{\text{atm}}$ tuning to a 5000-year delayed precession between 800 and 300 ka BP, 20 tie points associated with a 4000-year uncertainty from $\delta\text{O}_2/\text{N}_2$ alignment to local summer solstice insolation between 800 and 300 ka BP, and 14 tie points linked to an uncertainty between 3000 and 7000 years using TAC synchronized to integrated summer insolation between 430 and 0 ka BP. However, due to the lack of data for the orbital dating approach, the AICC2012 1σ uncertainty is of 1700 years on average, reaching 8000 years at the bottom of the core. The origins of AICC2012 uncertainty can be divided in the following points: (i) some inherent dissimilarities between $\delta^{18}\text{O}_{\text{atm}}$, $\delta\text{O}_2/\text{N}_2$ and TAC series and their curve-shaped orbital target; (ii) discontinuity and poor quality of the $\delta\text{O}_2/\text{N}_2$ and TAC records; (iii) uncertainty in the phasing between $\delta^{18}\text{O}_{\text{atm}}$ and precession; (iv) poor constraint on the LID scenario due to a disagreement between $\delta^{15}\text{N}$ data and firn modeling estimates (Bréant et al., 2017).

1.3 The new AICC2023 chronology

It is now possible to address each source of uncertainty thanks to recent advances. (i) Since AICC2012, the $\delta^{18}\text{O}_{\text{atm}}$ and TAC records have been extended, now covering the last 800 kyr (Extier et al., 2018b). In addition, new highly resolved $\delta^{18}\text{O}_{\text{atm}}$ and $\delta\text{O}_2/\text{N}_2$ measurements are available over several glacial terminations (TII, III, IV, V and VI) (Grisart, 2023). (ii) Extier et al. (2018a) recently suggested a $\delta^{18}\text{O}_{\text{atm}}$ -based timescale using $\delta^{18}\text{O}_{\text{calcite}}$ of East Asian speleothems as an alternative tuning target to precession. This choice reduces the chronological uncertainty between 640 and 100 ka BP. (iii) Finally, new highly resolved $\delta^{15}\text{N}$ data covering the terminations II to VI are available (Grisart, 2023). In parallel, firn densification models have been progressively improved, and the model described in Bréant et al. (2017) can be employed to estimate LID evolution in the past when $\delta^{15}\text{N}$ data are still missing.

In this work, we implement new absolute age constraints spanning the last 800 kyr derived from ^{81}Kr measured in air trapped in the EDC ice core as well as new orbital age constraints obtained by synchronizing up-to-date EDC records with their orbital target. We combine these data with recent volcanic matching and methane record synchronization, which provide additional stratigraphic links, relating EDC to other ice cores over the past 122 kyr (Baumgartner et al., 2014; Svensson et al., 2020). Finally, we propose the new chronology AICC2023 with reduced chronological uncertainties. AICC2023 is recommended as the new official age scale for the EPICA ice cores by the EPICA Scientific Steering Committee (Wolff, 2023).

2 Methods

2.1 Dating strategy

The Paleochrono Python software is a probabilistic dating tool similar to Datice and IceChrono1 with improved mathematical, numerical and programming capacities (Parrenin et al., 2021). The dating strategy of Paleochrono relies on the Bayesian inference of three glaciological functions forming the input background scenario: accumulation rate (A), thinning of annual ice layers (τ) and lock-in depth (LID). The three variables evolve along the ice core depth z and are used to estimate the ice (ψ) and gas (χ) age profiles as follows:

$$\psi(z) = \int_0^z \frac{D(z')}{\tau(z')A(z')} dz' \quad (1)$$

$$\chi(z) = \psi(z - \Delta\text{depth}(z)) \quad (2)$$

$$\int_{z-\Delta\text{depth}(z)}^z \frac{D(z')}{\tau(z')} dz' = \text{LID}(z) \times \left. \frac{D}{\tau} \right|_{\text{firn}}^0, \quad (3)$$

where D is the relative density of the snow/ice and $\left. \frac{D}{\tau} \right|_{\text{firn}}^0$ the average value of $\frac{D}{\tau}$ in the firn when the air particle was at the lock-in depth (this parameter is usually ~ 0.7 ; Parrenin et al., 2012). The age scales are further constrained to respect chronological constraints identified from observations. To specify the credibility of the background scenario for the age scales and the chronological constraints, the glaciological functions (accumulation, thinning and LID) and the chronological information can be mathematically expressed as probability densities, which are presumed to be Gaussian and independent (i.e., decorrelated between them). Thus, the inference is based on the least square optimization method (implying all probability densities are Gaussian). It is numerically solved using the trust region algorithm (assuming that the model is roughly linear around the solution), and the Jacobian of the model is evaluated analytically for an improved computation time. As a result, the best adjustment between the background scenario and chronological observations is found, providing the most probable scenario as a posterior evaluation of the three glaciological functions and hence chronologies for ice and air. For each ice core, the input files for Paleochrono are the following: (i) the background values of the three glaciological functions with depth; (ii) gas and ice stratigraphic links; (iii) gas- and ice-dated horizons, which are tie points derived for one core from absolute and synchronization dating methods; (iv) gas and ice intervals of known durations; and (v) depth difference estimates between the same event recorded in the gas and ice matrix (Δdepth). Specific relative or absolute uncertainties are attached to each of these parameters in each input file.

In this study, we added numerous gas- and ice-dated horizons for EDC as well as an updated background scenario for the LID. Then, to construct a new chronology for the EDC

ice core that is consistent with the timescales of the Vostok, TALDICE, EDML and NGRIP ice cores, we followed the same strategy as for the construction of AICC2012. Glaciological background parameters and dating constraints for the Vostok, TALDICE, EDML, NGRIP and EDC drillings are compiled in one run of Paleochrono to obtain AICC2023. The Vostok, TALDICE, EDML and NGRIP background parameters and dating constraints are extracted from Bazin et al. (2013), except for (i) new Vostok gas age constraints determined from the alignment of $\delta^{18}\text{O}_{\text{atm}}$ and East Asian $\delta^{18}\text{O}_{\text{calcite}}$ records as for EDC (see Fig. S10), (ii) new TALDICE background parameters and age constraints from Crotti et al. (2021), and (iii) corrected LID background scenarios for the Vostok and EDML sites (see Fig. S11). In order to prevent any confusion with reference ice core timescales, the new AICC2023 chronology for NGRIP is compelled to respect exactly the layer-counted GICC05 timescale through absolute tie points placed at 1 m intervals over the last 60 kyr (Andersen et al., 2006). For this reason, we did not use the methodology described by Lemieux-Dudon et al. (2015), who implemented layer counting as a constraint on the duration of events in the dating tool, inducing a slight shift (maximum 410 years) in the AICC2012 timescale. The resulting Paleochrono experiment provides the new official chronology AICC2023 for the EDC ice core. The contingent timescales obtained for the four other sites are not the subject of this study but are also provided (see “Data availability” section). We acknowledge the exclusion of the WAIS (West Antarctic Ice Sheet) Divide ice core (WDC) from the construction of the AICC2023 age scale as for the AICC2012 age scale. Over the last 60 kyr, though, we recommend the use of timescales tied to the WAIS Divide 2014 age model (WD2014; Buizert et al., 2015; Sigl et al., 2016). A correspondence between AICC2012, AICC2023 and WD2014 age models based on the volcanic synchronization of WDC and EDC using sulfate data (Buizert et al., 2018) is provided over the 0–58 ka BP period (that is to say for the section above the depth of 915 m for the EDC ice core; see “Data availability” section).

2.2 Analytical method

2.2.1 $\delta^{18}\text{O}_{\text{atm}}$, $\delta\text{O}_2/\text{N}_2$ and $\delta^{15}\text{N}$

The measurements of the isotopic and elemental compositions of O_2 and N_2 were performed by Grisart (2023) at the Laboratory for Sciences of Climate and Environment (LSCE) following the method described by Bréant et al. (2019) and Extier et al. (2018a). The air trapped in the EDC ice core is extracted using the semi-automatic line, which eliminates CO_2 and H_2O . Samples of 30 to 40 g are prepared in a cold environment (-20°C), their exterior layer (3–5 mm) is removed so that there is no exchange with atmospheric air, and each sample is cut in two replicates. Each day, three ice samples (and replicates) are placed in six flasks, and the at-

mospheric air is evacuated from the flasks. Samples are then melted and left at ambient temperature for approximately 1 h 30 min in order to extract the air trapped in ice samples. The extracted air is then cryogenically trapped within a dedicated manifold immersed in liquid helium (Bazin et al., 2016). Along the way to the cryogenic trap, the air goes through cold traps to remove CO_2 and H_2O . Two additional samples containing exterior modern air are processed through the same line every day for calibration and for monitoring the analytical set-up. Lastly, the $\delta^{15}\text{N}$, $\delta^{18}\text{O}$ of O_2 and $\delta\text{O}_2/\text{N}_2$ of each sample are measured by a dual-inlet Delta V plus (Thermo Electron Corporation) mass spectrometer.

Classical corrections are applied on the measurements (pressure imbalance, chemical slopes, as per Landais et al., 2003). In addition, $\delta^{15}\text{N}$ data are used to get the values of atmospheric $\delta^{18}\text{O}$ of O_2 and $\delta\text{O}_2/\text{N}_2$ after gravitational fractionation occurred in the firm so that $\delta^{18}\text{O}_{\text{atm}} = \delta^{18}\text{O}$ of $\text{O}_2 - 2 \times \delta^{15}\text{N}$ and $\delta\text{O}_2/\text{N}_{2(\text{corr})} = \delta\text{O}_2/\text{N}_{2(\text{raw})} - 4 \times \delta^{15}\text{N}$ (Landais et al., 2003; Bazin et al., 2016; Extier et al., 2018a). Note that our samples were stored at -50°C after drilling to minimize the gas loss effect. As a consequence, no correction for gas loss was applied (see Sect. S1 in the Supplement), and if gas loss may explain a slight scattering in the data, the peak positions are not affected.

Existing and new EDC data are compiled in Table 1. The dataset’s resulting pooled standard deviations for the new measurements are of 0.006 ‰, 0.03 ‰ and 0.4 ‰ for $\delta^{15}\text{N}$, $\delta^{18}\text{O}_{\text{atm}}$ and $\delta\text{O}_2/\text{N}_2$, respectively.

2.2.2 Total air content

The TAC record was measured in the entire EDC ice core at the IGE (Institute of Environmental Geosciences) following the barometric method first described by Lipenkov et al. (1995). The TAC record measured in the younger part of the core (400–0 ka BP) has been published in Raynaud et al. (2007) (Table 2). TAC estimates need to be corrected for the cut-bubble effect. After correction, the uncertainty in TAC values is of about 1 %, and the analysis replicability is better than 1 %.

2.2.3 ^{81}Kr extraction and analysis

The analytical method is the same as described by Crotti et al. (2021). Three 6 kg ice samples are taken from the bottom part of EDC, and a slight shaving (1 mm) of the external layer is performed before processing. The air extraction is performed through a manual extraction line following the protocol described in Tian et al. (2019). The ice sample is placed in a 40 L stainless-steel chamber. The atmospheric air is pumped while the chamber is kept at -20°C . The air is then slowly extracted, passing through a water trap, and compressed in a stainless-steel cylinder. The three cylinders are sent to the University of Science and Technology of China (USTC, Hefei, China) for krypton extraction and analysis.

Table 1. Information on isotopic and elemental compositions measured in air trapped in the EDC ice core. * Details on storage and measurement conditions of $\delta\text{O}_2/\text{N}_2$ are available in Sect. S1 in the Supplement.

	$\delta^{18}\text{O}_{\text{atm}}$			$\delta\text{O}_2/\text{N}_2^*$			$\delta^{15}\text{N}$		
	Depth (m)	AICC2012 gas age (ka BP)	Resolution (kyr)	Depth (m)	AICC2012 ice age (ka BP)	Resolution (kyr)	Depth (m)	AICC2012 gas age (ka BP)	Resolution (kyr)
AICC2012	2479–3260	300–800	1–1.5	2480–3260	300–800	2.5	346–578	11–27	0.35–0.38
Dreyfus et al. (2007, 2008, 2010), Landais et al. (2012), Bazin et al. (2013)							1090–1169 1389–3260	75–83 100–800	1.4 2.4
Bazin et al. (2016)	1300–1903 2657–3260	90–160 370–800	1.1	1300–1903 2595–3260	93–163 340–800	2.37 2.08			
Extier et al. (2018b, c)	1872–2665	153–374	0.16–0.7	1904–2562	164–332	2–2.5			
Bréant et al. (2019)							1904–2580	160.2–334.5	1.013
This work (Girard, 2023)	1489.95–1832.6 1995.95–2350.15 2555.85–2633.4 2744.5–2797.85 2873.75–2910.6	108.0–136.3 180.6–255.8 328.3–346.8 408.7–445.9 508.1–535.6	0.333 0.437 0.356 0.744 1.375	1489.95–1832.6 1995.95–2350.15 2555.85–2633.4 2744.5–2797.85 2873.75–2910.6	111.4–148.9 183.9–259.6 330.5–360.6 410.7–449.6 511.3–539.3	0.441 0.437 0.579 0.779 1.401	1489.95–1832.6 1995.95–2350.15 2555.85–2633.4 2744.5–2797.85 2873.75–2910.6	108.0–136.3 180.6–255.8 328.3–346.8 408.7–445.9 508.1–535.6	0.333 0.437 0.356 0.744 1.375

Table 2. Information on TAC measurements in the EDC ice core.

	TAC		
	Depth (m)	AICC2012 ice age (ka BP)	Resolution (kyr)
AICC2012 (Raynaud et al., 2007)	115–2800	0–440	2.000
Unpublished	2800–3260	440–800	2.000

Krypton extraction is performed after the methodology of Dong et al. (2019), who set up an automated system for dual separation of argon and krypton, composed of a titanium getter module followed by a gas-chromatography separator module. The extracted krypton is analyzed by the Atom Trap Trace Analysis (ATTA) instrument set up at the Laser Laboratory for Trace Analysis and Precision Measurement (LL-TAPM, USTC, Hefei, China), giving the ^{81}Kr abundance R_{81} in the sample. R_{81} is determined by the number of counted ^{81}Kr atoms in the sample as compared to the atmospheric reference. The anthropogenic ^{85}Kr is measured simultaneously with ^{81}Kr to control any present-day air contamination. Here, the ^{85}Kr abundance measured in ice samples is inferior to the detection limit, so contamination has occurred.

From the ^{81}Kr abundance, it is possible to estimate ^{81}Kr radioactive decay and to calculate the ice sample's age. As a noble gas isotope, ^{81}Kr is globally mixed in the atmosphere, and its decay cannot be affected by complex chemical reactions (Lu et al., 2014). The ^{81}Kr half-life ($t_{1/2}$) is estimated to be $\approx 229 \pm 11$ kyr (Baglin, 2008). ^{81}Kr age can be calculated as per the following equation:

$$\text{age} = -\frac{t_{1/2}}{\ln(2)} \times \ln(R_{81}). \quad (4)$$

The atmospheric abundance of ^{81}Kr is not constant in the past, and its value is corrected using reconstruction of the geomagnetic field intensity (Zappala et al., 2020). The error in ^{81}Kr age estimates is estimated from the statistical error in atom counting, from the uncertainty in ^{81}Kr half-life (inducing a systematic age error) and from the size of the sample (larger sample resulting in a smaller uncertainty).

2.3 Firm model

Firm densification models have been progressively improved over the years (Herron and Langway, 1980; Alley, 1987; Arthern et al., 2010; Ligtenberg et al., 2011; Kuipers Munneke et al., 2015; Oraschewski and Grinsted, 2022). While these models generally explain the evolution of $\delta^{15}\text{N}$ in time well through changes in the LID, they fail to reproduce values of $\delta^{15}\text{N}$ in some regions, including coastal areas and cold and low-accumulation sites such as EDC (Capron et al., 2013). This disagreement can be explained

by an inaccurate estimate of glacial temperature and accumulation rate at the surface (Buizert, 2021) and/or by the impossibility of tuning empirical firm models to sites with no present-day equivalent in terms of temperature and accumulation rate (Dreyfus et al., 2010; Capron et al., 2013). Recently, the firm model described in Bréant et al. (2017) was developed from the IGE model (Pimienta and Duval, 1987; Barnola et al., 1991; Arnaud et al., 2000; Goujon et al., 2003) by implementing a dependency of the firm densification rate on temperature and impurities. The temperature dependence is added to the classical formulation of the densification rate following an Arrhenius law with an activation energy Q as per $\exp(-Q/RT)$, with R the perfect gas constant and T the firm temperature. Rather than using a constant activation energy (Goujon et al., 2003), Bréant et al. (2017) stated that the value of the activation energy should be contingent on the firm temperature value as observed in material science, where the temperature dependency exhibits the predominance of one physical mechanism among others for a material compaction at a specific temperature. Through several sensitivity tests, Bréant et al. (2017) adjusted three values for activation energy in three different temperature ranges to reproduce best the $\delta^{15}\text{N}$ evolution over the last deglaciation at East Antarctic sites. The firm model also considers that firm densification is facilitated by the dissolution of impurities within the snow (Freitag et al., 2013). If the impurity content in snow (i.e., concentration of calcium ions) is greater than a certain threshold, the densification rate dependence on impurities is traduced by a relationship between the new activation energy Q' and the concentration of calcium ions $[\text{Ca}^{2+}]$: $Q' = f_1 \times \left(1 - \beta \ln\left(\frac{[\text{Ca}^{2+}]}{[\text{Ca}^{2+}]_{\text{threshold}}}\right)\right) \times Q$ (Freitag et al., 2013). Bréant et al. (2017) assumed the impurity effect equal for all physical mechanisms and tuned β and f_1 constants so that the modeled- $\delta^{15}\text{N}$ data mismatch is minimized over the last glacial termination at cold East Antarctic sites.

As a consequence, and in addition to our new extensive $\delta^{15}\text{N}$ dataset, we have chosen to use here the firm model approach of Bréant et al. (2017). In order to make a correct calculation of uncertainties linked to firm modeling at EDC, we ran two tests of the model with and without including the impurity concentration parameter (see Sect. S3.1).

The firm densification model takes as input scenarios of temperature and accumulation rate at the surface. It computes both the LID and the thermal gradient in the firm (ΔT) and then deduces the $\delta^{15}\text{N}_{\text{therm}} = \Omega \cdot \Delta T$ with Ω the thermal-fractionation coefficient (Grachev and Severinghaus, 2003). The final $\delta^{15}\text{N}$ is calculated as $\delta^{15}\text{N} = \delta^{15}\text{N}_{\text{therm}} + \delta^{15}\text{N}_{\text{grav}}$ and $\delta^{15}\text{N}_{\text{grav}} \approx \text{LID} \cdot \frac{g}{RT}$ (first-order approximation), with g the gravitational acceleration (9.8 m s^{-2}), R the gas constant ($8.314 \text{ J mol}^{-1} \text{ K}^{-1}$) and T the mean firm temperature (K).

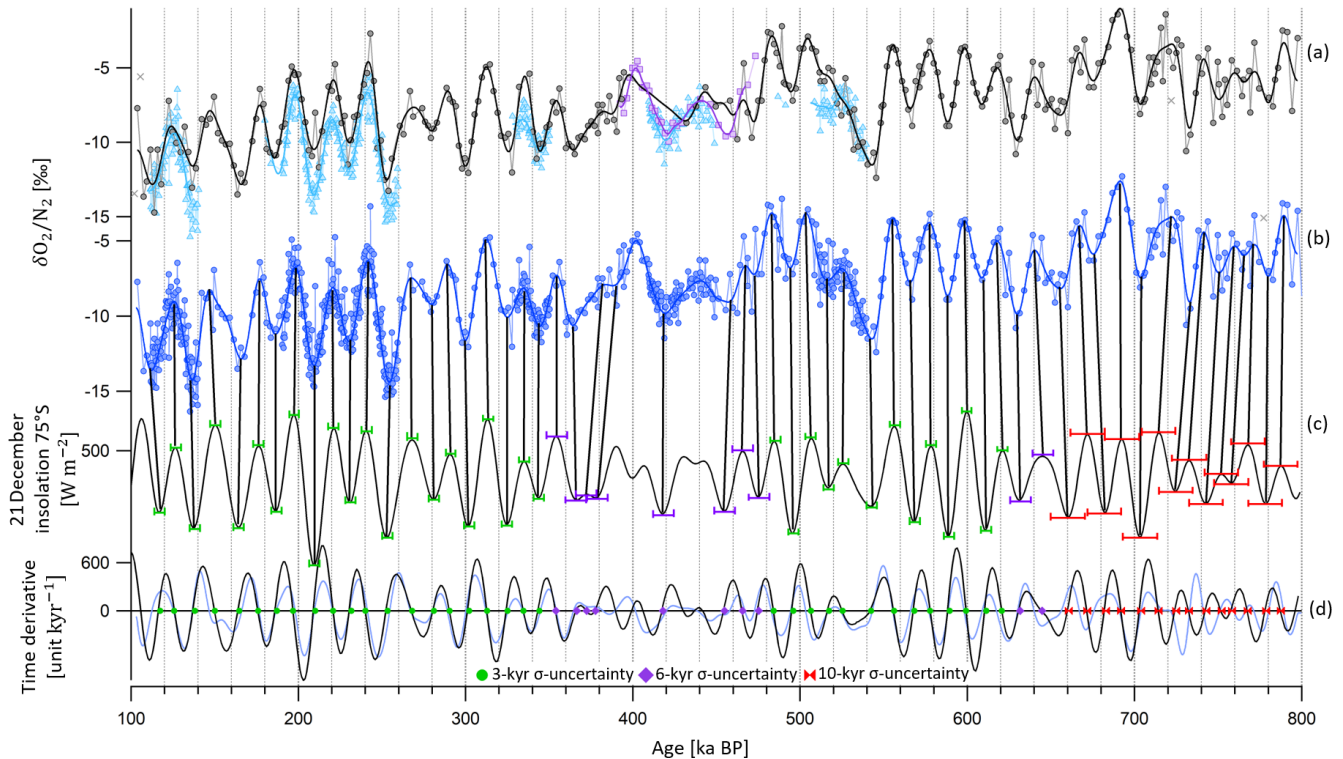


Figure 1. Alignment of $\delta\text{O}_2/\text{N}_2$ and insolation between 800 and 100 ka BP. **(a)** Old raw EDC $\delta\text{O}_2/\text{N}_2$ data between 800 and 100 ka BP (black circles for data of Extier et al., 2018c, and purple squares for data of Landais et al., 2012), outliers (gray crosses) and filtered signal (black and purple lines). New raw EDC $\delta\text{O}_2/\text{N}_2$ data (blue triangles, this study) and filtered signals (blue line). The $\delta\text{O}_2/\text{N}_2$ data are plotted on the AICC2012 ice timescale. Zooms between 270 and 100 ka BP and between 570 and 300 ka BP are shown in Fig. S2. **(b)** Extrema in the compiled filtered $\delta\text{O}_2/\text{N}_2$ dataset (plain blue line) are identified and matched to extrema in the **(c)** 21 December insolation at 75° S plotted on a reversed y axis and on the age scale given by Laskar et al. (2004) (black line). The peaks are matched by vertical black bars. **(d)** The zero value in the time derivative of insolation (black line) and of the filtered $\delta\text{O}_2/\text{N}_2$ dataset (blue line) corresponds to extreme values in the signals. The determined tie points between $\delta\text{O}_2/\text{N}_2$ and insolation are depicted by markers on the horizontal line. Green circles are attached to a 3 kyr 1σ uncertainty (horizontal green error bars show 2σ in panel c), purple squares are associated with a 6 kyr 1σ uncertainty (horizontal purple error bars show 2σ in panel c), and red markers are associated with a 10 kyr 1σ uncertainty (horizontal red error bars show 2σ in panel c). Between 390 and 475 ka BP, all extrema are not tuned to the target due to the poor resemblance between the signal and insolation.

3 Age constraints and background scenarios

3.1 ⁸¹Kr age constraints

Three ice samples from the bottom part of EDC have been analyzed and provide three age estimates displayed in Table 3: 629, 788 and 887 ka BP, with statistical age uncertainties between 30 and 50 kyr and a 4.8 % systematic error due to the uncertainty in the half-life of ⁸¹Kr. The deepest sample suggests the presence of ice older than 800 ka BP below the 3200 m depth level, and further studies would be valuable in exploring whether the stratigraphy of the lowermost EDC section is continuous (Tison et al., 2015), although this is beyond the scope of this work.

3.2 Determination of orbital age constraints using new data

3.2.1 $\delta\text{O}_2/\text{N}_2$

In this work, new highly resolved $\delta\text{O}_2/\text{N}_2$ data on the EDC ice core are presented over terminations II, III, IV, V and VI (Fig. 1). As these novel $\delta\text{O}_2/\text{N}_2$ measurements have been performed on ice samples stored at -50°C , there is little storage effect, and they can directly be merged with the 800 kyr long record of Extier et al. (2018c) (Table 1). The new dataset improves the resolution of the long EDC record, reaching sub-millennial-scale accuracy over marine isotope stages (MISs) 5, 7 and 9 and in particular over MIS 11 and MIS 13, periods of sparsity in the ancient record (Extier et al., 2018c). Although the two datasets agree well over recent periods (last 350 kyr), they show some discrepancies during older periods (between 550 and 375 ka BP; see

Table 3. Ice sample details and radio krypton dating results. Reported errors are 1σ errors. Upper limits have a 90 % confidence level. The average ^{85}Kr activity in the Northern Hemisphere is about 75 dpm cm^{-3} (decays per minute per cubic centimeter) in 2017. The measured ^{85}Kr concentrations are inferior to the detection limit, verifying that no relevant contamination with modern air has occurred. In addition to the statistical error in the ^{81}Kr age from atom counting, a systematic error due to the uncertainty in the half-life of ^{81}Kr is considered. This error would shift the calculated ^{81}Kr ages up or down for all ice samples. ^a dpm cm^{-3} : decays per minute per cubic centimeter standard temperature and pressure (STP) of krypton (conversion: 100 dpm cm^{-3} corresponds to $^{85}\text{Kr}/\text{Kr} = 3.03 \times 10^{11}$). ^b pMKr: percent modern krypton.

Depth (m)	Air extracted/ ice weight (mL kg^{-1})	Sample Used ($\mu\text{L STP}$, Kr)	Analysis date	^{85}Kr (dpm cm^{-3}) ^a	^{81}Kr (pMKr) ^b	^{81}Kr – age (ka BP) $\text{age}_{-stat-sys}^{+stat+sys}$
3013–3024	440/6.0	~ 0.46	18 Dec 2019	< 0.77	$15.1^{+1.4}_{-1.4}$	629^{+34+31}_{-29-31}
3144–3161	600/8.4	~ 0.67	30 Dec 2019	< 0.67	$9.6^{+1.0}_{-1.0}$	788^{+36+38}_{-33-38}
3216–3225	415/6.4	~ 0.43	16 Jan 2020	< 1.17	$7.1^{+1.0}_{-1.0}$	887^{+51+43}_{-44-43}

Fig. 1). Such dissimilarities are observed over MIS 11 (between 424 and 374 ka BP), where the sampling resolution of the previous dataset is particularly low (2500 years). In addition, MIS 11 is a period characterized by a low eccentricity in the Earth orbit, inducing subdued variations in insolation, causing $\delta\text{O}_2/\text{N}_2$ changes of smaller magnitude and leading to a lower signal-to-noise ratio. Data by Landais et al. (2012) (shown by purple squares in Figs. 1 and S2) are consistent with the highly resolved data presented here, supporting the relevance of the new dataset over this period. Over termination VI (from 550 to 510 ka BP), the old dataset continuously increases, while the novel dataset shows a brief maximum at around 525 ka BP followed by a minimum at around 520 ka BP. These newly revealed variations seem in phase with insolation variations, suggesting that the new dataset shows improved agreement with insolation. Still, highly resolved measurements are needed in the lowermost part of the ice core, where noise is significantly altering the temporal signal.

Following a data processing treatment consistent with the method described in Kawamura et al. (2007), the compiled dataset is linearly interpolated every 100 years and then smoothed using a finite-duration impulse response (FIR) filter with a KaiserBessel20 window (cut-off from 16.7 to 10.0 kyr period, 559 coefficients for the 800 kyr long record) designed with the software Igor Pro in order to reject periods inferior to 10 000 years and erase the noise present in the data. Note that using a low-pass (rejecting periods below 15 kyr) or a band-pass filter (keeping periods between 100 and 15 kyr periods, used by Bazin et al., 2013) does not alter the peak positions in the $\delta\text{O}_2/\text{N}_2$ curve (see Fig. S2). The noise is particularly significant for highly resolved $\delta\text{O}_2/\text{N}_2$ data, and without preliminary filtering, it becomes ambiguous to identify the exact peak position (which needs to be subjectively placed on a 1000- to 2000-year interval; see Sect. S2.1).

The filter is then applied to the local summer solstice insolation curve to check that it does not induce the shift in extrema positions by more than 100 years. This condition is verified over the last 800 kyr, except for the peaks located at the endpoints of the record (respectively around 107 and 788 ka BP), which are then not used for tie point determination. Outliers in the raw $\delta\text{O}_2/\text{N}_2$ dataset are discarded if they show an anomaly greater than 3.2 % when compared to the low-pass-filtered signal. Five outliers are rejected out of 294 points. The $\delta\text{O}_2/\text{N}_2$ is interpolated and filtered again after removal of the outliers.

The orbital target chosen is the 21 December insolation at 75°S , which is calculated every 100 years over the last 800 kyr (Laskar et al., 2004). The peak positions in the compiled filtered $\delta\text{O}_2/\text{N}_2$ signal and in the summer solstice insolation are detected via an automated method using the zero values of the time derivatives of the $\delta\text{O}_2/\text{N}_2$ and its orbital target. Each $\delta\text{O}_2/\text{N}_2$ maximum is matched to an insolation minimum and each $\delta\text{O}_2/\text{N}_2$ minimum to an insolation maximum. The data treatment and tie point identification method used here are consistent with the approach recently conducted by Oyabu et al. (2022) on a novel 207 kyr long $\delta\text{O}_2/\text{N}_2$ record of the Dome Fuji (DF) ice core.

Some periods, such as between 450 and 350 ka BP (encompassing MIS 11) and older ages (before 600 ka BP), are characterized by a poor resemblance between the signal and the target. For instance, two or three peaks in the insolation curve only correspond, respectively, to one or two peaks in the $\delta\text{O}_2/\text{N}_2$ data. This could be explained by a low eccentricity-induced subdued variability in the insolation target and hence in $\delta\text{O}_2/\text{N}_2$ signal over MIS 11 and by the poor resolution of the $\delta\text{O}_2/\text{N}_2$ measurements before 600 ka BP. In such cases, the uncertainty (1σ) associated with each tie point ranges from 6 to 10 kyr (precession half period), and some extrema in the target are not used to tune the $\delta\text{O}_2/\text{N}_2$ record (5 extrema over MIS 11 out of 63 over the last 800 kyr). Otherwise, $\delta\text{O}_2/\text{N}_2$ seems to evolve

in phase with the inverse summer solstice insolation variations, and the tie point uncertainty (1σ) is set at 3 kyr. A 3–4 kyr uncertainty was evaluated by Bazin et al. (2016) on the following arguments. They examined three $\delta\text{O}_2/\text{N}_2$ records from the Vostok, DF and EDC ice cores over MIS 5 and detected some site-specific $\delta\text{O}_2/\text{N}_2$ high-frequency variability that could not be explained by a timescale issue. This observation, along with the presence of a 100 kyr periodicity in the EDC $\delta\text{O}_2/\text{N}_2$ record and the difficulty of identifying $\delta\text{O}_2/\text{N}_2$ mid-slopes and maxima because of a scattering of the $\delta\text{O}_2/\text{N}_2$ signal at the millennial scale, led them to recommend the use of a 3–4 kyr uncertainty. Because our higher-resolution $\delta\text{O}_2/\text{N}_2$ data give the possibility of filtering the signal with more confidence and hence reduces the uncertainty in the identification of $\delta\text{O}_2/\text{N}_2$ tie points, we propose taking a 3 kyr uncertainty. The orbital tuning results in 58 new tie points over the last 800 kyr (displayed in Fig. 1 and compiled in Table S5), replacing the 20 tie points used to constrain AICC2012 between 800 and 300 ka BP that were derived from synchronizing mid-slopes of band-pass-filtered $\delta\text{O}_2/\text{N}_2$ with the insolation (Bazin et al., 2013).

The uncertainty arising from the filter used and from the tie point identification method can be estimated by a comparison of the $\delta\text{O}_2/\text{N}_2$ peak positions identified before and after filtering of the signal with two different methods (see Sect. S2.1). The resulting uncertainty is of 700 years on average (with a standard deviation of 250 years), reaching 2100 years around 230 ka BP.

The new highly resolved data presented here enable a better description of the signal variability and a reduction in the uncertainty associated with orbital tie points.

3.2.2 Total air content

The TAC record is extended over the last 800 kyr with a mean sampling resolution of 2000 years (Fig. 2). The raw data between 800 and 440 ka BP are not shown here and will be published in a separate study. The TAC series shows a good resemblance with the integrated summer insolation (ISI, obtained by a summation over a year of all daily insolation at 75° S above a chosen threshold). After comparing the EDC TAC record, within its frequency domain, with ISI curves obtained using different thresholds, the ISI curve calculated for a threshold of 375 W m⁻² (ISI375) exhibits the finest spectral agreement with the EDC TAC record over the past 800 kyr. The coherency between the TAC record and ISI is deficient over MIS 11 (between 430 and 370 ka BP) and in the deepest part of the core (prior to 700 ka BP), where the signal-to-noise ratio is low.

Following a data processing treatment consistent with the method described by Lipenkov et al. (2011), the 800 kyr long TAC dataset is interpolated every 100 years and then filtered with a band-pass filter rejecting periods below 15 000 and above 46 000 years (Igor Pro FIR filter with a KaiserBessel20 window, cut-off from 15 to 14 kyr and from 46 to 47 kyr,

559 coefficients). Outliers in the raw TAC dataset are discarded if they show an anomaly greater than 1.0 mL kg⁻¹ (standard deviation of TAC record) when compared to the band-pass-filtered signal. A total of 45 outliers are rejected out of 399 data points (among which 16 outliers are identified between 100 and 0 ka BP). The TAC is interpolated and filtered again after removal of the outliers.

Tie points are mostly determined by matching variation extrema of TAC and integrated summer insolation at 75° S (Fig. 2). Indeed, in the case of a non-linear relationship between TAC and insolation, extrema are better indicators of TAC response to insolation forcing. Moreover, filtering the dataset induces a bias in the mid-slope position. The method employed to determine extrema position is the same as for $\delta\text{O}_2/\text{N}_2$ insolation tie points. Only one of the tie points is identified by matching mid-slopes (i.e., derivative extremum) at 362 ka BP rather than minima at 375 ka BP due to the flatness of the insolation minimum, which precludes identification of an accurate tie point. Not all extrema are tuned to the target due to the poor resemblance between the signal and insolation, and 42 unambiguous tie points were kept out of 64 detected by the automated method. The tie point uncertainty finds its origin in the age errors associated with the filtering (~ 700 years), tie point identification and outlier rejection (~ 900 years). The 1σ uncertainty is evaluated to be 3 kyr when there is good agreement: (i) between the signal and its target, meaning that one peak in ISI375 is reflected by a singular peak in the TAC record, and (ii) between the tie points identified by the automated method and manually (age shift < 1300 years, average value) (see green circles, Fig. 2). A 6 kyr uncertainty (1σ) is attached to the tie points if the latter condition is not respected (age shift > 1300 years) (see purple squares, Fig. 2), and a 10 kyr uncertainty (1σ) (precession half period) is ascribed to the tie points if the ISI375 variations are not reflected by the TAC record, meaning that one peak in ISI375 could be associated with two peaks in the TAC record, or if the signal-to-noise ratio of the TAC record is too large (see red markers, Fig. 2). The choices of filter and orbital target have no significant impact on the chronological uncertainty; a further detailed study is thus beyond the scope of this work.

The orbital tuning results in 42 new tie points over the last 800 kyr (displayed in Fig. 2 and compiled in Table S5). They replace the 14 tie points used to constrain the EDC ice timescale in AICC2012 between 425 and 0 ka BP that were derived by directly matching mid-slope variations in unfiltered TAC and ISI target and attached to an uncertainty varying between 2.9 and 7.2 kyr.

3.2.3 $\delta^{18}\text{O}_{\text{atm}}$

In this work, new highly resolved $\delta^{18}\text{O}_{\text{atm}}$ data on the EDC ice core are presented over terminations II, III, IV, V and VI (Fig. 3). The available $\delta^{18}\text{O}_{\text{atm}}$ data can be sorted out in two groups: new $\delta^{18}\text{O}_{\text{atm}}$ data (Grisart, 2023) at high temporal

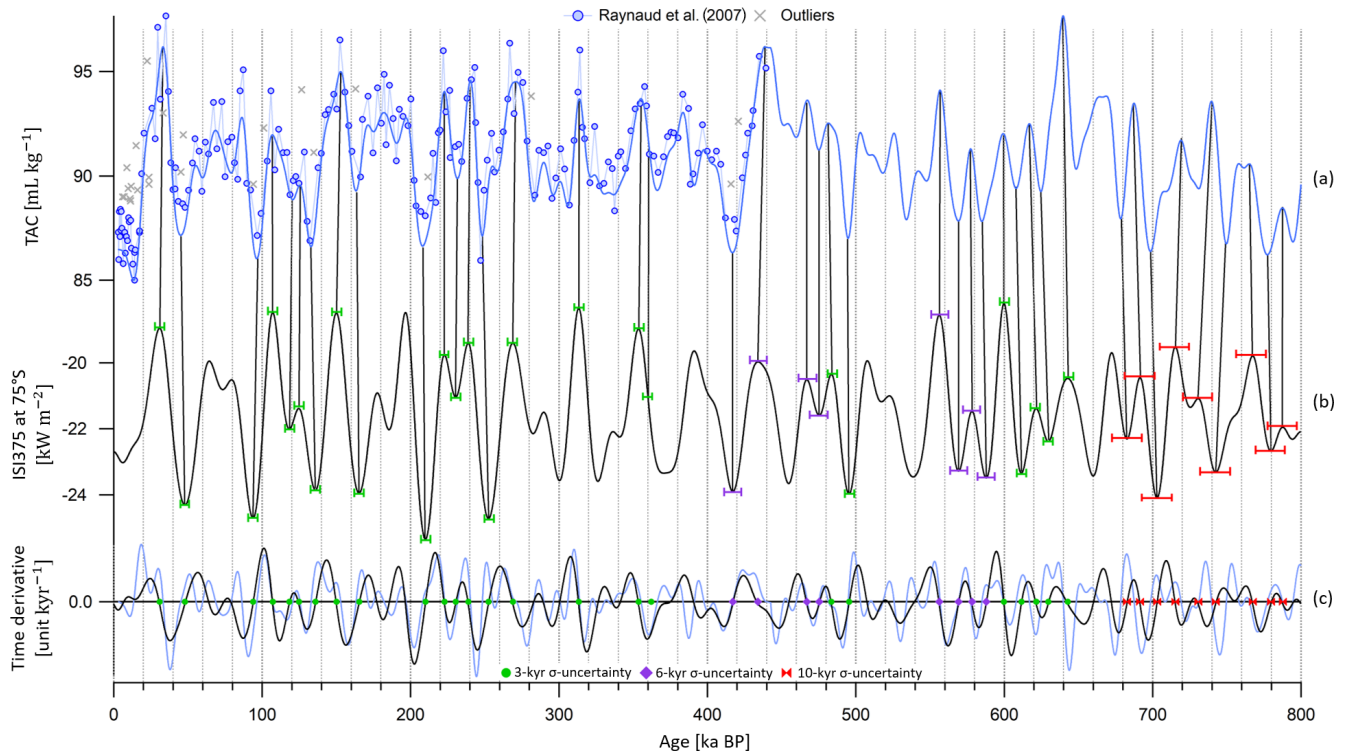


Figure 2. Alignment of TAC and insolation between 800 and 0 ka BP. **(a)** Raw EDC TAC data (blue circles; Raynaud et al., 2007), outliers (gray crosses) and filtered signal (blue line) on the AICC2012 ice timescale. The raw data between 800 and 440 ka BP are not shown here and will be published in a separate study. **(b)** ISI375 at 75° S on a reversed axis. The peaks and mid-slopes are matched by vertical bars. **(c)** Temporal derivative of insolation (black line) and TAC (blue line). Its zero value corresponds to extreme values in insolation and TAC. The determined tie points between TAC and insolation are depicted by markers on the horizontal line. Green circles are attached to a 3 kyr 1σ uncertainty (horizontal green error bars show 2σ in panel c), purple squares are associated with a 6 kyr 1σ uncertainty (horizontal purple error bars show 2σ in panel c), and red markers are associated with a 10 kyr 1σ uncertainty (horizontal red error bars show 2σ in panel c).

resolution (between 333 and 1375 years; see Table 1) and old measurements compiled by Extier et al. (2018b), characterized by a lower sampling resolution (between 1000 and 1500 years; see Table 1), except between 374 and 153 ka BP (resolution between 160 and 700 years; see Table 1). The new dataset improves the resolution of the long EDC record over MISs 5, 7 and 9 and in particular over MISs 11 and 13, periods of sparsity in the ancient record (Extier et al., 2018b). Although the two datasets agree well globally over the last 800 kyr, the new highly resolved dataset refines the signal between 255.5 and 243 ka BP where a lot of noise is present in the record of Extier et al. (2018b) (see inset in Fig. 3). This noise may be explained by the fact that highly resolved (mean sampling resolution of 381 years) measurements were performed on ice samples stored at -20°C in the compilation by Extier et al. (2018b), while the new measurements are performed on ice stored at -50°C . Therefore, we chose to remove the noisy dataset of Extier et al. (2018b) between 255.5 and 243 ka BP before combining the novel dataset with the remaining 800 kyr long record of Extier et al. (2018b).

Following the dating approach proposed by Extier et al. (2018a), $\delta^{18}\text{O}_{\text{atm}}$ and $\delta^{18}\text{O}_{\text{calcite}}$ are aligned using mid-

slopes of their variations over the last 640 kyr. To do so, the compiled EDC $\delta^{18}\text{O}_{\text{atm}}$ record and the Chinese $\delta^{18}\text{O}_{\text{calcite}}$ signal are linearly interpolated every 100 years and smoothed (25-point Savitzky–Golay) and extrema in their temporal derivative are aligned. It should be specified that synchronizing $\delta^{18}\text{O}_{\text{atm}}$ and East Asian $\delta^{18}\text{O}_{\text{calcite}}$ is not always obvious due to the long residence time of oxygen in the atmosphere (1–2 kyr), which may not be compatible with abrupt $\delta^{18}\text{O}_{\text{calcite}}$ variations over glacial inception and terminations. In particular, the slow increase in the $\delta^{18}\text{O}_{\text{atm}}$ record from 370 to 340 ka BP does not resemble the evolution of $\delta^{18}\text{O}_{\text{calcite}}$, which is first moderate then abrupt over the same period (Fig. 4, red area). For this reason, we chose not to use the two tie points identified by Extier et al. (2018a) at 351 and 370.6 ka BP. The new highly resolved data enable the identification of five new tie points and shifting of five tie points that have been determined beforehand by Extier et al. (2018a) (Fig. 4). Between 248 and 244 ka BP, the new $\delta^{18}\text{O}_{\text{atm}}$ measurements do not coincide with the $\delta^{18}\text{O}_{\text{calcite}}$ variations, and we decided to remove the tie point identified by Extier et al. (2018a) at 245.4 ka BP (Fig. 4, red area). Between 480 and 447 ka BP, the $\delta^{18}\text{O}_{\text{atm}}$ variations are

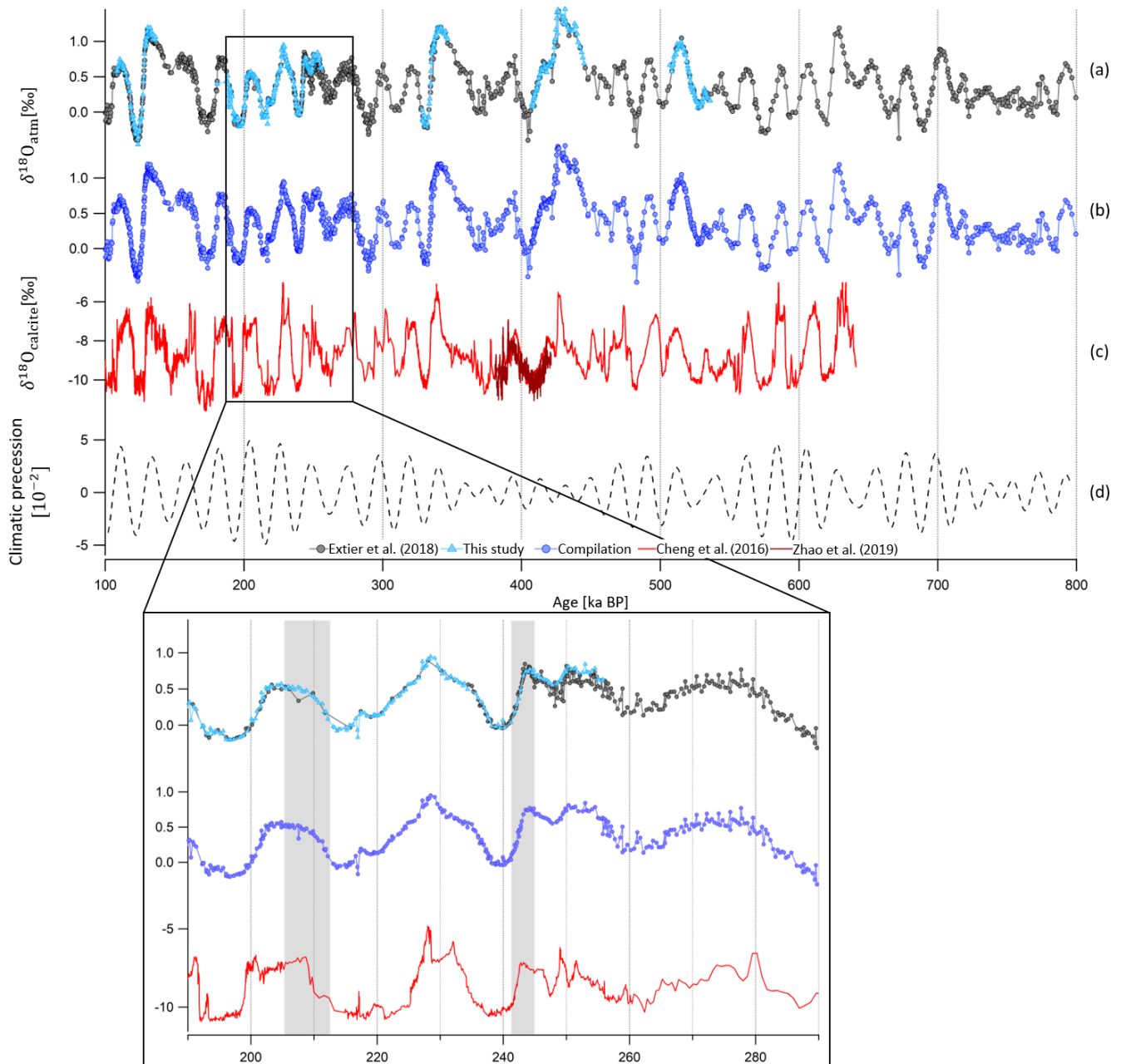


Figure 3. Evolution of EDC $\delta^{18}\text{O}_{\text{atm}}$ record between 800 and 100 ka BP. **(a)** Old raw EDC $\delta^{18}\text{O}_{\text{atm}}$ data (black circles; Extier et al., 2018b) and new raw EDC $\delta^{18}\text{O}_{\text{atm}}$ data (blue triangles; Grisart, 2023) on the AICC2012 gas timescale. **(b)** Compilation of the two datasets after removal of old measurements between 255.5 and 243 ka BP. **(c)** $\delta^{18}\text{O}_{\text{calcite}}$ composite record from speleothems from Sambao, Dongge, Hulu (red line) and Yongxing (brown line) caves (Cheng et al., 2016; Zhao et al., 2019) on U–Th age scales. **(d)** Climatic precession from Laskar et al. (2004) delayed by 5000 years. Inset is a zoom between 290 and 190 ka BP. Vertical gray rectangles highlight the improved agreement between new data of Grisart (2023) (blue triangles) and $\delta^{18}\text{O}_{\text{calcite}}$ (red line) compared to old data (gray circles) and $\delta^{18}\text{O}_{\text{calcite}}$.

characterized by a low resolution (1.1 kyr) and a weak amplitude, which prevents unambiguous matching of $\delta^{18}\text{O}_{\text{atm}}$ and $\delta^{18}\text{O}_{\text{calcite}}$. The four tie points identified by Extier et al. (2018a) at 447.3, 449.9, 455.9 and 462.8 ka BP are thus rejected (Fig. 4, red area). The remaining 39 tie points defined by Extier et al. (2018a) are preserved and used here

to constrain the EDC gas age. Their uncertainty (1σ) varies between 1.1 and 7.4 kyr.

Between 810 and 590 ka BP, the $\delta^{18}\text{O}_{\text{atm}}-\delta^{18}\text{O}_{\text{calcite}}$ dating uncertainty becomes larger than 6 kyr, and no East Asian speleothem $\delta^{18}\text{O}_{\text{calcite}}$ records are available before 640 ka BP. Over this time interval, we updated the following approach of

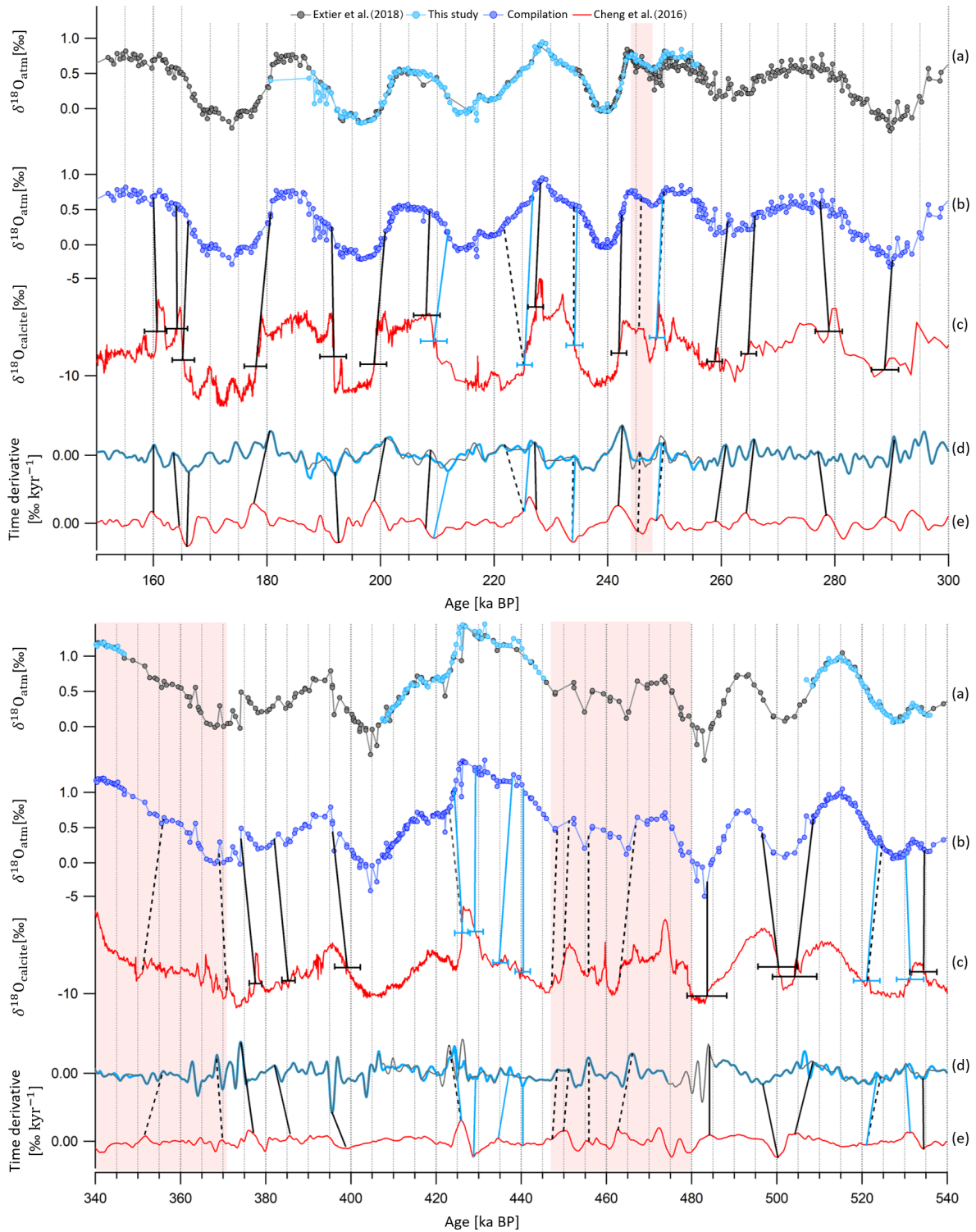


Figure 4. Alignment of EDC $\delta^{18}\text{O}_{\text{atm}}$ and Chinese $\delta^{18}\text{O}_{\text{calcite}}$ records over time periods where new tie points are defined. **(a)** New and old EDC $\delta^{18}\text{O}_{\text{atm}}$ datasets on the AICC2012 gas age scale. **(b)** Compiled EDC $\delta^{18}\text{O}_{\text{atm}}$. **(c)** Chinese $\delta^{18}\text{O}_{\text{calcite}}$ on U–Th age scale (Cheng et al., 2016). **(d)** Temporal derivatives of compiled EDC $\delta^{18}\text{O}_{\text{atm}}$ (blue curve) and of the old $\delta^{18}\text{O}_{\text{atm}}$ dataset (black curve). **(e)** Temporal derivative of Chinese $\delta^{18}\text{O}_{\text{calcite}}$ (red curve). Extrema in temporal derivatives are matched. Tie points represented by vertical black bars are determined by Extier et al. (2018a), and those by vertical blue bars are determined by this study. Both are used in the AICC2023 chronology. Dashed vertical bars show tie points identified by Extier et al. (2018a) that are not used in AICC2023; 2σ uncertainties attached to the tie points are shown by the horizontal error bars in panel c). Vertical red areas frame periods of lacking resemblance between $\delta^{18}\text{O}_{\text{atm}}$ and $\delta^{18}\text{O}_{\text{calcite}}$ variations.

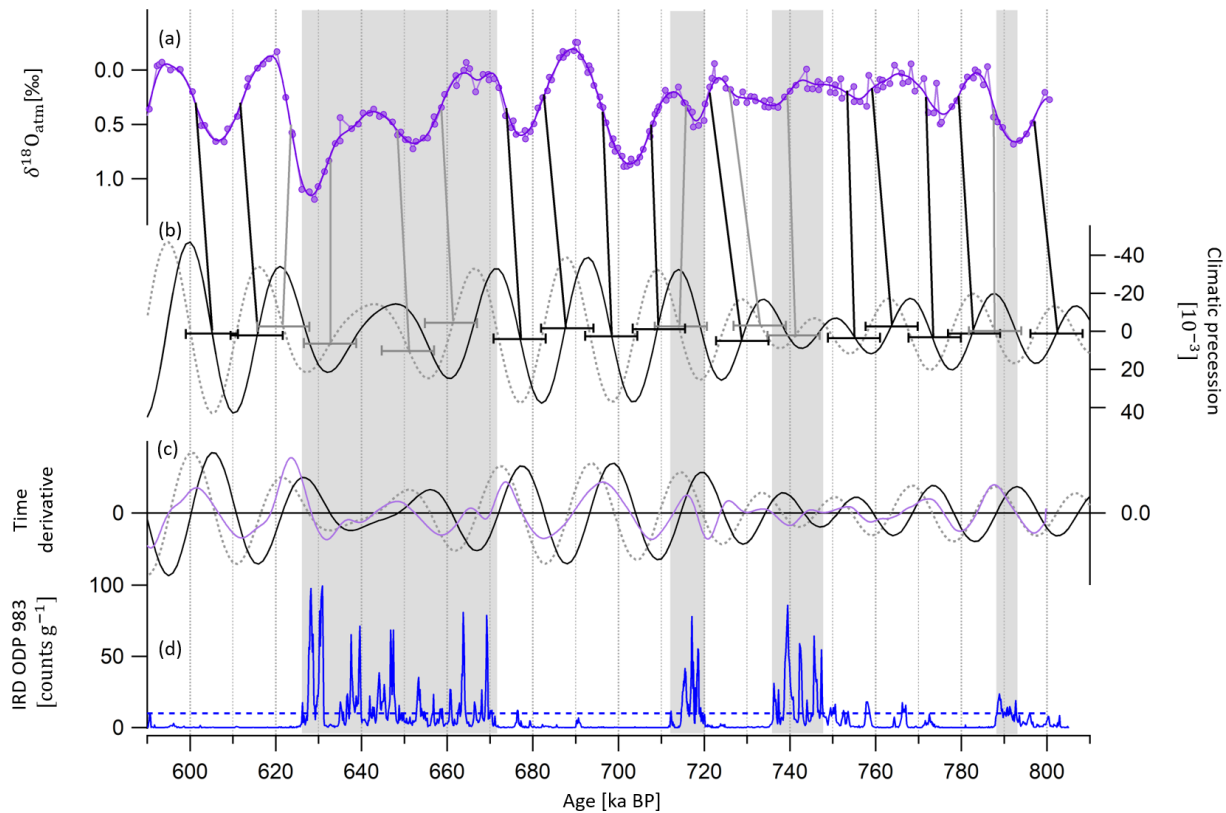


Figure 5. Alignment of EDC $\delta^{18}\text{O}_{\text{atm}}$ and climatic precession between 810 and 590 ka BP. **(a)** Compiled EDC $\delta^{18}\text{O}_{\text{atm}}$ on the AICC2012 gas timescale. **(b)** Precession delayed by 5000 years (dashed gray line) and not delayed (black line) (Laskar et al., 2004). **(c)** Temporal derivative of precession (black line), delayed precession (dotted gray line) and the compiled $\delta^{18}\text{O}_{\text{atm}}$ record (plain purple line). **(d)** Ice-rafted debris at ODP983 site (North Atlantic Ocean, southwest of Iceland) by Barker et al. (2019, 2021). The gray rectangles indicate periods where IRD counts are greater than the 10 counts per gram threshold shown by the dotted horizontal blue line. Vertical gray bars illustrate new tie points between EDC $\delta^{18}\text{O}_{\text{atm}}$ and delayed precession mid-slopes (i.e., derivative extrema) when IRD counts are greater than the threshold. Vertical black bars illustrate new tie points between EDC $\delta^{18}\text{O}_{\text{atm}}$ and precession mid-slopes (i.e., derivative extrema) when no Heinrich-like events are shown by the IRD record. The 12 kyr 2σ uncertainty attached to the tie points is shown by the horizontal error bars in panel **(b)**.

Bazin et al. (2013): EDC $\delta^{18}\text{O}_{\text{atm}}$ and 5 kyr delayed climatic precession are synchronized using mid-slopes of their variations. However, from the findings of Extier et al. (2018a), $\delta^{18}\text{O}_{\text{atm}}$ should rather be aligned to precession without delay when no Heinrich-like events occur. Indeed, $\delta^{18}\text{O}_{\text{atm}}$ is sensitive to both orbital- and millennial-scale variations in the low-latitude water cycle (Landais et al., 2010; Capron et al., 2012), and Heinrich-like events occurring during deglaciations delay the response of $\delta^{18}\text{O}_{\text{atm}}$ to orbital forcing through southward ITCZ shifts (Extier et al., 2018a). We thus chose to align $\delta^{18}\text{O}_{\text{atm}}$ to precession when no ice-rafted debris (IRD) peak is visible in the studied period in the ODP983 record (Barker et al., 2019, 2021) and keep a 5 kyr delay when IRD peaks are identified. This results in shifting 12 tie points of Bazin et al. (2013) by 5000 years towards older ages (Fig. 6). The eight remaining tie points of Bazin et al. (2013) that coincide with peaks in the IRD record are kept (Fig. 6). To confirm the validity of our approach, we tested three methodologies to align $\delta^{18}\text{O}_{\text{atm}}$ and precession over well-

dated periods when $\delta^{18}\text{O}_{\text{atm}}-\delta^{18}\text{O}_{\text{calcite}}$ matching was done (see Sect. S2.2.2). These tests support our approach, but in order to account for potential errors associated with this tuning method (Oyabu et al., 2022), a 6 kyr uncertainty (1σ) is attributed to the $\delta^{18}\text{O}_{\text{atm}}$ -derived tie points over the period between 810 and 590 ka BP.

A total of 69 new $\delta^{18}\text{O}_{\text{atm}}$ tie points are determined over the last 810 kyr (displayed in Figs. 4 and 5 and compiled in Table S5). They replace the 39 tie points used to constrain the EDC gas timescale in AICC2012 between 800 and 363 ka BP (Bazin et al., 2013). The age constraints are attached to an uncertainty varying between 1.1 and 7.4 kyr, which is the sum of the uncertainties in the speleothem ^{230}Th dating, the $\delta^{18}\text{O}_{\text{atm}}$ response to orbital forcing (1 kyr) and the $\delta^{18}\text{O}_{\text{atm}}-\delta^{18}\text{O}_{\text{calcite}}$ matching (0.5 kyr). The same alignment method is applied between Vostok $\delta^{18}\text{O}_{\text{atm}}$ (Petit et al., 1999) and Chinese $\delta^{18}\text{O}_{\text{calcite}}$, and 36 new tie points are determined (see Sect. S4.1.2), replacing the 35 tie points used to constrain the Vostok gas timescale in AICC2012.

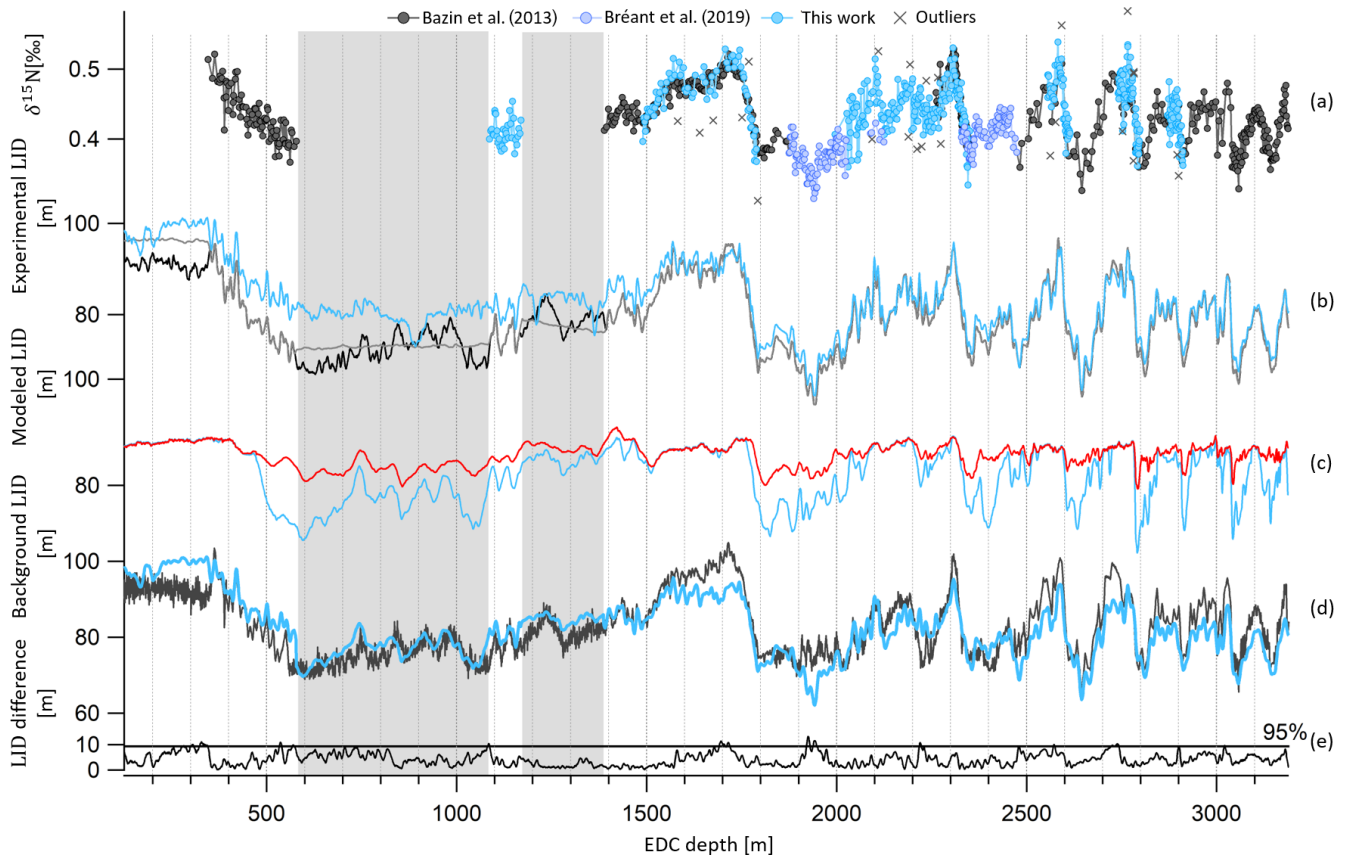


Figure 6. EDC $\delta^{15}\text{N}$ record and past LID evolution as a function of EDC depth. **(a)** New and highly resolved $\delta^{15}\text{N}$ dataset (blue circles), dataset of Bréant et al. (2019) (purple circles), old dataset (black circles) and outliers (rejection criterion of 1σ) (gray crosses). **(b)** LID calculated as per $\text{LID} \simeq \delta^{15}\text{N}_{\text{grav}} \cdot \frac{RT}{g}$ for three cases: (1) $\delta^{15}\text{N}_{\text{grav}} = \delta^{15}\text{N}$ with the $\delta^{15}\text{N}$ record constructed by interpolation between data when no data are available (gray), (2) $\delta^{15}\text{N}_{\text{grav}} = \delta^{15}\text{N}$ with the $\delta^{15}\text{N}$ record constructed by normalization of the δD record when no data are available (black), (3) $\delta^{15}\text{N}_{\text{grav}} = \delta^{15}\text{N} - \delta^{15}\text{N}_{\text{therm}}$ with $\delta^{15}\text{N}_{\text{therm}}$ estimated by the firm model (Bréant et al., 2017) and the $\delta^{15}\text{N}$ record constructed by interpolation between data when no data are available (blue). **(c)** Modeled LID with impurity concentration (blue) and without impurity concentration (red). **(d)** Background scenarios of LID used to construct AICC2012 (black) and inputs in PaleoChrono to obtain AICC2023 (blue). **(e)** Absolute difference between prior LID of AICC2012 and AICC2023. The gray line separates the top 5% values from the rest. The gray rectangles cover areas when no $\delta^{15}\text{N}$ data are available.

Finally, there was a redundancy in the dating of the bottom part of the EDC ice core in AICC2012, where both $\delta^{18}\text{O}_{\text{atm}}$ orbital tie points and ^{10}Be peaks corresponding to the Matuyama–Brunhes geomagnetic reversal event were used. Indeed, the two ^{10}Be dating constraints at 780.3 and 798.3 ka BP were directly derived from the $\delta^{18}\text{O}_{\text{atm}}$ orbital dating and not obtained independently (Dreyfus et al., 2008). We thus decided to remove the ^{10}Be age constraints.

3.3 Background scenario of LID

In this work, new highly resolved $\delta^{15}\text{N}$ data in the EDC ice core are presented over terminations II, III, IV, V and VI (Fig. 6a). The available $\delta^{15}\text{N}$ data can be sorted out in two groups: $\delta^{15}\text{N}$ measured by Grisart (2023) and Bréant et al. (2019) at high temporal resolution (between 333 and 1375 years; see Table 1) and the older measurements (Bazin

et al., 2013) used to estimate LID in AICC2012, characterized by a lower sampling resolution (between 1400 and 2400 years; see Table 1). The measurements of Bazin et al. (2013) and Bréant et al. (2019) have been shifted down by 0.04‰ to account for calibration errors. The new dataset permits the extension of the record by around 1100 m and between 1700 and 2500 m and improvement in the resolution over terminations II to VI.

Outliers are discarded if they show an anomaly greater than 0.045‰ when compared to the smoothed record (Savitzky–Golay algorithm with 25 points). This results in the rejection of 25 data points out of 475 measurements for the new dataset (Fig. 6). The two $\delta^{15}\text{N}$ datasets are merged, and the compiled record is interpolated every 100 years. Then, assuming that the firm is solely a diffusive zone (i.e., no convection layer at the top) at EDC during the last 800 kyr, in

agreement with current observations (Landais et al., 2006), past LID is calculated as per the first-order estimate of the barometric equation:

$$\text{LID} \simeq \delta^{15}\text{N}_{\text{grav}} \frac{RT}{g}, \quad (5)$$

with T the temperature at EDC estimated from combined measurements of ice $\delta^{18}\text{O}$ and δD after correction of the influence of the seawater $\delta^{18}\text{O}$ (Landais et al., 2021).

In the absence of a large thermal gradient within the firn (mostly present in Greenlandic ice cores during Dansgaard–Oeschger events), $\delta^{15}\text{N}$ is mainly modulated by gravitational fractionation of N_2 molecules occurring from the surface down to the lock-in zone, and $\delta^{15}\text{N}$ measured in bubbles hence approximately reflects the LID (Severinghaus et al., 1996; Landais et al., 2006) and $\delta^{15}\text{N}_{\text{grav}} \simeq \delta^{15}\text{N}$ in Eq. (5) (gray and black lines in Fig. 6b). To account for a small temperature gradient in the firn in the Antarctic ice core, the thermal-fractionation term $\delta^{15}\text{N}_{\text{therm}}$ can be estimated by the firn model (Bréant et al., 2017). Past LID is then calculated as per Eq. (5) with $\delta^{15}\text{N}_{\text{grav}} = \delta^{15}\text{N} - \delta^{15}\text{N}_{\text{therm}}$ (blue curve in Fig. 6b). Thermal fractionation represents a maximum correction of 4.2 m to the LID at EDC.

When $\delta^{15}\text{N}$ measurements are not available, Bazin et al. (2013) used a synthetic $\delta^{15}\text{N}$ signal based on the correlation between $\delta^{15}\text{N}$ and δD to estimate the LID background scenario at Dome C (black curve in Fig. 6b). Indeed, for different low-accumulation Antarctic sites, it has been observed that $\delta^{15}\text{N}$ and δD are well correlated over the last termination on a coherent timescale (Dreyfus et al., 2010; Capron et al., 2013). Since then, Bréant et al. (2019) presented new high-resolution EDC measurements of $\delta^{15}\text{N}$ extending the signal over termination III (around 2300 m, 250 ka BP). Their study unveiled the anatomy of this atypical deglaciation: the interplay between Heinrich-like events and the bipolar seesaw mechanism induced a strong warming of Antarctic temperature, resulting in divergent $\delta^{15}\text{N}$ and δD records. Therefore, using δD to construct a synthetic $\delta^{15}\text{N}$ scenario should be done carefully. For this reason, the firn densification model described in Bréant et al. (2017) is employed to estimate EDC LID evolution in the past when $\delta^{15}\text{N}$ data are missing, rather than using the $\delta^{15}\text{N}$ – δD relationship, as was done for AICC2012. After different sensitivity tests, we chose to keep the parameterization preferred by Bréant et al. (2017) (i.e., firn densification activation energy depending on the temperature and the impurity concentration) as it is believed to give the most probable evolution of LID over the last 800 kyr (see Sect. S3.1).

The final background LID scenario is calculated as a function of EDC depth (Table 4, Fig. 6d). It has been smoothed using a Savitzky–Golay algorithm (25 points) and then provided as an input file to Paleochrono.

The other necessary input files for Paleochrono, accumulation (A) and thinning (τ) background scenarios, are the same as in Bazin et al. (2013). A is estimated from water isotopes

(Parrenin et al., 2007b) and τ from unidimensional ice flow modeling (Parrenin et al., 2007a).

3.4 New stratigraphic links between the EDC and other ice cores

EDC can be linked to other ice cores via ice and gas stratigraphic links identified during abrupt climate changes recorded in Greenlandic and Antarctic ice cores. To establish AICC2012, Bazin et al. (2013) used 255 gas stratigraphic tie points coming from the matching of CH_4 (or $\delta^{15}\text{N}$ when CH_4 is not available at NGRIP) or $\delta^{18}\text{O}_{\text{atm}}$ variations between EDC, EDML, Vostok, NGRIP and TALDICE. Here we revise some of these tie points using the synchronization of CH_4 series of EDC, Vostok and TALDICE to up-to-date, highly resolved records from EDML and NGRIP ice cores over the last interglacial offset and the last glacial period (Baumgartner et al., 2014). From 122 to 10 ka BP, Baumgartner et al. (2014) identified 39 stratigraphic links between EDML and NGRIP by matching mid-points of the CH_4 abrupt changes with a precision of 300 to 700 years. When they also detected such rapid variations in lower-resolution CH_4 records of the TALDICE, Vostok and EDC ice cores, they extended the stratigraphic links to the five ice cores but assigned them a larger uncertainty (up to 1500 years). AICC2012 was further constrained by 534 ice stratigraphic links identified from volcanic matching and synchronization of cosmogenic isotopes between the five ice cores. Here we replace some of the stratigraphic links between NGRIP, EDML and EDC by highly resolved volcanic matching points (Svensson et al., 2020). The application of volcanic proxies and annual layer counting helped them identify large volcanic eruptions that left a specific signature in both Greenland and Antarctica. Such a signature is defined by sulfate patterns (indicating singular volcanic events separated by the same time interval in ice cores from both poles). Their study spotted 82 large bipolar volcanic eruptions over the second half of the last glacial period (from 60 to 12 ka BP), providing as many ice stratigraphic links synchronizing EDC with EDML and EDML with NGRIP within a small relative uncertainty (i.e., ranging from 1 to 50 years, 12 years on average). Between 43 and 40 ka BP, five cosmogenic tie points associated with the Laschamp geomagnetic excursion (Raisbeck et al., 2017) replace the volcanic matching over this period (Svensson et al., 2013), shifting the tie points by ~ 30 years.

4 Discussion

4.1 New AICC2023 chronology

4.1.1 Impact of absolute age constraints

A large uncertainty is linked with ^{81}Kr dating; therefore ^{81}Kr age estimates do not significantly change the chronology

Table 4. Method of determination of the background LID scenario according to the EDC depth range.

Depth range (m)	0–345	345–578	578–1086	1086–1169	1169–1386	1386–bottom
$\delta^{15}\text{N}$ data availability	No	Yes	No	Yes	No	Yes
Method of determination of the LID	From constant $\delta^{15}\text{N}$ (measured at 345 m) and corrected for thermal fractionation	From $\delta^{15}\text{N}$ data, corrected for thermal fractionation and smoothed	From firm modeling	From $\delta^{15}\text{N}$ data, corrected for thermal fractionation and smoothed	From firm modeling	From $\delta^{15}\text{N}$ data, corrected for thermal fractionation and smoothed

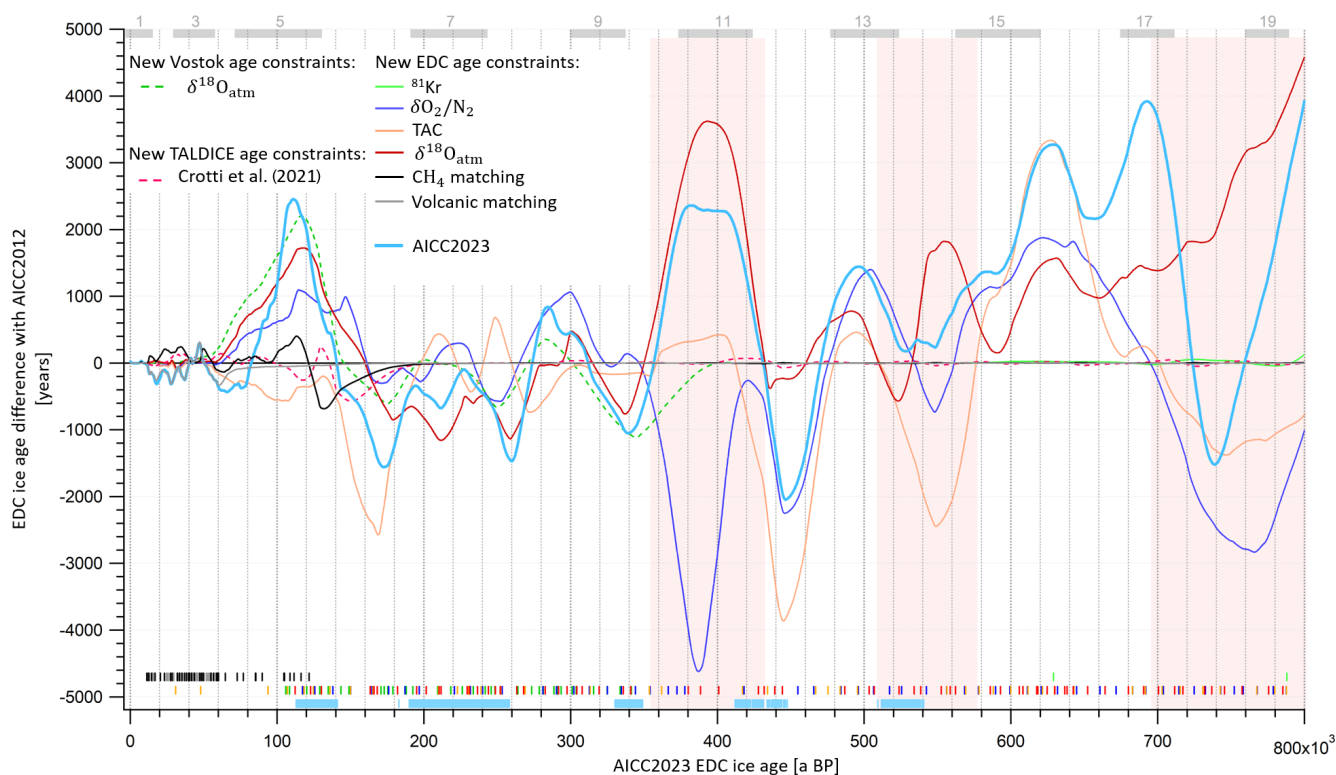


Figure 7. EDC ice age difference between AICC2012 and different test chronologies obtained with PaleoChrono over the last 800 kyr. The ice age difference is calculated as per test chronology – AICC2012. Two test chronologies are obtained by addition of either new Vostok $\delta^{18}\text{O}_{\text{atm}}-\delta^{18}\text{O}_{\text{calcite}}$ age constraints (dotted green line) or stratigraphic and absolute TALDICE constraints between 470 and 129 ka BP from Crotti et al. (2021) (dotted red line). The other “test chronologies” are constructed by replacing AICC2012 constraints by either (1) ^{81}Kr (green); (2) $\delta\text{O}_2/\text{N}_2$ (purple); (3) TAC (orange); (4) $\delta^{18}\text{O}_{\text{atm}}$ (red); (5) CH_4 tie points with NGRIP, EDML, TALDICE and Vostok (black); or (6) volcanic matching points with EDML and NGRIP (gray). Vertical bars represent the corresponding age horizons. AICC2023 is obtained by implementing the new constraints all together (light-blue line). Vertical light-blue bars show new data collected by Grisart (2023) and presented in this work. The three largest inconsistencies between $\delta\text{O}_2/\text{N}_2$, TAC and $\delta^{18}\text{O}_{\text{atm}}$ chronologies are shown by red areas. Gray rectangles indicate interglacials from MIS 19 to MIS 1.

(maximum 200 years) (Fig. 7). ^{81}Kr age estimates are systematically older than the new timescale (by 25 to 36 kyr; see Fig. 8). This observation could also indicate an undervaluation of ^{81}Kr half-life.

4.1.2 Consistency between orbital age constraints

To evaluate the consistency between the orbital age constraints, several “test chronologies” are produced. Each test chronology of the EDC ice core is obtained by running one

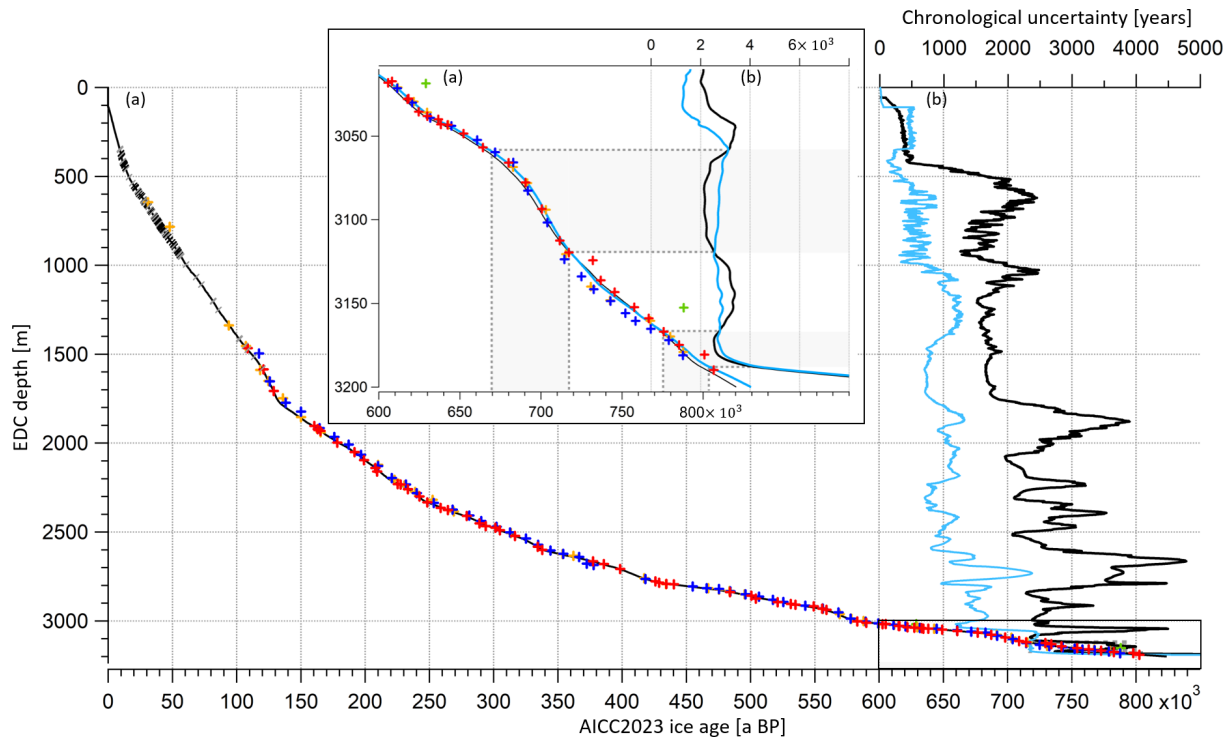


Figure 8. EDC ice age and uncertainty as a function of the depth. (a) EDC ice age (AICC2012 in black, AICC2023 in blue), (b) 1σ uncertainty (AICC2012 in black, AICC2023 in blue). Crosses and slashes represent new age constraints (ice stratigraphic links in black, gas stratigraphic links in gray, $\delta^{18}\text{O}_{\text{atm}}$ in red, $\delta\text{O}_2/\text{N}_2$ in blue, TAC in orange, ^{81}Kr in green). Inset is a zoom in between 800 and 600 ka BP. Gray rectangles frame periods where the new AICC2023 uncertainty is larger than the AICC2012 uncertainty. See Fig. S13 for EDC gas age profile.

multi-site (EDC, Vostok, EDML, TALDICE, NGRIP) experiment of Paleochrono. In each of these tests, we implemented one category of new age constraints presented in this work while keeping AICC2012 parameters for other categories. Several test chronologies are thus constructed: the ^{81}Kr -, $\delta\text{O}_2/\text{N}_2$ -, TAC-, $\delta^{18}\text{O}_{\text{atm}}$ -, CH_4 -matching- and volcanic-matching-based chronologies (Fig. 7). Two additional test chronologies are obtained by implementing and modifying age constraints either on Vostok or TALDICE with respect to the AICC2012 chronology, as explained in Sect. 2.1 (Fig. 7, dotted lines). The EDC ice age difference between each test chronology and the AICC2012 timescale is represented in Fig. 7 so that it is possible to read which type of dating tool suggests shifting the background chronology towards either older or younger ages.

Although the three orbital dating tools globally agree with each other over the last 800 kyr, meaning that they all tend to shift the background chronology towards either older or younger ages over a certain period of time, they are sometimes inconsistent (Fig. 7). The three largest inconsistencies involve age differences between $\delta\text{O}_2/\text{N}_2$ -, TAC- and $\delta^{18}\text{O}_{\text{atm}}$ -based chronologies reaching 4.15 to 8.3 kyr (Table 5). At 390 ka BP, a large 8.3 kyr discrepancy is observed between $\delta\text{O}_2/\text{N}_2$ - and $\delta^{18}\text{O}_{\text{atm}}$ -based chronologies. Over this

period, the low-resolution $\delta\text{O}_2/\text{N}_2$ record variations do not match its orbital target variations (two insolation minima against one $\delta\text{O}_2/\text{N}_2$ maximum; see Fig. 1). For this reason, the $\delta\text{O}_2/\text{N}_2$ age constraints identified between 480 and 350 ka BP were attached to a 6 kyr uncertainty (quarter of a recession period; Fig. 1). In contrast, the $\delta^{18}\text{O}_{\text{atm}}$ record agrees well with $\delta^{18}\text{O}_{\text{calcite}}$ (Fig. 3), and the uncertainty attached to the $\delta^{18}\text{O}_{\text{calcite}}$ inferred tie points over this interval is smaller. Hence, the new AICC2023 chronology suggests shifting AICC2012 towards older ages by 2.2 kyr, as per the $\delta^{18}\text{O}_{\text{atm}}$ -based chronology (Fig. 7). Around 550 ka BP, the TAC- and $\delta^{18}\text{O}_{\text{atm}}$ -based chronologies strongly diverge. This may be caused by the absence of TAC tie points due to the non-coincidence of TAC and ISI375 extrema (Fig. 3), while there is good agreement between $\delta^{18}\text{O}_{\text{atm}}$ and $\delta^{18}\text{O}_{\text{calcite}}$ records. Therefore, we decide to increase the uncertainty attached to the four TAC age constraints between 600 and 550 ka BP up to 6 kyr (Fig. 2), and AICC2023 follows the $\delta^{18}\text{O}_{\text{atm}}$ -based chronology, inducing older ages than AICC2012. At 765 ka BP, the discordance between $\delta\text{O}_2/\text{N}_2$ - (and TAC-) and $\delta^{18}\text{O}_{\text{atm}}$ -based chronologies is likely due to the poor quality of the records from the lowermost part of the core. Over these oldest time periods, $\delta^{18}\text{O}_{\text{atm}}$, TAC and $\delta\text{O}_2/\text{N}_2$ were tied up, respectively, with precession, inte-

grated insolation and insolation with a large uncertainty (6 to 10 kyr). This leads to a final chronology AICC2023, suggesting a larger chronological uncertainty than AICC2012 as well as younger ages (as per TAC and $\delta\text{O}_2/\text{N}_2$ chronologies) over MIS 18 and then older ages (as per $\delta^{18}\text{O}_{\text{atm}}$ chronology) over MIS 19.

4.1.3 Final chronology and uncertainty

The new AICC2023 chronology suggests significant age shifts when compared to AICC2012 over old periods, including 3.8 and 5 kyr shifts towards older ages around 800 and 690 ka BP as well as a 2.1 kyr shift towards younger ages around 730 ka BP. The chronology is also modified over MIS 5 and MIS 11, where AICC2023 is about 2 kyr older than AICC2012. These 2 kyr shifts are induced by $\delta\text{O}_2/\text{N}_2$ and $\delta^{18}\text{O}_{\text{atm}}$ dating constraints and stratigraphic links over MIS 5 and by TAC and $\delta^{18}\text{O}_{\text{atm}}$ constraints over MIS 11. When averaged over the past 800 kyr, the chronological uncertainty is reduced from 1.7 kyr for AICC2012 to 900 years here. Still, it remains significant (above 2 kyr) over MIS 11 and in the lowermost part of the core, between 800 and 650 ka BP. Specifically, between 800 and 670 ka BP, the uncertainty associated with the new AICC2023 timescale is sometimes larger than the AICC2012 uncertainty (Fig. 8). This is caused by a larger relative error attached to $\delta\text{O}_2/\text{N}_2$ and TAC age constraints as well as by the exclusion of the two redundant ^{10}Be age constraints at 780.3 and 798.3 ka BP associated with the Matuyama–Brunhes geomagnetic reversal event.

The age difference between ice and gas timescales (Δage) is 3 kyr on average, reaching its largest values (~ 4 kyr) during the cold eras of MISs 12, 8, 6 and 4 (at 440, 260, 145 and 70 ka BP, respectively; Fig. 9). A 4 kyr Δage is obtained at around 160 ka BP (Fig. 9), consistent with the use of new $\delta^{15}\text{N}$ data of Bréant et al. (2019), leading to a background scenario of LID that is 13 m smaller than the prior LID scenario used in AICC2012 between the depths of 1900 and 2000 m (Fig. 6). Using the definition of an interglacial period implying an EDC δD value surpassing the threshold of -403‰ (EPICA Community Members, 2004), we identify 10 substages of interglacials (MISs 1, 5e, 7a, 7c, 7e, 9e, 11c, 15a, 15e and 19; Fig. 9). The average duration of these substages is reduced by 320 years with the new AICC2023 timescale in comparison with the AICC2012 chronology (Fig. 9). More specifically, MISs 5e to 15a are shorter, while only MIS 15e and MIS 19 are longer. The largest decreases in duration affect the Last Interglacial (MIS 5e) and MIS 11c, whose lengths are decreased from 16.3 to 15.1 kyr and from 31.1 to 30.1 kyr, respectively, in agreement with the durations of 14.8 and 29.7 kyr proposed by Extier et al. (2018a).

4.2 Comparison with other chronologies

4.2.1 MIS 5 (from 130 to 80 ka BP)

When Veres et al. (2013) presented the AICC2012 chronology over the last climatic cycle, they identified a disagreement with the Greenland timescale GICC05-modelext between 115 and 100 ka BP. The comparison between the Greenland $\delta^{18}\text{O}_{\text{ice}}$ record and the $\delta^{18}\text{O}_{\text{calcite}}$ from U–Th-dated Alpine speleothems showed a delay of up to 2.7 kyr during the Dansgaard–Oeschger (D–O) events 23, 24 and 25. Later, this disagreement between abrupt changes in $\delta^{18}\text{O}_{\text{ice}}$ from NGRIP (Greenland surface temperature) and $\delta^{18}\text{O}_{\text{calcite}}$ from the Alps was re-evaluated based on a different use of $\delta^{18}\text{O}_{\text{atm}}$ in ice core chronology, and Extier et al. (2018a) presented better agreement between the two records with an older NGRIP timescale than AICC2012 by ~ 2200 years for D–O 23 to 25.

In Fig. 11, the NGRIP $\delta^{18}\text{O}_{\text{ice}}$ record is represented on the AICC2023 timescale and is compared to ancient and novel records of $\delta^{18}\text{O}_{\text{calcite}}$ from speleothems that grew along the northern rim of the Alps (NALPS; Boch et al., 2011; Moseley et al., 2020). Thanks to new $\delta\text{O}_2/\text{N}_2$ and $\delta^{18}\text{O}_{\text{atm}}$ age constraints, the new AICC2023 chronology is also older than AICC2012 between 115 and 100 ka BP and leads to improved agreement between the records along with a reduction in the uncertainty. This amelioration is particularly visible over D–O warmings 23 and 24, where the difference between NALPS and NGRIP chronologies is reduced from ~ 2000 years (AICC2012) to 430 and 325 years (AICC2023), respectively (Table 6).

The Greenland Interstadial (GI) 25 can be subdivided in three substages: GI-25a, GI-25-b and GI-25-c, where GI-25a is the earliest glacial so-called “rebound event” (Capron et al., 2010). This latter consists of a brief warm–wet excursion during the slow cooling trend of the longer GI-25 period before jumping back to a cool–dry climate. The GI-25a warm–wet interval corresponds to a temperature increase in Greenland and continental Europe and is hence identified by a positive excursion in NGRIP and NALPS $\delta^{18}\text{O}$ records (D–O 25 rebound) (Boch et al., 2011; Capron et al., 2012). At lower latitudes, this rebound likely affected the rainfall amount variations, as exhibited by the abrupt decrease in the $\delta^{18}\text{O}_{\text{calcite}}$ from a U–Th-dated Sardinian stalagmite from Bue Marino Cave (BMS1; Columbu et al., 2017). The 2 kyr shift in the new AICC2023 chronology towards older ages improves the coherency between NALPS, NGRIP and BMS1 timescales over the GI-25a onset (traceable in the $\delta^{18}\text{O}$ series; Fig. 10). The age discrepancy is reduced from ~ 3600 years (between AICC2012 and BMS1 timescale) to 1640 years (between AICC2023 and BMS1 timescale; Table 6).

Between 128 and 103 ka BP, the comparison between the AICC2012 timescale and the novel Dome Fuji ice core DF2021 chronology indicates that AICC2012 is likely too

Table 5. Description of the inconsistencies between $\delta\text{O}_2/\text{N}_2$ -, TAC- and $\delta^{18}\text{O}_{\text{atm}}$ -based chronologies. The age shift suggested by each dating tool with respect to AICC2012 age is detailed. The age position of the disagreement is given as per AICC2023. We did not highlight inconsistencies between $\delta\text{O}_2/\text{N}_2$ - and TAC-based chronologies as they remain within their respective orbital uncertainty.

$\delta\text{O}_2/\text{N}_2$	$\delta^{18}\text{O}_{\text{atm}}$		
	Non-coherent	Non-coherent	Non-coherent
TAC	Coherent	Non-coherent	Non-coherent
Disagreement type	$\delta\text{O}_2/\text{N}_2$ chronology younger than AICC2012 by 4700 years	TAC (and $\delta\text{O}_2/\text{N}_2$) chronology younger than AICC2012 by 2400 (and 800) years	$\delta\text{O}_2/\text{N}_2$ (and TAC) chronology younger than AICC2012 by 2850 (and 1300) years
	$\delta^{18}\text{O}_{\text{atm}}$ chronology older than AICC2012 by 3600 years	$\delta^{18}\text{O}_{\text{atm}}$ chronology older than AICC2012 by 1700 years	$\delta^{18}\text{O}_{\text{atm}}$ chronology older than AICC2012 by 2800 years
Interval of disagreement (ka BP)	430–350 (MIS 11)	580–510 (MIS 14)	800–700 (MISs 19–18)

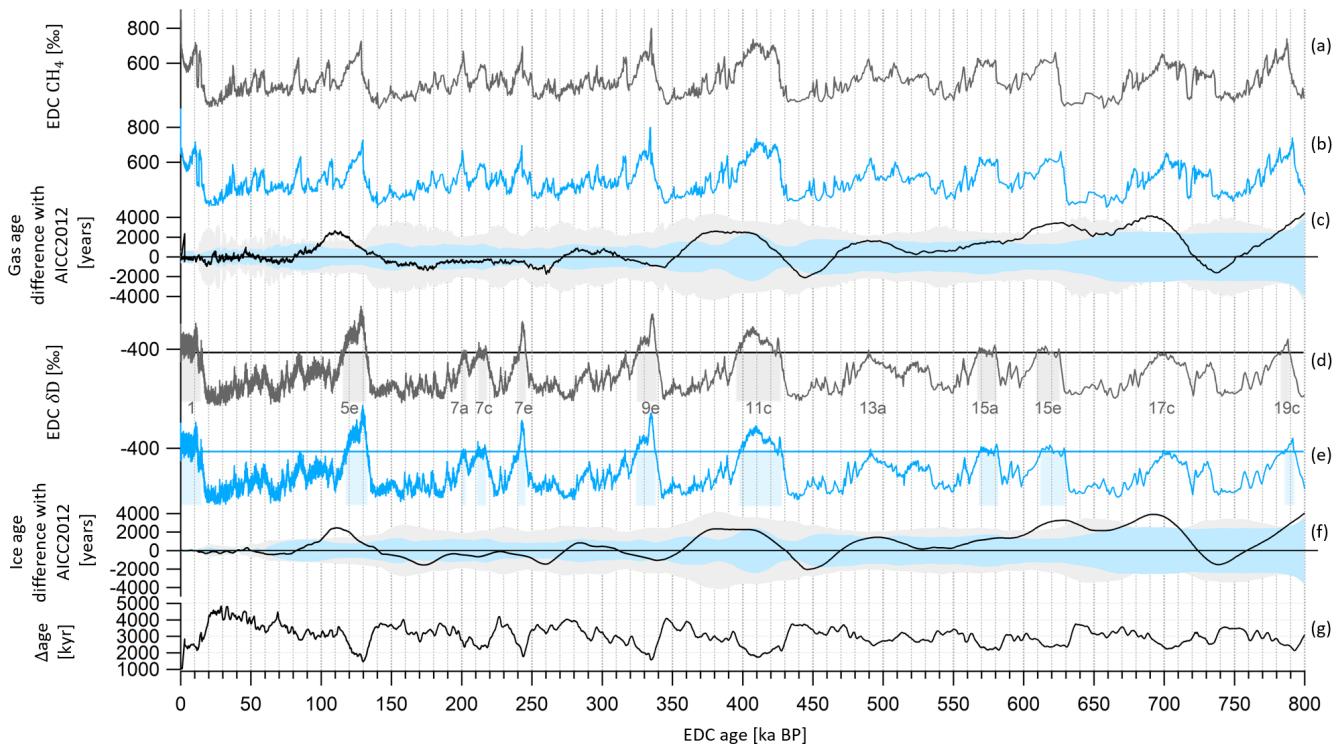


Figure 9. EDC gas and ice records on AICC2023 (blue) and AICC2012 (black) timescales over the last 800 kyr. **(a)** EDC CH_4 (Loulergue et al., 2008) on AICC2012 and **(b)** AICC2023 gas timescales. **(c)** Gas age difference AICC2023–AICC2012. Gray and blue envelopes are AICC2012 and AICC2023 chronological 1σ uncertainties, respectively. **(d)** EDC δD (Jouzel et al., 2007) on AICC2012 and **(e)** AICC2023 ice timescales. Gray and blue rectangles indicate interglacial periods defined when δD is greater than the threshold of -403‰ (horizontal lines) (EPICA Community Members, 2004). Interglacials are numbered from MISs 1 to 19 (Berger et al., 2016). **(f)** Ice age difference AICC2023–AICC2012. **(g)** Age difference between ice and gas AICC2023 timescales (Δage).

Table 6. Timing of D–O warmings 23 and 24 and D–O 25 rebound event onset. The GICC05-model ext age uncertainty is undetermined.

Event	Timing (a BP) and error (years)					
	NGRIP ice core timescale				Speleothem timescale	
	GICC05-model ext (Wolff et al., 2010)	AICC2012 (Veres et al., 2013)	Extier et al. (2018a)	AICC2023 (this study)	BMS1 (Columbu et al., 2017)	NALPS (Boch et al., 2011)
D–O 23 warming	103 995	101 850 ± 1310	104 090 ± 1200	103 980 ± 930	Not recorded	103 550 ± 375
D–O 24 warming	108 250	105 850 ± 1330	108 010 ± 1200	107 975 ± 850	Not recorded	108 300 ± 450
D–O 25 rebound onset	110 960	108 100 ± 1410	110 280 ± 1200	110 120 ± 900	111 760 ± 450	111 780 ± 630

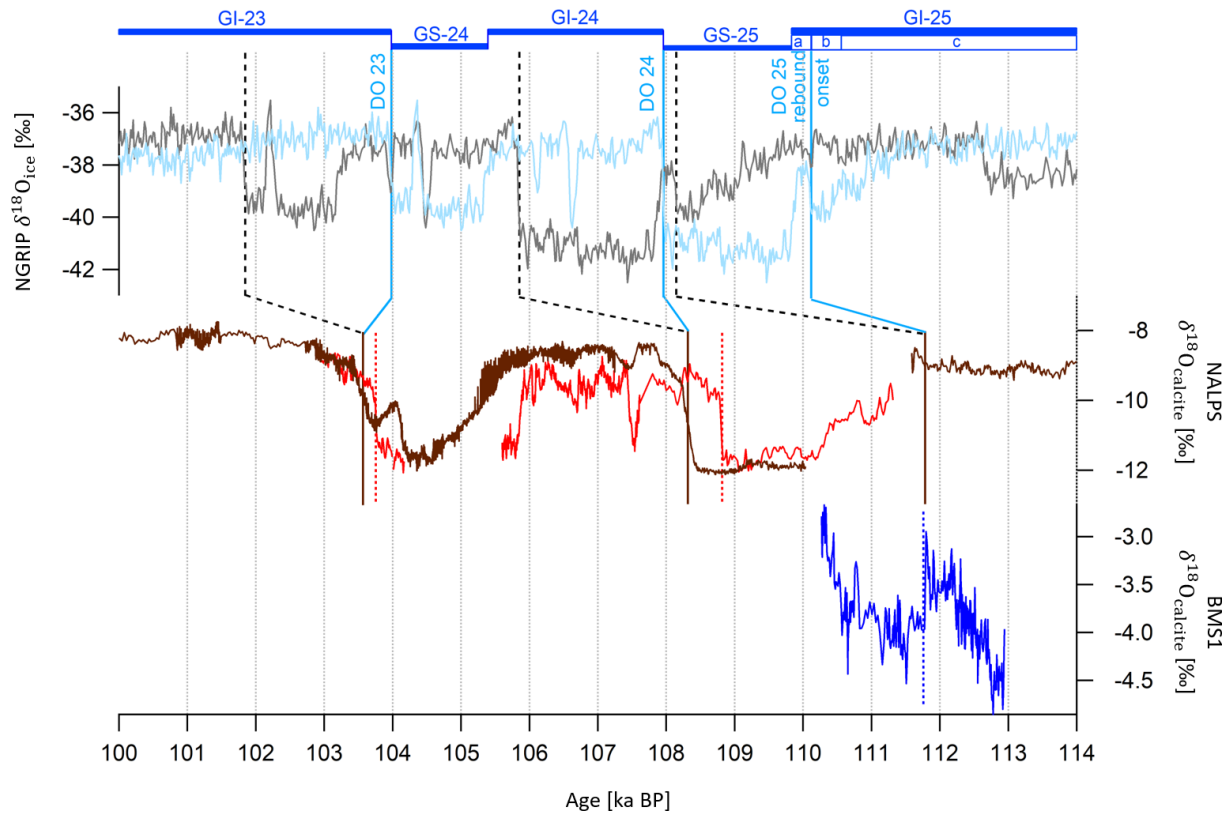


Figure 10. Northern Alpine speleothems (NALPS) and Bue Marino stalagmite (BMS1) $\delta^{18}\text{O}_{\text{calcite}}$ records and NGRIP $\delta^{18}\text{O}_{\text{ice}}$ evolution between 114 and 100 ka BP. NGRIP $\delta^{18}\text{O}_{\text{ice}}$ data by Andersen et al. (2004) on AICC2012 (gray) and AICC2023 (blue) chronologies. NALPS $\delta^{18}\text{O}_{\text{calcite}}$ data by Moseley et al. (2020) (red) and Boch et al. (2011) (brown). BMS1 $\delta^{18}\text{O}_{\text{calcite}}$ data by Columbu et al. (2017) (dark blue). Vertical bars indicate D–O 25 rebound, D–O 24 and D–O 23 warmings at the onset of the GI-25a warm–wet substage, GI-24, and GI-23. They correspond to abrupt increases in the NALPS $\delta^{18}\text{O}_{\text{calcite}}$ and NGRIP $\delta^{18}\text{O}_{\text{ice}}$ records and to a decrease in the BMS1 $\delta^{18}\text{O}_{\text{calcite}}$ series (for the GI-25a onset). Dashed black bars and blue bars show increases in $\delta^{18}\text{O}_{\text{ice}}$, respectively, on AICC2012 and AICC2023 chronologies. Brown bars and dotted red bars show increases in NALPS $\delta^{18}\text{O}_{\text{calcite}}$ datasets. The dotted blue bar indicates the decrease in BMS1 $\delta^{18}\text{O}_{\text{calcite}}$. GI–GS (Greenland stadial) boundaries and GI-25 subdivision are indicated on the new AICC2023 chronology by horizontal bars.

young by up to 4 kyr. Here, thanks to new highly resolved $\delta\text{O}_2/\text{N}_2$ data and to the alignment of $\delta^{18}\text{O}_{\text{atm}}$ and $\delta^{18}\text{O}_{\text{calcite}}$ records, we improve the consistency between AICC2023 and DF2021, now agreeing within 1.7 kyr over MIS 5e (Fig. 11). With the new chronologies, the records of $\delta^{18}\text{O}_{\text{atm}}$ and $\delta\text{O}_2/\text{N}_2$ from the Dome Fuji and EDC ice cores

show synchronous variations between 140 and 115 ka BP, although the $\delta\text{O}_2/\text{N}_2$ measurements from EDC are more scattered than DF data due to the use of smaller samples (see Sect. S1 in the Supplement). However, δD records are still slightly discordant, and the EDC record lags DF by up to 1700 years over MIS 5e and at the onset of the Antarctic

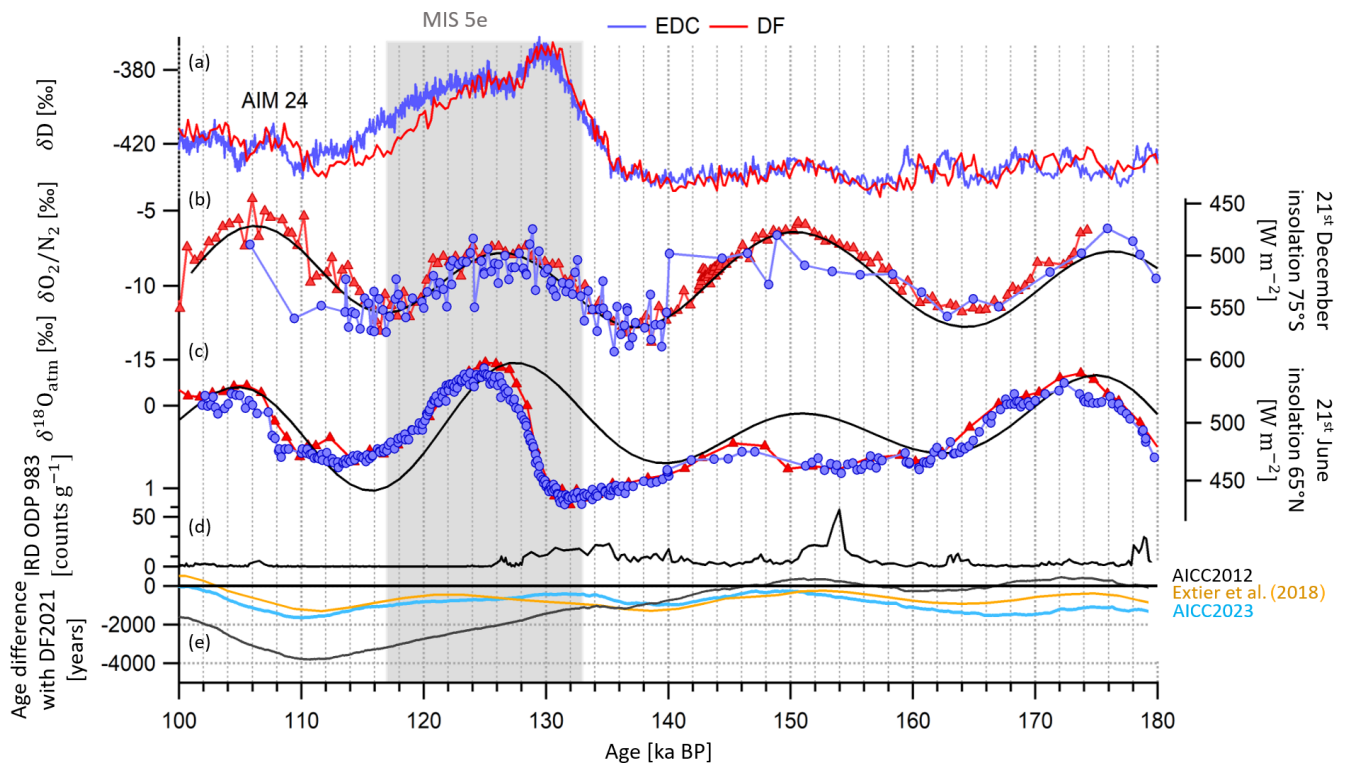


Figure 11. Evolution of EDC and DF records on AICC2023 and DF2021 chronologies between 180 and 100 ka BP. **(a)** δD records from DF (red; Uemura et al., 2018) and EDC (purple; Jouzel et al., 2007). **(b)** $\delta O_2/N_2$ records from DF (red triangles; Oyabu et al., 2022) and EDC (purple circles; this work). **(c)** $\delta^{18}O_{atm}$ records from DF (red triangles; Kawamura et al., 2007) and EDC (purple circles; this work). DF and EDC records are represented on DF2021 and AICC2023 timescales. **(d)** IRD from ODP 983 (Barker et al., 2019, 2021). **(e)** Ice age difference between DF2021 and (i) AICC2023 (blue), (ii) Extier et al. (2018a) chronology (orange) and (iii) AICC2012 (black). The age difference is calculated as per EDC age – DF2021 age. DF2021 age is transferred onto the EDC ice core via the volcanic synchronization of Fujita et al. (2015). The gray rectangle indicates MIS 5e.

Isotope Maximum (AIM) 24 (Fig. 11), suggesting some remaining chronology problems (AIM 24 onset) or regional climatic differences (δD decrease over MIS 5e). Between 180 and 150 ka BP, AICC2012 shows better agreement with the DF2021 chronology than the new AICC2023 chronology, which suggests younger ages as per TAC and $\delta^{18}O_{atm}$ dating constraints.

4.2.2 MIS 11 (from 425 to 375 ka BP)

Over the time interval from 430 to 360 ka BP, encompassing MIS 11, the new AICC2023 chronology predicts older ages than AICC2012 (by up to 2 kyr) with a diminished uncertainty (from 3.9 to 1.7 kyr). This shift towards older ages is induced by $\delta^{18}O_{atm} - \delta^{18}O_{calcite}$ (Hulu, Sambao and Dongge caves) tie points at 377.3, 385.7 and 398.5 ka BP and by the TAC age constraint at 362.1 ka BP (Figs. 7 and 12). As a result, two major rises in the EDC atmospheric CO_2 and CH_4 concentration records (corresponding to carbon dioxide jumps CDJ+ 11a.3 and 11a.4, labeled as per Nehrbass-Ahles et al., 2020) occur at 385.6 ± 1.4 and 389.8 ± 1.5 ka BP (Fig. 12). These two rapid jumps in CO_2 and CH_4 are

better aligned with two abrupt decreases in the highly resolved $\delta^{18}O_{calcite}$ record of Zhao et al. (2019) from Yongxing cave (independently dated with ^{230}Th at 386.4 ± 3.1 and 390.0 ± 3.0 ka BP) than when using the AICC2012 chronology (improvement by ~ 800 years). Such millennial-scale synchronicity is expected between CH_4 and $\delta^{18}O_{calcite}$ series from Chinese speleothems as they are both influenced by Asian monsoon area displacements (and associated methane emissions from wetlands) (Sánchez Goñi et al., 2008).

4.2.3 MIS 19 (from 780 to 760 ka BP)

The Matuyama–Brunhes event (geomagnetic field reversal) is reflected by a globally synchronous event in the ^{10}Be signal: an abrupt termination of the large ^{10}Be peak following a long-term increasing trend recorded in both ice and sedimentary cores (Giaccio et al., 2023). The $^{40}Ar/^{39}Ar$ age-constrained chronology of a lacustrine succession from Sulmona basin (Giaccio et al., 2023) gives an age of 770.9 ± 1.6 ka BP for the ^{10}Be peak termination. The new AICC2023 chronology provides an estimate of 767.3 ± 3 ka BP for the same ^{10}Be peak termination, an age which is closer to the

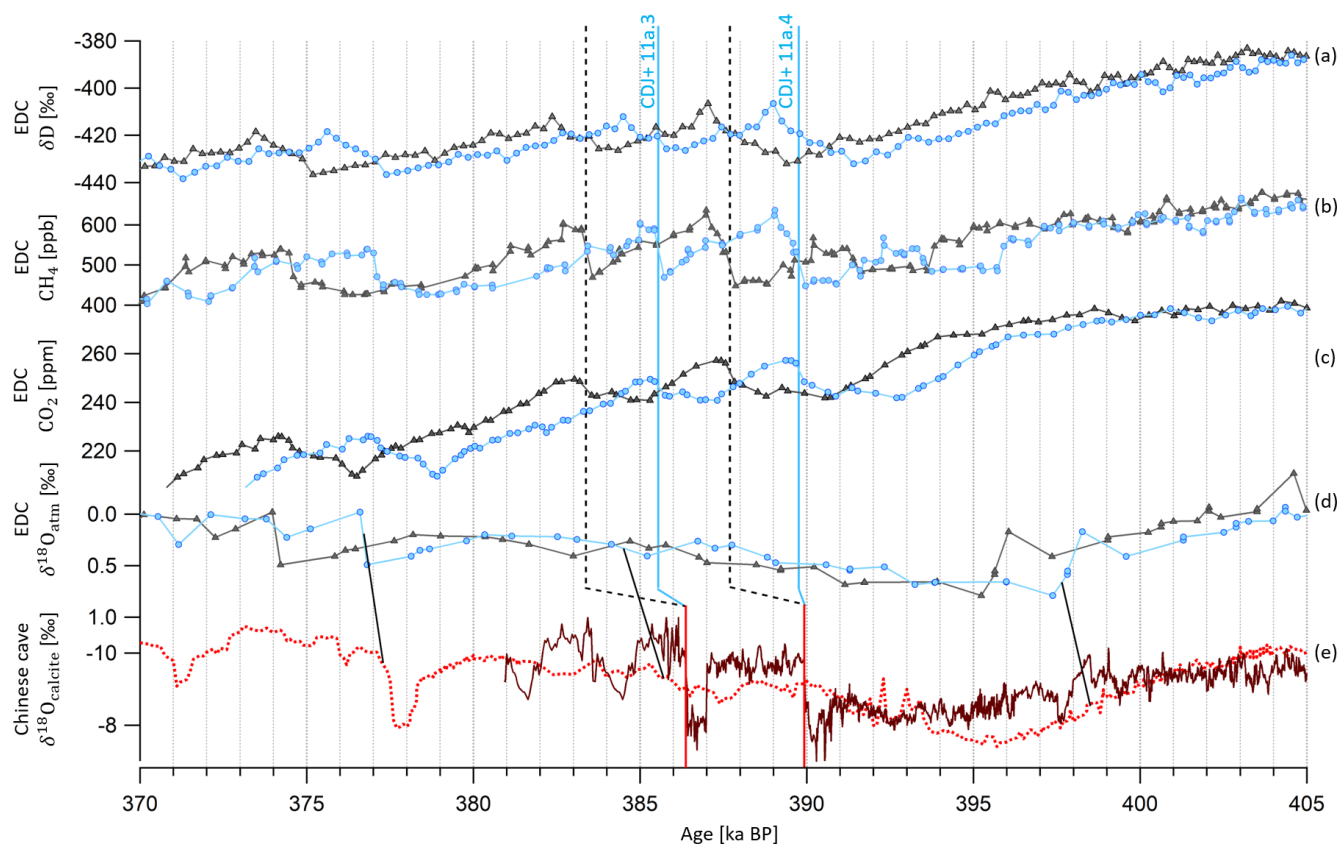


Figure 12. Evolution of climate tracers from the EDC ice core and Yongxing cave stalagmites between 405 and 370 ka BP. EDC records of (a) δD , (b) CH_4 (Nehrbass-Ahles et al., 2020), (c) CO_2 (Nehrbass-Ahles et al., 2020) and (d) $\delta^{18}O_{atm}$ on AICC2012 (gray triangles) and AICC2023 (blue circles) chronologies. (e) Speleothem $\delta^{18}O_{calcite}$ from Hulu, Dongge and Sambaog cave, used to constrain AICC2023 (dashed red curve; Cheng et al., 2016), and from Yongxing cave, independently dated with ^{230}Th dating and annual band counting (plain brown curve; Zhao et al., 2019). CDJ+ is labeled as per Nehrbass-Ahles et al. (2020). Vertical dashed black and blue bars show jumps in CO_2 on AICC2012 and AICC2023 chronologies, respectively; vertical red bars show corresponding decreases in $\delta^{18}O_{calcite}$. Black lines show the three tie points between $\delta^{18}O_{atm}$ and $\delta^{18}O_{calcite}$ (Cheng et al., 2016) used to constrain AICC2023.

$^{40}Ar/^{39}Ar$ age evaluation than the AICC2012 chronology estimate (766.2 ± 3 ka BP; Fig. 13). The new AICC2023 chronology indeed indicates an increasingly older age than AICC2012 over MIS 19 (from 790 to 761 ka BP) due to the new $\delta^{18}O_{atm}$ -based timescale (Fig. 7).

We acknowledge that the Chiba composite section also provides a high-resolution ^{10}Be record, as the Montalbano Jonico marine section (Simon et al., 2017), the Sulmona basin succession and the EDC ice core do. Although the ^{10}Be flux records of Sulmona and EDC show a similar pattern and the same asymmetrical shape (i.e., slow increase followed by an abrupt ^{10}Be peak termination), the sharp termination is less obvious in the Montalbano Jonico and Chiba records. In addition, the Chiba and Montalbano Jonico records are shallow marine deposits; hence expression of paleoclimatic proxies can be amplified and/or hampered by fluvial input (Nomade et al., 2019). Finally, substantial adjustments, up to 10.2 ± 5.5 kyr (i.e., exceeding the related uncertainty), are required to fit the millennial-scale variability in the Chiba

record within the Sulmona radioisotopic-based chronology. Giaccio et al. (2023) point out that, despite these relatively large temporal offsets for the Chiba record, the Sulmona-based age model is more linear and describes a simpler, and likely more realistic, history of sediment accumulation. Therefore, we rather use the Sulmona succession to compare with AICC2023.

5 Conclusions

In this study, we have established a new reference chronology for the EDC ice core, AICC2023, covering the last 800 kyr, which is consistent with the official GICC05 timescale over the last 60 kyr. A valuable update of the chronology construction has been the compilation of chronological and glaciological information, including new age markers from recent high-resolution measurements on the EDC ice core. As a result, the chronological uncertainty is reduced from 1.7 kyr in AICC2012 (standard deviation of 995 years) to 900 years

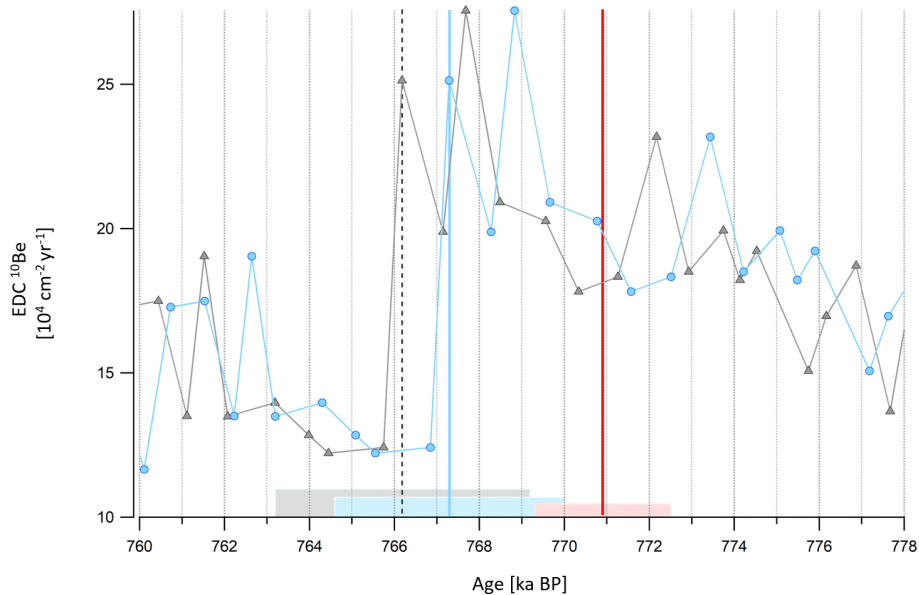


Figure 13. EDC ^{10}Be record on AICC2012 and AICC2023 chronologies between 778 and 760 ka BP. Vertical gray and blue bars indicate the age of the abrupt EDC ^{10}Be peak termination on AICC2012 (gray triangles) and AICC2023 (blue circles) chronologies, respectively. The horizontal gray and blue rectangles correspond to AICC2012 and AICC2023 2σ confidence intervals (± 3 and ± 2.7 ka, respectively). The vertical red bar and horizontal rectangle show the ^{10}Be peak termination age and its 2σ confidence interval (770.9 ± 1.6 ka BP; Giaccio et al., 2023).

on average in AICC2023 (standard deviation of 720 years). A total of 90 % of the new AICC2023 timescale is associated with an uncertainty lower than 2 kyr, compared to only 60 % in the AICC2012 chronology. First, the distinct orbital chronologies derived from $\delta\text{O}_2/\text{N}_2$, TAC and $\delta^{18}\text{O}_{\text{atm}}$ are coherent within their respective uncertainties except over three periods, including MIS 11 and MIS 19. Second, new $\delta^{15}\text{N}$ measurements along with new sensitivity tests with the firn densification model described by Bréant et al. (2017) and adapted for the EDC ice core provide the most plausible evolution of LID at EDC over the last 800 kyr.

The majority of the age disparities observed between the AICC2023 and AICC2012 chronologies are smaller than 500 years (median), hence minor given the average uncertainty in AICC2012 (1.7 kyr). Exceptions are significant age shifts reaching 3.4, 3.8 and 5 kyr towards older ages suggested over MIS 15, MIS 17 and MIS 19, respectively. However, most of these age discrepancies lead to an improved coherency between the new EDC timescale and independent absolute chronologies derived for other climate archives, especially over the following periods: MIS 5, MIS 11 and MIS 19.

We have identified time intervals where building the chronology is more complicated, such as termination VI (from 540 to 456 ka BP) and from 800 to 600 ka BP, corresponding to the lowermost section of the core, and we would like to draw attention to the requirement for new measurements over these periods. In particular, the links between the variability in $\delta\text{O}_2/\text{N}_2$ and TAC records and their orbital tar-

gets are not obvious over the 800–600 ka BP period (Fig. 1). This may be due to bad quality of the ice and/or diffusion of gases through the ice matrix (Bereiter et al., 2009). The imprecision of the signal may also be partially explained by the limited temporal resolution of the existing dataset in this deep section. To address these issues, highly resolved $\delta\text{O}_2/\text{N}_2$ and TAC measurements are needed in the lowermost section of the EDC ice core. In addition, $\delta\text{O}_2/\text{N}_2$ from ice samples over the period covering TVI should also be analyzed to investigate the mismatch between old and new datasets (Fig. 1).

A final important aspect would be to further extend the Paleochrono dating experiment by implementing other ice cores such as Dome Fuji, WAIS Divide and NEEM (North Greenland Eemian), for which a large amount of chronological and glaciological information is now available.

Code availability. The input and output files created during this study to obtain the new AICC2023 chronology are available on Zenodo (<https://doi.org/10.5281/zenodo.10091515>; Bouchet et al., 2023a). They include both updated and old age markers.

Data availability. A folder is available for each site in the PANGAEA data repository (Bouchet et al., 2023b). It includes new gas and ice age scales and their uncertainties as well as new gas data along with background and analyzed scenarios for accumulation rate, thinning function and

LID. A correspondence between AICC2023 and WD2014 age models is also given (<https://doi.org/10.1594/PANGAEA.961017>; Bouchet et al., 2023b). The new $\delta^{18}\text{O}_{\text{atm}}$ and $\delta\text{O}_2/\text{N}_2$ datasets for EDC are also available in the PANGAEA data repository (<https://doi.org/10.1594/PANGAEA.961023>; Bouchet et al., 2023c).

Supplement. The supplement related to this article is available online at: <https://doi.org/10.5194/cp-19-2257-2023-supplement>.

Author contributions. MB wrote the manuscript with the contribution of all co-authors. AL and FP contributed to the conceptualization of the study and the methodology. Measurements on the EDC ice core were performed at the LSCE by AG, FP, RJ and EF. EC, DR, VYL and MFL contributed to the collection, analysis and interpretation of the TAC record. ML provided resources. The krypton analysis was conducted by WJ, FR, ZTL and GMY. TE, AS, EL and PM contributed to the validation of the study.

Competing interests. At least one of the (co-)authors is a member of the editorial board of *Climate of the Past*. The peer-review process was guided by an independent editor, and the authors also have no other competing interests to declare.

Disclaimer. Publisher's note: Copernicus Publications remains neutral with regard to jurisdictional claims made in the text, published maps, institutional affiliations, or any other geographical representation in this paper. While Copernicus Publications makes every effort to include appropriate place names, the final responsibility lies with the authors.

Special issue statement. This article is part of the special issue "Ice core science at the three poles (CP/TC inter-journal SI)". It is a result of the IPICS 3rd Open Science Conference, Crans-Montana, Switzerland, 2–7 October 2022.

Acknowledgements. Krypton analysis has been supported by the Innovation Program for Quantum Science and Technology (2021ZD0303101) and by the National Natural Science Foundation of China (41727901). Development of the Paleochrono model was funded by CNRS/INSU/LEFE projects IceChrono and CO2Role. Emilie Capron and Etienne Legrain acknowledge financial support from the French National Research Agency under the "Programme d'Investissements d'Avenir" (ANR-19-MPGA-0001), through the Make Our Planet Great Again HOTCLIM project, as well as the financial support from the AXA research fund. We also acknowledge the assistance from the European Union FP5-EESD program (grant agreement no. EVK2-CT-2000-00077; EPICA), the French National Research Agency program "NE-ANDROOTS" (ANR-19-CE27-0011) and the French Polar Institute project no. 902 (GLACIOLOGIE CONCORDIA). Our special thanks go to Markus Grimmer, Marcel Haeberli, Daniel Baggen-

stos, Jochen Schmitt, Matthias Baumgartner, Hubertus Fischer, Kenji Kawamura and Ikumi Oyabu for sharing their thoughts and data and sustaining the discussion on the construction of new ice core age scales and to Sébastien Nomade and Alison Pereira for providing advice and expertise in geochronology.

Financial support. This research has received funding from the European Research Council under the European Union Horizon 2020 Excellent Science program (H2020/20192024)/ERC grant agreement no. 817493 (ERC ICORDA).

Review statement. This paper was edited by Christo Buizert and reviewed by two anonymous referees.

References

- Alley, R. B.: Firm densification by grain-boundary sliding: a first model, *Journal de Physique Colloque*, 48, 1–249, <https://doi.org/10.1051/JPHYSCOL:1987135>, 1987.
- Andersen, K. K., Azuma, N., Barnola, J.-M., Bigler, M., Biscaye, P., Caillon, N., Chappellaz, J., Clausen, H. B., Dahl-Jensen, D., Fischer, H., Flückiger, J., Fritzsche, D., Fujii, Y., Goto-Azuma, K., Grønvold, K., Gundestrup, N. S., Hansson, M., Huber, C., Hvidberg, C. S., Johnsen, S. J., Jonsell, U., Jouzel, J., Kipfstuhl, S., Landais, A., Leuenberger, M., Lorrain, R., Masson-Delmotte, V., Miller, H., Motoyama, H., Narita, H., Popp, T., Rasmussen, S. O., Raynaud, D., Rothlisberger, R., Ruth, U., Samyn, D., Schwander, J., Shoji, H., Siggard-Andersen, M.-L., Steffensen, J. P., Stocker, T., Sveinbjörnsdóttir, A. E., Svensson, A., Takata, M., Tison, J.-L., Thorsteinsson, Th., Watanabe, O., Wilhelms, F., White, J. W. C., and N. G. I. C. P. members: High-resolution record of Northern Hemisphere climate extending into the last interglacial period, *Nature*, 431, 147–151, <https://doi.org/10.1038/nature02805>, 2004.
- Andersen, K. K., Svensson, A., Johnsen, S. J., Rasmussen, S. O., Bigler, M., Röthlisberger, R., Ruth, U., Siggaard-Andersen, M.-L., Peder Steffensen, J., Dahl-Jensen, D., Vinther, B. M., and Clausen, H. B.: The Greenland Ice Core Chronology 2005, 15–42 ka. Part 1: constructing the time scale, *Quaternary Sci. Rev.*, 25, 3246–3257, <https://doi.org/10.1016/j.quascirev.2006.08.002>, 2006.
- Arnaud, L., Barnola, J. M., and Duval, P.: Physical modeling of the densification of snow/firm and ice in the upper part of polar ice sheets, *Physics of Ice Core Records*, 285–305, <http://hdl.handle.net/2115/32472> (last access: 9 November 2023), 2000.
- Arthern, R. J., Vaughan, D. G., Rankin, A. M., Mulvaney, R., and Thomas, E. R.: In situ measurements of Antarctic snow compaction compared with predictions of models, *J. Geophys. Res.-Earth*, 115, 3011, <https://doi.org/10.1029/2009JF001306>, 2010.
- Baglin, C. M.: Nuclear Data Sheets for $A = 81$, *Nucl. Data Sheets*, 109, 2257–2437, <https://doi.org/10.1016/J.NDS.2008.09.001>, 2008.
- Barker, S., Knorr, G., Conn, S., Lordsmith, S., Newman, D., and Thornalley, D.: Early interglacial legacy of deglacial climate instability, *Paleoceanogr. Paleoclimatol.*, 34, 1455–1475, <https://doi.org/10.1029/2019PA003661>, 2019.

- Barker, S., Zhang, X., Jonkers, L., Lordsmith, S., Conn, S., and Knorr, G.: Strengthening Atlantic inflow across the mid-Pleistocene transition, *Paleoceanogr. Paleoclimatol.*, 36, 2021e2020PA004200, <https://doi.org/10.1029/2020PA004200>, 2021.
- Barnola, J.-M., Pimienta, P., Raynaud, D., and Korotkevich, Y. S.: CO₂-climate relationship as deduced from the Vostok ice core: a re-examination based on new measurements and on a re-evaluation of the air dating, *Tellus B*, 43, 83–90, <https://doi.org/10.1034/J.1600-0889.1991.T01-1-00002.X>, 1991.
- Baumgartner, M., Kindler, P., Eicher, O., Floch, G., Schilt, A., Schwander, J., Spahni, R., Capron, E., Chappellaz, J., Leuenberger, M., Fischer, H., and Stocker, T. F.: NGRIP CH₄ concentration from 120 to 10 kyr before present and its relation to a $\delta^{15}\text{N}$ temperature reconstruction from the same ice core, *Clim. Past*, 10, 903–920, <https://doi.org/10.5194/cp-10-903-2014>, 2014.
- Bazin, L., Landais, A., Lemieux-Dudon, B., Toyé Mahamadou Kele, H., Veres, D., Parrenin, F., Martinerie, P., Ritz, C., Capron, E., Lipenkov, V., Loutre, M.-F., Raynaud, D., Vinther, B., Svensson, A., Rasmussen, S. O., Severi, M., Blunier, T., Leuenberger, M., Fischer, H., Masson-Delmotte, V., Chappellaz, J., and Wolff, E.: An optimized multi-proxy, multi-site Antarctic ice and gas orbital chronology (AICC2012): 120–800 ka, *Clim. Past*, 9, 1715–1731, <https://doi.org/10.5194/cp-9-1715-2013>, 2013.
- Bazin, L., Landais, A., Capron, E., Masson-Delmotte, V., Ritz, C., Picard, G., Jouzel, J., Dumont, M., Leuenberger, M., and Prié, F.: Phase relationships between orbital forcing and the composition of air trapped in Antarctic ice cores, *Clim. Past*, 12, 729–748, <https://doi.org/10.5194/cp-12-729-2016>, 2016.
- Bender, M. L.: Orbital tuning chronology for the Vostok climate record supported by trapped gas composition, *Earth Planet. Sc. Lett.*, 204, 275–289, [https://doi.org/10.1016/S0012-821X\(02\)00980-9](https://doi.org/10.1016/S0012-821X(02)00980-9), 2002.
- Bender, M. L., Barnett, B., Dreyfus, G., Jouzel, J., and Porcelli, D.: The contemporary degassing rate of ⁴⁰Ar from the solid Earth, *P. Natl. Acad. Sci. USA*, 105, 8232–8237, <https://doi.org/10.1073/PNAS.0711679105>, 2008.
- Bereiter, B., Schwander, J., Lüthi, D., and Stocker, T. F.: Change in CO₂ concentration and O₂/N₂ ratio in ice cores due to molecular diffusion, *Geophys. Res. Lett.*, 36, 2009L05703, <https://doi.org/10.1029/2008GL036737>, 2009.
- Berger, A.: Long-Term Variations of Daily Insolation and Quaternary Climatic Changes, *J. Atmos. Sci.*, 35, 2362–2367, [https://doi.org/10.1175/1520-0469\(1978\)035<2362:LTVODI>2.0.CO;2](https://doi.org/10.1175/1520-0469(1978)035<2362:LTVODI>2.0.CO;2), 1978.
- Berger, B., Crucifix, M., Hodell, D. A., Mangili, C., McManus, J. F., Otto-Bliesner, B., Pol, K., Raynaud, D., Skinner, L. C., Tzedakis, P. C., Wolff, E. W., Yin, Q. Z., Abe-Ouchi, A., Barbante, C., Brovkin, V., Cacho, I., Capron, E., Ferretti, P., Ganopolski, A., Gromalt, J. O., Hönisch, B., Kawamura, K. A., Landais, A., Margari, V., Martrat, B., Masson-Delmotte, V., Mokeddem, Z., Parrenin, F., Prokopenko, A. A., Rashid, H., Schulz, M., and Vazquez Riveiros, N.: Interglacials of the last 800,000 years, *Rev. Geophys.*, 54, 162–219, <https://doi.org/10.1002/2015RG000482>, 2016.
- Boch, R., Cheng, H., Spötl, C., Edwards, R. L., Wang, X., and Häuselmann, P.: NALPS: a precisely dated European climate record 120–60 ka, *Clim. Past*, 7, 1247–1259, <https://doi.org/10.5194/cp-7-1247-2011>, 2011.
- Bouchet, M., Parrenin, F., and Landais, A.: AICC2023 dating experiment using Paleochrono model, Zenodo [code], <https://doi.org/10.5281/zenodo.10091515>, 2023a.
- Bouchet, M., Landais, A., Grisart, A., Parrenin, F., Prié, F., Jacob, R., Fourné, E., Capron, E., Raynaud, D., Lipenkov, V. Y., Loutre, M.-F., Extier, T., Svensson, A. M., Martinerie, P., Leuenberger, M. C., Jiang, W., Ritterbusch, F., Lu, Z.-T., and Yang, G.-M.: The Antarctic ice core chronology (AICC2023), PANGAEA [data set], <https://doi.org/10.1594/PANGAEA.961017>, 2023b.
- Bouchet, M., Grisart, A., Landais, A., Prié, F., Jacob, R., and Fourné, E.: $\delta\text{O}_2/\text{N}_2$ and $\delta^{18}\text{O}$ of O₂ from EPICA Dome C ice core (Antarctica) (0–800 ka), PANGAEA [data set], <https://doi.org/10.1594/PANGAEA.961023>, 2023c.
- Bréant, C., Martinerie, P., Orsi, A., Arnaud, L., and Landais, A.: Modelling firn thickness evolution during the last deglaciation: constraints on sensitivity to temperature and impurities, *Clim. Past*, 13, 833–853, <https://doi.org/10.5194/cp-13-833-2017>, 2017.
- Bréant, C., Landais, A., Orsi, A., Martinerie, P., Extier, T., Prié, F., Stenni, B., Jouzel, J., Masson-Delmotte, V., and Leuenberger, M.: Unveiling the anatomy of Termination 3 using water and air isotopes in the Dome C ice core, East Antarctica, *Quaternary Sci. Rev.*, 211, 156–165, <https://doi.org/10.1016/J.QUASCIREV.2019.03.025>, 2019.
- Buizert, C.: The Ice Core Gas Age-Ice Age Difference as a Proxy for Surface Temperature, *Geophys. Res. Lett.*, 48, e2021GL094241, <https://doi.org/10.1029/2021GL094241>, 2021.
- Buizert, C., Sowers, T., and Blunier, T.: Assessment of diffusive isotopic fractionation in polar firn, and application to ice core trace gas records, *Earth Planet. Sc. Lett.*, 361, 110–119, <https://doi.org/10.1016/J.EPSL.2012.11.039>, 2013.
- Buizert, C., Baggenstos, D., Jiang, W., Purtschert, R., Petrenko, V. V., Lu, Z. T., Müller, P., Kuhl, T., Lee, J., Severinghaus, J. P., and Brook, E. J.: Radiometric ⁸¹Kr dating identifies 120,000-year-old ice at Taylor Glacier, Antarctica, *P. Natl. Acad. Sci. USA*, 111, 6876–6881, <https://doi.org/10.1073/pnas.1320329111>, 2014.
- Buizert, C., Cuffey, K. M., Severinghaus, J. P., Baggenstos, D., Fudge, T. J., Steig, E. J., Markle, B. R., Winstrup, M., Rhodes, R. H., Brook, E. J., Sowers, T. A., Clow, G. D., Cheng, H., Edwards, R. L., Sigl, M., McConnell, J. R., and Taylor, K. C.: The WAIS Divide deep ice core WD2014 chronology – Part 1: Methane synchronization (68–31 ka BP) and the gas age–ice age difference, *Clim. Past*, 11, 153–173, <https://doi.org/10.5194/cp-11-153-2015>, 2015.
- Buizert, C., Sigl, M., Severi, M., Markle, B. R., Wettstein, J. J., McConnell, J. R., Pedro, J. B., Sodemann, H., Goto-Azuma, K., Kawamura, K., Fujita, S., Motoyama, H., Hirabayashi, M., Uemura, R., Stenni, B., Parrenin, F., He, F., Fudge, T. J., and Steig, E.: Abrupt ice-age shifts in southern westerly winds and Antarctic climate forced from the north, *Nature*, 563, 681–685, <https://doi.org/10.1038/s41586-018-0727-5>, 2018.
- Capron, E., Landais, A., Chappellaz, J., Schilt, A., Buiron, D., Dahl-Jensen, D., Johnsen, S. J., Jouzel, J., Lemieux-Dudon, B., Loulergue, L., Leuenberger, M., Masson-Delmotte, V., Meyer, H., Oerter, H., and Stenni, B.: Millennial and sub-millennial scale climatic variations recorded in polar ice cores over the last glacial

- period, *Clim. Past*, 6, 345–365, <https://doi.org/10.5194/cp-6-345-2010>, 2010.
- Capron, E., Landais, A., Chappellaz, J., Buiron, D., Fischer, H., Johnsen, S. J., Jouzel, J., Leuenberger, M., Masson-Delmotte, V., and Stocker, T. F.: A global picture of the first abrupt climatic event occurring during the last glacial inception, *Geophys. Res. Lett.*, 39, L15703, <https://doi.org/10.1029/2012GL052656>, 2012.
- Capron, E., Landais, A., Buiron, D., Cauquoin, A., Chappellaz, J., Debret, M., Jouzel, J., Leuenberger, M., Martinerie, P., Masson-Delmotte, V., Mulvaney, R., Parrenin, F., and Prié, F.: Glacial-interglacial dynamics of Antarctic firn columns: Comparison between simulations and ice core air- $\delta^{15}\text{N}$ measurements, *Clim. Past*, 9, 983–999, <https://doi.org/10.5194/cp-9-983-2013>, 2013.
- Cheng, H., Edwards, R. L., Sinha, A., Spötl, C., Yi, L., Chen, S., Kelly, M., Kathayat, G., Wang, X., Li, X., Kong, X., Wang, Y., Ning, Y., and Zhang, H.: The Asian monsoon over the past 640,000 years and ice age terminations, *Nature*, 534, 640–646, <https://doi.org/10.1038/nature18591>, 2016.
- Columbu, A., Drysdale, R., Capron, E., Woodhead, J., De Waele, J., Sanna, L., Hellstrom, J., and Bajo, P.: Early last glacial intra-interstadial climate variability recorded in a Sardinian speleothem, *Quaternary Sci. Rev.*, 169, 391–397, <https://doi.org/10.1016/J.QUASCIREV.2017.05.007>, 2017.
- Crotti, I., Landais, A., Stenni, B., Bazin, L., Parrenin, F., Frezzotti, M., Ritterbusch, F., Lu, Z. T., Jiang, W., Yang, G. M., Fourré, E., Orsi, A., Jacob, R., Minster, B., Prié, F., Dreossi, G., and Barbante, C.: An extension of the TALDICE ice core age scale reaching back to MIS 10.1, *Quaternary Sci. Rev.*, 266, 107078, <https://doi.org/10.1016/J.QUASCIREV.2021.107078>, 2021.
- Dansgaard, W. and Johnsen, S. J.: A Flow Model and a Time Scale for the Ice Core from Camp Century, Greenland, *J. Glaciol.*, 8, 215–223, <https://doi.org/10.3189/S0022143000031208>, 1969.
- Dong, X. Z., Ritterbusch, F., Chu, Y. Q., Gu, J. Q., Hu, S. M., Jiang, W., Lu, Z. T., Yang, G. M., and Zhao, L.: Dual Separation of Krypton and Argon from Environmental Samples for Radioisotope Dating, *Anal. Chem.*, 91, 13576–13581, <https://doi.org/10.1021/ACS.ANALCHEM.9B02716>, 2019.
- Dreyfus, G. B., Parrenin, F., Lemieux-Dudon, B., Durand, G., Masson-Delmotte, V., Jouzel, J., Barnola, J. M., Panno, L., Spahni, R., Tisserand, A., Siegenthaler, U., and Leuenberger, M.: Anomalous flow below 2700 m in the EPICA Dome C ice core detected using $\delta^{18}\text{O}$ of atmospheric oxygen measurements, *Clim. Past*, 3, 341–353, <https://doi.org/10.5194/cp-3-341-2007>, 2007.
- Dreyfus, G. B., Raisbeck, G. M., Parrenin, F., Jouzel, J., Guyodo, Y., Nomade, S., and Mazaud, A.: An ice core perspective on the age of the Matuyama–Brunhes boundary, *Earth Planet. Sc. Lett.*, 274, 151–156, <https://doi.org/10.1016/J.EPSL.2008.07.008>, 2008.
- Dreyfus, G. B., Jouzel, J., Bender, M. L., Landais, A., Masson-Delmotte, V., and Leuenberger, M.: Firn processes and $\delta^{15}\text{N}$ potential for a gas-phase climate proxy, *Quaternary Sci. Rev.*, 29, 28–42, <https://doi.org/10.1016/j.quascirev.2009.10.012>, 2010.
- EPICA Community Members: Augustin, L., Barbante, C., Barnes, P. R. F., Barnola, J. M., Bigler, M., Castellano, E., Cattani, O., Chappellaz, J., Dahl-Jensen, D., Delmonte, B., Dreyfus, G., Durand, G., Falourd, S., Fischer, H., Flückiger, J., Hansson, M. E., Huybrechts, P., Jugie, G., Johnsen, S. J., Jouzel, J., Kaufmann, P., Kipfstuhl, J., Lambert, F., Lipenkov, V. Y., Littot, G., Longinelli, A., Lorrain, R., Maggi, V., Masson-Delmotte, V., Miller, H., Mulvaney, R., Oerlemans, J., Oerter, H., Orombelli, G., Parrenin, F., Peel, D. A., Petit, J. R., Raynaud, D., Ritz, C., Ruth, U., Schwander, J., Siegenthaler, U., Souchez, R., Stauffer, B., Steffensen, J. P., Stenni, B., Stocker, T. F., Tabacco, I. E., Udisti, R., van de Wal, R. S. W., van den Broeke, M., Weiss, J., Wilhelms, F., Winther, J. G., Wolff, E. W., and Zucchelli, M.: Eight glacial cycles from an Antarctic ice core, *Nature*, 429, 623–628, <https://doi.org/10.1038/nature02599>, 2004.
- Epifanio, J. A., Brook, E. J., Buizert, C., Edwards, J. S., Sowers, T. A., Kahle, E. C., Severinghaus, J. P., Steig, E. J., Winski, D. A., Osterberg, E. C., Fudge, T. J., Aydin, M., Hood, E., Kalk, M., Kreutz, K. J., Ferris, D. G., and Kennedy, J. A.: The SP19 chronology for the South Pole Ice Core – Part 2: Gas chronology, Δ age, and smoothing of atmospheric records, *Clim. Past*, 16, 2431–2444, <https://doi.org/10.5194/cp-16-2431-2020>, 2020.
- Extier, T., Landais, A., Bréant, C., Prié, F., Bazin, L., Dreyfus, G., Roche, D. M., and Leuenberger, M.: On the use of $\delta^{18}\text{O}_{\text{atm}}$ for ice core dating, *Quaternary Sci. Rev.*, 185, 244–257, <https://doi.org/10.1016/J.QUASCIREV.2018.02.008>, 2018a.
- Extier, T., Landais, A., Bréant, C., Prié, F., Bazin, L., Dreyfus, G., Roche, D. M., and Leuenberger, M. C.: $\delta^{18}\text{O}_{\text{atm}}$ records between 100–800 ka from EPICA Dome C ice core, PANGAEA [data set], <https://doi.org/10.1594/PANGAEA.887323>, 2018b.
- Extier, T., Landais, A., Bréant, C., Prié, F., Bazin, L., Dreyfus, G., Roche, D. M., and Leuenberger, M. C.: $\delta\text{O}_2/\text{N}_2$ records between 100–800 ka from EPICA Dome C ice core, PANGAEA [data set], <https://doi.org/10.1594/PANGAEA.887326>, 2018c.
- Freitag, J., Kipfstuhl, S., Laepple, T., and Wilhelms, F.: Impurity-controlled densification: a new model for stratified polar firn, *J. Glaciol.*, 59, 1163–1169, <https://doi.org/10.3189/2013JOG13J042>, 2013.
- Fujita, S., Parrenin, F., Severi, M., Motoyama, H., and Wolff, E. W.: Volcanic synchronization of Dome Fuji and Dome C Antarctic deep ice cores over the past 216 kyr, *Clim. Past*, 11, 1395–1416, <https://doi.org/10.5194/cp-11-1395-2015>, 2015.
- Giaccio, B., Zanchetta, G., Galli, P., Nomade, S., Regattieri, E., and Sagnotti, L.: The Quaternary evolution of Sulmona basin, central Italy, <https://inquinaroma2023.org/wp-content/uploads/2022/01/5-Post.pdf> (last access: 10 September 2023), 2023.
- Goujon, C., Barnola, J. M., and Ritz, C.: Modeling the densification of polar firn including heat diffusion: Application to close-off characteristics and gas isotopic fractionation for Antarctica and Greenland sites, *J. Geophys. Res.-Atmos.*, 108, 4792, <https://doi.org/10.1029/2002JD003319>, 2003.
- Grachev, A. M. and Severinghaus, J. P.: Determining the thermal diffusion factor for $^{40}\text{Ar}/^{36}\text{Ar}$ in air to aid paleoreconstruction of abrupt climate change, *J. Phys. Chem. A*, 107, 4636–4642, <https://doi.org/10.1021/JP027817U>, 2003.
- Grisart, A.: Étude à haute résolution des cycles hydrologiques et climatiques à partir d'une carotte de glace d'Antarctique avec un focus sur les déglaciations, Université Paris-Saclay, <https://theses.hal.science/tel-04042459> (last access: 9 November 2023), 2023.
- Heaton, T. J., Bard, E., Ramsey, C. B., Butzin, M., Köhler, P., Muscheler, R., Reimer, P. J., and Wacker, L.: Radiocarbon: A key tracer for studying Earth's dynamo, climate system, carbon cycle, and Sun, *Science*, 374, 6568, <https://doi.org/10.1126/SCIENCE.ABD7096>, 2021.

- Herron, M. M. and Langway, C. C.: Firn densification: an empirical model, *J. Glaciol.*, 25, 373–385, <https://doi.org/10.3189/S0022143000015239>, 1980.
- Jiang, W., Hu, S. M., Lu, Z. T., Ritterbusch, F., and Yang, G.: min: Latest development of radiokrypton dating – A tool to find and study paleogroundwater, *Quatern. Int.*, 547, 166–171, <https://doi.org/10.1016/J.QUAINT.2019.04.025>, 2020.
- Jouzel, J., Hoffmann, G., Parrenin, F., and Waelbroeck, C.: Atmospheric oxygen 18 and sea-level changes, *Quaternary Sci. Rev.*, 21, 307–314, [https://doi.org/10.1016/S0277-3791\(01\)00106-8](https://doi.org/10.1016/S0277-3791(01)00106-8), 2002.
- Jouzel, J., Masson-Delmotte, V., Cattani, O., Dreyfus, G., Falourd, S., Hoffmann, G., Minster, B., Nouet, J., Barnola, J. M., Chappellaz, J., Fischer, H., Gallet, J. C., Johnsen, S., Leuenberger, M., Loulergue, L., Luethi, D., Oerter, H., Parrenin, F., Raisbeck, G., Raynaud, D., Schilt, A., Schwander, J., Selmo, E., Souchez, R., Spahni, R., Stauffer, B., Steffensen, J. P., Stenni, B., Stocker, T. F., Tison, J. L., Werner, M., and Wolff, E. W.: Orbital and millennial antarctic climate variability over the past 800,000 years, *Science*, 317, 793–796, <https://doi.org/10.1126/SCIENCE.1141038>, 2007.
- Kawamura, K., Parrenin, F., Lisiecki, L., Uemura, R., Vimeux, F., Severinghaus, J. P., Hutterli, M. A., Nakazawa, T., Aoki, S., Jouzel, J., Raymo, M. E., Matsumoto, K., Nakata, H., Motoyama, H., Fujita, S., Goto-Azuma, K., Fujii, Y., and Watanabe, O.: Northern Hemisphere forcing of climatic cycles in Antarctica over the past 360,000 years, *Nature*, 448, 912–916, <https://doi.org/10.1038/nature06015>, 2007.
- Kuipers Munneke, P., Ligtenberg, S. R. M., Noël, B. P. Y., Howat, I. M., Box, J. E., Mosley-Thompson, E., McConnell, J. R., Steffen, K., Harper, J. T., Das, S. B., and Van Den Broeke, M. R.: Elevation change of the Greenland Ice Sheet due to surface mass balance and firn processes, 1960–2014, *The Cryosphere*, 9, 2009–2025, <https://doi.org/10.5194/tc-9-2009-2015>, 2015.
- Landais, A., Chappellaz, J., Delmotte, M., Jouzel, J., Blunier, T., Bourg, C., Caillon, N., Cherrier, S., Malaizé, B., Masson-Delmotte, V., Raynaud, D., Schwander, J., and Steffensen, J. P.: A tentative reconstruction of the last interglacial and glacial inception in Greenland based on new gas measurements in the Greenland Ice Core Project (GRIP) ice core, *J. Geophys. Res.-Atmos.*, 108, 4563, <https://doi.org/10.1029/2002JD003147>, 2003.
- Landais, A., Barnola, J. M., Kawamura, K., Caillon, N., Delmotte, M., Van Ommen, T., Dreyfus, G., Jouzel, J., Masson-Delmotte, V., Minster, B., Freitag, J., Leuenberger, M., Schwander, J., Huber, C., Etheridge, D., and Morgan, V.: Firn-air $\delta^{15}\text{N}$ in modern polar sites and glacial–interglacial ice: a model-data mismatch during glacial periods in Antarctica?, *Quaternary Sci. Rev.*, 25, 49–62, <https://doi.org/10.1016/J.QUASCIREV.2005.06.007>, 2006.
- Landais, A., Dreyfus, G., Capron, E., Masson-Delmotte, V., Sanchez-Goni, M. F., Desprat, S., Hoffmann, G., Jouzel, J., Leuenberger, M., and Johnsen, S.: What drives the millennial and orbital variations of $\delta^{18}\text{O}_{\text{atm}}$?, *Quaternary Sci. Rev.*, 29, 235–246, <https://doi.org/10.1016/J.QUASCIREV.2009.07.005>, 2010.
- Landais, A., Dreyfus, G., Capron, E., Pol, K., Loutre, M. F., Raynaud, D., Lipenkov, V. Y., Arnaud, L., Masson-Delmotte, V., Paillard, D., Jouzel, J., and Leuenberger, M.: Towards orbital dating of the EPICA Dome C ice core using $\delta\text{O}_2/\text{N}_2$, *Clim. Past*, 8, 191–203, <https://doi.org/10.5194/cp-8-191-2012>, 2012.
- Landais, A., Stenni, B., Masson-Delmotte, V., Jouzel, J., Cauquoin, A., Fourré, E., Minster, B., Selmo, E., Extier, T., Werner, M., Vimeux, F., Uemura, R., Crotti, I., and Grisart, A.: Inter-glacial Antarctic–Southern Ocean climate decoupling due to moisture source area shifts, *Nat. Geosci.*, 14, 918–923, <https://doi.org/10.1038/s41561-021-00856-4>, 2021.
- Lascu, I., Feinberg, J. M., Dorale, J. A., Cheng, H., and Edwards, R. L.: Age of the Laschamp excursion determined by U-Th dating of a speleothem geomagnetic record from North America, *Geology*, 44, 139–142, <https://doi.org/10.1130/G37490.1>, 2016.
- Laskar, J., Robutel, P., Joutel, F., Gastineau, M., Correia, A. C. M., and Levrard, B.: A long-term numerical solution for the insolation quantities of the Earth, *Astron. Astrophys.*, 428, 261–285, <https://doi.org/10.1051/0004-6361:20041335>, 2004.
- Laskar, J., Fienga, A., Gastineau, M., and Manche, H.: La2010: a new orbital solution for the long-term motion of the Earth, *Astron. Astrophys.*, 532, A89, <https://doi.org/10.1051/0004-6361/201116836>, 2011.
- Lemieux-Dudon, B., Blayo, E., Petit, J. R., Waelbroeck, C., Svensson, A., Ritz, C., Barnola, J. M., Narcisi, B. M., and Parrenin, F.: Consistent dating for Antarctic and Greenland ice cores, *Quaternary Sci. Rev.*, 29, 8–20, <https://doi.org/10.1016/J.QUASCIREV.2009.11.010>, 2010.
- Lemieux-Dudon, B., Bazin, L., Landais, A., Toyé Mahamadou Kele, H., Guillevic, M., Kindler, P., Parrenin, F., and Martinerie, P.: Implementation of counted layers for coherent ice core chronology, *Clim. Past*, 11, 959–978, <https://doi.org/10.5194/cp-11-959-2015>, 2015.
- Ligtenberg, S. R. M., Helsen, M. M., and Van Den Broeke, M. R.: An improved semi-empirical model for the densification of Antarctic firn, *The Cryosphere*, 5, 809–819, <https://doi.org/10.5194/tc-5-809-2011>, 2011.
- Lipenkov, V., Candaudap, F., Ravoire, J., Dulac, E., and Raynaud, D.: A new device for the measurement of air content in polar ice, *J. Glaciol.*, 41, 423–429, <https://doi.org/10.3189/S0022143000016294>, 1995.
- Lipenkov, V. Y., Raynaud, D., Loutre, M. F., and Duval, P.: On the potential of coupling air content and O_2/N_2 from trapped air for establishing an ice core chronology tuned on local insolation, *Quaternary Sci. Rev.*, 30, 3280–3289, <https://doi.org/10.1016/J.QUASCIREV.2011.07.013>, 2011.
- Loulergue, L., Schilt, A., Spahni, R., Masson-Delmotte, V., Blunier, T., Lemieux, B., Barnola, J. M., Raynaud, D., Stocker, T. F., and Chappellaz, J.: Orbital and millennial-scale features of atmospheric CH_4 over the past 800,000 years, *Nature*, 453, 383–386, <https://doi.org/10.1038/nature06950>, 2008.
- Lu, Z. T., Schlosser, P., Smethie, W. M., Sturchio, N. C., Fischer, T. P., Kennedy, B. M., Purtschert, R., Severinghaus, J. P., Solomon, D. K., Tanhua, T., and Yokochi, R.: Tracer applications of noble gas radionuclides in the geosciences, *Earth Sci. Rev.*, 138, 196–214, <https://doi.org/10.1016/J.EARSCIREV.2013.09.002>, 2014.
- Moseley, G. E., Spötl, C., Brandstätter, S., Erhardt, T., Luetscher, M., and Lawrence Edwards, R.: NALPS19: Sub-orbital-scale climate variability recorded in northern Alpine speleothems during the last glacial period, *Clim. Past*, 16, 29–50, <https://doi.org/10.5194/cp-16-29-2020>, 2020.
- Nehrbass-Ahles, C., Shin, J., Schmitt, J., Bereiter, B., Joos, F., Schilt, A., Schmidely, L., Silva, L., Teste, G., Grilli, R., Chappellaz, J., Hodell, D., Fischer, H., and Stocker, T. F.:

- Abrupt CO₂ release to the atmosphere under glacial and early interglacial climate conditions, *Science*, 369, 1000–1005, <https://doi.org/10.1126/SCIENCE.AAY8178>, 2020.
- Nomade, S., Bassinot, F., Marino, M., Simon, Q., Dewilde, F., Maiorano, P., Isguder, G., Blamart, D., Girone, A., Scao, V., Pereira, A., Toti, F., Bertini, A., Combourieu-Nebout, N., Peral, M., Bourlès, D. L., Petrosino, P., Gallicchio, S., and Ciaranfi, N.: High-resolution foraminifer stable isotope record of MIS 19 at Montalbano Jonico, southern Italy: A window into Mediterranean climatic variability during a low-eccentricity interglacial, *Quaternary Sci. Rev.*, 205, 106–125, <https://doi.org/10.1016/j.quascirev.2018.12.008>, 2019.
- Nye, J. F.: The motion of ice sheets and glaciers, *J. Glaciol.*, 3, 493–507, <https://doi.org/10.3189/S002214300001724X>, 1959.
- Oraschewski, F. M. and Grinsted, A.: Modeling enhanced firn densification due to strain softening, *The Cryosphere*, 16, 2683–2700, <https://doi.org/10.5194/tc-16-2683-2022>, 2022.
- Oyabu, I., Kawamura, K., Buizert, C., Parrenin, F., Orsi, A., Kitamura, K., Aoki, S., and Nakazawa, T.: The Dome Fuji ice core DF2021 chronology (0–207 kyr BP), *Quaternary Sci. Rev.*, 294, 107754, <https://doi.org/10.1016/J.QUASCIREV.2022.107754>, 2022.
- Parrenin, F., Rémy, F., Ritz, C., Siebert, M. J., and Jouzel, J.: New modeling of the Vostok ice flow line and implication for the glaciological chronology of the Vostok ice core, *J. Geophys. Res.-Atmos.*, 109, D20102, <https://doi.org/10.1029/2004JD004561>, 2004.
- Parrenin, F., Dreyfus, G., Durand, G., Fujita, S., Gagliardini, O., Gillet, F., Jouze, J., Kawamura, K., Lhomme, N., Masson-Delmotte, V., Ritz, C., Schwander, J., Shoji, H., Uemura, R., Watanabe, O., and Yoshida, N.: 1-D-ice flow modelling at EPICA Dome C and Dome Fuji, East Antarctica, *Clim. Past*, 3, 243–259, <https://doi.org/10.5194/cp-3-243-2007>, 2007a.
- Parrenin, F., Barnola, J.-M., Beer, J., Blunier, T., Castellano, E., Chappellaz, J., Dreyfus, G., Fischer, H., Fujita, S., Jouzel, J., Kawamura, K., Lemieux-Dudon, B., Loulergue, L., Masson-Delmotte, V., Narcisi, B., Petit, J.-R., Raisbeck, G., Raynaud, D., Ruth, U., Schwander, J., Severi, M., Spahni, R., Steffensen, J. P., Svensson, A., Udisti, R., Waelbroeck, C., and Wolff, E.: The EDC3 chronology for the EPICA Dome C ice core, *Clim. Past*, 3, 485–497, <https://doi.org/10.5194/cp-3-485-2007>, 2007b.
- Parrenin, F., Barker, S., Blunier, T., Chappellaz, J., Jouzel, J., Landais, A., Masson-Delmotte, V., Schwander, J., and Veres, D.: On the gas-ice depth difference (Δ_{depth}) along the EPICA Dome C ice core, *Clim. Past*, 8, 1239–1255, <https://doi.org/10.5194/cp-8-1239-2012>, 2012.
- Parrenin, F., Bazin, L., Capron, E., Landais, A., Lemieux-Dudon, B., Masson-Delmotte, V., Parrenin, F., Bazin, L., Capron, E., Landais, A., Lemieux-Dudon, B., and Masson-Delmotte, V.: IceChrono1: a probabilistic model to compute a common and optimal chronology for several ice cores, *Geosci. Model Dev.*, 8, 1473–1492, <https://doi.org/10.5194/gmd-8-1473-2015>, 2015.
- Parrenin, F., Bazin, L., Capron, É., Landais, A., Lemieux-Dudon, B., and Masson-Delmotte, V.: Icechrono1: un modèle probabiliste pour calculer une chronologie commune et optimale pour plusieurs carottes de glace, *Quaternaire*, 28, 179–184, <https://doi.org/10.4000/QUATERNAIRE.8121>, 2017.
- Parrenin, F., Bazin, L., Buizert, C., Capron, E., Chowdry Bee-man, J., Corrick, E., Drysdale, R., Kawamura, K., Landais, A., Mulvaney, R., Oyabu, I., and Rasmussen, S.: The Paleochrono probabilistic model to derive a consistent chronology for several paleoclimatic sites, EGUGA, EGU21-822, <https://doi.org/10.5194/EGUSPHERE-EGU21-822>, 2021.
- Petit, J. R., Jouzel, J., Raynaud, D., Barkov, N. I., Barnola, J. M., Basile, I., Bender, M., Chappellaz, J., Davis, M., Delaygue, G., Delmotte, M., Kotiyakov, V. M., Legrand, M., Lipenkov, V. Y., Lorius, C., Pépin, L., Ritz, C., Saltzman, E., and Stievenard, M.: Climate and atmospheric history of the past 420,000 years from the Vostok ice core, Antarctica, *Nature*, 399, 429–436, <https://doi.org/10.1038/20859>, 1999.
- Pimienta, P. and Duval, P.: Rate controlling processes in the creep of polar glacier ice, *Journal de Physique Colloques*, 48, C1-243–C1-248, <https://doi.org/10.1051/jphyscol:1987134>, 1987.
- Raisbeck, G. M., Yiou, F., Jouzel, J., and Stocker, T. F.: Direct north–south synchronization of abrupt climate change record in ice cores using Beryllium 10, *Clim. Past*, 3, 541–547, <https://doi.org/10.5194/cp-3-541-2007>, 2007.
- Raisbeck, G. M., Cauquoin, A., Jouzel, J., Landais, A., Petit, J. R., Lipenkov, V. Y., Beer, J., Synal, H. A., Oerter, H., Johnsen, S. J., Steffensen, J. P., Svensson, A., and Yiou, F.: An improved north–south synchronization of ice core records around the 41 kyr 10Be peak, *Clim. Past*, 13, 217–229, <https://doi.org/10.5194/cp-13-217-2017>, 2017.
- Raynaud, D., Lipenkov, V., Lemieux-Dudon, B., Duval, P., Loutre, M. F., and Lhomme, N.: The local insolation signature of air content in Antarctic ice. A new step toward an absolute dating of ice records, *Earth Planet. Sc. Lett.*, 261, 337–349, <https://doi.org/10.1016/J.EPSL.2007.06.025>, 2007.
- Reutenauer, C., Landais, A., Blunier, T., Bréant, C., Kageyama, M., Woillez, M. N., Risi, C., Mariotti, V., and Braconnot, P.: Quantifying molecular oxygen isotope variations during a Heinrich stadial, *Clim. Past*, 11, 1527–1551, <https://doi.org/10.5194/cp-11-1527-2015>, 2015.
- Sánchez Goñi, M. F., Landais, A., Fletcher, W. J., Naughton, F., Desprat, S., and Duprat, J.: Contrasting impacts of Dansgaard–Oeschger events over a western European latitudinal transect modulated by orbital parameters, *Quaternary Sci. Rev.*, 27, 1136–1151, <https://doi.org/10.1016/J.QUASCIREV.2008.03.003>, 2008.
- Schwander, J., Jouzel, J., Hammer, C. U., Petit, J. R., Udisti, R., and Wolff, E.: A tentative chronology for the EPICA Dome Concordia Ice Core, *Geophys. Res. Lett.*, 28, 4243–4246, <https://doi.org/10.1029/2000GL011981>, 2001.
- Severinghaus, J. P., Bender, M. L., Keeling, R. F., and Broecker, W. S.: Fractionation of soil gases by diffusion of water vapor, gravitational settling, and thermal diffusion, *Geochim. Cosmochim. Ac.*, 60, 1005–1018, [https://doi.org/10.1016/0016-7037\(96\)00011-7](https://doi.org/10.1016/0016-7037(96)00011-7), 1996.
- Shackleton, N. J.: The 100,000-year ice-age cycle identified and found to lag temperature, carbon dioxide, and orbital eccentricity, *Science*, 289, 1897–1902, <https://doi.org/10.1126/SCIENCE.289.5486.1897>, 2000.
- Sigl, M., Fudge, T. J., Winstrup, M., Cole-Dai, J., Ferris, D., McConnell, J. R., Taylor, K. C., Welten, K. C., Woodruff, T. E., Adolphi, F., Bisiaux, M., Brook, E. J., Buizert, C., Caffee, M. W., Dunbar, N. W., Edwards, R., Geng, L., Iverson, N., Koffman, B., Layman, L., Maselli, O. J., McGwire, K., Muscheler, R., Nishiizumi, K., Pasteris, D. R., Rhodes, R. H., and Sowers,

- T. A.: The WAIS Divide deep ice core WD2014 chronology – Part 2: Annual-layer counting (0–31 ka BP), *Clim. Past*, 12, 769–786, <https://doi.org/10.5194/cp-12-769-2016>, 2016.
- Simon, Q., Bourlès, D. L., Bassinot, F., Nomade, S., Marino, M., Ciaranfi, N., Girone, A., Maiorano, P., Thouveny, N., Choy, S., Dewilde, F., Scao, V., Isguder, G. and Blamart, D., Authigenic $^{10}\text{Be}/^9\text{Be}$ ratio signature of the Matuyama–Brunhes boundary in the Montalbano Jonico marine succession, *Earth Planet. Sc. Lett.*, 460, 255–267, <https://doi.org/10.1016/j.epsl.2016.11.052>, 2017.
- Suwa, M. and Bender, M. L.: Chronology of the Vostok ice core constrained by O_2/N_2 ratios of occluded air, and its implication for the Vostok climate records, *Quaternary Sci. Rev.*, 27, 1093–1106, <https://doi.org/10.1016/J.QUASCIREV.2008.02.017>, 2008.
- Svensson, A., Andersen, K. K., Bigler, M., Clausen, H. B., Dahl-Jensen, D., Davies, S. M., Johnsen, S. J., Muscheler, R., Parrenin, F., Rasmussen, S. O., Röthlisberger, R., Seierstad, I., Steffensen, J. P., and Vinther, B. M.: A 60 000 year Greenland stratigraphic ice core chronology, *Clim. Past*, 4, 47–57, <https://doi.org/10.5194/cp-4-47-2008>, 2008.
- Svensson, A., Bigler, M., Blunier, T., Clausen, H. B., Dahl-Jensen, D., Fischer, H., Fujita, S., Goto-Azuma, K., Johnsen, S. J., Kawamura, K., Kipfstuhl, S., Kohno, M., Parrenin, F., Popp, T., Rasmussen, S. O., Schwander, J., Seierstad, I., Severi, M., Steffensen, J. P., Udisti, R., Uemura, R., Vallelonga, P., Vinther, B. M., Wegner, A., Wilhelms, F., and Winstrup, M.: Direct linking of Greenland and Antarctic ice cores at the Toba eruption (74 ka BP), *Clim. Past*, 9, 749–766, <https://doi.org/10.5194/cp-9-749-2013>, 2013.
- Svensson, A., Dahl-Jensen, D., Steffensen, J. P., Blunier, T., Rasmussen, S. O., Vinther, B. M., Vallelonga, P., Capron, E., Gkinis, V., Cook, E., Kjær, H. A., Muscheler, R., Kipfstuhl, S., Wilhelms, F., Stocker, T. F., Fischer, H., Adolphi, F., Erhardt, T., Sigl, M., Landais, A., Parrenin, F., Buizert, C., McConnell, J. R., Severi, M., Mulvaney, R., and Bigler, M.: Bipolar volcanic synchronization of abrupt climate change in Greenland and Antarctic ice cores during the last glacial period, *Clim. Past*, 16, 1565–1580, <https://doi.org/10.5194/cp-16-1565-2020>, 2020.
- Tian, L., Ritterbusch, F., Gu, J. Q., Hu, S. M., Jiang, W., Lu, Z. T., Wang, D., and Yang, G. M.: ^{81}Kr Dating at the Guliya Ice Cap, Tibetan Plateau, *Geophys. Res. Lett.*, 46, 6636–6643, <https://doi.org/10.1029/2019GL082464>, 2019.
- Tison, J.-L., de Angelis, M., Littot, G., Wolff, E., Fischer, H., Hansson, M., Bigler, M., Udisti, R., Wegner, A., Jouzel, J., Stenni, B., Johnsen, S., Masson-Delmotte, V., Landais, A., Lipenkov, V., Loulergue, L., Barnola, J.-M., Petit, J.-R., Delmonte, B., Dreyfus, G., Dahl-Jensen, D., Durand, G., Bereiter, B., Schilt, A., Spahni, R., Pol, K., Lorrain, R., Souchez, R., and Samyn, D.: Retrieving the paleoclimatic signal from the deeper part of the EPICA Dome C ice core, *The Cryosphere*, 9, 1633–1648, <https://doi.org/10.5194/tc-9-1633-2015>, 2015.
- Uemura, R., Motoyama, H., Masson-Delmotte, V., Jouzel, J., Kawamura, K., Goto-Azuma, K., Fujita, S., Kuramoto, T., Hirabayashi, M., Miyake, T., Ohno, H., Fujita, K., Abe-Ouchi, A., Iizuka, Y., Horikawa, S., Igarashi, M., Suzuki, K., Suzuki, T., and Fujii, Y.: Asynchrony between Antarctic temperature and CO_2 associated with obliquity over the past 720,000 years, *Nat. Commun.*, 9, 1–11, <https://doi.org/10.1038/s41467-018-03328-3>, 2018.
- Veres, D., Bazin, L., Landais, A., Toyé Mahamadou Kele, H., Lemieux-Dudon, B., Parrenin, F., Martinerie, P., Blayo, E., Blunier, T., Capron, E., Chappellaz, J., Rasmussen, S. O., Severi, M., Svensson, A., Vinther, B., and Wolff, E. W.: The Antarctic ice core chronology (AICC2012): an optimized multi-parameter and multi-site dating approach for the last 120 thousand years, *Clim. Past*, 9, 1733–1748, <https://doi.org/10.5194/cp-9-1733-2013>, 2013.
- Wolff, E.: Recommendation of AICC2023 by EPICA SSC, <https://doi.org/10.5194/egusphere-2023-1081-CC1>, 2023.
- Wolff, E. W., Chappellaz, J., Blunier, T., Rasmussen, S. O., and Svensson, A.: Millennial-scale variability during the last glacial: The ice core record, *Quaternary Sci. Rev.*, 29, 2828–2838, <https://doi.org/10.1016/J.QUASCIREV.2009.10.013>, 2010.
- Yan, Y., Bender, M. L., Brook, E. J., Clifford, H. M., Kemeny, P. C., Kurbatov, A. v., Mackay, S., Mayewski, P. A., Ng, J., Severinghaus, J. P., and Higgins, J. A.: Two-million-year-old snapshots of atmospheric gases from Antarctic ice, *Nature*, 574, 663–666, <https://doi.org/10.1038/s41586-019-1692-3>, 2019.
- Yiou, F., Raisbeck, G. M., Baumgartner, S., Beer, J., Hammer, C., Johnsen, S., Jouzel, J., Kubik, P. W., Lestringuez, J., Stievenard, M., Suter, M., and Yiou, P.: Beryllium 10 in the Greenland Ice Core Project ice core at Summit, Greenland, *J. Geophys. Res.-Oceans*, 102, 26783–26794, <https://doi.org/10.1029/97JC01265>, 1997.
- Zappala, J. C., Baggenstos, D., Gerber, C., Jiang, W., Kennedy, B. M., Lu, Z. T., Masarik, J., Mueller, P., Purtschert, R., and Visser, A.: Atmospheric ^{81}Kr as an Integrator of Cosmic-Ray Flux on the Hundred-Thousand-Year Time Scale, *Geophys. Res. Lett.*, 47, e2019GL086381, <https://doi.org/10.1029/2019GL086381>, 2020.
- Zhao, X., Cheng, H., Sinha, A., Zhang, H., Baker, J. L., Chen, S., Kong, X., Wang, Y., Edwards, R. L., Ning, Y., and Zhao, J.: A High-Resolution Speleothem Record of Marine Isotope Stage 11 as a Natural Analog to Holocene Asian Summer Monsoon Variations, *Geophys. Res. Lett.*, 46, 9949–9957, <https://doi.org/10.1029/2019GL083836>, 2019.

Appendix B : First-author publication : Legrain, E., Blard, P. H., & Charreau, J. (2022). Glacial equilibrium line-based relationship for paleoclimate reconstructions (Sierra Nevada, USA). *Quaternary Research*, 109, 183-194.

Research Article

Glacial equilibrium line–based relationship for paleoclimate reconstructions (Sierra Nevada, USA)

Etienne Legrain^a, Pierre-Henri Blard^{a,b*}  and Julien Charreau^a

^aCRPG, CNRS, Université de Lorraine, 54500 Vandoeuvre-lès-Nancy, France and ^bLaboratoire de glaciologie, DGES-IGEOS, Université Libre de Bruxelles, 1050 Brussels, Belgium

Abstract

We use PRISM climatic data (1981–2010) and Landsat images (2012–2013) to establish an empirical relationship linking annual temperature and precipitation to the equilibrium line altitude (ELA) of glaciers in the Sierra Nevada (36–41°N, California, USA). For this, we determined the present-day ELAs of 57 glaciers and the local 0°C isotherms elevation I_{so_0} , averaged over the 1981–2010 period. The difference, for each glacier, is Y , the normalized snowline altitude ($Y = ELA - I_{so_0}$). We then empirically calibrated a logarithmic relationship between this normalized snowline altitude and mean annual precipitation using data from partially covered glaciers. Our calibration is statistically distinct from that previously established for the tropical and midlatitude Andes (Fox and Bloom [1994], *Journal of Geography (Chigaku Zasshi)*, 103, 867–885; Condom et al. [2007], *Global and Planetary Change*, 59, 189–202). This new relationship for North America is an easy-to-use tool to permit paleoclimatic reconstructions from paleo-ELAs. For a specific paleoglacial site, paleotemperature can be computed knowing the paleoprecipitation range, and vice versa. We also performed a test showing that, if precipitation is well known, the uncertainty associated with paleotemperature is about 1°C (1σ).

Keywords: Glacier, Sierra Nevada, ELA, Temperature, Precipitation, Calibration

(Received 14 July 2021; accepted 28 February 2022)

INTRODUCTION

Past extents of glaciers are reliable climatic proxies (e.g., Oerlemans, 2005; Blard et al., 2007) to reconstruct past climatic changes in continental areas (e.g., Martin et al., 2018). Glacial extents are driven by the surface mass balance of glaciers, which is controlled by multiple climatic variables, including snowfall, temperature, albedo, relative humidity, insolation, and wind (e.g., Ohmura et al., 1992). Ideally, physical models can be developed to accurately link these climatic variables to glacial mass balances. This is the goal of surface-energy models that explicitly account for all atmospheric variables controlling glacial mass balance (e.g., Plummer and Phillips, 2003; Rupper et al., 2009; Fitzpatrick et al., 2017). However, some of the variables required by such models are often difficult to constrain, notably for past conditions. Other approaches, such as positive degree-day (PDD), models are simplified, easy-to-use alternatives (e.g., Braithwaite, 1995; Hock, 2003; Gabbi et al., 2014). In certain climatic settings (e.g., low relative humidity, high solar insolation), however, PDD models may yield inaccurate estimates of surface mass balance, because they do not accurately capture processes such as sublimation or wind ablation (Sicart et al., 2005; Blard et al., 2011).

Several studies have shown that the response of alpine glaciers to climatic parameters is well captured by a glacier's equilibrium line altitude (ELA) (Meier, 1962; Miller et al., 1975; Porter, 1975). ELA is the elevation at which annual accumulation is exactly balanced by annual ablation (e.g., Ohmura et al., 1992; Condom et al., 2007). This opens the door to even simpler empirical relationships linking ELAs and two climatic variables: summer temperatures and winter precipitation (e.g., Ohmura et al., 1992). Empirical studies have established regional relationships linking ELA to mean annual temperature (T) and precipitation (P) (e.g., Fox and Bloom, 1994; Condom et al., 2007). Indeed, the simple logarithmic calibration of Fox and Bloom (1994), based on current glaciers in a restricted part of the tropical Andes (Peru, 5–17°S), accurately describes the spatial variability of present-day ELAs over the entire Andes Cordillera (10°N to 55°S; Condom et al., 2007).

Such a simple relationship between glacial mass balance and two climatic variables is useful, because it enables quick and accurate climatic projections (e.g., Condom et al., 2007) and paleoclimatic reconstructions (e.g., Martin et al., 2018). However, such empirical relationships between ELA, P , and T are, in principle, only regionally valid, and regional variations of other confounding factors such as relative humidity, insolation, wind, and cloud cover may modify them. Thus, specific empirical relationships linking ELA, P , and T should ideally be determined for each climatic region using accurate present-day observations.

The Sierra Nevada is a midlatitude (36–41°N) North American mountain range situated between the Pacific Ocean and the arid

*Corresponding author at E-mail address: blard@crpg.cnrs-nancy.fr (P.-H. Blard)

Cite this article: Legrain E, Blard P-H, Charreau J (2022). Glacial equilibrium line–based relationship for paleoclimate reconstructions (Sierra Nevada, USA). *Quaternary Research* 1–12. <https://doi.org/10.1017/qua.2022.10>

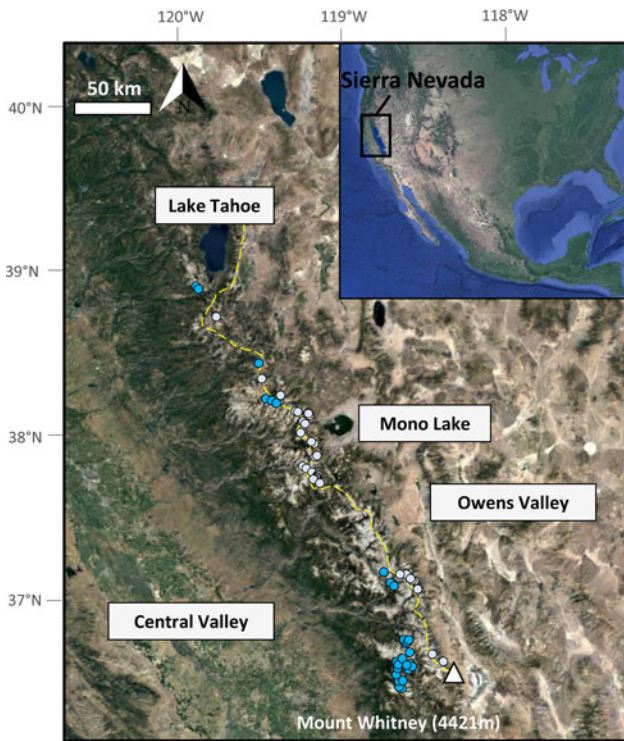


Figure 1. Google Earth® images showing the regional setting of the Sierra Nevada range (western United States, inset) and the locations of the 57 glaciers studied (gray and blue dots). The yellow dashed line represents the crest of the Sierra Nevada. Glaciers east of the crest are gray dots; glaciers west of the crest are blue dots.

deserts of Nevada, with summit elevations exceeding 4000 m above sea level (m asl) in the central part of the range (Fig. 1). At such high altitudes (i.e., 2900–4000 m asl), the westerly oceanic winds bring sufficient precipitation for promoting permanently glaciated areas between 36.4°N and 38.9°N (Pandey *et al.*, 1999). This study aims to empirically calibrate the relationship between ELA, temperature, and precipitation for the Sierra Nevada, following the approach of Fox and Bloom (1994) and Condom *et al.* (2007). This empirical relationship can be used in future studies to reconstruct past climatic variables from the paleo-ELAs of glaciers from North America: that is, paleoprecipitation if paleotemperature is independently determined, or vice versa. This approach relies on the assumption that secondary climatic variables (other than precipitation and temperatures) are the same in the past as in the present.

DATA AND METHODS

The main objective of this study was to determine an empirical relationship between local precipitation, 0°C isotherms, and present-day ELAs of Sierra Nevada glaciers. This section describes the data and methods used to establish this relationship.

Data

PRISM temperature data

We chose to use the PRISM data set for climatological data, as it is a robust and widely used reanalyzed climatological product (PRISM Climate Group, Oregon State University, <http://prism.oregonstate.edu>, created July 2012) (Daly *et al.*, 2008, 2015). We

used the reanalyzed PRISM temperatures averaged over the 30 year normal period (1981–2010), gridded at a spatial resolution of 800 × 800 m. Glaciers behave as low-pass filters of the interannual climatic signal, averaging the climatic signal over the decadal timescale. This justifies the use of climatic data averaged over a period that precedes the date of the observed ELAs. Given their geometries and sizes, the 57 analyzed Sierra Nevada glaciers integrate climate over a period that is representative of the previous 30 years (e.g., Zekollari and Huybrechts, 2015), meaning that the ELAs derived from the 2013 and 2012 images are likely representative of the 1981–2010 climatic period. The mean annual temperature corresponding to each glacier was assumed to be the value of the grid cell containing the glacier.

PRISM precipitation data

Mean annual precipitation was derived from PRISM data over the 30 year normal period (1981–2010) at a gridded spatial resolution of 800 × 800 m. This data set is spatially continuous, which is important for capturing the sharp spatial changes that are frequent in high-elevation terrains such as the Sierra Nevada. Moreover, the 30 year integration period of the data set smooths the interannual variability. The annual precipitation corresponding to each glacier was assumed to be the value of the cell in which the glacier is located.

Elevation data

For each precipitation and temperature value, we associated the elevation value of the PRISM data set of the corresponding cell. The digital elevation model (DEM) used for the PRISM normal data set is the National Elevation Dataset (Daly *et al.*, 2008). The average vertical uncertainty of the DEM expressed as the root mean-square error is 2.4 m (Gesch *et al.*, 2002); the horizontal resolution is 10 m, and 3 m in some local areas where really high resolution is available (Gesch *et al.*, 2002).

Landsat images of Sierra Nevada glaciers (2012–2013)

To derive the ELAs of 57 Sierra Nevada glaciers, we used clear-sky Landsat Thematic Mapper color images with a horizontal resolution of 15 m and the associated DEM available in Google Earth® (elevation uncertainty < 6 m; Sharma and Gupta, 2014). Most glaciers were mapped and identified from images acquired between August and September 2013, although we also used images from August 2012, when 2013 images were not available in some areas. Summer 2013 was favored, as it corresponds to a relatively dry year, minimizing the risk of overestimating the glacial extent because of relict snow. When images from both years were available for the same glacier, comparison showed that the Sierra Nevada ELAs of 2012 and 2013 were undistinguishable within uncertainties.

ELAs data set of 1972 for testing the ELA versus climate calibration

To test the robustness and the versatility of the calibration law derived from the 2012–2013 ELAs (see “Relationship between ELAs and Climate” for a description of this calibration; Eq. 3), we also considered another data set based on the oblique and vertical photographs of glaciers obtained during the aerial campaign of 1972 (August 23–24) in Sierra Nevada (Raub *et al.*, 2006). These black-and-white pictures allowed determination of ELAs from 1972 with an uncertainty of 15 m (Raub *et al.*, 2006). Raub *et al.*'s (2006) study identified 13 main basins in the Sierra Nevada, and we chose for each basin the glacier having

the largest area in 1972. Two of them being debris-covered glaciers, our final 1972 test data set comprised 11 glaciers. Their areas range from 0.02 to 1.32 km², with a mean of 0.38 km² (Supplementary Table 2). Among these 11 glaciers, 4 have now disappeared (East Walker River Basin, Mokelumne River Basin, East Carson River Basin, Merced River Basin). The ELAs of these 11 glaciers were calculated using the same approach as the one applied for the glaciers’ data set based on the 2012–2013 images (see “Determination of ELAs”). For this test data set, we used PRISM Temperature and Precipitation reanalysis data from the 1941–1970 period (average of previous 30 year period), with a grid resolution of 4 × 4 km. PRISM temperatures of the 1941–1970 period were used to compute 0°C isotherms, applying the same method as the one applied to the 1981–2010 data set (see “Determination of 0°C Isotherm”).

Methods

Determination of ELAs

Perennial ice bodies were identified as glaciers if they fulfilled the following conditions (Figs. 2 and 3): (1) they were already described in a previous compilation of aerial photos from August 1972 (Raub et al., 2006); (2) they had an elevation range >30 m (Figs. 2 and 3); (3) they presented typical glacial features, such as crevasses (Fig. 2); and (4) their surfaces were only partially covered by debris. Because debris coverage may modulate ice melting (Clark et al., 1994), we paid special attention to this criterion by analyzing the colors of the glaciers and clearly identify debris-covered areas. We discarded the fully covered glaciers from this calibration and included partially covered glaciers in the data set, with “partially covered” referring to glaciers whose surface is 10–90% debris free (Fig. 4).

We then calculated the ELA of each glacier using the toe-to-headwall altitude ratio (THAR) method, with a THAR coefficient of 0.5 (Charlesworth, 1957). While the THAR coefficient may range from 0.4 to 0.8 for glaciers worldwide (Benn and Lehmkuhl, 2000), a value of 0.5 was shown to be the most accurate for the Sierra Nevada (Moore and Moring, 2013).

Determination of 0°C isotherm

To calculate the elevation of the 0°C isotherm at each glacier’s location, we used the PRISM temperature and elevation data (Eq. 2). To compute this local 0°C isotherm, we used the temperature of the PRISM grid cell in which the glacier is located and combined this with the local mean annual environmental lapse rate (Lr). For this, we determined Lr for the Sierra Nevada range, using a linear regression between the 57 collected temperature and elevation cells (elevation also derived from the PRISM data set). We obtained a best-fit value of Lr = −5.20 ± 0.14°C/km (Fig. 5). This uncertainty corresponds to the 1σ confidence interval of the regression coefficient of the linear fit. To evaluate the accuracy of this Lr estimate, we also computed the Lr from 29 high-altitude (1128–2940 m asl) climatic stations of the Sierra Nevada from the National Weather Service Cooperative Observer Program (<https://www.ncdc.noaa.gov>, last accessed February 2021) (Supplementary Table 3). Using the same regression methodology, we found a best-fit value of Lr = −5.3 ± 0.5°C/km, which is similar within uncertainties to the Lr value derived from the PRISM data.

Relationship between ELAs and climate

We followed the method of Fox and Bloom (1994) and Condom et al. (2007) to establish a simple relationship between the

observed ELA (m asl), the elevation of the annual 0°C isotherm (Iso₀, m asl), and mean annual precipitation (P, mm/yr). We first determined the modern ELA of Sierra Nevadan glaciers by analyses of Landsat satellite images available in Google Earth® from 2012 and 2013 using the THAR method (Charlesworth, 1957). Then, we subtracted the local 0°C isotherm (defined in “Determination of 0°C Isotherm”) from the ELA for each glacier to define the normalized snowline altitude (Y) as (Fox and Bloom, 1994):

$$Y = ELA - Iso_0 \tag{Eq.1}$$

where Iso₀ is inferred from PRISM temperature data as:

$$ISO_0 = \frac{T}{Lr} + Z, \tag{Eq.2}$$

where T is the local PRISM grid cell’s mean annual temperature averaged over the 1981–2010 period (°C), Z is the mean elevation of the PRISM grid cell (m asl), and Lr is the average annual Lr of the studied region (°C/m) (Fig. 5).

To smooth the data variability, we grouped and averaged the climatic and ELA data sets in five subclimatic regions based on mean annual precipitation. These subclimatic regions range from 800 to 1800 mm/yr, with a bin size of 200 mm/yr (Table 1). Using this data set, we established a relationship between Y and P:

$$Y = A - B \times \log_{10}(P) \tag{Eq.3}$$

where A and B are empirical variables specific to the region of interest. From their detailed survey of modern Peruvian and Bolivian glaciers in 21 subclimatic regions (5–17°S), Fox and Bloom (1994) determined regional values of A (3427 m) and B (1148 m). Here, we used the same approach to calculate the values of A and B specific to Sierra Nevadan glaciers (Fig. 6).

Paleoclimatic reconstruction from ELAs derived from glacial landforms

For paleoclimatic reconstructions, once A and B are determined, it is possible to compute T from the paleo-ELA and P by combining Eqs. 1, 2, and 3:

$$T = Lr \times [ELA - Z - A + B \cdot \log_{10}(P)] \tag{Eq.4}$$

Alternatively, if paleotemperature is constrained from an independent proxy, it is possible to compute P from Eq. 4:

$$P = 10^{\frac{\frac{T}{Lr} + Z + A - ELA}{B}} \tag{Eq.5}$$

Equations 4 and 5 may thus be used for paleoclimatic reconstructions.

In other situations, ELA positions may also be computed as a function of T and P. This could be useful to perform sensitivity tests, using independent proxies for paleotemperature and paleoprecipitation. Additionally, future projected P and T from global climate models may also be used as input in this equation to

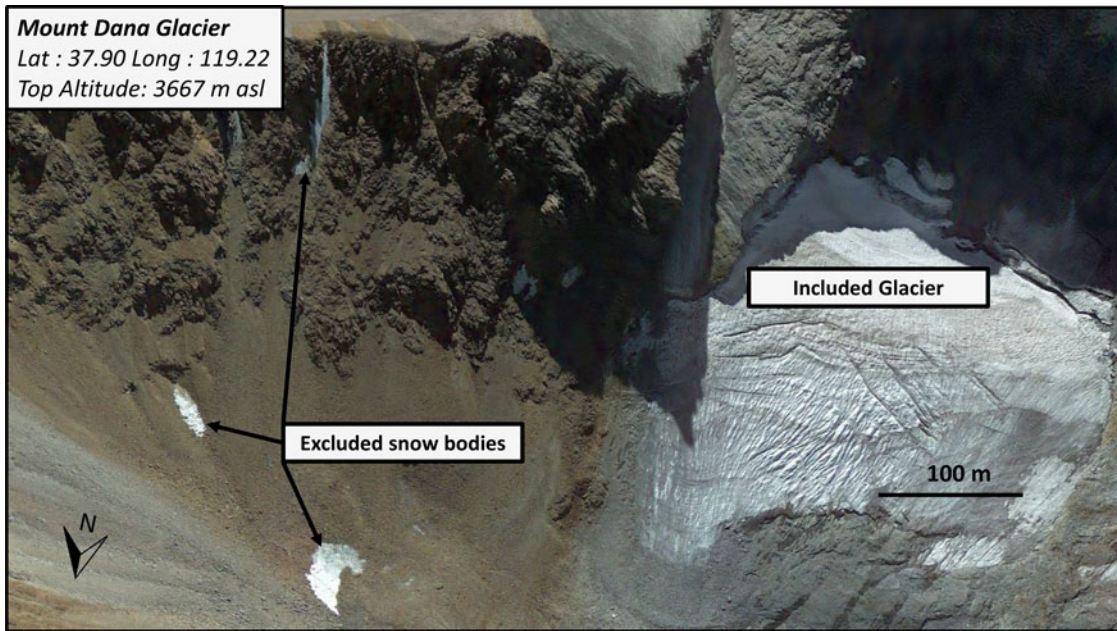


Figure 2. September 2013 Landsat-Google Earth® image of four representative Sierra Nevadan glaciers. We used Google Earth digital elevation model (elevation uncertainty <6 m). Only the glacier on the right was included in the data set, as it is of sufficient size (elevation range >30 m), presents glacial features (crevasses), and is within a glacial cirque. The three excluded snow bodies on the left have elevation ranges <30 m.

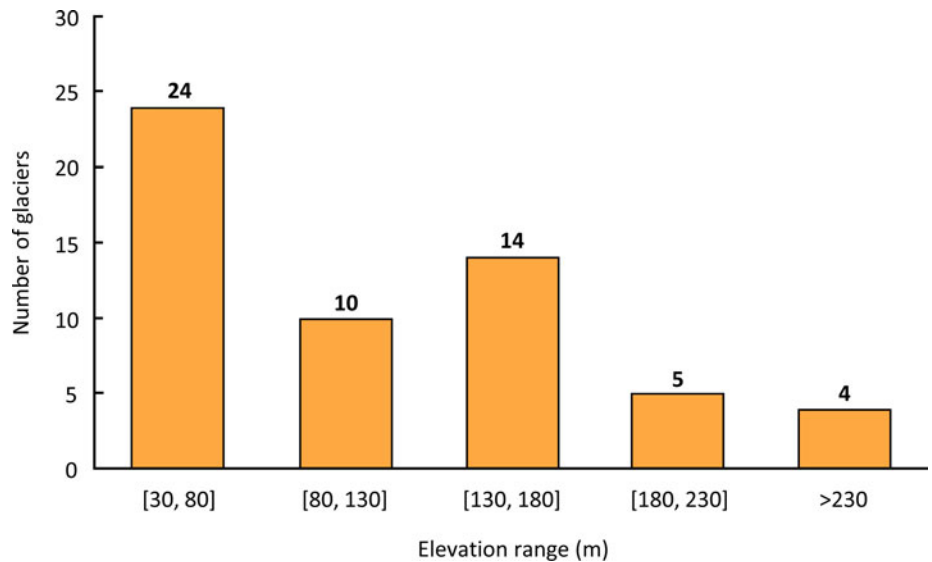


Figure 3. Distribution of the elevation ranges of Sierra Nevadan glaciers in 2012 and 2013. Elevation range represents the difference between the headwall and toe elevations of each glacier. We used the digital elevation model displayed in Google Earth® (elevation uncertainty <6 m).

make first-order estimates of future ELA changes:

$$ELA = \frac{T}{Lr} + Z + A - B \times \log_{10}(P) \quad (Eq.6)$$

Results

Glacial inventory and ELAs

Our calibration data set consists of a total of 57 Sierra Nevadan glaciers, all located from 36.4°N to 38.9°N (Supplementary Table 1). Sierra Nevadan glaciers are most abundant around 37°N and are absent in two low-elevation zones between 37.4°N and 37.6°N and between 38.4°N and 38.8°N (Raub et al., 2006; Figs. 1 and 7). The 2012–2013 ELAs of these glaciers range

from 2908 to 3957 m asl. They display a noticeable geographic variability, with two superimposed eastward and southward gradients (Fig. 7): along a west-east transect, ELAs rise from about 3000 m (120°W) to ~3800 m (118.5°W) (356 ± 31 m/decimal degree [DD] west-east gradient). Latitude has no visible impact on ELAs between 36.5°N and 37.5°N, but ELAs then drop from ~3800 m (37.5°N) to ~3000 m (38.5°N), corresponding to a south-north gradient of about –400 m/DD. This spatial variability results from increased precipitation to the west and decreased temperature to the north. Twenty-nine glaciers are located north-east of the crest in the rain shadow, whereas 28 of them are located southwest of the crest (Fig. 1). However, we did not observe any significant differences between these two sub-data sets, both yielding similar relationships between ELAs and

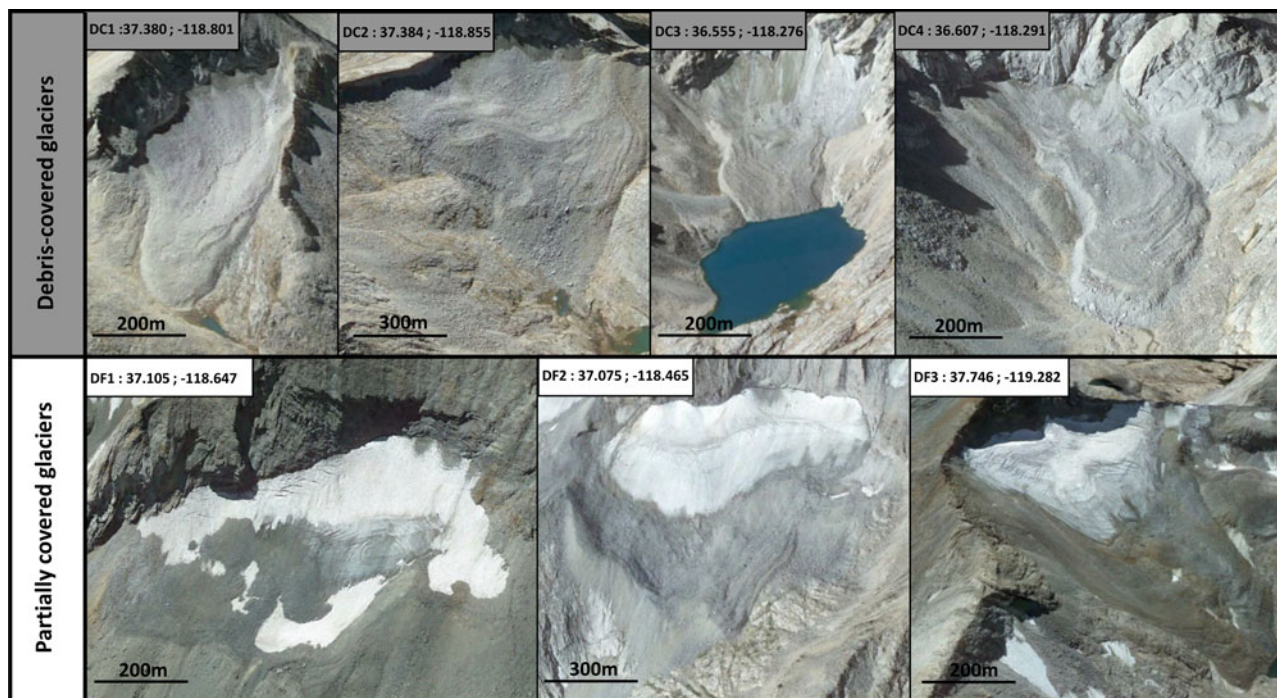


Figure 4. Examples of four debris-covered glaciers (top) and three partially covered glaciers (bottom) (Landsat-Google Earth® images). We consider a glacier as “partially covered” when 10–90% of its surface is free of debris. Only partially covered glaciers were included in the calibration.

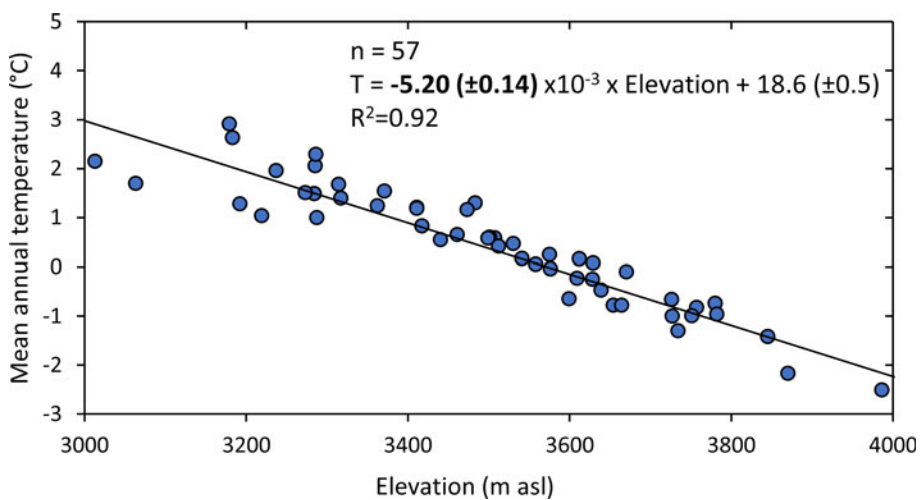


Figure 5. Mean annual temperature (T) vs. elevation (Z) for the 57 glaciers studied, derived from the PRISM data set (1981–2010). These data permit us to determine the average mean annual lapse rate (L_r) for the Sierra Nevada. Best-fit L_r is $-5.20 \pm 0.14^\circ\text{C}/\text{km}$ (1σ).

climatic parameters. We thus considered the whole data set when establishing the calibration, without making any distinction between western and eastern glaciers.

Uncertainties on the normalized snowline altitude and mean annual precipitation

Each of the two variables involved in the calibration (Eq. 3)—mean annual precipitation and the normalized snowline altitude—has its own uncertainties that we estimated during each computation step.

To compute the 0°C isotherms (Eq. 2), we corrected the temperature of each glacier using the regional L_r (1σ uncertainty, $0.14^\circ\text{C}/\text{km}$; Fig. 5). The uncertainties on the normalized snowline altitude arising from this L_r correction range from 16 to 52 m. Additionally, we observe a scatter of the normalized snowline

altitudes, Y , in each 200 mm/yr subclimatic region. This observed variability in each subregion represents another source of error. This uncertainty was computed for each subregion as the standard error of the mean, that is, $\sigma(Y)/\sqrt{n}$, $\sigma(Y)$ being the standard deviation of the observed normalized snowline altitudes in each subclimatic region. Hence, the total uncertainty of the normalized snowline altitude of each subclimatic region combines the standard error of the mean and the uncertainty resulting from the L_r correction (Table 1). These errors were propagated using a Taylor series expansion.

The uncertainty associated with the PRISM precipitation data attributed to each subregion was computed as the standard deviation of all PRISM data points within each subregion. These uncertainties range from 35 to 61 mm/yr for the five subclimatic regions (Table 1).

Table 1. Averaged annual precipitation (mm/yr) and normalized snowline altitude (Y) (m) data used for the present Sierra Nevada calibration for the five subclimatic regions, considering partially covered glaciers only ($n=57$; see “Other Sources of Uncertainty”).^a

Range of precipitation (mm/yr)	Number of glaciers per region	Mean annual precipitation (mm/yr)	σ (mm/yr) ^b	Y (m)	σ (m) ^c
800–1000	7	936	35	242	95
1000–1200	17	1097	59	156	72
1200–1400	19	1282	61	115	62
1400–1600	13	1460	39	-96	67
1600–1800 ^d	1	1791	48.5	-185	51

^aMean annual precipitation and normalized snowline altitude are the arithmetic average values across all partially covered glaciers in each subclimatic region (based on mean annual precipitation bins of 200 mm/yr). Precipitation values are from the PRISM data set and cover the 1981–2010 climatic period, while normalized snowline altitudes are derived from 2012 and 2013 pictures. The 1σ values indicate the most realistic uncertainties associated with each subregion (see “Uncertainties on the Normalized Snowline Altitude and Mean Annual Precipitation” for uncertainty estimates).

^bComputed as the standard deviation of each precipitation value of each subregion.

^cComputed as the quadratic sum (Taylor series expansion) of the standard deviation/racine(n) of normalized snowline altitudes and of the analytical uncertainties in each subregion.

^dThe 1600–1800 subclimatic region is only composed of one glacier, inducing a null standard deviation for this subregion. The associated uncertainty is the error of the normalized equilibrium line altitude (ELA) computation itself.

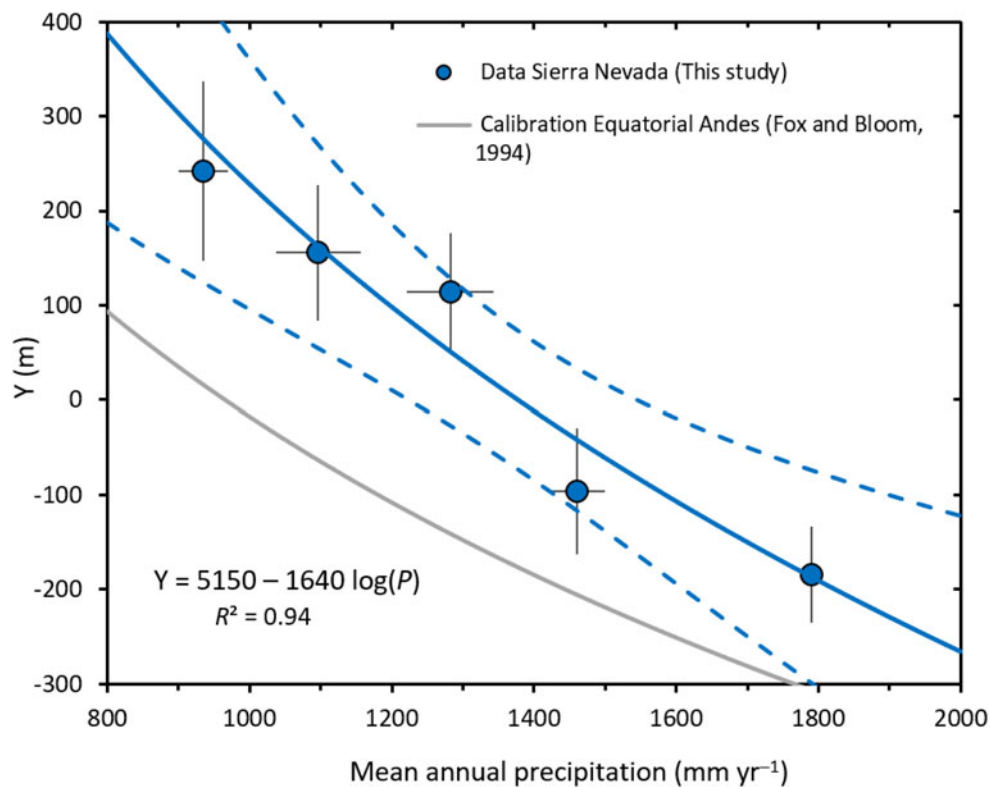


Figure 6. Calibrated relationship between normalized snowline altitude (Y) and mean annual precipitation for the five subclimatic regions (see Table 1) of the Sierra Nevada (blue dots). The best-fit logarithmic calibration is shown by the blue curve ($R^2=0.94$; P value = 6.7×10^{-5} ; mean standard deviation of the mean (MSWD) = 0.62). The relationship was computed by taking into account the data uncertainties (Vermeesch, 2018). Dashed blue curves represent the 2σ confidence interval for external errors only. The gray curve is the calibration established for the tropical Andes by Fox and Bloom (1994). The best-fit values of the empirical variables A and B in Eq. 6 for Sierra Nevada are 5150 ± 767 m and 1640 ± 244 m (1σ), respectively.

Other sources of uncertainty

The resolution of the Landsat images used induces a vertical maximum uncertainty of 6 m on ELAs. Because the observed ELAs cover a range of more than 1000 m in this data set, this resolution does not represent an important source of uncertainty. We also tested the impact of the value of the THAR coefficient on our results. Using a THAR coefficient of 0.7 instead of 0.5 (global values range between 0.4 and 0.8; Benn and Lehmkühl, 2000) shifts the computed ELA values by 0.7% on average and by 2.2% at most (Supplementary Table 1).

For each glacier, we attributed the temperature of the PRISM cell (800×800 m) in which the center of the glacier is located. This approximation may be a source of uncertainty, as a given glacier could belong to more than one grid cell. All the glaciers in our data set are smaller than a grid cell surface (0.64 km^2). The largest glacier of the data set, Palisade Glacier, is 0.6 km^2 (Supplementary Table 1). In an extreme case, however, a glacier could belong to up to four PRISM cells. Even if this case is unlikely, we estimated a maximum uncertainty by calculating the average absolute temperature difference of four adjacent

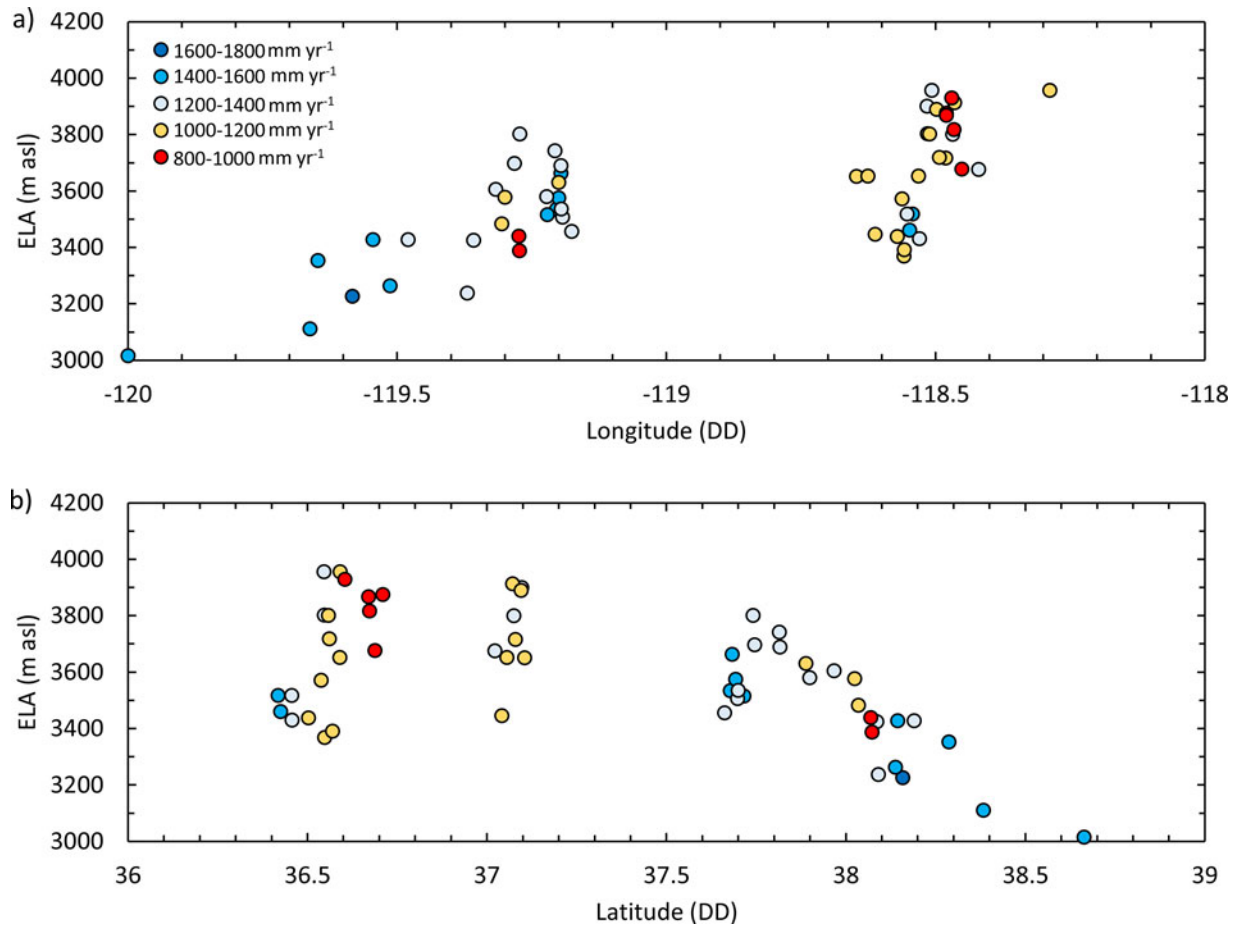


Figure 7. Equilibrium line altitude (ELA) vs. (a) longitude and (b) latitude for the 57 glaciers analyzed (2012–2013). Colored dots represent glaciers of each sub-climatic region: red for 800–1000, yellow for 1000–1200, blue-gray for 1200–1400, blue for 1400–1600, and dark blue for 1600–1800 mm/yr. From west to east, ELAs increase from ~3000 m asl (120°W) to ~3800 m asl (118.5°W), a west-east gradient of 356 ± 31 m/decimal degree (DD). Latitude has no visible impact on ELAs between 36.5°N and 37.0°N, but ELAs then decrease from ~3800 m asl (37.0°N) to ~3000 m asl (38.5°N), a south-north gradient of about -500 m/DD. This spatial variability results from increased precipitation toward the west and increased cooling toward the north. ELA uncertainties are provided in Supplementary Table 1.

cells of the PRISM grid data set (between 121–117°W and 40–36°N). This yields an average value of $0.25 \pm 0.28^\circ\text{C}$. This spatially induced temperature uncertainty is on the order of 0.25°C , which remains reasonable. However, it may explain part of the data dispersion in the normalized snowline altitude versus precipitation space (Figs. 6 and 8).

Uncertainties associated with the PRISM temperature and precipitation over the normal period (1981–2010) are difficult to evaluate. Daly et al. (2008) estimated uncertainties for the last PRISM climate-normal period (1971–2000) using cross-validation mean absolute error and a 70% prediction interval. Their results indicated that the highest uncertainties within the PRISM data set occur in the mountainous western United States, including the Sierra Nevada range, where uncertainties surrounding precipitation may reach 30% of the mean annual value and those for temperature may reach 1°C . We tested this PRISM-specific relative error of 30% for precipitation: it induced a drop of the mean standard deviation of the mean (MSWD) far below 1 (MSWD = 0.05). The MSWD, which is also known as the “reduced chi-square statistic,” is an indicator of the match between the model and the data, taking into account the agreement between the dispersion of the data and their attached

uncertainties. This low MSWD value indicates that the data dispersion is much lower than expected from these uncertainties and that the 30% value reported by Daly et al. (2008) for precipitation probably overestimates the actual uncertainty. Hence, we consider that our error computation based on the standard deviation of precipitation in each subclimatic region (Table 1) is an accurate and sufficient predictor of the precipitation data dispersion.

Globally, the grid resolution of 800×800 m for the PRISM data could be a source of uncertainty if we consider that glaciers have a vertical extension and thus the top and the front of the glacier do not receive the same amount of precipitation and temperature. Although we did not try to explicitly quantify this uncertainty, this source of random error could also explain part of the data dispersion (Fig. 6).

Finally, although we did not identify a systematic correlation between the proportion of debris cover and the ELA position, we cannot exclude that the variability of the debris cover may explain part of the data scatter. Given that the elevation range covered by these small glaciers is on average ~ 100 m, the ELA scatter induced by the variable debris cover is limited and probably included in the noise of the data set (Supplementary Tables 1 and 2).

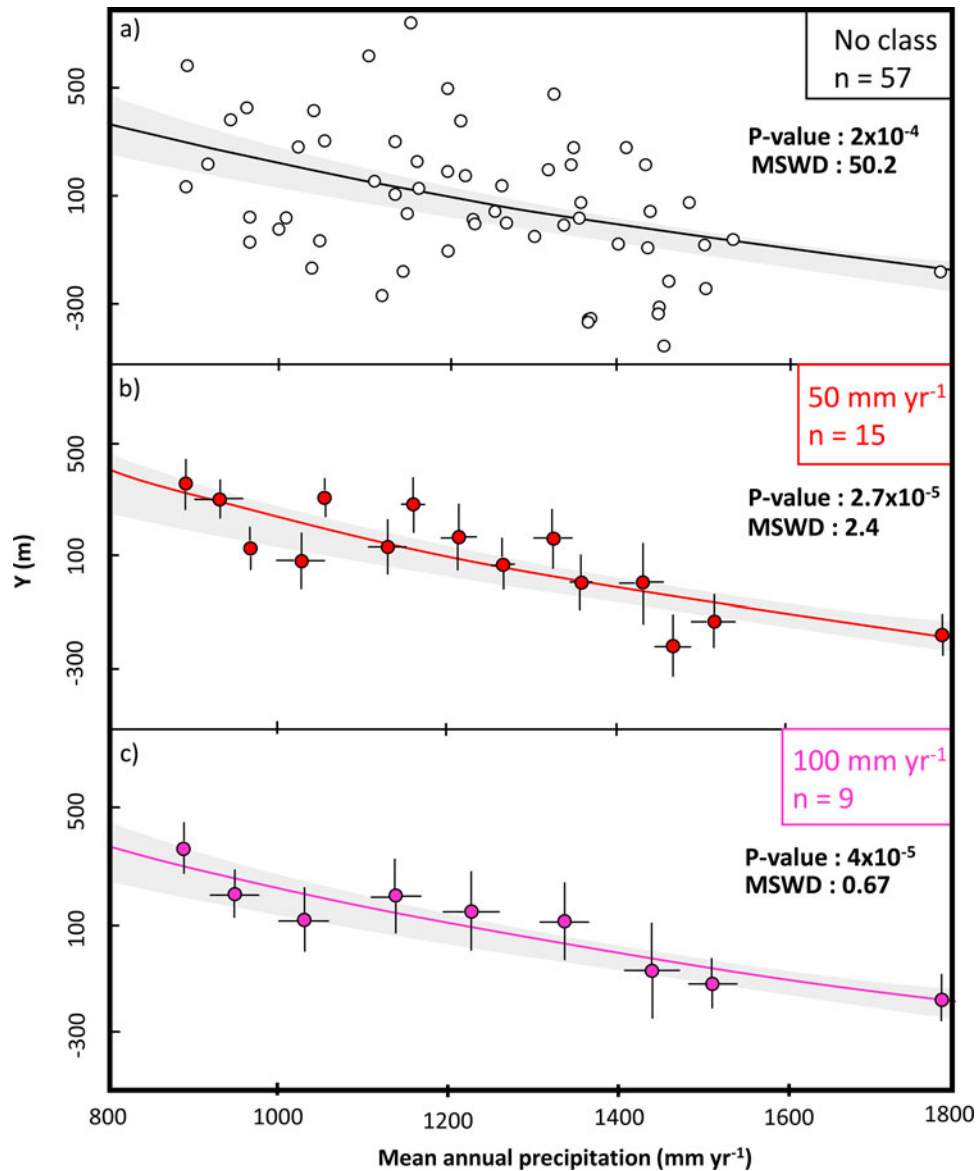


Figure 8. Relationships between normalized snowline altitude and mean annual precipitation computed from (a) the raw precipitation data set (no pre-averaging) and (b, c) precipitation data pre-averaged in subclimatic regions with bin sizes of (b) 50 and (c) 100 mm/yr. All three relationships are within the 2σ confidence interval of the relationship obtained with a subregional bin size of 200 mm/yr (shaded gray area; see Fig. 7). Each dot represents one subclimatic region. MSWD, mean standard deviation of the mean.

Normalized snowline versus P calibration

The normalized snowline values calculated for all glaciers using Eqs. 1 and 2 range between -457 and $+753$ m, with a mean value of 162 ± 227 m. Mean annual precipitation for these glaciers ranges between 850 and 1791 mm/yr. After grouping the 57 glaciers into the five subclimatic regions of 200 mm/yr precipitation bins, we established the best fit between normalized snowline altitude and precipitation using the logarithmic model defined by Eq. 3 and a regression algorithm that accounts for data uncertainties (Vermeesch, 2018; Fig. 6). The best-fit values we obtained are $A = 5150 \pm 767$ m and $B = 1640 \pm 244$ m. Statistical parameters of this regression ($R^2 = 0.94$, P value = 6.7×10^{-3} , MSWD = 0.62) indicate that it is accurate in describing the relationship between normalized snowline altitude and precipitation. An MSWD of 0.62, close to 1, shows that the magnitude of the uncertainties is realistic and is in agreement with the data dispersion.

DISCUSSION

Representativeness of the data set

We studied a representative glacier data set from the Sierra Nevada to obtain an accurate calibration. Our inclusion criteria avoid temporary snow bodies, thus yielding a total number of glaciers much lower than those in the previous compilation of Raub et al. (2006; 497 glaciers) and the Randolph Inventory Database 6.0 (GLIMS and NSIDC, 2005, updated 2018; 923 glaciers). However, these two inventories do not distinguish permanent glaciers from nonpermanent snowfields, and therefore may overestimate the actual number of glaciers. Fountain et al. (2017) counted 157 glaciers in the Sierra Nevada based on a shear stress–threshold criterion to distinguish glaciers from perennial snowfields. However, they included debris-covered glaciers, whereas we only consider partially covered glaciers.

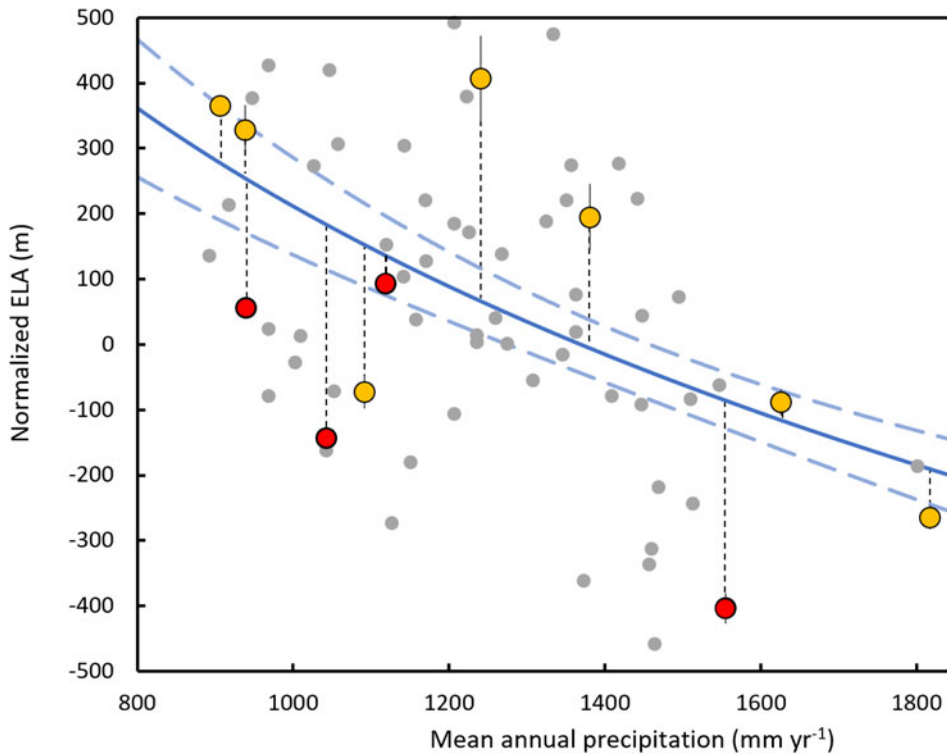


Figure 9. Comparison of the calibrated relationship with a test data set of 11 glacial equilibrium line altitudes (ELAs) observed in 1972. The 11 glaciers (red and yellow data points) used for this testing are based on PRISM climatic data of 1941–1970 and aerial photography of August 1972 (Raub et al., 2006). Yellow and red dots are respectively still existing ($n=7$) and vanished glaciers ($n=4$). Gray dots show the 2012–2013 glacial ELAs used to establish the calibration curve. Average residual between tested glaciers and the calibrated relationship (blue curve, dashed-blue curves represent 2σ confidence interval) is represented by the dark dashed-line distance and is on average 175 ± 197 m (standard deviation).

Moreover, the main reason that our data set is smaller than the Randolph Inventory Database is that we did not include glaciers with elevation ranges <30 m. The 57 partially covered glaciers used in our calibration have a mean elevation range of 107 m (standard deviation: 64 m). Their areas range from 3500 to 590,000 m^2 , for a mean value of 67,000 m^2 (Supplementary Table 1). Glaciers having these typical sizes and geometries integrate climatic variables over the past 10 to 50 years (e.g., Oerlemans, 2012; Zekollari and Huybrechts, 2015). Hence, the selected calibration data set has the advantage of limiting the variability due to interannual fluctuations and justifies the use of the PRISM data set, which is averaged over the 30 years preceding the 2012–2013 glacier pictures.

Impact of the size of the subclimatic region on the calibration

The relationship between normalized snowline altitude and P (Eq. 3) is an easy-to-use tool to link precipitation and temperature to any glacial extent. However, secondary factors such as a glacier’s orientation, atmospheric conditions, or local albedo can shift a particular glacier from the average relationship. Thus, we decided to minimize the noise generated by these secondary factors by averaging data from several glaciers based on the mean annual precipitation criteria. For our calibration, we used a 200 mm/yr interval to create subclimatic regions in which the P and normalized snowline altitude sub-data sets are averaged before performing the regression (see “Data”). As the width of this interval is an arbitrary choice, we tested the sensitivity of our model to the interval size by computing the calibration for intervals of 200 (Fig. 6), 100, and 50 mm/yr and for the raw data set (i.e., no binning interval; Fig. 8). The four relationships obtained are compatible within the 95% confidence interval, yielding similar parameters A and B (dashed blue lines in Fig. 6, light-gray shaded areas in Fig. 8). Notably, the calibration variables obtained for the

raw data set (no binning) are $A = 4905$ and $B = 1560$, compatible within uncertainties with those derived from the 200 mm/yr binned data, $A = 5150 \pm 767$ m and $B = 1640 \pm 244$ m (Fig. 8). The computed P values are not significantly different between these different precipitation bin sizes, ranging from 2×10^{-4} for the whole data set to 2.7×10^{-5} for the 50 mm/yr bin (Fig. 8). This test indicates that the data preclustering did not bias the obtained calibration, and we prefer to retain the parameters obtained with this 200 mm/yr interval. Moreover, the MSWD value decreases from 50.8 for the raw data to 0.62 for the 200 mm/yr bin (Fig. 8). An MSWD value of 0.62 indicates that this 200 mm/yr clustering accurately captures the variability arising from the data uncertainties, suggesting that our choice of bin size is representative of the real data dispersion (Fig. 8). Although different clustering bins may be used in further studies, our tests show that using a 200 mm/yr bin is justified and permits us to minimize the data scatter due to the secondary parameter control on the glacial mass balance.

Testing the calibration with a 1972 normalized snowline altitude data set of 11 representative glaciers

Figure 9 shows the agreement between the calibration curve and the test data set represented by 11 Sierra Nevadan normalized snowline altitudes observed in 1972. To test the robustness of our empirical normalized snowline altitude versus P relationship, we calculated the residuals between these 11 additional data and the calibration curve (Fig. 9). The obtained average residual value is 175 m. Using the present Sierra Nevadan L_r of $5.20 \pm 0.14^\circ C/km$ (see “Determination of $0^\circ C$ Isotherm”), this corresponds to a paleotemperature uncertainty of $0.9^\circ C$. The size of this test data set (11 glaciers) is typical of a comprehensive paleoclimatic study that would reconstruct paleo-ELAs by dating moraines in a mountain range of a comparable area (e.g.,

Stansell *et al.*, 2007; Roy and Lachniet, 2010; Zech *et al.*, 2017). It is thus statistically representative and pertinent to provide a first-order estimate of the uncertainty attached to paleotemperature reconstruction from paleo-ELAs ($\sim \pm 1^\circ\text{C}$).

We also explored the cause of the disappearance of four glaciers within this data set (East Walker River basin, Mokelumne River basin, East Carson River basin, Merced River basin). Between the 1941–1970 and 1981–2010 periods, the PRISM data set indicates that temperature rose on average $1.1 \pm 0.5^\circ\text{C}$ at the locations of these four glaciers, while precipitation remained nearly constant or increased slightly (Supplementary Table 2). Combining temperature and precipitation measured over the 1981–2010 period at these four sites, our relationship (Fig. 6) yields theoretical $\text{ELA}_{1981-2010}$ values that are on average +188 m higher than the summits of these four drainages. The disappearance of these four glaciers between 1972 and 2012 thus probably results from local warming that occurred over the last 40 years. This synchronous response of ELAs to warming confirms that these glaciers integrate the climatic parameters over 30 years or fewer.

Comparison of logarithmic and linear fits

Following several previous regional studies performed in the equatorial Andes (e.g., Fox and Bloom, 1994; Condom *et al.*, 2007), we calibrated the normalized snowline altitude versus P relationship using a logarithmic fit. However, we also tested the statistical parameters of a linear fit, using the same data set: logarithmic fit, $R^2 = 0.94$, P value = 6.3×10^{-3} ; linear fit, $R^2 = 0.94$, P value = 6.7×10^{-3} . The global calibration proposed by Greene *et al.* (2002) is linear. In some particular cases, such as midlatitude glaciers fed by moderate to high precipitation (800–1800 mm/yr), a linear calibration seems to be a reliable approximation (Greene *et al.*, 2002). However, their global linear calibration has only limited validity in extreme climatic conditions, notably in dry regions with precipitation of less than 200 mm/yr. For instance, their calibration is not able to reproduce the absence of glaciers in the central arid Andes (Ammann *et al.*, 2001). Linear glacier–climate calibrations should thus be considered with caution at regional scales, especially in arid areas. Although the Sierra Nevada is not subject to such a dry climate, our study aims to capture the regional specificity of the glacier–climate relationship. We therefore consider that the logarithmic calibration is probably a more accurate ELA–climate predictor (Fig. 6).

Comparison of the Sierra Nevadan and tropical Andean calibrations

Our ELA–climate calibration for Sierra Nevadan glaciers is statistically distinct from that established for the equatorial Andes by Fox and Bloom (1994; Fig. 6). Our values for the empirical variables A and B (5150 ± 767 m and 1640 ± 244 m, respectively) are higher than their values for the Andes ($A = 3427$ m and $B = 1148$ m). In these two regions, the situations where ELAs and 0°C isotherms are equal are encountered at different annual precipitations (mean $P = 1362 \pm 94$ mm/yr and 966 mm/yr for Sierra Nevada and tropical Andes, respectively). The differences between the two relationships should be considered with caution, as the discrepancy could lie in the nature of the climatological data set: our new calibration for the Sierra Nevada is based on reanalyzed temperature and precipitation, whereas the Andean

calibration was established from discrete meteorological data from weather stations.

These potential intercontinental differences underscore the importance of local calibrations, when they exist, in computing paleoclimatic conditions from paleo-ELAs. However, despite these differences, the tropical Andean and Sierra Nevadan normalized snowline altitude values display quite comparable sensitivities to precipitation changes, the slopes of the relationships (the B parameters) being quite close for the two regions (Fig. 6). Our new calibration thus offers new and complementary constraints on the sensitivity to precipitation and temperature changes of alpine glaciers in an area of the American Cordillera that is wetter than the tropical Andes.

Implications for future paleoclimatic studies

Many paleoclimatic studies consider paleoglaciers to be paleothermometers, hypothesizing an equivalence between ELA and 0°C isotherm (Ramage *et al.*, 2005; Vázquez-Selem and Lachniet, 2017), while other studies limit their interpretation to ELA depression (Martini *et al.*, 2017). However, a glacier's extent is mainly controlled by two parameters: mean annual precipitation and temperature (Ohmura *et al.*, 1992; Fox and Bloom, 1994; Condom *et al.*, 2007). Hence, assuming that equilibrium lines and 0°C isotherms are strictly identical may induce inaccuracies in some situations. In particular, in regions fed by low precipitation (< 200 mm/yr), the difference between the 0°C isotherm and ELA may reach 1000 m (Amman *et al.*, 2001; Carrasco *et al.*, 2005). Such a simplification could lead to bias larger than 5°C in temperature reconstruction. It is thus important to take into account both paleoprecipitation and paleotemperature in interpreting paleoglacial fluctuations.

Our empirical model is based on a relationship that only requires a paleo-ELA and a paleoprecipitation estimate to provide accurate reconstruction of paleotemperature. Compared with simpler approaches that directly consider paleo-ELAs as paleothermometers, this easy-to-use method has the potential to reduce the uncertainty of paleotemperature reconstruction from paleoglacial extents. Previous calibrations of the same model have either shown slight differences (Greene *et al.*, 2002) or similarities (Condom *et al.*, 2007) between midlatitude regions and the tropics, suggesting that paleoclimatic reconstruction from these models should use the closest empirical calibration. Although our relationship is established for the Sierra Nevada, its use for paleoclimatic reconstruction should be encouraged for all midlatitude mountains ranges of North America, notably in American regions that are ice-free today (Owen *et al.*, 2003; Marchetti *et al.*, 2007).

CONCLUSION

Our calibration study established and tested a simple empirical model to link glacial ELAs of the U.S. Sierra Nevada with the main local climatic parameters (annual temperature and precipitation averaged over the previous 30 years). We demonstrated that the elevation difference between mean annual 0°C isotherm and ELA, the normalized snowline, is tightly linked with the mean annual precipitation ($R^2 = 0.94$, P value = 6.3×10^{-5}). We provide here a simple tool to compute temperature from ELA and precipitation or precipitation from ELA and temperature. The uncertainty of temperature computed in this way is about 1°C at 1σ . This relationship will be especially useful for paleoclimatic

studies, notably in regions where paleoglaciers are the unique paleoclimatic proxy.

Our study also compared the calibration relationships obtained from Sierra Nevadas and Andean glaciers (Condom et al., 2007). This comparison shows that different regions may require using specific calibration studies. When possible, using a local calibration has the potential to maximize the accuracy of glacial ELA-based paleoclimatic reconstructions. Further studies should be conducted in other mountain ranges to better document the interregional variability of this relationship between precipitation, temperature, and ELA.

Supplementary Material. The supplementary material for this article can be found at <https://doi.org/10.1017/qua.2022.10>

Acknowledgments. We thank Harry Zekollari for his very insightful comments on an earlier version of this article and Sylvie Cappelle for her expertise in handling several software programs used in this study. Robert Dennen carefully checked and edited the English. This work was funded by the ANR EroMed (PI: P-HB). The authors declare no competing interests.

REFERENCES

- Ammann, C., Jenny, B., Kammer, K., Messerli, B., 2001. Late Quaternary glacier response to humidity changes in the arid Andes of Chile (18–29 S). *Paleogeography, Paleoclimatology, Paleoecology* **172**, 313–326.
- Benn, D.I., Lehmkühl, F., 2000. Mass balance and equilibrium-line altitudes of glaciers in high-mountain environments. *Quaternary International* **65**, 15–29.
- Blard, P.H., Lavé, J., Pik, R., Wagnon, P., Boulès, D., 2007. Persistence of full glacial conditions in the central Pacific until 15,000 years ago. *Nature* **449**, 591.
- Blard, P.H., Wagnon, P., Lavé, J., Soruco, A., Sicart, J.E., Francou, B., 2011. Degree-day melt models for paleoclimate reconstruction from tropical glaciers: calibration from mass balance and meteorological data of the Zongo glacier (Bolivia, 16° S). *Climate of the Past Discussions* **7**, 2119–2158.
- Braithwaite, R.J., 1995. Positive degree-day factors for ablation on the Greenland ice sheet studied by energy-balance modelling. *Journal of Glaciology* **41**, 153–160.
- Carrasco, J.F., Casassa, G., Quintana, J., 2005. Changes of the 0° C isotherm and the equilibrium line altitude in central Chile during the last quarter of the 20th century/Changements de l'isotherme 0° C et de la ligne d'équilibre des neiges dans le Chili central durant le dernier quart du 20ème siècle. *Hydrological Sciences Journal* **50**(6), 948.
- Charlesworth, J.K., 1957. *The Quaternary Era with Special Reference to Its Glaciation*. Vol. 2. Edward Arnold, London, pp. 595–1700.
- Clark, D.H., Clark, M.M., Gillespie, A.R., 1994. Debris-covered glaciers in the Sierra Nevada, California, and their implications for snowline reconstructions. *Quaternary Research* **41**, 139–153.
- Condom, T., Coudrain, A., Sicart, J.E., Théry, S., 2007. Computation of the space and time evolution of equilibrium-line altitudes on Andean glaciers (10 N–55 S). *Global and Planetary Change* **59**(1–4), 189–202.
- Daly, C., Halbleib, M., Smith, J.I., Gibson, W.P., Doggett, M.K., Taylor, G.H., Curtis, J., Pasteris, P.P., 2008. Physiographically sensitive mapping of climatological temperature and precipitation across the conterminous United States. *International Journal of Climatology* **28**, 2031–2064.
- Daly, C., Smith, J.I., Olson, K.V., 2015. Mapping atmospheric moisture climatologies across the conterminous United States. *PLoS ONE* **10**(10), e0141140.
- Fitzpatrick, N., Radić, V., Menounos, B., 2017. Surface energy balance closure and turbulent flux variableization on a mid-latitude mountain glacier, Purcell Mountains, Canada. *Frontiers in Earth Science* **5**, 67.
- Fountain, A.G., Glenn, B., Basagic H.J., IV, 2017. The geography of glaciers and perennial snowfields in the American West. *Arctic, Antarctic, and Alpine Research* **49**, 391–410.
- Fox, A.N., Bloom, A.L., 1994. Snowline altitude and climate in the Peruvian Andes (5–17 S) at present and during the latest Pleistocene glacial maximum. *Journal of Geography (Chigaku Zasshi)* **103**, 867–885.
- Gabbi, J., Carenzo, M., Pellicciotti, F., Bauder, A., Funk, M., 2014. A comparison of empirical and physically based glacier surface melt models for long-term simulations of glacier response. *Journal of Glaciology* **60**(224), 1140–1154.
- Gesch, D., Oimoen, M., Greenlee, S., Nelson, C., Steuck, M., Tyler, D., 2002. The national elevation dataset. *Photogrammetric Engineering and Remote Sensing* **68**, 5–32.
- [GLIMS and NSIDC] Global Land Ice Measurements from Space and National Snow and Ice Data Center, 2005 [updated 2018]. Global Land Ice Measurements from Space Glacier Database. Compiled and made available by the international GLIMS community and the National Snow and Ice Data Center, Boulder CO. <http://dx.doi.org/10.7265/N5V98602>.
- Greene, A.M., Seager, R., Broecker, W.S., 2002. Tropical snowline depression at the Last Glacial Maximum: comparison with proxy records using a single-cell tropical climate model. *Journal of Geophysical Research: Atmospheres* **107**(D8), ACL-4.
- Hock, R., 2003. Temperature index melt modelling in mountain areas. *Journal of Hydrology* **282**(1–4), 104–115.
- Martin, L.C., Blard, P.H., Lavé, J., Condom, T., Prémaillon, M., Jomelli, V., Brunstein, D., et al., 2018. Lake Tauca highstand (Heinrich Stadial 1a) driven by a southward shift of the Bolivian High. *Science Advances* **4**(8), eaar2514.
- Martini, M.A., Kaplan, M.R., Strelin, J.A., Astini, R.A., Schaefer, J.M., Caffee, M.W., Schwartz, R., 2017. Late Pleistocene glacial fluctuations in Cordillera oriental, subtropical Andes. *Quaternary Science Reviews* **171**, 245–259.
- Meier, M.F., 1962. Proposed definitions for glacier mass budget terms. *Journal of Glaciology* **4**(33), 252–263.
- Miller, G.H., Bradley, R.S., Andrews, J.T., 1975. The glaciation level and lowest equilibrium line altitude in the high Canadian Arctic: maps and climatic interpretation. *Arctic and Alpine Research* **7**, 155–168.
- Moore, J.G., Moring, B.C., 2013. Rangewide glaciation in the Sierra Nevada, California. *Geosphere* **9**, 1804–1818.
- Oerlemans, J., 2005. Extracting a climate signal from 169 glacier records. *Science* **308**, 675–677.
- Oerlemans, J., 2012. Linear modelling of glacier length fluctuations. *Geografiska Annaler: Series A, Physical Geography* **94**, 183–194.
- Ohmura, A., Kasser, P., Funk, M., 1992. Climate at the equilibrium line of glaciers. *Journal of Glaciology* **38**(130), 397–411.
- Pandey, G.R., Cayan, D.R., Georgakakos, K.P., 1999. Precipitation structure in the Sierra Nevada of California during winter. *Journal of Geophysical Research: Atmospheres* **104**(D10), 12019–12030.
- Plummer, M.A., Phillips, F.M., 2003. A 2-D numerical model of snow/ice energy balance and ice flow for paleoclimatic interpretation of glacial geomorphic features. *Quaternary Science Reviews* **22**, 1389–1406.
- Porter, S.C., 1975. Equilibrium-line altitudes of late Quaternary glaciers in the Southern Alps, New Zealand. *Quaternary Research* **5**, 27–47.
- Ramage, J.M., Smith, J.A., Rodbell, D.T., Seltzer, G.O., 2005. Comparing reconstructed Pleistocene equilibrium-line altitudes in the tropical Andes of central Peru. *Journal of Quaternary Science* **20**, 777–788.
- Raub, W., Brown, C.S., Post, A., 2006. *Inventory of Glaciers in the Sierra Nevada, California*. U.S. Geological Survey Open File Report 2006-1239. U.S. Geological Survey, Woods Hole, MA.
- Roy, A.J., Lachniet, M.S., 2010. Late quaternary glaciation and equilibrium-line altitudes of the Mayan ice cap, Guatemala, Central America. *Quaternary Research* **74**, 1–7.
- Rupper, S., Roe, G., Gillespie, A., 2009. Spatial patterns of Holocene glacier advance and retreat in Central Asia. *Quaternary Research* **72**, 337–346.
- Sharma, A., Gupta, D., 2014. Derivation of topographic map from elevation data available in Google Earth. *Civil Engineering and Urban Planning* **1**(2), 14–21.
- Sicart, J.E., Wagnon, P., Ribstein, P., 2005. Atmospheric controls of the heat balance of Zongo Glacier (16 S, Bolivia). *Journal of Geophysical Research: Atmospheres* **110**(D12).

- Stansell, N.D., Polissar, P.J., Abbott, M.B.**, 2007. Last glacial maximum equilibrium-line altitude and paleo-temperature reconstructions for the Cordillera de Mérida, Venezuelan Andes. *Quaternary Research* **67**, 115–127.
- Vázquez-Selem, L., Lachniet, M.S.** 2017. The deglaciation of the mountains of Mexico and Central America. *Cuadernos de Investigación Geográfica* **43**, 553–570.
- Vermeesch, P.**, 2018. IsoplotR: a free and open toolbox for geochronology. *Geoscience Frontiers* **9**, 1479–1493.
- Zech, J., Terrizzano, C.M., Garcia Morabito, E., Veit, H., Zech, R.**, 2017. Timing and extent of late Pleistocene glaciation in the arid Central Andes of Argentina and Chile (22–41 S). *Cuadernos de Investigación Geográfica* **43**, 697–718
- Zekollari, H., Huybrechts, P.**, 2015. On the climate–geometry imbalance, response time and volume–area scaling of an alpine glacier: insights from a 3-D flow model applied to Vadret da Morteratsch, Switzerland. *Annals of Glaciology* **56**(70), 51–62.

Appendix C : First-author publication: Legrain, E., Blard, P. H., Kageyama, M., Charreau, J., Leduc, G., Bourdin, S., & Bekaert, D. V. (2023). Moisture amplification of the high-altitude deglacial warming. *Quaternary Science Reviews*, *318*, 108303.



Contents lists available at ScienceDirect

Quaternary Science Reviews

journal homepage: www.elsevier.com/locate/quascirev

Moisture amplification of the high-altitude deglacial warming

Etienne Legrain^{a,*}, Pierre-Henri Blard^{b,c,**}, Masa Kageyama^d, Julien Charreau^b, Guillaume Leduc^e, Stella Bourdin^d, David V. Bekaert^b^a Université Grenoble Alpes, CNRS, IRD, Grenoble INP, IGE, 38000, Grenoble, France^b CRPG, CNRS, Université de Lorraine, 54000, Nancy, France^c Laboratoire de Glaciologie, DGES-IGEOS, Université Libre de Bruxelles, 1050, Brussels, Belgium^d LSCE/IPSL, UMR CEA-CNRS-UVSQ 8212, Université de Paris-Saclay, 91190, Gif-sur-Yvette, France^e Aix-Marseille Université, CNRS, IRD, INRAE, Coll. France, CEREGE, 13545, Aix-en-Provence, France

ARTICLE INFO

Handling editor: Mira Matthews

ABSTRACT

In response to anthropogenic warming, glaciers are shrinking almost everywhere, endangering water accessibility in areas located downstream. Glacier fluctuations are at first order controlled by local precipitation and temperature, but large uncertainties persist on the potential role of local moisture in amplifying or dampening temperature changes at high-elevation. Here, we combine glacier extents and Sea Surface Temperature (SST) during the Last Glacial Maximum (LGM) to quantify altitudinal thermal gradients (lapse rate) from 40°N to 40°S along the American Cordillera. We also constrain modern lapse rates based on present day temperature and SST database to explore how the lapse rate has changed since the LGM along this North South transect. Based on proxy-based quantitative paleo-precipitation estimations above 2000 m, we investigate how these lapse rate changes compare with moisture modifications around the Cordillera and discuss the mechanisms that potentially controlled lapse rate changes during the post-LGM deglacial warming.

We find that lapse rate changes are linearly related to changes in precipitation and derive a quantitative relationship between these two parameters. To further explore the processes involved in controlling lapse rate variations, we use the IPSL global climate model outputs, for the LGM and pre-industrial states in this region. The IPSL model also yields a shallower modern lapse rate in the wetter tropical region, confirming the observed correlation between precipitation changes and lapse rate variations. The IPSL model also supports a close coupling of continental relative moisture and mean annual precipitation in the studied area, indicating that moisture is involved in the precipitation – lapse rate relationship. Our results suggest that future warming may be enhanced in high altitude regions where precipitation is expected to increase. Using our most reliable relationship linking precipitation and lapse rate changes, we conclude that, assuming a 1 °C warming at sea level, a mean annual precipitation increases of 500 mm.a⁻¹ could lead to a warming amplification of 4.1 ± 0.8 °C at 4000 m asl (mean elevation of modern glaciers). In this case, a 2 °C warming at sea level would yield >6 °C degrees warming at 4000 m asl. This study therefore confirms that special attention should be given to the climate projections of glacier melting in tropical and mid latitude regions.

1. Introduction

Global warming massively disrupts the cryosphere at low and mid-latitude, as alpine glaciers shrinking is now accelerating worldwide (Hugonnet et al., 2021; Thompson et al., 2011). Over the last two decades, melting of mountain glaciers (excluding ice cap) has contributed to 21 ± 3% of the global sea level rise, i.e. more than Greenland and

Antarctica considered separately (Hugonnet et al., 2021; Slater et al., 2020). In mountainous regions where precipitation is highly seasonal, alpine glaciers represent the main water supply during the dry season (Kaser et al., 2010; Pritchard, 2019; Rabatel et al., 2013). It is therefore crucial to identify factors that modulate glacier melting in order to better understand and anticipate their stability, for the decades to come (Kraaijenbrink et al., 2017; Zekollari et al., 2019).

* Corresponding author.

** Corresponding author. CRPG, CNRS, Université de Lorraine, 54000, Nancy, France.

E-mail addresses: legrain.etienne@hotmail.fr (E. Legrain), pierre-henri.blard@cnrs.fr (P.-H. Blard).<https://doi.org/10.1016/j.quascirev.2023.108303>

Received 12 May 2023; Received in revised form 1 September 2023; Accepted 2 September 2023

0277-3791/© 2023 Elsevier Ltd. All rights reserved.

The annual mass balance of a glacier is primarily controlled by mean local temperature and precipitation (Condom et al., 2007; Ohmura, 1992). Globally, the temperature increase associated with anthropogenic fossil fuel combustion recently surpassed +1 °C, at an average warming rate of +0.18 °C/decade (Intergovernmental Panel on Climate Change (IPCC), 2022). This warming rate is not spatially homogenous: it is notably amplified over the continent, reaching on average 1.4 °C in the 40°S-40°N zone at low elevation (Seltzer et al., 2023a). At high elevation, in mountainous areas, anthropogenic warming has reached up to +0.7 °C/decade (Intergovernmental Panel on Climate Change (IPCC), 2022). However, high elevation warming rates are very variable from one region to another, ranging between +0.1 and +0.7 °C/decade above 2000 m (Pepin et al., 2015). Many potential causes for high-altitude temperature amplification have been proposed, including surface albedo feedbacks, latent heat release, moisture-enhanced radiative changes, and aerosol feedbacks (Pepin et al., 2015). These

mechanisms may at least partly explain the contrasting regional patterns of high-altitude warming, but the relative contributions of each of these forcing remain unknown.

Several studies have hypothesized that warming at high altitude should be greater than observed at sea level because warmer conditions at the regional scale will increase the atmospheric moisture content and yield a shallower lapse rate. The modern global annual average free atmospheric lapse rate (LR) is $-6.5 \text{ }^\circ\text{C.km}^{-1}$, but it locally varies between the moist adiabatic value around $-4-6 \text{ }^\circ\text{C.km}^{-1}$ and the dry adiabatic value of $-9.8 \text{ }^\circ\text{C.km}^{-1}$ (Stone et al., 1979). The temporal and spatial LR variations remains poorly known. Accurate and precise reconstructions of paleo LR under different global and regional paleo-climate conditions are useful to quantify and understand how the atmospheric moisture content may affect LR variations at the regional scale (Blard et al., 2007; Loomis et al., 2017; Tripathi et al., 2014).

Recent compilations of oceanic and continental paleothermometers

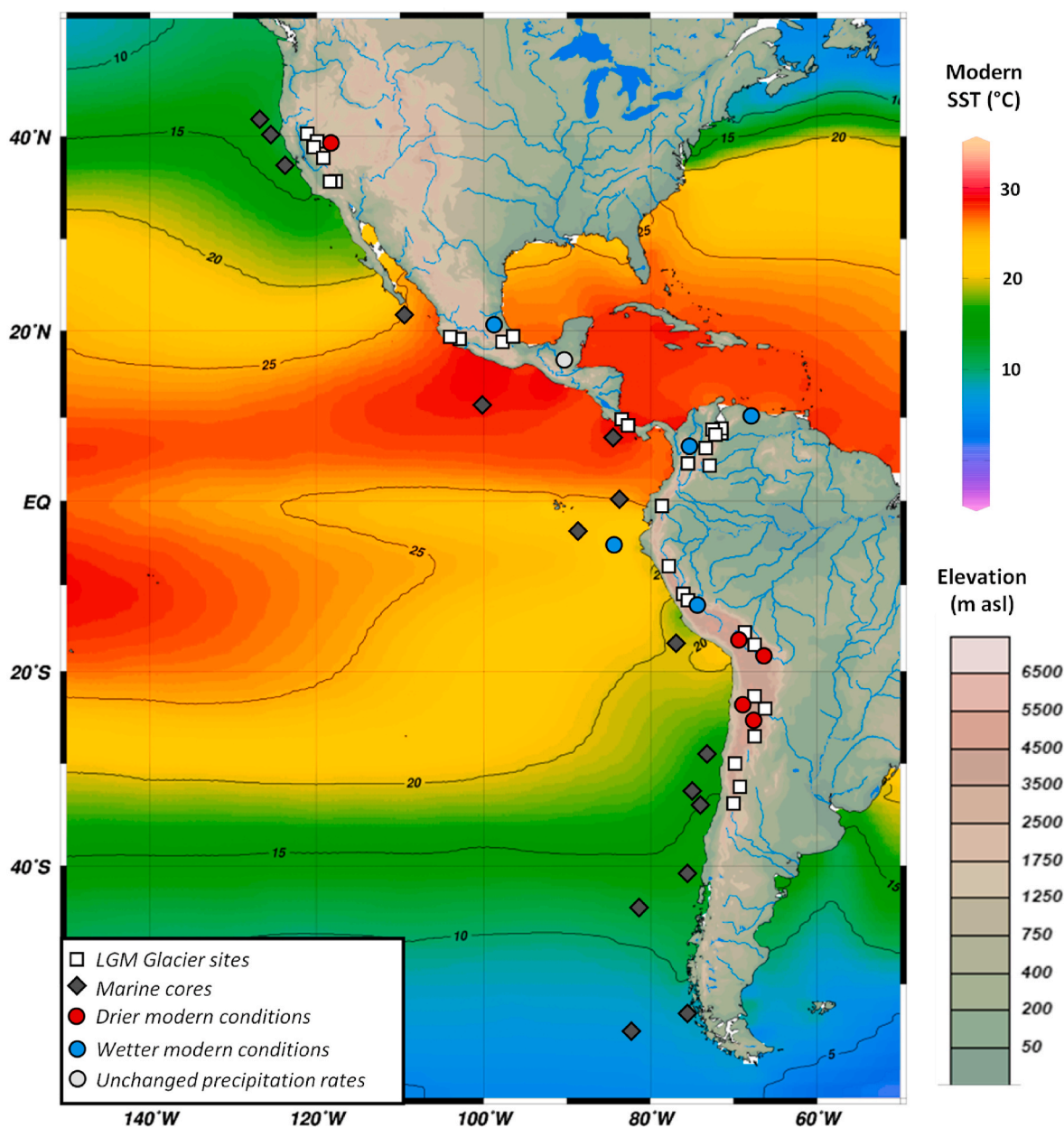


Fig. 1. Location of the studied sites. Grey diamonds identify marine core locations used for the SST calibration (Fig.4). White squares are the 31 Δ LR computation sites. Dots are sites with LGM paleoprecipitation estimates. Blue, red and grey dots respectively indicate sites where the modern period is wetter, drier, and unchanged than LGM.

proposed that the global post-Last Glacial Maximum (LGM) warming was between 4 and 6 °C, with large regional disparities (Annan et al., 2022; Seltzer et al., 2021; Tierney et al., 2020). Even if the exact amplitude of the post LGM warming could still be refined in future studies, the LGM climate is an ideal benchmark for studying the sensitivity of global temperatures to the net radiative forcing, and the specific responses of certain regions, partly driven by the polar amplification (Smith et al., 2019), the terrestrial amplification (Seltzer et al., 2023a,b) or by the altitudinal dependent warming (Pepin et al., 2015). LGM temperature reconstructions at high elevations have yielded contrasting results: some tropical and mid latitude regions display an amplified post-LGM warming at high elevation (steeper LR during the LGM) (Blard et al., 2007; Kuhlemann et al., 2008; Loomis et al., 2017), while others suggest no dependence of the post-LGM warming on elevation (i.e., no LR change since the LGM) (Tripathi et al., 2014). These studies provide local reconstructions in different regions of the globe, with contrasting hydrological regimes. Thus, they may not be globally representative, hampering our ability to anticipate potentially upcoming LR changes under future climatic conditions.

In this study, we aim to fill this gap by investigating the main physical parameters and mechanisms controlling LR changes. For that, we compare precipitation and LR data between the LGM and present. We focus our study on the American Cordillera, along a near-continuous, 8000 km-long latitudinal transect ranging from 40°N to 40°S. From Alaska to Patagonia, the American Cordillera is the sole mountain range that continuously covers both Hemispheres over a large latitudinal range (70°N – 50°S, Fig. 1), with a mean altitude of 4000 m and summits above 6000 m asl. The American Cordillera thus provides a unique collection of glaciers, encompassing both the tropics and mid-latitude regions. The Cordillera also have sub-regions with very contrasting precipitation regimes, which is ideal to test the potential impact of moisture variations on LR changes. It is also located near the Eastern Pacific Ocean, where records of SSTs permit constraining low altitude LGM temperatures. Local continental precipitation proxies (e.g., lake levels, speleothems, and pollen records) are also available in the vicinity of LGM paleoglaciers. Here, based on glacier paleo-extents, we reconstruct LGM equilibrium lines of the American cordillera glaciers and convert them into 0 °C isotherm altitudes using independent estimates of paleoprecipitation, following the approach of Condom et al. (2007) and Legrain et al. (2022). We then combine these paleo-isotherm estimates with alkenone-based paleo SST data to compute LGM LR estimates along the latitudinal transect. These LR estimates are then compared with present-day LR values (computed with a comparable methodology) to identify where and how LR have changed during the last deglaciation. The mechanisms causing the observed spatial and temporal LR variability are then investigated using the IPSL global climate model outputs, for LGM and pre-industrial states.

2. Materials and methods

To reconstruct LR variations between the LGM and today, our approach includes four main steps (summarized in the synoptic flow diagram presented in Supplementary Fig. 1), which involve both already published and newly computed data:

1. Identifying sites with LGM glacial extents, well-dated by cosmogenic ^{10}Be , ^{36}Cl or radiocarbon (section 2.1.). The locations of the paleoclimatic data used in this study are presented in Supplementary Figs. 3-4.
2. Compiling/determining modern (section 2.2.) and LGM (section 2.3.) SST, 0 °C isotherm and precipitation for each site. For the LGM, this step notably requires reconstructing LGM ELAs using the Accumulation-Area Ratio (AAR) method and converting these into LGM 0 °C isotherms using empirical relationship linking ELA, temperature, and paleoprecipitation data (Fox and Bloom, 1994; Legrain et al., 2022).

3. Converting SST data into equivalent continental sea-level temperatures at the sites where glacial landforms are studied using an empirical transfer function (section 2.4.).
4. Computing modern and LGM lapse rates (with LGM LR defined as the slope between SST – taken at –125 m below present-day sea level – and the glacier-derived isotherm 0 °C elevation) to derive ΔLR values by subtracting the LGM LR from the modern LR (section 2.5.).

We then proceed to a model-data comparison (section 2.6.) using outputs of the IPSLCM5A2 model (Sepulchre et al., 2020) to investigate the underlying mechanism(s) controlling LR temporal and spatial variations.

2.1. Studied LGM glacial landforms and their ages constraints

This study is based on the compilation of well-dated LGM landform extents dated by *in situ* cosmogenic nuclides (27/31 sites) and radiocarbon (4/31 sites) (Supplementary Tables 1 and 2). The inclusion criteria for these LGM glacial extents is to consider that every glacial morphology dated between 26-18 ka belongs to the LGM. This 26-18 ka range represents the broad duration of the global LGM (Clark et al., 2009). Considering this whole time window has the advantage to account for the inter-site age variability produced by the slight diachronism of the so-called “local” LGMs identified along the American Cordillera (Palacios et al., 2020).

^{10}Be cosmogenic data used here comprise all the published LGM ages stored within the online ICE-D database <http://alpine.ice-d.org/>. All these ^{10}Be exposure ages are updated and homogenized using the KNSTD07 standardization (Nishiizumi et al., 2007), and are recomputed with the online calculator Cosmic Ray Exposure Program (CREP) <https://crep.otelo.univ-lorraine.fr/#/> (Martin et al., 2017) using the regional production rate of the Andes (Martin et al., 2015), as well as the world wide mean value, for comparison (Supplementary Table 2) (Martin et al., 2017). We also compute these ^{10}Be ages using two different scaling schemes: *Lal stone time corrected* (Lal, 1991) and *Lifton-Sato-Dunai* (Lifton et al., 2014) (Supplementary Table 2). In all cases, we use the ERA40 atmosphere model and the atmospheric ^{10}Be based Virtual Dipolar Moment (VDM) (Muscheler et al., 2005) to account for time variations of the production rate. Our comparison shows that the choice of the scaling and production rates does not affect the final ages beyond uncertainties (Supplementary Table 2). We retain the ages computed with the *Lal stone time variable* scaling with the regional Andes production rate (Martin et al., 2015). In the few cases where no regional production rate is available (southern Andes), we use the ^{10}Be ages computed with the worldwide mean production rate (Supplementary Table 2). ^{36}Cl ages of landforms ($n = 7$) are considered without any additional processing (Supplementary Table 1) as there is no consensus on ^{36}Cl elemental production rates (Marrero et al., 2016; Schimmelpfennig et al., 2009).

When no direct cosmogenic surface exposure age of a given glacial morphology is available (as is the case for 4 sites in Ecuador and Colombia; Supplementary Table 1), the age of the LGM glacial extent is determined by ^{14}C dating on paleosoils bracketing the glacier moraines.

2.2. Modern temperatures and precipitation at the studied sites

2.2.1. Modern Sea Surface Temperatures

We use the modern SST data from the Extended Reconstructed Sea Surface Temperature version 4 (ERSST_V4) (Huang et al., 2015; Smith and Reynolds, 2003), available at <https://www.esrl.noaa.gov/psd/>. This database is based on SST values extended from the Comprehensive Ocean–Atmosphere Data Set (COADS) database. Modern SSTs correspond to the mean annual value from the climatic period 1989–2018 (Supplementary Table 3). Data are compiled for each 0.5 latitudinal degree from 40°N to 40°S along the American Pacific coast and the Venezuelan and Colombian Caribbean coasts. We use the Pacific Ocean

SSTs, except for the Santa Maria Colombian site and the Venezuelan sites, that are closest to the Caribbean Sea (Supplementary Table 3). At these two locations, we compute a mean SST between the Pacific and the Caribbean zone. It is noteworthy that SST values from the Pacific Ocean and the Caribbean Sea are similar ($\Delta\text{SST} \leq 1^\circ\text{C}$) at these latitudes ($12\text{--}9^\circ\text{N}$). Thus, the potential bias induced by combining the Pacific Ocean and Caribbean Sea data is not considered as a significant source of uncertainty in our study.

2.2.2. Modern 0°C isotherms

Modern 0°C isotherms are directly compiled from literature data (Supplementary Table 5), except for the Sierra Nevada and San Bernardino sites, for which no previous estimate of the 0°C isotherm is available. For the sites from Sierra Nevada and San Bernardino, we estimate the 0°C isotherm using normal PRISM reanalysis data (1980–2011). We extract data for 118 sites of high-altitude glaciers and perform a regression of elevation as a function of mean annual temperature (Supplementary Fig. 6), yielding an averaged value of 0°C isotherm of $3578 \pm 11\text{ m}$ (standard deviation) for Sierra Nevada. At the scale of the whole American Cordillera, computed and compiled modern 0°C isotherms range from 3452 to 5100 m with an average of $4530 \pm 587\text{ m}$ (1σ standard deviation). We estimate an approximate uncertainty of 50 m for modern 0°C isotherms directly compiled from literature.

2.2.3. Modern precipitation

The values of modern precipitation at the LGM precipitation sites are from the PRISM product, that is compiled from high-resolution radar measurements (Western Regional Climate Center, <https://wrcc.dri.edu/>), from global modelling of precipitation (Climate Change Knowledge Portal, <https://climateknowledgeportal.worldbank.org/>), and from climatic station measurements (Supplementary Table 6).

2.3. LGM temperatures and precipitation at the studied sites

2.3.1. LGM Sea Surface Temperatures

To reconstruct SSTs during LGM, we use alkenone data from 16 marine cores located along the American cordillera at a restricted distance (<1000 km) from the coastline (Fig. 1; Supplementary Fig. 2). We use a single SST proxy approach to avoid potential biases due to inter-proxy disparities (Bova et al., 2021; Leduc et al., 2010, 2017). Moreover, alkenone is the only SST proxy available from marine cores along the whole American Cordillera (Fig. 1) and comparison of SST proxies suggest that alkenones provide accurate SST estimates in the tropics (Lea

et al., 2014). The LGM alkenone-derived SSTs are averaged from 26 to 18 ka (Supplementary Table 8). To estimate LGM SSTs corresponding to the sites studied for glacial landforms, we first consider a simple linear extrapolation between the reconstructed SSTs for the two nearest LGM SST cores.

This simple approach may suffer biases due to the heterogeneous spatial distribution of marine cores. To circumvent this issue and smooth local discrepancies, we consider time variations of the SST and how they may relate to latitude. Because the Holocene variability of temperature is low, we assume in this calculation that the modern SSTs are equivalent to Holocene average SSTs derived from alkenone data. For the Holocene, we average the alkenone-derived SST for the time period 11.7 to 0 ka. We consider the Holocene as a whole because global temperature changes during this period were marginal (1σ standard deviation $< 1^\circ\text{C}$) and the averages should therefore represent robust and representative SST values. Then we consider the LGM SST as the mean of the 26–18 ka period. The ΔSST (Holocene–LGM) are then calculated as the difference between the mean Holocene SST and the mean LGM SST (Supplementary Table 8).

As expected, the minimal ΔSST values are found around the equator and increase exponentially towards higher latitudes, suggesting that alkenone data provide LGM SST estimates that are precise enough to capture the polar temperature amplification (Fig. 2). At $\sim 34^\circ\text{N}$, we observe a cluster of LGM SST anomalies that are much lower than surrounding estimates from other marine sites. These LGM SST anomalies of $\sim -1^\circ\text{C}$ compared to modern SST are caused by an early warming in the area, more than 10 ka before the end of the LGM (Herbert et al., 2001). This early SST warming was likely caused by the collapse of the California Current during glacial maximum, in response to a local climate change occurring on land (Herbert et al., 2001). Using the local LGM SST defined for $\sim 25\text{ ka}$ from these 3 cores would yield LGM anomalies of about -4°C , a value in good agreement with other SST estimates at those latitudes (Herbert et al., 2001, Fig. 2). As this LGM SST anomaly is very localized and is not representative of the large-scale latitudinal trend, we remove these three sites from our LGM SST database (labelled in red in Fig. 2). As the ΔSST are driven at first order by latitude, we can use it to compute the LGM SST at each latitude location from the modern SST. From these data, we then define a relationship between ΔSST and the latitude (Fig. 2):

$$\Delta\text{SST}(\text{latitude}) = A \times \exp(|\text{Latitude}| \times B) \quad (\text{S1})$$

where Latitude is expressed in decimal degrees (DD) and A and B are empirical parameters specific to the eastern Pacific SST latitudinal

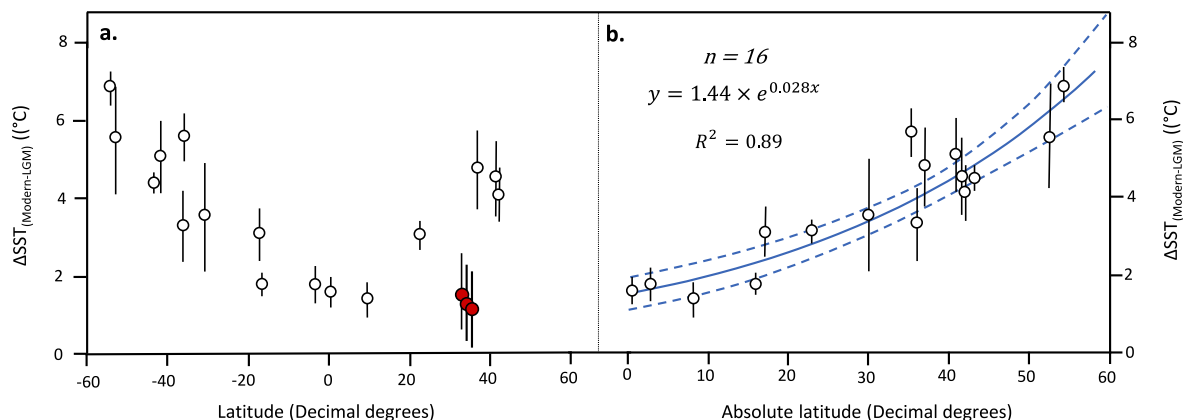


Fig. 2. Calibration of the $\Delta\text{SST}_{(\text{Modern-LGM})}$. **a.** White and red dots are SST estimates from marine cores included in, and excluded from, the calibration, respectively (see Methods). All SST estimates are based on alkenone reconstructions. The U-shaped relationship between the $\Delta\text{SST}_{(\text{Modern-LGM})}$ and latitude highlights the polar amplification. **b.** $\Delta\text{SST}_{(\text{Modern-LGM})}$ is plotted as a function of absolute latitude used to estimate the $\Delta\text{SST}_{(\text{Modern-LGM})}$ at each latitude (blue line). Dashed lines represent the 1σ envelope ($R^2 = 0.89$; MSWD = 1.3; p value = 2×10^{-12}).

gradient (Fig. 2). LGM SST at any given latitude, especially at studied sites for glacier paleoextent, can be calculated by subtracting the latitude-specific Δ SST from the modern SST at the same latitude.

2.3.2. LGM 0 °C isotherms

ELA, 0 °C isotherm and mean annual precipitation are linked with robust empirical relationships (Condom et al., 2007; Fox and Bloom, 1994; Legrain et al., 2022). Knowing this relationship and LGM precipitation (see section 3.3.3 below, Supplementary Tables 5 and 6) allows using LGM ELAs and LGM precipitation to compute LGM 0 °C isotherm elevations. To estimate paleo ELAs from paleo glacial extents we use the Accumulation Ablation Ratio (AAR) (Meier and Post, 1962) method, that is a robust and easy-to-use technique (Benn and Lehmkuhl, 2000). The AAR defines the ELA as the elevation at which the ratio between (i) the glacier area above this ELA and (ii) the total surface of the glacier, equals the AAR (Meier and Post, 1962) (i.e., the ratio of the accumulation area to the area of glacier). Thus, the LGM ELA can be computed if both the total surface of the LGM glacier and the AAR parameter are known.

The LGM glacial extent and total surface of each studied glacier are determined by glacial morphology analysis and identification of lateral and frontal moraines mapped using high-resolution Landsat imagery (Supplementary Fig. 7). Then, we assume that the AAR remained constant through time and estimate paleo-ELA based on the modern AAR. Since AAR may vary spatially, we use the most accurate AAR estimates available (from the World Glacier Monitoring Service (WGMS) mass balance measurements) to calibrate regional AAR values (Supplementary Fig. 8). Following Martin et al. (2020), we compile interannual AAR and annual mass balances to estimate the AAR value (Supplementary Fig. 8) of each glacier, at equilibrium with the climate state. Data from modern glaciers available in WGMS permitted to calibrate AARs in the following five regions: the Sierra Nevada ($n = 1$ glacier), Mexico ($n = 1$), the Central Andes ($n = 1$), the Bolivian and the Peruvian Andes ($n = 2$) (Supplementary Table 7). In the case of Venezuela and Central America, for which modern data are absent from the WGMS database, we use AAR regional values directly compiled from the literature (Stansell et al. (2007) (Venezuela) and Lachniet and Vazquez-Selem (2005) (Central America) (Supplementary Table 7).

Local LGM ELAs for each glacial valley are given in Supplementary Table 7. The final uncertainties associated with these ELAs are computed using the quadratic sum of the standard deviation associated with each regional AAR coefficient (ranging from 0.03 to 0.06) and a spatial uncertainty of 50 m to account for the lack of precision of paleo glacier mapping.

For South and Central America (20°N – 36°S), we use the relationship calibrated by Fox and Bloom (1994) to calculate the elevation of the LGM 0 °C isotherm, Iso_{LGM} (m asl), as:

$$Iso_{LGM} = ELA_{LGM} - 3427 + (1148 \times \log_{10} P_{LGM}) \quad (S2)$$

where P_{LGM} is the mean annual precipitation ($\text{mm}\cdot\text{a}^{-1}$) and ELA_{LGM} is the Equilibrium Line Altitude (m asl), both during the LGM. This equation is established for the latitudinal range of 5–17°S but was proven to yield robust and accurate results between 10°N and 50°S (Condom et al., 2007). In Central America (20°N – 10°N), climatic conditions are fairly similar to the calibration area (Tropical Andes), implying that this equation is likely to also provide robust results for this region.

For the Sierra Nevada and San Bernardino Mountains (40°N – 34°N), we use the relationship established by Legrain et al. (2022) who used data from Northern America glaciers to define a regional version of the Fox and Bloom (1994) equation:

$$Iso_{LGM} = ELA_{LGM} - 5150 + (1640 \times \log_{10} P_{LGM}) \quad (S3)$$

Total uncertainties on LGM 0 °C isotherms are computed by propagating uncertainties on LGM precipitation, LGM ELA, as well as the

calibration relationship.

2.3.3. LGM precipitation

A few LGM precipitation databases exist (Bartlein et al., 2011; Cleator et al., 2019) and were used in climate-model comparison exercises (e.g. Kageyama et al., 2021). Unfortunately, only very few quantitative LGM precipitation estimates are included in these databases for western America. A few isotopic records based on speleothems (Lachniet et al., 2013) and leaf wax (Bhattacharya et al., 2018) are available, but as the isotopic composition of rainfall records mixed source signals, precipitation temperatures, and extents of Rayleigh-type distillation, comparing isotopic results from the LGM and Holocene is not straightforward. In particular, the deglacial warming and continental ice sheet melting invariably obscure precipitation signals and eventually compromise quantitative precipitation rate estimates. For this reason, we ignore rainfall estimates based on stable isotopes. Instead, we derive LGM precipitation from other proxies (pollen assemblage, paleolake shoreline, packrat midden) (Supplementary Table 6) that provide relative precipitation change between the LGM and modern conditions. In practice, we compute LGM precipitation by correcting modern precipitation from these changes derived from these proxies (Supplementary Table 6, Fig. 3). When uncertainties are not provided in the original publication, we arbitrarily attribute a relative uncertainty of 20% for LGM precipitation estimates.

2.4. Continental effect: translation of SST into continental-equivalent temperature

We restrict our compilation to the American Cordillera in order to minimize the potential bias introduced by the effect of continentality between SST and 2 m air temperatures above continents. Despite the relative proximity (≤ 500 km) between the glaciated sites in the American Cordillera and the Pacific Ocean (or the Caribbean Sea), a correction must be applied to convert modern and LGM coastal SST into equivalent continental sea-level temperatures. This correction accounts for the fact that continents have a different radiative budget and climatic inertia compared to the ocean (Seltzer et al., 2023a,b).

In order to compute this continental-ocean correction for the present day, we compile weather station data at variable altitudes along the American cordillera, and defined 9 regions (Supplementary Fig. 5-6) whereby the LR appears to be distinct from those of the adjacent areas (spatial LR variability > 1 °C.km⁻¹). Each region is also characterized by a specific climate. For instance, the distinction between San Bernardino Mountains and Sierra Nevada corresponds to an abrupt change in precipitation rates (Pandey et al., 1999) associated with an orographic depression (< 1000 m asl) between these two regions. For Mexico, we separate an Eastern and a Western Transmexican region, since available climatic data show strong differences in the atmosphere thermal structures of these two regions (spatial LR variability ≥ 1.5 °C.km⁻¹). These differences are probably due to the influences of Caribbean Sea and Pacific Ocean on the corresponding coastal sites. In this case, the boundary between the two regions at a given latitude is defined as the equidistant point between the two coasts. The Central America region conforms to the specific climate of Central America, with a geographical setting characterized by high moisture transport across the Central America isthmus (Leduc et al., 2007). Equatorial Andes are divided into two distinct regions: the Northern and the Southern Equatorial Andes, representing the Colombian Venezuelan Andes (Caribbean Sea influence and discontinuous Andes) and the Peruvian Bolivian Andes (Pacific coast and high-altitude plateau), respectively. The Northern Central Andes correspond to the climatic region of the Chilean Dry Andes, characterized by a near absence of glaciers due to extremely dry conditions (Ammann et al., 2001). The Southern Central Andes correspond to the glaciated region South of the North Central Andes.

For each region, we compile mean annual temperature data from weather stations (wrrc.dri.edu; explorador.cr2.cl; <http://berkeleyearth.org>).

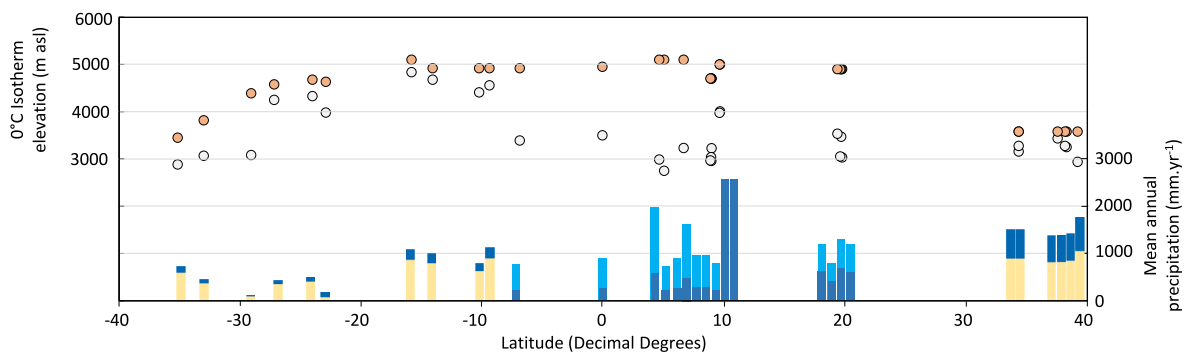


Fig. 3. Modern and LGM 0 °C Isotherm elevation and associated precipitation changes. Red and grey circles are modern and LGM 0 °C isotherm values, respectively. Dark blue sticks are LGM precipitation at the Isotherm 0 °C computation sites. Light blue and yellow sticks are modern precipitation when they are higher and lower than during LGM, respectively.

lbl.gov). Combining the elevation and temperature of these station, we obtain the temperature of the theoretical 0 m asl altitude within the mountain range, for each of the 9 sub-climatic regions (Supplementary Fig. 9). This theoretical temperature is referred to as the CNET (Continental Null Elevation Temperature). Then, we compare this value with the modern SST of the East Pacific at the same latitude and expressed the Correction Factor of Continental Effect (CFCE) as:

$$CFCE(i) = CNET(i) - SST(i) \quad (S4)$$

where (i) corresponds to the index of a given climatic region. The mean CFCE value is $+4.3 \pm 5.2$ °C, ranging from $+14.8$ °C (Bolivian and Peruvian Andes) down to -2.3 °C (Central America) (Supplementary Table 4). Then, we compute the modern SST_{corr} for each of the 31 studied sites:

$$SST_{corr}(\text{modern})(i) = SST_{\text{Modern}} - CFCE(i) \quad (S5)$$

where CFCE is given in °C and varies for each calibrated region. Modern SSTs data corrected for the continental effect using the regional computed CFCE value are reported in Supplementary Table 3.

To compute the continental-ocean correction for the LGM, we use the same approach as for modern data but we apply an additional correction to account for continental amplification. Recently, it has been shown that during a major climatic change, the temperature change over the continent is about 37% larger than that of the ocean (Seltzer et al., 2023a). To compute the SST during the LGM period we thus account for the terrestrial amplification of the post-deglacial warming. Hence, the SST_{corr} (LGM) is:

$$SST_{corr}(\text{LGM}) = SST_{\text{Modern}} + CFCE - 1.37 \times (\Delta SST) \quad (S6)$$

with ΔSST_{LGM} defined by equation (S1).

SST_{corr} (LGM) values are reported in Supplementary Table 3.

2.5. Lapses rate and ΔLR computations

We compute both modern and LGM LR using a linear interpolation between a high-altitude temperature (glacier data) and a zero-altitude temperature (continental temperature reconstruction derived from coastal SSTs), following:

$$LR(t) = \frac{-SST_{corr}(t)}{Iso0(t) - Z(SST_{corr}(t))} \quad (S7)$$

Where (t) refers to either the LGM or modern time, $Iso0(t)$ is the 0 °C isotherm elevation in m asl. at the considered time t, $SST_{corr}(t)$ and $Z(SST_{corr}(t))$ are the SST corrected from the CFCE (°C) and the altitude of the $SST_{corr}(t)$ at the considered time t. In practice, we use $Z(SST)$ values of 0 and -125 m for the modern and LGM sea level (Dutton et al., 2015; Fleming et al., 1998), respectively. The last step of our procedure is to

compute the difference between the two LR in order to get the ΔLR (in °C.km⁻¹) for the 31 glacial sites along the American cordillera (Supplementary Table 9).

2.6. IPSLCM5A2 climate model

The model results used in this study are based on the IPSLCM5A2 model (Sepulchre et al., 2020). The pre-industrial simulation is described in the same reference. The LGM simulations follows the PMIP4 protocol (Kageyama et al., 2017) and is further described in the first overview of PMIP4 LGM simulations (Kageyama et al., 2021). The main changes in boundary conditions to obtain this LGM simulation are those due to the LGM ice sheets: the altitude, land ice extent and coastlines are set up following the PMIP3 ice sheet reconstruction (Abe-Ouchi et al., 2015). Greenhouse gases and insolation parameters are set up to their LGM values (Kageyama et al., 2017). The Pre-industrial simulation has been run for 2800 years up to equilibrium (Sepulchre et al., 2020). The LGM simulation has been run for 1200 years, starting from pre-industrial conditions. The final 100 years of the pre-industrial and LGM experiments are used to define the averages used in the present work. We examine the 3D (longitude, latitude, altitude) annual mean temperatures and relative humidity simulated by the model for both periods, over the Americas and adjacent oceans, as well as the annual mean precipitation.

We compute the free atmospheric lapse rate for each grid point as the slope of the regression of the vertically dependent temperature vs altitude of the grid point, computed by using the mean geopotential height. Grid points with altitude below 6000m are retained.

3. Results

3.1. Low altitude vs high altitude temperature changes

Fig. 4a displays the post-LGM warming on the continent at low elevation and at high elevation (computed from the 0° isotherm shift), respectively, from -40° to 40° latitude. This shows that low elevation T changes are comparable or slightly higher than those at high elevation, from 40°S to 10°S of latitude and beyond 35°N of latitude, with warming ranging from 1 to 6 °C. A contrasting pattern is visible in the inner tropics, between, 8°S to 20°N, where high elevation post LGM warming are significantly larger (8–14 °C) than those observed at low elevation (1–6 °C). Consequently, the lapse rate changes consecutive to the deglacial warming are much larger in this inner tropic region than those observed at higher latitudes; and are locally driven by the large temperature changes that occurred at high elevation (Fig. 4a).

3.2. Comparing LGM and modern lapse rates

Reconstructed LR values for LGM and modern time stand between

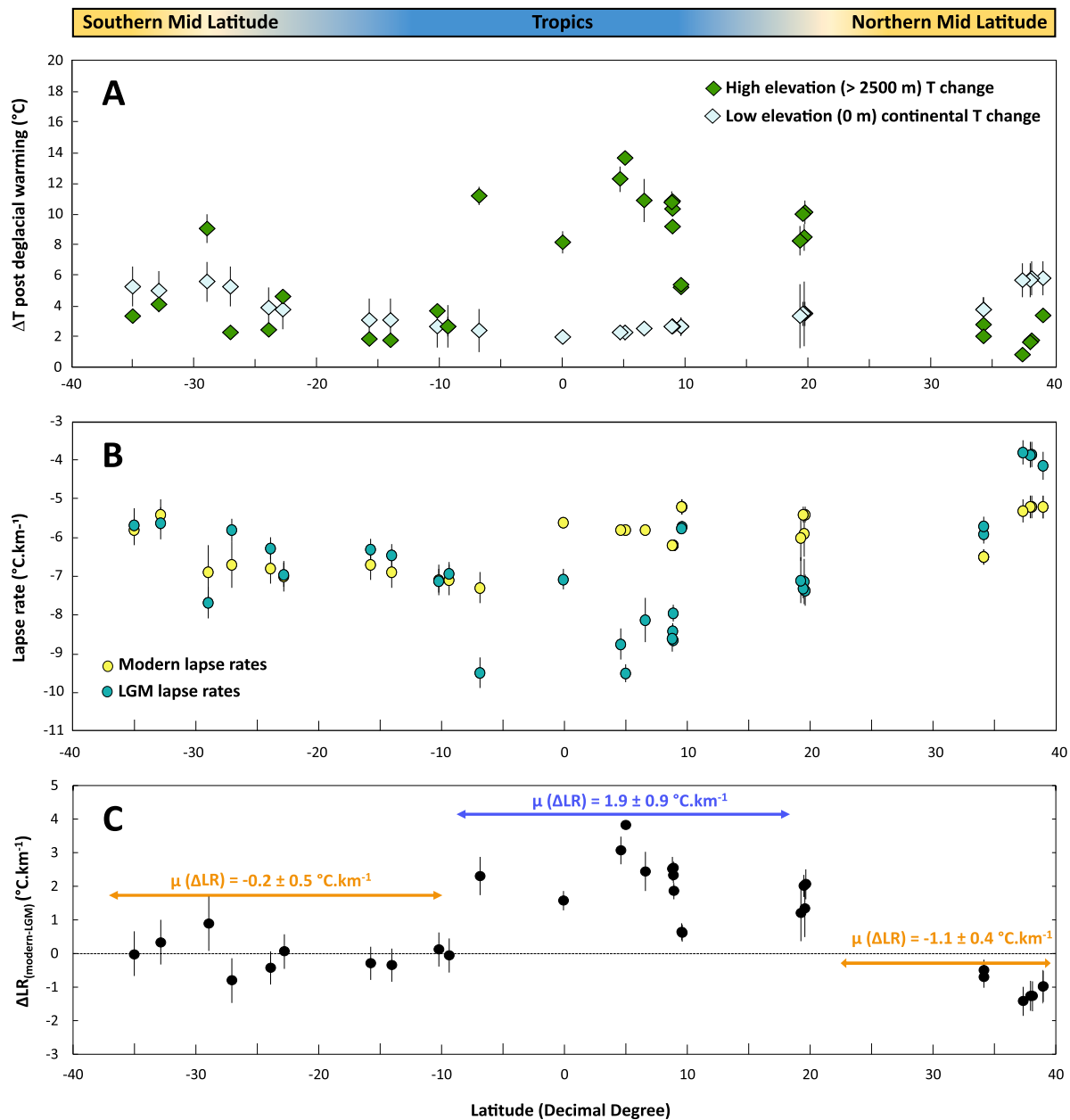


Fig. 4. A) Low elevation vs high elevation post LGM warming. Low elevation T changes are calculated from nearby SST, applying the continental correction factor (CFCE), while high elevation T changes are computed from the glacier-derived 0° isotherm shift, using modern local lapse rates. B) Modern and LGM lapse rates C) $\Delta LR_{(\text{modern-LGM})}$ for the 31 studied sites. Central tropics (20°N - 9°S) present the highest value of $\Delta LR_{(\text{modern-LGM})}$ and thus a steeper lapse rate during the LGM. Post-deglacial warming is thus amplified at high-altitude, between 20°N and 9°S .

-9.5 ± 0.8 and -3.8 ± 0.3 $^{\circ}\text{C.km}^{-1}$ (average LR of -6.7 ± 1.6 $^{\circ}\text{C.km}^{-1}$; 1σ) and between -7.3 and -5.2 $^{\circ}\text{C.km}^{-1}$ (average LR of -6.1 ± 0.7 $^{\circ}\text{C.km}^{-1}$; 1σ), respectively (Table S9; Figs. 4b and 5). The interquartile range of LGM LR is markedly larger than the one for modern LR (Fig. 5). The ΔLR ranges from -1.5 to $+3.7$ $^{\circ}\text{C.km}^{-1}$ (Supplementary Table 9; Fig. 4c). Positive ΔLR values, indicative of shallower modern lapse rates relative to LGM, are observed in the Colombian Andes (Inner Northern Tropics), whereas slightly negative ΔLR s are recorded in Northern and Southern mid-latitudes. Shallower modern lapse rates indicate amplified post LGM warming at high elevation, compared to sea level. In the search for a spatial relationship between ΔLR and latitude along the American Cordillera, we identify three distinct regions (Fig. 4c): (i) between ~ 40 and 20°N (Sierra Nevada and San Bernardino mountains), where the modern LR is slightly steeper than the LGM LR (mean ΔLR of -1.1 ± 0.4 $^{\circ}\text{C.km}^{-1}$), (ii) between 20°N and 9°S , where the modern LR

is shallower than the LGM LR (mean ΔLR of 1.9 ± 0.9 $^{\circ}\text{C.km}^{-1}$), and (iii) between 14°S and 35°S , where the modern LR is similar to the LGM LR (ΔLR average of -0.2 ± 0.5 $^{\circ}\text{C.km}^{-1}$). In summary, a high-altitude amplification of post LGM warming is observed at low latitudes (20°N to 9°S), in the central and the northern South American Cordillera (Fig. 4).

The ΔLR simulated by IPSLCM5A2 (Fig. 6g) is positive over the tropical Americas, the maximum value being reached over northern South America. On the other hand, negative values are simulated over mid-latitude North America. Even if the simulated ΔLR are much smaller than the reconstructed values, these model results suggest that changes in lapse rates are indeed spatially heterogeneous.

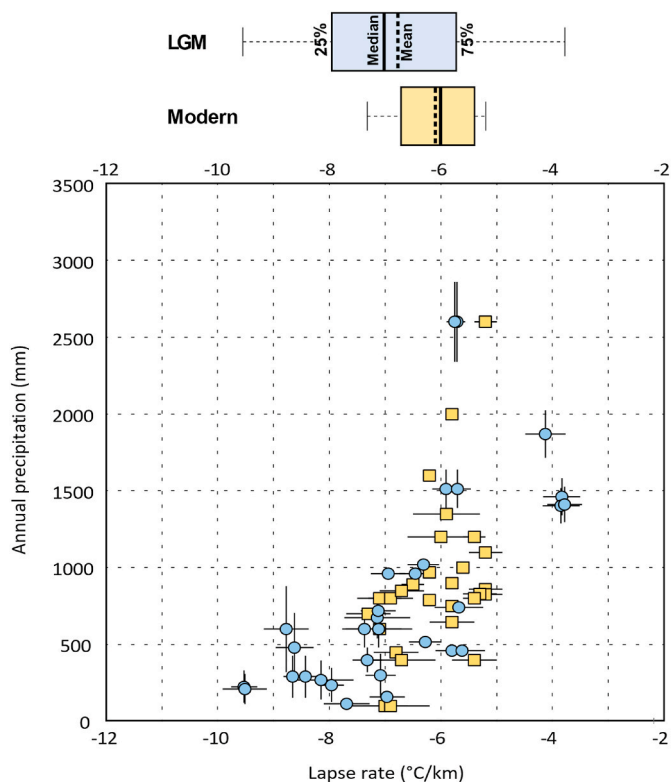


Fig. 5. Annual precipitation (mm) plotted against lapse rates, for both modern (orange circles) and LGM (blue circles) lapse rates (Lower panel). Box plot showing the distribution of modern and LGM lapse rates (Upper panel).

4. Discussions

4.1. Robustness of the reconstructed ΔLR

The robustness of our ΔLR could be questioned because our approach includes several computation steps with inherent uncertainties, assumptions and corrections. However, several independent arguments and observations support our results and suggest our approach is robust.

First, as a sensitivity test, we also calculated the modern LR directly from weather station data (Supplementary Fig. 5). The average difference between these modern LR estimates and our modern SST versus 0 °C isotherm-based LR is only 0.2 °C.km⁻¹ on average, with a maximum of 0.94 °C.km⁻¹ for Costa Rican sites (Supplementary Fig. 10). Such a small difference between two independent methods appears negligible and within the uncertainty of our regional ΔLR computation. It is much lower than the modern versus LGM variations of the LR we report here for the Tropics (Fig. 4C). In other words, using the alternative stations-based methodology would not significantly affect the ΔLR changes computed in this study between 20°N and 9°S (Supplementary Fig. 10). Nonetheless, we prefer to keep the SST and 0 °C isotherm-based approach to compute modern LR, for two main reasons: (i) we consider it preferable to use the same methodology for LGM and modern LR computation, and (ii) the weather station-based methodology does not permit to take into account the local LR variability due to the large geographical range.

Second, we show that the final ΔLR values are not very sensitive to the choice of the method used to estimate the LGM SST at the studied site (either latitudinal correction to account for polar amplification or linear interpolation) (Fig. 7).

Third, we also performed a sensitivity analysis to assess how each parameter involved in the lapse rate reconstructions contribute to our ΔLR estimates, and hence identify potential bias. For this, we computed

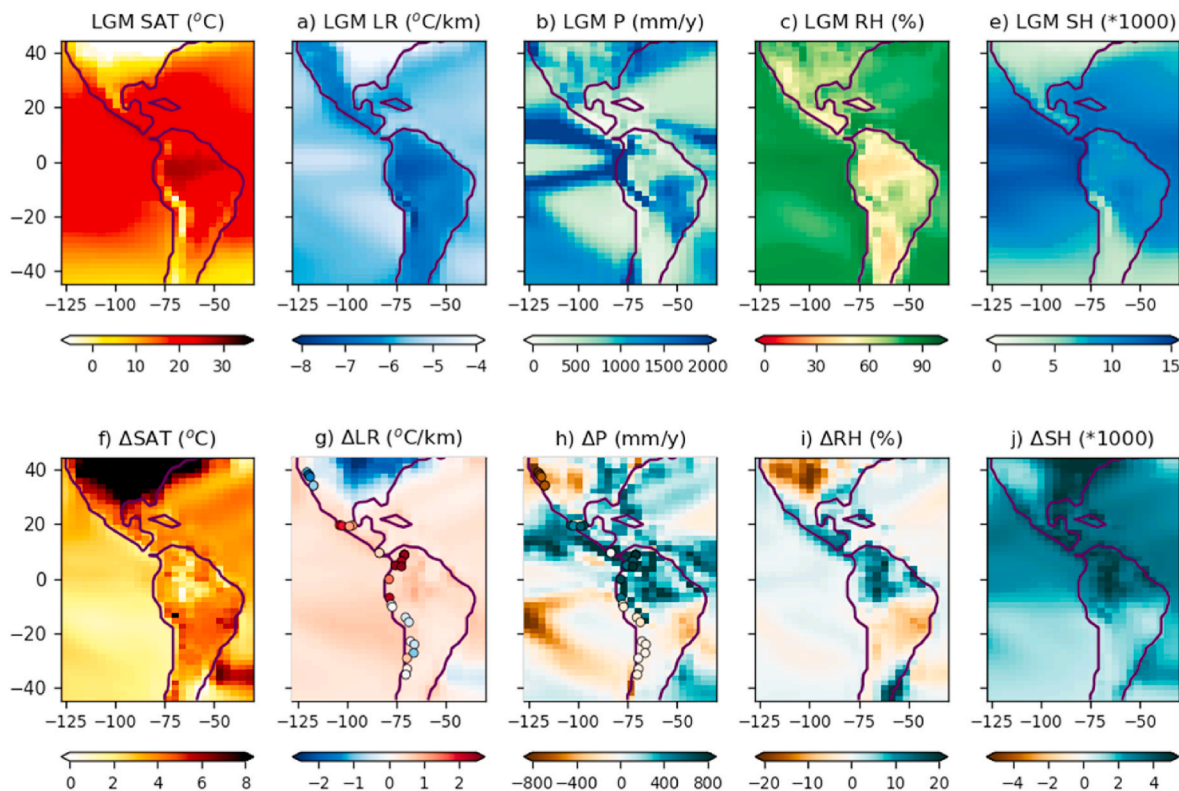


Fig. 6. IPSLCM5A2 coupled model results for the LGM climate (top row) and the PI – LGM anomaly (bottom row). Surface air temperature (a: LGM, f: PI – LGM), lapse rate (b: LGM, g: PI – LGM), annual precipitation (c: LGM, h: PI – LGM), relative humidity (d: LGM, i: PI – LGM), and specific humidity (e: LGM, j: PI – LGM). All fields are annual means. Reconstructions compiled in this study for the lapse rate and precipitation are superimposed on panels e and f, based on the same colour scale as for the maps.

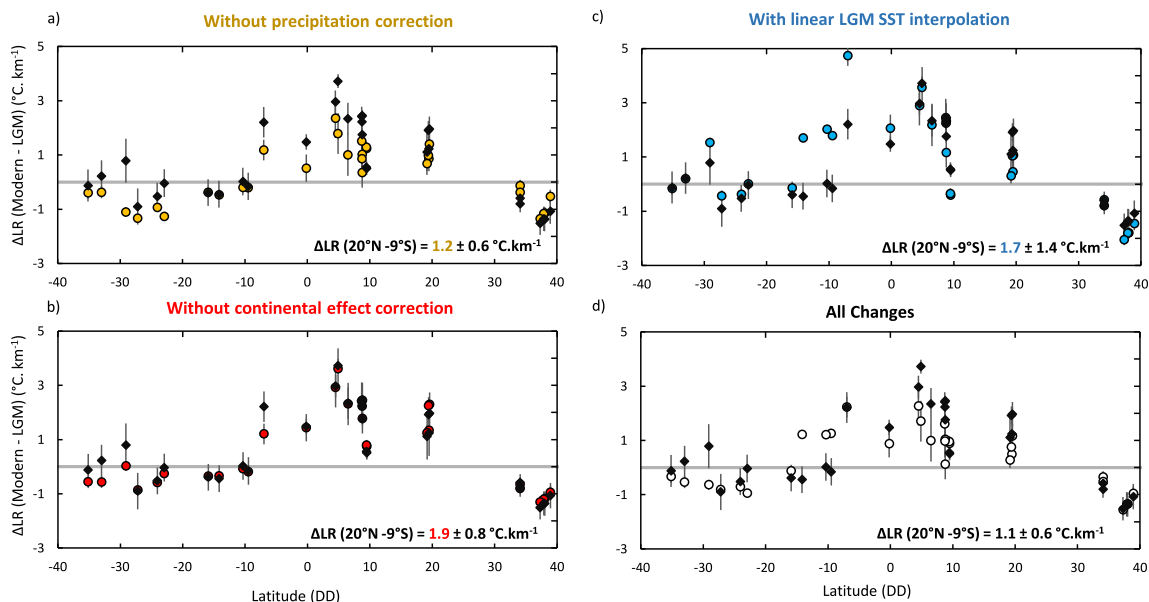


Fig. 7. Testing the model dependence of ΔLR results. Dark diamonds are the computed ΔLR of the study (see methods, Fig.5). Coloured dots show ΔLR computed removing iteratively each correction: a) ΔLR computed without precipitation correction (yellow dots), b) ΔLR computed without CFCE correction (red dots), c) ΔLR computed assuming that corresponding LGM SSTs are interpolated from the 2 nearest cores, without using the SST calibration relationship (blue dots). d) ΔLR computed without performing any of the 3 corrections (white dots). Note that ΔLR between 20°N and 9°S is significantly superior to zero independently of the modelling choices used.

the ΔLR by iteratively suppressing each of the following corrections (Fig. 7): (i) the conversion of LGM glacier paleoELAs into 0 °C isotherms using independent precipitation estimates, (ii) the latitudinal interpolation of ΔSST , and (iii) the conversion of modern and LGM SST into “equivalent” continental air temperatures with the CFCE. This sensitivity analysis indicates that the computed regional ΔLR pattern remains

similar, within uncertainty, when any of these three corrections is not accounted for (Fig. 7). In the extreme scenario where the ΔLR are computed without any of these three corrections being applied, positive ΔLR s values are still present beyond uncertainties in the equatorial region (Fig. 7). These sensitivity tests therefore demonstrate that the patterns of our ΔLR calculations are robust.

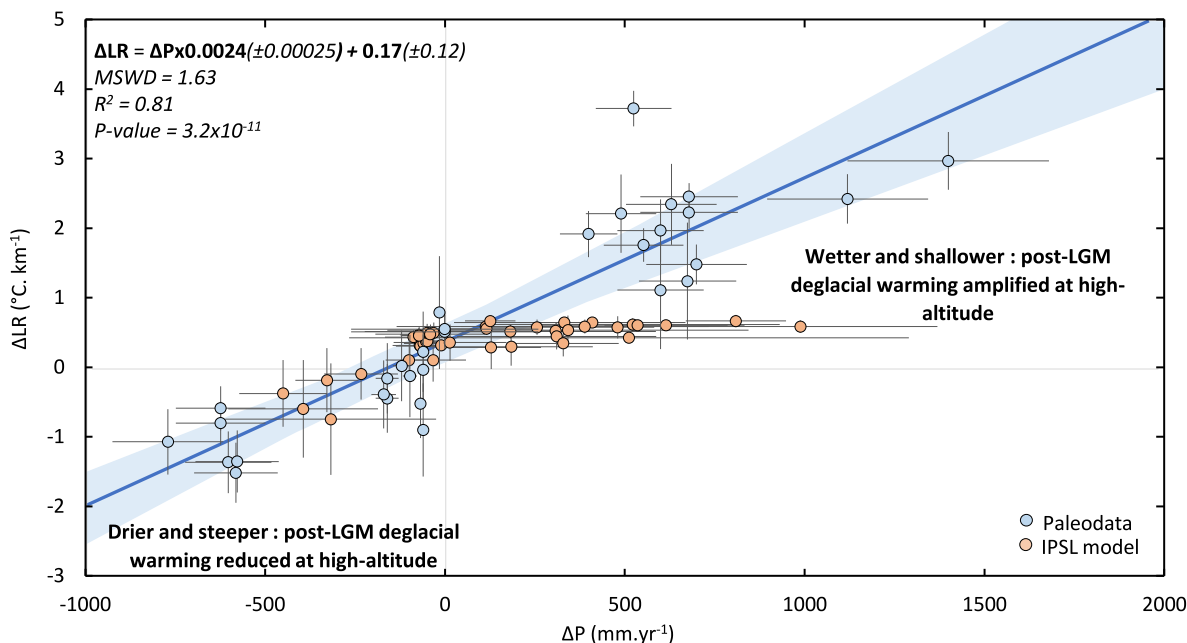


Fig. 8. Correlation between ΔLR and ΔP . (a) Data, blue dots: LGM precipitation has been calculated directly from modern precipitation and independent paleo-precipitation proxy (See Methods). The 31 sites of calculation are shown as blue dots. Note that steeper and shallower modern LR are systematically associated with drier and wetter areas than during LGM, respectively. IPSL model, orange dots: precipitation and lapse rate variations have been extracted at each data site location to perform the comparison.

4.2. The role of precipitation and humidity on LR changes

4.2.1. Correlation between LR and precipitation variations

For both LGM and modern values, the steepest LR values (≤ -6.5 °C.km⁻¹) are only observed in the driest regions ($P \leq 1000$ mm.yr⁻¹; Fig. 5). However, the relationship between absolute LR and annual precipitation remains unclear for both LGM and modern data (Fig. 5). The modern LR displays a lower spread than LGM LR and the relationship between LR and annual precipitation is less significant under the warmer climatic state of the modern compared to the colder LGM (Fig. 5). This different LR vs precipitation sensitivity suggests that boundary conditions matter, but the main drivers (average temperature, atmospheric CO₂ concentrations, differences in atmospheric dynamics) still need further research to be identified. To better understand the mechanism(s) that control(s) spatial and temporal variations of LR, we evaluate the correlation between the computed Δ LR and absolute precipitation changes ($\Delta P =$ modern precipitation – LGM precipitation) (Fig. 8). Precipitation proxies indicate that rainfall significantly increased between the LGM and the Holocene in the inner tropics (20°N – 9°S: ΔP range from 0 to +1400 mm.yr⁻¹), while it slightly decreased in the outer tropics and at mid-latitudes (10°S – 35°S and 34°N – 40°N: ΔP range from –15 to –770 mm.yr⁻¹) (Fig. 3, Supplementary Table 6, Supplementary Fig. 4). Notably, pollen records and lake shoreline levels in Central America (20°N–9°S) indicate a significant precipitation increase from the LGM to the Holocene (Supplementary Table 6). Although these absolute precipitation estimates are based on different proxies with their own characteristics and potential biases, their good overall agreement depicts a consistent picture. In detail, differences between the absolute precipitation estimates for the inner and the outer tropics display a precipitation pattern which potentially reflects a global southward shift of the Intertropical Convergence Zone (ITCZ) during the LGM, from Central America to South America, and/or an intensification of the South American Summer Monsoon (SASM). This scenario is corroborated by several precipitation records in Southern America (Blard et al., 2011; Martin et al., 2018, 2020; McGee, 2020; Woods et al., 2020).

Importantly, Δ LR values display a linear relationship with ΔP ($R^2 = 0.81$; p -value = 3.2×10^{-11}) (Fig. 8). Shallower modern lapse rates are associated with higher modern precipitation rates compared to the LGM. Conversely, areas characterized by a limited precipitation change (or a slight aridification) in the modern period (still relative to the LGM) yield unchanged or only slightly negative Δ LR values (Fig. 8).

4.2.2. Robustness of the Δ LR versus ΔP relationship

The precipitation values are used in the computation of the LR values to convert ELAs into 0 °C isotherms. One could hence wonder whether the Δ LR versus ΔP relationship (Fig. 8) could result from a bias inherent to the method. To evaluate the influence of the precipitation-correction on the Δ LR versus ΔP relationship, we compute a similar relationship but using Δ LR values that have not been corrected for the effect of precipitation (Supplementary Fig. 12). This methodological choice represents an extreme case where ELAs are considered as equivalent to 0 °C isotherm, which is not physically realistic (Condom et al., 2007; Legrain et al., 2022). However, this approach allows us to evaluate the extent to which the observed correlation between ΔP and Δ LR is due to the precipitation involved in the computation of Δ LR values. Using this approach, we find that the correlation between ΔP and Δ LR qualitatively stands similar, (i.e., wetter sites still are associated with shallower lapse rate; Supplementary Fig. 12). This sensitivity test thus reinforces the robustness of the observed correlation between Δ LR and ΔP . Nevertheless, the slope of the linear relationship is modified, implying that quantitative estimates is affected by the precipitation correction. Since the glacier ELAs are sensitive to absolute precipitation, we still consider the relationship using precipitation values in the LR computation as the most reliable approach (Fig. 8).

4.2.3. Role of moisture in the Δ LR variations

Based on the relationship results, we propose that shallower lapse rates may result from a post-LGM increase of the atmospheric water content. When the atmospheric water content increases, the capacity of the atmosphere to transfer heat from low to high elevations by convective and radiative transfer is enhanced, yielding less steep lapse rates (Kattell et al., 2013; Stone et al., 1979). Our suggestion of a shallower modern LR relative to the LGM in the inner tropics (20°N – 9°S) corroborates local studies of Blard et al. (2007) and Loomis et al. (2017), who established less steep modern LR compared to LGM in Hawaii and Kenya, respectively. Alternatively, constant modern LR could have prevailed in some tropical regions (e.g., between 11°S and 30°S in this study, but also in Papua New Guinea, in the Western Pacific (Tripathi et al., 2014)). The main difference between these two regions is that the summits of New Guinea are subject to much higher precipitation than those of Hawaii and Mount Kenya (>1000 mm.yr⁻¹ versus <500 mm.yr⁻¹), and the local LR is hence close to the moist adiabatic typical range (around 4–6 °C.km⁻¹). While our results demonstrate a linear relationship between Δ LR and ΔP , some of the noise in this correlation may be attributed to differences in the absolute climatic conditions of the glaciers. Specifically, mountainous areas experiencing high precipitation (>1000 mm/yr) are likely to be less influenced by changes in precipitation, making them less susceptible to recording a change in lapse rate. Moreover, paleo-precipitation records suggest that the modern climate conditions in Papua New Guinea are not significantly wetter than during the LGM (Denham and Haberle, 2008; Hope, 2009). The absence of precipitation changes between the LGM and the modern would explain the absence of significant variation of the LR computed in these areas.

4.3. What can we learn by comparing the paleoLR derived from paleoELA and those from the IPSLCM5A2 climate model?

The GCM modeled Δ LR and ΔP (Pre-industrial – LGM) map indicates a first order spatial agreement between the variations of these two metrics (Fig. 9). This is in line with the empirical correlation that we derive from our reconstruction based on high altitude continental proxies between Δ LR and ΔP (Fig. 8). The GCM outputs also indicate a tight spatial correlation between ΔP and the relative humidity change (noted Δ RH) (Fig. 6). This correlation between RH and precipitation changes is supported by the scatter plot (Fig. 9b) between these individual outputs retrieved from the GCM grid ($R^2 = 0.65$). The observed correlation in the paleoclimate record between ΔP and Δ LR could hence reflect a close control of Δ RH on Δ LR. The fact that RH changes may be a major driver of LR changes is also confirmed by plotting these metrics extracted from the IPSLCM5A2 model output over and close to the American cordillera from 40°N to 40°S (Fig. 9c) ($R^2 = 0.80$). The same plot realized between the modeled specific humidity and LR changes display a poorer correlation, mainly arising from the sites located north of 20°N where Δ LR is negative (Supplementary Fig. 11; $R^2 = 0.27$). These observations provide a strong support for the involvement of a moisture control on LR changes, increased relative humidity conditions implying shallower lapse rates (or drier conditions implying steeper lapse rates) (Fig. 9).

However, the agreement between the IPSL model outputs and our proxy-based reconstruction does not hold for regions that experienced a post LGM precipitation increase. In such cases, the model shows a saturation effect for Δ LR, hence causing the overall Δ LR response to be underestimated (Fig. 8). A comparison between present day precipitation rates and those modeled for PI conditions (Fig. 10) shows that the IPSL model underestimates precipitation rates over the Amazonian basin, while overestimating precipitation rates in the Northern part of the Andes (Ecuador, Columbia). This could result from the low resolution of the topography, which causes a poor representation of the real altitude of the range, and, hence, an inaccurate representation of the orographic effect in this narrow part of the Cordillera (Fig. 10). There are also other long-recognized biases of the IPSL models, as discussed by

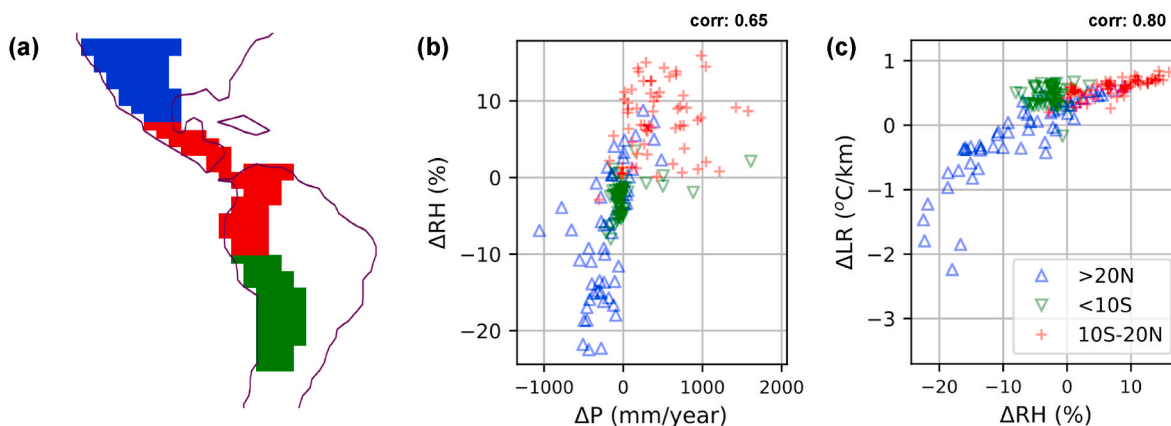


Fig. 9. Relationships between variables simulated by IPSLCM5A2 over and close to the American Cordillera, on the grid points highlighted on the map. The American Cordillera is separated into three main domains highlighted in green, red and blue (a), respectively. Δ indicate PI - LGM anomalies. RH: relative humidity at first level, P: precipitation, LR: lapse rate.

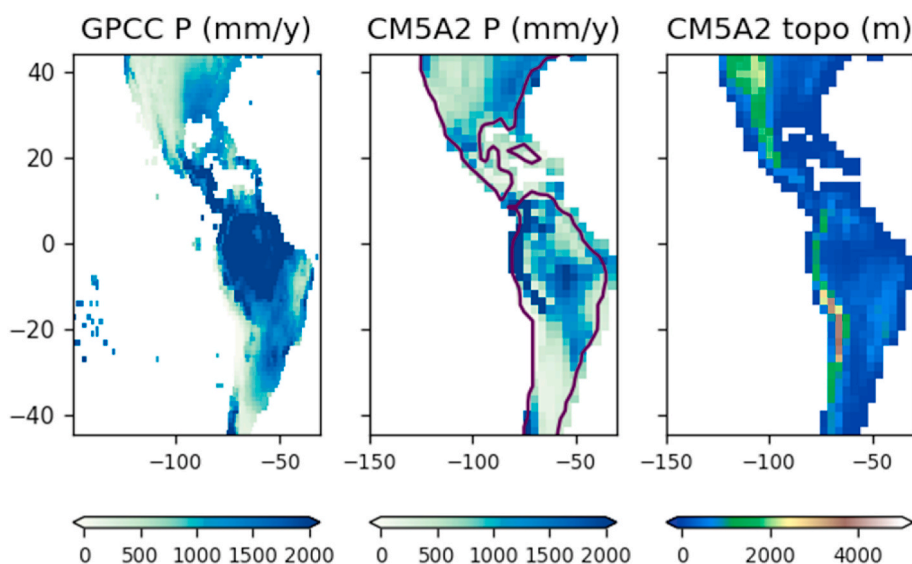


Fig. 10. Comparison of observed (GPCC dataset, https://opendata.dwd.de/climate_environment/GPCC/html/gpcc_normals_v2022_doi_download.html) and modeled (GCM IPSLCM5A2) modern precipitation field in the American Cordillera.

(Sepulchre et al., 2020). This low resolution could cause post-LGM LR changes to be underestimated in Ecuador and Columbia, where GCM-modeled precipitation are overestimated at the location of glaciers (>1500 mm/a, compared to < 1000 mm/a), implying that the modeled LRs are already close to a moist adiabatic value (around $5^{\circ}\text{C.km}^{-1}$), thus hampering any post-LGM LR change to be observed in the simulations. Finally, it is important to acknowledge that lapse rates measured along mountain slope may be decoupled from those observed in the adjacent free atmosphere (Pepin et al., 2015), especially in valleys. Since the IPSL model is run at ~ 300 km resolution, it only has an incomplete description of the real topography, and therefore of the processes occurring within the mountain atmospheric boundary layer, well below the subgrid scale. This observation may partly explain some of the discrepancies between modeled LR and those derived from paleoELA reconstruction. Future studies could test this by performing high-resolution GCM simulations with a much higher resolution topography (i.e., <10 km grid cell).

4.4. Amplification of high-altitude temperature changes: implications for anthropogenic warming

During the past decade, several studies have developed the concept of an elevation-dependant warming (Pepin et al., 2015; Wang et al., 2014, 2016). Recent observations have shown an amplification of the high-altitude warming, albeit this pattern seems to yield contrasting outcomes (Ohmura, 2012). A recent study based on noble gas reconstruction of continental temperature evidenced a larger post LGM warming over the continent relative to the oceans, even at elevations <1000 m (Seltzer et al., 2021). In order to test the robustness of the amplification of temperature changes that we obtain here at high elevations, we compute the post LGM warming values derived from paleo-glaciers and plotted them against the altitude of observation (Fig. 11). Our data correspond to high elevation (2500 m–5000 m) post LGM warming ranging between 6 and 14°C in locations that were drier during the LGM, and 0 – 5°C in locations that were wetter. For Brazil, noble gas paleotemperatures indicate a low altitude LGM cooling of $5.4 \pm 0.6^{\circ}\text{C}$, at an average elevation of 600 m (Seltzer et al., 2021; Stute et al., 1995). This value is at the low end of the range of post LGM warming computed in our study for higher altitudes. This observation

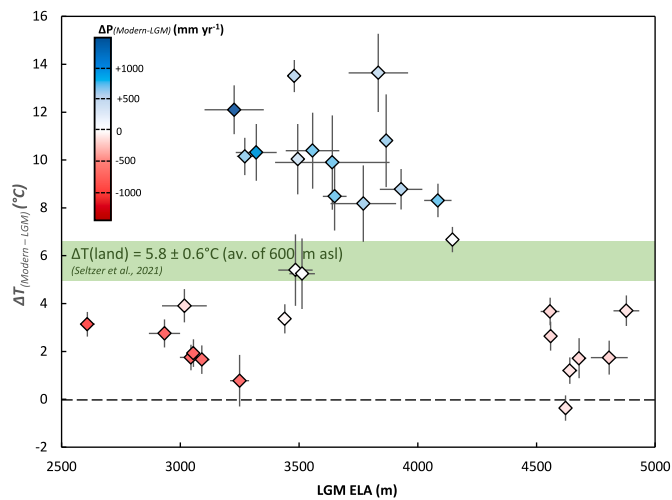


Fig. 11. Correlation between $\Delta T_{(\text{Modern-LGM})}$ and LGM ELA (m). $\Delta T_{(\text{Modern-LGM})}$ is computed from the ELA depression value using the modern lapse rate value. Blue and red dots represent sites that were drier and wetter during the LGM relative to present-day, respectively. LGM precipitation was calculated directly from modern precipitation and independent paleoprecipitation proxies (see Methods). Note that the highest values of ΔT are higher than the land ΔT from the study of Seltzer et al. (2021) (green shaded area).

thus implies that the amplification of the post LGM warming is significant at high elevation, and exceeds the effect of pure continental amplification (Seltzer et al., 2023a,b) (Fig. 11).

Many factors have been proposed to explain the peculiar trends of anthropogenic warming, including surface-based land use feedbacks (Zeng et al., 2021), as well as atmospheric radiative forcings and convective process (Keil et al., 2021; Pepin et al., 2015). A recent study also mentioned the potential role of seasonality in modulating short term warming amplification at high-altitude (Qixiang et al., 2018).

Several studies had already identified correlations between lapse rate and humidity, both for present day (Colman and Soden, 2021; Li et al., 2015) and the LGM (Blard et al., 2007; Kuhlemann et al., 2008; Loomis et al., 2017). Previous reconstructions of LGM lapse rates yielded contrasting results from different regions (Blard et al., 2007; Kuhlemann et al., 2008; Loomis et al., 2017; Tripathi et al., 2014) but the scarcity of these LGM reconstructions and their lack of quantitative precipitation estimate did not permit to demonstrate a clear forcing mechanism. Our synthesis identifies for the first time a robust quantitative relationship between changes in lapse rate and changes in local precipitation (and probably relative humidity) during the post LGM warming. This finding permits to better understand and constrain the roles of precipitation and moisture on lapse rate modifications, temporal and spatial changes in moisture being able to drive variable interregional lapse rate changes at different elevations. Consequently, as evidenced by our dataset (Fig. 4a), the magnitude of the LGM cooling at high elevation has a high probability to have been spatially heterogeneous, which represents a significant caveat to keep in mind when deriving a uniform and universal temperature change on land (Seltzer et al., 2023a,b). Using the obtained relationship between precipitation rates and lapse rate changes (Fig. 8), we estimate the high-altitude amplification of the future warming, assuming mean annual precipitation changes modeled by 2100 projection scenarios. For instance, a precipitation increases of $500 \text{ mm}\cdot\text{a}^{-1}$ would lead to $-1.1 \text{ }^\circ\text{C}\cdot\text{km}^{-1}$. Hence, based on our most reliable $\Delta\text{LR}-\Delta\text{P}$ relationship (Fig. 8), we find that a sea level $+1 \text{ }^\circ\text{C}$ warming could induce an additional warming of $4.1 \pm 0.8 \text{ }^\circ\text{C}$ at 4000 m asl (1σ standard deviation). Following this reasoning, we speculate that regions becoming increasingly wet as a result of climate change may coincide with regions where the low altitude anthropogenic warming will be amplified at high-altitude and potentially accelerate mountainous glaciers melting there, despite the increase in precipitation. Reversely, in

regions that will become drier in the future, global warming could be attenuated at high elevation. Future modelling studies should help to quantify these amplification/attenuation mechanisms and better address future high-altitude climatic changes.

5. Conclusions

We summarize the main outcomes of our study in these four key findings:

- **Quantitative relationship between lapse rate and precipitation changes:** by using LGM 0° isotherm from glacier paleo-equilibrium line, SST and paleoprecipitation proxies, we establish a relationship linking post LGM changes in precipitation (ΔP) and changes in lapse rates (ΔLR).
- **Amplified post-LGM warming in wetter areas:** the deglacial warming amplitude at high-altitude is correlated with changes in mean annual precipitation: in areas that have become wetter, the lapse rate has become shallower, and reversely. This mechanism is also encountered in the IPSL-GCM model outputs, although some discrepancies exist in regions that experienced the largest post LGM moisture increase.
- **Spatial heterogeneities in post-LGM lapse rate variations:** by linking moisture and lapse rate changes, our study provides key insights to explain the heterogeneities in post-LGM lapse rate variations inferred from previous studies.
- **Implications for anthropogenic-induced high-elevation warming:** our results suggest that the current high-altitude warming is underestimated in areas that will become wetter. Future modeled projections need to ensure that this moisture amplification mechanism is well captured by numerical models.

Author contributions

P-H.B., M.K and E.L. designed research; P-H.B., M.K and E.L. performed research; E.L. wrote a draft of the paper, with subsequent inputs from P-H.B., M.K, J.C, G.L, S.B, D.V.B.

Declaration of competing interest

The authors declare that they have no known competing financial interests or personal relationships that could have appeared to influence the work reported in this paper.

Data availability

All data are available on the open repository: <https://doi.org/10.24396/ORDAR-130>.

Acknowledgments

We thank the two anonymous reviewers for their constructive suggestions that improved the quality of our manuscript and Miryam Bar-Matthews for editing this manuscript. EL acknowledges funding by the French National Research Agency under the "Programme d'Investissements d'Avenir" (ANR-19-MPGA-0001). DVB acknowledges funding by grant ANR-22-CPJ2-0005-01. The IPSLCM5A2 simulations were run on the CEA/TGCC supercomputer joliotcurie (PI) and IDRIS supercomputer JeanZay (LGM) via the GENCI allocation gen2212. The IPSL Climate Modelling Centre computer scientists are thanked for their help with setting up the simulations and Pierre Sepulchre for his endeavour on IPSLCM5A2. The Paleoclimate Modelling Intercomparison Project (PMIP) is thanked for its coordination in establishing the LGM experimental set up. MK is funded by CNRS and SB by CEA. Lukas Kulft is thanked for fruitful interactions at the beginning of the project.

Appendix A. Supplementary data

Supplementary data to this article can be found online at <https://doi.org/10.1016/j.quascirev.2023.108303>.

References

- Abe-Ouchi, A., Saito, F., Kageyama, M., Braconnot, P., Harrison, S.P., Lambeck, K., Otto-Bliesner, B.L., Peltier, W.R., Tarasov, L., Peterschmitt, J.-Y., Takahashi, K., 2015. Ice-sheet configuration in the CMIP5/PMIP3 last glacial maximum experiments. *Geosci. Model Dev.* (GMD) 8, 3621–3637. <https://doi.org/10.5194/gmd-8-3621-2015>.
- Ammann, C., Jenny, B., Kammer, K., Messerli, B., 2001. Late Quaternary Glacier response to humidity changes in the arid Andes of Chile (18–29°S). *Palaeogeogr. Palaeoclimatol. Palaeoecol.* 172, 313–326. [https://doi.org/10.1016/S0031-0182\(01\)00306-6](https://doi.org/10.1016/S0031-0182(01)00306-6).
- Annan, J.D., Hargreaves, J.C., Mauritsen, T., 2022. A new global surface temperature reconstruction for the Last Glacial Maximum. *Clim. Past* 18, 1883–1896. <https://doi.org/10.5194/cp-18-1883-2022>.
- Bartlein, P.J., Harrison, S.P., Brewer, S., Connor, S., Davis, B.A.S., Gajewski, K., Guiot, J., Harrison-Prentice, T.I., Hendersson, A., Peyron, O., Prentice, I.C., Scholze, M., Seppä, H., Shuman, B., Sugita, S., Thompson, R.S., Viau, A.E., Williams, J., Wu, H., 2011. Pollen-based continental climate reconstructions at 6 and 21 ka: a global synthesis. *Clim. Dynam.* 37, 775–802. <https://doi.org/10.1007/s00382-010-0904-1>.
- Benn, D.I., Lehmkuhl, F., 2000. Mass balance and equilibrium-line altitudes of glaciers in high-mountain environments. *Quat. Int.* 65 (66), 15–29. [https://doi.org/10.1016/S1040-6182\(99\)00034-8](https://doi.org/10.1016/S1040-6182(99)00034-8).
- Bhattacharya, T., Tierney, J.E., Addison, J.A., Murray, J.W., 2018. Ice-sheet modulation of deglacial North American monsoon intensification. *Nat. Geosci.* 11, 848–852. <https://doi.org/10.1038/s41561-018-0220-7>.
- Blard, P.-H., Lavé, J., Pik, R., Wagnon, P., Bourlès, D., 2007. Persistence of full glacial conditions in the central Pacific until 15,000 years ago. *Nature* 449, 591–594. <https://doi.org/10.1038/nature06142>.
- Blard, P.-H., Sylvestre, F., Tripathi, A.K., Claude, C., Causse, C., Coudrain, A., Condom, T., Seidel, J.-L., Vimeux, F., Moreau, C., Dumoulin, J.-P., Lavé, J., 2011. Lake highstands on the altiplano (tropical Andes) contemporaneous with heinrich 1 and the younger dryas: new insights from ^{14}C , U–Th dating and $\delta^{18}\text{O}$ of carbonates. *Quat. Sci. Rev.* 30, 3973–3989. <https://doi.org/10.1016/j.quascirev.2011.11.001>.
- Bova, S., Rosenthal, Y., Liu, Z., Godad, S.P., Yan, M., 2021. Seasonal origin of the thermal maxima at the Holocene and the last interglacial. *Nature* 589, 548–553. <https://doi.org/10.1038/s41586-020-03155-x>.
- Clark, P.U., Dyke, A.S., Shakun, J.D., Carlson, A.E., Clark, J., Wohlfarth, B., Mitrovica, J. X., Hostetler, S.W., McCabe, A.M., 2009. The last glacial maximum. *Science* 325, 710–714. <https://doi.org/10.1126/science.1172873>.
- Cleator, S., Harrison, S., Nichols, N., Prentice, I.C., Roulstone, I., 2019. A new multi-variable benchmark for Last Glacial Maximum climate simulations. <https://doi.org/10.17864/1947.229>.
- Colman, R., Soden, B.J., 2021. Water vapor and lapse rate feedbacks in the climate system. *Reviews of Modern Physics* 93 (4), 045002.
- Condom, T., Coudrain, A., Sicart, J.E., Théry, S., 2007. Computation of the space and time evolution of equilibrium-line altitudes on Andean glaciers (10 N–55 S). *Global and Planetary Change* 59 (1–4), 189–202.
- Denham, T., Haberle, S., 2008. Agricultural emergence and transformation in the Upper Wahgi valley, Papua New Guinea, during the Holocene: theory, method and practice. *Holocene* 18, 481–496. <https://doi.org/10.1177/0959683607087936>.
- Dutton, A., Carlson, A.E., Long, A.J., Milne, G.A., Clark, P.U., DeConto, R., Horton, B.P., Rahmstorf, S., Raymo, M.E., 2015. Sea-level rise due to polar ice-sheet mass loss during past warm periods. *Science* 349, aaa4019. <https://doi.org/10.1126/science.aaa4019>.
- Fleming, K., Johnston, P., Zwart, D., Yokoyama, Y., Lambeck, K., Chappell, J., 1998. Refining the eustatic sea-level curve since the Last Glacial Maximum using far- and intermediate-field sites. *Earth Planet Sci. Lett.* 163, 327–342. [https://doi.org/10.1016/S0012-821X\(98\)00198-8](https://doi.org/10.1016/S0012-821X(98)00198-8).
- Fox, A., Bloom, A., 1994. Snowline altitude and climate in the Peruvian Andes (5°–17° S) at present and during the latest pleistocene glacial maximum. *J. Geogr.* 103, 867–885.
- Herbert, T.D., Schuffert, J.D., Andreasen, D., Heusser, L., Lyle, M., Mix, A., Ravelo, A.C., Stott, L.D., Herguera, J.C., 2001. Collapse of the California current during glacial maxima linked to climate change on land. *Science* 293, 71–76. <https://doi.org/10.1126/science.1059209>.
- Hope, G., 2009. Environmental change and fire in the Owen Stanley ranges, Papua New Guinea. *Quat. Sci. Rev.* 28, 2261–2276. <https://doi.org/10.1016/j.quascirev.2009.04.012>.
- Huang, B., Banzon, V.F., Freeman, E., Lawrimore, J., Liu, W., Peterson, T.C., Smith, T.M., Thorne, P.W., Woodruff, S.D., Zhang, H.-M., 2015. Extended Reconstructed Sea Surface temperature version 4 (ERSST.v4). Part I: upgrades and intercomparisons. *J. Clim.* 28, 911–930. <https://doi.org/10.1175/JCLI-D-14-00006.1>.
- Hugonnet, R., McNabb, R., Berthier, E., Menounos, B., Nuth, C., Girod, L., Farinotti, D., Huss, M., Dussallant, I., Brun, F., Kääb, A., 2021. Accelerated global glacier mass loss in the early twenty-first century. *Nature* 592, 726–731. <https://doi.org/10.1038/s41586-021-03436-z>.
- Intergovernmental Panel on Climate Change (IPCC), 2022. The Ocean and Cryosphere in a Changing Climate: Special Report of the Intergovernmental Panel on Climate Change, first ed. Cambridge University Press. <https://doi.org/10.1017/9781009157964>.
- Kageyama, M., Albani, S., Braconnot, P., Harrison, S.P., Hopcroft, P.O., Ivanovic, R.F., Lambert, F., Marti, O., Peltier, W.R., Peterschmitt, J.-Y., Roche, D.M., Tarasov, L., Zhang, Xu, Brady, E.C., Haywood, A.M., LeGrande, A.N., Lunt, D.J., Mahowald, N. M., Mikolajewicz, U., Nisanicoglu, K.H., Otto-Bliesner, B.L., Renssen, H., Tomas, R. A., Zhang, Q., Abe-Ouchi, A., Bartlein, P.J., Cao, J., Li, Q., Lohmann, G., Ohgaito, R., Shi, X., Volodin, E., Yoshida, K., Zhang, Xiao, Zheng, W., 2017. The PMIP4 contribution to CMIP6 – Part 4: scientific objectives and experimental design of the PMIP4-CMIP6 Last Glacial Maximum experiments and PMIP4 sensitivity experiments. *Geosci. Model Dev.* (GMD) 10, 4035–4055. <https://doi.org/10.5194/gmd-10-4035-2017>.
- Kageyama, M., Harrison, S.P., Kapsch, M.-L., Lofverstrom, M., Lora, J.M., Mikolajewicz, U., Sherriff-Tadano, S., Vadsaria, T., Abe-Ouchi, A., Bouttes, N., Chandan, D., Gregoire, L.J., Ivanovic, R.F., Izumi, K., LeGrande, A.N., Lhardy, F., Lohmann, G., Morozova, P.A., Ohgaito, R., Paul, A., Peltier, W.R., Poulsen, C.J., Quiquet, A., Roche, D.M., Shi, X., Tierney, J.E., Valdes, P.J., Volodin, E., Zhu, J., 2021. The PMIP4 Last Glacial Maximum experiments: preliminary results and comparison with the PMIP3 simulations. *Clim. Past* 17, 1065–1089. <https://doi.org/10.5194/cp-17-1065-2021>.
- Kaser, G., Großhauser, M., Marzeion, B., 2010. Contribution potential of glaciers to water availability in different climate regimes. *Proc. Natl. Acad. Sci. U.S.A.* 107, 20223–20227. <https://doi.org/10.1073/pnas.1008162107>.
- Kattel, D.B., Yao, T., Yang, K., Tian, L., Yang, G., Joswiak, D., 2013. Temperature lapse rate in complex mountain terrain on the southern slope of the central Himalayas. *Theor. Appl. Climatol.* 113, 671–682. <https://doi.org/10.1007/s00704-012-0816-6>.
- Keil, P., Schmidt, H., Stevens, B., Bao, J., 2021. Variations of tropical lapse rates in climate models and their implications for upper tropospheric warming. *J. Clim.* 1–50. <https://doi.org/10.1175/JCLI-D-21-0196.1>.
- Kraaijenbrink, P.D.A., Bierkens, M.F.P., Lutz, A.F., Immerzeel, W.W., 2017. Impact of a global temperature rise of 1.5 degrees Celsius on Asia's glaciers. *Nature* 549, 257–260. <https://doi.org/10.1038/nature23878>.
- Kuhlemann, J., Rohling, E.J., Krumrei, I., Kubik, P., Ivy-Ochs, S., Kucera, M., 2008. Regional synthesis of mediterranean atmospheric circulation during the last glacial maximum. *Science* 321, 1338–1340. <https://doi.org/10.1126/science.1157638>.
- Lachniet, M.S., Vazquez-Selem, L., 2005. Last Glacial Maximum equilibrium line altitudes in the circum-Caribbean (Mexico, Guatemala, Costa Rica, Colombia, and Venezuela). *Quat. Int.* 138–139, 129–144. <https://doi.org/10.1016/j.quaint.2005.02.010>.
- Lachniet, M.S., Asmerom, Y., Bernal, J.P., Polyak, V.J., Vazquez-Selem, L., 2013. Orbital pacing and ocean circulation-induced collapses of the Mesoamerican monsoon over the past 22,000 y. *Proc. Natl. Acad. Sci. U.S.A.* 110, 9255–9260. <https://doi.org/10.1073/pnas.1222804110>.
- Lal, D., 1991. Cosmic ray labeling of erosion surfaces: in situ nuclide production rates and erosion models. *Earth Planet Sci. Lett.* 104, 424–439.
- Lea, D.W., Kienast, M., De Garidel-Thoron, T., Kageyama, M., Paul, A., Bard, E., 2014. Compare 2013: constraining tropical ocean cooling during the last glacial maximum. *PAGES Mag.* 22. <https://doi.org/10.22498/pages.22.1.43>, 43–43.
- Leduc, G., Vidal, L., Tachikawa, K., Rostek, F., Sonzogni, C., Beaufort, L., Bard, E., 2007. Moisture transport across Central America as a positive feedback on abrupt climatic changes. *Nature* 445, 908–911. <https://doi.org/10.1038/nature05578>.
- Leduc, G., Schneider, R., Kim, J.-H., Lohmann, G., 2010. Holocene and Eemian sea surface temperature trends as revealed by alkenone and Mg/Ca paleothermometry. *Quat. Sci. Rev.* 29, 989–1004. <https://doi.org/10.1016/j.quascirev.2010.01.004>.
- Leduc, G., Garidel-Thoron, T. de, Kaiser, J., Bolton, C., Contoux, C., 2017. Databases for sea surface paleotemperature based on geochemical proxies from marine sediments: implications for model-data comparisons. *Quaternaire* 201–216. <https://doi.org/10.4000/quaternaire.8034>.
- Legrain, E., Blard, P.-H., Charreau, J., 2022. Glacial equilibrium line-based relationship for paleoclimate reconstructions (Sierra Nevada, USA). *Quat. Res.* 109, 183–194. <https://doi.org/10.1017/qua.2022.10>.
- Li, Y., Zeng, Z., Zhao, L., Piao, S., 2015. Spatial patterns of climatological temperature lapse rate in mainland China: A multi-time scale investigation. *Journal of Geophysical Research: Atmospheres* 120 (7), 2661–2675.
- Lifton, N., Sato, T., Dunai, T.J., 2014. Scaling in situ cosmogenic nuclide production rates using analytical approximations to atmospheric cosmic-ray fluxes. *Earth Planet Sci. Lett.* 386, 149–160. <https://doi.org/10.1016/j.epsl.2013.10.052>.
- Loomis, S.E., Russell, J.M., Verschuren, D., Morrill, C., De Cort, G., Sissinghe Damsté, J. S., Olago, D., Eggermont, H., Street-Perrott, F.A., Kelly, M.A., 2017. The tropical lapse rate steepened during the Last Glacial Maximum. *Sci. Adv.* 3, e1600815. <https://doi.org/10.1126/sciadv.1600815>.
- Marrero, S.M., Phillips, F.M., Caffee, M.W., Gosse, J.C., 2016. CRONUS-Earth cosmogenic ^{36}Cl calibration. *Quat. Geochronol.* 31, 199–219. <https://doi.org/10.1016/j.quageo.2015.10.002>.
- Martin, L.C.P., Blard, P.-H., Lavé, J., Braucher, R., Lupker, M., Condom, T., Charreau, J., Mariotti, V., Aster Team, Davy, E., 2015. In situ cosmogenic ^{10}Be production rate in the High Tropical Andes. *Quat. Geochronol.* 30, 54–68. <https://doi.org/10.1016/j.quageo.2015.06.012>.
- Martin, L.C.P., Blard, P.-H., Balco, G., Lavé, J., Delunel, R., Lifton, N., Laurent, V., 2017. The CREP program and the ICE-D production rate calibration database: a fully parameterizable and updated online tool to compute cosmic-ray exposure ages. *Quat. Geochronol.* 38, 25–49. <https://doi.org/10.1016/j.quageo.2016.11.006>.
- Martin, L.C.P., Blard, P.-H., Lavé, J., Condom, T., Prémaillon, M., Jomelli, V., Brunstein, D., Lupker, M., Charreau, J., Mariotti, V., Tibari, B., Aster Team, Davy, E., 2018. Lake tauca highstand (heinrich stadial 1a) driven by a southward shift of the Bolivian high. *Sci. Adv.* 4, eaar2514. <https://doi.org/10.1126/sciadv.aar2514>.
- Martin, L.C.P., Blard, P.-H., Lavé, J., Jomelli, V., Charreau, J., Condom, T., Lupker, M., Arnold, M., Aumaitre, G., Bourlès, D.L., Keddadouche, K., 2020. Antarctic-like

- temperature variations in the Tropical Andes recorded by glaciers and lakes during the last deglaciation. *Quat. Sci. Rev.* 247, 106542 <https://doi.org/10.1016/j.quascirev.2020.106542>.
- McGee, D., 2020. Glacial–Interglacial precipitation changes. *Ann. Rev. Mar. Sci.* 12, 525–557. <https://doi.org/10.1146/annurev-marine-010419-010859>.
- Meier, M., Post, A., 1962. Recent variations in mass net budgets of glaciers in western North America. *Int. Assoc. Sci. Hydrol. Publ.* 58.
- Muscheler, R., Beer, J., Kubik, P.W., Synal, H.-A., 2005. Geomagnetic field intensity during the last 60,000 years based on 10Be and 36Cl from the Summit ice cores and 14C. *Quat. Sci. Rev.* 24, 1849–1860. <https://doi.org/10.1016/j.quascirev.2005.01.012>.
- Nishiizumi, K., Imamura, M., Caffee, M.W., Southon, J.R., Finkel, R.C., McAninch, J., 2007. Absolute calibration of 10Be AMS standards. In: *Nuclear Instruments and Methods in Physics Research Section B: Beam Interactions with Materials and Atoms*, vol. 258, pp. 403–413. <https://doi.org/10.1016/j.nimb.2007.01.297>.
- Ohmura, A., 1992. Climate at the equilibrium line of glaciers. *J. Glaciol.* 38.
- Ohmura, A., 2012. Enhanced temperature variability in high-altitude climate change. *Theor. Appl. Climatol.* 110, 499–508. <https://doi.org/10.1007/s00704-012-0687-x>.
- Palacios, D., Stokes, C.R., Phillips, F.M., Clague, J.J., Alcalá-Reygosa, J., Andrés, N., Angel, I., Blard, P.-H., Briner, J.P., Hall, B.L., Dahms, D., Hein, A.S., Jomelli, V., Mark, B.G., Martini, M.A., Moreno, P., Riedel, J., Sagredo, E., Stansell, N.D., Vázquez-Selem, L., Vuille, M., Ward, D.J., 2020. The deglaciation of the Americas during the last glacial termination. *Earth Sci. Rev.* 203, 103113 <https://doi.org/10.1016/j.earscirev.2020.103113>.
- Pandey, G.R., Cayán, D.R., Georgakakos, K.P., 1999. Precipitation structure in the Sierra Nevada of California during winter. *J. Geophys. Res.* 104, 12019–12030. <https://doi.org/10.1029/1999JD900103>.
- Mountain Research Initiative EDW Working Group, Pepin, N., Bradley, R.S., Diaz, H.F., Baraer, M., Caceres, E.B., Forsythe, N., Fowler, H., Greenwood, G., Hashmi, M.Z., Liu, X.D., Miller, J.R., Ning, L., Ohmura, A., Palazzi, E., Rangwala, I., Schöner, W., Severskiy, I., Shahgedanova, M., Wang, M.B., Williamson, S.N., Yang, D.Q., 2015. Elevation-dependent warming in mountain regions of the world. *Nat. Clim. Change* 5, 424.
- Pritchard, H.D., 2019. Asia's shrinking glaciers protect large populations from drought stress. *Nature* 569, 649–654. <https://doi.org/10.1038/s41586-019-1240-1>.
- Qixiang, W., Wang, M., Fan, X., 2018. Seasonal patterns of warming amplification of high-elevation stations across the globe. *Int. J. Climatol.* 38, 3466–3473. <https://doi.org/10.1002/joc.5509>.
- Rabatel, A., Francou, B., Soruco, A., Gomez, J., Cáceres, B., Ceballos, J.L., Basantes, R., Vuille, M., Sicart, J.-E., Huggel, C., Scheel, M., Lejeune, Y., Arnaud, Y., Collet, M., Condom, T., Consoli, G., Favier, V., Jomelli, V., Galarraga, R., Ginot, P., Maisincho, L., Mendoza, J., Ménégoz, M., Ramirez, E., Ribstein, P., Suarez, W., Villacis, M., Wagnon, P., 2013. Current state of glaciers in the tropical Andes: a multi-century perspective on glacier evolution and climate change. *Cryosphere* 7, 81–102. <https://doi.org/10.5194/tc-7-81-2013>.
- Schimmelpennig, I., Benedetti, L., Finkel, R., Pik, R., Blard, P.-H., Bourlès, D., Burnard, P., Williams, A., 2009. Sources of in-situ 36Cl in basaltic rocks. Implications for calibration of production rates. *Quat. Geochronol.* 4, 441–461. <https://doi.org/10.1016/j.quageo.2009.06.003>.
- Seltzer, A.M., Ng, J., Aeschbach, W., Kipfer, R., Kulongoski, J.T., Severinghaus, J.P., Stute, M., 2021. Widespread six degrees celsius cooling on land during the last glacial maximum. *Nature* 593, 228–232. <https://doi.org/10.1038/s41586-021-03467-6>.
- Seltzer, A.M., Blard, P.-H., Sherwood, S.C., Kageyama, M., 2023a. Terrestrial amplification of past, present, and future climate change. *Sci. Adv.* 9, eadf8119 <https://doi.org/10.1126/sciadv.adf8119>.
- Seltzer, A.M., Blard, P.-H., Sherwood, S.C., Kageyama, M., 2023b. Terrestrial amplification of past, present, and future climate change. *Sci. Adv.* 9, eadf8119 <https://doi.org/10.1126/sciadv.adf8119>.
- Sepulchre, P., Caubel, A., Ladant, J.-B., Bopp, L., Boucher, O., Braconnot, P., Brockmann, P., Cozic, A., Donnadieu, Y., Dufresne, J.-L., Estella-Perez, V., Ethé, C., Fluteau, F., Foujols, M.-A., Gastineau, G., Ghattas, J., Hauglustaine, D., Hourdin, F., Kageyama, M., Khodri, M., Marti, O., Meurdesoif, Y., Mignot, J., Sarr, A.-C., Servonnat, J., Swingedouw, D., Szopa, S., Tardif, D., 2020. IPSL-CM5A2 – an Earth system model designed for multi-millennial climate simulations. *Geosci. Model Dev. (GMD)* 13, 3011–3053. <https://doi.org/10.5194/gmd-13-3011-2020>.
- Slater, D.A., Felikson, D., Straneo, F., Goelzer, H., Little, C.M., Morlighem, M., Fettweis, X., Nowicki, S., 2020. Twenty-first century ocean forcing of the Greenland ice sheet for modelling of sea level contribution. *Cryosphere* 14, 985–1008. <https://doi.org/10.5194/tc-14-985-2020>.
- Smith, T.M., Reynolds, R.W., 2003. Extended reconstruction of global sea surface temperatures based on COADS data (1854–1997). *J. Clim.* 16.
- Smith, D.M., Screen, J.A., Deser, C., Cohen, J., Fyfe, J.C., García-Serrano, J., Jung, T., Kattsov, V., Matei, D., Msadek, R., Peings, Y., Sigmond, M., Ukita, J., Yoon, J.-H., Zhang, X., 2019. The Polar Amplification Model Intercomparison Project (PAMIP) contribution to CMIP6: investigating the causes and consequences of polar amplification. *Geosci. Model Dev. (GMD)* 12, 1139–1164. <https://doi.org/10.5194/gmd-12-1139-2019>.
- Stansell, N.D., Polissar, P.J., Abbott, M.B., 2007. Last glacial maximum equilibrium-line altitude and paleo-temperature reconstructions for the Cordillera de Mérida, Venezuelan Andes. *Quat. Res.* 67, 115–127. <https://doi.org/10.1016/j.yqres.2006.07.005>.
- Stone, Carlson, P., John, 1979. Atmospheric lapse rate regimes and their parametrization. *J. Atmos. Sci.* 36, 415–423.
- Stute, M., Forster, M., Frischkorn, H., Serejo, A., Clark, J.F., Schlosser, P., Broecker, W.S., Bonani, G., 1995. Cooling of tropical Brazil (5°C) during the last glacial maximum. *Science* 269, 379–383. <https://doi.org/10.1126/science.269.5222.379>.
- Thompson, L.G., Mosley-Thompson, E., Davis, M.E., Brecher, H.H., 2011. Tropical glaciers, recorders and indicators of climate change, are disappearing globally. *Ann. Glaciol.* 52, 23–34. <https://doi.org/10.3189/172756411799096231>.
- Tierney, J.E., Zhu, J., King, J., Malevich, S.B., Hakim, G.J., Poulsen, C.J., 2020. Glacial cooling and climate sensitivity revisited. *Nature* 584, 569–573.
- Tripati, A.K., Sahany, S., Pittman, D., Eagle, R.A., Neelin, J.D., Mitchell, J.L., Beaufort, L., 2014. Modern and glacial tropical snowlines controlled by sea surface temperature and atmospheric mixing. *Nat. Geosci.* 7, 205–209. <https://doi.org/10.1038/ngeo2082>.
- Wang, Q., Fan, X., Wang, M., 2014. Recent warming amplification over high elevation regions across the globe. *Clim. Dynam.* 43, 87–101. <https://doi.org/10.1007/s00382-013-1889-3>.
- Wang, Q., Fan, X., Wang, M., 2016. Evidence of high-elevation amplification versus Arctic amplification. *Sci. Rep.* 6, 19219 <https://doi.org/10.1038/srep19219>.
- Woods, A., Rodbell, D.T., Abbott, M.B., Hatfield, R.G., Chen, C.Y., Lehmann, S.B., McGee, D., Weidhaas, N.C., Tapia, P.M., Valero-Garcés, B.L., Bush, M.B., Stoner, J.S., 2020. Andean drought and glacial retreat tied to Greenland warming during the last glacial period. *Nat. Commun.* 11, 5135. <https://doi.org/10.1038/s41467-020-19000-8>.
- Zekollari, H., Huss, M., Farinotti, D., 2019. Modelling the future evolution of glaciers in the European Alps under the EURO-CORDEX RCM ensemble. *Cryosphere* 13, 1125–1146. <https://doi.org/10.5194/tc-13-1125-2019>.
- Zeng, Z., Wang, D., Yang, L., Wu, J., Ziegler, A.D., Liu, M., Ciais, P., Searchinger, T.D., Yang, Z.-L., Chen, D., Chen, A., Li, L.Z.X., Piao, S., Taylor, D., Cai, X., Pan, M., Peng, L., Lin, P., Gower, D., Feng, Y., Zheng, C., Guan, K., Lian, X., Wang, T., Wang, L., Jeong, S.-J., Wei, Z., Sheffield, J., Caylor, K., Wood, E.F., 2021. Deforestation-induced warming over tropical mountain regions regulated by elevation. *Nat. Geosci.* 14, 23–29. <https://doi.org/10.1038/s41561-020-00666-0>.

Appendix D : Co-atorship : Bekaert, D. V., Blard, P. H., Raoult, Y., Pik, R., Kipfer, R., Seltzer, A. M., Legrain, E. & Marty, B. (2023). Last glacial maximum cooling of 9° C in continental Europe from a 40 kyr-long noble gas paleothermometry record. *Quaternary Science Reviews*, 310, 108123.



Contents lists available at ScienceDirect

Quaternary Science Reviews

journal homepage: www.elsevier.com/locate/quascirev

Last glacial maximum cooling of 9 °C in continental Europe from a 40 kyr-long noble gas paleothermometry record



D.V. Bekaert ^{a, b, *}, P.-H. Blard ^{a, c}, Y. Raoult ^{a, d}, R. Pik ^a, R. Kipfer ^{e, f, g}, A.M. Seltzer ^b, E. Legrain ^h, B. Marty ^a

^a Université de Lorraine, CNRS, CRPG, F-54000, Nancy, France

^b Marine Chemistry and Geochemistry Department, Woods Hole Oceanographic Institution, Woods Hole, MA, USA

^c Laboratoire de Glaciologie, DGES-IGEOS, Université Libre de Bruxelles, 1050, Brussels, Belgium

^d UMR 7619 METIS, Sorbonne Université, 4 Place Jussieu, 75005, Paris, France

^e Institute of Biogeochemistry and Pollutant Dynamics, Department of Environmental Systems Science, Swiss Federal Institute Technology, ETHZ, Zurich, Switzerland

^f Institute of Geochemistry and Petrology, Department of Earth Sciences, Swiss Federal Institute Technology, ETHZ, Zurich, Switzerland

^g Department of Water Resources and Drinking Water, Swiss Federal Institute of Environmental Science and Technology (EAWAG), Dübendorf, CH-8600, Switzerland

^h Université Grenoble Alpes, CNRS, IRD, IGE, Grenoble, France

ARTICLE INFO

Article history:

Received 13 December 2022

Received in revised form

31 January 2023

Accepted 5 May 2023

Handling Editor: Giovanni Zanchetta

Keywords:

Noble gas paleothermometry

Continental Europe

Last glacial maximum

Climate sensitivity

ABSTRACT

The Last Glacial Maximum (LGM; ~26–18 kyr ago) is a time interval of great climatic interest characterized by substantial global cooling driven by radiative forcings and feedbacks associated with orbital changes, lower atmospheric CO₂, and large ice sheets. However, reliable proxies of continental paleotemperatures are scarce and often qualitative, which has limited our understanding of the spatial structure of past climate changes. Here, we present a quantitative noble gas temperature (NGT) record of the last ~40 kyr from the Albian aquifer in Eastern Paris Basin (France, ~48°N). Our NGT data indicate that the mean annual surface temperature was ~5 °C during the Marine Isotope Stage 3 (MIS3; ~40–30 kyr ago), before cooling to ~2 °C during the LGM, and warming to ~11 °C in the Holocene, which closely matches modern ground surface temperatures in Eastern France. Combined with water stable isotope analyses, NGT data indicate δD/NGT and δ¹⁸O/NGT transfer functions of $+1.6 \pm 0.4\text{‰}/^{\circ}\text{C}$ and $+0.18 \pm 0.04\text{‰}/^{\circ}\text{C}$, respectively. Our noble-gas derived LGM cooling of ~9 °C (relative to the Holocene) is consistent with previous studies of noble gas paleothermometry in European groundwaters but larger than the low-to-mid latitude estimate of 5.8 ± 0.6 °C derived from a compilation of noble gas records, which supports the notion that continental LGM cooling was more extreme at higher latitudes. While an LGM cooling of ~9 °C in Eastern France appears compatible with recent data assimilation studies, this value is greater than most estimates from current-generation climate model simulations of the LGM. Comparing our estimate for the temperature in Eastern France during MIS3 (6.4 ± 0.5 °C) with GCM outputs presents a promising avenue to further evaluate climate model simulations and constrain European climate evolution over the last glacial cycle.

© 2023 Elsevier Ltd. All rights reserved.

1. Introduction

Constraining the evolution of past climate is key for evaluating modern estimates of equilibrium climate sensitivity (ECS) and

improving predictions of future climate change. For decades, our understanding of past climate evolution has improved thanks to the analysis of polar ice cores (e.g., [Lorius et al. \(1990\)](#); [Dansgaard et al. \(1993\)](#); [Petit et al. \(1999\)](#)) and oceanic sediment archives (e.g., [McManus et al. \(1999\)](#); [Peterson et al. \(2000\)](#); [Martrat et al. \(2007\)](#)). Both archives have the advantage of providing near continuous high-resolution records of paleoclimatic information. The analysis of air bubbles trapped in ice cores notably helped unraveling the role of CO₂ in driving and/or amplifying global

* Corresponding author. Université de Lorraine, CNRS, CRPG, F-54000, Nancy, France.

E-mail address: david.bekaert@univ-lorraine.fr (D.V. Bekaert).

climate variations (Caillon et al. (2003); Shakun et al. (2012); Parrenin et al. (2013)). However, polar and marine paleoclimate records alone are insufficient to determine the spatial structure of climate changes at Earth's surface, especially on the continents. The development of quantitative proxies of continental paleoclimates is essential to constrain the magnitude and spatial structure of past climate changes in terrestrial regions that are heavily populated today (e.g., Cleator et al. (2020); Seltzer et al. (2021a)).

One of the best-documented, geologically-recent global climate transitions is the last deglaciation, that started ~20 kyr ago, when the Earth transitioned from a ~100 kyr-long glacial period. The last glacial maximum (LGM; ~26 kyr ago if defined by the strict maximum in global ice volume (Grant et al. (2014)) was characterized by low levels of pCO₂ (~185 ppm), which subsequently increased to pre-industrial levels (~280 ppm) in conjunction with rising global temperatures (e.g., Parrenin et al. (2013)). For this reason, paleoclimatologists have long sought to refine estimates of regional temperature changes during the LGM as a way to constrain Earth's ECS. It is however worth noting that the very definition of the LGM may vary slightly across scientific communities. Defining the LGM in a way that integrates constraints from geomorphological records of glaciations, changes in global sea level, and δ¹⁸O signals in the marine record has proven challenging (Clark et al. (2009); Hughes and Gibbard (2015)). Overall, estimates for the timing of the LGM across the globe spread over more than 10 kyr (Shakun and Carlson (2010)), implying that a distinction must often be made between local, regional, and global "LGMs". Here we consider the global LGM period to range from 28 to 23 kyr ago, as defined by (Hughes and Gibbard (2015)) as the maximum of global ice volume and atmospheric dust concentration.

Recent data assimilation studies of the LGM have incorporated large collections of sea surface temperature (SST) proxy to simulate the spatial distribution of surface temperature changes since the global LGM (Tierney et al. (2020); Osman et al. (2021)). As a way to assess the validity of the simulation outputs, these results are compared with independent ice core and speleothem δ¹⁸O data (Tierney et al. (2020)). Although many terrestrial paleoclimate archives exist (e.g., fossil pollen records (Bartlein et al. (2011); Cleator et al. (2020)), speleothems (James et al. (2015)), glacier equilibrium lines (e.g., Porter (2000); Martin et al. (2020)), noble gases in groundwater (Stute et al. (1995)), these have been largely overlooked in most data assimilation studies, leading to large uncertainties about the magnitude and dynamics of past climate changes in populated regions. The main reason for ignoring these paleoclimate proxy data is that most of them do not provide quantitative, reliable, and spatially-distributed estimates of past temperatures.

In multiple regions of the globe, existing LGM paleotemperature records from terrestrial proxies exhibit disagreements potentially attributed to proxy specific biases. At low elevation, historical pollen data have for instance been used to suggest a tropical cooling ≤3 °C during the LGM (e.g., Bartlein et al. (2011)), whereas noble gas abundances in groundwater indicate a larger LGM tropical cooling of 5.8 ± 0.6 °C (Stute et al. (1995); Seltzer et al. (2021a)). At higher elevations (>3000 m), LGM glacier equilibrium lines (Porter (2000); Blard et al. (2007)) and organic matter in lakes (Loomis et al. (2017)) also suggest large tropical cooling, from ~6 to 9 °C. These apparent discrepancies could potentially reflect an amplification of LGM cooling (and thus, of equilibrium warming) with altitude (lapse rate) or distance from the shoreline (continental amplification). Loomis et al. (2017) for instance proposed that their estimate of LGM tropical cooling from organic matter in lakes could be compatible with a ~2 °C LGM cooling at low elevation (i.e., sea level), consistent with pollen paleoclimatic records (Bartlein et al. (2011)). Such a low estimate of LGM tropical cooling at low

elevation is however inconsistent with most noble gas reconstructions (Seltzer et al. (2021a)). Recently, Cleator et al. (2020) presented a new global reconstruction of LGM seasonal climates using data assimilation of pollen records with the ensemble average of the PMIP3—CMIP5 simulations. This new reconstruction yielded a larger tropical LGM cooling (~4.7 °C) than previous pollen-based reconstructions (Bartlein et al. (2011)), in closer agreement with independent constraints from noble gas records (Seltzer et al. (2021a)). The same potential complications of proxy specific biases and vertical or continental amplifications of equilibrium warming arise for the mid-to high-latitude regions, where estimates of LGM cooling are even more variable than in the tropics (Seltzer et al. (2021a)). While the polar amplification of climate change is a robust feature of model simulations (e.g., Holland and Bitz (2003); Pithan and Mauritsen (2014)) and data (Tierney et al. (2020)), the cause(s) and latitudinal extent of polar amplification remain debated (Stuecker et al. (2018)). These considerations underline a crucial need for robust paleotemperature reconstructions of glacial cooling at mid-to high latitudes, in the continental realm.

Due to their temperature-dependent solubilities in water and insensitivity to biological and chemical processes, noble gases dissolved in ancient groundwater have long been recognized as a reliable archive of past climates, with a well established, quantitative link to past land surface temperatures (e.g. Aeschbach-Hertig et al. (2000); Mazor (1972); Stute et al. (1995); Loosli et al. (2001); Aeschbach-Hertig and Solomon (2013)). Today, about a third (27.0–36.3%) of Earth's land area is estimated to hold LGM-aged groundwater (Befus et al. (2017)). By applying a physical recharge model that account for both the temperature-dependent solubility equilibrium between air and water, as well as bubble injection and partial dissolution (Ingram et al. (2007)), measured noble gas concentrations can be interpreted with an inverse model to quantitatively reconstruct past Mean Annual Surface Temperatures on land (MAST, (Aeschbach-Hertig and Solomon (2013)). Here, we present a brief summary of the noble gas thermometry approach, and report a new ~40-kyr long noble gas record of past MAST from the Albian aquifer of the Paris Basin, in Eastern France. We use these new data to discuss the spatial gradients of equilibrium warming across Western Europe (as a function of altitude, latitude, and distance from the shore), and to assess the capability of atmospheric global climate model (GCMs) to reproduce past LGM conditions.

2. Material and methods

2.1. Noble gas thermometry

The early recognition that the stable isotope composition of water molecules in rainwater (i.e., δ¹⁸O and δD) depends on several climatic factors, including air temperature, rain amount, altitude, and latitude of precipitations (e.g., Craig (1961)) paved the way for isotope hydrology and hydroclimatology. Dissolved atmospheric neon (Ne), argon (Ar), krypton (Kr) and xenon (Xe) concentrations in groundwater have long been recognized as reliable proxies of past climate, with a physics-based link to past land surface temperature (e.g. Mazor (1972); Stute et al. (1995); Loosli et al. (2001); Seltzer et al. (2021a)). Because atmospheric noble gases are inert and lack appreciable sinks or sources, their concentrations in fresh water at solubility equilibrium reflect well-understood physical constants that primarily depend on temperature, barometric pressure, and "additional" dissolved noble gases acquired by bubble entrainment and dissolution during recharge (referred to as "excess air" or "ΔNe", because neon is a sensitive indicator of excess air dissolution owing to its low solubility (Andrews and Lee (1979); Heaton and Vogel (1981); Klump et al. (2008)). Owing to the

attenuation of seasonal temperature fluctuations in soil with depth, typical temperatures at the water table (that is, the upper surface of the saturated zone) closely match MAST (Aeschbach-Hertig and Solomon (2013)). In most cases, MAST appear to be 1–2 °C warmer than Mean Annual surface Air Temperatures (MAAT) (Seltzer et al. (2021a)), with slight decoupling notably arising at high latitudes due to changes in snow cover or vegetation (e.g., Stute and Sonntag (1992)). However, changes in MAST and MAAT can be reasonably assumed to be of equal magnitudes, such that $\Delta\text{NGT}_{\text{LGM}}$ are directly comparable to MAAT changes since the LGM.

When groundwater is isolated from soil air by subsequent recharge or flow beneath a confining layer, dissolved noble gases are preserved. Because they lack subsurface sources or sinks, the concentrations (of Ne, Ar, Kr, and Xe) are preserved after the time of recharge and affected only by dispersive mixing and advection. Unlike stable noble gases, atmosphere-derived radioactive isotopes in groundwater will decay according to their respective half-lives (e.g. $t_{1/2} (^{14}\text{C}) = 5730 \text{ yr}$), providing a way to determine both (i) the “age” of groundwater recharge from the activities of radioactive species, and (ii) the noble gas temperatures (NGT) from bulk noble gas concentrations. Although the 5730 year half-life of ^{14}C and the ubiquity of carbon in groundwater make it a powerful - and widely applied - age tracer on the timescale of ~1000 to ~40 000 years, the potential for hydrogeochemical reactions and physical processes to alter measured ^{14}C activities (Geyh (2000)) require caution when interpreting ^{14}C -dated sample chronologies.

Over the past ~40 yr, multiple noble gas studies have aimed at (i) improving numerical approaches to deconvolve “excess air” and “equilibrium” (i.e., temperature) signals in groundwater data, and (ii) reconstructing glacial/interglacial NGT changes across the continents (e.g., Edmunds and Milne (2001); Corcho Alvarado et al. (2011); Seltzer et al. (2021a) and references therein). Multiple conceptual models (e.g., unfractionated air (UA) (Heaton and Vogel (1981)), partial re-equilibration (PR) (Stute et al. (1995)), and oxygen depletion (OD) (Hall et al. (2005))) have been proposed to account for the variable compositions of soil air and excess air at the water table, including the variable extents of air entrapment and bubble dissolution during recharge (Klump et al. (2008)). Today, however, it is the so-called closed-system equilibration (CE) model (Aeschbach-Hertig et al. (2000)), whereby water table fluctuations entrain bubbles of soil air that partially dissolve under elevated hydrostatic pressure at solubility equilibrium, that has been established as the most robust and reliable approach (Kipfer et al. (2002); Aeschbach-Hertig and Solomon (2013)). Using late Holocene groundwater noble gas data from 30 study areas worldwide, Seltzer et al. (2021a) showed that CE model NGTs closely match modern ground surface and shallow groundwater temperature measurements, further demonstrating the robustness of this approach to using groundwater noble gases as an unbiased palaeothermometer.

2.2. Groundwater sampling of the Albian aquifer

The Albian aquifer of the Paris Basin (France), which has been exploited since 1841, shows drastic drawdown with a clear cone of piezometric depression near the Paris region, where $\sim 23 \times 10^6 \text{ m}^3$ of water are extracted every year for human use (cumulative volume abstraction of $>450 \times 10^6 \text{ m}^3$ over the period 1841–1935; Contoux et al. (2013)), among which ~80% are for domestic/human use. Water parcels from several flowlines converge towards this zone, where they mix with the underlying aquifer of Neocomian age (Fig. 1). More generally, the Albian aquifer consists of alternating layers of sand and clays, with a total porosity between 3% and 35% (average 25%) and a kinematic porosity – i.e., the porosity

that actually contributes to the flow network – around 15%. The rate at which groundwater can flow through the Albian aquifer (referred to as transmissivity) has been previously estimated to be in the range $[3.2\text{--}7.2] \times 10^{-5} \text{ m}^2/\text{s}$ (Raoult (1999)).

Water samples from the Albian aquifer have been collected in the late 1990s, in the frame of the Raoult et al. (1998) project. We present here the results from water samples collected in 17 wells distributed along a South–North/West transect of the Paris Basin (average recharge elevation of 270 m), parallel to the sub-horizontal flowlines of the aquifer (Fig. 1). Two samples (Ns1 and Ns2) originate from the Neocomian aquifer, and two others (Cs1 and Cs2) originate from a shallower aquifer associated with chalk Raoult (1999)). All of the other samples originate from the Albian aquifer. Water samples dedicated to radiocarbon (^{14}C) dating were prepared by precipitating carbonates (CaCO_3 and BaCO_3 , via BaCl_2 addition) from 80 L water containers, previously set at pH = 12 by NaOH addition. Radiocarbon activity was then measured using a conventional liquid scintillation analyzer; all ^{14}C ages were here calibrated using the most recent IntCal20 calibration curve (Reimer et al. (2020)). $\delta^{13}\text{C}$ was measured from CO_2 released under vacuum from 100-mL water samples via addition of H_3PO_4 . Radiocarbon and $\delta^{13}\text{C}$ were measured at the Center de Recherches Géodynamiques (Thonon-les-Bains, France) following the procedure described by Olive (1999). $\delta^{18}\text{O}$ and δD values were determined at the Laboratoire de Biochimie isotopique (Université Paris VI) following procedures described by Gat and Gonfiantini (1981) and Coleman et al. (1982), respectively. Water samples collected in 3/8” copper tubes were analyzed at ETH Zurich for noble gas abundance determination (i.e., ^3He , ^4He , ^{20}Ne , ^{36}Ar , ^{40}Ar , ^{84}Kr , ^{132}Xe), following the procedure described by Weyhenmeyer et al. (2000). The conversion of noble gas abundances in groundwater into past temperatures was carried out assuming the closed-system equilibration (CE) model using the software PANGA (Jung and Aeschbach (2018)), and compared to results from a recent approach by Seltzer et al. (2021a).

3. Results

All data (^{14}C , δD , $\delta^{18}\text{O}$, noble gases, computed recharge paleo-temperature) are reported in Tables S1–S5. The spatial distribution of ^{14}C activity within the Albian aquifer indicates that water parcels range in age from ~40 kyr ago (near the detection limit of radiocarbon) down to present-day (~90 pmc) with a general decrease of ^{14}C activity towards the center of the Paris Basin (Raoult et al. (1998)), consistent with previous ^{14}C measurements of the Albian aquifer (Vuillaume (1971)) and hydrological models of the Paris Basin (Castro et al. (1998)). The absence of notable $\delta^{13}\text{C}$ variations across all of our samples as well as their negative values well below 0‰ VPDB (with most data falling within the range of –15‰ to –10‰ VPDB) indicates that no significant correction for dead carbon input via carbonate dissolution is required in the present case (Fig. 2a). In detail, the highest DIC concentrations and highest $\delta^{13}\text{C}$ values appear in samples with the highest ^{14}C activities (Table S4). Among older samples, the lack of apparent trend in either DIC nor $\delta^{13}\text{C}$ with ^{14}C activity (Fig. S5) indicates that (a) input of ^{14}C -free DIC is not a major concern for dating, and (b) the younger groundwaters likely have a distinct source of DIC than groundwater samples from the Albian aquifer (perhaps from agricultural influence via seepage of irrigation water to shallow groundwater; e.g., Seltzer et al. (2021b)). However, if the addition of ^{14}C -free DIC was biasing ^{14}C ages towards low values in the Albian aquifer, then the highest DIC should be associated with the oldest samples, which is not observed (Fig. S5). Thus, there is no basis for making a correction for dead carbon addition in the present case.

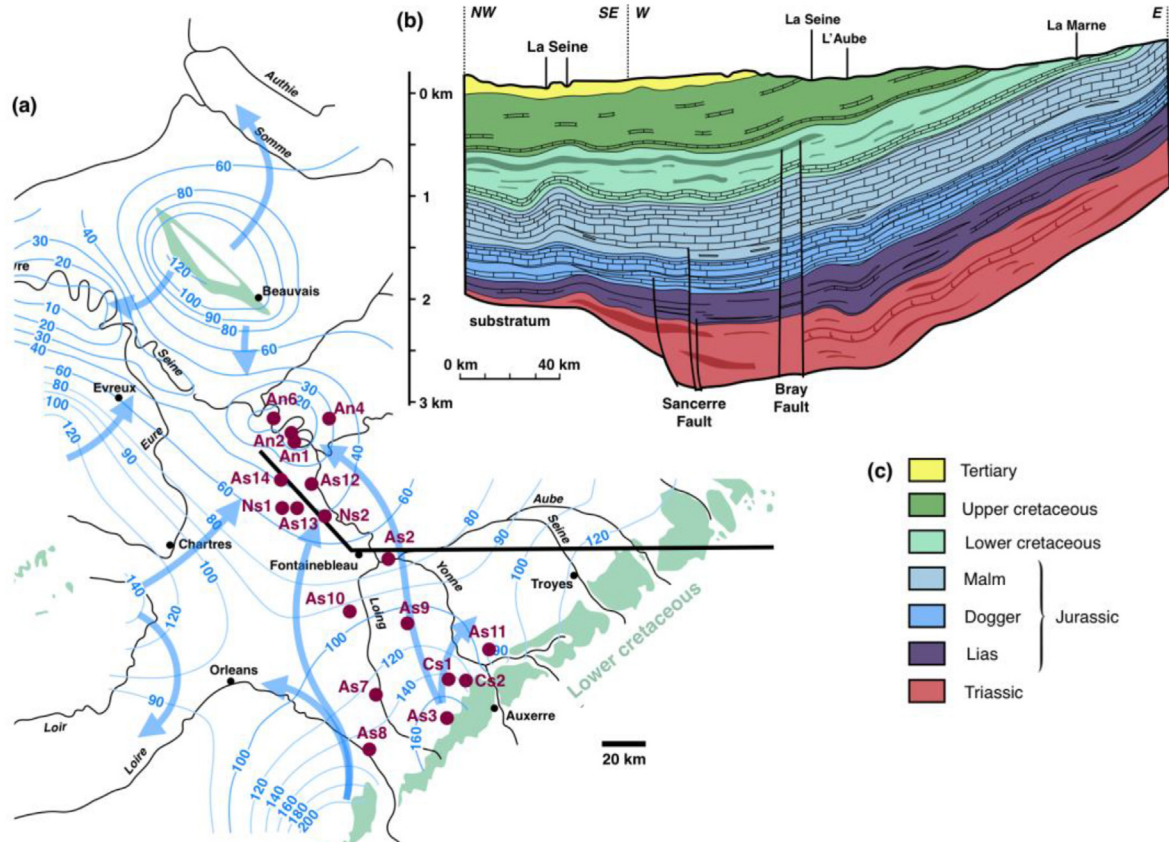


Fig. 1. Location of groundwater sampling sites in the Paris Basin. (a) Piezometric map of the Paris Basin showing the flowlines in the confined Albian aquifer (cretaceous inf.) and piezometric contour (given in meters below surface). Sample names correspond to: A = Albian, N = Neocombian, C = “chalk”, s = South, n = North. (b) Cross section of the Paris Basin (broadly following the cross section profile reported on panel (a)). (c) Stratigraphic levels represented on the cross section of panel (b). The Albian aquifer is located on the upper part of the Lower cretaceous. Adapted from Raoult (1999).

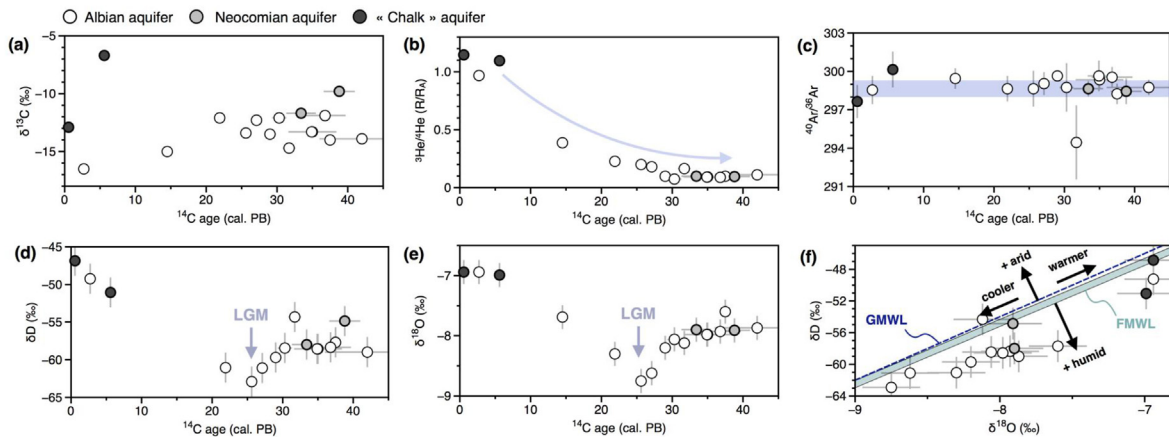


Fig. 2. Evolution of geochemical parameters in the Albian aquifer, as a function of ^{14}C age. Evolution of $\delta^{13}\text{C}$ (‰ VPDB) (a), He isotope ratios (b) (here given as R/R_A , where R and R_A correspond to the $^3\text{He}/^4\text{He}$ of the sample and atmosphere, respectively; Boucher et al. (2018)), $^{40}\text{Ar}/^{36}\text{Ar}$ (c), δD (‰ SMOW) (d) and $\delta^{18}\text{O}$ (‰ SMOW) (e), as a function of calibrated ^{14}C age. (f) Groundwater stable isotope composition relative to the Global Meteoritic Water Line (GMWL) and French Meteoritic Water Line (FMWL) (Millot et al. (2010)).

The absence of evidence for dead carbon input via carbonate dissolution in the Albian aquifer is notably consistent with the paucity of carbonated lithologies within this aquifer.

The decreasing He isotope ratios of groundwater as a function of ^{14}C age (from $R/R_A \sim 1$ down to ≤ 0.1 , where R and R_A correspond to the $^3\text{He}/^4\text{He}$ of the sample and atmosphere, respectively; Boucher et al. (2018)) reflects the progressive addition of radiogenic ^4He from U–Th decay along the water flowline (Fig. 2b). Conversely, the

absence of significant $^{40}\text{Ar}/^{36}\text{Ar}$ evolution as a function of ^{14}C age indicates that, if present, the potential effect of $^{40}\text{Ar}^*$ additions from ^{40}K decay is here below detection (Fig. 2c). The evolutions of δD (Fig. 2d) and $\delta^{18}\text{O}$ (Fig. 2e) as a function of ^{14}C age indicates that groundwater parcels analyzed in this study hold a paleoclimatic signal, with lighter $\delta^{18}\text{O}$ and δD in the glacial period relative to the Holocene, and the lowest values corresponding to the LGM. The stable isotope compositions of Albian groundwater plot very close

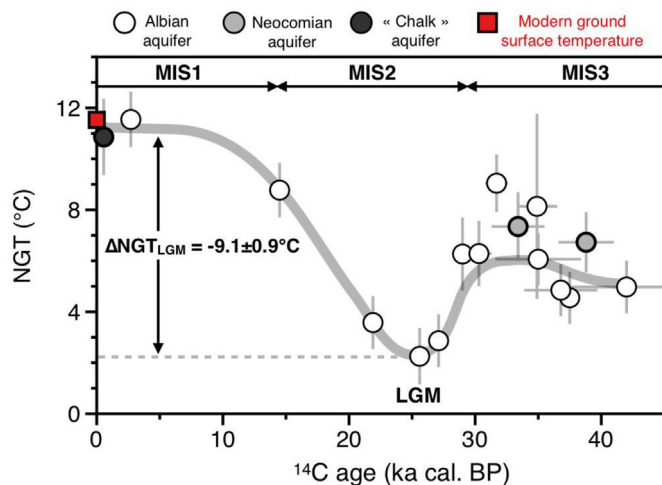


Fig. 3. Noble gas paleotemperature (NGT) computed using the closed-system equilibration (CE) model, a function of ^{14}C age (in kyr ago cal. BP). The NGT record depicts a clear temporal trend, from ~ 5 °C between 42 and 30 kyr ago down to ~ 2 °C between 28 and 25 kyr ago, and then up to a steady ~ 11 °C for the last 10 kyr (in excellent agreement with the average modern (1950–2019) ground surface temperature (red square) of 11.53 °C in Eastern France, as derived from ERA5-Land reanalysis (Hersbach et al. (2020))). The $\Delta\text{NGT}_{\text{LGM}}$ of -9.1 ± 0.9 °C is computed following approach by Seltzer et al. (2021a). Recharge elevation for PANGA calculations is taken at 271 m (i.e., $P = 0.9680$ atm). NGT reconstructions using the UA model are given for comparison in Fig. S1.

to the Global Meteoritic Water Line (GMWL) and French Meteoritic Water Line (FMWL) (Millot et al. (2010)), indicating limited – if any – evaporative loss, in line with a meteoritic origin of groundwater in the Albian aquifer (Innocent et al. (2021)).

Noble gas paleotemperatures (NGT) computed with the CE model using the software PANGA (Jung and Aeschbach (2018)) show a clear temporal trend (Fig. 3) that mimics the evolutions of δD (Fig. 2d) and $\delta^{18}\text{O}$ (Fig. 2e), from consistent NGTs ~ 6 °C between 42 and 30 kyr ago (i.e., during the Marine Isotope Stage 3, MIS3) down to ~ 2 °C between 28 and 25 kyr ago (MIS2), and then up to a steady ~ 11 °C for the last ~ 10 kyr (Fig. 3). These Holocene temperatures are in excellent agreement with the average modern (1950–2019) ground surface temperature of 11.53 °C in Eastern

France, as derived from ERA5-Land reanalysis (Hersbach et al. (2020)). However, we note that two samples analyzed in this study appear to have been affected by degassing, as reflected in the occurrence of F values $\gg 1$ (Table S6). In the CE model, the dimensionless parameter F (also referred to as the “fractionation parameter”) corresponds to the ratio between B (the final trapped gas to water volume ratio) and A (the volume ratio of air entrapped in the groundwater in the recharge zone to water) (e.g., Aeschbach-Hertig and Solomon (2013)). Hence, the model describes excess air for $F < 1$ and degassing for $F > 1$. While several samples reported in this study yield F values < 1 , potentially attributed to the occurrence of excess air, the conspicuous occurrence of degassing in several samples prevents interpretation of potential excess air signatures. However, the observation that, despite their variable F values (Table S1), samples of similar ages yield consistent NGTs (Fig. 3) indicates that NGT reconstructed in this study are not significantly affected by degassing or potential excess air corrections.

4. Discussion

4.1. Comparison with previous NGT reconstructions in Europe

Our data indicate that the LGM in Eastern France was characterized by a MAST cooling ($\Delta\text{NGT}_{\text{LGM}}$) of about -9 °C, similar to the glacial cooling of -8.4 ± 1.1 °C recorded in Belgian groundwater (Blaser et al. (2010); Fig. 4d). To date, $\Delta\text{NGT}_{\text{LGM}}$ reconstructions in Europe have shown significant variability, with for instance lower $\Delta\text{NGT}_{\text{LGM}}$ in Portugal (-5.9 ± 1.6 °C, De Melo Condesso et al. (2001); Fig. 4c) and England (-5.9 ± 1.1 °C, Andrews and Lee (1979); Fig. 4d) compared to “continental” Europe (Seltzer et al. (2021a)). Although Portugal and England are further South and West than Eastern France, respectively, these discrepancies could reflect spatial gradients of LGM cooling, controlled at the first-order by a continental amplification of equilibrium warming at increasing distances from the shoreline (e.g., Sutton et al. (2007); Byrne and O’Gorman (2018)). However, gaps in recharge during cold periods of permafrost have been suggested for the England record (Andrews and Lee (1979)), implying that the true LGM cooling for this region may be greater than 6 °C. Two paleo-reconstructions of NGT from Hungary also yielded contrasted $\Delta\text{NGT}_{\text{LGM}}$ (-6.5 ± 0.9 °C and -9.2 ± 1.0 °C; values recently updated by Seltzer et al. (2021a) using the datasets

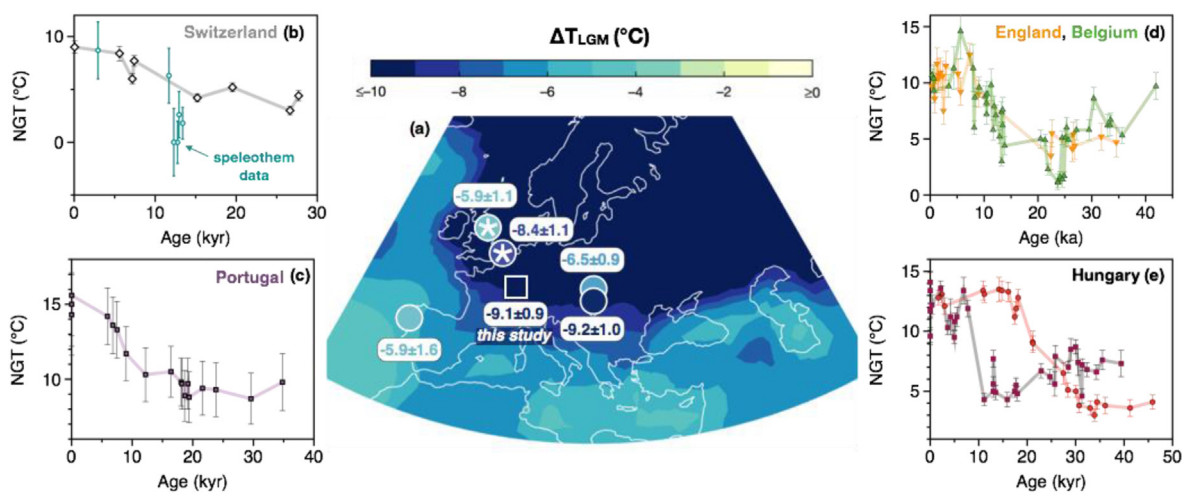


Fig. 4. NGT reconstructions across Europe and comparison of corresponding $\Delta\text{NGT}_{\text{LGM}}$ with results from the data assimilation results of Tierney et al. (2020) plotted using the MATLAB Mapping Toolbox following Seltzer et al. (2021a). Asterisks indicate sites with LGM recharge gaps, which coincide with the lateral extent of the LGM ice sheet (Stadelmaier et al. (2021)). NGT records from (b) Switzerland groundwater (Beyerle et al., 1998) and speleothem data (Ghadiri et al. (2018)) (c) Portugal (De Melo Condesso et al. (2001)), (d) England (Andrews and Lee (1979)) and Belgium (Blaser et al. (2010)), and (e) Hungary (Stute and Deak (1989); Varsányi et al. (2011)).

of Varsányi et al. (2011) and Stute and Deak (1989), respectively) as well as very different deglaciation timelines (Fig. 4e), emphasizing potential methodological bias, or more probably, issues with age models (Varsányi et al. (2011)). Overall, a LGM cooling of about -7 to -9 °C has been found previously by noble gas studies in Hungary, comparable to the magnitude of glacial cooling found in Belgium and Eastern France. Although more observations are required to draw a definitive conclusion, this dataset suggests a limited effect of continental amplification across central Europe.

Determining $\Delta\text{NGT}_{\text{LGM}}$ in Switzerland (intermediate location between Belgium-France and Hungary) has proven challenging given the difficulties in identifying LGM groundwaters in this mountainous area (Beyerle et al. (1998)) (Fig. 4b). Over the last decades, important analytical efforts have been achieved to extract and quantify noble gases from speleothem fluid inclusions, and derive NGTs (proxy of cave temperature) with a similar precision to groundwater data (after deconvolution of air-filled vs. water-filled inclusion signals) (e.g., Kluge et al. (2008); Vogel et al. (2013)). This promising approach enabled NGT's application to Holocene stalagmites in Switzerland for paleo-temperature reconstructions (e.g., Ghadiri et al. (2018), Fig. 4b) and investigations of past temperature–altitude gradients (Ghadiri et al. (2020)). Applying this technique to LGM-aged speleothems is a promising approach that could better constrain the amplitude of glacial cooling in the continental realm, at higher altitudes than groundwater noble gas data.

4.2. Comparison with other paleoclimate proxy data

A $\Delta\text{NGT}_{\text{LGM}}$ of about -9 °C in Eastern France is consistent with pollen-stratigraphic records from La Grande Pile and Les Echets (-10 ± 2 °C, Eastern France; Guiot et al. (1989)), as well as with the -7.8 to -11 °C cooling derived from inversion of the paleo-ice extent over the European Alps during the LGM (Višnjić et al. (2020)). Since our NGT record reflects temperatures of <500 m elevation, the agreement with glacier equilibrium line temperatures (reflecting paleoclimate at altitudes >1000 m) is a particularly interesting observation, as it would suggest a preservation of the vertical temperature gradient (i.e., the lapse rate) during the LGM, in Western Europe. However, this conclusion should be considered with caution given the relatively small altitudinal range covered by these two records. Systematic comparisons between low- and high-altitude paleotemperature reconstructions are required to determine whether the lapse rate was steeper during the LGM (i.e., amplification of glacial cooling with altitude (Blard et al. (2007); Loomis et al. (2017)), or indeed similar to present-day (Tripathi et al. (2014); Banerjee et al. (2022)). Remarkably, a $\Delta\text{NGT}_{\text{LGM}}$ of -9 °C for Eastern France appears in line with recent data assimilation studies that developed field reconstructions of global LGM temperatures (Tierney et al. (2020)) from a large collection of geochemical paleo-SST proxies (Fig. 4). This finding potentially extends the low-to-mid latitude ($<30^\circ\text{N}$) terrestrial proxy support for this recent SST-based simulation (Seltzer et al. (2021a)) to high latitude continental lands, like Eastern France. Including continental ΔT_{LGM} records (such as NGTs) in future efforts to synthesize global proxy data and simulate climate changes since the LGM (Tierney et al. (2020)) is a promising opportunity to assess and improve our understanding of terrestrial climate dynamics.

4.3. Temperature sensitivity of water stable isotopes and D-excess

The temporal evolution of NGT derived for the Albian aquifer using the CE model (Fig. 3) broadly mimics the evolutions of δD (Fig. 2d) and $\delta^{18}\text{O}$ (Fig. 2e), suggesting that these can be interpreted altogether in order to document past climates (Fig. 5). Variations in

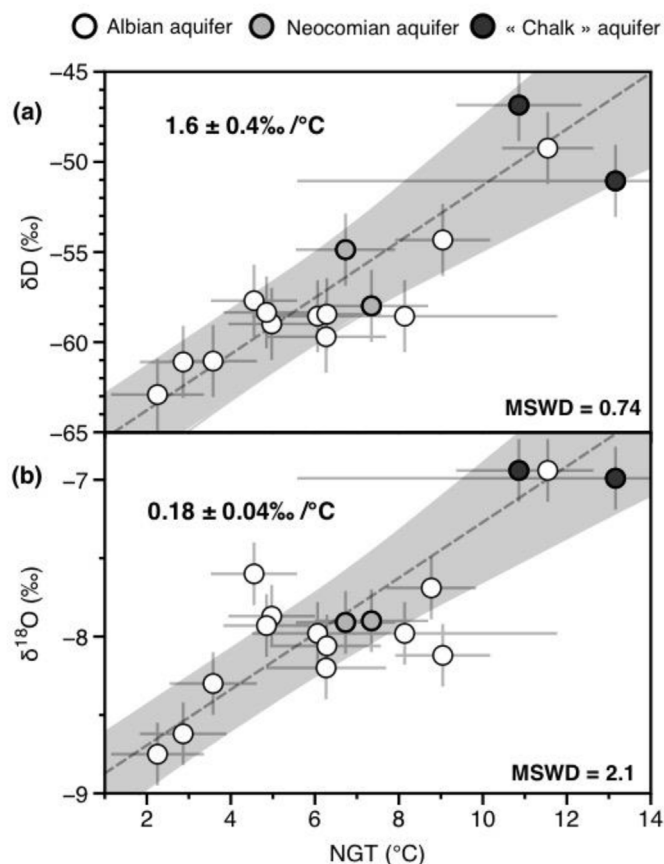


Fig. 5. δD and $\delta^{18}\text{O}$ as a function of NGT. Linear regressions ($\delta\text{D} = (1.6 \pm 0.4) \times \text{NGT} - (66.9 \pm 2.5)$ and $\delta^{18}\text{O} = (0.18 \pm 0.04) \times \text{NGT} - (9.1 \pm 0.3)$) were computed using the error weighted least squares algorithm of York et al. (2004).

the stable isotopes of water are however challenging to interpret by themselves as they may reflect multiple processes, including changes in temperature, moisture source(s), evaporation rates, precipitation amount, and atmospheric convection, which may all vary seasonally, annually and spatially (e.g., Dansgaard (2012); Rozanski et al. (1992); Araguás-Araguás et al. (2000)). Here, we observe that NGTs are linearly correlated with both δD (Fig. 5a) and $\delta^{18}\text{O}$ (Fig. 5b), indicating that temperature (rather than precipitation amount) is likely to be the main parameter controlling the evolution of water stable isotopes in Eastern France since the LGM. Although the exact series of mechanisms linking water stable isotope variations in precipitations to local temperature (as well as spatial temperature gradients) remain complex, the strong correlations between NGTs and water stable isotopes since MIS3 potentially open the door to using water stable isotope variations in precipitation as an empirical paleothermometer in other paleoclimate studies (e.g., using lake sediment archives (Leng and Marshall (2004))). Here, we compute linear $\delta\text{D}/\text{NGT}$ and $\delta^{18}\text{O}/\text{NGT}$ transfer functions of $+1.6 \pm 0.4$ ‰/°C and $+0.18 \pm 0.04$ ‰/°C, respectively. On the one hand, these values are markedly lower than those that have been previously considered to calculate paleotemperatures from the analysis of water stable isotope in speleothems fluid inclusions from Central Europe (2.88 – 4.80 ‰/°C for δD and 0.36 – 0.60 ‰/°C for $\delta^{18}\text{O}$; Affolter et al. (2019)). These $\delta^{18}\text{O}/\text{NGT}$ transfer functions were derived by comparing $\delta^{18}\text{O}$ in modern precipitation and corresponding temperature time series for the Global Network of Isotopes in Precipitation stations in Basel (1986–2017) and Bern (1971–2017), and then considering

equilibrium fractionation factor of eight to transpose $\delta^{18}\text{O}$ in δD values (Affolter et al. (2019)). On the other hand, the $\delta^{18}\text{O}/\text{NGT}$ derived in this study is markedly greater than the transfer function of $0.0708 \pm 0.0034\text{‰}/^\circ\text{C}$ computed from the paleoclimate data assimilation outputs of Osman et al. (2021) for the grid cell corresponding to our study area (Lat: 48.3, Lon: 5), over the last 23.9 kyr (Fig. S2). These discrepancies underline the fact that the exact temperature sensitivity of water stable isotopes in precipitations remains underconstrained, hence calling for extra caution when using $\delta^{18}\text{O}$ as a quantitative paleothermometer (Affolter et al. (2019)). Importantly, we note that changes in the seasonality between the last glacial period and the present day may have modified the transfer functions between water stable isotopes and temperature. For instance, an enhanced seasonality during the LGM in comparison to the late Holocene (Ford et al. (2015)) would cause winter precipitations to become a relatively smaller contributor to annual precipitations, thus affecting the slope of the $\delta^{18}\text{O}/T$ relationship and biasing the weighted annual mean $\delta^{18}\text{O}$ of paleowaters towards the (higher) $\delta^{18}\text{O}$ of summer precipitations.

At last, since δD and $\delta^{18}\text{O}$ are highly correlated with temperature and with one another in our study (Figs. 2 and 5), the deuterium excess ($\text{D-excess} = \delta\text{D} - 8 \times \delta^{18}\text{O}$) appears rather invariant in time (Fig. S3), consistent with previous comparisons of water isotope systematics in modern infiltration waters and in old groundwaters in Western and Central Europe (e.g., Rozanski (1985)). Because D-excess is typically used as an indicator of both the source of precipitation and the conditions during vapor transport (e.g., Froehlich et al. (2002)), a constant D-excess excess over the last ~40 Myr is indicative of no major change in the moisture source of precipitations over the study area since the last glacial period.

4.4. Comparison with global Climate model outputs

SST changes since the last glacial cycle are rather well documented (e.g., Ho and Laepple (2015)), with different temperature proxies yielding quite comparable LGM cooling from 2 °C (under the tropics) down to 5 °C at high latitudes. As discussed in this study, in-land proxies of paleotemperatures since the LGM suggest significant on land variability, and so the spatial evolution of equilibrium warming on the continental realm remains shrouded in uncertainty. Recently, a new generation of global climate models has been used to generate LGM simulations in the Paleoclimate Modelling Intercomparison Project (PMIP 4) contribution to the Coupled Model Intercomparison Project (CMIP) (Kageyama et al. (2021)). Most of these GCM experiments (as well as previous generation of simulations) yield significantly warmer LGM temperatures in Eastern France (48°N, 4°E) than our $\Delta\text{NGT}_{\text{LGM}}$ reconstruction (Fig. 6). Four models (HadCM3-PMIP3, CESM1-2, INM-CM4-8, HadCM3-ICE6GC) are however compatible within error with our $\Delta\text{NGT}_{\text{LGM}}$ of -9.1 ± 0.9 °C (Fig. 6), suggesting that these models may most accurately simulate Western Europe's surface temperatures during the LGM. We speculate that these four models provide the best estimates of future equilibrium warming in this region of the globe. In line with previous conclusions from Zhu et al. (2021), the CESM2-1 model provides an unreasonably large LGM cooling in Eastern Europe (about -20 °C), most likely as a result of a too strong shortwave cloud feedback. As such, the projected future warming in CESM2 (and models with a similarly high equilibrium warming) is likely too large. Direct comparisons between several types of paleoclimate proxies and outcomes of GCM models (as proposed in this study) is a consistent way to evaluate climatic models and their ability to describe past, present, and future climates, including both temperatures and precipitations.

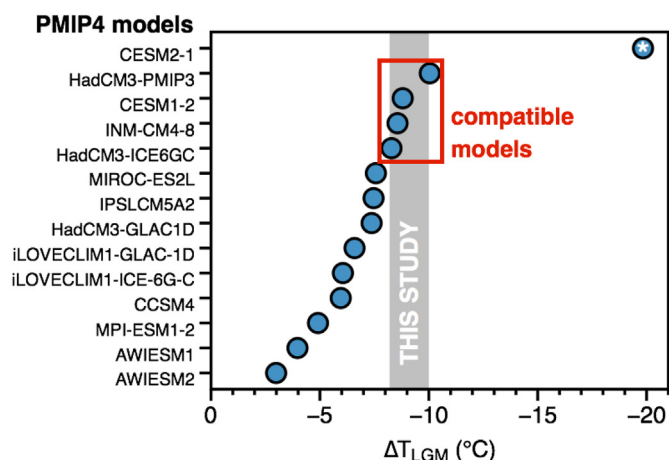


Fig. 6. Comparison of PMIP4 estimates of Eastern France (48°N, 4°E) LGM cooling with our $\Delta\text{NGT}_{\text{LGM}}$ of the Albian aquifer. While most of the PMIP4 models (Kageyama et al. (2021); <http://dods.lscce.ipsl.fr/pmip4/db/>) predict lower ΔT_{LGM} than observed in the present study, four models (HadCM3-PMIP3, CESM1-2, INM-CM4-8, HadCM3-ICE6GC) appear compatible with our noble gas data. The CESM2-1 model (marked with an asterisk) provides an unreasonably high estimate of LGM cooling in Eastern Europe (-20 °C), consistent with previous findings that this model likely overestimates the amount of equilibrium warming at Earth's surface (Zhu et al. (2021)).

4.5. Quantification of European temperatures during MIS3

In addition to providing important insight into $\Delta\text{NGT}_{\text{LGM}}$, the noble gas record of the Albian aquifer offers a rare opportunity to constrain European temperatures during MIS3 (between 29 and 42 kyr ago in this dataset). Accurate ^{14}C dating of groundwaters over such timescales is challenging. However, the observation that significant ^4He excesses from U–Th decay (computed as the measured ^4He concentration minus the equilibrium ^4He concentrations obtained from the CE model) are only observed in samples with ^{14}C ages older than 26 kyr ago is an independent, empirical confirmation that these samples are indeed significantly older than Holocene ones (Fig. S4).

During the last glacial period, the North Atlantic region experienced abrupt, north-to-south Dansgaard–Oeschger (DO) climatic oscillations that affected both atmosphere and ocean global circulations (e.g., Andersen et al. (2004)), but whose cause(s) and dynamics remain largely uncertain (e.g., Capron et al. (2021)). These abrupt and potentially globally distributed events have been previously observed during MIS3 in Greenland ice core data (Buizert et al. (2015)), marine sediments from the Atlantic Ocean (e.g., Peterson et al. (2000); Martrat et al. (2007); Deplazes et al. (2013)), and speleothem records (e.g., Wang et al. (2006); Fig. 7). In western continental Europe, DO events have been qualitatively recorded in speleothems (Genty et al. (2003)), lake sediments (Thouveny et al. (1994)), and paleosols-loess sequences (Moine et al. (2017)). In principle, we cannot exclude the possibility that some NGTs recorded here during MIS3 (Fig. 3) are also affected, to some extent, by the influence of DO events. This may, at least in part, explain the slight variability of NGTs between ~29 and 42 kyr-old, with for instance the highest NGT (at ~32 kyr ago) corresponding to the # 5.2 DO event recorded in other paleoclimate archives (Fig. 3). However, high frequency (DO-like) climatic signals are highly unlikely to be preserved in ancient groundwater parcels due to the dispersive and advective nature of mixing during storage at depth. For a typical groundwater dispersivity of 100 m²/yr and velocity of 1 m/s (Stute and Schlosser (1993)), the e-folding attenuation

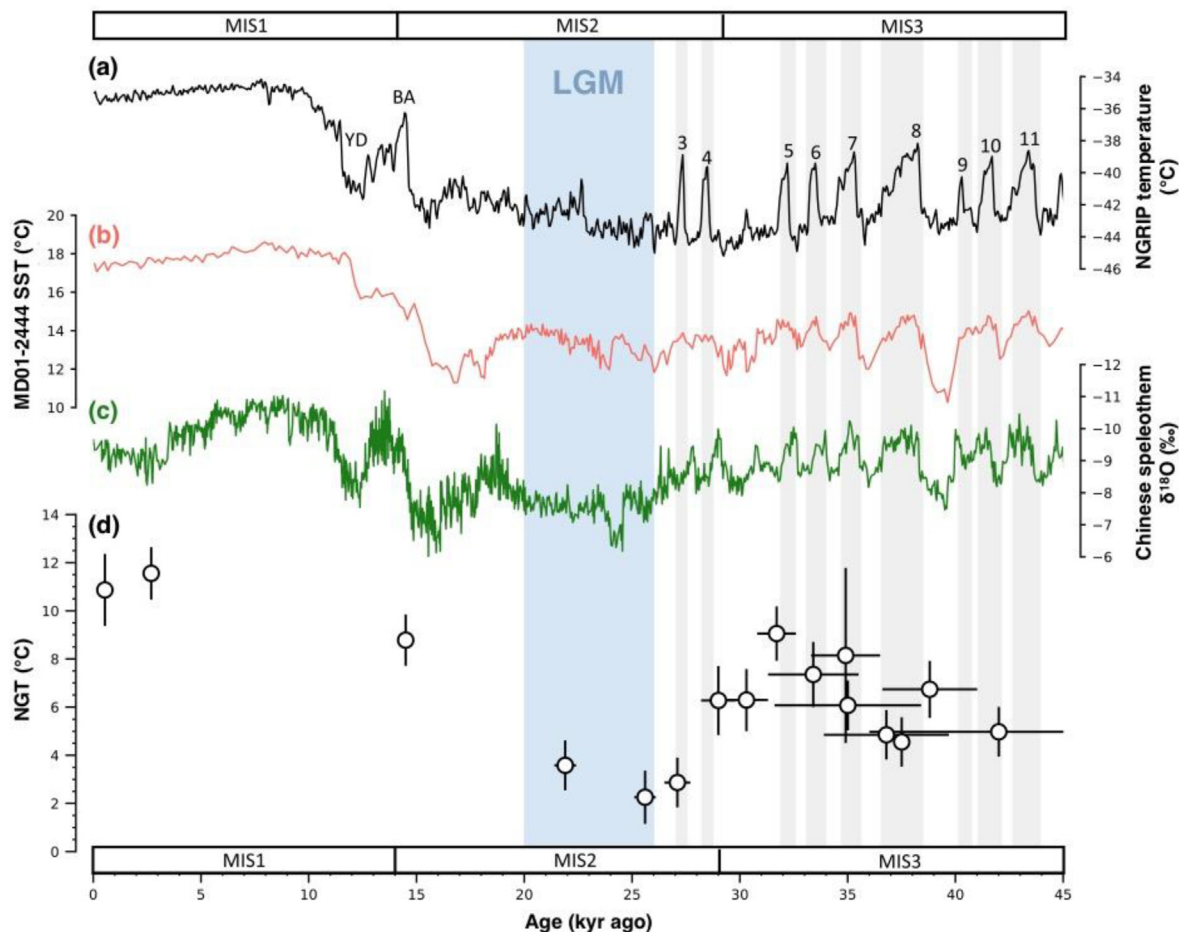


Fig. 7. Comparison of our NGT reconstruction from the Albian aquifer with paleotemperature records of the last ~45 kyr from Greenland ice core, ocean sediments, and speleothem data. (a) Temperature reconstruction from the $\delta^{15}\text{N}$ record of the NGRIP Greenland ice core (Kindler et al. (2014), black). (b) Sea surface temperature of the Iberian margin from the MD01-2444 core (Martrat et al. (2007), red). (c) Composite continental $\delta^{18}\text{O}$ record from Chinese speleothems (Cheng et al. (2016), green). (d) Noble gas paleotemperature (NGT) from the Eastern Paris Basin (white dots, this study). Numbers on the NGRIP Greenland ice core record and vertical gray areas indicate D-O events. Light blue area indicates LGM as defined in this study (26–20 kyr ago). BA: Bølling–Allerød. YD: Younger Dryas.

timescale (i.e., the timescale for a groundwater signal to decrease to $1/e$ ($\sim 1/2.72$) of its previous value) of a 1000 yr-long climatic event is for instance $\sim 10\,000$ years (Fig. S7). After 30 kyr, the magnitude of a DO event-like climatic signal with a period of 1000 yr would therefore be attenuated by a factor >8 , implying that the variability potentially induced by the preservation of a DO-like event in groundwater would likely be inferior to the uncertainty on NGT determination (i.e., <1 °C). Here, we compute an error-weighted average of all NGT between 29 and 42 kyr ago of 6.4 ± 0.5 °C, about 4 °C warmer than MIS2. A warmer MIS3 than MIS2 in Eastern Europe may appear inconsistent with the recent proposal that paleo-glacial extents in the North Western French Alps reached their maximum extent during MIS3 rather than during MIS2 (Gribenski et al. (2021)), an observation that may question the respective cooling between MIS3 and MIS2. The good statistical agreement between NGTs reported in this study for MIS3 (Fig. 7) however suggests that the error-weighted average of NGTs between 29 and 42 kyr ago ($n = 10$, mean = 6.4 ± 0.5 °C) can be used as a quantitative constraint on the extent of cooling during that period of time. Comparing this estimate for the temperature in Eastern France during MIS3 with GCM simulations of MIS3 appears to be another promising avenue to further constrain models of climate evolution since the last glaciation.

5. Conclusion

We have reported a new reconstruction of Eastern France temperature evolution over the last ~40 kyr, using noble gas abundances in the Albian aquifer (Paris Basin) as a quantitative proxy of past temperatures at the time and location of groundwater recharge. This noble gas temperature (NGT) record, independently supported by water stable isotope systematics, depicts a clear glacial-interglacial transition history with mean annual temperatures close to 5 °C during MIS 3, followed by a period of cooling to about 2 °C during the LGM, and then, post glacial warming to Holocene temperatures (~ 11 °C) between 20 and 10 kyr ago. Altogether, these data indicate an LGM cooling of -9.1 ± 0.9 °C, which supports the notion that continental LGM cooling was more extreme at higher latitudes relative to the tropics (where the ΔT_{LGM} was -5.8 ± 0.6 °C; (Seltzer et al. (2021a)). While our data appear compatible with outputs from the data assimilation of (Tierney et al. (2020)), we find that most climate model simulations of the LGM largely underestimate the extent of glacial cooling in Western Europe during the LGM. Combining our NGT reconstruction with water stable isotopes, we find linear $\delta\text{D}/\text{NGT}$ and $\delta^{18}\text{O}/\text{NGT}$ transfer functions of $+1.6 \pm 0.4\text{‰}/\text{°C}$ and $+0.18 \pm 0.04\text{‰}/\text{°C}$, respectively. Additional inter-proxy and data-model comparisons (using both LGM and MIS3 data as anchor points), as well as new noble gas

records from well-dated archives of variable resolutions, are required to reach a comprehensive assessment of spatial gradients of equilibrium warming across Europe.

Credit author statement

All authors contributed to the manuscript. YR, RP, BM and RK initiated this project and produced the original datasets. DVB, P-HB and AMS processed the data and established the main interpretations. DVB made the tables, figures, and wrote the original draft of the manuscript. All co-authors revised the manuscript and approved its submission.

Declaration of competing interest

The authors declare that they have no known competing financial interests or personal relationships that could have appeared to influence the work reported in this paper.

Data availability

All the data are readily available from the Supplementary Information

Acknowledgements

We thank the two anonymous reviewers for their constructive suggestions that improved the quality of our manuscript. We are grateful to Eawag and ETHZ teams for their effort to operate the noble gas laboratory at ETHZ. Part of this recherche was funded by grant ANR-22-CPJ2-0005-01 to DVB. AS acknowledges funding by NSF grant 2102457. EL acknowledges funding by the French National Research Agency under the "Programme d'Investissements d'Avenir" (ANR-19-MPGA-0001). Funding for open access charge: grant ANR-22-CPJ2-0005-01.

Appendix A. Supplementary data

Supplementary data to this article can be found online at <https://doi.org/10.1016/j.quascirev.2023.108123>.

References

Aeschbach-Hertig, W., Peeters, F., Beyerle, U., Kipfer, R., 2000. Paleotemperature reconstruction from noble gases in groundwater accounting for equilibration with entrapped air. *Nature* 405, 1040–1044.

Aeschbach-Hertig, W., Solomon, D.K., 2013. Noble gas thermometry in groundwater hydrology. *Adv. Isotope Geochem.* 81–122.

Affolter, S., Häuselmann, A., Fleitmann, D., Lawrence Edwards, R., Cheng, H., Leuenberger, M., 2019. Central Europe temperature constrained by speleothem fluid inclusion water isotopes over the past 14,000 years. *Sci. Adv.* 5.

Andersen, K.K., et al., 2004. High-resolution record of Northern Hemisphere climate extending into the last interglacial period. *Nature* 431, 147–151.

Andrews, J.N., Lee, D.J., 1979. Inert gases in groundwater from the Bunter Sandstone of England as indicators of age and palaeoclimatic trends. *J. Hydrol.* 41, 233–252.

Araguás-Araguás, L., Froehlich, K., Rozanski, K., 2000. Deuterium and oxygen-18 isotope composition of precipitation and atmospheric moisture. *Hydrol. Process.* 14, 1341–1355.

Banerjee, A., Yeung, L.Y., Murray, L.T., Tie, X., Tierney, J.E., Legrande, A.N., 2022. Clumped-isotope constraint on upper-tropospheric cooling during the last glacial maximum. *AGU Advances* 3, 1–15.

Bartlein, P.J., et al., 2011. Pollen-based continental climate reconstructions at 6 and 21 ka: a global synthesis. *Clim. Dynam.* 37, 775–802.

Befus, K.M., Jasechko, S., Luijendijk, E., Gleeson, T., Bayani Cardenas, M., 2017. The rapid yet uneven turnover of Earth's groundwater. *Geophys. Res. Lett.* 44, 5511–5520.

Beyerle, U., Purtschert, R., Aeschbach-Hertig, W., Imboden, D.M., Loosli, H.H., Wieler, R., Kipfer, R., 1998. Climate and groundwater recharge during the last glaciation in an ice-covered region. *Science* 282, 731–734.

Blard, P.H., Lavé, J., Pik, R., Wagnon, P., Bourlès, D., 2007. Persistence of full glacial

conditions in the central Pacific until 15,000 years ago. *Nature* 449, 591–594.

Blaser, P.C., Kipfer, R., Loosli, H.H., Walraevens, K., Van Camp, M., Aeschbach-Hertig, W., 2010. A 40 ka record of temperature and permafrost conditions in northwestern Europe from noble gases in the Ledo-Paniselian Aquifer (Belgium). *J. Quat. Sci.* 25, 1038–1044.

Boucher, C., Lan, T., Mabry, J., Bekaert, D.V., Burnard, P.G., Marty, B., 2018. Spatial analysis of the atmospheric helium isotopic composition: geochemical and environmental implications. *Geochem. Cosmochim. Acta* 237, 120–130.

Buizert, C., et al., 2015. Precise inter-polar phasing of abrupt climate change during the last ice age. *Nature* 520, 661–665.

Byrne, M.P., O'Gorman, P.A., 2018. Trends in continental temperature and humidity directly linked to ocean warming. *Proc. Natl. Acad. Sci. U. S. A.* 115, 4863–4868.

Caillon, N., Severinghaus, J.P., Jouzel, J., Barnola, J.M., Kang, J., Lipenkov, V.Y., 2003. Timing of atmospheric CO₂ and antarctic temperature changes across termination III. *Science* 299, 1728–1731.

Capron, E., et al., 2021. The anatomy of past abrupt warmings recorded in Greenland ice. *Nat. Commun.* 12, 1–12. Springer US.

Castro, M.C., Jambon, A., De Marsily, G., Schlosser, P., 1998. Noble gases as natural tracers of water circulation in the Paris Basin. 1. Measurements and discussion of their origin and mechanisms of vertical transport in the basin. *Water Resour. Res.* 34, 2443–2466.

Clark, P.U., Dyke, A.S., Shakun, J.D., Carlson, A.E., Clark, J., Wohlfarth, B., Mitrovica, J.X., Hostetler, S.W., McCabe, A.M., 2009. The last glacial maximum. *Science* 325, 710–714.

Cleator, S.F., Harrison, S.P., Nichols, N.K., Colin Prentice, I., Roulstone, I., 2020. A new multivariable benchmark for Last Glacial Maximum climate simulations. *Clim. Past* 16, 699–712.

Coleman, M.L., Shepherd, T.J., Durham, J.J., Rouse, J.E., Moore, G.R., 1982. Reduction of water with zinc for hydrogen isotope analysis. *Anal. Chem.* 54, 993–995.

Contoux, C., Violette, S., Vivona, R., Goblet, P., Patriarche, D., 2013. How basin model results enable the study of multi-layer aquifer response to pumping: the Paris Basin, France. *Hydrogeol. J.* 21, 545–557.

Corcho Alvarado, J.A., Leuenberger, M., Kipfer, R., Paces, T., Purtschert, R., 2011. Reconstruction of past climate conditions over central Europe from groundwater data. *Quat. Sci. Rev.* 30, 3423–3429. Elsevier Ltd.

Craig, H., 1961. Isotopic variations in meteoric waters. *Science* 133, 1702–1703.

Dansgaard, W., et al., 1993. Evidence for general instability of past climate from a 250-kyr ice-core record. *Nature* 364, 218–220.

Dansgaard, W., 2012. Stable isotopes in precipitation. *Tellus Dyn. Meteorol. Oceanogr.* 16, 436.

De Melo Condesso, M.T., Carreira Paquete, P.M.M., Da Silva Marques, M.A., 2001. Evolution of the Aveiro Cretaceous Aquifer (NW Portugal) during the Late Pleistocene and Present Day: Evidence from Chemical and Isotopic Data, vol. 189. Geological Society Special Publication, pp. 139–154.

Deplazes, G., et al., 2013. Links between tropical rainfall and North Atlantic climate during the last glacial period. *Nat. Geosci.* 6, 213–217. Nature Publishing Group.

Edmunds, W.M., Milne, C.J., 2001. Palaeowaters in Coastal Europe: Evolution of Groundwater since the Late Pleistocene. Geological Society of London.

Ford, H.L., Ravelo, A.C., Polissar, P.J., 2015. Reduced el niño-southern oscillation during the last glacial maximum. *Science* 347, 255–258.

Froehlich, K., Gibson, J.J., Aggarwal, P.K., 2002. Deuterium Excess in Precipitation and its Climatological Significance. *No. IAEA-CSP-13/*.

Gat, J.R., Gonfiantini, R., 1981. Stable Isotope Hydrology Deuterium and Oxygen-18 in the Water Cycle. International Atomic Energy Agency, Vienna.

Genty, D., Blamart, D., Ouahdi, R., Gilmour, M., Baker, A., Jouzel, J., Van-Exter, S., 2003. Precise dating of Dansgaard – oeschger climate oscillations in western Europe from stalagmite data. *Nature* 421, 833–837.

Geyh, M.A., 2000. An overview of ¹⁴C analysis in the study of groundwater. *Radiocarbon* 42, 99–114.

Ghadiri, E., Affolter, S., Brennwald, M.S., Fleitmann, D., Häuselmann, A.D., Cheng, H., Maden, C., Leuenberger, M., Kipfer, R., 2020. Estimation of temperature – altitude gradients during the Pleistocene–Holocene transition from Swiss stalagmites. *Earth Planet Sci. Lett.* 544, 116387. Elsevier B.V.

Ghadiri, E., Vogel, N., Brennwald, M.S., Maden, C., Häuselmann, A.D., Fleitmann, D., Cheng, H., Kipfer, R., 2018. Noble gas based temperature reconstruction on a Swiss stalagmite from the last glacial–interglacial transition and its comparison with other climate records. *Earth Planet Sci. Lett.* 495, 192–201. Elsevier B.V.

Grant, K.M., et al., 2014. Sea-level variability over five glacial cycles. *Nat. Commun.* 5. Nature Publishing Group.

Gribenski, N., Valla, P.G., Preusser, F., Roattino, T., Crouzet, C., Buoncristiani, J.F., 2021. Out-of-phase Late Pleistocene glacial maxima in the Western Alps reflect past changes in North Atlantic atmospheric circulation. *Geology* 49, 1096–1101.

Guiot, J., Pons, A., De Beaulieu, J.L., Reille, M., 1989. A 140,000-year continental climate reconstruction from two European pollen records. *Nature* 338, 309–313.

Hall, C.M., Castro, M.C., Lohmann, K.C., Ma, L., 2005. Noble gases and stable isotopes in a shallow aquifer in southern Michigan: implications for noble gas paleo-temperature reconstructions for cool climates. *Geophys. Res. Lett.* 32, 1–4.

Heaton, T.H.E., Vogel, J.C., 1981. Excess air" in groundwater. *J. Hydrol.* 50, 201–216.

Hersbach, H., et al., 2020. The ERA5 global reanalysis. *Q. J. R. Meteorol. Soc.* 146, 1999–2049.

Ho, S.L., Laepple, T., 2015. Glacial cooling as inferred from marine temperature proxies TEXH86 and UK'37. *Earth Planet Sci. Lett.* 409, 15–22. Elsevier B.V.

Holland, M.M., Bitz, C.M., 2003. Polar amplification of climate change in coupled models. *Clim. Dynam.* 21, 221–232.

- Hughes, P.D., Gibbard, P.L., 2015. A stratigraphical basis for the last glacial maximum (LGM). *Quat. Int.* 383, 174–185. Elsevier Ltd.
- Ingram, R.G.S., Hiscock, K.M., Dennis, P.F., 2007. Noble gas excess air applied to distinguish groundwater recharge conditions. *Environ. Sci. Technol.* 41, 1949–1955.
- Innocent, C., Millot, R., Kloppmann, W., 2021. A multi-isotope baseline (O, H, C, S, Sr, B, Li, U) to assess leakage processes in the deep aquifers of the Paris basin (France). *Appl. Geochem.* 131.
- James, E.W., Banner, J.L., Hardt, B., 2015. A global model for cave ventilation and seasonal bias in speleothem paleoclimate records. *G-cubed* 16, 1044–1051.
- Jung, M., Aeschbach, W., 2018. A new software tool for the analysis of noble gas data sets from (ground)water. *Environ. Model. Software* 103, 120–130. Elsevier Ltd.
- Kageyama, M., et al., 2021. The PMIP4 Last Glacial Maximum experiments: preliminary results and comparison with the PMIP3 simulations. *Clim. Past* 17, 1065–1089.
- Kipfer, R., Aeschbach-Hertig, W., Peeters, F., Stute, M., 2002. Noble gases in lakes and ground waters. *Rev. Mineral. Geochem.* 47, 615–700.
- Kluge, T., Marx, T., Scholz, D., Niggemann, S., Mangini, A., Aeschbach-Hertig, W., 2008. A new tool for palaeoclimate reconstruction: noble gas temperatures from fluid inclusions in speleothems. *Earth Planet Sci. Lett.* 269, 408–415.
- Klump, S., Cirpka, O.A., Surbeck, H., Kipfer, R., 2008. Experimental and numerical studies on excess-air formation in quasi-saturated porous media. *Water Resour. Res.* 44, 1–15.
- Leng, M.J., Marshall, J.D., 2004. Palaeoclimate interpretation of stable isotope data from lake sediment archives. *Quat. Sci. Rev.* 23, 811–831.
- Loomis, S.E., et al., 2017. The tropical lapse rate steepened during the Last Glacial Maximum. *Sci. Adv.* 3, 1–8.
- Loosli, H.H., et al., 2001. Isotopic methods and their hydrogeochemical context in the investigation of palaeowaters. *Geol. Soc. London, Special Pub.* 189, 193–212.
- Lorius, C., Jouzel, J., Raynaud, D., Hansen, J., Le Treut, H., 1990. The ice-core record: climate sensitivity and future greenhouse warming. *Nature* 347, 139–145.
- Martin, L.C.P., et al., 2020. Antarctic-like temperature variations in the Tropical Andes recorded by glaciers and lakes during the last deglaciation. *Quat. Sci. Rev.* 247.
- Martrat, B., Grimalt, J.O., Shackleton, N.J., De Abreu, L., Hutterli, M.A., Stocker, T.F., 2007. Four climate cycles of recurring deep and surface water destabilizations on the Iberian margin. *Science* 317, 502–507.
- Mazor, E., 1972. Paleotemperatures and other hydrological parameters deduced from noble gases dissolved in groundwaters; Jordan Rift Valley, Israel. *Geochim. Cosmochim. Acta* 36, 1321–1336.
- McManus, J.F., Oppo, D.W., Cullen, J.L., 1999. A 0.5-Million-year record of millennial-scale climate variability in the North Atlantic. *Science* 283, 971–975.
- Millot, R., Petelet-Giraud, E., Guerrot, C., Négrel, P., 2010. Multi-isotopic composition ($\delta^{17}\text{Li}$ - $\delta^{11}\text{B}$ - δD - $\delta^{18}\text{O}$) of rainwaters in France: origin and spatio-temporal characterization. *Appl. Geochem.* 25, 1510–1524. Elsevier Ltd.
- Moine, O., Antoine, P., Hatté, C., Landais, A., Mathieu, J., Prud, C., 2017. The Impact of Last Glacial Climate Variability in West-European Loess Revealed by Radiocarbon Dating of Fossil Earthworm Granelles, pp. 1–6.
- Olive, P., 1999. La datation des eaux souterraines à long temps de résidence par le radiocarbone. *Mode d'emploi. Hydrogéologie* 1, 3–19.
- Osman, M.B., Tierney, J.E., Zhu, J., Tardif, R., Hakim, G.J., King, J., Poulsen, C.J., 2021. Globally resolved surface temperatures since the last glacial maximum. *Nature* 599, 239–244.
- Parrenin, F., et al., 2013. Synchronous change of atmospheric CO₂ and antarctic temperature during the last deglacial warming. *Science* 339 (6123), 1060–1063.
- Peterson, L.C., Haug, G.H., Hughen, K.A., Ursula, R., 2000. Tropical atlantic during the last glacial rapid changes in the hydrologic cycle of the tropical atlantic during the last glacial. *Science* 290, 1947–1951.
- Petit, J.R., et al., 1999. Climate and atmospheric history of the past 420,000 years from the Vostok ice core, Antarctica the recent completion of drilling at Vostok station in East. *Nature* 399, 429–436.
- Pithan, F., Mauritsen, T., 2014. Arctic amplification dominated by temperature feedbacks in contemporary climate models. *Nat. Geosci.* 7, 181–184.
- Porter, S.C., 2000. Snowline depression in the tropics during the last glaciation. *Quat. Sci. Rev.* 20, 1067–1091.
- Raoult, Y., 1999. La nappe de l'Albien dans le bassin de Paris, de nouvelles idées pour de vieilles eaux. Thèse de doctorat de l'université Paris VI, pp. 117–119.
- Raoult, Y., Lauerjat, J., Boulegue, J., Olive, P., Barriac, T., 1998. Etude hydrogéologique d'une ligne d'écoulement de l'aquifère de l'Albien dans le bassin de Paris entre Gien-Auxerre et Paris. *Bull. Soc. Geol. Fr.* 169 (3), 453–457.
- Reimer, P.J., et al., 2020. The IntCal20 northern hemisphere radiocarbon age calibration curve (0–55 cal kBP). *Radiocarbon* 62, 725–757.
- Rozanski, K., 1985. Deuterium and oxygen-18 in European groundwaters - links to atmospheric circulation in the past. *Chem. Geol. Isot. Geosci.* 52, 349–363.
- Rozanski, K., Araguás-Araguás, L., Gonfiantini, R., 1992. Relation between long-term trends of oxygen-18 isotope composition of precipitation and climate. *Science* 258, 981–985.
- Seltzer, A.M., Ng, J., Aeschbach, W., Kipfer, R., Kulongoski, J.T., Severinghaus, J.P., Stute, M., 2021a. Widespread six degrees celsius cooling on land during the last glacial maximum. *Nature* 593, 228–232. Springer US.
- Seltzer, A.M., Bekaert, D.V., Barry, P.H., Durkin, K.E., Mace, E.K., Aalseth, C.E., Zappala, J.C., Mueller, P., Jurgens, B., Kulongoski, J.T., 2021b. Groundwater residence time estimates obscured by anthropogenic carbonate. *Sci. Adv.* 7 (17) eabf3503.
- Shakun, J.D., Carlson, A.E., 2010. A global perspective on Last Glacial Maximum to Holocene climate change. *Quat. Sci. Rev.* 29, 1801–1816.
- Shakun, J.D., Clark, P.U., He, F., Marcott, S.A., Mix, A.C., Liu, Z., Otto-Bliesner, B., Schmittner, A., Bard, E., 2012. Global warming preceded by increasing carbon dioxide concentrations during the last deglaciation. *Nat. Nat. Publish. Group* 484, 49–54.
- Stadelmaier, K.H., Ludwig, P., Bertran, P., Antoine, P., Shi, X., Lohmann, G., Pinto, J.G., 2021. A new perspective on permafrost boundaries in France during the Last Glacial Maximum. *Clim. Past* 17, 2559–2576.
- Stuecker, M.F., et al., 2018. Polar amplification dominated by local forcing and feedbacks. *Nat. Clim. Change* 8, 1076–1081. Springer US.
- Stute, M., Deak, J., 1989. Environmental isotope study (^{14}C , ^{18}O , D , noble gases) on deep groundwater circulation systems in Hungary with reference to paleoclimate. *Radiocarbon* 31, 902–918.
- Stute, M., Forster, M., Frischkorn, H., Serejo, A., Clark, J.F., Schlosser, P., Broecker, W.S., Bonani, G., 1995. Cooling of tropical Brazil (5°C) during the last glacial maximum. *Science* 269, 379–383.
- Stute, M., Schlosser, P., 1993. Principles and Applications of the Iodide Process. Washington DC American Geophysical Union Geophysical Monograph Series, pp. 89–100.
- Stute, M., Sonntag, C., 1992. Paleotemperatures derived from noble gases dissolved in groundwater and in relation to soil temperature. *Isotopes of noble gases as tracers in environmental studies* 111–122.
- Sutton, R.T., Dong, B., Gregory, J.M., 2007. Land/sea warming ratio in response to climate change: IPCC AR4 model results and comparison with observations. *Geophys. Res. Lett.* 34, 2–6.
- Thouveny, N., et al., 1994. Climate variations in Europe over the past 140 kyr deduced from rock magnetism. *Nature* 293, 503–506.
- Tierney, J.E., Zhu, J., King, J., Malevich, S.B., Hakim, G.J., Poulsen, C.J., 2020. Glacial cooling and climate sensitivity revisited. *Nature* 584, 569–573. Springer US.
- Tripati, A.K., Sahany, S., Pittman, D., Eagle, R.A., Neelin, J.D., Mitchell, J.L., Beaufort, L., 2014. Modern and glacial tropical snowlines controlled by sea surface temperature and atmospheric mixing. *Nat. Geosci.* 7, 205–209.
- Varsányi, I., Palcsu, L., Kovács, L.O., 2011. Groundwater flow system as an archive of paleotemperature: noble gas, radiocarbon, stable isotope and geochemical study in the Pannonian Basin, Hungary. *Appl. Geochem.* 26, 91–104.
- Višnjević, V., Herman, F., Prasicek, G., 2020. Climatic patterns over the European Alps during the LGM derived from inversion of the paleo-ice extent. *Earth Planet Sci. Lett.* 538.
- Vogel, N., Brennwald, M.S., Fleitmann, D., Wieler, R., Maden, C., Süssli, A., Kipfer, R., 2013. A combined vacuum crushing and sieving (CVCS) system designed to determine noble gas paleotemperatures from stalagmite samples. *G-cubed* 14, 2432–2444.
- Vuillaume, Y., 1971. Application des méthodes isotopiques et hydrochimiques à l'étude de la nappe de l'Albien du bassin de Paris, vol. 71. *Sgn 304 Hyd* 140pp.
- Wang, X., Auler, A.S., Edwards, R.L., Cheng, H., Ito, E., Solheid, M., 2006. Inter-hemispheric anti-phasing of rainfall during the last glacial period. *Quat. Sci. Rev.* 25, 3391–3403.
- Weyhenmeyer, C.E., Burns, S.J., Waber, H.N., Aeschbach-Hertig, W., Kipfer, R., Loosli, H.H., Matter, A., 2000. Cool glacial temperatures and changes in moisture source recorded in Oman groundwaters. *Science* 287 (5454), 842–845.
- York, D., Evensen, N.M., Martinez, M.L., De Basabe Delgado, J., 2004. Unified equations for the slope, intercept, and standard errors of the best straight line. *Am. J. Phys.* 72, 367–375.
- Zhu, J., Otto-Bliesner, B.L., Brady, E.C., Poulsen, C.J., Tierney, J.E., Lofverstrom, M., DiNezio, P., 2021. Assessment of equilibrium climate sensitivity of the community Earth system model version 2 through simulation of the last glacial maximum. *Geophys. Res. Lett.* 48, 1–10.

Résumé en français

Il est sans équivoque que les activités humaines ont réchauffé notre climat [IPCC report, AR6 WGI]. Les activités anthropiques ont transféré le carbone initialement stocké dans le réservoir lithosphérique dans l'atmosphère. Ces émissions de carbone fossile ont provoqué une perturbation majeure du climat préindustriel. L'augmentation des concentrations atmosphériques de dioxyde de carbone (CO₂) et de méthane (CH₄) combinée aux autres facteurs humains (aérosols, ozone et changements d'utilisation des terres) a entraîné une augmentation totale de la température de surface mondiale de 1,14 (de 0,9 à 1,4) °C de 2013 à 2022 par rapport à 1850-1900 [Forster et al., 2023]. Les conséquences de la libération actuelle des gaz à effet de serre dans l'atmosphère se poursuivront après l'arrêt des émissions, à cause de l'inertie du climat et du cycle du carbone, dont les mécanismes de rétroactions en jeu entre ces composantes impliquent une réponse retardée par rapport à la perturbation initiale (par exemple, la fonte des calottes polaires) [IPCC SPR1.5, 2018] (Figure 1). Les projections climatiques futures au-delà de la fin du siècle demeurent complexes car les observations des interactions entre le climat et le cycle du carbone sont limitées aux dernières décennies. Or, ces interactions seront un facteur déterminant de l'évolution du climat terrestre à court terme (fin du siècle) et à long terme (sur plusieurs millénaires). Une meilleure compréhension de ces interactions à différentes échelles temporelles est donc essentielle pour caractériser le climat futur et aider l'adaptation de nos sociétés face au changement climatique en cours.

La vitesse et l'amplitude des émissions anthropiques de carbone et leurs conséquences sur le climat terrestre n'ont pas d'équivalent dans le passé. Cependant, les variations du climat terrestre et la dynamique du cycle du carbone sont enregistrées dans les archives paléoclimatiques depuis des millions d'années. En particulier, le climat des 2 derniers millions d'années (Ma) est ponctué d'une alternance de périodes chaudes (interglaciaires) et froides (glaciaires). Ces climats couvrent une large gamme de températures, de schémas de précipitations et d'extension du volume de glace, ainsi qu'une grande diversité de concentrations atmosphériques de CO₂ et de CH₄. Par exemple, certaines des périodes chaudes passées, d'une durée de 5 à 30 milliers d'années (ka), ont enregistré des températures de surface

polaire similaires à celles attendues à la fin du siècle [Past Interglacial Working Group of PAGES, 2016]. Parallèlement, les transitions des périodes froides aux périodes chaudes, connues sous le nom de Terminaisons glaciaires, se caractérisent par une augmentation de 4 à 7 °C de la température moyenne mondiale et une augmentation de 60 à 100 ppm des concentrations de CO₂ en environ 10 ka. Elles représentent des transitions climatiques majeures impliquant d'importants changements dans la dynamique du cycle du carbone.

En raison de sa proximité relative avec le présent, les 2 derniers Ma offrent de nombreux enregistrements extraits des archives paléoclimatiques naturelles. Ces archives couvrent une large gamme d'intervalles de temps et de lieux géographiques à différentes résolutions temporelles. Ces caractéristiques permettent d'étudier les interactions entre le cycle du carbone et le climat des échelles centennale à orbitale. Ainsi, caractériser et comprendre les interactions entre le cycle du carbone et le climat au cours des 2 derniers Ma peut fournir des informations uniques pour mieux contraindre les variations climatiques allant des échelles centennale à orbitale en réponse à la perturbation actuelle du cycle du carbone.

Mon projet de thèse s'inscrit dans ce contexte, en s'appuyant sur l'utilisation de plusieurs intervalles climatiques clés des 2 derniers Ma en tant que laboratoires naturels pour caractériser et comprendre les interactions entre le cycle du carbone et le climat à différentes échelles temporelles. Ce projet de thèse s'est déroulé à l'IGE où j'ai mesuré de nouveaux enregistrements de CO₂ et de CH₄ sur la carotte de glace Antarctique EPICA Dome C (EDC). J'ai également bénéficié de données mesurées au LSCE par F. Prié, A. Grisart et A. Landais, où j'ai passé trois semaines dans le cadre de ce projet.

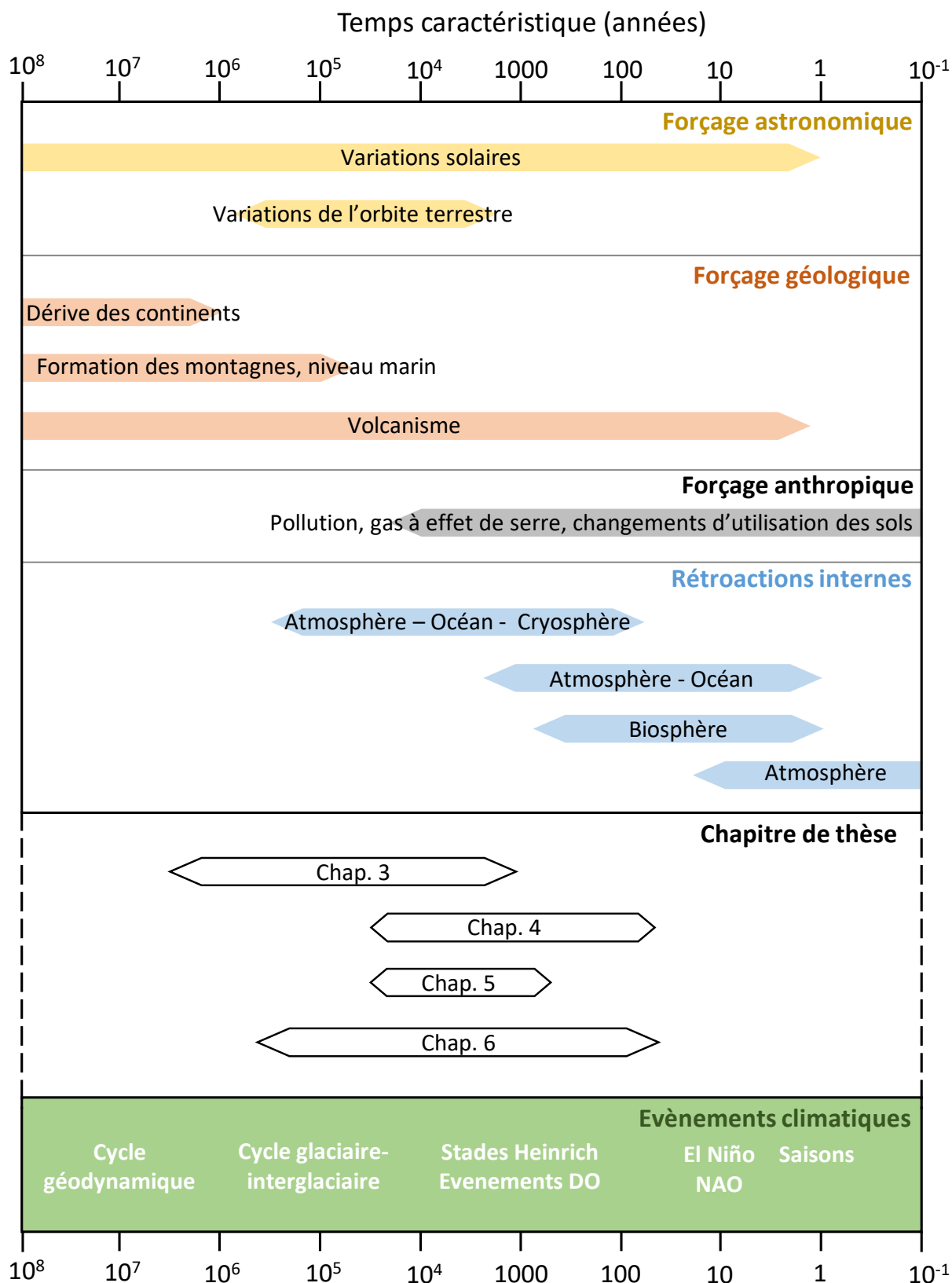


Figure 1: Forçage externe, rétroactions internes du climat, événements climatiques majeurs et chapitres de thèse présentés en fonction de leur échelle de temps caractéristique. Événements DO : Événements Dansgaard-Oeschger. NAO : Oscillation Nord-Atlantique. Modifié et adapté de Bard, leçon inaugurale du Collège de France, 2002.

Dans le chapitre 3, qui est le premier chapitre de résultat, je présente les résultats publiés dans *Communications Earth & Environment* en mars 2023 ainsi que les analyses complémentaires associées. Le mécanisme déclencheur à l'origine de la Transition du Mid-Pleistocène (MPT) est étudié à travers un modèle conceptuel simple utilisé pour reproduire une reconstruction basée sur les données du volume mondial de glace. Sur la base de ces résultats, j'insiste sur le rôle majeur joué par le forçage orbital dans cette transition. De plus, des simulations supplémentaires montrent qu'une légère modification dans le forçage orbital empêche l'apparition de la MPT dans le modèle conceptuel. Ainsi, bien qu'un changement dans le système climatique interne soit nécessaire pour compléter entièrement la MPT, je propose que les fréquences orbitales spécifiques non dominantes sur les 2 derniers Ma sont essentielles dans la survenue de cette transition. En d'autres termes, le forçage orbital joue un rôle clé dans l'établissement des cycles climatiques à 100 ka.

De plus, je propose qu'un changement graduel survenu au cours des 2 derniers Ma est plus susceptible d'avoir provoqué la MPT qu'un événement abrupt. En tenant compte de la structure temporelle des mécanismes étudiés, les résultats pointent vers la diminution progressive des concentrations de CO₂ glaciaire au cours des 2 Ma comme le mécanisme sous-jacent qui a déclenché la MPT (Figure 2). Les preuves d'une telle diminution dans les données restent peu claires [Chalk et al., 2017 ; Berends et al., 2021 ; Yamamoto et al., 2022]. Sous l'égide du défi IPICS Oldest Ice Challenge, les projets de forage internationaux en cours devraient fournir des carottes de glace continues couvrant la MPT au cours de la prochaine décennie. Les mesures directes des concentrations de CO₂ devraient contribuer à confirmer ou à rejeter l'hypothèse d'un rôle majeur joué par le cycle du carbone dans le déclenchement de la MPT.

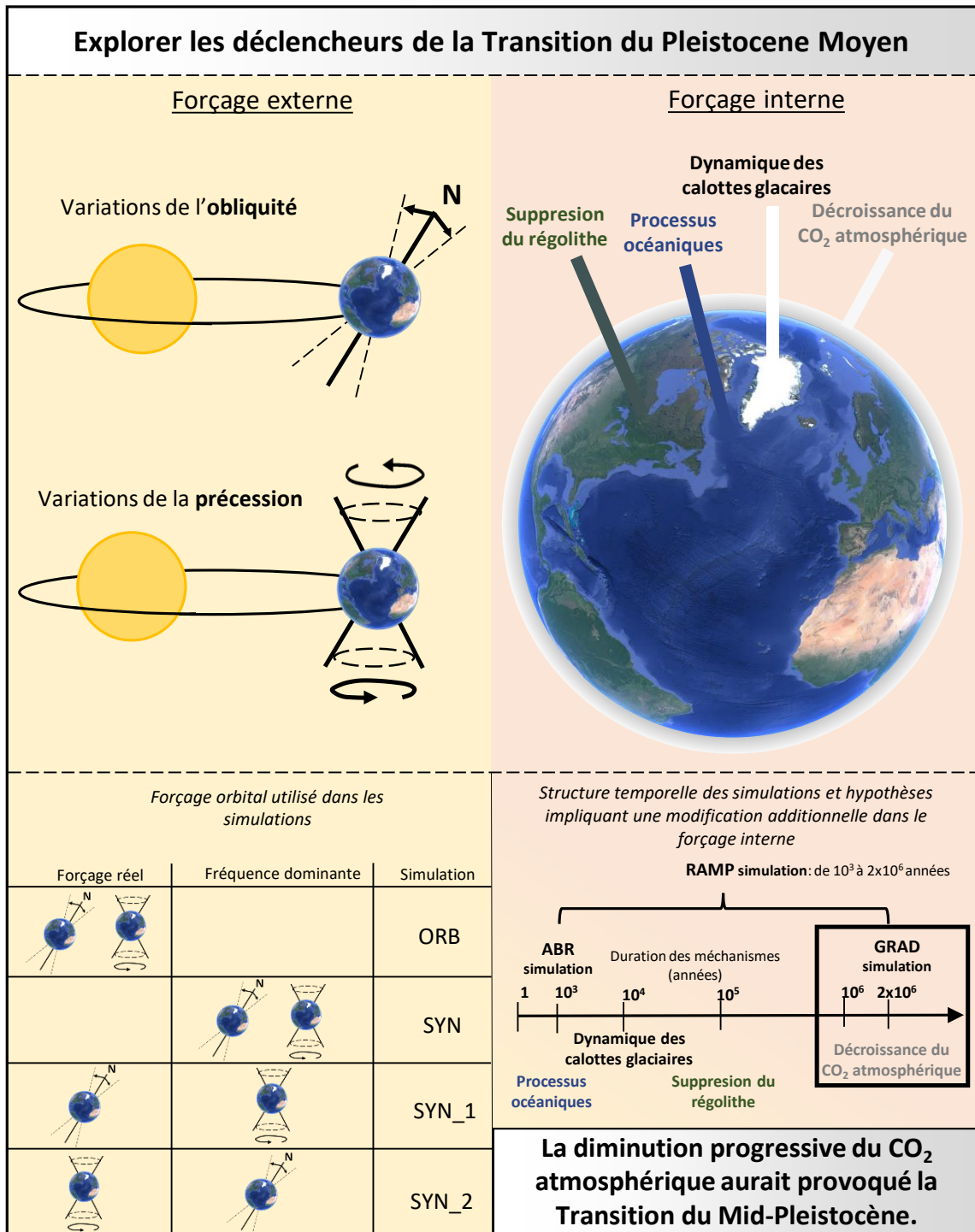


Figure 2: Résumé conceptuel de l'analyse réalisée dans le chapitre 3. Les zones jaunes/rouges se réfèrent aux forçages externes/internes. La partie gauche présente le forçage orbital considéré (haut de la figure) et les simulations basées uniquement sur ce forçage orbital (ORB, SYN, SYN_1, SYN_2) (bas de la figure). La distinction est faite entre les simulations utilisant le forçage réel des paramètres orbitaux et le forçage synthétique des paramètres orbitaux, qui est composé uniquement de la fréquence dominante (~21 ka pour la précession et la précession décalée en phase, ~41 ka pour l'obliquité). La partie supérieure droite illustre les forçages externes couramment évoqués comme des déclencheurs potentiels de la MPT. La partie inférieure droite présente l'hypothèse combinant un changement dans les forçages externes et internes. Le rectangle noir représente la simulation la plus pertinente et son mécanisme associé.

Dans le chapitre 4, j'examine le rôle du cycle du carbone et des processus responsables de ses variations au cours des transitions climatiques majeures du Pléistocène, en quantifiant le phasage entre le climat antarctique et les concentrations atmosphériques de CO₂ durant les cinq dernières terminaisons glaciaires. Pour ce faire, j'utilise de nouveaux enregistrements de CO₂ et de δ¹⁵N à haute résolution provenant de la carotte de glace EDC récemment publiés. Des études antérieures ont examiné ce phasage au cours des trois dernières terminaisons, révélant des résultats significativement différents d'une étude à l'autre. Néanmoins, l'utilisation de carottes de glace, de méthodes statistiques et de proxies différents pour le climat antarctique, rend difficile la distinction entre l'hétérogénéité induite par la méthode et le signal climatique réel. Mon approche repose sur l'utilisation de trois outils statistiques de détection des changements de pente dans les enregistrements, afin de distinguer les résultats dépendants de la méthode des schémas de phasage robustes. Les analyses ont montré que le phasage au début des terminaisons varie en fonction de la méthodologie utilisée et de la terminaison considérée. À l'inverse, un important décalage multi-centennal de la décroissance du CO₂ atmosphérique par rapport au refroidissement du climat antarctique est observé à la fin des terminaisons (Figure 3). Un phasage d'échelle temporelle similaire a été décrit précédemment lors des événements à l'échelle millénaire de la dernière période glaciaire. En suivant la théorie développée par Wolff et al. [2009], je propose que les terminaisons soient achevées par des événements climatiques se produisant à l'échelle millénaire. Néanmoins, l'occurrence de variations à l'échelle millénaire au cours de la Terminaison I et la Terminaison III révèle la complexité des interactions entre la variabilité à l'échelle orbitale et à l'échelle millénaire. Je suggère que la variabilité à l'échelle millénaire pourrait soit temporairement interrompre, soit achever définitivement le processus de la terminaison en fonction de son contexte orbital d'occurrence. Enfin, une analyse de la séquence d'événements des proxies paléoclimatiques à la fin des terminaisons suggère qu'un renforcement d'un puits de carbone localisé dans les moyennes à basses latitudes pourrait contraindre le moment exact de la diminution du CO₂ atmosphérique à la fin des terminaisons. De nouveaux efforts de modélisation ainsi que de nouveaux enregistrements climatiques sur les terminaisons les plus anciennes (Terminaisons III, IV et V) sont nécessaires pour quantifier les conséquences à l'échelle multi-centennale du développement d'un puits de carbone localisé dans les moyennes et basses latitudes sur les concentrations atmosphériques de CO₂.

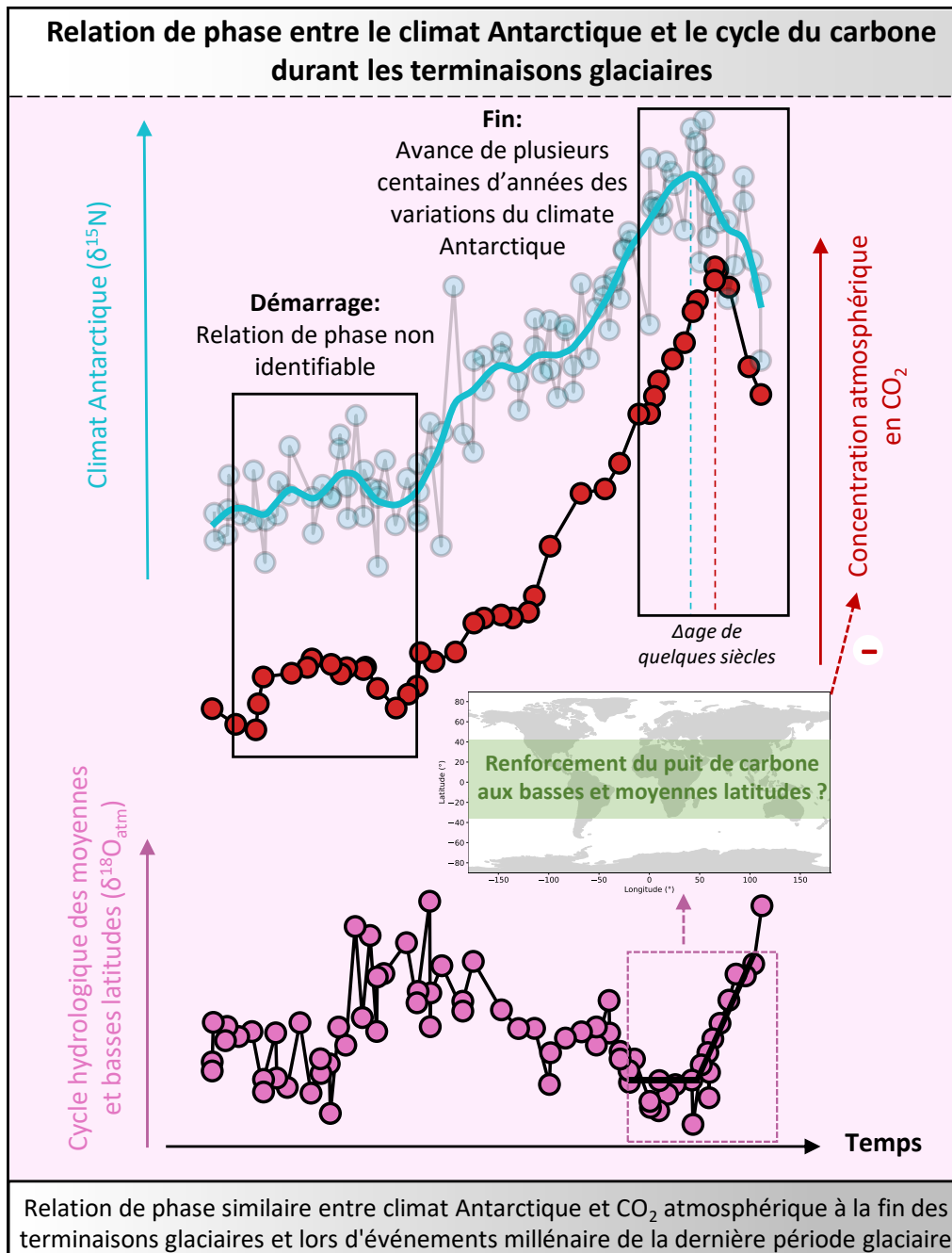


Figure 3: Résumé conceptuel de l'analyse réalisée dans le chapitre 4. Les courbes bleues, rouges et roses et représentent la morphologie des enregistrements de $\delta^{15}\text{N}$, CO_2 atmosphérique et $\delta^{18}\text{O}_{\text{atm}}$ durant la Terminaison III, pris comme exemple des variations des différents proxies au cours des terminaisons. Les rectangles noirs représentent respectivement la fin et le début de la terminaison. Le rectangle rose représente la période de variation dans le $\delta^{18}\text{O}_{\text{atm}}$ associée à une augmentation potentielle du puits de carbone des moyennes et basses latitudes. Le signe - indique l'effet négatif du puits de carbone sur les concentrations de CO_2 atmosphérique. Les axes x et y sont délibérément purement qualitatifs pour mettre en évidence l'aspect conceptuel et représentatif de ce schéma.

Dans le chapitre 5, je présente les résultats d'une synthèse multi-archives caractérisant l'évolution spatiale de la température de surface au cours du MIS 7 et de la Terminaison III. Sur la base de cette synthèse, j'ai mis en évidence la variabilité à l'échelle latitudinale de l'intensité relative entre les MIS 7e et 7a-7c. Le MIS 7e est plus chaud dans les hautes latitudes de l'hémisphère sud par rapport au MIS 7a-7c, suivant les changements d'amplitude observés dans les concentrations atmosphériques de CO₂ et les enregistrements de température de l'Antarctique. À l'inverse, les basses et les hautes latitudes enregistrent des températures de surface équivalentes pendant les MIS 7e et 7a-7c. Deuxièmement, j'ai montré que les hautes latitudes de l'hémisphère sud présentent des températures de surface locales plus chaudes que pendant la période préindustrielle lors du MIS 7^e (Figure 4). Troisièmement, les enregistrements de température des hautes latitudes dans les deux hémisphères sont mieux corrélés avec les concentrations atmosphériques de CO₂ et les estimations du volume global de glace que ceux des basses latitudes. Enfin, les analyses de corrélation entre les enregistrements orbitaux et les motifs de température de surface confirment l'empreinte forte de l'obliquité dans la morphologie de l'évolution de la température pendant le MIS 7. En combinant cette forte empreinte d'obliquité et l'amplitude relativement faible du réchauffement, je propose que le dernier interglaciaire possède des spécificités qui ressemblent à celles associées aux interglaciaires pré-MPT (Figure 4).

Cette synthèse s'inscrit dans un effort plus global pour caractériser les climats interglaciaires au cours des 500 derniers ka grâce au projet MOPGA HOTCLIM. Bien que cette étude se soit concentrée sur le schéma spatio-temporel des enregistrements de paléotempérature basés sur des données, des travaux futurs devraient (i) comparer les résultats avec les sorties spatialisées de modèles de complexité intermédiaire et (ii) comparer l'évolution climatique spatio-temporelle pendant le MIS 7 avec celles d'autres interglaciaires, dans le but d'améliorer notre compréhension des forçages, de la réponse du système climatique et des impacts pendant les périodes chaudes du passé.

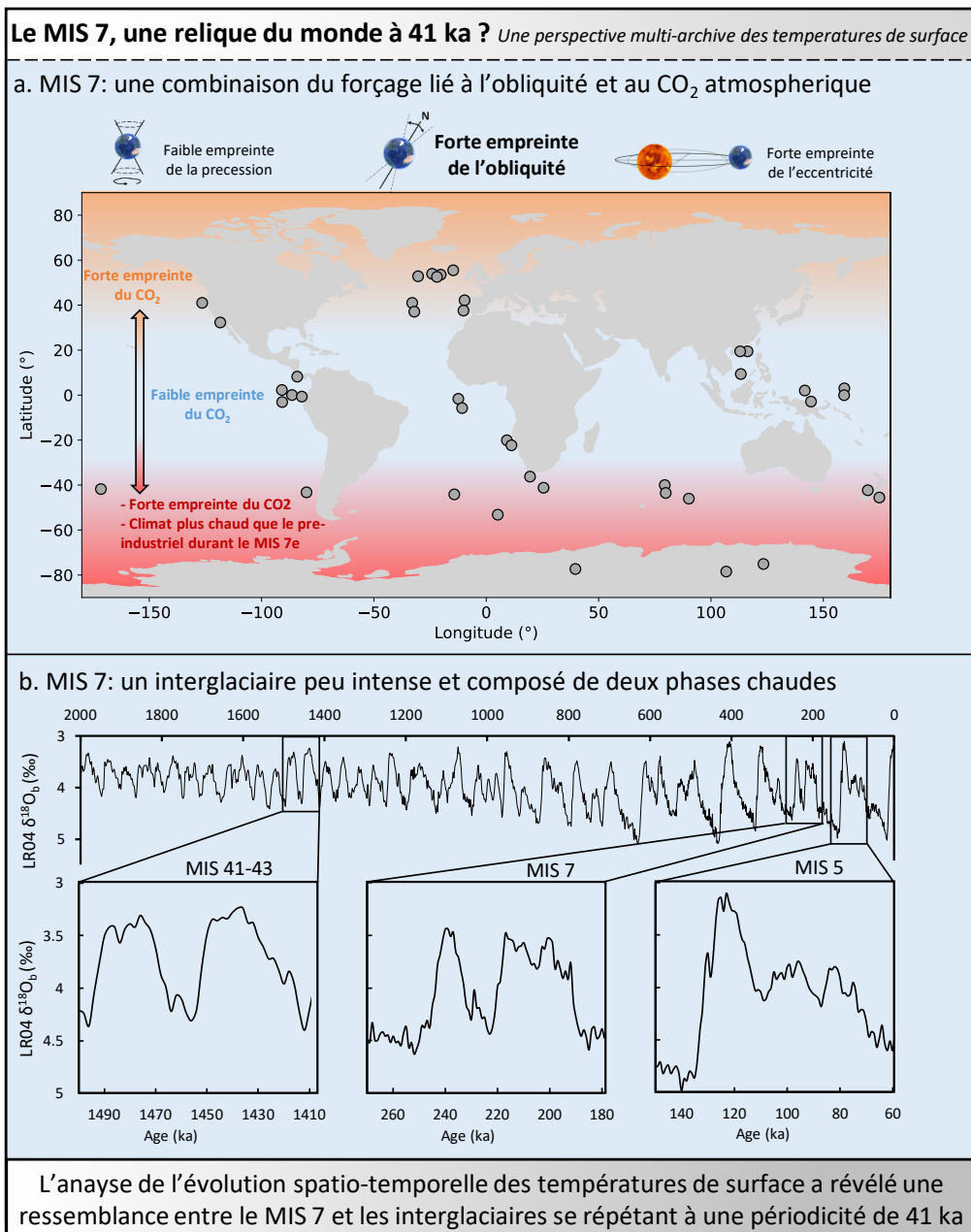


Figure 4: Résumé conceptuel de l'analyse réalisée dans le chapitre 5. a. Les points gris sur la carte représentent les enregistrements de température de surface compilés inclus dans la synthèse multi-archives. La zone orange représente les latitudes nordiques, où l'enregistrement de température de surface est fortement corrélé avec les concentrations atmosphériques de CO₂. De même, la zone rouge représente les hautes latitudes méridionales, où les enregistrements de température de surface sont fortement corrélés avec les concentrations atmosphériques de CO₂ et où un climat plus chaud qu'avant l'ère industrielle a été enregistré à 242 ka. La zone bleu clair représente les tropiques, où une faible empreinte du CO₂ sur les enregistrements de température de surface a été enregistrée. En haut de la carte sont représentées les similarités relatives de morphologie entre les différents paramètres orbitaux et les enregistrements de température de surface. b. La compilation benthique LR04 de Lisiecki et Raymo [2004] a été représentée sur les 2 derniers Ma avec un zoom sur trois périodes spécifiques comprenant MIS 7, MIS 41-43 et MIS 5. MIS 41-43 et MIS 5 ont été choisis comme exemples « typiques » des interglaciaires du monde à 41 kyr et du monde à 100 kyr, bien que chaque période ait enregistré une variabilité interne dans leurs schémas interglaciaires. Ces exemples sont choisis pour illustrer la différence d'amplitude et de fréquence des interglaciaires se produisant avant la MPT (par exemple, MIS 41-43) et après le MPT (par exemple, MIS 5), bien que la diversité des interglaciaires soit beaucoup plus complexe. Les échelles verticales et horizontales sont similaires pour faciliter la comparaison. Veuillez noter la similitude plus élevée entre le MIS 7 et le MIS 41-43 qu'entre le MIS 5 en termes d'amplitude et de fréquence de pic.

Dans le chapitre 6, je présente les résultats d'un article actuellement en cours de révision pour *Nature*. En me basant sur un nouvel enregistrement de CO₂ à haute résolution sur la période 260 - 190 ka, j'ai identifié sept libérations de CO₂ atmosphérique à l'échelle centennale (CDJs) mesurées dans la carotte de glace antarctique EDC. Pour fournir une compréhension complète de la variabilité à l'échelle centennale dans le cycle du carbone, j'ai analysé les enregistrements de CO₂ atmosphérique à haute résolution des 500 derniers ka. En particulier, 18 des 20 CDJs identifiés se sont produits pendant des périodes de forte obliquité, suggérant une influence des conditions orbitales de fond sur les libérations rapides de CO₂ atmosphérique. Pour explorer les sources potentielles de ces augmentations rapides de CO₂, j'ai analysé des simulations d'un modèle de système terrestre de complexité intermédiaire (LOVECLIM) réalisées par Laurie Menviel (Université de Nouvelle-Galles du Sud, Australie). Les simulations visaient à reproduire le CDJ associé au stade Heinrich 5 sous de vraies phases d'obliquité et sous des phases d'obliquité artificiellement faibles. Les résultats suggèrent que pendant un stade Heinrich, à la fois la biosphère continentale et l'océan Austral agissent comme des sources primaires de carbone contribuant aux occurrences de CDJ. De plus, seule la biosphère continentale semble être une source de CO₂ dépendante de l'obliquité lors d'événements à l'échelle centennale (Figure 5). Cette étude met en évidence l'impact potentiel du forçage externe à long terme sur les variations abruptes passées du CO₂. Notamment, elle suggère que la phase actuelle de forte obliquité pourrait amplifier les variations des concentrations atmosphériques de CO₂ à l'échelle centennale en cas de modification de la circulation océanique due à des perturbations anthropogéniques. D'autres simulations étudiant l'influence de l'obliquité sur l'événement atmosphérique à l'échelle centennale associé à un événement DO et explorant l'impact de la précession sur les variations à l'échelle centennale dans le cycle du carbone fourniraient des informations précieuses. De plus, cette étude s'inscrit dans un effort global plus large visant à produire des enregistrements à haute résolution sur la période couverte par les carottes de glace antarctiques. Le développement d'un enregistrement composite à partir de plusieurs carottes de glace augmenterait considérablement la résolution de la courbe composite actuelle du CO₂ [Bereiter et al., 2015]. Le développement d'une nouvelle courbe composite de CO₂ atmosphérique basée sur les données de la carotte de glace EDC couvrant les 800 derniers ka fournirait le plus vaste enregistrement continu de CO₂ atmosphérique obtenu à partir d'une seule carotte de glace.

Le forçage de l'obliquité à l'échelle orbitale et les variations du cycle du carbone à l'échelle centennale

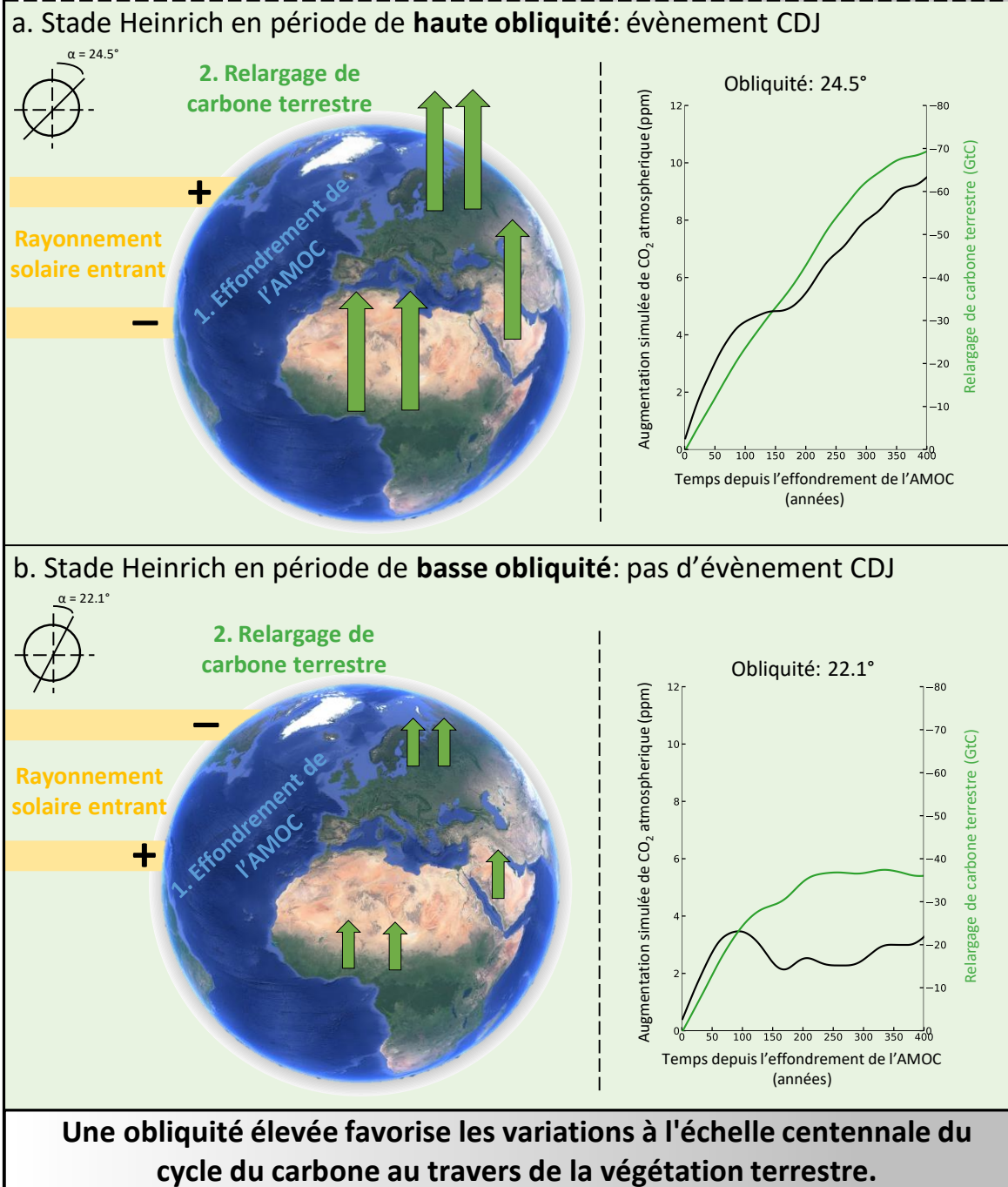


Figure 5: Résumé conceptuel de l'analyse réalisée dans le chapitre 6. Le panneau supérieur/inférieur présente les conséquences d'un stade Heinrich se produisant pendant (a) des états d'obliquité élevée et (b) d'obliquité basse. La zone en jaune représente le forçage solaire entrant à la surface de la Terre. Le signe + et - se réfère à une augmentation/diminution de l'insolation entrante à cette latitude par rapport à l'autre état d'obliquité. Les flèches vertes représentent la zone où la libération de carbone terrestre dans l'atmosphère est sensible à l'état d'obliquité, déduit des simulations du modèle LOVECLIM. Le panneau de droite représente l'évolution à partir de l'effondrement de l'AMOC des concentrations atmosphériques simulées de CO_2 et de la libération de carbone terrestre dans les simulations HighObl (en haut) et LowObl (en bas) effectuées sous haute et basse obliquité avec le modèle LOVECLIM. AMOC : circulation méridienne de retour atlantique.

Ma recherche doctorale s'est basée sur une approche multi-méthodes (expérimentale, modélisation, statistique) appliquée à différentes échelles temporelles (échelles centennale, millénaire, orbitale) afin de caractériser les interactions entre le cycle du carbone et le climat au cours des 2 derniers Ma. Au-delà de la diversité des angles de recherche, deux caractéristiques prédominantes du climat du Pléistocène ont émergé, que je discute ici en tant que conclusion finale de ce manuscrit.

Sur le rôle du forçage orbital. Toutes les études paléoclimatiques présentées dans ce manuscrit ont pour objectif d'investiguer le couplage entre le climat et le cycle du carbone. Néanmoins, quelle que soit l'échelle de temps considérée, une influence prédominante des conditions orbitales de fond a été mise en évidence : (i) sur l'établissement de la MPT (Chapitre 3), (ii) sur la variabilité à l'échelle millénaire à la fin des terminaisons glaciaires (Chapitre 4), (iii) sur les évolutions de température de surface pendant le MIS 7 (~245-190 ka) (Chapitre 5), et (iv) sur les occurrences et l'amplitude de la variabilité du cycle du carbone à l'échelle centennale (Chapitre 6). Alors qu'il est établi que le climat du Pléistocène est principalement influencé par le forçage orbital, la récurrence de son impact sur le cycle du carbone, le climat et leurs interactions, à des échelles de temps plus courtes que l'échelle orbitale est un résultat majeur de mon travail de doctorat. Le climat du Pléistocène est généralement résumé en deux principales périodes : le « monde » pré-MPT à 41 ka, correspondant à la périodicité de l'obliquité, et le « monde » post-MPT à 100 ka, qui répond de manière non linéaire à la combinaison des forçages orbitaux. Mes résultats de doctorat suggèrent que l'impact du forçage d'obliquité est omniprésent dans le « monde » post-MPT, à l'échelle orbitale et sous-orbitale, sur (i) l'ampleur des variations du cycle du carbone à l'échelle centennale, (ii) la morphologie spécifique du MIS 7 et (iii) l'amplification des cycles climatiques post-MPT par sa fréquence à long terme.

Sur l'interaction entre les échelles temporelles et les périodes temporelles. Cette étude se limite au climat des 2 derniers millions d'années et, au sein de ce manuscrit, les différents chapitres sont axés sur des périodes temporelles spécifiques qui sont étudiées à différentes échelles de temps. Néanmoins, une interaction entre les différentes périodes et échelles temporelles considérées a été mise en évidence : (i) le MPT, bien qu'il survienne quelque part entre 1,2 et 0,8 Ma, est probablement influencé par une tendance graduelle à long terme dans le climat interne et doit donc être considéré dans le contexte global de l'établissement du climat du Pléistocène (Chapitre 3). (ii) Un parallèle entre la variabilité à l'échelle millénaire et les

terminaisons glaciaires a été établi (Chapitre 4). (iii) L'étude du MIS 7 a mis en évidence des motifs climatiques similaires avec les interglaciaires survenus avant le MPT (~1,6-1,2 Ma) (Chapitre 5). (iv) Le contexte orbital impacte directement l'amplitude des variations du cycle du carbone à l'échelle centennale, tandis que les variations centennales sont elles-mêmes induites par des événements à l'échelle millénaire (Chapitre 6). L'interaction entre les variations climatiques survenant à différentes échelles de temps apparaît ainsi comme une caractéristique majeure du climat du Pléistocène.

En conclusion, mes résultats ont mis en évidence deux principales caractéristiques des variations et des interactions entre le cycle du carbone et le climat pendant le Pléistocène :

- Une influence omniprésente du forçage orbital sur les variations climatiques et du cycle du carbone, indépendamment de l'échelle de temps considérée.
- Une interférence forte entre les processus agissant à différentes échelles de temps dans les interactions entre le cycle du carbone et le climat.